

*A theoretical model of vascularized tumors: simulation
of blood vessel network remodeling, interstitial fluid
flow and oxygenation*

Dissertation
zur Erlangung des Grades des Doktors der Naturwissenschaften
der Naturwissenschaftlich-Technischen Fakultät
der Universität des Saarlandes

von

Michael Welter

Saarbrücken
2015

Tag des Kolloquiums: 30. Nov. 2016

Dekan: Prof. Dr. Guido Kickelbick

Mitglieder des

Prüfungsausschusses: Prof. Dr. Romanus Dyczij-Edlinger
Prof. Dr. Heiko Rieger
Prof. Dr. Ludger Santen
Dr. Hendrik Hähl

Abstract

This thesis covers the development of a theoretical model of macroscopic vascularized tumor growth, the analysis of morphological characteristics, blood flow and tissue oxygenation in dependence on the vascular network in which the tumor grows, as well as an analysis of potential barriers to drug delivery caused by the transport characteristics of tumor blood vessel networks and tissue. An extended model is developed, incorporating processes of angiogenesis, vaso-dilation, vessel regression and collapse, for tumors embedded in artificial arterio-venous networks. It is predicted that substances dissolved in blood are rapidly conducted in maximal concentrations through most parts of the tumor network. Simulations of interstitial fluid flow and spatio-temporally variable drug concentrations showed that the local tumor vascular density predominantly determines the dose delivered and that non-diffusive substances may not reach all areas of tumors due to the heterogeneity of interstitial fluid flow. Moreover a new computational model to determine coupled intravascular and tissue oxygen concentrations was conceived which is applied to simulated tumor blood vessel networks guided by optical mammography data. Random differences of initial vessel layouts can accordingly explain the blood oxygen saturation fluctuations observed in tumors of a cohort of patients, to some degree. However other factors such as vessel compression need to be taken into account.

Zusammenfassung

Diese Arbeit umfasst die Entwicklung eines theoretischen Modells für makroskopisches vaskularisiertes Tumorwachstum, Untersuchung von morphologischen Kenngrößen, Blutfluss und Sauerstoffversorgung in Abhängigkeit des Gefäßnetzes in dem der Tumor wächst, sowie auch die Analyse von möglichen, durch Transporteigenschaften des Tumorblutgefäßnetzes und Gewebes verursachten Barrieren zur Medikamentablieferung. Ein erweitertes, die Prozesse Angiogenesis, Vasodilatation, Gefäßrückentwicklung, und Kollaps umfassendes Model wird für Tumore erarbeitet, die in künstlichen arterio-venösen Netzwerken wachsen. Es werden Modellvorhersagen getroffen, dass in Blut gelöste Substanzen schnell in maximaler Konzentration durch größte Teile des Tumornetzwerkes geleitet werden. Simulationen des Flusses von Gewebeflüssigkeit und raum-zeitlich veränderlichen Medikamentkonzentrationen zeigten, dass die abgelieferte Dosis maßgeblich von der lokalen Gefäßdichte bestimmt ist und dass nicht-diffundierende Substanzen aufgrund des interstitiellen Flüssigkeitsflusses i.A. nicht alle Bereiche eines Tumors erreichen können. Weiterhin wurde ein neues Rechenmodell zur Bestimmung von gekoppelten intravaskulären-und Gewebesauerstoffkonzentrationen entwickelt, welches geführt von optischen Mammographiedaten, auf simulierte Tumorblutgefäßnetzwerke angewand wird. Demzufolge können zufällige Unterschiede in der Anordnung der Anfangsvaskulatur die beobachteten Blutsauerstoffsättigungen in einer Schar von Patienten zu gewissem Grad erklären. Jedoch müssen andere Faktoren wie Gefäßkompression in Betracht gezogen werden.

Acknowledgements

First, i would like to thank Prof. Heiko Rieger who gave me the opportunity to work on this important topic. He was always open to questions and discussions and supervised my work. Secondly, i would like to thank our collaborators, Thierry Fredrich, Dr. Katalin Bartha and Prof. Herbert Rinneberg for contributing their expertise through stimulating discussions and suggestions. They also helped a lot with the work on our publications. In particular i learned a lot through the seemingly tireless work of Herbert Rinneberg. Special thanks goes to Dr. Marc Wagner who proofread this thesis all the way to the end. Moreover i also thank the Deutsche Forschungsgemeinschaft (DFG) for their financial support in the framework of the Graduiertenkolleg 1276 and the Sonderforschungsbereich 1027. Without it, my work would not have been possible. Finally, i thank my parents for their support.

Contents

Abstract	i
Zusammenfassung	ii
Acknowledgements	iii
Table of Contents	v
List of figures	vii
I Thesis	1
1 Introduction	1
1.1 Physics of cancer	1
1.2 Anatomy of cancer	1
1.3 The difficulty of cancer treatment	7
1.4 Goals of this thesis	11
2 State of the art research	12
2.1 Theoretical models of tissues	12
2.2 Theoretical models of blood vessel networks	15
2.3 A model of tumor induced angiogenesis and vascular remodeling	15
2.4 Computation of blood flow and hematocrit	17
2.5 Vascular networks of normal tissue	19
2.6 Time dependent intravascular tracer concentration	21
2.7 Interstitial fluid pressure	22
2.8 Transvascular fluid exchange	22
2.9 Oxygen transport	23
3 Summary of the publications that are part of this thesis	26
3.1 Emergent vascular network inhomogeneities and resulting blood flow patterns in a growing tumor	26
3.2 Vascular remodelling of an arterio-venous blood vessel network during solid tumour growth	28
3.3 Physical determinants of vascular network remodeling during tumor growth	30
3.4 Interstitial Fluid Flow and Drug Delivery in Vascularized Tumors: A Computational Model	32
3.5 Relation between tumor oxygenation, vascular remodeling and blood flow: A computational model with applications to breast cancer	34
4 Summarizing discussion	36
4.1 Tumor growth in vascularized tissues	36
4.2 Arterio-venous blood vessel networks	38
4.3 Intravascular drug conduction and blood flow	39
4.4 Interstitial fluid flow	40
4.5 Interstitial drug transport	40
4.6 Detailed model of oxygen distribution	41
4.7 Limitations and outlook	43
Bibliography	46
A Correlation of vascular density and blood pressure	56
II Papers	59

5	Emergent vascular network inhomogeneities and resulting blood flow patterns in a growing tumor	
6	Vascular remodelling of an arterio-venous blood vessel network during solid tumour growth	
7	Physical determinants of vascular network remodeling during tumor growth	
8	Interstitial Fluid Flow and Drug Delivery in Vascularized Tumors: A Computational Model	
8.1	Supplemental Information S1	
9	Relation between tumor oxygenation vascular remodeling and blood flow: A Compartment and computational model with applications to breast cancer	
9.1	S1 Oxygen Mass Transfer Coefficient	
9.2	S2 Explicit Formulas for Relevant Biophysical Quantities	
9.3	S3 Compartment Model	
9.4	S4 Regional Blood Volume of Confined Perfect Binary Trees	
9.5	S5 Blood Pressure Radius Relation	

III Demarcation from the work of the co-authors

List of Figures

1	Illustration of a capillary and the oxygen concentration distribution inside and around it	2
2	Experimentally measured oxygen partial pressures and pH	2
3	Depth-coded microscopy images of vascular networks	4
4	Histological sections of rat glioma brain tumors	5
5	Experimental morphological data of human melanoma in mouse models . . .	6
6	Illustration of interstitial fluid flow	8
7	Electron microscopy image of fibroblasts embedded in the extracellular matrix	8
8	Experimental distributions of drug in a histological section	10
9	Basic components of a theoretical model of vascularized tumor growth	10
10	Simulated tumor growth and vascular remodeling	14
11	Final simulated tumor and tumor blood vessel network	16
12	Representation of tumor blood vessel network and tissue domains	18
13	Blood vessel network construction by stochastic growth on a lattice	20
14	Oxygen transport and extravasation in a tube	24
15	Coupling of the numerical solution of intravascular oxygen distributions with tissue oxygen concentration	24
16	Reconstruction of a cranial blood vessel network from three-dimensional microscopy data	45
17	Reconstruction of a blood vessel network of a breast tumor	45
18	Tumor vascular density versus normalized average of the gradient magnitude	56
19	Distributions of local vascular density versus the normalized average of the gradient magnitude	57

Part I

Thesis

1 Introduction

1.1 Physics of cancer

"Physics of Cancer" has recently become a major interdisciplinary research field [see Ins08]. The reason is, even after decades of research, since the declaration of the "war against cancer" in 1971 in the US, cancer is a leading cause of death worldwide and is an ever-growing problem in the aging population. Altogether, average patient survival times have improved only little. However, some cancers have very high cure rates, when detected at an early stage, notably testicular cancer. In contrast, great progress has been made in the treatment of conditions of the heart and the circulatory system. At the surface, cancer is simple. Cells of the body mutate and start to proliferate uncontrolled. Eventually they migrate to distant parts of the body where they form secondary tumors. Tumors must have deep evolutionary roots since they occur naturally even in ancient, primitive, multi-cellular organisms [Dom+14]. Today, drug resistance and obstacles to delivery are still major challenges to overcome. Moreover there is no general theory of cancer with predictive power.

A growing tumor is in reality a complex entity which comprises many phenomena on different scales from biochemistry to the mechanics of macroscopic tissues. It is not merely a blob of cloned cells, but rather resembles a growing organ, for instance in its composition into different cell lines and in the interaction with its environment [ENW10]. There are other types of cancer than these so-called solid tumors, for example leukemia. But the latter is not the topic of this thesis. There are several hallmarks of cancer, one of them is Angiogenesis, the formation of new blood vessels, which helps to fuel tumor growth with additional nutrients [HW11]. As we will see, angiogenesis, and other processes, give rise to tumor blood vessel networks which are abnormally chaotic and spatially heterogeneous, and therefore inadequate to supply the entire tumor, leading to the emergence of hypoxia (lack of oxygen) and necrosis. Unfortunately, drugs are normally supplied through these networks, too. Moreover, hypoxia is detrimental for several reasons. It impedes the efficacy of radiation therapy and drugs, and promotes tumor invasiveness, to name a few issues encountered in clinical treatment.

Physics comes into play where transport and growth processes are considered. For example a growing tumor spheroid can be described by partial differential equations or particle models for tumor cell population distributions and for various other components which evolve in time according to forces and growth terms present in the system. Blood vessel networks are commonly represented by one-dimensional network models and often include computation of blood flow according to the analogy of Kirchhoff's laws. They are essential building blocks of mathematical models, acting as sources and drains of substances. Transport through tissue, can be described by diffusion-advection-reaction equations for concentration distributions of drugs, oxygen or other substances. Hence, many phenomena relevant to tumor growth are physical in nature and can be analyzed with mathematical theoretical models. See also the Refs. [Tra09; Low+10; SBP13; RW15] for reviews of recent work.

1.2 Anatomy of cancer

A solid tumor typically starts off as an avascular multicellular spheroid, i.e. it is a blob of tumor cells with no blood vessels in it. Its growth starts, when cells undergo mutations disabling their regulatory circuits for proliferation and apoptosis (programmed cell death). Such cells are in principle able to divide infinite number of times. After an initial phase of exponential growth, the radius of the spheroid continues to grow linearly [Bru+03; DH05] since proliferation of tumor cells (TCs) is restricted to a few cell layers behind the tumor-tissue interface. Also vascularized tumors show this linear growth regime [Döm+02; Hol+99]. TCs

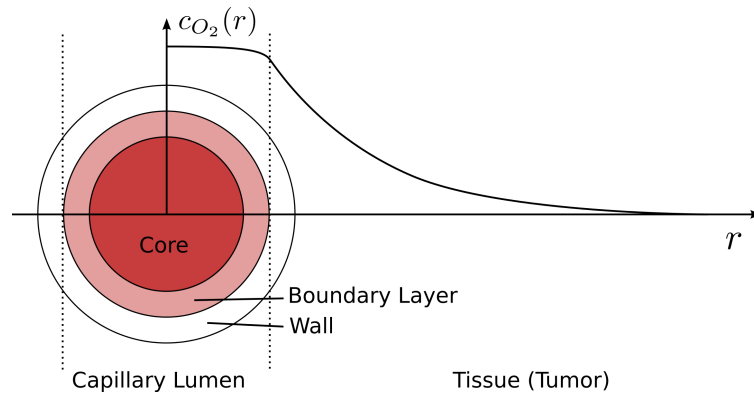


Figure 1. Illustration of a capillary and the oxygen concentration distribution inside and around it: Extravasation of oxygen and other solutes is driven by radial concentration gradients. The left hand side shows a schematic cross section of a capillary lumen extending to the right into a section of surrounding tissue. Blood flow develops a core rich of red blood cells (RBCs) where most of the oxygen is carried. The boundary layer between core and vessel wall is free of RBCs. In our model, the vessel wall is treated as part of the tissue, i.e. it is not explicitly represented. However the rate of oxygen consumption in arterial walls has been subject of controversy [Pit11]. Oxygen diffuses through those compartment including RBCs where it is also bound to hemoglobin. In tissue, oxygen is consumed with rate $M(P)$, where P is its partial pressure (PO₂). Near isolated vessels, oxygen consumption leads to an approximately exponential decay of the concentration curve $c_{O_2}(r)$. In tumors, the distance, where c_{O_2} reaches practically zero, denoted diffusion distance, is ca. $100\mu m$ [CJ00]. Beyond this, tissue becomes necrotic due to hypoxia. Under physiological conditions, the spacing between blood vessels is less than the (tissue specific) diffusion distance such that a sufficiently high oxygen concentration is present everywhere. The depicted oxygen concentration curve $c_{O_2}(r)$ was drawn for illustration, following theoretical calculations [MEG11]. The rather weak intravascular concentration gradient justifies the approximation that intravascular oxygen concentration is assumed constant in the radial direction, and therefore only depending on the longitudinal position on the vessel axis.

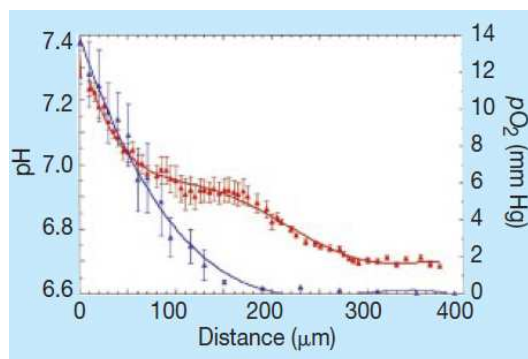


Figure 2. Experimentally measured oxygen partial pressures and pH: Partial pressure (pO_2 ; blue curve) and pH (red) were measured in human tumor xenografts and plotted versus distance to the nearest blood vessels [Hel+97]. Tumor cells further away than the diffusion distance of oxygen of ca. $100\mu m$ become hypoxic. Tumor cells survive under such low oxygen conditions by switching to glycolytic metabolism, the byproducts of which lower the pH to acidic levels [HW11]. (Reprinted from [CJ00] with permission. Copyright 2000 Macmillan Magazines Ltd.)

within the tumor interior either enter a quiescent state due to nutrient and space restrictions or die off (necrosis). Thus a necrotic core develops, and an equilibrium between proliferation and death is established, limiting the size of the spheroid to approximately 1 mm^3 . In the following we consider only oxygen as representative of nutrients although it is not the only one. For instance, TCs need glucose as well, but the limitation to oxygen-only is a common approximation for theoretical models. Not all tumors start as avascular spheres though. Some types, e.g. glioma brain tumors and breast tumors, incorporate (coopt) the blood vessel network of the host at the beginning of growth [HWY99; RCR09]. It was indeed shown that TCs preferably proliferate around blood vessels, apparently while displacing or destroying normal tissue [Döm+07]. The ability to metastasize may develop at a later point in time.

Normally, maintenance of the vasculature depends on a balance of pro- and antiangiogenic factors such as blood flow and metabolic demand, mediated by complex biochemical signaling networks not yet fully understood. This system adapts the microvascular density (MVD) to the nutrient demand of tissue and regulates development of blood vessels into arteries, capillaries and veins for an efficient blood flow. The walls of capillaries consist of endothelial cells (ECs). Arterioles that connect capillaries to arteries, get progressively thicker with additional cell layers composed of pericytes, smooth muscle cells and other components. Venules also exhibit supporting cell layers which are however thinner than on arterioles [MH13]. Capillaries, where most of the substance exchange occurs, must be homogeneously distributed since the range of diffusion of nutrients is limited. Oxygen for instance is a very light molecule and thus distributes quickly by diffusion, but it is also bound and consumed in cells which leads to an approximately exponential decay of the concentration around blood vessels (s. Figs. 1 and 2). The typical diffusion range within tumors is approximately $100 \mu\text{m}$ [CJ00] which is also the distance from blood vessels up to which TCs can remain viable. The diffusion range in normal tissues lies between $50 \mu\text{m}$ (brain) and $150 \mu\text{m}$ (breast). In tumors, the angiogenic balance is disrupted, resulting in the transformation of the original vasculature into a heterogeneous chaotic network (see below). Three processes which normally act together but are spatially separated in tumors take part in this transformation: sprouting of new vessels (angiogenesis), circumferential growth and vessel regression.

In general, tumor growth is hampered by the lack of oxygen, be it due to vessel regression, increased metabolic demand, or the start as avascular sphere. But eventually TCs switch to a phenotype that induces angiogenesis. The resulting increase of vascular density allows further growth. Induction of angiogenesis depends on the release of compounds known as growthfactors (GFs) which are essential mediator molecules of angiogenic signals. VEGF is a well-known major player [CJ00; MC03; CJ11; Log+14]. GFs are generally produced under lack of oxygen (hypoxia) and diffuse through tissue where they are bound and degraded. This leads to a finite range of the angiogenic signal amounting to several $100 \mu\text{m}$ [Döm+02; Hol+99]. Various GFs have different purposes. In angiogenesis, they loosen the cell layers of vascular walls, and stimulate ECs to proliferate and to migrate away from their parent vessel. ECs follow GF gradients to the source of GF (chemotaxis) trailed by more ECs that form a new sprout [NHH98; Ger+03; SM11]. If the tip encounters another vessel it will fuse with it and mature into a perfused capillary. Otherwise the sprout retracts after some time. Neovasculature as well as preexisting vessels are coopted when the tumor grows past them. Other modes of vascularization such as branch splitting (intussusception) [BHD04] or assembly of capillaries from free moving ECs (vasculogenesis) [TAP06] play a lesser role in tumor growth. However, sprouting takes place mostly uncontrolled, resulting in dense chaotic vascular excrescence, that is often dysfunctional. Some evidence suggest that it can be even detrimental to growth [SH07].

A few $100 \mu\text{m}$ into the tumor interior, angiogenesis stops and endothelial cells switch to circumferential growth leading to vaso-dilation. Tumor vessels of Melanoma and Glioma tend to dilate to a maximum of ca. $25 \mu\text{m}$ radius but no further. Moreover, vessels undergo a period of regression until eventual collapse of the lumen and pinch off of blood flow [Döm+02; HWY99]. Only few dilated vessels survive this thinning process, leading to a very sparse network of isolated vessels. Viable TCs remain as cuffs around these vessels. Be-

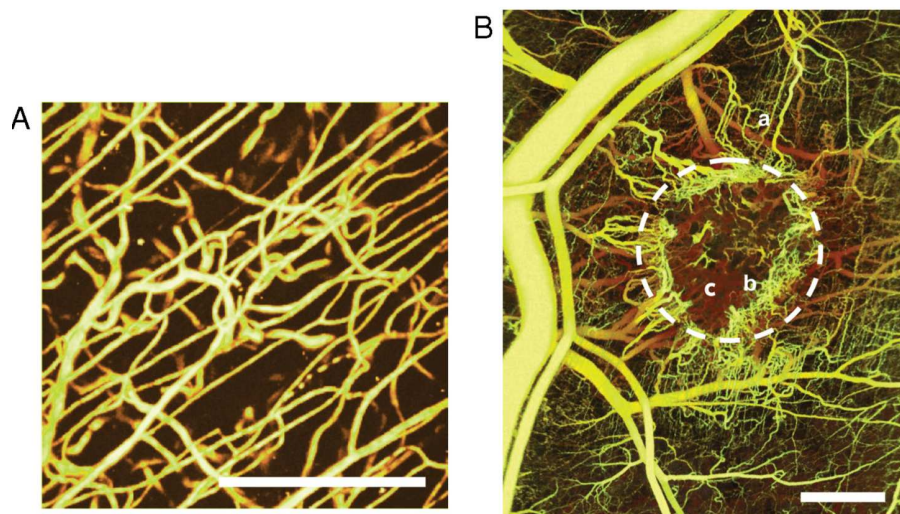


Figure 3. Depth-coded microscopy images of vascular networks: (A) A normal capillary network with some supplying and draining arterioles and venules, respectively. Capillaries appear as thin straight segments, which is typical, for instance, for muscle tissue (Scale bar = $100 \mu m$). (B) Blood vessel network in a mammary carcinoma bearing mouse (tumor location indicated by dashed circle). Vascular remodeling is apparent in proximity of the tumor. Numerous dilated, tortuous vessels proceed from a few parent vessels toward the tumor (a). The tumor rim is densely and chaotically vascularized due to excessive branching. The vascular density drops dramatically into the tumor, leaving large regions void of vessels (c, b; scale bar = $1 mm$). (Reprinted from [Bai+11] with permission. Copyright 2011 James W. Baish et al.)

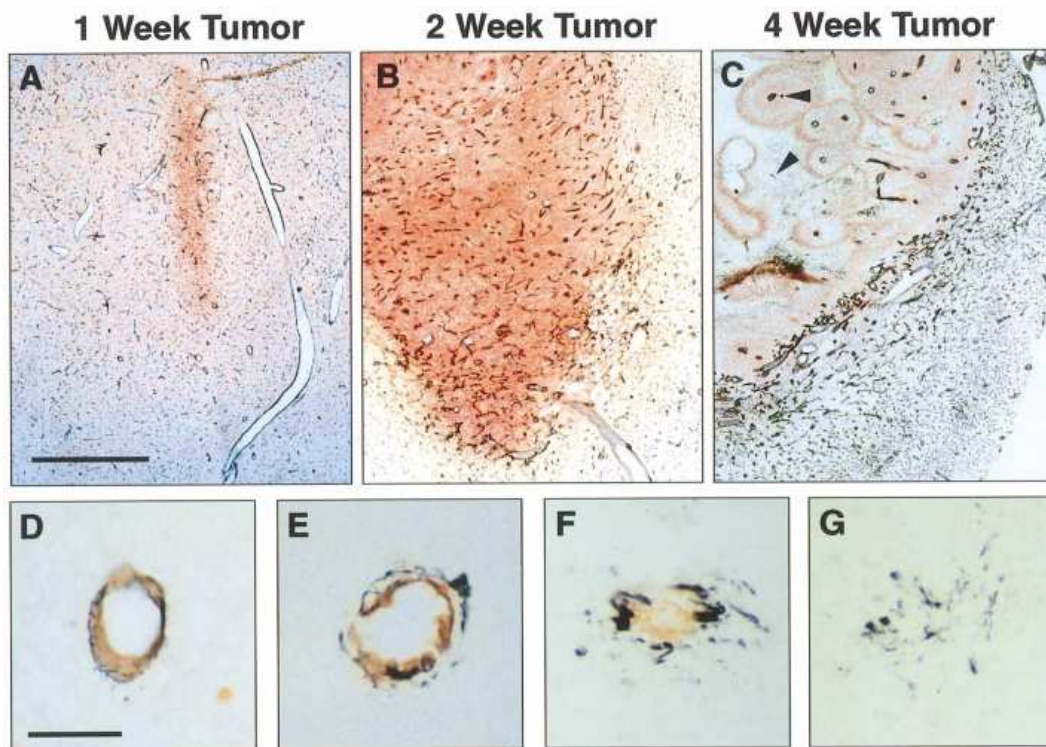


Figure 4. Histological sections of rat glioma brain tumors: (A-C) depict the progression of a tumor (viable tumor cells stained red; endothelial cells stained black; scale bar = 1 mm). Small 1-week tumors exhibit normal appearing blood vessels. After two weeks, decreased density and vaso-dilation are visible. In 4-week tumors, vessels are mostly isolated and have cuffs of viable tumor cells around them. Distal regions are necrotic. The tumor rim is densely vascularized. (D-G) depicts regression of a blood vessel with detachment of pericytes and smooth muscle cells (black) from the vessel wall (brown). (Scale bar = 50 μm ; Reprinted from [HWY99] with permission. Copyright 2005 American Association for the Advancement of Science)

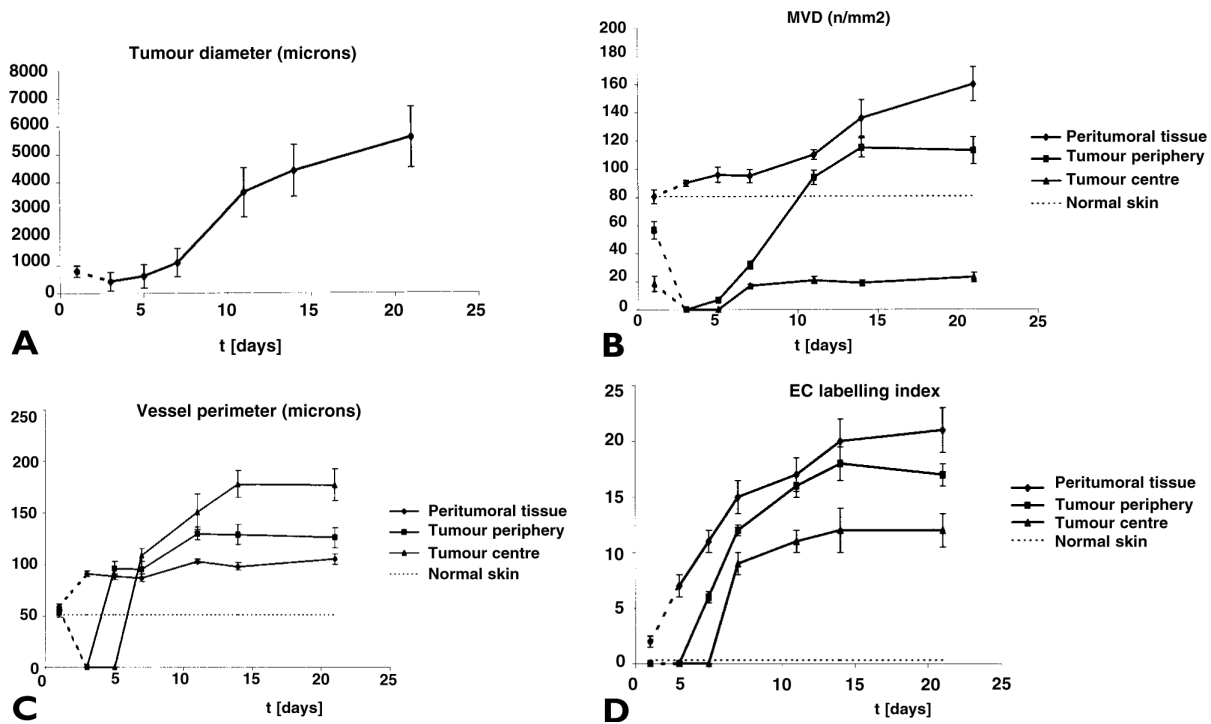


Figure 5. Experimental morphological data of human melanoma in mouse models:

The vessel network development was followed during tumor growth from an intradermal inoculation of 10^4 tumor cells until the tumor reached 4 – 5 mm in diameter. At day 10, tumor growth transitions to a linear regime, consistent with the confinement of proliferative activity to an annular shell behind the invasive edge (A). (B-D) display data for different regions: Tumor center; the tumor periphery - a 100 μm wide band of tumor immediately adjacent to the invasive edge; peritumoral tissue - a 200 μm wide band of host connective tissue immediately adjacent to the tumor periphery. After 15 days, MVD (B) and Vessel perimeters (C) assume plateau values. Vessels are generally abnormally dilated, and the MVD is high near the invasive edge whereas it stays low in the tumor center. The tumor coopts the dense peripheral vasculature and subsequently dilutes it. Thus the activity of vascular remodeling moves with the invasive edge. EC labeling index (D) is essentially the percentage of proliferating endothelial cells (ECs), i.e. the plot indicates angiogenic activity all across the tumor and beyond. (Reprinted from [Döm+02] with permission. Copyright 2002 John Wiley & Sons, Ltd)

yond the diffusion range of oxygen, TCs die of hypoxia, whereupon large necrotic regions emerge in the tumor interior. The details of the regulatory systems that lead to such malfunctioning are still not well understood. But it is known that GFs are continued to be produced (expressed) in TCs of the tumor interior, which, as aforementioned, can destabilize vessels, but also promote ECs survival. The switch from angiogenesis to circumferential growth is mediated by the ephB4 guidance molecule [Erb+06] and depends on the sensed direction of the GF concentration gradient [SM11]. Blood flow is crucial for vessel survival and maturation, where Angiopoietins (Ang-1/2) among others act as regulatory molecules [Goe+08; Buc+14]. They are expressed by ECs which react to the shear stress which is exerted by the blood flow on the vessel wall [AY13]. Ang-2, a negative regulator, promoting regression, is frequently overexpressed in tumors [HWY99]. Thus, a normal blood vessel network is progressively transformed into a tumor specific vasculature by the angiogenic activity at the tumor edge.

The result is a compartmentalization into a ca. $200 \mu m$ wide band around the periphery where the MVD is elevated. The MVD decreases from there sharply into the tumor interior where the vasculature is approximately only half as dense than in normal tissue [Hol+99; Döm+02]. Tumor vessels are generally tortuous, chaotically connected and dilated. Images of experimental tumors are reprinted in Figs. 3 and 4. Quantitative morphological data from [Döm+02] is reprinted in Fig. 5.

Tumor vessels are also leaky, i.e. huge gaps are present in their walls due to missing ECs [CJ00]. Through these leaks, blood plasma can easily escape into intercellular spaces. The liquid that normally fills these spaces is called interstitial fluid (s. Figs. 6 and 7). Normally, only a small amount of blood plasma leaks through nanometer sized gaps between ECs whereupon it becomes part of the interstitial fluid (IF). IF is absorbed into lymphatic channels which eventually feed the liquid back into the blood stream. In tumors, the permeability of the vessel walls is increased by two orders of magnitude [JTM07] since missing ECs leave holes of the size of micrometers. Moreover, tumors often lack lymphatic vessels, although they can induce lymphangiogenesis similar to regular angiogenesis and can metastasize through lymphatics in the tumor periphery [TA10]. The lack of lymphatics and the hyperpermeability leads to the phenomenon of elevated interstitial fluid pressure (IFP), i.e. the hydrostatic pressure of the liquid is elevated to the level of vessels [SL12]. The IFP in the tumor interior is relatively homogeneous at levels between $10 - 40 mmHg$. Across the tumor boundary it drops down to the level in normal tissue where the IFP is zero in good approximation. The interstitial fluid flows through tissue like water or oil flows through a porous medium, e.g. through rock. In tissues, cells and ECM assume the role of the medium. Consequently, IF flows predominantly in the radial direction out of the tumor spheroid, with measured velocities between 0.1 to $0.2 \mu m/s$ near the boundary of a $1 cm$ sized tumor [Jai87]. This can drive TCs into the surrounding lymphatics and move drug out of the tumor (see below).

1.3 The difficulty of cancer treatment

This section reviews biophysically relevant obstacles to treatment, most of which are founded in the peculiarities of tumor blood vessel networks. In tumors, an efficient delivery of drugs is not guaranteed, as it is in normal tissue with a normal vasculature. However, current cancer-killing drugs have poor selectivity, i.e. they are toxic to normal cells, too. Therefore, it is not possible to simply increase the dose to compensate for inadequacies of the vasculature. Traditionally, the efficacy of drugs is analyzed using cell monolayers. Thus their performance in patients is often overestimated. It is imperative that cancer therapies ideally kill every single tumor cell because even a few surviving tumor cells can grow a new tumor or metastases [see the review MT06].

At the time of diagnosis and prognosis, the MVD is used as an indicator of malignancy and tumor progression. Authoritative for further actions is the local MVD in areas where the MVD is highest, so called hot spots [Döm+02]. This mandates a solid understanding of tumor vascular network formation.

The reasons for poor drug delivery are severalfold. Since the vasculature in the tumor

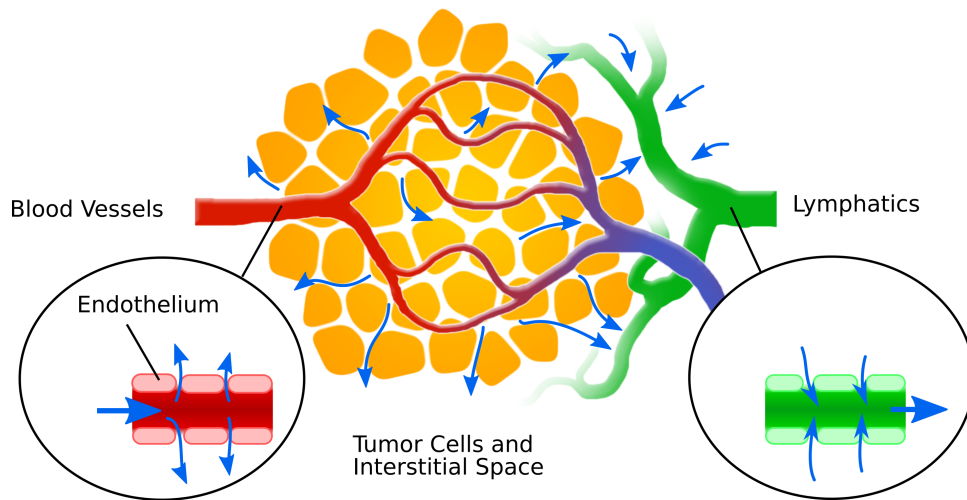


Figure 6. Illustration of interstitial fluid flow: Interstitial fluid (IF) is the liquid in which tissue cells bath [MH13]. It is derived from blood, i.e. it escapes through gaps in-between endothelial cells, which line the lumen of blood vessels, into extracellular space (left). IF contains various signaling substances, nutrients and waste products which are exchanged with tissue cells. Extracellular spaces are not only filled with IF but also contain adhesion molecules and a network of fibers composed of various proteins such as collagen and elastin. Together these three components are denoted extracellular matrix. Pores and fibers pose a resistance to the flow of the IF akin to the flow of water or oil through a porous rock. IF is absorbed into lymphatic channels (right) from where it is brought back into the blood stream. In normal tissue, a large resistance to transvascular flow leads to a large drop of the hydrostatic pressure across the vessel wall, so that the interstitial fluid pressure (IFP) approximately assumes the reference value of zero purported by the lymphatic system. In tumors (yellow), the interstitial fluid flow (IFF) is altered dramatically due to extremely large gaps in vascular walls and lack of functional lymphatics [Hel+04]. Consequently, the IFP is pulled up to the level of the blood pressure. 0 to 94 *mmHg* were measured in human tumors [JTM07]. Concomitantly, IF flows from the tumor center across the tumor interface until it is completely absorbed by lymphatics in normal tissue. This facilitates metastasation into lymphatics, and is likely detrimental to drug delivery. [Hel+04].

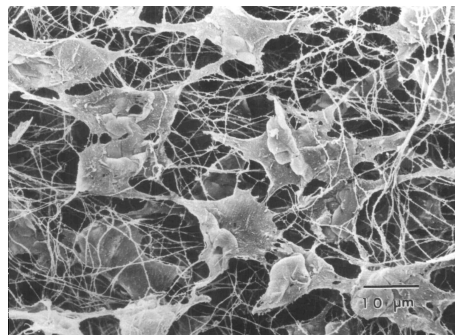


Figure 7. Electron microscopy image of fibroblasts embedded in the extracellular matrix: Fibroblasts are responsible for production of extracellular matrix constituents such as collagen fibers. Empty spaces are filled with the interstitial fluid. Functional tissues (or tumors) would contain other, specialized, cell lines (or tumor cells) as well. (Scale bar = 10 μm ; Reprinted from [Nis+88] with permission. Copyright Association for Research in Vision and Optalmology)

center is very sparse, the efficacy of drugs depends on the ability to penetrate tissue well. However this is often not the case. Instead, strong drug concentration gradients emerge around blood vessels, and persist over long periods of time [Pri+05] (s. Fig. 8). Most drug molecules are diffusive but still the flow of the IF might additionally impede their distribution by washout of drug into the surrounding normal tissue. Washout is likely a bigger issue for nano-scale particles which have much lower diffusion coefficient due to their mass [BJ89]. Finally low blood flow rates and excessive extravasation might lead to premature release of all drug before adequate concentrations can reach all parts of a tumor. In particular, compression of blood vessels can cause impairment of blood flow. This is now regarded as therapeutic opportunity [Jai14]. Solid components of the tumor push each other due space limitations and thus give rise to the so-called solid pressure which also acts on blood vessels. The fibers of the ECM transmit these forces, and it was shown that a reduction of the amount of fibers can increase blood flow [Cha+13; Sty+12; Cha+14]. There is also some evidence that elevated IFP aids in the compression of vessels [Gri+99; Del+14]. The discovery of tumor induced angiogenesis [Fol71], and VEGF, sparked the development of a new type of treatment in which the vasculature is targeted with angiogenesis suppressing agents to deprive the tumor of nutrients. This is a so-called anti-angiogenic therapy, today often used concomitantly to other measures, such as chemotherapy. A recent concept is "vascular normalization", where a balance between excessive pruning and a reduction of angiogenic activity is to be effectuated in order to reduce leakiness and thus improve blood flow [Jai13]. However the underlying mechanisms are still poorly understood. What works for one kind of tumor can have an adverse effect in another type of tumor [MT06].

Moreover, the success of ordinary therapeutic strategies is tied to the oxygenation status of the tumor. For instance, some chemotherapeutics work poorly in oxygen deprived environments due the chemical reactions involved. Other drugs can only kill cycling (proliferating) cells and are therefore uneffective against tumor cells (TCs) which are quiescent which can be caused by hypoxia or high solid pressure. Hypoxic TCs are also resistant to radiation therapy since oxygen is required so that ionizing radiation can produce DNA damaging compounds [KR15]. Hypoxia also promotes invasive growth, i.e. the tendency and ability of TCs to migrate increases, which can lead to the penetration of barriers between different organs and the growth of fingering protrusions of the tumor spheroid [Pen+03]. Hence, hypoxia is generally associated with poor prognosis [BW04; Har02].

It is possible to obtain important tumor characteristic data such as perfusion, blood volume and hypoxia status from patients using positron emission tomography (PET) and other imaging methods. However the interpretation of raw sensor data requires theoretical models. Moreover the resolution of current methods is limited to a voxel size of ca. 1 mm^3 . On the other hand, microscopic information are hardly accessible experimentally. Direct measurement of oxygen partial pressure PO_2 is performed by invasive probes, making it impractical to obtain a large enough sample size for heterogeneous environments like tumors. Worse, invasive probes can distort the true values [TJI03]. Interstitial fluid flow velocities are measured by invasive microscopy [Jai99]. Concentration distributions of drugs were measured by microscopy of dissected tumorous tissue [Pri+05], exploiting auto-fluorescence. In this regard theoretical models and computer simulation can provide insight into the tumor micro environment in order to foster the understanding of macroscopic phenomena and therapy failures.

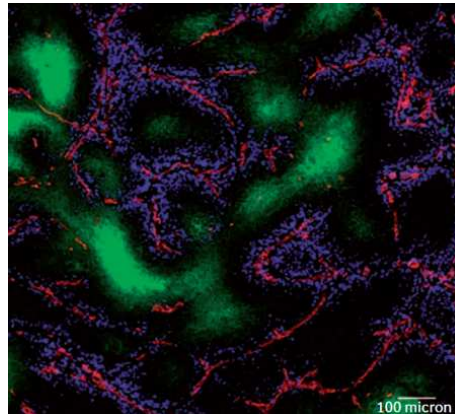


Figure 8. Experimental distributions of drug in a histological section: A microscopy image was taken from a section of tumor tissue of a tumor bearing mouse that received a dose of Doxorubicin, an ordinary chemotherapeutic, 180 minutes prior to excision. The color value of blue is proportional to the Doxorubicin concentration. Endothelial cells of the vessel walls are stained red, viable tumor cells are stained black and necrotic tissue is green. Concentration gradients changed minimally from 5 minutes up to three hours after the injection. (Scale bar = 100 μm ; reprinted from [Pri+05] with permission. Copyright 2005 American Association for Cancer Research)

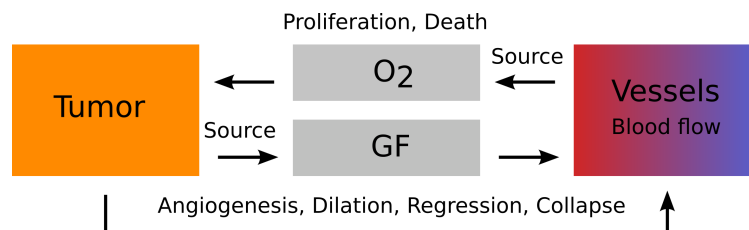


Figure 9. Basic components of a theoretical model of vascularized tumor growth: Following [BR06], tumor and vascular network interact via concentration distributions of growth-factors (GF) and oxygen (O₂), where tumor cells are sources of GF and the vascular network is the source of O₂. Blood flow is (re)computed after alterations of the vascular network to reflect the changes in blood pressure, flow rates and shear stresses. The dynamical interactions used in our model are described in detail in [WR13, Suppl.1, Fig.1] (s. reprint in Sec. 8.1). Briefly, tumor cells can proliferate in response to a sufficient O₂ supply, and will die to O₂ deprivation. GF either stimulates growth of new vascular sprouts (angiogenesis) or causes vascular dilatation, depending on if the vessel is located within the tumor or outside. Furthermore, low shear stress on vessel walls (low blood flow) leads to regression and collapse. In general, the tumor mass can be represented in various ways, i.e. discrete particles or continuous density distributions governed by partial differential equations. The vasculature is represented by a graph, or network model. However some other work incorporates it as continuous vessel density distribution, in which case a model of blood flow has to be omitted or severely simplified. Interactions, as described, are sufficient to predict realistic vascular morphologies of melanoma and glioma tumors.

1.4 Goals of this thesis

While the ultimate goal would be the construction of a predictive patient specific simulation of tumor growth and treatment, the focus of this work is to elucidate fundamental relationships between tumor vascular morphology, processes of tumor vascular remodeling, vasculature of the host, blood flow, adequacy of drug transport and oxygenation. Extending upon the work of Bartha, Lee, and Rieger [BR06; LRB06] (s. Fig. 9) this thesis covers, over a series of four papers [WBR08; WBR09; WR10; WR13], the development of a theoretical model of three-dimensional tumor growth within an artificial arterio-venous network on macroscopic scales. The focus of [WR13] is interstitial fluid flow and drug delivery, and in a fifth paper we considered tumor oxygenation exclusively [Wel+15].

We abolished oversimplifications of blood flow and oxygen concentration computations. Moreover, we analyzed the dependence of MVD and fractal dimension d_f on parameters for vessel regression [WBR08]. The restriction to pure capillary networks was a serious limitation of our work and other theoretical models of tumor growth. Therein, initial capillary segments of the host are laid out in regular square or hexagonal patterns. It is hardly possible to emulate realistic blood flow conditions on macroscopic scales in such a network. If, for instance, a homogeneous blood pressure gradient is imposed on the boundary then artifacts arise where tumor blood vessels clearly follow preferred directions imposed by the global flow. In reality, the capillary plexus is however supplied and drained by adjacent arterioles and venules. Therefore, we considered a vascular tumor growth model augmented with an artificial algorithmically constructed arterio-venous initial network of normal tissue in two dimensions [WBR09]. Original predictions of Refs. [BR06; LRB06] of vascular morphology had to be confirmed with this supposedly more faithful model. In [WR10] we laid the foundation allowing us to simulate macroscopic (ca. 0.5 mm^3) systems in three dimensions. A continuum model of the tumor spheroid [WR13] was implemented which may be used in future to study morphological growth instabilities which are exhibit by highly invasive tumors.

During this work, we realized that the predicted spatial distribution of tumor vessels depends strongly on the layout of initial ($t = 0$) vascular trees in which the tumor grows. Therefore, this thesis also touches the inverse problem, i.e. how initial networks must look like to obtain agreement with experimental data, such as blood oxygen saturations obtained from mammography. For this purpose, we generated various initial network configurations and determined biophysical quantities in dependence thereof [Wel+15]. Moreover we attempted to develop a means to predict the emergence of cluster of locally increased MVD (vascular hot-spots) by correlation with blood pressure differences within the initial networks (s. Appendix A).

In regard of the tortuous and chaotic nature of the tumor vasculature it is questionable if blood flow can distribute drug sufficiently within a reasonable period of time. Indeed, extremely low blood flow velocities of 0.1 mm/s were observed in animal models [JS10]. Therefore, we considered the flow of an intravascular tracer substance through final computed tumor vascular networks using a time dependent simulation of concentration distributions [WBR08; WBR09; WR10]. This allows to gauge the performance of conduction of drugs in vascular networks that are more realistic for actual patients, than in networks considered previously. The question for barriers to drug delivery is considered further in Ref. [WR13], where we performed simulations of interstitial fluid flow and spatio-temporal drug concentration distributions in tissue. It is often assumed that elevated IFP is a barrier to drug delivery since the extravasated flux density per vessel surface area is proportional to the hydrostatic pressure difference across vessel walls. However this cannot be the root cause of bad drug performance since the system behaves essentially like a series of resistors of which one resistor (tumor blood vessel walls) has particularly low resistance. Therefore other possible barriers to drug delivery are considered and targets for therapeutic strategies are explored.

In previous work, extremely good perfusion of tumor vessels was predicted, guided by data for Melanoma and Glioma. Under conditions of low blood flow however, consideration of spatially varying intravascular levels of oxygen and other substances is required because a substantial fraction may be lost during the transit through the tumor vasculature. This is

addressed in our fifth paper [Wel+15], using a new computational model of coupled intravascular and tissue oxygen concentrations. It is applied to elucidate the statistical distribution of average oxygen saturations in simulated tumors, guided by breast cancer. Grosenick et al. [Gro+05] and others [Spi+05; Tar+05] obtained such data from a cohort of patients using optical mammography. It exists the prospect of being able to deduce aspects of vascular morphology and blood flow based on such indirect measurements. However, this requires adequate predictive models.

2 State of the art research

This section will briefly review the basic theory and modeling approaches of mathematical models of tumor growth.

2.1 Theoretical models of tissues

There are two approaches to describe tissues. In continuum mechanics conservation equations are formulated for mass, momentum and sometimes energy, and on the other hand, in particle methods, particles represent either cells or macroscopic sections of tissue and move according to Newtons equations of motion. Fluids and deformable bodies are described in this way, too. But for living tissues, addition and removal of mass and momentum due to growth and death needs to be taken into account. The simplest form of mass conservation to satisfy this is the partial differential equation (PDE)

$$\frac{d\rho}{dt} = -\rho\nabla\mathbf{u} + \alpha, \quad (1)$$

where $\rho = \rho(\mathbf{x}, t)$ is the density depending on space and time, $d\rho/dt$ is total derivative in time which can be expanded into $d\rho/dt = \partial\rho/\partial t + \mathbf{u}\nabla\rho$, ∇ is the Nabla operator, \mathbf{u} is the local velocity, and α embodies local sources and drains. The general form of momentum equations is

$$\frac{d(\rho\mathbf{u})}{dt} = \nabla \cdot \boldsymbol{\sigma} + \mathbf{f}, \quad (2)$$

where $\boldsymbol{\sigma}$ is the Cauchy stress tensor and \mathbf{f} is the total body force, accounting for gravity for instance. In reality, biological tissues are highly complex materials [Ver+09, see the review]. On short time scales, they show elastic behavior which is usually neglected in models of tumor growth. On long time scales, i.e. days, residual stresses are relaxed by rearrangement of ECM fibers and cell adhesion molecules, leading to viscous behavior. Moreover, cells show active responses to stimuli, e.g. migratory behavior. In practice, growing tumors are therefore modeled like (viscous) liquids, including an isotropic (solid) pressure, friction, and adhesion forces. Inertial forces are conveniently neglected since biological growth and migrations happens in a regime of very low Reynolds numbers ($Re \ll 1$). Conservation of energy is in general not considered, assuming a constant temperature and equations of state oblivious to the inner energy. The growth of multicellular spheroids [AM04; APS06; Amb+11; Cia+13; Vol06] and tumors in general [ZWC05; Swa+11; PT09] was described using continuum models of a single homogeneous material.

Current state of the art are multi-phase or mixture models where total mass, momentum and stress, are given as summations over contributions from cells of different types, ECM and water. All of these phases are allowed to coexist in space, where their relative amount within the unit volume is given by respective volume fractions. The motion of the cell population is often modeled analogous to fluid flow through a porous medium, where the ECM takes the role of the medium. The “flow” thus represents migratory motion in response to solid pressure. Depending on the choice of components and their stress tensors, mixture models describe various growth phenomena, and indeed found numerous applications to study avascular [BP03; ML07; AP09; Wis+08; Cia+13; Sci+13] and vascular tumor growth

[BBL03; CGP06; Sta+07; Mac+09; HB13]. It is relatively straight forward to implement cell-cell adhesion, modeled by effective surface tension forces to study growth induced morphological instabilities of the interface between cell populations. Such instabilities can occur because either protruding perturbations have better access to nutrients than recessions, facilitating the growth of the perturbation, or as viscous instabilities akin to a less viscous fluid injected into a more viscous fluid. The result is the growth of finger-like protrusions. Following [PT09] we implemented a simple mixture model [WR13] with the intent to study such instabilities. But it is still topic for future work.

Dissolved substances like oxygen, GFs, or drugs are an essential component of many tumor growth models. In case of drugs or oxygen, their concentration distributions may be the entire subject of study, for instance in our papers [WR13] and [Wel+15]. The simplest general equation to describe the transport of the concentration $c(x, t)$ of one species is the diffusion-advection-reaction equation

$$\frac{\partial c}{\partial t} + \nabla \cdot (c\mathbf{u}) = \nabla \cdot (D\nabla c) + R, \quad (3)$$

where the substance diffuses with diffusion constant D and is carried with the flow of the solute with velocity \mathbf{u} . The reaction term R can comprise sources and drains, e.g. vessels are sources of oxygen whereas tissue consumption is represented by a homogeneous drain distribution. In multi-components system, each component i is associated with the concentration c_i each of which is governed by an equation of type (3) [PT09]. Then R (or rather R_i) also comprise transition rates between compartments. This way, drug binding to different intracellular compartments was described in simulations of drug concentrations in tumors [Sin+09]. The advection term in calculations of oxygen distributions is usually neglected since oxygen transport is dominated by diffusion due to its low molecular weight. Moreover, it is sufficient to consider quasi stationary distributions where $\partial c/\partial t = 0$ since equilibration times are much shorter than growth processes in tissues [BR06]. Thus we obtain

$$0 = D\nabla^2 c + R, \quad (4)$$

assuming equal concentration c in all compartments and a constant oxygen diffusion coefficient D . Such partial PDEs can only be solved analytically in special cases. In general, the equations are solved numerically with the help of finite difference (FD) or finite element methods (FEM) or some variation thereof. In both methods, space is divided into numerical cells defined by regular grids or unstructured meshes. In FD methods, the solution is approximated by function values at discrete grid points and derivative operators of the original equations are replaced by differences between functions values on neighboring grid points. In FEM, an approximate solution is computed in a finite dimensional function space over the considered domain. FEM have the advantage that they can be applied straight forwardly to unstructured meshes and therefore work well for arbitrary domain shapes. FD methods are much easier to implement on regular grids and arguably more efficient. We and many other authors consider tumor growth in square (cubic) domains, hence FD formulations are used. The application of difference operators leads to systems of linear or non-linear equations in the solution values at grid points. The core of numerical solutions consists often of routines for the inversion of sparse matrices. Such routines comprise specialized factorization methods, multi-grid, or Fourier transformation. See e.g. the nice book [LeV07] for an introduction to FD methods.

In particle based models matter is described from a frame of reference that moves with a given initial piece of material. Such a piece of material is represented by a particle with a given position, velocity and various other associated quantities. The collection of thousands to millions of particles thus describes the entire body. This is the traditional approach in fluid dynamics. In biological applications, the particle count is not conserved in general. Instead particles are allowed to replicate or vanish to reflect growth and regression of real tissues. In microscopic systems, particles can be conveniently identified with individual cells. Otherwise particles can represent macroscopic volumes as it is the case in dissipative particle dynamics. The time dynamics can be described simply by Newtons equation of

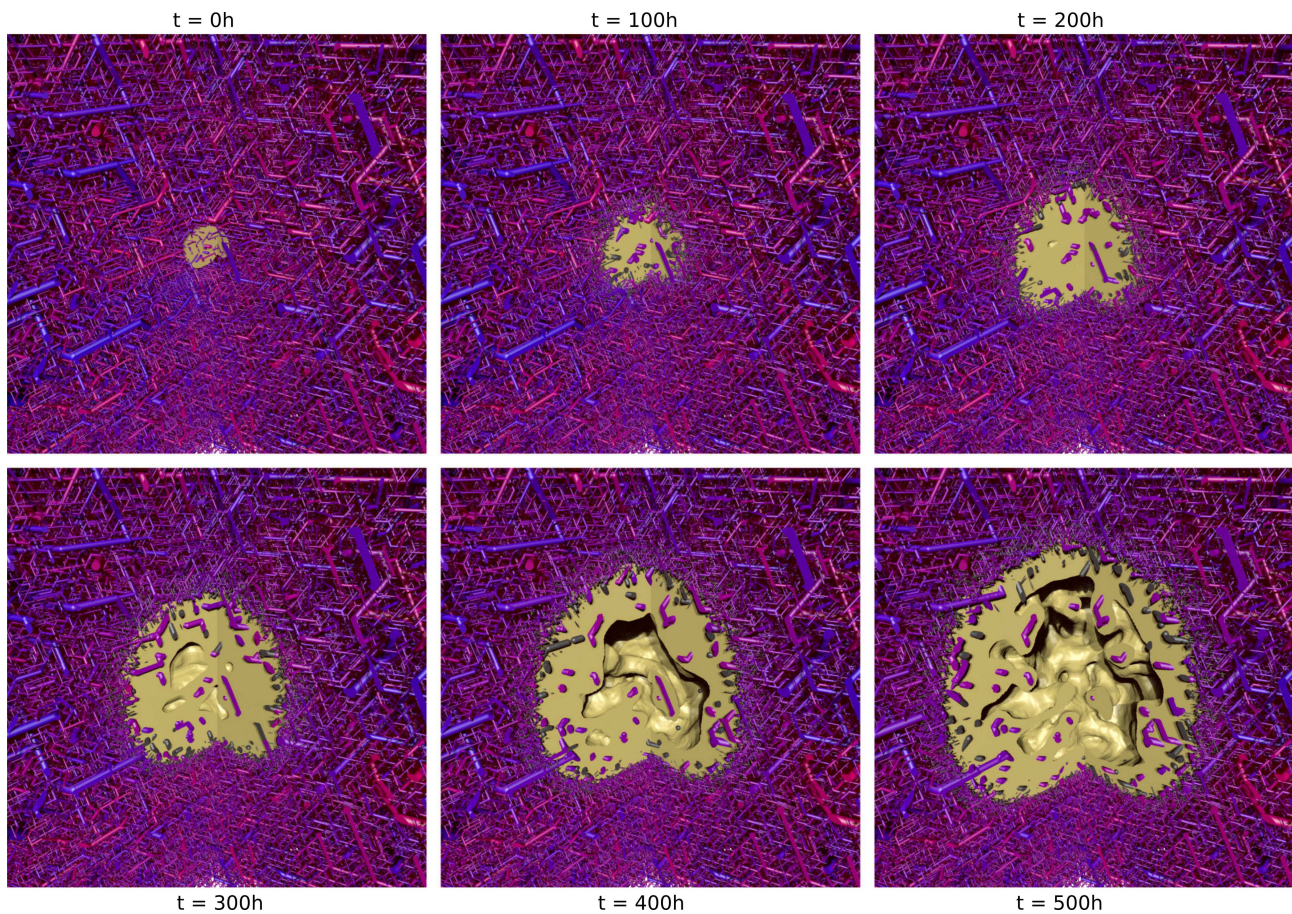


Figure 10. Simulated tumor growth and vascular remodeling: The image sequence shows the temporal evolution of the vascular network and of the interface between viable tumor cells and normal or necrotic tissue (yellow blob). It is a three-dimensional system, computed for [WR13], of which a quadrant is cut out so that the tumor interior can be seen. The view is zoomed in slightly, whereas the full system can be seen in Fig. 11. For scale: the tumor radius at $t = 500 h$ is ca. $1.8 mm$. Vessel segments are color coded by blood pressure (red is high; approximately $10 kPa$, or $75 mmHg$). At $t = 0 h$ the simulation is initialized with a small tumor nucleus in the center and a pre-generated vasculature of the host. The oxygen consumption of tumor cells is elevated compared to normal tissue, leading to a drop of the tissue oxygen concentration, secretion of diffusing GF and stimulation of angiogenesis. As a result, at $t = 100$, the vascular density (MVD) has increased near the tumor rim. Unperfused segments, i.e. blind ends, are displayed in dark gray. Some of them are newly extending angiogenic sprouts. Others pertain to vessel segment chains where one segment has been removed according to the vascular regression and collapse process, pinching off blood flow. Angiogenesis, dilation and regression act mostly near the expanding tumor-tissue interface, transforming the host vasculature into a typical compartmentalized tumor network. Necrotic regions occur as a result of hypoxia. Since only viable areas are shown, necrotic regions appear as hollow interior.

motion for each particle as in molecular dynamics simulations, i.e.

$$\frac{\partial m_i v_i}{\partial t} = F_i(x_0, \dots, x_N, \dots),$$

where m_i , v_i , x_i denote the mass, velocity and position of the i -th particle, and F_i denotes the force on the particle depending on the current state of the system. These equations must be solved numerically in a discrete time-stepping scheme. In between time steps, an extra step can be added to account for proliferation and death of particles. Continuous space particle models were used to study the growth dynamics of multicellular spheroids [RCM07; DH05] and of tissues that are in competition with each other [Bas+11]. Alternatively, the time dynamics can be described by stochastic processes and be simulated by Monte-Carlo methods (see below).

In cellular automata models, particles are confined to sites on a lattice. Particles may be able to hop or proliferate to neighboring sites. Due to its simplicity this is a popular approach to study tumor growth [ABM03; BR06; Bet+06; LRB06; Wei+09; Owe+09; EHH09; End+09] and angiogenesis [AC98; PVS04; Wei+09; Per+11]. In the latter case, particles represent pipe segments of a network. It is however more adequate to think of the network as a dynamically changing graph as in mathematical graph theory. The space-time dynamics can be determined by deterministic rules which are applied once per discrete time step, or by stochastic processes, or a mix of both. A stochastic process is formally described by the Master Equation for the rate of change of the probability P_k to find the system in state $k = 1..n$

$$\frac{dP_k}{dt} = \sum_l A_{kl} P_l.$$

The matrix A_{kl} contains the transition rates according to which the system transitions from state l to k with probability $A_{kl} dt$.

2.2 Theoretical models of blood vessel networks

Microscopic sections of micro vascular networks can in principle be represented by individual endothelial cells in particle models or by distributions in continuum mechanics frameworks. This is well suited for simulation of vasculogenesis [SBP13] or angiogenesis when the migration of individual cells is considered. However, in models of tumor induced angiogenesis and vascular network formation many biological details are omitted in favor of a simple network representation as collection of pipe segments. This approach was first applied to tumor angiogenesis by Anderson and Chaplain [AC98] and has since then been adopted into many other works [SRM+02; SAC06; BR06; LRB06; ABM03; Cai+11; Per+11; ABM03; BBL03; CGP06; Sta+07; Mac+09]. Mathematically the network is represented as a graph $G(E, V)$ with edges E and vertices (or nodes) V . An edge is defined as pair of vertices $e = (i, j)$ with $i, j \in V$ forming a connection between i and j . Thus standard graph algorithms, such as depth-first-traversal [TS09], can be used as building blocks for model processes and for analysis. To model biological systems, edges and vertices are associated with biophysical variables like for instance a radius and a blood flow rate.

2.3 A model of tumor induced angiogenesis and vascular remodeling

Bartha and Rieger [BR06] considered the spatio-temporal evolution of the blood vessel network of a tumor and of the surrounding tissue as stochastic process, where edges (vessel segments) are added and removed depending on blood flow and on concentration of growth-factors (s. Fig. 9). Therefore, they associated edges with the vascular tube radius r , blood flow rate q , and wall shear stress f . In our work [WBR09; WR10; WR13; Wei+15], we also incorporate variables for the life time of angiogenic sprouts, time since entering the tumor, and degeneracy state of the vessel wall. Furthermore, Bartha and Rieger [BR06] defined

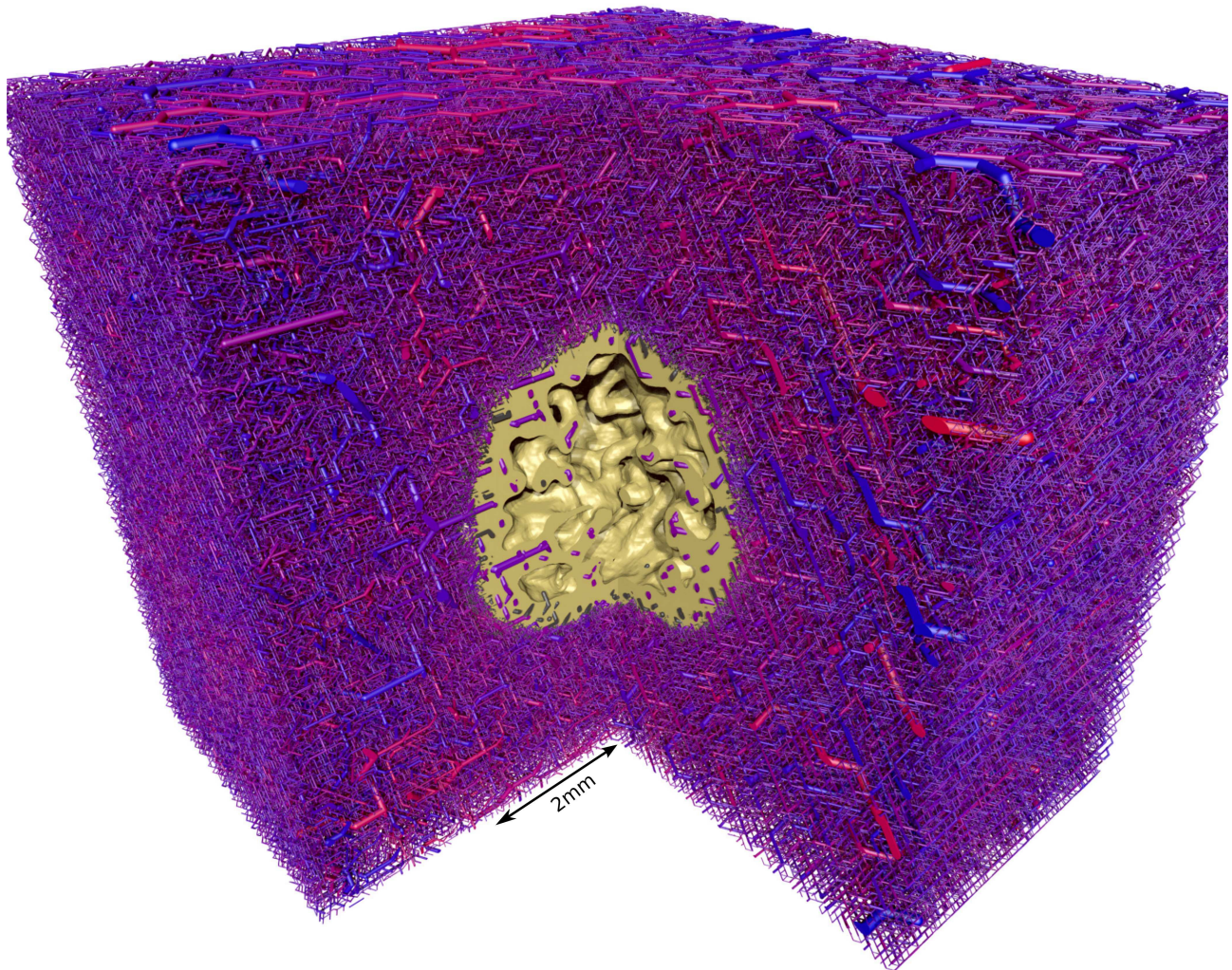


Figure 11. Final simulated tumor and tumor blood vessel network: Depicted is a visualization of the final state of the simulation shown in Fig. 10 at $t = 700 h$, where the simulation is stopped. The full simulation cube of $8 mm$ lateral length is shown. As before, a quadrant is cut out, the interface to viable tumor mass is shown in yellow and the vascular network is displayed as collection of cylinders, color coded according to blood pressure. The bulk of volume surrounding the (yellow) tumor spheroid is filled with the initial vascular network. It appears solid, but actually fills only ca. 10% of the available volume. The tumor vasculature exhibits the typical compartmentalization found in melanoma and glioma [Hol+99; Döm+07] as briefly described in Fig. 10. Networks such as this are the basis of further studies of interstitial fluid pressure and drug transport [WR13] and tumor oxygenation [Wei+15].

transition probabilities reflecting the processes of sprouting angiogenesis, vessel dilation, collapse, and regression. A discrete time stepping scheme was used, where a sweep over all vessels is performed per step and process, modifying the network accordingly. These processes are, in brief, defined as follows:

Angiogenesis: A new straight segment is introduced with non-zero probability, connecting the current site x and a distant site x' if both sites are occupied by circulated vessels, if the GF concentration at x is sufficiently high, but only if there are no other branching points nearby, the distance $|x-x'|$ is small enough, and no site on the path is occupied by TCs.

Dilation: There is a non-zero probability that the radius r of a vessel segment is increased by a magnitude that corresponds to the addition of the diameter of a single EC to the circumference, if the local GF concentration is sufficiently high, if TCs are nearby, and if r is smaller than the upper limit r_{max} .

Collapse: A vessel segment surrounded by TCs has a non-zero probability to be removed if the wall shear stress f is less than the threshold f_{crit} .

Regression: An uncirculated vessel segment has a non-zero probability to be removed if the oxygen concentration is less than a threshold.

The probabilities are simply given as fractions $\Delta t/\tau_{proc}$ of the time step Δt and process specific time constants τ_{proc} under the precondition that $\Delta t \ll \tau_{proc}$. Consequently angiogenesis occurs near the invasive front where the tumor is not yet grown over the network. On the other hand, circumferential growth (dilation) occurs only within the tumor. Bartha and Rieger [BR06] found that this initially leads to decreased flow rates, also decreasing the shear stress f . This further leads to removal of segments according to the collapse rule, redirecting blood flow to other vessels. Blood flow in these vessels is thus stabilized. Remaining unperfused segments are rapidly removed according to the regression rule. Circulated vessel are determined with the help of the biconnected component graph algorithm [HT73]. A biconnected component is a subset of V such that for a pair of vertices $a, b \in V$, there are two disjoint paths from a to b . Hence all tumor vessels that are in the biconnected component of the remaining regular initial network are circulated [BR06]. Bartha, Lee and Rieger [BR06; LRB06] furthermore considered individual TCs with the help of a simple particle model. Therein, lattice sites are identified with the potential location of one and only one TC, assuming that TCs cannot move but proliferate to neighboring sites. Given a small initial tumor nucleus, proliferation is consequently confined to the tumor rim, yielding linear growth dynamics of tumor spheroids. Moreover, TCs can be flagged as dead in case that the oxygen concentration becomes too low. Dead TC occupy lattice sites, prohibiting proliferation thereto, but are otherwise inert. Thus the size and spatial distribution of necrotic regions can be analyzed. In our papers [WBR08; WBR09] we followed this approach, but later adopted a more sophisticated continuum mixture model [PT09] incorporating cell motility, cell-cell adhesion and homeostatic pressure dependent proliferation. Figs. 10 and 11 illustrate tumor vascular remodeling based on simulation data obtained from our extended model. As illustrated in Fig. 12, vessel network and the remaining tissue can be defined on disparate but spatially coexisting domains.

2.4 Computation of blood flow and hematocrit

Depending on the application, blood flow can be considered on various scales, i.e. from computation of the velocity field on micrometer scale to bulk perfusion measured in $ml\ blood\ ml\ tissue^{-1}min^{-1}$ as e.g. obtained from positron emission tomography (PET). For pipe networks of tumors models, blood flow is approximated as ideal laminar flow, where the flow rates q define the blood volume throughput per time through each pipe. Blood pressure variables, p , are associated with nodes. Thus, q is determined by Poiseuille's law

$$q = \frac{\pi r^4 \Delta p}{8\eta l}, \quad (5)$$

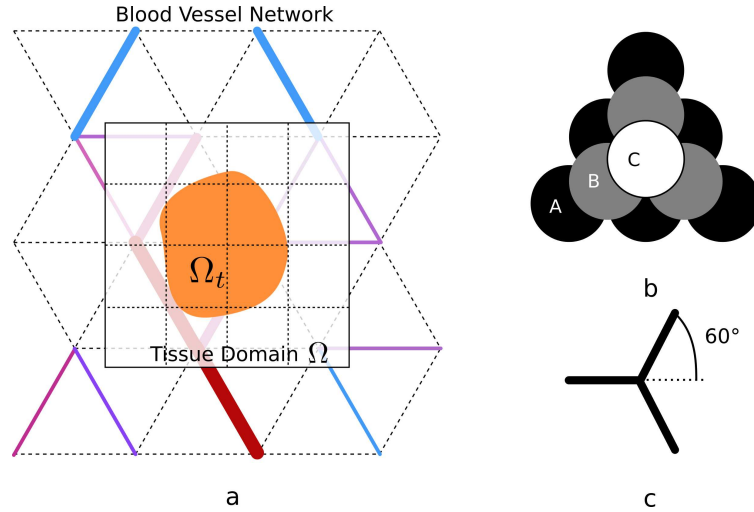


Figure 12. Representation of tumor blood vessel network and tissue domains: Vasculature and tumor may be defined on different spatially overlapping domains as illustrated in (a). In [WBR08; WBR09], we considered two-dimensional systems where vessel segments occupy bonds on a triangular lattice \mathbb{L} as depicted here. The vascular network is indicated by solid lines of varying thickness and color, reflecting the hierarchical nature of arterio-venous networks. The color code reflects the blood pressure drop from arteries (red) to veins (blue), as displayed in other figures as well. At inlets and outlets of the network, we use radius dependent boundary conditions of constant blood pressure (analog of constant voltage sources). Vessel segments can span several bonds in a straight line, and can be added or removed during the temporal evolution of the network. In three-dimensional simulations [WR13; Wel+15], vessel segments occupy bonds on a face centered cubic (FCC) lattice. Such lattices can be represented by flat layers stacked in the vertical as depicted in (b). The layers are offset from each other in the horizontal which repeats itself after three layers, denoted by the stacking order ABC as indicated. Triangular (and FCC) lattices have a high degree of symmetry and allow realistic vascular branching angles (c). In two dimensions [WBR08; WBR09], individual tumor cells can be represented on vertices of \mathbb{L} with a lattice constant $h_v = 10 \mu m$ corresponding to the diameter of a tumor cell. Also, \mathbb{L} must be sufficiently fine to resolve angiogenic sprouts in regions of high vascular density even though the original vascular network is not as dense. In three-dimensions it is hardly possible to represent individual cells of a solid mass of a significant size, simply due to the cost of the sheer number of items to store. Therefore, we switched to a representation by cell density distributions on a coarser cubic lattice as indicated [WR10; WR13]. The tumor mass Ω_t is indicated as orange blob. Figure (c) illustrates our definition of branching angle, i.e. the angle between daughter branch and the axis of the parent vessel.

where r is the vessel radius, η the viscosity, l the length, and Δp denotes the blood pressure difference between the ends of the segment. Conservation of mass requires that the flow into a node equals the flow out of the node, i.e.

$$\sum_i q_i = 0, \quad (6)$$

analogous to Kirchoff's laws of electricity, where i indexes vessels adjacent to a given node under consideration. Together with boundary conditions, a system of equations is obtained which is sparse and can be solved with standard numerical methods, e.g. using a sparse LU-factorization of the corresponding system matrix. Because of the red blood cell (RBC) content, blood is a non-Newtonian fluid, i.e. its viscosity $\eta(r, H)$ depends on the vessel radius r and on blood hematocrit H . The hematocrit is the blood volume fraction of RBCs. The viscosity is commonly expressed by the decomposition into the product of the blood plasma viscosity η_{plasma} , which is constant, and a correction factor, the relative viscosity $\eta_{rel}(r, H)$. Pries et al. [Pri+94] derived a well-known phenomenological formula for $\eta_{rel}(r, H)$ which is easy to incorporate. As a first approximation, it can be sufficient to consider a constant prescribed hematocrit as in [BR06; WR10; WR13] since the viscosity varies only by about a factor of 5 over relevant radii ranges from 4 to 25 μm , whereas the dependence of the flow rate on r^4 plays a much greater role.

In other work [ABM03; Bet+06; Owe+09; Per+11] and our recent paper [Wel+15] a varying hematocrit distribution was computed in order to capture the oxygen concentration dependence on the number of red blood cells, in which the majority of oxygen is stored. A low hematocrit can consequently lead to rapid depletion of blood oxygen. The distribution of hematocrit is sensitive to blood flow rates, i.e., at bifurcations, RBCs tend to flow into the faster perfused vascular branch which is the well-known phase separation effect. Computational models use a phenomenological formula by Pries et al. [Pri+90], describing the hematocrit in each down stream branch depending on flow rates q in vessels adjacent to the bifurcation and upstream hematocrit H . With its help, the hematocrit can be propagated downstream through the network, given an inlet hematocrit. The computation of the flow rates and computation of the hematocrit distribution can be performed in alternating order until convergence to a self-consistent solution, usually in a few iterations [Pri+90]. See also [BR06; Wel+15].

2.5 Vascular networks of normal tissue

To adequately represent a tumor bearing tissue, a model of tumor growth should incorporate the vascular network of healthy tissue. The capillary bed, where most of the solute exchange with blood takes place, is connected to supplying arterioles and draining venules. Arterioles and venules join into larger arteries and veins which are eventually connected to the heart [MH13]. An idealized simple model of a vascular tree is a space filling fractal. In order to supply tissue efficiently, with minimal power dissipation, power law scaling relations for vascular radii and vessel lengths have to hold true [WBE97]. For instance, the well-known Murray's law states that the radius r_c of a parent vessel is related to the radii of the child vessels at a bifurcation, r_a and r_b , by $r_c^\alpha = r_a^\alpha + r_b^\alpha$ with an exponent α between two and three.

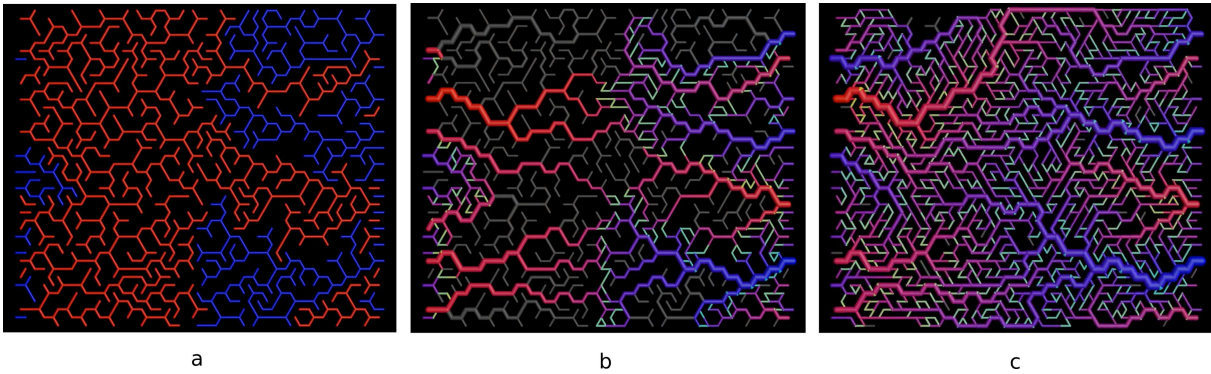


Figure 13. Blood vessel network construction by stochastic growth on a lattice: Following [GK01], the algorithm initializes the network by growing random arterial (red) and venous (blue) trees under exclusion of volume (a). In this initial stage, segments are attached in random directions to randomly chosen tree tips. Starting (root) nodes, which become the top level arterial inlets or venous outlets, need to be specified a-priori. For the lack of better knowledge we consider different hand picked configuration types specifying the number and locations of such root nodes, see [WBR09, Fig. 5], [Wel+15, Fig. 7], and [WR13, S1] for an illustration of the algorithm. Characteristics of the emerging tumor network, e.g. tissue perfusion, depend significantly on the choice of these configurations and some of them may not be physiologically realistic. Eventually the lattice is filled, the growth stage terminates, capillary connections are added between tree tips of opposing types (arteries and veins), and blood flow is computed. The result is depicted in (b) where capillaries are light green and the arterio-venous trees are color coded by blood pressure (high is red, low is blue). In a second stage, trees are remodeled, i.e. tree tips exhibiting low shear stress are removed whereas tips exhibiting high shear stress can grow by further random additions of vascular segments. Capillaries in this stage are temporarily created for the computation of blood flow and removed again afterwards. This is carried out in sweeps where all current tree tips are visited, blood flow is computed and the process is repeated. Eventually the iteration converges to a state with interdigitating trees and homogeneously distributed capillaries. In three dimensions, our construction algorithm of initial arterio-venous networks [WR13] is able to fill the entire simulation box. In two dimensions [WBR09], volume exclusion frequently causes arterial and venous trees to deny each other access to growth into the corners of the simulation box.

In early models of angiogenesis, the initial network consisted only of a single parent vessel [AC98]. These models adequately describe angiogenesis in the rabbit eye model [Gim+74]. Essentially, a small tumor on the cornea of the rabbit eye stimulates vascular sprouting in a few large parent vessels from up to 1 *mm* away. These sprouts branch excessively and form a dense capillary mesh between the tumor and the parent vessels. Similar configurations were used in later work [SRM+02; SAC06; Wu+08; Wu+09]. However, in the bulk of tissue, the distance to sites of angiogenic activity is evidently only a few hundred micrometers [Döm+02; Hol+99]. Therefore, the capillary plexus of normal tissue is often represented by vessel segments arranged in regular patterns, e.g. as square grid, or hexagonal grid, omitting supplying arteries and draining veins [ABM03; Byr+06; Owe+09; Wei+09; Bet+06; BR06; LRB06; Wu+13; Wu+08]. Blood flow is computed assuming a fixed blood pressure at boundaries of the simulation box. We used a regular hexagonal pattern [WBR08], and later considered arterio-venous networks [WBR09; WR13; Wel+15]. Other authors use random arrangements of lines e.g. [Gev11] or voronoi cells as basis for vascular networks [Saf12].

Two decades ago, algorithmic construction of arterial trees was already considered by Schreiner [Sch93]. The basic idea of this algorithm is to grow a tree, branch by branch. At each step, the existing tree is first geometrically scaled to increase in dimension. This increases the distance between vessels, implying that tissue oxygenation would worsen each step. However a new segment is added according to some optimality criterion in order to supply the voxel in space that is most in need of oxygen. Thus, oxygenation stays approximately constant. This process is repeated until the desired size is reached. Later Götde and Kurz [GK01] developed a lattice based growth model which represents the entire connected vessel network including arteries, capillaries and veins so that blood can flow (s. Fig. 13). We adopted this model in [WBR09; WR13; Wel+15] as replacement for previous capillary networks that were based on honeycomb lattices. The basic principle is again shear-stress based vascular remodeling. First, random arterial and venous trees are grown by successive attachment of new bifurcations at existing tree leafs. Then connections, representing capillaries, are added between leafs of the arterial and venous trees to allow for computation of blood flow. In a following iterative process, vessels exhibiting low shear stress are pruned while leafs exhibiting high shear stress are allowed to grow. This way, interdigitating trees develop until eventually the vasculature converges to a (mostly) stationary configuration. Details on our recent implementation are given in Ref. [Wel+15]. Note that our construction scheme differs from the original by Götde and Kurz [GK01] since not all details are provided by them.

In future it might be possible to obtain real scanned blood vessel networks of sufficient accuracy and size. However, current state of the art microscopy methods can only see through a tissue slab up to a maximal depth of ca. 250 μm [Cas+06]. Recently, data obtained from micro computed tomography ($\mu\text{-CT}$) was used by Stamatelos et al. [Sta+14] to reconstruct large parts of the vascular system of an animal-model breast tumor. However, it is questionable if all capillaries were captured since the resolution of the scanner was only 8 μm , and many dead ends were in the reconstructed network. Results of these works are reprinted in Figs. 16 and 17. Similar results were obtained for other cranial [GFP10] and coronary [Lee+07] blood vessel networks.

2.6 Time dependent intravascular tracer concentration

Rather than computing stationary concentration distributions, we are here interested in following an injected bolus of some substances during the transit through the vascular network. For this purpose, S.R.McDougall et al. [SRM+02] already adopted a method from petrol engineering, originally developed to predict solute transport through porous rock. It allows the computation of time dependent concentrations of a tracer c associated with segments of a vascular networks. The basic idea is to collect amounts of tracer m in nodes of the network and distribute it downstream in proportion to the flow rates q of downstream vessels. This procedure, akin to the upwind-differencing scheme for advection equations, is applied repeatedly in time steps of length Δt . The amounts of substance from upstream vessels,

added into downstream nodes, is accordingly $\Delta m = cq\Delta t$. Thus, given a time dependent inlet concentration $c_{in}(t)$, the method yields concentrations $c(t)$ of each vessel. Transvascular loss was not considered although the method would be straight forward to extend to take this into account.

We applied the method to networks created by our tumor growth simulation for regular [WBR08; WR10] and arterio-venous initial networks [WBR09]. However, in our network model, the assumption that network edges are of constant length, and short compared to their radius is violated, leading to an amplified propagation velocity. Therefore we track the position of the interface that separates clean blood from tracer “contaminated” blood and moves with the velocity of blood flow. Similar models were developed for the simulation of capillary rise in network models of porous materials [Ake+98] and are widely used there [e.g. RTS15].

2.7 Interstitial fluid pressure

Interstitial fluid flow (IFF) is prevalently modeled as liquid flowing through a porous medium [JB88; JTM07; Wu+08; Cai+11; Wu+13; ZSS07; Sef+14; Sef+15], where tissue cells and the fibers of the extracellular matrix assume the role of the medium. Fluid and medium are described in general within the framework of mixture theory with the help of distributions of their local volume fraction and their velocity distributions. However, the medium is often assumed rigid. The volume fraction of the liquid is identified with the porosity ϵ which describes the amount of space available per unit volume within the medium. This space is filled by definition with the liquid. Assuming rigidity and (quasi) stationary flow, the system is characterized by the spatial velocity field of the liquid, $v(x)$, where x is the space coordinate. The velocity v is determined by the gradient of the hydrostatic pressure p according to the well-known Darcy’s Law

$$v = -K\nabla p, \quad (7)$$

where the permeability constant K is the product of an intrinsic permeability constant of the medium, the porosity and the inverse fluid viscosity. Usually, K is obtained directly from experimental data for a specific tissue type. Assuming incompressibility and constant permeability, the mass conservation equation obtained is a Poisson equation in p :

$$\nabla \cdot v = -K\nabla^2 p = Q, \quad (8)$$

where Q was added to represent sources (vessels) and drains (vessels, lymphatics). Discretization leads to a symmetric positive definite system of equations which is straight forward to solve by state of the art methods, e.g. FFT or preconditioned conjugate gradient [KL00]. We adopted this simple approach to determine IFP and IFF in vascular networks of simulated tumors [WR13]. Some authors consider IFF within a fully coupled mixture model, where v is the relative velocity between the IF and a moving cell population [Wis+08]. Other authors incorporate IFF into models of tumor growth and allow compression of blood vessels due to elevated IFP [Wu+13].

2.8 Transvascular fluid exchange

Normally only a miniscule amount of blood plasma can leave the blood stream through tiny gaps between ECs. But in tumor vessels, large quantities escape through gaps where entire ECs are missing. The net loss of fluid volume per time J_v within a given control volume is given by the Starling equation

$$J_v = L_p S [p_v - p_i + \sigma_T(\pi_v - \pi_i)], \quad (9)$$

where L_p is the hydraulic permeability of the vasculature, S is the vascular surface area within the control volume, p_v is the blood pressure, p_i is the interstitial pressure, σ_T is the average osmotic reflection coefficient and π_v and π_i are the osmotic pressures of plasma

and IF, respectively [JB88]. The osmotic term $\sigma_T(\pi_v - \pi_i)$ represents forces generated by various dissolved substances and can be considered as a constant offset from p_v at an experimentally determined value [JB88]. This form of transvascular coupling is straight forward to apply in models where the vasculature is considered as a homogeneous phase.

In network models of the vasculature, the flux from each individual segment has to be taken into account in Eq.(8) as a local source of fluid. A simple means to facilitate this is to let the vessel network occupy the same lattice used for the numerical discretization of Eq.(8) which was done in Refs. [Wu+08; Cai+11; Wu+13]. Then each node of the vessel network j corresponds to a discretization site of Eq.(8), and local transvascular fluxes between them can be defined according to Eq.(9), where S now stands for the local surface area of the segments in the vicinity of node j . Using the standard finite difference stencil for the Laplace operator in (8) one obtains a combined system of equations, equivalent to Kirchhoff's laws. It is a common scheme in simulations of tumor growth, not limited to computation of IF, but also applied in theoretical studies of drug delivery [Sin+09; Sef+15] and oxygation [DTK03; KB06; Mon+11; Ske+12; EPK13].

More generally, vessels can be considered as line-like sources akin to the Dirac δ distribution, a concept which has been formulated mathematically rigorously for the solution of elliptic equations with Dirac terms by finite element methods [DAn12] and applied to IFF [CZ14]. We can thus replace (9) by the distribution

$$J(\mathbf{y}) = \int_{\Gamma} L_p 2\pi r (\tilde{p}_v - p_i) \delta(\mathbf{x} - \mathbf{y}) dx \quad (10)$$

where \mathbf{x} , \mathbf{y} are spatial coordinates on the network and in tissue space respectively, Γ is the set of one-dimensional curves (or line segments) that describes the vascular network, \tilde{p}_v is the effective blood pressure including the osmosis terms, and r is the vessel radius. The permeability L_p , blood pressure \tilde{p}_v and radius r can vary depending on the position on the network \mathbf{x} . In our IFP paper [WR13] we considered the efflux from a vascular network on a tetrahedral lattice into a tissue domain discretized by a cubic grid. This was done for a convenient solution of the diffusion-advection equation describing drug transport. Taking inspiration from immersed boundary methods [Pes02], and following [Bea01], we replaced the Dirac δ distribution with a smoothed kernel δ_ϵ with finite width of ϵ . Thus the flux J is distributed from each point on the network to several nearby tissue discretization points. We use an analog scheme to compute the efflux of drug [WR13].

2.9 Oxygen transport

Oxygenation of tissues has been studied in great detail theoretically [Hel+96; Gol08], beginning with the work of Krogh [Kro19] who conceived a simple model of muscle tissue that is reduced to a central straight capillary and an outer concentric cylinder representing muscle fibers. Recent refined versions of such one-capillary models achieve very good agreement with experimental studies of artificial capillaries [NHO89; Nai+90; Hel+96; MEG11]. The typical radial distribution of oxygen in such a scenario is illustrated in Fig. 1. The cylinder model adequately describes muscle fibers where capillaries run mostly in parallel, but many tissues such as tumors have more complex vasculature. The relevant literature, can be roughly divided into two approaches. Some authors [HS89; GP00; Sec+04; GBE04; GBE06; Tso+07; SSD11; FGE13; SD13; Wel+15] seek self-consistent solutions of the equations for advection of oxygen in blood within a realistic blood vessel network and diffusion of oxygen in tissue. This includes acquisition of networks either by artificial construction or experiments, as well as computation of blood flow. On the other hand, many authors use simplified models, where capillaries constitute sources of oxygen of an a-priori determined strength corresponding to a certain intravascular oxygen concentration. Depending on the application it is adequate to model the vasculature as disjoint set of points (in 2d) or lines (in 3d) that are placed in the tissue domain according to some statistical distribution or scanned images [DTK03; EPK13; KB06; Mon+11; Ske+12]. Thus only a stationary diffusion equation needs to be solved to determine the tissue oxygen concentration distribution. See [Wel+15] for a more comprehensive review (reprinted in Sec. 9).

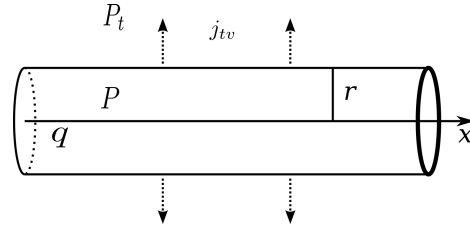


Figure 14. Oxygen transport and extravasation in a tube: Blood flows with the total volumetric rate of q volume units per time through the vessel of radius r . The intravascular oxygen (O₂) concentration $c(x)$ is determined by the partial pressure of O₂ $P(x)$ depending on the position x on the vessel axis. The concentration $c(P)$ is given by the sum of dissolved O₂ αP and hemoglobin-bound O₂ $c_0 H S(P)$, where c_0 is the O₂ concentration in RBCs, H is the hematocrit and $S(P)$ is the Hill-curve of hemoglobin saturation. The flux density of oxygen leaving the vessel at each point on the longitudinal axis is $2\pi r \cdot j_{tv}$, where j_{tv} is the flux density per unit area, modeled using an empirical mass transfer coefficient $\gamma(r)$, times the difference to the partial pressure of O₂ in the surrounding tissue P_t , hence $j_{tv} = \gamma(r) \cdot (P - P_t)$. This leads to a decay of the intravascular concentration $c(x)$ with a local slope dc/dx proportional to $\gamma(P - P_t)/q$. In most theoretical tumor growth models, including ours, except [WBR08], these details are omitted and a constant vascular O₂ partial pressure is assumed. Since the concentration of bound O₂ is much larger than dissolved O₂ $c_0 H S(P) \gg \alpha P$, a better approximation is to assume a O₂ concentration that is proportional to H , see [WBR08; Wel+15]. In [Wel+15] we focused on computation of O₂ distributions in stationary tumor networks including a varying vascular O₂ concentration.

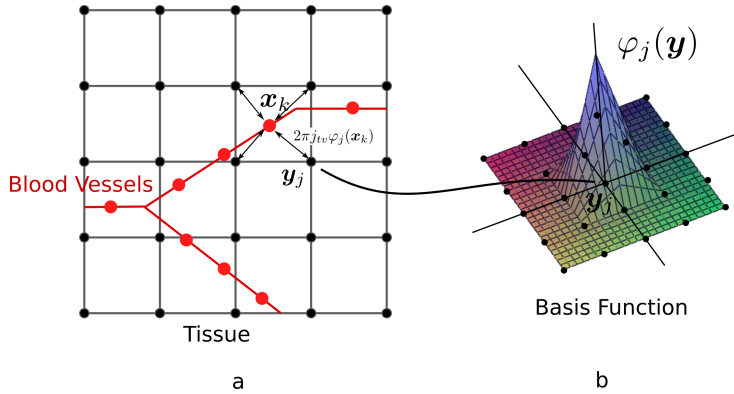


Figure 15. Coupling of the numerical solution of intravascular oxygen distributions with tissue oxygen concentration: This figure relates to the computation of (variable) intravascular and tissue oxygen (O₂) concentrations [Wel+15]. Numerical integration of intravascular O₂ partial pressure $P(x)$ uses integration points, denoted x_k (a, red dots). Spatial coordinates, corresponding to a location on the vascular network are denoted as vector x . Extra- and intravasation are represented by line-like sources and drains, including Dirac- δ distributions. The tissue O₂ partial pressure P_t is approximated as weighted superposition of basis functions φ_j , defined over the tissue domain Ω , with spatial coordinates y , and centered at grid points y_j (b). Following standard finite element methods (FEM), we use piecewise tri-linear functions (in three dimensions) that interpolate control values at grid points. The volumetric transvascular oxygen flux density is given by $2\pi r j_{tv} \delta(y - x)$, where δ is the Dirac- δ distribution, and j_{tv} is proportional to $P(x) - P_t(x)$. From the standard Galerkin method [KL00] it follows that the transvascular flux of a finite segment of length Δx given by $2\pi r j_{tv} \Delta x$ at x_k is added as source contribution according to the weight $\varphi_j(x_k)$ to each corner point j of the enclosing grid cell. In our study of interstitial fluid flow [WR13] we used a slightly different approach in that the δ -distribution was replaced with a smooth kernel yielding a volumetric interstitial fluid source density that is a smooth function of y .

For the study of intravascular oxygen transport it is crucial to take into account that oxygen is, for the most part, bound to hemoglobin in red blood cells (RBCs). Each of the four heme groups of the hemoglobin molecule can bind one oxygen molecule. The steady state of the binding and unbinding processes is described in good approximation by the Hill-curve [Gol08]

$$S(P) = \frac{P^n}{P^n + P_{50}^n}, \quad (11)$$

where P is the partial pressure of oxygen, $S(P)$ is the fraction of oxygen bound relative to the maximal capacity, c_0 is the concentration of oxygen in RBCs at full saturation, n is the Hill exponent and P_{50} denotes the partial pressure of oxygen where $S(P_{50}) = 1/2$. Hence, the total concentration of oxygen c is given by

$$c = \alpha P + H c_0 S(P), \quad (12)$$

where H is the hematocrit and $\alpha = \alpha_p + H\alpha_{rbc}$ is the effective solubility in blood and α_p, α_{rbc} the solubility in plasma and RBCs, respectively. The transvascular flux density j_{tv} of oxygen leaving blood through the blood-vessel interface is strongly diffusion dominated. It is commonly expressed in units of $ml O_2 min^{-1} cm^{-2} mmHg^{-1}$, and follows Fick's law $j_{tv} = -\alpha \nabla P$ at the interface (s. Fig. 14). In single capillary models, the concentration distribution of oxygen is described by advection-diffusion partial differential equations in three dimensions. Thus the expression $-\alpha \nabla P$ yields the oxygen flux at any point in space. However, in large scale network models it is too expensive to compute all microscopic details of the oxygen distribution. Therefore an effective mass transfer coefficient (MTC) γ , similar to L_p of Eq.(9), is used to obtain the transvascular flux density j_{tv} from average tissue and blood oxygen partial pressures [Gol08] according to

$$j_{tv} = \gamma(P_v - P_t), \quad (13)$$

where P_t is the partial pressure of oxygen at the inner wall of the vessel lumen, and P_v is the partial pressure at the center of the vessel. Note that γ represents an effective radial diffusion coefficient of oxygen in blood. L_p of the Starling equation, on the other hand, represents the permeability of the wall. In small vessels, blood tends to form an RBC-rich core and a RBC-free boundary layer. For larger vessels ($r > 100 \mu m$), the discrete nature of RBCs plays a lesser role. Therefore the MTC is function of the vessel radius r , hematocrit H , and blood oxygen saturation S [Hel+96]. The functional dependency $\gamma(r, H, S)$ can be obtained from single capillary simulations and experiments. Assuming radial symmetry, and further assuming that radial variations of the oxygen concentration in blood are negligible, the change of the oxygen flux along the vessel axis is simply given by the differential equation

$$q \frac{dc}{dx} = -2\pi r j_{tv}, \quad (14)$$

where q is the blood flow rate, and x denotes the longitudinal space coordinate on the vessel axis. In order to determine the oxygen distribution across an entire network, assumptions must be made on the distribution at vessel junctions, e.g. instant equilibration of the partial pressure of oxygen flowing into a junction. With the help of mass balance equations, the concentration of outflowing oxygen can be computed. Thus the solution for the oxygen concentration can be propagated downstream. We describe this in more detail in [Wel+15].

Furthermore, the tissue oxygen concentration $c_t = \alpha_t P_t$ is determined by the diffusion equation for the partial pressure P_t

$$0 = \alpha_t D \nabla^2 P_t - M(P_t) + J_{tv}, \quad (15)$$

where D is the diffusion coefficient of oxygen, $M(P)$ is a partial pressure dependent consumption rate, and J_{tv} is the source and drain strength distribution of vessels. J_{tv} can be formulated with the help of the Dirac δ distribution in analogy to (10) (s. Fig. 15). A general

good approximation to the consumption rate of oxygen $M(P)$ is the well-known Michaelis-Menten relation

$$M(P) = M_0 \frac{P}{P + P'_{50}}, \quad (16)$$

which tends to zero for small P , assumes the value $M_0/2$ for $P = P'_{50}$ and goes asymptotically to the maximal consumption rate M_0 . For some problems like tumor oxygenation it is usually assumed that the oxygen concentration rather low, i.e. $P_t < P'_{50}$. Then it is sufficient to use a linear approximation $M(P) \approx -\lambda P$ for some rate coefficient λ . In physiological conditions, $M(P)$ is often approximated by zero order kinetics $M(P) \approx M_0$. This is only applicable in case of good oxygenation since the solution for P_t can otherwise drop below zero.

The system of combined equations for the concentration of intravascular oxygen and tissue oxygen is very challenging to solve and it can only be done numerically. David, Hsu, Safaeian and David [HS89; Sec+04; SD13] used a Green's function method based on the Green's function G of the Laplacian ∇^2 , where G is the solution to $\nabla^2 G(\mathbf{x}) = \delta(\mathbf{x})$. The solution to Eq.(15) is thus formally given by the convolution of G with $M(P_t) + J_{tv}$ [Sec+04]. Goldman [Gol08] and the authors in the references therein use very fine grid tessellations of $3 \mu m$, and consider vessels as sources of oxygen with non-zero radius. This facilitates the numerical treatment of the transvascular flux coupling with help of the gradient boundary condition $-\alpha \nabla P_t = j_{tv}$ at vessel surfaces. We further explored the concepts used in our IFF paper [WR13] and followed [Sec+04; Bea01; CZ14] in the development of a new method to compute intra-and extravascular oxygen distributions [RW15]. Methods developed for the study of oxygen distributions can also be employed to consider distribution of other substances like drugs. Moreover oxygen adds the complication of hemoglobin binding which leads to nonlinear systems of equations. For other substances this can be omitted and linear equations are obtained. As aforementioned, in many cases it may be adequate to consider constant intravascular concentrations.

3 Summary of the publications that are part of this thesis

This section reviews the development of our model of tumor growth and summarizes the things considered in our publications.

3.1 Emergent vascular network inhomogeneities and resulting blood flow patterns in a growing tumor

In previous work Lee, Bartha, and Rieger [LRB06; BR06] suggested a theoretical simulation model of tumor growth and vascular remodeling (s. Sec. 2.3) which predicts realistic vascular density distributions. However this model was quite simplified in several key areas. First, the supply of oxygen (O₂) was modeled using sources of constant O₂ extravasation rate, whereas the net transvascular oxygen flux proper is proportional to the difference of oxygen partial pressure PO₂ between blood and tissue [Gol08]. Hence the attenuation of the net flux due to back diffusion was neglected, leading to overestimation of the O₂ concentration. Secondly, blood is a non-Newtonian fluid, i.e. when blood flows through a capillary, its viscosity η depends on the tube radius and hematocrit (s. Sec. 2.4). This dependence was neglected in [BR06; LRB06] by using a constant viscosity, in spite of the variation of the relative viscosity η_{rel} by a factor of approximately five for the capillary radii considered [PS05, Fig. 4] ($\eta_{rel}(r = 25 \mu m, H = 0.15) \approx 1.5$, $\eta_{rel}(r = 5 \mu m, H = 0.6) = 8$). Vascular radii in tumors are subject to a spatial compartmentalization similar to the MVD (radii are small in the neovascular plexus and dilated within the tumor). Therefore, the interplay of shear force correlated vascular collapse with viscosity variations due to radius and hematocrit variation could affect simulation results unpredictably. Finally, the phase separation effect (segregation of RBC into the faster perfused branch at bifurcations; s. Sec. 2.4) was neglected. In

real tumor, this effect could lead to uneven distribution of hematocrit and thus uneven distribution of blood flow and oxygen availability. In the first part of this paper (reprinted in Sec. 5) we present model extensions where these issues are addressed, and we further analyze these extensions in comparison to before. In the second part we consider the flow of an intravascular tracer substance in order to gauge the ability of networks generated by our simulation to deliver drugs into tumors. The vasculature model closely follows the original work [BR06; LRB06], i.e. the vascular network is formed by segments on a lattice subject to a time dependent dynamical evolution steered by processes given in [WBR08, Sec 2.] and illustrated in [WBR08, Fig. 2].

The following enumeration should familiarize the reader with the alterations and extensions made in this paper: in contrast to [BR06; LRB06] we used a triangular lattice instead of a square lattice since it allows for more realistic branching angles for the arterio-venous vasculature model implemented in later work [WBR09]. Moreover, for efficiency, vascular segments occupy lattice bonds and are allowed to span multiple bonds with which a line segment is formed between two lattice sites that are the end points [WBR08, Fig. 1]. Previously the network was represented by sequences of $10 \mu m$ wide pieces, representing endothelial cells, and occupying lattice sites, which was prohibitively expensive for larger systems. In addition, the previous angiogenesis process was extended with an initial sprout creation and subsequent grow over an extended period of time where previously a “bridge” between perfused parallel vessels was created instantly. The new version is useful to emulate tip splitting since sprouting can now be initiated from a sprouting unperfused branch. It also allows for fusion of sprouting branches. These alterations yielded qualitative model predictions as before [WBR08, Fig. 12. bottom left], and hardly quantitative differences.

It should be noted here that blood flow in [BR06] was computed using a local relaxation method, i.e. Gauss-Seidel [KL00], to solve the equivalent of Kirchoff’s laws (6). It is well-known that local relaxation methods remove high-frequency components of the error, in the sense of a Fourier decomposition, rapidly, but which then continue to converge orders of magnitude slower for smooth components of the error [BHM01]. This lead to a premature halt of the iteration and overestimation of the blood pressure gradient. In this paper this was fixed by using a direct solver (essentially Gauss elimination) specialized for sparse systems of equations [Dav04]. As a result tumor vessels bend inwards toward the middle of the tumor spheroid, an artifact of flow boundary conditions which has not been observed previously (cf. [BR06, Fig. 3] vs. [WBR08, Fig. 12.]). Also the critical collapse threshold (here $f^{(c)}$), according to which it is determined if vessel segments are prone to collapse, had to be adjusted to decreased levels of wall shear stress.

In the base case of this paper we also incorporated the aforementioned radius and hematocrit dependent relative viscosity η_{rel} as well as the phase separation effect. For this purpose, we computed vascular hematocrit distributions [WBR08, Eqs. 2-6] according to the procedure developed by Pries et al. [Pri+90]. We further abolished constant-rate oxygen sources by using a source density per unit tissue area of the form $\alpha(c_o^{(B)} - c_o)$ that is proportional to the difference between blood oxygen concentration $c_o^{(B)}$ and tissue oxygen concentration c_o . The prefactor α is positive for lattice sites that coincide with vessel segments and zero otherwise. Therefore, c_o is henceforth computed by solution of the stationary diffusion equation [WBR08, Eq. 7]. This is less straight forward than previously [BR06] since now the oxygen source strength depends on the concentration itself. The discretized analog of the diffusion equation [WBR08, Eq. 7] is a sparse system of linear equations which was also solved numerically by the routines in [Dav04]. Since RBCs carry the majority of blood oxygen in hemoglobin bound form, we considered a blood oxygen concentration $c_o^{(B)}$ proportional to hematocrit H . We think this is justified as crude approximation to a detailed intravascular oxygen simulation since the rate of oxygen depletion of blood dc/dx (14) depends on the hematocrit according to Eqs. (11, 12, 14), i.e. the average oxygen concentration taken over a given section of the vascular network increases with the hematocrit.

A simulation result is depicted in [WBR08, Fig. 3]. On the left column, the vascular network, color coded by flow rate q , and tumor cells are shown, The oxygen concentration c_o is shown on the right hand side. The visualization of the distribution of oxygen also

reflects vascular hematocrit levels because the source strength of oxygen is proportional to hematocrit. Immediately apparent is the preferred direction of tumor vessels which is imposed by blood pressure boundary conditions generating a homogeneous blood pressure gradient along the diagonal in the initial ($t = 0$) capillary network. We recognize that the hematocrit and tissue oxygen are distributed asymmetrically (there is more on the left hand side of the tumor) which must be the consequence of the rectangular simulation domain. On the other hand hematocrit variations within tumor vessels are barely recognizable, and the average hematocrit equals the inlet hematocrit. However these predictions will not hold true for simulations using arterio-venous networks in subsequent work [Wel+15]. There, model predictions show a drastic decrease of hematocrit in the peripheral capillary plexus.

This paper then continues with the analysis of the dependence of the microvascular density (MVD) and fractal dimension d_f on the critical collapse wall shear stress $f^{(c)}$ [WBR08, Fig. 6] and collapse probability p_{coll} [WBR08, Fig. 7]. Both variables $f^{(c)}$ and p_{coll} are space dependent, assuming maximal values of $f^{(c,max)}$ and $p^{(c,max)}$ in the tumor periphery [WBR08, Eq. 12]. In the first case, the collapse probability $p^{(c,max)}$ was held constant and $f^{(c,max)}$ was varied. In the second case $p^{(c,max)}$ was varied and $f^{(c,max)}$ was set to 10 times the parameter value of the base case. Vessels are only allowed to collapse according to p_{coll} when their wall shear stress f is lower than $f^{(c)}$. Thus the probabilistic nature of collapses is given more weight. Vascular morphology indeed differs between both cases, where $f^{(c,max)}$ variation yielded networks with clearly imposed flow direction and $p^{(c,max)}$ variation cases produced tortuous networks with many loops. Fractal dimension d_f correlated well with vascular density (MVD) and $f^{(c,max)}$ or $p^{(c,max)}$, respectively. Furthermore, although both cases yielded visually distinct results, the dimension d_f varied over similar value ranges.

The paper then proceeds with the analysis of cases where the relative viscosity as function of vessel radius r and hematocrit H is simplified to include only the r dependence or is simply constant [WBR08, Fig. 9]. We also analyzed different variants of the dependence of $f^{(c)}$, p_{coll} on the spatial position in relation to the tumor and on vessel radii [WBR08, Fig. 10]. While these experiments yielded somewhat different networks neither of them changed the quality of our predictions. Moreover we also considered the neglect of oxygen backflow, i.e. a model variant where vessels are constant rate producers of oxygen as originally proposed [BR06]. For realistic parameters, the inclusion of backflow reduced the available tissue oxygen concentration in the tumor periphery significantly [WBR08, Fig. 11]. Therefore tumor growth, i.e. the net expansion rate of the spheroid, is much more sensitive to the choice of oxygen concentration thresholds of hypoxia and quiescence.

In the final part of the paper we considered the flow of a tracer through static final ($t = 800 h$) simulated tumor vascular networks. The computational model used yields time dependent vascular concentration distributions given a time dependent concentration at the inlets (s. Sec. 2.6). The results are quickly summarized, namely that the tracer travels very fast, within ca. two minutes through the entire network with the exception of insignificantly small vascular loops where it takes longer. However the neglect of extravasation makes these results only applicable for cases where the transvascular losses are actually small.

3.2 Vascular remodelling of an arterio-venous blood vessel network during solid tumour growth

In this paper [WBR09] we considered the augmentation of our model of tumor growth with an arterio-venous initial network of normal tissue in two dimensions (reprinted in Sec. 6). The limitation to exclusively capillary networks is a serious limitation shared by previous work by us and other theoretical models of tumor vascular remodeling [RW15], i.e. initial capillary segments of the host are laid out in regular square or hexagonal patterns. It is hardly possible to select realistic blood flow boundary conditions for such networks. As we have seen, imposing a homogeneous blood pressure gradient yields tumor vascular networks where the global flow direction is imposed on the direction of tumor blood vessels. In reality, the capillary plexus is however supplied and drained by adjacent arterioles and venules. Therefore we expect the absence of a global flow direction but rather that local capillary blood flow depends on the geometrical layout of arteriolar and venous vascular trees. We addressed this

issue as aforementioned by incorporating arterio-venous vascular trees of the initial ($t = 0$) host tissue (s. Sec. 2.5). In the first part of this paper, we explore vascular morphologies obtained by tumor vascular remodeling of different vascular tree configurations [WBR09, Sec.3] and attempt to correlate the occurrence of locally increased MVD with blood pressure in initial vascular networks. In the second part we show predictions of intravascular tracer flow.

For this purpose, we retained the foundation of previous work, i.e. vessels are represented as pipe segments occupying bonds on a triangular lattice, and the tumor spheroid is represented by cells occupying sites on the lattice. Tumor vascular remodeling processes are adopted without change except for vascular collapse (see below). We closely follow the method conceived by Godde and Kurz [GK01] to computer generate vascular trees as already outlined in Sec. 2.5 and more comprehensively described in [WBR09, Appendix A]. The principal idea is stochastic growth and remodeling of trees by successive addition of structural elements under exclusion of volume. Structural elements are single segments and bifurcations composed of three segments. These elements are added successively to already existing tree tips in random order and orientation until the latticed is filled up [s. WBR09, Fig.15, a-c]. The algorithm has a second stage which is similar, but tip segments can be removed as well, depending on wall shear stress [s. WBR09, Fig.15, d-f]. Connections between arterial and venous trees, representing the capillary bed, are maintained during growth. Thus blood flow can be determined based on boundary conditions at just a few in-and outlets for which experimental pressure or flow values can be used [Wel+15, S5 Appendix]. Later we proposed an alteration to produce less tortuous high-caliber vessels and the extension to three dimensions [WR13, Sec. 'Initial Blood Vessel Network Construction'].

Previously, initial blood vessel networks consisted exclusively of capillaries of radius $5 \mu m$ but vessels of arterio-venous networks considered in this paper also include arterioles of up to $100 \mu m$ radius. The walls of arterioles exhibit additional layers of pericytes and smooth muscle cells which is why they are thicker than capillaries. We therefore assumed that arterioles are more resistant to collapse than capillaries which necessitates an alteration of the previous collapse process. Hence we introduced a wall stability variable w associated with vessel segments that works like a countdown ticking down as soon as the tumor spheroid expands over segments and allows collapse only if $w = 0$ and $f < f^{(c)}$. The initial stability $w(t = 0)$ depends on the radius r and vessel type [WBR09, Sec. 2.2. and Fig. 2.]. Furthermore, we omitted the computation of hematocrit distributions for simplicity assuming an average hematocrit of 0.45. We omitted the functional dependence of the critical collapse shear stress $f^{(c)}$ on the distance from the tumor, i.e. $f^{(c)} = f^{(c,max)}$ according to Sec. 3.1.

Snapshots of simulation states can be viewed in [WBR09, Figs. 3, 4, and 5]. We considered four different vascular configurations of initial networks ($t = 0$) which differ in the location of vascular tree roots [WBR09, Fig. 5]. These tree roots are the starting point of the aforementioned vascular growth procedure. The selection of their number, type (arterial or venous), and location was completely arbitrary. But in principle statistical data such as frequency distributions of vascular radii could help reject configurations that are unrealistic for a given tissue. In later work [Wel+15] we explored the dependence of other parameters such as regional blood volume rBV , perfusion rBF and blood oxygen saturation Y on a greater number of root configurations (s. 3.5). Evidently the imposition of a global flow direction is abolished, but rather vessels emanate from arterioles protruding into the tumor [WBR09, Fig. 5].

The new model predicts vascular morphologies which obey the same compartmentalization of vascular density (MVD) and vascular radii as before on regular initial networks, i.e. vascularization is high in at the tumor periphery and diluted in the tumor center. Capillaries in the tumor center are generally dilated, but now the tumor center also exhibits higher-caliber vessels co-opted from the initial network. Such vessels exhibit a radius r larger than the maximal dilation threshold r_{max} and are therefore not subject to dilation. Radially averaged quantities MVD, vessel radius O_2 concentration, flow rate q , tumor cell density and wall shear stress f are in good agreement with earlier work, see [WBR09, Fig. 4] vs. [WBR08, Fig. 4]. However flow rates q are increased overall by a factor of 10 due to the presence of

vessels much thicker than capillaries.

Flow rates within the peripheral vascular plexus are predicted to be of the magnitude of normal capillaries. The model fails to predict severely decreased blood flow velocities found in animal models [JS10; Yua+94]. On the other hand the model predicts arterio-venous short-cuts within the tumor, i.e. vaso-dilation gives rise to mostly very well perfused vascular threads connecting arterioles with venules [WBR08, Fig. 8]. Such shunts were suggested in the experimental literature where “flow hotspots” are frequently found in tumors of patients [Sah+05].

Considering severe heterogeneity of local vascular densities [WBR09, Fig. 5] depending on initial networks, we attempted to correlate local MVD with differences in blood pressure between neighboring vessels in initial networks. For this purpose, we computed an auxiliary “pressure” field $p(x)$ as function of space x at $t = 0$ that interpolates approximately the blood pressure p_v in spaces between vessels. Hence p is given as the solution of $\nabla^2 p + a \cdot (p_v - p) = 0$, where a is zero in empty space and $a \gg 1$ at sites coincident with vessels. Since a is large, p assumes the value of the blood pressure in good approximation. Then we plotted the magnitude of the gradient $||\nabla p||$ as local averages taken over small boxes versus the local MVD at $t = 1200 h$ as shown in [WBR09, Figs. 10 and 11]. This yielded a low correlation coefficient between 0.2 and 0.4 per simulation run. A much better correlation (0.9) was obtained for MVD and $||\nabla p||$ when averages were taken over the area of entire tumors. We obtain similar results from simulated three-dimensional tumors generated for our recent paper [Wel+15]. See Appendix A.

Finally, we determined frequency distributions of (a) MVD, (b) size of clusters of necrotic regions and (c) size of clusters of high MVD [WBR09, Fig. 12]. These distributions follow power laws with a common exponent of -1.4 . Such algebraic distributions are commonly found in systems near a phase transition or in classical percolation at the critical threshold.

The second part of the paper is the straight forward application of intravascular tracer flow computations following [WBR08]. (s. Sec. 2.6). Qualitatively, predictions agree with earlier results [WBR08], i.e. blood saturated with tracer flows through, in good approximation, the entire tumor vasculatures within very short times. In contrast to earlier predictions blood flow velocities in arterio-venous network are higher ($\geq 1 \text{ mm/s}$) which is why the transit times are now of the order of seconds instead of minutes.

3.3 Physical determinants of vascular network remodeling during tumor growth

Two-dimensional simulations of tumor growth are, without doubt, useful but two-dimensional geometry does not adequately represent real tumors. Properties like vascular density, vessel radius, blood volume, and so on are subject to a compartmentalization into annular shells around the center of the tumor spheroid. But nevertheless, the tumor vascular network exhibits no spatial symmetry. This is a difference to the situation in tissue like muscles where capillaries run in-between muscle fibers mostly in parallel to each other. In such cases the longitudinal dimension may be integrated out or it may be sufficient to consider a thin slab under periodic boundary conditions. Two-dimensionality also leads to restrictions for initial ($t = 0$) networks because arterial and venous trees cannot cross each other or wind around each other as they can in three dimensions. Moreover, Lee, Rieger, and Bartha [LRB06] already performed simulations using initial blood vessels arranged as cubic lattice. Their results should be confirmed for arterio-venous networks.

These concerns are addressed in this paper [WR10] where we present an extension of the construction algorithm for artificial three-dimensional arterio-venous networks on cubic lattices and a new simple continuum model of the tumor spheroid (reprinted in Sec. 7). As previously, we consider morphological characteristics of the emergent tumor networks. The final part of our paper continues with simulations of intravascular tracer flow.

For this paper we switched to a cubic lattice for the arrangement of vessel segments, following Lee, Rieger, and Bartha [LRB06]. This is much simpler than the extension of triangular lattices to three dimensions but excludes realistic 60° branching angles between daughter branches at bifurcations (s. Fig. 12). Later this restriction was removed using

face centered cubic (FCC) lattices [WR13]. The previous procedure for the construction of vascular trees (s. 3.2) was altered for three dimensions. Y-shaped bifurcations as structural elements were replaced by two new elements that can be appended to tree tips. First, a T-junction consisting of three segments and secondly, a fork-shaped junction (–□) consisting of five segments. The additional space dimension provides additional rotational degrees of freedom for the orientation of appended elements relative to their parent segment. We simply handle this analogous as before, by enumeration of all possible configurations and picking of an admissible configuration which produces no overlap with other vessels, weighted so that the forward direction relative to the parent segment is ten times more likely than taking a 90° turn [WR10, Sec. 2.7]. Furthermore, it is too computationally costly to represent each single tumor cell in three dimensions. Therefore we sought an effective description of tissue on a macroscopic scale, of which a multiplicity exists in the literature (s. Sec 2.1). We implemented a simple reaction-diffusion model for the density distribution of tumor cells $c(\mathbf{x}, t)$ depending on space \mathbf{x} and time t [WR10, Eq. 1]. We assume that c can vary between 0 and the maximal tolerable density $c^{(max)}$ beyond which cells stop proliferating. Moreover we assume that the extracellular matrix behaves like a porous medium, posing a resistance to cell migration, and that TCs are driven by a solid pressure P which is assumed as function of their density, following e.g. [AP09]. This leads to a migration velocity $v = -D\nabla P(c)$, where D is a mobility constant. (Note that P is not to be mistaken for the the oxygen partial pressure elsewhere). Analogous to the previous discrete model, cells of normal tissue are not explicitly represented. Hence c is computed as solution to the partial differential equation

$$\frac{\partial c}{\partial t} = -D\nabla \cdot [c\nabla P(c)] + k_p c \left(1 - c/c^{(max)}\right) - k_n c, \quad (17)$$

where k_p and k_n are oxygen dependent rate constants for proliferation and necrosis [s. the rates WR10, Eqs. 2 and 3]. A solution to this equation, provided sufficient oxygen and an initial spherical nucleus, is a spherical soliton wave expanding from an initial spheroid. The actual computed solutions also approximately describe a spherical tumor. We identify necrotic regions simply as areas where the oxygen concentration o level is below the necrosis threshold $o_{TC}^{(death)}$, neglecting the time TCs can survive under hypoxia. This works well since the local oxygen concentration within the tumor center can only decrease (by vessel collapse). Otherwise we would have to track the density distribution of necrotic TCs as well. The solution of (17) is carried out by finite differencing methods on a cubic grid discretization with a cell width of $h = 30 \mu m$. Other parts of our model remained in principle the same, but with some technical exceptions. First the vascular network of the tumor growth simulation is maintained at a lattice constant of $h_v = 10 \mu m$ for sufficiently high resolution of the tumor neovascular plexus. Hence, we cease to assume that vessel lattices and grids for numerical solution of continuous variables coincide. To conserve memory we only store pointers to vascular segments in a dictionary (hash table [TS09]) using indices of lattice sites as keys. In the determination whether a vessel lies within the tumor we check if $c(\mathbf{x}) < 1/2 \cdot c^{(max)}$, where $c(\mathbf{x})$ is obtained by piecewise linear interpolation of control values at grid points. Moreover the numerical solution of the diffusion equation for the oxygen concentration distributions is defined on the same numerical grid used to represent c . Therefore oxygen source flux density contributions of vessels are distributed to nearby grid sites analog to the source flux density of interstitial fluid according to Sec. 2.8.

The extended model predicts vascular and tumor morphology consistent with earlier predictions, i.e. a well vascularized rim and a tumor core with few isolated dilated vessels, as shown in visualizations [WR10, Figs. 3 and 4] and radial distributions [WR10, Fig. 5]. Correction: regardless of what the paper states, the vascular density MVD was actually calculated as line density L_D , i.e. vascular network length per measurement volume, in unit of $10^2 \mu m^{-2}$, [Wel+15, s. also Appendix S2, Eq. 1]. Hence the predicted normal tissue line density L_D is actually $150 mm^{-2}$ in fair agreement with the histological MVD of normal skin amounting to $80 mm^{-2}$. In the worst case L_D overestimates the histological MVD by a factor of three simply because the cutting-plane of the histological MVD misses vessels in parallel to the plane. Nevertheless L_D was used as representation of the MVD in at least another publication [Sta+14], and we continued to use it in following work [WR13; Wel+15], correctly

designated.

Moreover we determined (box-counting) fractal dimensions, [WR10, Sec. 3.3] for which we obtain $d_f(\text{tumor}) = 2.5 \pm 0.03$ as average and standard deviation taken over entire tumor networks which is in good agreement with previous $d_f = 2.52 \pm 0.05$ [LRB06] based on remodeled capillary networks, and which corresponds to the dimension of the critical percolation cluster in three dimensions. We also computed fractal dimensions of arterio-venous trees $d_f(av) = 1.64$ which happened to be in good agreement with experimental data $d_f = 1.65 \pm 0.05$ [Gaz+95]. However different method were used. We used box-counting in three-dimensions, whereas Gazit et al. [Gaz+95] considered binary valued images of two-dimensional projections.

The last part of this section of this paper, [WR10, Sec. 3.4], presents our attempt to confirm the correlation of local tumor *MVD* versus local blood pressure differences at $t = 0$. We computed $\|\nabla p\|$ according to the definition in Sec. 3.2, and plotted it versus the local tumor *MVD* at $t = 800 h$. However we failed to reproduce the correlation found in the two-dimensional case [WBR09]. We suspect an error, because we repeated the calculations for the tumor vascular networks generated for our recent study of tumor oxygenation [Wel+15], using new program codes, and obtained a correlation coefficient amounting to 0.41 for local $MVD(t = 800 h)$ versus $\|\nabla p\|(t = 0)$ taken over $(100 \mu m)^3$ voxels. For the $MVD(t = 800 h)$ versus the average of $\|\nabla p\|(t = 0)$ taken over the area of entire tumors at $t = 800 h$ we obtained a correlation coefficient of 0.93 consistent with previous results (s. Appendix A).

In the second part of this paper we consider again the conduction of a tracer substance through the tumor vascular network using previous methods (s. Sec. 2.6). Consistent with predictions based on two-dimensional networks, high tracer concentrations are conducted within seconds through the entire vascular network.

3.4 Interstitial Fluid Flow and Drug Delivery in Vascularized Tumors: A Computational Model

Interstitial fluid flow (IFF) in tumorous tissue has been considered theoretically to some extent but only either using constant capillary density distributions within simple continuum models, or under unrealistic assumptions for a patients capillary network (s. Sec. 2.7). Moreover, at the current time, experimental acquisition of detailed maps of IFF of human tumors appears infeasible since invasive methods are state of the art. However, IFF can, depending on the type of drug, affect its distribution potentially negatively [JB88]. Also, the spatial concentration distribution of drugs has rarely been considered in the literature. Previous theoretical models are limited to regular capillary initial ($t = 0$) networks, e.g. [Sin+09] or consider a continuous vascular density [JB88]. Experimentally, penetration experiments are performed for homogeneous cells layers and genetic causes for drug resistance are examined but heterogeneity of drug distributions were only considered in few cases [MT06; Zhe+01; Pri+05]. An example of experimental drug distributions in tissues is reprinted in Fig. 8.

In this paper [WR13] (reprinted in Sec. 8) we focus on IFF and drug delivery in solid tumors like melanoma or glioma, using simulated tumor blood vessel networks based on artificial arterio-venous vasculatures of normal tissue. We also abolished deficiencies of our previous continuum model of the tumor spheroid [WR10], and switched to face centered cubic (FCC) lattices for the arrangement of vessels. One such deficiency is that the model equations would allow solutions where the tumor cell (TC) density c rises sharply at the invasive edge. For instance, assuming quiescent tumor cells (low oxygen availability), a stationary solution to the differential equation (17) is $c(\mathbf{x}) = c_0$ for \mathbf{x} within some arbitrary region T and $c = 0$ elsewhere. We can find c_0 by definition of P so that $P(c_0) = 0$. Thus, TCs feel no pressure and therefore stay in place. Another problem with this approach is the curvature of the interface ∂T which can be arbitrarily high. Therefore the solution $c(\mathbf{x})$ may not be representable on the numerical grid. Also, in real tumors, cell-cell adhesion causes a certain degree of smoothness of the tumor interface. In this paper this is corrected by a new continuum model of the tumor spheroid, closely following [PT09] and the refs. therein. In principle, a common density distribution ϕ (actually fractional volume per unit volume) with

a common migration velocity v_ϕ is defined for TCs and normal tissue cells. The interface between TCs and normal cells is defined via an auxiliary function, i.e. using the Level Set method [SS03]. Thus the interface is defined as 0-level of the auxiliary function providing the closest distance from the interface within some proximity of the interface. We found that this already works well. For future considerations it is possible to include a surface tension force, following [BKZ92]. The switch to vascular FCC lattices was undertaken to revert back to 60° branching angles. This may seem overly complicated at first, but FCC lattices can be represented by layers of two-dimensional triangular lattices which are set off from each other according to the well known-stacking order ABCABC... (s. Fig. 12). We organize sites logically as sites of a three-dimensional cubic lattice that is spatially distorted to coincide with the conceptual FCC lattice. Neighbors of a given site must correspond to the FCC lattice. Therefore, exploiting translational symmetry, we store precomputed neighbor lists for a minimal number of exemplary sites. Generation of arterio-venous initial networks was carried out again using Y-junctions as structural elements of growth, true to the original proposal [GK01] [WR13, see also S1 Fig. 2].

A cohort of initial ($t = 0$) arterio-venous networks were generated. Subsequently tumor growth and vascular remodeling were simulated using previous methods in conjunction with the new model of tissue described above [WR13, Fig. 2]. Computed tumor spheroids and vascular networks exhibit morphological compartmentalization in agreement with previous predictions [WR13, Fig. 3]. Interstitial fluid flow and drug delivery were considered for stationary final ($t = 800 h$) simulated tumors, i.e. although we determined concentration distributions depending on time, we still kept the tissue and network configuration frozen in time. Interstitial fluid pressure $p(\mathbf{x})$ and its velocity field $v_l(\mathbf{x})$ were determined according to Sec. 2.7, i.e. by finite difference solution of (8). Note that p is not to be mistaken for the (interpolated) blood pressure used elsewhere. It should be clear from context which one is meant. Drug content is divided into an extracellular compartment with concentration s_1 [WR13, Eqn. 20] and an intracellular compartment with concentration s_2 [WR13, Eqn. 21] where drug is bound immobile. The concentration s_1 is subject to diffusion and advection with the liquid velocity v_l . Vessels are sources and drains of drug (s. Sec 2.8, and 2.9) comprising diffusive and advective transvascular flux densities [WR13, Eqn. 23]. Lymphatics can sink drug by advection, assuming that the drug concentration within lymphatics is approximately equal to the concentration in tissue. Consequently, drug diffusion into lymphatics is neglected. Both compartments 1 and 2 exchange drug via rates k_{12} and k_{21} depending on assumed trans-membrane diffusion coefficient and cell surface area. For simplicity, degradation of drug molecules is neglected. In future this should be straight forward to add, provided experimental data. The initial condition is a system clean of drug. Drug is inserted via the vasculature where the intravascular concentration $s^v(t)$ is homogeneous in space and follows a exponentially decaying pulse in time, imitating an injection.

A major simplifying assumption in our model is that extravasation of blood plasma affects blood flow negligibly, i.e. we computed blood flow under neglect of extravasation. We determined the fraction of plasma loss due to extravasation, amounting to an order of magnitude of one promille. Moreover we estimated the length scale on which the blood pressure would decrease, amounting to ca. $500 \mu m$ in the worst case where the interstitial fluid pressure is constant zero [WR13, Pg. 12 and Fig. 6]. Therefore the simplification seems justified from a computational point of view, although in animal models blood flow velocities are generally lower amounting to $0.1 - 1 mm/s$. There severe extravasation causes a rise in hematocrit and blood viscosity, which can even cause stasis of blood flow [Net+96; BNJ97].

Predicted interstitial fluid pressure (IFP) distributions exhibit an average radial profile that increases sharply from the tumor edge into the tumor center. There, the IFP approaches a plateau value asymptotically, close to the level of blood pressure, amounting to ca. $6.5 kPa$ ($49 mmHg$) [WR13, Fig. 4 and 5]. This is expected due to the high vascular permeability, implying a small pressure drop across the vessel wall. The plateau value lies above experimentally observed mean values taken over various human tumors, but it is still lower than the absolute maximal observed IFP [JTM07, Tbl. 1]. Since the IFP is generally assumed to rise very close to the level of blood pressure, this is rather indicative of overestimated blood pressure. IFP distributions, i.e. the scaled negative gradient of the IFP, follow trivially and

exhibit the expected sharp rise at the tumor rim amounting to a maximal value of $0.2 \mu\text{m}/\text{s}$ in good agreement with the literature. Due to the discrete vasculature model used, the IFP and IFF distributions exhibit heterogeneity, i.e. they vary spatially in-between vessels of different blood pressure values. Thus vessels are predicted to drain the interstitial fluid in some instances [WR13, Fig. 4C]. The distributions shown are discontinuous because we assumed a different interstitial permeability for tumor than for normal tissue.

Anti-cancer drugs come in a variety of kinds, from light molecules e.g. Cisplatin or Doxorubicin ($\approx 543 \text{ g/mol}$) to heavy nano particles and viruses as carrier systems. We considered Doxorubicin as base case since it is experimentally well studied and widely used. Maps of predicted concentration distributions are depicted in [WR13, Fig. 7]. The computation was stopped after a simulated time of 96 h . Corresponding radial averages, are displayed in [WR13, Fig. 8A] whereas Fig. 8B shows average concentration distributions depending on the distance from vessels. The distribution of local concentrations is apparently mostly determined by the local vascular density (MVD) distribution. Thus, drug concentration are generally high within an annular shell around the tumor interface and otherwise low except for areas in proximity of tumor blood vessels. Moreover we computed maps of intracellular drug doses, denoted ICMAX and ICAUC which are the local maximal concentration s_2 taken over time and the local time integral of s_2 , respectively. Both distributions are qualitatively similar and likewise reflect the distribution of the MVD [WR13, Fig. 9].

We considered also concentration distributions arising from non-diffusing particles, e.g. from nano-particles (case i). Due to their high molecular mass we assumed a vanishing diffusion coefficient so that they are transported purely by advection. The main qualitative difference to the base case is that predicted concentrations and dose distributions precisely follow stream lines of the flow of interstitial fluid. As a result there are frequently small sections of viable tumor, where no noteworthy drug concentration arrives within the simulation time of 96 h [WR13, Fig. 11]. In case (ii) we considered a prolonged infusion of drug which yielded similar results as the base case except with higher magnitudes of concentrations and doses.

Further simulations were performed for simple parameter variations based on the base case where each time we varied one permeability coefficient in the system (cases iii to v) as well as the number of lymphatic channels (cases vi and vii) [WR13, Figs. 10, 13 and 14]. The main conclusion here is that increased permeability increases interstitial fluid flow and fluxes of drug. The model system of interstitial fluid flow is in all respects analogous to an electrical circuit, and therefore this result is not surprising (s. Sec. 4). Moreover predicted doses are very sensitive to the variation of tumor tissue permeability, suggesting a possible therapeutic target.

3.5 Relation between tumor oxygenation, vascular remodeling and blood flow: A computational model with applications to breast cancer

In previous papers we assumed that intravascular oxygen (O_2) concentrations are constant [WBR09; WR10; WR13] or proportional to hematocrit [WBR08]. In the limit of small transit times this may be justified. But as mentioned before, this assumption is certainly not valid for all tumors because during the transit of a control volume of blood through vascular tubes, its O_2 content decreases due to extravasation of O_2 (s. Sec. 2.9). Moreover, oxygenation of tumors is currently not well understood. For instance, Grosenick et al. [Gro+05] and Spinelli et al. [Spi+05] measured tumor oxygenation by optical mammography in a cohort of patients. They determined average concentrations of total hemoglobin c_{Hb} , oxyhemoglobin c_{HbO} , deoxyhemoglobin c_{HbD} , and average blood oxygen saturations Y within normal and tumorous tissue sections. The saturation Y is simply defined as the ratio $Y = c_{\text{HbO}}/c_{\text{Hb}}$. They found that the tumor hemoglobin concentration $c_{\text{Hb}}(\text{tumor})$ is always larger than the hemoglobin concentration in normal tissue $c_{\text{Hb}}(\text{normal})$. This is already explained by an increase in regional blood volume rBV due to vaso-dilation. The blood oxygen saturation in tumors $Y(\text{tumor})$, however, can be larger or lower than the blood oxygen saturation in normal tissue $Y(\text{normal})$, split approximately to one half among the patients. Moreover, high hemoglobin concentrations are correlated with high saturations, but tumors with low

hemoglobin concentration exhibit a wider range of blood oxygen saturations. These statistical variations of the saturations were previously not explained, and no attempt was made to link them to vascular architectures of different kinds, for instance.

In this unpublished preprint [Wel+15] (reprinted in Sec. 9) we tackle these problems with extensions of previous methods including the computation of varying intravascular oxygen concentrations [Wel+15, Sec. "Models"]. Note that oxygen concentration and partial pressure (PO2) are denoted as c and P here, not to be confused with quantities of previous papers. Similar as before [WR13] we consider tumor vascular networks ($t = 800 h$) obtained from simulation of tumor growth and vascular remodeling. Regional blood volume rBV , perfusion rBF , hemoglobin concentrations c_{Hb} , oxy-hemoglobin concentrations, deoxy-hemoglobin concentrations, oxygen saturation Y , as well as tissue and vascular oxygen partial pressure distributions P , and P_t were calculated for initial networks and final tumor networks ($t = 800 h$), to name the most important quantities. Transient behavior such as transient hypoxia due to temporary occlusion of blood vessels is not considered. In previous work [WBR09] predicted vascular morphologies were sensitive to different initial ($t = 0$) arterio-venous blood vessel network configurations in which the tumor grows. Therefore we again consider different initial network configurations, in greater number, denoted RC1 through RC9 [see Wel+15, Fig. 7], emulating a cohort of patients, and present calculated parameters as function of these configurations.

Following the work of Hsu and Secomb [HS89] and Goldman [Gol08], our mathematical model describes stationary consistent states of oxygen PO2 distributions within the vascular network, P , and of tissue, P_t . The intravascular PO2 is assumed as constant across the cross sectional area of vascular pipes. Thus the vasculature model reduces to a collection of one-dimensional segments of which $P(x)$ gives the O2 partial pressure at some longitudinal position x along the axis of some vessel. Both distributions P , and P_t , are coupled by the net transvascular flux density of oxygen per vessel unit length $2\pi r \cdot j_{tv}$, depending on the difference of PO2 levels across the vascular wall. The effective resistance to radial oxygen transport and extravasation is captured by the phenomenological mass transfer coefficient γ , according to which the flux density is $2\pi r j_{tv} = 2\pi r \gamma (P - P_t)$. The intravascular oxygen content decreases longitudinally according to the flux density j_{tv} , and simultaneously, the extravasated oxygen flux is a source of oxygen for the tissue oxygen distribution P_t . Tissue oxygen consumption rates, $M(P)$, are determined according to the well-known Michaelis-Menten relation [Gol08]. For more details we refer to Sec. 2.9. A concise model definition is provided in [Wel+15, Sec. "Models"]. Discretization of the model equations yields a complex system of non-linear equations. We combined ideas from previous work [HS89; Sec+04; Gol08; Bea01] into a new numerical solution procedure which is sufficiently efficient, allowing us to study three-dimensional networks in a simulation box of ca. 0.5 cm^3 . However the method suffers from sub-linear convergence with the grid constant h of the discretization grid of the tissue domain. [Wel+15, S1 Appendix, Fig.4] shows solutions for PO2 distributions of a single vessel for different h . Solutions are spaced slightly further apart the smaller h becomes. The difference between the average partial pressure for some h and the solution at $h = 10 \mu\text{m}$ taken over the vessel length $|\langle P \rangle(h) - \langle P \rangle(h = 10 \mu\text{m})|$, scales in proportion to $h^{0.6}$. In standard finite difference methods an exponent of 2 is common, where solution would be spaced less apart the smaller h becomes. However, here convergence is spoiled by singular source terms.

Complementing the network model, a simple zero-dimensional, i.e. mean-field, model was developed by Rinneberg [see Wel+15, Sec. "Homogeneous Three-Compartment Model of Blood Oxygenation"]. In essence this model divides tissue into identical sections, each supplied by a capillary which are also all identical, similar to the basic idea of the Krogh model (s. Sec. 2.9). However, in contrast to the Krogh model, variations of tissue oxygen partial pressure PO2 are neglected, and the net transvascular O2 flux density j_{tv} is determined by an effective mass transfer coefficient γ (13). Thus the longitudinal variation of the blood oxygen saturation $S(x)$ along the vessel axis coordinate x can be determined, provided that the inlet O2 saturation S_{in} and a homogeneous tissue O2 partial pressure P_t are given. Under the model assumptions, microscopic quantities like blood flow rate q are easy to related to their macroscopic counterparts. For example, the tissue perfusion

is $rBF = q/V$, where V is the volume of the considered tissue sections. Thus, the average saturation Y , oxygen extraction OEF and several more parameters were calculated. Predictions are compared against simulation results and experimental data [see Wel+15, Sec. “Predictions of Compartment Model and Comparison with Experimental Data”]. By this model it is easy to see that the average blood oxygen saturation $Y = \langle S \rangle$ increases with perfusion rBF asymptotically to the saturation value $Y = 1$. Moreover, Y decreases with increasing vascular surface area to volume ratio.

For each vascular tree configuration RC1 through RC9, we simulated five realizations of different tumor vascular networks. Moreover, we considered three model variations of tumor growth and oxygen consumption. For the base case (BASE), we adopted our previous model with some parameter changes guided by experimental data for breast tumor [Wel+15, Tbl. 1 and 3]. Although we reduced the maximal vascular dilation radius $r^{(max)}$ to only $14 \mu m$, down from 25, predicted blood flow rates q and tissue perfusion are much larger than experimentally measured [Wel+15, Tbl. 4]. Consequently, oxygenation Y is also predicted to high. In the second case (CMPR) we essentially consider a shrinkage in radius of high caliber arterioles and venules which is motivated as the effect of compression forces caused by the tumor (s. Sec. 1.3). In this case predictions of oxygenation agree well with mammography data, and flow rates are lower. In the third case (METAB) we picked a different maximal rate of oxygen consumption M_0 of the Michaelis-Menten relation for each simulated tumor on the basis of a statistical log-normal distribution. Using a plausible spread, i.e. a standard deviation of 30% and a mean of M_0 of the base case, this case fails to lower oxygenation of tumors Y sufficiently for experimental agreement, i.e. at the given flow rates, the system is too insensitive to variations of the O₂ consumption rate. We further observe that the use of different initial ($t = 0$) networks yields a significant spread across all computed quantities [see Wel+15, Figs. 12 to 15]. We show that this variation can be traced back to the varying number of vascular trees R within the fixed simulation volume [Wel+15, Fig. 15D, and Appendix S4]. Note that initial networks generally consists of multiple arterial and venous trees, the inlets and outlets (tree roots) of which are prescribed arbitrarily [Wel+15, Fig. 7]. It is indeed quite easy to see that, with increasing R , vascular volume must decrease. This implies the presence of smaller average vascular radii, which has a drastic effect on blood flow due to the r^4 dependence of the blood flow resistance.

Moreover we considered a comparison of the full model to a simplified model of oxygen distribution where the intravascular PO₂ is constant. In contrast to the simplified model, the full model predicts O₂ depletion of the neovascular plexus at the tumor edge due to decreased hematocrit levels and depletion of isolated vascular threads simply due to their length. The predicted hematocrit H of intra-tumoral vessels is generally elevated. Therefore simplified models where P is proportional to H fail to predict O₂ depletion of isolated vascular threads.

4 Summarizing discussion

This section provides a concluding discussion of the papers of this thesis. First, implications of the incorporation of arterio-venous initial ($t = 0$) blood vessel networks are discussed. It follows a discussion of the results of simulations of drug transport, interstitial fluid flow and detailed intra- and extravascular oxygen distributions.

4.1 Tumor growth in vascularized tissues

Previously, Lee, Bartha and Rieger [BR06; LRB06] developed a model of vascularized solid tumor growth and capillary network remodeling. This model includes all essential ingredients to predict the morphological compartmentalization of tumor blood vessel networks in agreement with experimental data of melanoma and glioma [Döm+02; HWY99; Hol+99]. This compartmentalization is characterized by dense chaotic vascular sprouting at the tumor interface, a sharp decrease of vascular density into tumor spheroid where isolated dilated blood vessels are predominant, and finally the occurrence of necrotic regions caused by

hypoxia (s. Figs. 3, 4, and 5). The ingredients to obtain such characteristics from a theoretical model comprise tumor cells, an initial capillary network, blood flow, a growthfactor concentration field, an oxygen concentration field, and processes reflecting co-option, angiogenesis, vaso-dilation, regression and collapse.

It was concluded to extend the basic theoretical model with more faithful biophysical model details (s. Sec 3.1, 3.2 and below) and eliminate shortcomings such as unphysiological blood flow boundary conditions (s. Sec. 3.2). Thus, relevance for clinical applications is increased, in particular predictions of drug transport and oxygen distributions are more relevant for tumors in humans than previous work which was mostly guided by experimental animal models. Model extensions implemented comprise transvascular oxygen diffusion, as opposed to constant rate production (not to be mistaken for recent work [RW15]), computation of intravascular hematocrit distributions (phase separation effect), hematocrit and vessel radius dependent blood viscosity, acute-angled vascular bifurcations (s. Fig. 12c), arterio-venous initial blood-vessel networks of the host, a versatile continuum model of the tumor spheroid, and the extension to three dimensions (s. Sec. 3.3, 3.4).

Model predictions of average quantities such as radial distributions of microvascular density (MVD), blood flow, oxygenation and tumor density are robust against these model alterations. The parameters for vessel collapse probability $p^{(col)}$, wall degradation rate Δw , critical collapse shear stress $f^{(col)}$ and contact inhibition length of angiogenesis $l^{(spr)}$ naturally determine the MVD. However, we demonstrated that the abnormal qualities of tumor blood vessel networks are preserved, as described in the introduction, over a wide range of parameter values. This is true in particular for the rather drastic alteration of the introduction of arterio-venous blood vessel networks (AVNs) [WBR09]. Previously, state of the art were capillary-only networks (CNs) even for centimeter sized sections of tissue, without supplying or draining vessels. Therein, vessel segments are arranged in a lattice pattern, e.g. square or hexagonal. Initial CNs consist of identical capillaries. AVNs however, introduce vessels of varying caliber, wall thickness, and presumably resistance to collapse. Varying degrees of stability were therefore incorporated by the addition of a wall stability variable w associated with vascular segments. Thus vessels undergo a degeneration period before blood flow is pinched-off. A certain invariance against model details is expected and even required, because it would be implausible if the results were dependent on a specific abstraction of the biological reality (within reasonable accuracy).

Moreover, following [BR06], fractal dimension numbers were computed for vascular networks. Fractal dimension d_f is an extension of the conventional dimension to self-similar (fractal) objects, i.e. a line has $d_f = 1$, but a fractal curve within the two-dimensional plane can have d_f between 1 and 2 depending on how densely it permeates space. $d_f = 2$ corresponds to a solid object like a disc. For real objects of finite size several approximate metrics exists, e.g. the number obtained by box-counting [Man83]. Gazit et al. [Gaz+95] measured the dimension of photographs of tumor vascular networks and obtained $d_f^{exp} = 1.89 \pm 0.04$. Furthermore, in conventional percolation, sites of a lattice are randomly occupied with probability p . At some critical probability p_c , a percolating cluster forms that spans across the lateral size of the considered domain. The dimension of this cluster is exactly known $d_f^{perc} = 1.891$ [SA94]. [Gaz+95] hypothesized that fractal properties of tumor vascular networks emerge from an in-growth process through a heterogeneous extracellular matrix because d_f^{exp} is close to the dimension of invasive percolation, i.e. a fractal structure created by a random growth process with $d_f^{inv-perc} = 1.81$ [Fur+88]. On the other hand, Bartha and Rieger [BR06] obtained $d_f = 1.85$ by box-counting from the entire vasculature that was changed by tumor vascular remodeling. Since no ECM heterogeneities were modeled, it was hypothesized that the mechanism leading to the fractal properties is a random dilution process similar to conventional percolation. Lee, Rieger, and Bartha [LRB06] computed box-counting dimensions for three-dimensional networks and obtained $d_f = 2.52$, corresponding to the three-dimensional percolation cluster. Later, we computed box-counting dimensions for tumor networks obtained from the extended models [WBR08; WBR09; WR10]: For CNs based tumor vascular networks, d_f was obtained in the range between 1.6 and 1.9, depending on the MVD, where we varied either the critical collapse shear-stress $f^{(col)}$ or the collapse probability $p^{(col)}$ [WBR08]. Fractal dimensions

of tumor vascular networks obtained from simulations based on three-dimensional AVNs [WR10] yielded $d_f = 2.51 \pm 0.03$, in good agreement with percolation theory and [LRB06] where tumors in CNs are considered. However, accurate measurement of fractal dimensions of real and simulated tumor vascular networks is hardly possible due to their limited size [BR06]. It was suggested previously [BR06] that fractal dimension is mostly a function of MVD, which is supported in this thesis. Therefore it appears doubtful that d_f is a reliable means to discern subtle differences like invasive versus normal percolation.

Morphological analysis was approached from another angle in [WBR09], where spatial frequency distributions of (i) local MVD, (ii) area of clusters of necrotic tissue, and (iii) area of hot-spots of high MVD were computed for tumors grown in two-dimensional AVNs (s. Sec. 3.2). Predicted distributions show good agreement with a power law, and exhibit all the same exponent of -1.4 . A such algebraic decrease, in contrast to an exponential decrease, is known for systems at a critical threshold where systems undergo a phase transition. In the case of percolation, the critical threshold at $p = p_c$ marks the transition from isolated clusters to a single connected region. [BR06] suggested that the tumor vasculature is driven automatically into a state akin to the critical percolation cluster because vessels permeate the entire tumor. The mechanism responsible for this is shear-stress correlated vascular collapse, i.e. when vessels collapse, their blood flow is redirected through nearby vessels, increasing their shear-stress and stability. It is interesting to see this idea supported by predictions of algebraic distributions. These predictions are experimentally testable and, if confirmed, would support that real vascular networks of the interior of tumors are the result of a dilution process rather than the result of sprouting growth into a heterogeneous environment.

4.2 Arterio-venous blood vessel networks

Theoretical models for the construction of artificial arterial trees [SB93] and arterio-venous blood vessel networks (AVNs) [GK01] were conceived previously. We adopted the model developed by Godde and Kurz [GK01] with which they simulated realistic arterio-venous vascular patterns of the chorioallantoic membrane of chicken eggs. This model fits our requirements well since it is lattice-based and entire vascular networks are obtained from it, not just arterial trees. Later, we extended the model to three dimensions [WR10] and face centered cubic (FCC) lattices [Wel+15]. In principle the construction can be carried out on a cubic lattice, as done in [WR10], but the restriction to 90° branching angles (T-junctions) is quite unrealistic in contrast to narrower 60° angles (s. Fig. 12c) [ZM82]. Hence the later implementation was made for FCC lattices. By setting appropriate values for the lattice constant and capillary radii, the MVD and vascular volume of generated networks can be adjusted. Recently, we demonstrated simultaneous good agreement of quantities obtained from simulated initial networks [Wel+15] with MVD, relative blood volume (rBV), venous volume fraction ($vrBV$), perfusion (rBF) and oxygen saturation (Y) found in human breast tissue [Gro+05; Bea84; Vuj+03; Man+02; Wil+92].

Blood flow boundary conditions in CNs were implemented by imposing a global constant blood pressure gradient on boundary nodes of the network. This, however, leads to a selection of surviving tumor vessels preferably in the direction parallel to the imposed gradient [BR06; WBR08]. The explanation is simply that junctions of vessels that run perpendicular to the gradient lie on approximately equal blood pressure potentials and therefore no significant blood flow can occur, resulting in collapse of the vessels. AVNs abolish this artifact since there is no global flow direction.

On the other hand, simulations of tumor growth in AVNs exhibit high-caliber ($> 50 \mu\text{m}$ radius) vessels protruding into the tumor which form a backbone of stable vessels in-between which thinner vessels form short and straightforward paths [WBR09]. The flow resistance decreases in proportion to $1/r^4$ with radius r and is therefore, in comparison to capillaries, extremely low in such high-caliber vessels. Therefore, in analogy to electrical networks, the blood pressure (voltage) drop across them is also low. In zero-th order approximation the blood pressure is constant, i.e. high-caliber vessels act like a pressure boundary condition for adjacent capillaries. Short, directed paths, have a survival advantage as discussed above

for CNs. The distribution of tumor vessels thus becomes dependent on initial ($t = 0$) vascular networks and is generally heterogeneous and anisotropic. We attempted to quantify this behavior by correlation of tumor MVD ($t > 0$) versus the magnitude of blood pressure differences in-between vessels of initial ($t = 0$) AVNs (s. Sec. 3.2 and A). For instance, assuming an arteriole runs near a venule then a large spatial blood pressure gradient is present. When a tumor grows near this area, a connection (short cut) is formed by angiogenesis, imposing the spatial gradient onto blood flow through the newly formed vessel which is the more stable the steeper the gradient. An auxiliary field, interpolating the blood pressure of vessels, was computed of which the average gradient $\langle ||\nabla p|| \rangle$ was plotted versus the MVD. For local averages we obtain correlation coefficients ranging from 0.2 to 0.5 taken per simulation. A correlation coefficient of 0.9 was obtained for averages over entire tumors of a cohort of simulations [WBR09]. This finding suggests that an analysis of the blood vessel network surrounding the tumor might be useful in a clinical application, e.g. to calibrate MVD-based prognosis.

Moreover, we suggest that different architectures of tumor vascular networks which are observed in real tumors of the same tissue, e.g. breast tumors [Du+08] are the result of the, to some degree random, layout of the micro vasculature in which the tumor grows, rather than motivated in genetic origins. This idea is similar to the proposal of [Gaz+95] (see above). However, our work suggests that heterogeneity of the initial vascular network has a strong impact on the emerging tumor vasculature rather than heterogeneity of the ECM through which vascular sprouts grow.

Furthermore, regional blood volume rBV , perfusion rBF , hemoglobin concentrations c_{Hb} , average blood oxygen saturations Y and other derived quantities were computed for a cohort of simulated tumors [see Wel+15, Figs. 12 to 15]. A significant spread of these quantities was predicted due to the selection of different initial ($t = 0$) vascular tree configurations obtained from different, arbitrary, sets of tree root locations (RC1 through RC9) [see Wel+15, Fig. 7]. The origin of this spread lies founded in the variation of blood volume rBV with the number of vascular trees within the fixed simulation volume. Fewer trees require that the existing trees exhibit higher depth. Murray's law demands that each additional tree level exhibits vascular radii larger than the radii of child branches. The radii of capillaries is fixed by definition of the construction method. For these three reasons, the total vascular volume rBV increases with decreasing number of trees. We use Dirichlet blood pressure boundary conditions and therefore obtain a corresponding variation of blood flow rBF and of all other dependent variables. Differences among vascular root configurations are also reflected in local and global distributions of the gradient of the interpolated blood pressure $\langle ||\nabla p|| \rangle$ (s. Appendix A). Naturally, higher tree depths imply more high-caliber vessels, which implies the presence of steeper blood pressure differences in-between vessels. Whether simulated conditions reflect the physiological reality is currently unknown, however uncertainties, as demonstrated, should be taken into account for clinical applications.

Bartha and Rieger [BR06] suggested that MVD is presumably an unreliable tool for diagnostic because if the initial vascular network can satisfy the metabolic demand of tumor cells then tumor growth rate, MVD of the interior, and MVD of the tumor periphery is uncorrelated. Our model of AVNs supports this supposition since vascular hot-spots, i.e. clusters of locally increased MVD, appear in differing size and density depending on the initial network layout [see WBR09, Fig. 4 and 5]. The density of such hot-spots is used as a diagnostic tool [Döm+02]. A recent meta-study [Nic+08] of clinical data comes to the same conclusion. We agree with Bartha and Rieger [BR06] that correlations between MVD and the outcome of the disease is likely due to metastases which was not considered.

4.3 Intravascular drug conduction and blood flow

McDougall et al. [SRM+02; SAC06] first considered conduction of a tracer substance through tumor vascular networks using a simulation model of a time-dependent intravascular concentration distribution that was previously used in geo-engineering. Following them, we studied intravascular tracer conduction in stationary tumor vascular networks based on CNs [WBR08] and AVNs [WBR09; WR10]. Simply, a pulse, or a constant infusion, is applied

at inlet vessels, which is from there propagated down-stream through the vascular network. The unspectacular model predictions show tracer flowing through networks within a duration of seconds (AVNs) and ca. one minute (CNs). McDougall et al., on the other hand, consider a model system based on angiogenesis experiments on the cornea of a rabbit eye [Gim+74] which is denoted in the following as rabbit-eye model of vascularization. There, the tumor is not connected to an extensive vascular network, but instead, a single parent vessel spawns a few sprouts (angiogenesis) which travel a long distance of ca. 1 mm and branch into a dense network permeating a tumor spheroid and adjacent tissue. It was concluded that the tumor vasculature conducts drug poorly and that most drug bypasses the tumor. The cause of this contradiction appears to be dilution of the tracer concentration within the dense network near the tumor and much lower flow rates leading to transit times of the order of $10 - 30\text{ min}$. Moreover a vascular adaptation model was considered, leading to formation of shunts that bypass the tumor network [SAC06]. In our model this does not happen because the tumor is embedded within an efficiently conducting host network.

A good perfusion is consistent with several clinical studies of human tumors based on PET measurements [Wil+92; Man+02; Lee+85; Ito+82] where elevated perfusion rBF by factors of 4.7 to 5.2 were observed [s. Wel+15, Tbl. 4]. Blood flow velocities predicted by our model are of the order of magnitude of 1 mm/s , which is also the order of magnitude of blood flow velocities in normal capillaries [MH13]. However, it is well-known that blood flow in animal models is can be severely reduced to only 0.1 to 1 mm/s . The exact causes for discrepancy are presumably vessel compression and excessive blood plasma extravasation [JS10], both of which were not considered here.

4.4 Interstitial fluid flow

We incorporated arterio-venous networks (AVNs) as sources and drains of interstitial fluid [WR13] into a system that was previously considered within the scope of continuum models [Jai99; JTM07; ZSS07], network models based the rabbit-eye model [Wu+08; Wu+09], and capillary networks (CNs) [Wu+13]. Our model predicts an elevation of interstitial fluid pressure (IFP) to 49 mmHg within the experimentally measured range for human tumors [JTM07], and close to the average blood pressure within the simulated tumor. A peak radial flow velocity of $0.2\text{ }\mu\text{m/s}$ is predicted at the tumor edge, also in agreement with the literature.

It was often suggested that an elevated IFP poses a barrier to drug delivery [MT06; Hel+04; Jai99; Wu+13]. However, the reason for this cannot simply be a decreased transvascular hydrostatic pressure gradient that drives extravasation according to the Starling equation (9). To the contrary, in the standard models of the literature (s. Sec. 2.7), interstitial fluid flow is analogous to an electrical current through a chain of resistors, of which one resistor, namely leaky tumor vessel walls, is particularly small. Thus, an increase in leakiness, i.e. an elevation of IFP, would actually increase the liquid flux throughout the tumor, as predicted by our model. However, our analysis is restricted to good perfusion, where only a negligible liquid fraction escapes in spite of leakiness. Otherwise the way through tumorous tissue into lymphatics could presumably present an alternative well conducting pathway, draining downstream vessels of blood plasma, resulting in reported low flow velocities [JS10].

The recent theoretical work [Wu+13], using CNs and a sophisticated model of tumor growth that incorporates vessel compression due to IFP, comes to similar conclusions about the role of various permeabilities. However, it was concluded that IFP is a barrier with little supporting numerical evidence, i.e. no simulation of actual drug transport was performed. Results from other work [Wu+08; Wu+09] may not be directly applicable for human tumors since the physiologically unrealistic rabbit-eye model was considered.

4.5 Interstitial drug transport

In order to shed light on barrier to drug delivery, transport through tissue by advection and diffusion after extravasation must be taken into account. For this purpose, we analyzed a simple model, according to which, we computed time-dependent concentration distributions

of drug in simulated tissues containing a vascularized tumor, grown in three-dimensional AVNs [WR13]. The considered tumors were static, and obtained by simulations guided by melanoma and glioma. In addition to concentration distributions, we also computed time-integrated local doses as time-independent metrics of drug delivery. The base case is guided by data for Doxorubicin [Pri+05; Zhe+01; Sin+09], and many more cases and parameter variations were explored. Experimentally, the spatio-temporal distribution of drugs has not been studied much due to the lack of suitable markers for direct observation. Doxorubicin concentration distributions were observed exploiting auto fluorescence. Predictions of our model are in fair agreement with the above Refs. However, quantitative data are hardly available.

The model predicts that, in general, the dose delivered is subject to a compartmentalization similar to the vascular density (MVD). For the base case and most other cases, the average dose within the center of the tumor spheroid is significantly lower than in normal tissue, and doses are highest at the tumor edge. This result provides an additional explanation of the incompletely understood success of combination therapies of anti-angiogenic agents and chemotherapy, whereas a single drug fails to improve survival [Jai13]. TCs behind the tumor edge might be killed by high doses of chemotherapeutics, effective against cycling cells, whereas the TC population of the tumor center is reduced by necrosis caused by hypoxia. A monotherapy might leave the one or the other part of the TC population unaffected. The mechanism by which combination therapies are known to act is suppression of the activity caused by vascular growth factors, leading to a decreased vascular permeability. This allows throughout better delivery of chemotherapeutics due to improved perfusion [Jai13].

Variation of the various permeabilities shows that average doses delivered increase in differing sensitivity with the permeability. Doses showed the highest sensitivity with respect to interstitial hydraulic and diffusive permeabilities which were varied simultaneously. As Wu et al. [Wu+13] already suggested this could be exploited for therapy, however care must be taken to not accidentally aggravate tumor invasiveness [SS11] or metastatic shedding of TCs. Moreover, angiogenic normalization therapy, i.e. a reduction of permeability and pruning of superfluous vessels [Jai13], might be ineffective or even detrimental for tumors where blood flow is negligibly impaired.

Doxorubicin molecules have a molar mass of 543 g/mol . Such, and lighter molecules have the advantage that diffusion helps to distribute a substantial dose homogeneously around blood vessels. Recent simulations of another group [Sin+09] predicted very smooth and homogeneous concentration distributions of the more diffusive drug Cisplatin (300 g/mol) arising from extravasation from a CN. Since the diffusion coefficient decreases with the molar mass of the solute, transport of drugs like nano-particles is strongly advection dominated. Such a case was considered previously with the help of a simple one-dimensional continuum model, predicting that hardly any drug is released by the vascular network into the tumor center [Jai99]. Our model predicts interstitial drug concentrations that follow the stream of interstitial fluid in significant concentrations through the largest parts of the tumor spheroid, starting from the initial insertion through the vasculature. However, simulations frequently yielded small isolated islands behind the tumor edge where no noteworthy dose had been delivered within the time frame of the simulation of 96 h . Presumably, this discrepancy to earlier work [Jai99] is caused by the discrete nature of the blood vessel network allowing for flow in-between vessel of different blood pressure levels. However the radial flow component vanishes by chance at some places as dictated by the random layout of the vascular network. Thus locations further outwards are hardly supplied with drug [WR13, Fig. 11]. This suggests that a mono-therapy with agents of high molar mass would be prone to recurring cancer.

4.6 Detailed model of oxygen distribution

Extremely good perfusion of tumor vessels cannot be assumed for tumors in general. This necessitates consideration of spatially varying substance concentrations because a substantial fraction may be lost during the transit through the tumor. Our recently developed computational method attempts to solve this problem for oxygen concentration distributions

on macroscopic scales by solution of coupled systems of differential equations for intravascular and extravascular oxygen transport and diffusion to obtain a self-consistent numerical solution [Wel+15]. This is computationally very expensive, however, this expense is justified since few simplifying assumptions need to be made for the vascular network and blood flow.

Maps of tissue oxygen partial pressure (PO₂) distributions emerging for various vascular networks and tissues were calculated previously according to the mathematical description of oxygen transport that we also use [Sec+04; Gol08, and the refs. therein]. Our numerical solution is a compromise between computational demand and presumably more accurate methods [Sec+04; Gol08]. The method allows computation of oxygenation in simulation boxes of ca. 0.5 cm^3 on standard hardware (i7-2600K, 3.4 GHz, 4GB Ram) within an hour. This was by far not achievable with the Green’s function based method [Sec+04]. However, our method suffers from sub-linear convergence with the numerical grid constant h , i.e. the results depend strongly on the fineness of the discretization [s. Wel+15, S1 Appendix, Fig.4]. For a small artificial vasculature we obtained good qualitative agreement with the Green’s function method but the computed PO₂ differs up to 10% of the value at the inlet. In spite of that, we obtain good agreement with experimentally data of normal breast tissue, and use the method to analyze oxygenation of breast tumors (see below).

Critical to performance and accuracy is the regularization of the singular source term $2\pi r j_{tv}$ of the tissue O₂ diffusion equation, containing Dirac δ distributions, in conjunction with an efficient numerical scheme for the solution of the diffusion equation. In general the method should yield a sparse system matrix to enable numerical solutions in $O(n \log n)$ time in the number of unknowns n . Moreover, the method should allow for coarse grid constants h of 5 to 30 μm to keep the number of unknowns low and simultaneously resolve O₂ concentration gradients around tumor vessels. D’Angelo [DAn12] achieved optimal convergence by adaptive tessellation of the tissue domain, i.e. the discretization becomes more fine grained near singular source terms (blood vessels).

Our method was applied to the case of breast tumors for which several groups measured hemoglobin concentrations c_{Hb} and average blood oxygen saturations Y in large cohorts of patients [Gro+05; Spi+05; Tar+05; Tar12]. The average saturation Y within these tumors can be above or below the saturation measured within healthy tissue. Moreover, saturations Y are high when the hemoglobin concentration c_{Hb} is also high, but tumors exhibiting low c_{Hb} exhibit broader ranges of saturations Y . In our base case (BASE), the use of different initial ($t = 0$) root node configurations (RC1 through RC9) leads to a spread in tumor oxygen saturations, but it does not predict the experimentally observed dependency of $Y(\text{tumor})$ versus $Y(\text{normal})$ since predicted $Y(\text{tumor})$ is always larger than $Y(\text{normal})$ [Wel+15, Fig.12]. Therefore we considered a phenomenological ad-hoc extension of the model by vaso-compression, i.e. essentially a reduction of the radii of arterioles and venules. This leads to good agreement with mammography data (case CMPR) [Wel+15, Fig.13]. The reason for this is the reduction of blood flow, thus draining a greater fraction of the supplied O₂ in order to meet metabolic demand. Thus, rather subtle variations in arterial radii can lead to large blood flow variations, in addition to fluctuations introduced by varying initial networks of the host. The experimental data might imply that tumor vascular networks that exhibit higher saturations than normal are vastly different in their vascular architecture than networks that exhibit low saturations. However, our simulations suggest that these networks nevertheless share the traits of typical tumor vascular networks, i.e. as outlined in the introduction.

It is standard for tumor growth models to assume a constant vascular PO₂. By definition, this approximation does not explain variation of saturations Y in the cohort of patients, since then Y becomes an input parameter. In comparison with the full model, the constant-PO₂ approximation over-predicts PO₂ in the neo-vascular plexus around the tumor periphery, and it fails to predict local oxygen depletion in vessels threading the tumor center. This should be taken into account in applications like therapy planing and other pharmacokinetical studies, or else, the efficacy of the therapy might be overestimated.

Previously, Secomb’s Greensfunction method [HS89] was used to study oxygen concentration distributions in microscopic tissue sections using blood vessel networks of tumors in animal models [Sec+04] as well as theoretical idealizations of the vasculature of the human brain [SD13; SSD11]. The finite difference method by Goldman and Popel [GP00] was

used in several publications [Gol08; FGE13, and the Refs. therein] to study oxygen concentrations in capillary networks of muscle fibers. There are several other papers in which specifically the oxygen distribution in tumors is considered [DM89; Ske+12; KB06; Mon+11; DTK03; EPK13; Lag+13; LKB14]. However, in these works, the vasculature is represented by extremely simplified idealizations, i.e. by arrays of disjoint, often parallel, capillaries. The vascular oxygen saturation (or partial pressure) is an input parameter in these models and the macroscopic compartmentalization of the tumor vasculature is neglected. Therefore, such models are more suited to determine precise statistical frequency distributions of oxygen concentration levels in tissue, given a specific microvascular density and blood oxygen concentration.

4.7 Limitations and outlook

During the course of this thesis, models and computer programs were developed which could be further developed into an integrated model with which tumor growth and the efficacy of drugs could be simulated in great detail and physiological relevance. For this purpose, several modules, e.g. interstitial fluid flow, detailed oxygen distribution modeling, etc. should be integrated into the time dependent simulation of tumor growth. In a proper framework, modules could be swapped, for instance for specific pharmacokinetics models. Other groups, who however are not considering arterio-venous networks, are developing similar models [Low+10; Wu+13; Sin+09; San+06] with the final goal of patient specific predictive power.

To obtain a more faithful cohort of initial blood vessel networks, a systematic analysis of initial networks could be carried out. Experimental data of blood volume, rBV , perfusion rBF , and so on, could be used to select a cohort of networks that satisfies experimentally observed statistical distributions. Current networks are unrealistic in some aspects, e.g. they contain no anastomosis, i.e. cross-links between vascular trees [MH13]. Therefore it would be ideal to use real scanned and digitized blood vessel networks. In principle it is possible to automatically reconstruct networks from voxel data, as done previously [Cas+06; Lee+07; GFP10; Sta+14]. A data base of many large scale networks of normal tissues and corresponding tumor networks at different growth stages could be built in future. Not only would this eliminate the need to construct artificial initial networks, but it would also allow a very detailed comparison between model predictions and real tumor networks. At best, scanned network should be obtained from human tissue and be complete, i.e. including all capillaries. However, this is likely not yet possible at the present time.

A major limitation of our model is the restricted applicability to only well perfused tumors. The prediction of good perfusion is inherent to our basic model of vascular remodeling since tumor vessels can only dilate, not shrink, and surviving vessels must route the blood volume coming from the surrounding vasculature. Therefore it would be worthwhile to explore biophysically motivated extensions to vascular dilation and regression processes rather than limiting blood flow by ad-hoc shrinkage of arterial radii. One such possible extension already exists in the vascular adaptation model [PRS05], variations of which are frequently used in other mathematical models of tumor growth. Essentially, in this model, a shrinking-tendency is balanced by a wall shear-stress dependent growth signal. Moreover, compression of blood vessels is insufficiently understood. Forces involved were studied quantitatively, separately, to some degree (see Refs. below). Obviously, the deformation of vessel walls is governed by a balance of forces which are tensile and compressive stress within the vessel wall, blood pressure, interstitial fluid pressure, and solid pressure. Solid pressure compresses vessels [Cha+13; Sty+12; Cha+14] and there is evidence that an elevated IFP aids in compression of vessels [Gri+99; Del+14]. However, the interplay of these forces still seems somewhat elusive, and there is, to our knowledge, no predictive model of the response of the vessel wall that takes these factors into account. A physical consideration based on first principles e.g. with the help of a elasto-plastic mechanical model of vascular walls in combination with a mechanical model of tissue could help elucidate the forces involved and ultimately yield better predictions of blood flow.

Even with ad-hoc compression, our model predicts regional blood flow rBF that is about

a factor of 5 to 10 above measured data from breast tumors [s. Wel+15, Tbl. 4]. This failure might also lie founded in the size of the considered tumors (4 mm in diameter, simulated, versus centimeter sized real tumors). Kallinowski et al. [Kal+89] showed that blood flow r^{BF} of experimental tumors ($2-0.3\text{ ml/g/min}$) correlates negatively with size ($0.1-10\text{ cm}^3$ tumor volume), consistent with our results. The reasons for this size dependency are currently unknown. However, it suggests that vasculatures can only provide a fixed blood flow per surface area [s. Wel+15, Sec. "Results of the computational model"]. Hence r^{BF} would decrease with increasing surface to volume ratio of the tumor spheroid. If, in future, tumors with low flow rates will be considered, our models of blood flow, interstitial fluid flow and drug transport will likely need revision to take loss of blood plasma and intravascular concentration variations into account. Mathematically this could be treated in the style of our detailed simulation of oxygen distributions.

In conclusion, it was demonstrated that tumor vascular morphology and all derived biophysical quantities such as oxygenation depend on the initial vasculature in which the tumor grows. The basic transformation mechanism is wall shear-stress correlated vessel regression. Furthermore, concentric compartmentalization of predicted drug doses provides explanation for the efficacy of combined anti-angiogenic, cytotoxic therapies. Heterogeneous interstitial fluid flow patterns might be a barrier to delivery of nano-scale therapeutic agents. Finally our model requires further work to make it applicable to tumors that exhibit low blood flow rates.

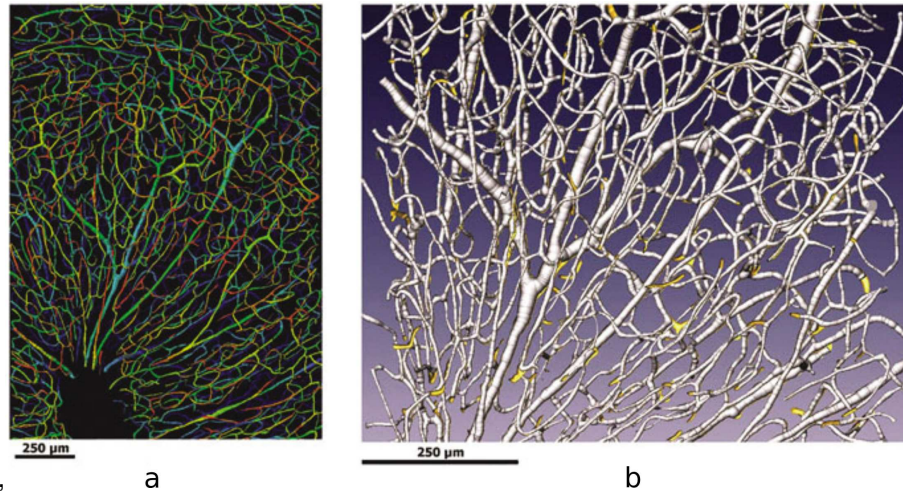


Figure 16. Reconstruction of a cranial blood vessel network from three-dimensional microscopy data: (a) Projection view of the mosaic obtained from microscopy, color coded by depth. (b) 3D visualization of the reconstructed network with associated vessel radii (white cylinders) and original data (yellow isosurfaces). (Reprinted from [Cas+06] with permission. Copyright 2006 Taylor & Francis LLC)

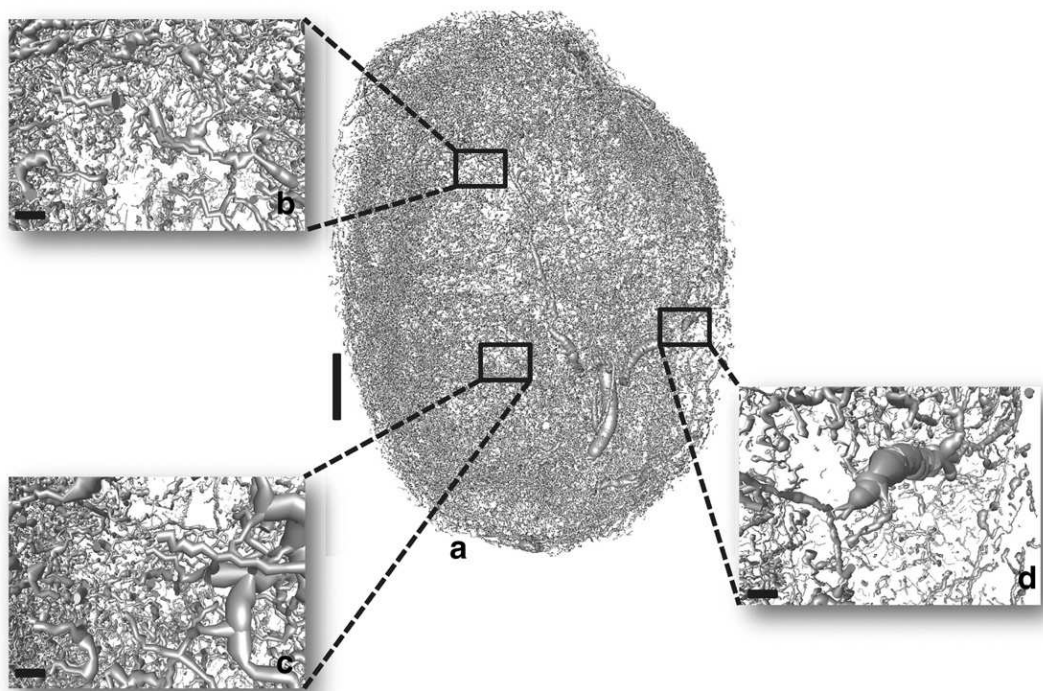


Figure 17. Reconstruction of a blood vessel network of a breast tumor: The network was reconstructed from 3D micro-CT data obtained from a blood vessel network of a breast cancer bearing mouse (scale bar = 1 mm). The insets (b-d) show magnified views (scale bars = 100 μm).

References

- [ABM03] T. Alarcon, H. Byrne, and P. Maini. “A cellular automaton model for tumour growth in inhomogeneous environment”. *Journal of Theoretical Biology* 225 (2003), pp. 257–274.
- [AC98] A. Anderson and M. A. J. Chaplain. “Continuous and Discrete Mathematical Models of Tumor-induced Angiogenesis”. *Bulletin of Mathematical Biology* 60.857-900 (1998), pp. 857–899.
- [Ake+98] E. Aker et al. “A Two-Dimensional Network Simulator for Two-Phase Flow in Porous Media”. English. *Transport in Porous Media* 32.2 (1998), pp. 163–186. DOI: 10.1023/A:1006510106194. URL: <http://dx.doi.org/10.1023/A:1006510106194>.
- [AM04] D. Ambrosi and F. Mollica. “The role of stress in the growth of a multicell spheroid”. *J Math Biol* 48.5 (May 2004), pp. 477–499.
- [Amb+11] D. Ambrosi et al. “Perspectives on biological growth and remodeling”. *J Mech Phys Solids* 59.4 (Apr. 2011), pp. 863–883.
- [AP09] D. Ambrosi and L. Preziosi. “Cell adhesion mechanisms and stress relaxation in the mechanics of tumours”. *Biomech Model Mechanobiol* 8.5 (Oct. 2009), pp. 397–413.
- [APS06] N. J. Armstrong, K. J. Painter, and J. A. Sherratt. “A continuum approach to modelling cell-cell adhesion”. *J. Theor. Biol.* 243.1 (Nov. 2006), pp. 98–113.
- [AY13] J. Ando and K. Yamamoto. “Flow detection and calcium signalling in vascular endothelial cells”. *Cardiovasc. Res.* 99.2 (July 2013), pp. 260–268.
- [Bai+11] J. W. Baish et al. “Scaling rules for diffusive drug delivery in tumor and normal tissues”. *Proc. Natl. Acad. Sci. U.S.A.* 108.5 (Feb. 2011), pp. 1799–1803.
- [Bas+11] M. Basan et al. “Dissipative particle dynamics simulations for biological tissues: rheology and competition”. *Phys Biol* 8.2 (Apr. 2011), p. 026014.
- [BBL03] C. J. Beward, H. M. Byrne, and C. E. Lewis. “A multiphase model describing vascular tumour growth”. *Bull. Math. Biol.* 65.4 (July 2003), pp. 609–640.
- [Bea01] D. A. Beard. “Computational framework for generating transport models from databases of microvascular anatomy”. *Ann Biomed Eng* 29.10 (Oct. 2001), pp. 837–843.
- [Bea84] R. P. Beaney. “Positron emission tomography in the study of human tumors”. *Semin Nucl Med* 14.4 (Oct. 1984), pp. 324–341.
- [Bet+06] R. Betteridge et al. “The impact of cell crowding and active cell movement on vascular tumour growth”. *Networks and Heterogeneous Media* 1.4 (2006), pp. 515–535.
- [BHD04] P. H. Burri, R. Hlushchuk, and V. Djonov. “Intussusceptive angiogenesis: its emergence, its characteristics, and its significance”. *Dev. Dyn.* 231.3 (Nov. 2004), pp. 474–488.
- [BHM01] W. L. Briggs, V. E. Henson, and S. F. McCormick. *A Multigrid Tutorial*. The Society for Industrial and Applied Mathematics (SIAM), 2001.
- [BJ89] L. T. Baxter and R. K. Jain. “Transport of fluid and macromolecules in tumors. I. Role of interstitial pressure and convection”. *Microvasc. Res.* 37 (1989), pp. 77–104.
- [BKZ92] J. U. Brackbill, D. B. Kothe, and C. Zemach. “A continuum method for modeling surface tension”. *Journal of Computational Physics* 100 (June 1992), pp. 335–354. DOI: 10.1016/0021-9991(92)90240-Y.
- [BNJ97] J. W. Baish, P. A. Netti, and R. K. Jain. “Transmural coupling of fluid flow in microcirculatory network and interstitium in tumors”. *Microvasc. Res.* 53 (1997), pp. 128–141.

- [BP03] H. Byrne and L. Preziosi. “Modelling solid tumour growth using the theory of mixtures”. *Math Med Biol* 20.4 (Dec. 2003), pp. 341–366.
- [BR06] K. Bartha and H. Rieger. “Vascular network remodeling via vessel cooption, regression and growth in tumors”. *J. Theor. Biol.* 241 (2006), pp. 903–918. DOI: <http://dx.doi.org/10.1016/j.jtbi.2006.01.022>. URL: <http://www.sciencedirect.com/science/article/pii/S0022519306000373>.
- [Bru+03] A. Bru et al. “The Universal Dynamics of Tumor Growth”. *Biophysical Journal* 85 (2003), pp. 2948–2961.
- [Buc+14] C. F. Buchanan et al. “Flow shear stress regulates endothelial barrier function and expression of angiogenic factors in a 3D microfluidic tumor vascular model”. *Cell Adh Migr* 8.5 (2014), pp. 517–524.
- [BW04] J. M. Brown and W. R. Wilson. “Exploiting tumour hypoxia in cancer treatment”. *Nat. Rev. Cancer* 4.6 (June 2004), pp. 437–447.
- [Byr+06] H. M. Byrne et al. “MODELLING THE RESPONSE OF VASCULAR TUMOURS TO CHEMOTHERAPY: A MULTISCALE APPROACH”. *Mathematical Models and Methods in Applied Sciences* 16.supp01 (2006), pp. 1219–1241.
- [Cai+11] Y. Cai et al. “Coupled modelling of tumour angiogenesis, tumour growth and blood perfusion”. *Journal of Theoretical Biology* 279.1 (2011), pp. 90–101. DOI: <http://dx.doi.org/10.1016/j.jtbi.2011.02.017>. URL: <http://www.sciencedirect.com/science/article/pii/S0022519311001196>.
- [Cas+06] F. Cassot et al. “A novel three-dimensional computer-assisted method for a quantitative study of microvascular networks of the human cerebral cortex”. *Microcirculation* 13.1 (Jan. 2006), pp. 1–18.
- [CGP06] M. A. Chaplain, L. Graziano, and L. Preziosi. “Mathematical modelling of the loss of tissue compression responsiveness and its role in solid tumour development”. *Math Med Biol* 23 (Sept. 2006), pp. 197–229.
- [Cha+13] V. P. Chauhan et al. “Angiotensin inhibition enhances drug delivery and potentiates chemotherapy by decompressing tumour blood vessels”. *Nat Commun* 4 (2013), p. 2516.
- [Cha+14] V. P. Chauhan et al. “Compression of pancreatic tumor blood vessels by hyaluronan is caused by solid stress and not interstitial fluid pressure”. *Cancer Cell* 26.1 (July 2014), pp. 14–15.
- [Cia+13] P. Ciarletta et al. “Mechano-transduction in tumour growth modelling”. *Eur Phys J E Soft Matter* 36.3 (Mar. 2013), p. 23.
- [CJ00] P. Carmeliet and R. Jain. “Angiogenesis in cancer and other diseases”. *Nature* 407 (2000), pp. 249–257.
- [CJ11] P. Carmeliet and R. K. Jain. “Molecular mechanisms and clinical applications of angiogenesis”. *Nature* 473.7347 (May 2011), pp. 298–307.
- [CZ14] L. Cattaneo and P. Zunino. “A computational model of drug delivery through microcirculation to compare different tumor treatments”. *Int J Numer Method Biomed Eng* 30.11 (Nov. 2014), pp. 1347–1371.
- [DAn12] C. D’Angelo. “Finite Element Approximation of Elliptic Problems with Dirac Measure Terms in Weighted Spaces: Applications to One- and Three-dimensional Coupled Problems”. *SIAM Journal on Numerical Analysis* 50.1 (2012), pp. 194–215.
- [Dav04] T. A. Davis. “Algorithm 832: UMFPACK V4.3—an Unsymmetric-pattern Multifrontal Method”. *ACM Trans. Math. Softw.* 30.2 (June 2004), pp. 196–199. DOI: [10.1145/992200.992206](http://dx.doi.org/10.1145/992200.992206). URL: <http://doi.acm.org/10.1145/992200.992206>.

- [Del+14] K. E. DelGiorno et al. "Response to Chauhan et Al.: interstitial pressure and vascular collapse in pancreas cancer-fluids and solids, measurement and meaning". *Cancer Cell* 26.1 (July 2014), pp. 16–17.
- [DH05] D. Drasdo and S. Höhme. "A single-cell-based model of tumor growth in vitro: monolayers and spheroids". *Physical Biology* 2 (2005), pp. 133–147.
- [DM89] P. Degond and S. Mas-Gallic. "The Weighted Particle Method for Convection-Diffusion Equations. Part 1: The Case of an Isotropic Viscosity". *Mathematics of Computation* 53.188 (1989), pp. 485–507.
- [Döm+02] B. Döme et al. "Vascularization of cutaneous melanoma involves vessel co-option and has clinical significance". *The Journal of Pathology* 197.3 (2002), pp. 355–362.
- [Döm+07] B. Döme et al. "Alternative vascularization mechanisms in cancer: Pathology and therapeutic implications". *Am. J. Pathol.* 170.1 (Jan. 2007), pp. 1–15.
- [Dom+14] T. Domazet-Lošo et al. "Naturally occurring tumours in the basal metazoan Hydra". *Nat Commun* 5 (2014), p. 4222.
- [DTK03] A. Dasu, I. Toma-Dasu, and M. Karlsson. "Theoretical simulation of tumour oxygenation and results from acute and chronic hypoxia". *Phys Med Biol* 48.17 (Sept. 2003), pp. 2829–2842.
- [Du+08] J. Du et al. "Microvascular architecture of breast lesions: evaluation with contrast-enhanced ultrasonographic micro flow imaging". *J Ultrasound Med* 27.6 (June 2008), pp. 833–842.
- [EHH09] H. Enderling, L. Hlatky, and P. Hahnfeldt. "Migration rules: tumours are conglomerates of self-metastases". *Br. J. Cancer* 100.12 (June 2009), pp. 1917–1925.
- [End+09] H. Enderling et al. "Paradoxical dependencies of tumor dormancy and progression on basic cell kinetics". *Cancer Res.* 69.22 (Nov. 2009), pp. 8814–8821.
- [ENW10] M. Egeblad, E. S. Nakasone, and Z. Werb. "Tumors as organs: complex tissues that interface with the entire organism". *Dev. Cell* 18.6 (June 2010), pp. 884–901.
- [EPK13] I. Espinoza, P. Peschke, and C. P. Karger. "A model to simulate the oxygen distribution in hypoxic tumors for different vascular architectures". *Med Phys* 40.8 (Aug. 2013), p. 081703.
- [Erb+06] R. Erber et al. "EphB4 controls blood vascular morphogenesis during postnatal angiogenesis". *EMBO J.* 25.3 (Feb. 2006), pp. 628–641.
- [FGE13] G. M. Fraser, D. Goldman, and C. G. Ellis. "Comparison of generated parallel capillary arrays to three-dimensional reconstructed capillary networks in modeling oxygen transport in discrete microvascular volumes". *Microcirculation* 20.8 (Nov. 2013), pp. 748–763.
- [Fol71] J. Folkman. "Tumor angiogenesis: therapeutic implications". *N. Engl. J. Med.* 285.21 (Nov. 1971), pp. 1182–1186.
- [Fur+88] L. Furuberg et al. "Dynamics of invasion percolation". *Phys. Rev. Lett.* 61.18 (Oct. 1988), pp. 2117–2120.
- [Gaz+95] Y. Gazit et al. "Scale-Invariant Behavior and Vascular Network Formation in Normal and Tumor Tissue". *Physical Review Letters* 75.12 (1995), pp. 2428–2431.
- [GBE04] D. Goldman, R. M. Bateman, and C. G. Ellis. "Effect of sepsis on skeletal muscle oxygen consumption and tissue oxygenation: interpreting capillary oxygen transport data using a mathematical model". *Am. J. Physiol. Heart Circ. Physiol.* 287.6 (Dec. 2004), H2535–2544.

- [GBE06] D. Goldman, R. M. Bateman, and C. G. Ellis. "Effect of decreased O₂ supply on skeletal muscle oxygenation and O₂ consumption during sepsis: role of heterogeneous capillary spacing and blood flow". *Am. J. Physiol. Heart Circ. Physiol.* 290.6 (June 2006), H2277–2285.
- [Ger+03] H. Gerhardt et al. "VEGF guides angiogenic sprouting utilizing endothelial tip cell filopodia". *The Journal of Cell Biology* 161.6 (2003), pp. 1163–1177.
- [Gev11] J. L. Gevertz. "Computational modeling of tumor response to vascular-targeting therapies—part I: validation". *Comput Math Methods Med* 2011 (2011), p. 830515.
- [GFP10] R. Guibert, C. Fonta, and F. Plouraboue. "Cerebral blood flow modeling in primate cortex". *J. Cereb. Blood Flow Metab.* 30.11 (Nov. 2010), pp. 1860–1873.
- [Gim+74] M. Gimbrone et al. "Tumor growth and neovascularization: an experiment model using the rabbit cornea". *Journal of the National Cancer Institute* 52 (1974), pp. 413–427.
- [GK01] R. Gödde and H. Kurz. "Structural and Biophysical Simulation of Angiogenesis and Vascular Remodeling". *Developmental Dynamics* 220 (2001), pp. 387–401.
- [Goe+08] W. Goettsch et al. "Flow-dependent regulation of angiopoietin-2". *J. Cell. Physiol.* 214.2 (Feb. 2008), pp. 491–503.
- [Gol08] D. Goldman. "Theoretical models of microvascular oxygen transport to tissue". *Microcirculation* 15.8 (Nov. 2008), pp. 795–811.
- [GP00] D. Goldman and A. S. Popel. "A computational study of the effect of capillary network anastomoses and tortuosity on oxygen transport". *J. Theor. Biol.* 206.2 (Sept. 2000), pp. 181–194.
- [Gri+99] G. Griffon-Etienne et al. "Taxane-induced apoptosis decompresses blood vessels and lowers interstitial fluid pressure in solid tumors: clinical implications". *Cancer Res.* 59.15 (Aug. 1999), pp. 3776–3782.
- [Gro+05] D. Grosenick et al. "Time-domain scanning optical mammography: II. Optical properties and tissue parameters of 87 carcinomas". *Phys Med Biol* 50.11 (June 2005), pp. 2451–2468.
- [Har02] A. L. Harris. "Hypoxia—a key regulatory factor in tumour growth". *Nat. Rev. Cancer* 2.1 (Jan. 2002), pp. 38–47.
- [HB13] M. Hubbard and H. Byrne. "Multiphase modelling of vascular tumour growth in two spatial dimensions". *Journal of Theoretical Biology* 316 (2013), pp. 70–89. DOI: <http://dx.doi.org/10.1016/j.jtbi.2012.09.031>. URL: <http://www.sciencedirect.com/science/article/pii/S0022519312005097>.
- [Hel+04] C. H. Heldin et al. "High interstitial fluid pressure - an obstacle in cancer therapy". *Nat. Rev. Cancer* 4.10 (2004), pp. 806–813.
- [Hel+96] J. D. Hellums et al. "Simulation of intraluminal gas transport processes in the microcirculation". *Ann Biomed Eng* 24.1 (1996), pp. 1–24.
- [Hel+97] G. Helmlinger et al. "Interstitial pH and pO₂ gradients in solid tumors in vivo: high-resolution measurements reveal a lack of correlation". *Nat. Med.* 3.2 (Feb. 1997), pp. 177–182.
- [Hol+99] J. Holash et al. "Vessel Cooption, Regression, and Growth in Tumors Mediated by Angiopoietins and VEGF". *Science* 284 (1999), pp. 1994–1998.
- [HS89] R. Hsu and T. W. Secomb. "A Green's function method for analysis of oxygen delivery to tissue by microvascular networks". *Mathematical Biosciences* 96.1 (1989), pp. 61–78.
- [HT73] J. Hopcroft and R. Tarjan. "Algorithm 447: Efficient Algorithms for Graph Manipulation". *Commun. ACM* 16.6 (June 1973), pp. 372–378. DOI: 10.1145/362248.362272. URL: <http://doi.acm.org/10.1145/362248.362272>.

- [HW11] D. Hanahan and R. A. Weinberg. "Hallmarks of cancer: the next generation". *Cell* 144.5 (Mar. 2011), pp. 646–674.
- [HWY99] J. Holash, S. Wiegand, and G. Yancopoulos. "New model of tumor angiogenesis: dynamic balance between vessel regression and growth mediated by angiopoietins and VEGF". *Oncogene* 18 (1999), pp. 5356–5362.
- [Ins08] N. C. Institute. *Physical Sciences in Oncology*. 2008. URL: <http://physics.cancer.gov/>.
- [Ito+82] M. Ito et al. "Measurement of regional cerebral blood flow and oxygen utilisation in patients with cerebral tumours using ^{15}O and positron emission tomography: analytical techniques and preliminary results". *Neuroradiology* 23.2 (1982), pp. 63–74.
- [Jai13] R. K. Jain. "Normalizing tumor microenvironment to treat cancer: bench to bedside to biomarkers". *J. Clin. Oncol.* 31.17 (June 2013), pp. 2205–2218.
- [Jai14] R. K. Jain. "An indirect way to tame cancer". *Sci. Am.* 310.2 (Feb. 2014), pp. 46–53.
- [Jai87] R. K. Jain. "Transport of molecules across tumor vasculature". *Cancer Metastasis Rev.* 6.4 (1987), pp. 559–593.
- [Jai99] R. K. Jain. "Transport of molecules, particles, and cells in solid tumors". *Annu Rev Biomed Eng* 1 (1999), pp. 241–263.
- [JB88] R. K. Jain and L. T. Baxter. "Mechanisms of heterogeneous distribution of monoclonal antibodies and other macromolecules in tumors: significance of elevated interstitial pressure". *Cancer Res.* 48.24 Pt 1 (Dec. 1988), pp. 7022–7032.
- [JS10] R. K. Jain and T. Stylianopoulos. "Delivering nanomedicine to solid tumors". *Nat Rev Clin Oncol* 7.11 (Nov. 2010), pp. 653–664.
- [JTM07] R. K. Jain, R. T. Tong, and L. L. Munn. "Effect of vascular normalization by antiangiogenic therapy on interstitial hypertension, peritumor edema, and lymphatic metastasis: insights from a mathematical model". *Cancer Res.* 67.6 (2007), pp. 2729–2735.
- [Kal+89] F. Kallinowski et al. "Tumor blood flow: the principal modulator of oxidative and glycolytic metabolism, and of the metabolic micromilieu of human tumor xenografts in vivo". *Int. J. Cancer* 44.2 (Aug. 1989), pp. 266–272.
- [KB06] C. J. Kelly and M. Brady. "A model to simulate tumour oxygenation and dynamic [^{18}F]-Fmiso PET data". *Phys Med Biol* 51.22 (Nov. 2006), pp. 5859–5873.
- [KL00] P. Knabner and A. L. *Numerik partieller Differentialgleichungen*. Springer Verlag, 2000.
- [KR15] S. V. Karakashev and M. J. Reginato. "Progress toward overcoming hypoxia-induced resistance to solid tumor therapy". *Cancer Manag Res* 7 (2015), pp. 253–264.
- [Kro19] A. Krogh. "The number and distribution of capillaries in muscles with calculations of the oxygen pressure head necessary for supplying the tissue". *J. Physiol. (Lond.)* 52.6 (May 1919), pp. 409–415.
- [Lag+13] J. H. Lagerlöf et al. "Image-based 3D modeling study of the influence of vessel density and blood hemoglobin concentration on tumor oxygenation and response to irradiation". *Med Phys* 40.2 (Feb. 2013), p. 024101.
- [Lee+07] J. Lee et al. "Automatic segmentation of 3D micro-CT coronary vascular images". *Med Image Anal* 11.6 (Dec. 2007), pp. 630–647.
- [Lee+85] K. L. Leenders et al. "Dexamethasone treatment of brain tumor patients: effects on regional cerebral blood flow, blood volume, and oxygen utilization". *Neurology* 35.11 (Nov. 1985), pp. 1610–1616.

- [LeV07] R. J. LeVeque. *Finite difference methods for ordinary and partial differential equations - steady-state and time-dependent problems*. SIAM, 2007.
- [LKB14] J. H. Lagerlöf, J. Kindblom, and P. Bernhardt. “The impact of including spatially longitudinal heterogeneities of vessel oxygen content and vascular fraction in 3D tumor oxygenation models on predicted radiation sensitivity”. *Med Phys* 41.4 (Apr. 2014), p. 044101.
- [Log+14] E. A. Logsdon et al. “A systems biology view of blood vessel growth and remodelling”. *Journal of Cellular and Molecular Medicine* 18.8 (2014), pp. 1491–1508.
- [Low+10] J. S. Lowengrub et al. “Nonlinear modelling of cancer: bridging the gap between cells and tumours”. *Nonlinearity* 23.1 (2010), R1–R9.
- [LRB06] D. Lee, H. Rieger, and K. Bartha. “Flow correlated percolation during vascular remodeling in growing tumors”. *Physical Review Letters* 96 (2006), pp. 0581041–0581044. DOI: 10.1103/PhysRevLett.96.058104. URL: <http://link.aps.org/doi/10.1103/PhysRevLett.96.058104>.
- [Mac+09] P. Macklin et al. “Multiscale modelling and nonlinear simulation of vascular tumour growth”. *J Math Biol* 58 (Apr. 2009), pp. 765–798.
- [Man+02] D. A. Mankoff et al. “Blood flow and metabolism in locally advanced breast cancer: relationship to response to therapy”. *J. Nucl. Med.* 43.4 (Apr. 2002), pp. 500–509.
- [Man83] B. B. Mandelbrot. *The Fractal Geometry of Nature*. San Francisco: Freeman, 1983.
- [MC03] D. M. McDonald and P. L. Choyke. “Imaging of angiogenesis: from microscope to clinic”. *Nature Medicine* 9.6 (2003), pp. 713–725.
- [MEG11] T. E. Moschandreou, C. G. Ellis, and D. Goldman. “Influence of tissue metabolism and capillary oxygen supply on arteriolar oxygen transport: a computational model”. *Math Biosci* 232.1 (July 2011), pp. 1–10.
- [MH13] E. Marieb and K. Hoehn. *Human Anatomy & Physiology*. Pearson, 2013.
- [ML07] P. Macklin and J. Lowengrub. “Nonlinear simulation of the effect of microenvironment on tumor growth”. *J. Theor. Biol.* 245 (Apr. 2007), pp. 677–704.
- [Mon+11] D. Monnich et al. “Modelling and simulation of [18F]fluoromisonidazole dynamics based on histology-derived microvessel maps”. *Phys Med Biol* 56.7 (Apr. 2011), pp. 2045–2057.
- [MT06] A. I. Minchinton and I. F. Tannock. “Drug penetration in solid tumours”. *Nat. Rev. Cancer* 6.8 (Aug. 2006), pp. 583–592.
- [Nai+90] P. K. Nair et al. “A simple model for prediction of oxygen transport rates by flowing blood in large capillaries”. *Microvasc. Res.* 39.2 (Mar. 1990), pp. 203–211.
- [Net+96] P. A. Netti et al. “Effect of transvascular fluid exchange on pressure-flow relationship in tumors: a proposed mechanism for tumor blood flow heterogeneity”. *Microvasc. Res.* 52.1 (July 1996), pp. 27–46.
- [NHH98] V. Nehls, R. Herrmann, and M. Hühnen. “Guided migration as a novel mechanism of capillary network remodeling is regulated by fibroblast growth factor”. *Histochem Cell Biol* 109 (1998), pp. 319–329.
- [NHO89] P. K. Nair, J. D. Hellums, and J. S. Olson. “Prediction of oxygen transport rates in blood flowing in large capillaries”. *Microvasc. Res.* 38.3 (Nov. 1989), pp. 269–285.
- [Nic+08] B. Nico et al. “Evaluation of microvascular density in tumors: pro and contra”. *Histol. Histopathol.* 23.5 (May 2008), pp. 601–607.

- [Nis+88] T. Nishida et al. "The network structure of corneal fibroblasts in the rat as revealed by scanning electron microscopy." *Investigative Ophthalmology & Visual Science* 29.12 (1988), p. 1887. eprint: /data/Journals/IOVS/933370/1887.pdf.
- [Owe+09] M. R. Owen et al. "Angiogenesis and vascular remodelling in normal and cancerous tissues". *J Math Biol* 58.4-5 (Apr. 2009), pp. 689–721.
- [Pen+03] S. Pennacchietti et al. "Hypoxia promotes invasive growth by transcriptional activation of the met protooncogene". *Cancer Cell* 3.4 (Apr. 2003), pp. 347–361.
- [Per+11] H. Perfahl et al. "Multiscale modelling of vascular tumour growth in 3D: the roles of domain size and boundary conditions". *PLoS ONE* 6.4 (2011), e14790.
- [Pes02] C. S. Peskin. "The immersed boundary method". *Acta Numerica* 11 (2002), pp. 479–517. DOI: 10.1017/S0962492902000077. URL: <http://dx.doi.org/10.1017/S0962492902000077>.
- [Pit11] R. N. Pittman. "Oxygen gradients in the microcirculation". *Acta Physiol (Oxf)* 202.3 (July 2011), pp. 311–322.
- [Pri+05] A. J. Primeau et al. "The distribution of the anticancer drug Doxorubicin in relation to blood vessels in solid tumors". *Clin. Cancer Res.* 11.24 Pt 1 (Dec. 2005), pp. 8782–8788.
- [Pri+90] A. Pries et al. "Blood flow in microvascular networks. Experiments and simulation". *Circulation Research* 67 (1990), pp. 826–834.
- [Pri+94] A. R. Pries et al. "Resistance to blood flow in microvessels in vivo". *Circ. Res.* 75.5 (Nov. 1994), pp. 904–915.
- [PRS05] A. R. Pries, B. Reglin, and T. W. Secomb. "Remodeling of blood vessels: responses of diameter and wall thickness to hemodynamic and metabolic stimuli". *Hypertension* 46.4 (Oct. 2005), pp. 725–731.
- [PS05] A. R. Pries and T. W. Secomb. "Microvascular blood viscosity in vivo and the endothelial surface layer". *Am. J. Physiol. Heart Circ. Physiol.* 289.6 (Dec. 2005), H2657–2664.
- [PT09] L. Preziosi and A. Tosin. "Multiphase modelling of tumour growth and extracellular matrix interaction: mathematical tools and applications". *J Math Biol* 58 (Apr. 2009), pp. 625–656.
- [PVS04] S. M. Peirce, E. J. Van Gieson, and T. C. Skalak. "Multicellular simulation predicts microvascular patterning and in silico tissue assembly". *FASEB J.* 18.6 (Apr. 2004), pp. 731–733.
- [RCM07] T. Roose, S. Chapman, and P. Maini. "Mathematical Models of Avascular Tumor Growth". *SIAM Review* 49.2 (2007), pp. 179–208. DOI: 10.1137/S0036144504446291. eprint: <http://epubs.siam.org/doi/pdf/10.1137/S0036144504446291>. URL: <http://epubs.siam.org/doi/abs/10.1137/S0036144504446291>.
- [RCR09] M. Raica, A. M. Cimpian, and D. Ribatti. "Angiogenesis in pre-malignant conditions". *Eur. J. Cancer* 45.11 (July 2009), pp. 1924–1934.
- [RTS15] H. Rieger, C. Thome, and Z. Sadjadi. "Meniscus arrest dominated imbibition front roughening in porous media with elongated pores". *Journal of Physics: Conference Series* 638.1 (2015), p. 012007. URL: <http://stacks.iop.org/1742-6596/638/i=1/a=012007>.
- [RW15] H. Rieger and M. Welter. "Integrative models of vascular remodeling during tumor growth". *Wiley Interdisciplinary Reviews: Systems Biology and Medicine* 7.3 (2015), pp. 113–129. DOI: 10.1002/wsbm.1295. URL: <http://dx.doi.org/10.1002/wsbm.1295>.
- [SA94] D. Stauffer and A. Aharony. *Introduction to percolation theory*. CRC press, 1994.

- [SAC06] S.R.McDougall, A. Anderson, and M. A. J. Chaplain. "Mathematical Modelling of dynamic adaptive tumour-induced angiogenesis: Clinical implications and therapeutic targeting strategies". *Journal of Theoretical Biology* 241 (2006), pp. 564–589.
- [Saf12] Safaeian, N. *Computational Modelling of Capillaries in Neuro-vascular Coupling: A Thesis Presented for the Degree of Doctor of Philosophy in Mechanical Engineering at the University of Canterbury, Christchurch, New Zealand*. University of Canterbury, 2012.
- [Sah+05] D. V. Sahani et al. "Assessing Tumor Perfusion and Treatment Response in Rectal Cancer with Multisection CT: Initial Observations". *Radiology* 234 (2005), pp. 785–792.
- [San+06] S. Sanga et al. "Mathematical modeling of cancer progression and response to chemotherapy". *Expert Review of Anticancer Therapy* (2006), pp. 1361–1376.
- [SB93] W. Schreiner and P. Buxbaum. "Computer-optimization of vascular trees". *Biomedical Engineering, IEEE Transactions on* 40.5 (1993), pp. 482–491.
- [SBP13] M. Scianna, C. G. Bell, and L. Preziosi. "A review of mathematical models for the formation of vascular networks". *J. Theor. Biol.* 333 (Sept. 2013), pp. 174–209.
- [Sch93] W. Schreiner. "Computer generation of complex arterial tree models". *J Biomed Eng* 15.2 (Mar. 1993), pp. 148–150.
- [Sci+13] G. Sciume et al. "A multiphase model for three-dimensional tumor growth". *New J Phys* 15 (Jan. 2013), p. 015005.
- [SD13] N. Safaeian and T. David. "A computational model of oxygen transport in the cerebrocapillary levels for normal and pathologic brain function". *J. Cereb. Blood Flow Metab.* 33.10 (Oct. 2013), pp. 1633–1641.
- [Sec+04] T. W. Secomb et al. "Green's Function Methods for Analysis of Oxygen Delivery to Tissue by Microvascular Networks". *Annals of Biomedical Engineering* 32.11 (2004), pp. 1519–1529.
- [Sef+14] M. Sefidgar et al. "Effect of tumor shape, size, and tissue transport properties on drug delivery to solid tumors". *J Biol Eng* 8 (2014), p. 12.
- [Sef+15] M. Sefidgar et al. "Numerical modeling of drug delivery in a dynamic solid tumor microvasculature". *Microvascular Research* 99 (2015), pp. 43–56.
- [SH07] R. C. Sainson and A. L. Harris. "Anti-Dll4 therapy: can we block tumour growth by increasing angiogenesis?" *Trends Mol Med* 13.9 (Sept. 2007), pp. 389–395.
- [Sin+09] J. P. Sinek et al. "Predicting drug pharmacokinetics and effect in vascularized tumors using computer simulation". *J Math Biol* 58.4-5 (2009), pp. 485–510.
- [Ske+12] A. C. Skeldon et al. "Modelling and detecting tumour oxygenation levels". *PLoS ONE* 7.6 (2012), e38597.
- [SL12] M. A. Swartz and A. W. Lund. "Lymphatic and interstitial flow in the tumour microenvironment: linking mechanobiology with immunity". *Nat. Rev. Cancer* 12.3 (Mar. 2012), pp. 210–219.
- [SM11] J. W. Song and L. L. Munn. "Fluid forces control endothelial sprouting". *Proc. Natl. Acad. Sci. U.S.A.* 108.37 (Sept. 2011), pp. 15342–15347.
- [Spi+05] L. Spinelli et al. "Characterization of female breast lesions from multi-wavelength time-resolved optical mammography". *Phys Med Biol* 50.11 (June 2005), pp. 2489–2502.
- [SRM+02] S.R.McDougall et al. "Mathematical Modelling of Flow Through Vascular Networks: Implications for Tumor-induced Angiogenesis and Chemotherapy Strategies". *Bulletin of Mathematical Biology* 64 (2002), pp. 673–702.

- [SS03] J. A. Sethian and P. Smereka. “Level Set Methods for Fluid Interfaces”. *Annual Review of Fluid Mechanics* 35.1 (2003), pp. 341–372. URL: <http://www.annualreviews.org/doi/abs/10.1146/annurev.fluid.35.101101.161105%7D>.
- [SS11] A. C. Shieh and M. A. Swartz. “Regulation of tumor invasion by interstitial fluid flow”. *Phys Biol* 8.1 (Feb. 2011), p. 015012.
- [SSD11] N. Safaeian, M. Sellier, and T. David. “A computational model of hemodynamic parameters in cortical capillary networks”. *J. Theor. Biol.* 271.1 (Feb. 2011), pp. 145–156.
- [Sta+07] I. J. Stamper et al. “Modelling the role of angiogenesis and vasculogenesis in solid tumour growth”. *Bull. Math. Biol.* 69.8 (Nov. 2007), pp. 2737–2772.
- [Sta+14] S. K. Stamatelos et al. “A bioimage informatics based reconstruction of breast tumor microvasculature with computational blood flow predictions”. *Microvasc. Res.* 91 (Jan. 2014), pp. 8–21.
- [Sty+12] T. Stylianopoulos et al. “Causes, consequences, and remedies for growth-induced solid stress in murine and human tumors”. *Proc. Natl. Acad. Sci. U.S.A.* 109.38 (Sept. 2012), pp. 15101–15108.
- [Swa+11] K. R. Swanson et al. “Quantifying the role of angiogenesis in malignant progression of gliomas: in silico modeling integrates imaging and histology”. *Cancer Res.* 71.24 (Dec. 2011), pp. 7366–7375.
- [TA10] T. Tammela and K. Alitalo. “Lymphangiogenesis: Molecular mechanisms and future promise”. *Cell* 140.4 (Feb. 2010), pp. 460–476.
- [TAP06] A. Tosin, D. Ambrosi, and L. Preziosi. “Mechanics and chemotaxis in the morphogenesis of vascular networks”. *Bull. Math. Biol.* 68.7 (Oct. 2006), pp. 1819–1836.
- [Tar+05] P. Taroni et al. “Time-resolved optical mammography between 637 and 985 nm: clinical study on the detection and identification of breast lesions”. *Phys Med Biol* 50.11 (June 2005), pp. 2469–2488.
- [Tar12] P. Taroni. “Diffuse optical imaging and spectroscopy of the breast: a brief outline of history and perspectives”. *Photochem. Photobiol. Sci.* 11.2 (Feb. 2012), pp. 241–250.
- [TJI03] A. G. Tsai, P. C. Johnson, and M. Intaglietta. “Oxygen gradients in the microcirculation”. *Physiol. Rev.* 83.3 (July 2003), pp. 933–963.
- [Tra09] P. Tracqui. “Biophysical models of tumour growth”. *Reports on Progress in Physics* 72.5 (2009), p. 056701.
- [TS09] R. L. R. Thomas H. Cormen Charles E. Leiserson and C. Stein. *Introduction to Algorithms, third edition*. The MIT Press, 2009.
- [Tso+07] N. M. Tsoukias et al. “A computational model of oxygen delivery by hemoglobin-based oxygen carriers in three-dimensional microvascular networks”. *J. Theor. Biol.* 248.4 (Oct. 2007), pp. 657–674.
- [Ver+09] C. Verdier et al. “Review: Rheological properties of biological materials”. *Comptes Rendus Physique* 10.8 (2009). Complex and biofluids Fluides complexes et biologiques, pp. 790–811. DOI: <http://dx.doi.org/10.1016/j.crhy.2009.10.003>. URL: <http://www.sciencedirect.com/science/article/pii/S1631070509001492>.
- [Vol06] K. Y. Volokh. “Stresses in growing soft tissues”. *Acta Biomater* 2.5 (Sept. 2006), pp. 493–504.
- [Vuj+03] Z. Vujaskovic et al. “Ultrasound guided pO₂ measurement of breast cancer re-oxygenation after neoadjuvant chemotherapy and hyperthermia treatment”. *Int J Hyperthermia* 19.5 (2003), pp. 498–506.

- [WBE97] G. B. West, J. H. Brown, and B. J. Enquist. "A general model for the origin of allometric scaling laws in biology". *Science* 276.5309 (Apr. 1997), pp. 122–126.
- [WBR08] M. Welter, K. Bartha, and H. Rieger. "Emergent vascular network inhomogeneities and resulting blood flow patterns in a growing tumor". *J. Theor. Biol.* 250.2 (Jan. 2008), pp. 257–280. DOI: <http://dx.doi.org/10.1016/j.jtbi.2007.09.031>. URL: <http://www.sciencedirect.com/science/article/pii/S0022519307004584>.
- [WBR09] M. Welter, K. Bartha, and H. Rieger. "Vascular remodelling of an arterio-venous blood vessel network during solid tumour growth". *J. Theor. Biol.* 259.3 (Aug. 2009), pp. 405–422. DOI: <http://dx.doi.org/10.1016/j.jtbi.2009.04.005>. URL: <http://www.sciencedirect.com/science/article/pii/S0022519309001635>.
- [Wei+09] R. Weislo et al. "A 3-D model of tumor progression based on complex automata driven by particle dynamics". *J Mol Model* 15.12 (Dec. 2009), pp. 1517–1539.
- [Wel+15] M. Welter et al. "Relation between tumor oxygenation, vascular remodeling, and blood flow: a computational model with applications to breast cancer." Submitted to PLOS Comp. Biol. 2015. URL: http://www.uni-saarland.de/fak7/rieger/Paper/welter2015_submitted.pdf.
- [Wil+92] C. B. Wilson et al. "Measurements of blood flow and exchanging water space in breast tumors using positron emission tomography: a rapid and noninvasive dynamic method". *Cancer Res.* 52.6 (Mar. 1992), pp. 1592–1597.
- [Wis+08] S. M. Wise et al. "Three-dimensional multispecies nonlinear tumor growth—II Model and numerical method". *J. Theor. Biol.* 253 (Aug. 2008), pp. 524–543.
- [WR10] M. Welter and H. Rieger. "Physical determinants of vascular network remodeling during tumor growth". *Eur Phys J E Soft Matter* 33.2 (Oct. 2010), pp. 149–163. DOI: 10.1140/epje/i2010-10611-6. URL: <http://dx.doi.org/10.1140/epje/i2010-10611-6>.
- [WR13] M. Welter and H. Rieger. "Interstitial fluid flow and drug delivery in vascularized tumors: a computational model". *PLoS ONE* 8.8 (2013), e70395. DOI: 10.1371/journal.pone.0070395. URL: <http://dx.doi.org/10.1371/journal.pone.0070395>.
- [Wu+08] J. Wu et al. "Coupled modeling of blood perfusion in intravascular, interstitial spaces in tumor microvasculature". *J Biomech* 41.5 (2008), pp. 996–1004.
- [Wu+09] J. Wu et al. "Study of tumor blood perfusion and its variation due to vascular normalization by anti-angiogenic therapy based on 3D angiogenic microvasculature". *Journal of Biomechanics* 42.6 (2009), pp. 712–721. DOI: <http://dx.doi.org/10.1016/j.jbiomech.2009.01.009>. URL: <http://www.sciencedirect.com/science/article/pii/S0021929009000281>.
- [Wu+13] M. Wu et al. "The effect of interstitial pressure on tumor growth: Coupling with the blood and lymphatic vascular systems". *Journal of Theoretical Biology* 320 (2013), pp. 131–151. DOI: 10.1016/j.jtbi.2012.11.031. URL: <http://www.sciencedirect.com/science/article/pii/S0022519312006200>.
- [Yua+94] F. Yuan et al. "Vascular permeability and microcirculation of gliomas and mammary carcinomas transplanted in rat and mouse cranial windows". *Cancer Res.* 54.17 (Sept. 1994), pp. 4564–4568.
- [Zhe+01] J. H. Zheng et al. "Time- and concentration-dependent penetration of doxorubicin in prostate tumors". *AAPS PharmSci* 3.2 (2001), E15.
- [ZM82] M. Zamir and J. A. Medeiros. "Arterial branching in man and monkey". *J. Gen. Physiol.* 79.3 (Mar. 1982), pp. 353–360.
- [ZSS07] J. Zhao, H. Salmon, and M. Sarntinoranont. "Effect of heterogeneous vasculature on interstitial transport within a solid tumor". *Microvasc. Res.* 73 (2007), pp. 224–236.

[ZWC05] X. Zheng, S. M. Wise, and V. Cristini. “Nonlinear simulation of tumor necrosis, neo-vascularization and tissue invasion via an adaptive finite-element/level-set method”. *Bull. Math. Biol.* 67 (2005), pp. 211–259.

A Correlation of vascular density and blood pressure

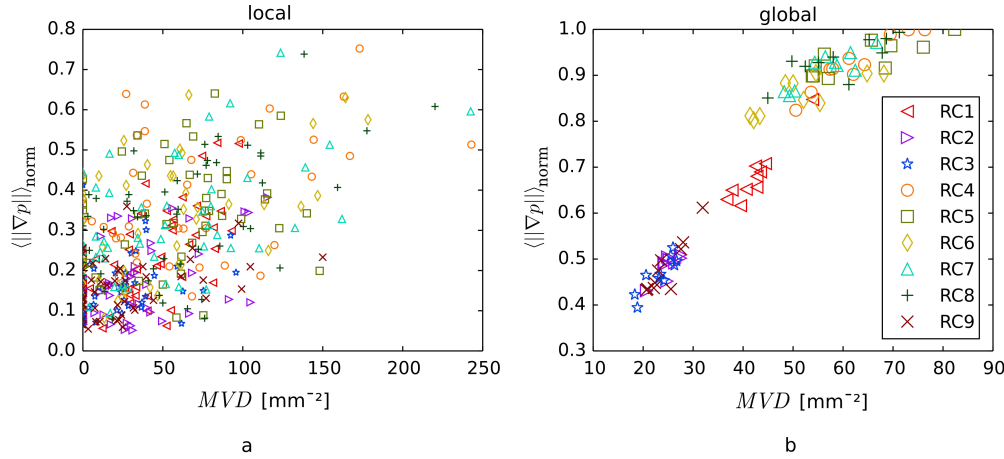


Figure 18. Tumor vascular density MVD versus normalized average of the gradient magnitude $\langle \|\nabla p\| \rangle_{\text{norm}}$. The quantity p interpolates in good approximation the blood pressure in-between vessels. It is the solution of the partial differential equation $\nabla^2 p + a \cdot (p_v - p) = 0$, where a is proportional to local volume fractions of the vascular network within numerical grid cells. A grid constant of $h = 40 \mu\text{m}$ was used. The proportionality factor is much larger than one, so that p of cells that intersect with the vascular network is approximately equal to the blood pressure p_v . This definition is similar to the one given in previous work (s. Sec. 3.2), but not identical because here the numerical grid of p is different from the lattice used to arrange vessel segments. MVD was determined as line density L_D [see Wel+15, Appendix S2] at $t = 800 h$ and p was determined for $t = 0$. The gradient magnitude of p , $\|\nabla p\|$, computed by finite differences, was averaged over local control volumina that are voxels of $200 \mu\text{m}$ width. Each point in the plot of (a) thus corresponds to a different voxel of different tumors, of which only a subset is shown. In the plot (b) the averaging was instead performed over the entire tumor, i.e. there is one data point per tumor. The legend indicates the initial network configuration of the networks generated for our paper [Wel+15], see [Wel+15, Fig. 7]. The value of the average $\langle \|\nabla p\| \rangle$ was normalized against the maximal obtained average. The computed correlations coefficients are 0.56 (local) and 0.96 (global).

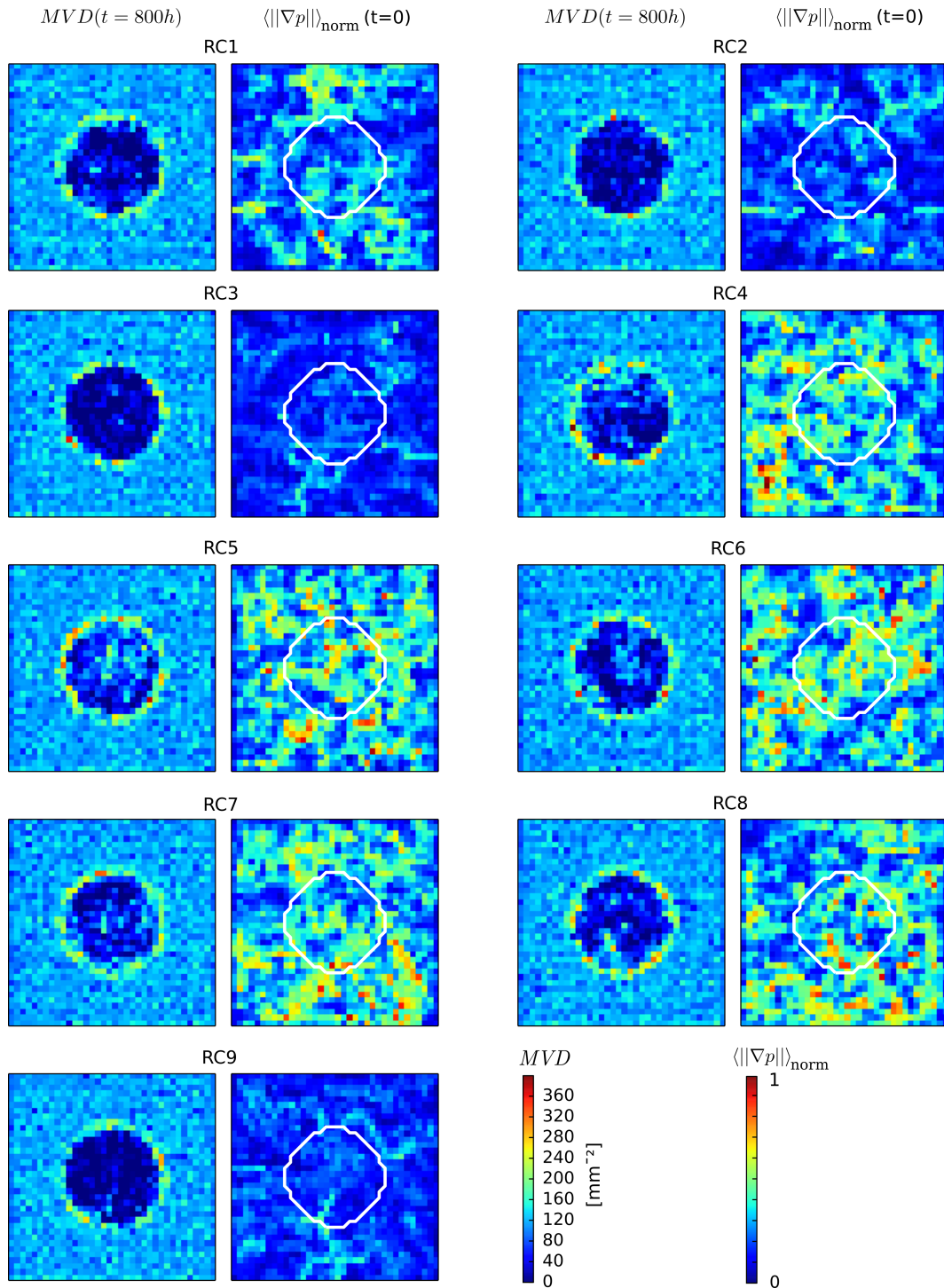


Figure 19. Distributions of local MVD versus the normalized average of the gradient magnitude $\|\nabla p\|$: This figure shows renderings of voxel data used for the scatter plots of Fig. 18. Of each initial network configuration (RC1 through RC9), [see Wel+15, Fig. 7], one simulated realization is shown with the vascular density MVD on the left and the “pressure” gradient $\langle \|\nabla p\| \rangle$ on the right. MVD and $\langle \|\nabla p\| \rangle$ were obtained as described in Fig. 18. Color scales are shown in the bottom right. White outlines indicate the location of the tumor spheroid. Its diameter is ca. 4 mm . The images shown correspond to slices through the center of the simulation boxes.

Part II

Papers

Reprinted with permission. [WBR08] Copyright 2007 Elsevier Ltd.; [WBR09] Copyright 2009 Elsevier Ltd.; [WR10] Copyright 2010 Springer-Verlag; [WR13] Copyright 2013 Welter and Rieger (open-access); [Wel+15] Copyright 2015 Welter, Thierry, Rinneberg and Rieger (unpublished preprint; submitted to PLOS Comp. Biol.)

Emergent vascular network inhomogeneities and resulting blood flow patterns in a growing tumor

M. Welter^a, K. Bartha^b, H. Rieger^{a,*}

^a*Theoretische Physik, Universität des Saarlandes, PF 151150, 66041 Saarbrücken, Germany*

^b*Department of Medical Biochemistry, Semmelweis University, Budapest, Hungary*

Received 9 March 2007; received in revised form 31 July 2007; accepted 21 September 2007

Available online 26 September 2007

Abstract

Tumors acquire sufficient oxygen and nutrient supply by coopting host vessels and neovasculature created via angiogenesis, thereby transforming a highly ordered network into chaotic heterogeneous tumor specific vasculature. Vessel regression inside the tumor leads to large regions of necrotic tissue interspersed with isolated surviving vessels. We extend our recently introduced model to incorporate Fahraeus–Lindqvist- and phase separation effects, refined tissue oxygen level computation and drug flow computations. We find, unexpectedly, that collapse and regression accelerates rather than diminishes the perfusion and that a tracer substance flowing through the remodeled network reaches all parts of the tumor vasculature very well. The reason for decreased drug delivery well known in tumors should therefore be different from collapse and vessel regression. Implications for drug delivery in real tumors are discussed.

© 2007 Elsevier Ltd. All rights reserved.

Keywords: Cancer; Angiogenesis modeling; Blood flow heterogeneities; Remodeling of vessel networks; Drug flow simulations

1. Introduction

A malignant tumor, cancer, remodels actively the blood vessel network of normal tissue into a characteristic tumor vasculature (Holash et al., 1999a, b): A well perfused region of the network at the tumor periphery provides sufficient oxygen and nutrient for further tumor growth, whereas an extremely sparse network with a low vascular density in the tumor center produces a necrotic core. The process leading to a high vascular density at the outer rim is known as angiogenesis, the production of new vessels from old ones via the stimulus of tumor secreted growth factors (Carmeliet and Jain, 2000). The regression of vessels inside the tumor is related to unstable vessel morphology and abnormal blood flow dynamics as well as increased solid stress generated by the tumor—for a discussion see Bartha and Rieger (2006). The emerging vascular tumor network is thus extremely inhomogeneous and has geometric, in particular fractal, properties that are very different from normal vasculature (Baish and Jain,

2000). As a consequence also blood flow patterns inside this network are highly irregular and might have an impact upon drug delivery (Minchinton and Tannock, 2006).

This paper is concerned with a mathematical model for a situation sketched above. There is already a large amount of work on the mathematical modeling of tumor-induced angiogenesis (for reviews see, e.g., Mantzaris et al., 2004; Preziosi, 2003) and can roughly be classified into two groups: The first group concentrates on blood vessel densities rather than vessel morphology, as in continuum partial differential equation (Byrne and Chaplain, 1995; Levine et al., 2001) or in locally coupled map lattice (Sansone et al., 2001) approaches. Today's most sophisticated models (Breward et al., 2003), so-called multi-phase models even track density profiles of different tissue types. Mechanical interaction is included in terms of constitutive laws. Hence, also the effect of solid pressure on cells can be respected. The current research situation is reviewed in (Byrne et al., 2006). Due to the absence of individual blood “vessels” these models do not contain neither the information on the geometrical and morphological properties of the vascular network nor on hydrodynamic blood flow characteristics.

*Corresponding author. Tel.: +49 681 302 3969; fax: +49 681 302 4899.
E-mail address: h.rieger@mx.uni-saarland.de (H. Rieger).

The second group of works represents vessels as interconnected lattice patterns, line segments, or continuous curves. As a crucial simplification either a static tumor is assumed (Anderson and Chaplain, 1998; McDougall et al., 2002; Tong and Yuan, 2001; Sun et al., 2005), or a proliferating tumor is considered in a static network topology. An example for the latter is the work of (Alarcon et al., 2003), where a cellular automaton model was introduced in which automaton elements, are identified with vessels, extracellular matrix (ECM), tumor cells (TCs) or normal cells. TCs and normal cells can proliferate or die according to the O_2 level and other factors, creating a competition between TCs and normal cells. The vessel network is initialized to a hexagonal grid and remains static. The O_2 concentration is computed by a standard diffusion equation with vessel sites as sources and other tissues as consumers. Based on this the invasiveness of TCs under different O_2 conditions is studied. This work has been progressively extended into a complex multi-scale model (Betteridge et al., 2006) which includes an improved model for dynamic vessel radius adaptation in response to various stimuli (Pries et al., 1998), “pressure” effects i.e. competition for space, a vascular endothelial growth factor (VEGF) concentration field, implemented in analogy to O_2 , biochemical details, including cell cycles and factors related to proliferation and apoptosis, modeled via ordinary differential equations. Despite these improvements the basic limitation of a topologically static vessel network remains and for many tumor types the applicability of this model is restricted to the first few days of the existence of the tumor.

A paradigmatic angiogenesis model with a static tumor (Anderson and Chaplain, 1998) describes actually the experimental situation in the so-called “rabbit eye model” (Gimbrone et al., 1974), in which a small growth factor (or TAF, i.e. tumor angiogenic factor) source is implanted in the cornea of the eye. Stimulated by TAF, angiogenesis occurs, whereupon multiple sprouts migrate toward the tumor. Excessive branching and loop formation happens close to the tumor, culminating in an extremely dense network. Since the cornea is initially free of normal vessels this situation can also be denoted as “pure vessel-ingrowth”. The continuous theoretical model of (Anderson and Chaplain, 1998) includes three fields for: endothelial cell (EC) density, fibronectin, a component of the ECM also secreted by ECs; TAF concentration. The TAF field is initialized once with a decreasing profile from the tumor to the parent vessel. Later on, TAF is locally consumed by ECs. Fibronectin is produced and consumed locally by ECs and does not diffuse. EC fluxes are driven by a random motility (diffusion), chemotaxis via GF gradients, and haptotaxis via fibronectin gradients (gradients of adhesion). The discretized version uses probabilities (derived from discretized diffusion equations with source and sink terms) for biased random walks of individual ECs at sprouting tips. These tip ECs leave a path occupied with trailing ECs, which can randomly initiate further sprouts if

TAF concentration is high enough. The basic model has received considerable upgrades; see (Chaplain et al., 2006) for a review. The most recent version (McDougall et al., 2006) includes blood flow rate computations and the sophisticated dynamic vessel radius adaptation procedure (Pries et al., 1998) as used in (Betteridge et al., 2006), making it feasible to study drug delivery by simulations of a tracer substance flowing through the vasculature. A shortcoming that needs to be addressed is that vessels do not penetrate the tumor. In the latest studies (with the most realistic network), the tumor is actually not explicitly represented, instead the lower boundary of the simulated domain is identified with the invasive edge. Hence drug uptake by the tumor varies by three orders of magnitude, depending on whether a thick vessels is near the boundary or not.

This general concept has been adopted in third group of tumor simulators for modeling pure vessel in-growth into a non-static tumor, neglecting existing host vessels. For instance Zheng et al. (2005), designed a hybrid tumor simulator to study highly invasive tumor types like glioma brain cancers. There, an extensive framework is developed, where the tumor is treated as viscous fluid and the topology of the sharp tissue-tumor interface is described by sophisticated level-set techniques. The discrete part involves the angiogenesis model by Anderson and Chaplain (1998), where the generated capillary network serves as additional source for nutrients and influences the evolution of the tumor considerably. In recent work Lowengrub et al. (2007) presented a glioma model where temporal and spatial development of cell densities as well as nutrients is described by convection–reaction–diffusion equations also including mechanical properties like intercellular adhesion forces. For angiogenesis a discrete lattice free variant has been adopted (Plank and Sleeman, 2003, 2004).

Here we also want to go beyond the “static network” and the “static tumor” models and combine a dynamically evolving network in the presence of a dynamically changing tumor. Most relevant for our work is the cellular automaton model that was introduced recently by two of us (Bartha and Rieger, 2006) for a two-dimensional and later for a three-dimensional set-up (Lee et al., 2006), designed to reproduce experimental results for solid human melanoma type tumors (Döme et al., 2002, 2007). There it was found that in cutaneous melanoma during tumor growth, there are no signs of directed vessel ingrowth; instead, these tumors appear to grow by co-opting the massive vascular plexus present in the peritumoral connective tissue. The intention in Bartha and Rieger (2006) was to clarify the basic mechanisms leading to the abnormal tumor vasculature, and discuss the implications for assessment of tumor growth. In the model TCs and ECs occupy sites on a regular lattice. ECs form a vessel network circulated by blood. Tumor and vessels interact via O_2 and GF diffusion fields. The temporal evolution of the system is governed by stochastic rules for certain events like TC death, proliferation, sprout formation or vessel collapse.

It turned out that these comparably simple rules and little numerical effort are sufficient to explain many important aspects of tumor vessel morphology.

In this paper we modify and extend this model and incorporate the details taken into account by Alarcon et al. (2003) for static network topologies as described above, and discuss their relevance for the tumor vessel morphology. Then we analyze on the basis of our model how a drug injected into the blood stream distributes over time within the tumor vasculature and compare the results with those for a pure vessel ingrowth-model (McDougall et al., 2006).

The paper is organized as follows: In Section 2 we describe our model. In Section 3 we present the results of the model which can be compared to experimental data, discuss the effect of parameter variations and the relevance of various model details for the global model behavior. In Section 4 we describe how drug flow is modeled and present results of the simulation of an injection of a tracer substance into one part of the vasculature. Section 5 summarizes our results and provides an outlook to further research.

2. The model

The following model definition is conceptually similar to Bartha and Rieger (2006) but implements higher level of detail in the modeling of physiology.

2.1. Description of the system state

Basics: Elements are managed on a regular two dimensional triangular lattice of $l \times l = n$ sites, i.e. we define the set of sites as

$$L = \left\{ \left\{ \begin{array}{ll} (\delta(x), & \delta \sin(60^\circ)y) & \text{if } y \text{ even} \\ (\delta(x + \frac{1}{2}), & \delta \sin(60^\circ)y) & \text{else} \end{array} \right. \mid x, y \in [0, l] \right\}. \quad (1)$$

Each site can be occupied by a single tumor cell, and each bond by a vessel segment. Unoccupied space is part of the extracellular matrix and/or healthy tissue. Fig. 1 illustrates how TCs and vessels are aligned on the lattice. The lattice constant is $\delta = 10 \mu\text{m}$, chosen deliberately to be of the order of the typical diameter of TCs and ECs.

Definition of the tumor: The tumor is defined as a set of sites $T = \{x \in L, \text{ TC present at } x\}$. This means sites in T are associated with single TCs. For any given site $x \in T$ it is assumed that the space occupied by the cells corresponds roughly to the Voronoi region around x , i.e. the points in space that are closer to x than any other site. The hexagon shown in Fig. 1 is exactly such a Voronoi region and indicates a TC. During the growth of the tumor necrotic regions will arise. At the time t , we refer to these by the set of sites T_{necro} where a TC was removed at some time in the past $t' < t$, excluding the current set of tumor cells: $T_{necro} = \bigcup_{t' < t} T(t') \setminus T(t)$. To determine whether a site x is inside of the tumor we use a polar map $x_T(\theta)$ which tracks

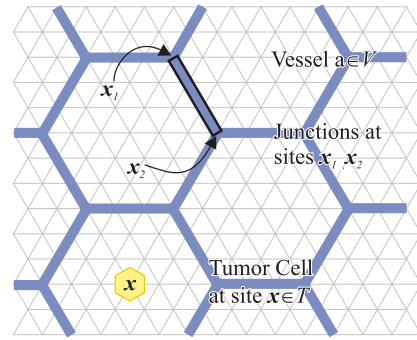


Fig. 1. Illustration of vessels and TCs. A tumor cell (TC) is indicated as yellow hexagon. TCs are centered at lattice sites. Sites always represent single cells. Thereby the diameter of the cells is of the order of the lattice constant. Vessels are indicated as blue bars. In contrast to TCs, they are associated with the bonds of the lattice, thereby constraining their orientation to the main lattice directions. A single vessel $a = (i, j)$ is highlighted by a black outline. This vessel spans between sites labeled x_i and x_j . Vessel may span multiple sites like those that are indicated here. The initial networks for the studies in Section 3.2 consists of a hexagonal pattern. The hexagonal vessel arrangement here would represent a tiny part of such a network. Note that the tumor grows in it's own layer unhampered by vessel. Interactions are predominantly mediated by growth factor and oxygen fields, although information about the spatial coverage also plays an important role.

the extend of the tumor in radial direction, where θ is the polar angle measured relative to the center of the tumor.

Definition of the micro-vascular system: The micro-vascular system evolves in a separate layer, i.e. vessel elements can pass sites where TCs are also present. From the theoretical point of view the vessel network is a graph where the edges represent vessel segments with associated hemodynamic and geometry properties. Hence, the topology is described by the graph $G = (N, V)$, where $V = \{(i, j), i, j \in N\}$ is the set of vessel segments, i, j denote attached junction nodes in N . We denote the position of a node i with $x_i \in L$. Analogously we refer to various properties of vessels, nodes or TCs via sub-scripts, i.e. q_a for the flow-rate in some vessel a .

In our current implementation vessels are allowed to span multiple bonds/sites. For convenience $x \in a$ denotes a site that is covered by a vessel $a \in V$, including the endpoints x_i, x_j . For each vessel in the set of potentially perfused vessels $V_{circ} \subset V$ it is required that least two disjoint paths to the system boundaries must exist.

Blood flow modeling: Blood flow for vessels in V_{circ} is modeled as laminar steady flow through ideal pipes of radius r and length l . Therefore Hagen–Poiseuille's Law is applicable to compute flow rate q and wall shear stress f from the blood pressure difference of the endpoints $p_i - p_j$:

$$q = \frac{\pi}{8} \cdot \frac{r^4}{\eta} \cdot \left(\frac{p_i - p_j}{l} \right), \quad (2)$$

$$f = \frac{r}{2} \cdot \left(\frac{p_i - p_j}{l} \right). \quad (3)$$

To account for the fact that blood is a non-Newtonian fluid with complex flow behavior, it is common to introduce an effective viscosity $\eta = \eta_0 \cdot \eta_{rel}(H, r)$ depending on local

vessel radius r and hematocrit H (red blood cell volume fraction). In simulations which incorporate this effect, we base our calculations on the formula in Pries et al. (1994). It is derived from in vivo data and is used in various other works (Ji et al., 2006; Alarcon et al., 2003; McDougall et al., 2006). Since the definition of η_{rel} is rather lengthy we refer to Fig. 8 and to the original work of Pries et al.

In blood vessel networks the distribution of hematocrit is usually not homogeneous, instead RBCs tend to enter the branch with faster flow—known as phase-separation or plasma-skimming effect (Fung, 1993). To calculate the hematocrit we rely again on an empirical formula. Pries et al. (1990) found a “bifurcation law”:

$$QH_b = g(QH_a, r_a, r_b, r_c, q_a, q_b, q_c), \quad (4)$$

which relates the RBC flow $QH_b = q_b H_b$ in a branch b to the RBC flow QH_a in a parent vessel a in dependence on the radii and the flow rates of all three vessels a, b, c at the bifurcation.

For the definition of the function g we refer again to the original work. Note that the relation is valid only for arterial bifurcation. The case where two or more branches merge into a larger one is trivial for obvious reasons. Furthermore g is symmetric in b and c such that RBC mass is conserved $QH_b + QH_c = QH_a$. During the simulation it is ensured that no more than three vessels meet at some node.

To compute the global hematocrit distribution when the blood flow rates are known, vessels must be processed in consecutive order such that the upstream hematocrit has already been determined when a downstream child is processed. That is because via (4) the hematocrit in a given vessel depends on the hematocrit of all vessels stream upwards. The hematocrit H_0 at the uppermost in-flow vessels is fixed as a boundary condition. Graph-theoretically this problem of traversal order is known as finding a topological sorting and standard algorithms can be applied (Cormen et al., 1990).

Furthermore mass preservation dictates that the sum of inflow and outflow equals zero for each node $i \in N$ (Kirchhoff's Law):

$$0 = \sum_{j \in Nb(i)} q_{ij} = \sum_{j \in Nb(i)} S_{ij} \cdot (p_i - p_j), \quad (5)$$

where $Nb(i)$ are adjacent nodes of i in the network. To find the flow and pressure distribution when the flow conductivities S_{ij} —and therefore hematocrits—are known, the system of linear equations in the nodal pressures (5) must be solved with appropriate boundary conditions.

Together (2), (5) and the hematocrit computation procedure form a complex system of non-linear equations where it is impossible to solve for flow and hematocrit simultaneously. Hence an iterative approach was suggested in the literature Pries et al. (1990) which is commonly used now (Ji et al., 2006; Alarcon et al., 2003): First an initial guess for the hematocrit is chosen. Until convergence, flow and hematocrit are updated successively assuming constant

hematocrit and constant flow respectively. To solve the pressure–potential equations we use a modern sparse LU factorization library (Davis, 2004) which can efficiently handle large systems with 10,000 of variables. The naive outer fix-point iteration however resulted in poor convergence due to over- and undershooting. Therefore we employ a dampened iteration which has the same fix-points:

$$\begin{aligned} \mathbf{q}_{i+1} &= \mathbf{q}(\mathbf{H}_i), \\ \mathbf{H}_{i+1} &= \mathbf{H}_i \cdot 2/3 + 1/3 \cdot \mathbf{H}(\mathbf{q}_{i+1}), \end{aligned} \quad (6)$$

with the stopping condition $\|\mathbf{H}_{i+1} - \mathbf{H}_i\|_2 < 10^{-3}$, where i is the iteration number while \mathbf{H} and \mathbf{q} denote vectors which contain data values from the individual vessel segments. We choose dirichlet type boundary-conditions, where the pressure in boundary nodes is prescribed and decreases from $p^{(max)}$ at $(0, 0)$ to $(p^{(max)} + p^{(min)})/2$ at $(0, l)$ and $(l, 0)$ further to $p^{(min)}$ at (l, l) .

Definition of the oxygen field: The tumor and the vascular system interact via oxygen and growth factor fields. Our unit-less oxygen field c_o is given by the solution of the stationary diffusion-equation:

$$\Delta c_o - \kappa c_o + \alpha(c_o^{(B)} - c_o) = 0, \quad (7)$$

with the consumption-rate coefficient κ , the source coefficient α , and the blood oxygen level $c_o^{(B)}$. We update the O_2 field by finding the stationary state because the O_2 diffusion constant is of the order of $2.4 \times 10^{-5} \text{ cm}^2/\text{s}$ which means that the relaxation time after a configuration change is negligible compared to cell proliferation rates, which is of the order of an hour.

For simplicity and efficiency we define a linear O_2 -uptake $-\kappa c_o$, as approximation to a more realistic non-linear Michaelis–Menten type relationship (i.e. $-Ac_o/[B + c_o]$). At least within, or close to the tumor the saturation regime of a MM-uptake would be irrelevant, since tumor cells usually suffer from hypoxia. Furthermore κ varies with the tissue type: it is set to $\kappa^{(T)}$ for $\mathbf{x} \in T$ (tumor), 0 for $\mathbf{x} \in T_{necro}$ (necrotic tumor) and $\kappa^{(M)}$ otherwise (ECM/normal tissue). The O_2 transport through the vessels wall is predominantly a diffusion process driven by the PO_2 difference between blood ($c_o^{(B)}$) and tissue (c_o) at the vessel wall. Therefore it is common to model the oxygen release as the source term $\alpha(c_o^{(B)} - c_o)$. In the context of our continuum description the coefficient α has the meaning of O_2 amount released per time per volume element, which implicitly includes parameters like wall permeability and circumference. For simplicity we treat all vessels equal i.e. $\alpha(\mathbf{x}) = \alpha^{(0)}$ at vessel occupied sites $\mathbf{x} \in a \in V_{circ}$, where $\alpha^{(0)}$ is a constant. Naturally $\alpha(\mathbf{x}) = 0$ at non-vessel-sites.

For the blood- O_2 level $c_o^{(B)}$, we assume that it is essentially proportional to the blood hematocrit—following (Alarcon et al., 2003)—and neglecting the fact that oxygen leaves the vessel. Considering that the PO_2 drops only by about a factor of 2 while blood flows through the

body this is likely not to pose a problem. Performing computations with a sophisticated model as presented by Secomb et al. (2004), would be numerically very hard. Their model includes intravascular O₂ variability, as well as the nonlinear saturation behavior of hemoglobin. In our simple approach however we set $c_o^{(B)}(\mathbf{x}) = H_a$ for a given $\mathbf{x} \in a \in V_{circ}$. At junctions, the average hematocrit is used. An additional pre-factor is not necessary because (i) it would only scale the field values globally; (ii) c_o is unit-less.

Discretizing the diffusion equation by finite differences for the Laplace operator yields the linear system of equations

$$\left(\frac{2}{\delta^2} + \alpha(\mathbf{x}) + \kappa(\mathbf{x})\right)c_o(\mathbf{x}) - \frac{2}{|Nb(\mathbf{x})|\delta^2} \sum_{\mathbf{x}' \in Nb(\mathbf{x})} c_o(\mathbf{x}') = \alpha(\mathbf{x})c_o^{(B)}(\mathbf{x}), \quad (8)$$

where $Nb(\mathbf{x})$ is the set of neighbor sites. It is solved numerically by a multi-grid V-Cycle with a fixed number of Jacobi iterations at each level (Briggs et al., 2001). Since the sources have only a spatially limited effect, the field does not change much when vessels are added or removed. Hence, the solution from the previous time-step is taken as initial guess. This allows rather efficient updates with a small number of iterations.

Definition of the growth factor field: The modeling of growth factor distribution c_g is also based on a reaction–diffusion equation:

$$0 = \Delta c_g - \tilde{\kappa}c_g + \tilde{\alpha}, \\ \tilde{\alpha}(\mathbf{x}) = \tilde{\alpha}^{(0)} \quad \text{for } \mathbf{x} \in T_{uo}, \quad 0 \text{ else,} \\ \tilde{\kappa} = const, \quad (9)$$

where $T_{uo} \subset T$ denotes the set of tumor sites for which $c_o < \theta_o^{(prol)}$. We assume that (i) under-oxygenized TCs produce GF at a constant rate $\tilde{\alpha}^{(0)}$, (ii) free GF is removed with the rate $\tilde{\kappa}c_g$ due to binding and degradation. This simple formulation facilitates the solution following a “Greens-function” approach for the operator $\Delta - \tilde{\kappa}$ by super-positioning contributions of individual TCs:

$$c_g(\mathbf{x}) = \sum_{\mathbf{x}' \in T_{uo}} \tilde{g}(\mathbf{x} - \mathbf{x}'), \quad (10)$$

$$\tilde{g} = r \mapsto \max[0, 1 - r/R^{(g)}], \quad (11)$$

where $R^{(g)}$ is the GF diffusion radius. For our convenience we use a linearly decaying “Greens-function” instead of the correct exponential decay. The model is not critically dependent on the exact GF profile nor on the value range of c_g and this simplification allows us to tune the distance up to which angiogenesis is triggered intuitively via $R^{(g)}$. $R^{(g)}$ also provides a natural cutoff for the “Greens-function” \tilde{g} so updating the field after removal(addition) of TCs is very efficient because it is sufficient to simply subtract(add) the contribution of the respective cells.

2.2. Description of dynamical processes

The system dynamics are governed by the following procedures which are executed in sequence for each time-step of length $\Delta t = 1h$.

TC proliferation: New TCs are put on empty neighbor sites $\mathbf{x} \notin T$ of existing TCs with probability $\Delta t/t_{TC}^{(prol)}$ if the local oxygen level is high enough $c_o(\mathbf{x}) > \theta_o^{(prol)}$: $T \leftarrow T \cup \{\mathbf{x}\}$. Naturally this restricts proliferation to the outer rim. Experiments (Bru et al., 2003) and simulations (Drasdo and Höhme, 2005) have shown that following an exponential growth, proliferation is indeed confined to a small band behind the invasive edge. The simple model here, reminiscent of the Eden model (Eden, 1961) does not capture all the aspects of tumor growth dynamics. For example cell motility is not included. But we consider this as an acceptable approximation for studying vessel morphology under a growing solid tumor (Fig. 2a).

TC death: TCs are removed with probability $p_{TC}^{(Death)} = 1/2$ if the local O₂ concentration is low enough $c_o < \theta_o^{(death)}$ for longer than $t_{TC}^{(uo)}$: $T \leftarrow T \setminus \{\mathbf{x}\}$. Since TCs adapt to low oxygen conditions (Iyer et al., 1998), $\theta_o^{(death)} = \theta_o^{(prol)}/10$ is very small. The survival time under hypoxia actually depends strongly on the cell genotype (Yu et al., 2002), promoting the selection of certain species. However for simplicity $t_{TC}^{(uo)}$ has been given a fixed value (Fig. 2b).

Angiogenesis: While adult vessels are normally quiescent, angiogenesis is induced in close proximity to tumors via increased growth factor levels. Thereby the migration of ECs at the sprouting tip is guided by GF gradients (Gerhardt et al., 2003). Tumors also coopt existing vessels (Paku, 1998) but no explicit modeling is required for this phenomenon because tumor cell proliferation is not occluded by vessels. Incorporation of angiogenesis is split into two subprocesses: sprout initiation and migration. Sprouts are initiated with probability $\Delta t/t_{EC}^{(sprout)}$ at vessel-sites if (i) the location $\mathbf{x} \in a \in V$ is outside of the tumor (i.e. no sprouting inside the tumor (Holash et al., 1999a)); (ii) the GF level is above a threshold $c_g(\mathbf{x}) > \theta_g^{(prol)}$; (iii) the path length to the next bifurcation is greater than $l^{(spr)}$. At the respective sites segments with $l = \delta$, $r = r^{(init)}$ are appended in the direction of the steepest GF increase (Fig. 2c).

At each sprouting tip one further δ segment is added with probability $\Delta t/t_{EC}^{(migr)}$. If another vessel is located at a neighboring site in front of the tip, the new segment creates a junction to the other vessel, forming a potentially blood circulated loop. Here we assume that the sprout direction remains constant, which is not a severe simplification because due to the two-dimensional setting sprouts usually migrate at most ca. 100 μm until another vessel is hit (the situation is different in three space dimensions). Sprouts have been observed to regress after a certain time of not having formed connections (Nehls et al., 1998). To model this, vessels have an associated countdown s (in analogy to hypoxic TCs) which is incremented each time-step. While $s < s^{(max)}$ vessels are guaranteed not to be removed due to

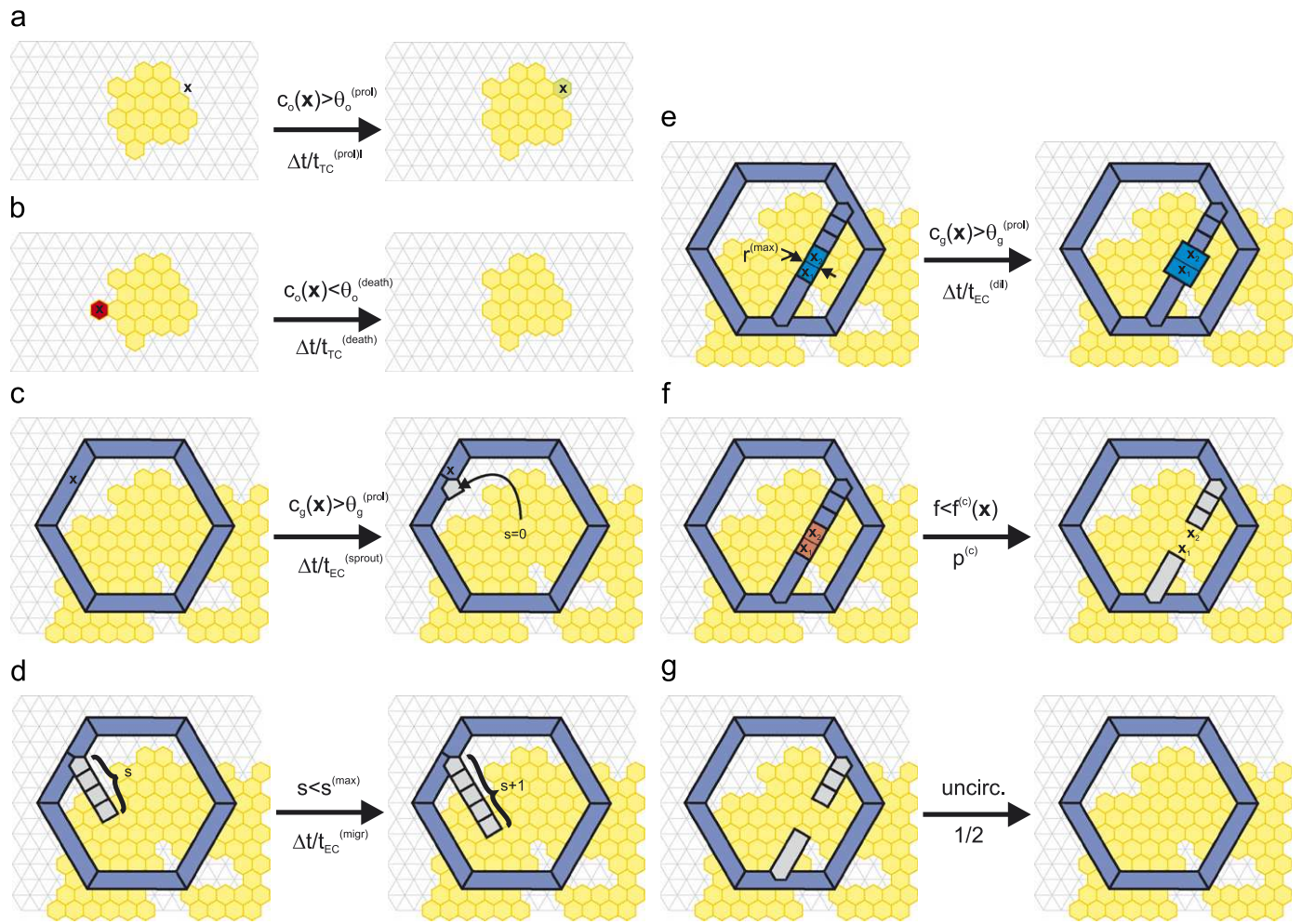


Fig. 2. Illustration of the dynamic processes of the system. Tumor cells are indicated as yellow hexagons. Circulated vessels are indicated as blue bars. Vessels are drawn in gray color if uncirculated. This also includes sprouting tips. The meaning of each subfigure is as follows: (a) Tumor cells proliferate by occupying neighbor sites if $c_o(\mathbf{x}) > \theta_o^{(prol)}$ with a rate $\Delta T / t_{TC}^{(prol)}$; (b) tumor cells die if they have been exposed to low oxygen $c_o(\mathbf{x}) < \theta_o^{(death)}$ for longer than $t_{TC}^{(death)}$ with a rate $\Delta T / t_{TC}^{(death)}$; (c) sprouts form if $c_g(\mathbf{x}) > \theta_g^{(prol)}$ with rate $\Delta T / t_{EC}^{(sprout)}$; (d) sprouts grow further with by appending segments with rate $\Delta T / t_{EC}^{(migr)}$ until $s > s^{(max)}$; (e) vessels dilate with rate $\Delta T / t_{EC}^{(dil)}$ for each subsegment where $c_g(\mathbf{x}) > \theta_g^{(prol)}$; (f) vessels collapse with rate $p^{(c)}(a, \mathbf{x})$ if for some subsegment $f_a < f^{(c)}(\mathbf{x})$ and (g) Uncirculated network components are eliminated with rate 1/2.

being uncirculated. During this period vessels can also start new sprouts which inherit s from their parents. Vessels for which $s \geq s^{(max)}$ (i.e. normal non-sprouting vessels) regress rapidly if not circulated (Fig. 2d).

Vessel collapse: Long-term reduction of wall shear stress can cause vessel regression. In tumors solid stresses might cause vessel collapses resulting in reduced perfusion and thereby low shear stresses. Also local angiogenesis inhibitors might be involved in EC apoptosis (Dimmeler and Zeiher, 2000). Furthermore dilated tumor vessels, although tortuous and leaky with inadequate support structures, apparently remain stable (Holash et al., 1999b). In the model this behavior is realized as follows: Let $a \in V$ be a vessel then each occupied lattice bond $(k, l) \in a$ causes a to be removed with probability $p^{(c)}(a, (\mathbf{x}_k + \mathbf{x}_l)/2)$. For uncirculated vessels with $s_a \geq s^{(max)}$ it is $p^{(c)} = 1/2$. Sprouts are protected from removal, i.e. $p^{(c)} = 0$ for $s_a < s^{(max)}$. For normal circulated vessels $p^{(c)} = p^{(c)}(a, \mathbf{x})$ depending on local system properties as follows: If either shear force or vessel

radius is above a critical threshold $f_a > f^{(c)}(\mathbf{x})$ or $r_a > r^{(stable)}$ then $p^{(c)} = 0$. Thereby we let $f^{(c)}$ vary spatially to account for increased solid stresses in the tumor. Several functional dependencies are studied, but the basic case involves a radial triangular profile g_1 , with limited support $2\delta^{(c)}$ and peak height $f^{(c, max)}$ centered $\delta^{(c)}$ microns behind the invasive edge:

$$\begin{aligned} f^{(c)}(\mathbf{x}, a) &= f^{(c)}(\mathbf{x} - \mathbf{x}_{center}) \\ &= f^{(c, max)} \cdot g_1(\|\mathbf{x} - \mathbf{x}_{center}\|, \theta), \\ g_1 := x, \theta &\mapsto \max\left(0, 1 - \frac{|x - x_T(\theta) - \delta^{(c)}|}{\delta^{(c)}}\right). \end{aligned} \quad (12)$$

This is inspired by Breward et al. (2003) where it is assumed that the replacement of TCs with necrotic material reduces the solid pressure exerted on vessels. If $f_a \leq f^{(c)}(\mathbf{x}, a)$ and $r_a \leq r^{(stable)}$ and $a \in V_{circ}$ then $p^{(c)} = p^{(c, max)} \cdot g_1(\|\mathbf{x} - \mathbf{x}_{center}\|, \theta) g_2(r_a) > 0$. For the basic case we also tried to

modulate $p^{(c)}$ with a vessel radius dependent linear function g_2 for which $g_2(r^{(stable)}) = 0$ and $g_2(r^{(init)}) = 1$ (Fig. 2f).

Vessel regression: Uncirculated vessels cannot contribute to nutrient delivery and there is no mechanism in the model that would “repair” such vessels. Hence uncirculated vessels $V \setminus V_{circ}$ are simply removed with probability $1/2$ (Fig. 2g).

Vessel dilation: Vascularization and remodeling of the vascular system surrounding the growing tumor is primarily dependent upon angiogenic sprouting as modelled above. Within the tumor the vascularization program switches to circumferential growth of the initial vasculature by proliferation of endothelial cells within the vessel walls (Erber et al., 2006). This we model by a stepwise vessel dilation in the presence of a high enough VEGF concentration. Experimentally it is found that the radius of tumor vessels is limited by a maximum radius $r^{(max)}$ (Döme et al., 2002). Using the polar map x_θ defined above it is decided whether a vessel segment lies within the tumor. If it does vessel dilatation can occur: each bond $(k, l) \in a$ occupied by a vessel a increases the radius of the respective vessel with probability $\Delta t/t_{EC}^{(dil)}$ if $c_g((\mathbf{x}_k + \mathbf{x}_l)/2) > \theta_o^{(prol)}$ and $r_a < r^{(max)}$. The added value $\delta^2/2\pi l_a$ corresponds to the surface area contribution of an additional EC. To account for surface tension, a smoothing effect is generated by dilating the thinnest vessel at junction bonds (Fig. 2e).

3. Results

Following (Bartha and Rieger, 2006), the base case scenario is one for a malignant melanoma, guided by data from Döme et al. (2002). Further parameter variations and simplifications are presented after the base case results.

3.1. Parameters

The size of the lattice is $l = 1000$ in all of the following experiments. With the mentioned bond length $\delta = 10 \mu\text{m}$, this corresponds to a $10 \times 8 \text{ mm}^2$ rectangular area of tissue.

Following (Alarcon et al., 2003), we chose a hexagonal pattern as initial network which is physiologically more reasonable than the “Manhattan” or square pattern in (Bartha and Rieger, 2006) since only three vessels meet at junctions. Also not at least because this facilitates the incorporation of the blood phase-separation effect straight forward as described. Fig. 1 depicts a tiny network section, whereas in Fig. 3 half of the domain is visible. We determined the size of the hexagons according to the microvascular density (MVD) of normal skin. Experimentally MVD is measured by counting the number of vessels which cross a thin slice of tissue. Data from Döme et al. (2002) indicate an MVD of ca. 100 vessels per mm^2 . This means the average inter vessel distance is ca. $100 \mu\text{m}$. With $60 \mu\text{m}$ edge-length for the hexagons, the vessel–vessel distance through the center of a hexagon lies between 100 and $120 \mu\text{m}$. Furthermore the fraction of vessel occupied

sites is ca. 0.15. The rectangular grid in our previous work yielded the value 0.2.

The initial tumor is generated by placing a single TC in the center of the system and attaching new TCs at randomly chosen surface sites until the tumor contains $|T(t = 0)| = 1000$ cells.

We set the TC proliferation time to $t_{TC}^{(prol)} = 10$ h, and assume that ECs proliferate four times slower. Hence, sprout generation time is $t_{EC}^{(sprout)} = 40$ h. The sprout migration time $t_{EC}^{(migr)} = 1$ h is motivated by the experimental results of Nehls et al. (1998): Apparently the sprouts extend roughly $200 \mu\text{m}$ per 20 h. This matches with the migration rate here, where a $10 \mu\text{m}$ segment is added per hour. The duration for which sprouts remain active $s^{(max)}$ is set to 20 h, also in line with these experiments. The minimum distance from a new sprout to existing junctions $l^{(spr)}$, is a crucial parameter as it controls the MVD in the growth region. It is set to $l^{(spr)} = 30 \mu\text{m}$, in order to match MVD data for the peritumoral region in Döme et al. (2002).

The time for dilation $t_{EC}^{(dil)} = 20$ h as well as the maximum radius $r^{(max)} = 30 \mu\text{m}$ are estimated from vessel perimeter measurements in that paper. The stable vessel radius is set to $r^{(stable)} = 20 \mu\text{m}$ due to the absence of thin vessels in tumors. The boundary pressures $p^{(max)}$ and $p^{(min)}$ must now generate typical flow and shear stress values for capillaries. In contrast to Bartha and Rieger (2006) the hemodynamics is here based on empirical formulas. $p^{(min)}$ is set to 0 arbitrarily. $p^{(max)}$ is set to 90 kPa such that the shear force in the initial network is within realistic ranges for capillaries: approximately 10 Pa (Gödde and Kurz, 2001).

$(p^{(max)} - p^{(min)})$ gives rise to a gradient in the diagonal of about $\partial P/\partial l \approx \sqrt{2} \times 9 \text{ Pa}/\mu\text{m}$. Multiplying this by $\cos(45^\circ)$ for a horizontal vessel and multiplying by $\frac{1}{2}r = \frac{5}{2} \mu\text{m}$ to get the shear force, results in $f \approx 20 \text{ Pa}$. The actual value obtained is $\langle f \rangle = 10 \text{ Pa}$, due to the network geometry.

Clearly the pressure values are not realistic, but this has no negative impact on the model because pressures influence the model only indirectly via flow and shear force. The critical shear force $f^{(c, max)}$ is set to 1 Pa and the collapse probability to $p^{(c, max)}$ to 0.01. The collapse probability determines how far the high MVD zone reaches into the tumor. This value is chosen deliberately, because higher values lead to drastic vessel regression just at the invasive edge. Whereas lower values (e.g. < 0.005) would be unfeasible because the mean survival time must not be longer than the time to reach the stable radius. Having $p^{(c, max)}$ fixed means that the critical shear force is the prominent factor determining the central MVD. Parameter variations thereof will be presented after the base case results. The support width $\delta^{(c)} = 1 \text{ mm}$ of the collapse region is motivated by results from Breward et al. (2003).

$\alpha^{(0)}$ controls the strength by which c_o scales with increasing MVD. Giving an estimate is difficult due to the quasi two-dimensional layer that is supplied by a network of three dimensional pipes. We factorized $\alpha^{(0)}$ into (i) the volume of a lattice cell $C \cong \delta^2 h$, (ii) the length of a

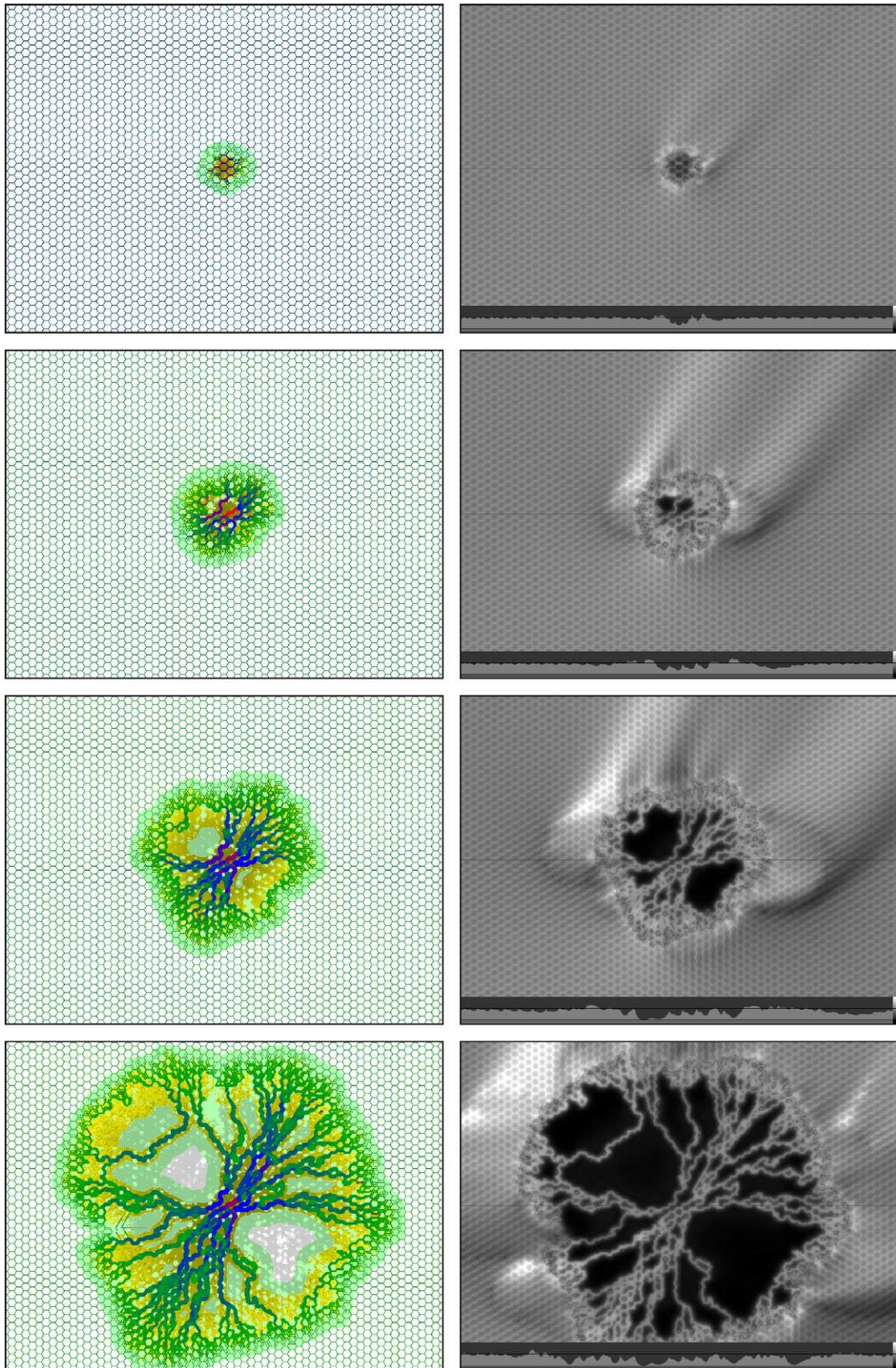


Fig. 3. Left: Tumor and vessel network at $t = 50, 200, 400, 800$. The width of the picture equals 5 mm of tissue. Tumor is yellow, older cells are darker. Vessels are color coded by flow rate. 0 is green, half the maximum is blue, the global maximum value is red. The global flow goes from the bottom left to the top right. Light green regions indicate GF influence zones. Gray indicated necrotic tissue. Right: Tissue oxygen level: 0.55 is white. The tumor is indicated as thin dark outline. The lower bar shows a cross section profile through the center of the system. The vertical lines indicate the thresholds for proliferation $\theta_o^{(prol)}$ and death $\theta_o^{(death)}$.

vessel subsegment over one lattice-bond $L = \delta$, (iii) the resistance to radial O_2 transport through the vessel wall per axial length $K = 3 \times 10^8$ [cm s mmHg]/ml O_2 (Secomb et al., 2004), and (iv) the Krogh diffusion coefficient $D\alpha = 5 \times 10^{-10}$ ml O_2 /[cm s mmHg]: $\alpha^{(0)} = L/(K C D \alpha)$. The parameter h corresponds to the height of the supplied tissue layer and is deliberately set to 333 μm . Our choice is motivated by two considerations: increasing the MVD should result in noticeable increase in $\langle c_o \rangle$ and the oxygen diffusion range should support 150 μm tissue above and below the vasculature. With parameters as chosen above, we obtain $\alpha^{(0)} = 0.002$. The diffusion radius can be related to the consumption coefficient κ via the Green's function of the operator $[\Delta - \kappa]$ which exhibits asymptotically exponential decay on the length scale $\sqrt{1/\kappa}$. Therefore we set $\kappa^{(M)}$ to $(80 \mu\text{m})^{-2}$. The tumor consumption is set to $\kappa^{(T)} = 4\kappa^{(M)}$, i.e. the diffusion radius is halved within the tumor. These parameters yield a mean O_2 concentration of $\langle c_o \rangle = 0.27$ in normal tissue and 0.16 at the tumor center. With the proliferation threshold $\theta_o^{(prol)} = 0.29$ the tumor cannot grow without neovascularization. The threshold for extreme under-oxygenation is set to a value much smaller

than the proliferation threshold: $\theta_o^{(death)} = \theta_o^{(prol)}/10 \ll \langle c_o \rangle$. TCs remain viable under low oxygen conditions for $t_{TC}^{(uo)} = 100$ h. Because the absolute values of the oxygen field are arbitrary, comparisons to experimental data can only be done by observing relative variations.

The growth factor radius is $R^{(g)} = 200 \mu\text{m}$, motivated by the size of the peritumoral region with increased MVD in Döme et al. (2002). The vessel proliferation threshold is very low $\theta_g^{(prol)} = 10^{-4}$, so that essentially all vessels within the full GF radius are affected. In Table 1 all parameter values of the base case scenario are summarized.

3.2. Base-case scenario

System configurations for one representative run at different times are shown in the left column in Fig. 3. The right column shows a map of the oxygen level. Since most TCs are initially under-oxygenized, new vessels emerge within the GF radius in the region around the tumor. Sprouts grow toward the tumor and eventually make contact with other vessels. Once blood flow is established, vessels contribute to the O_2 supply. This leads to increased

Table 1
List of parameters and their symbol together with the values used for the base case scenario

Parameter	Value	Description	Reference
δ	10 μm	Lattice const.	
l	1000	Lattice size	
Δt	1 h	Time step	
$ T(t=0) $	1000	Initial # TCs	
$\alpha^{(0)}$	0.02	O_2 source coefficient	(Secomb et al., 2004)
$\kappa^{(M)}$	$(80 \mu\text{m})^{-2}$	Consumption in normal tissue	(Carmeliet and Jain, 2000)
$\kappa^{(T)}$	$4\kappa^{(M)}$	Consumption tumor tissue	
$\theta_o^{(prol)}$	$0.29 \approx 1.07\langle c_o \rangle$	TC O_2 proliferation threshold	
$\theta_o^{(death)}$	$\theta_o^{(prol)}/10$	TC hypoxia threshold	
$R^{(g)}$	200 μm	Growthfactor diffusion radius	(Döme et al., 2002)
$\theta_g^{(prol)}$	10^{-4}	Sprouting GF threshold	
$H^{(0)}$	0.45	Initial hematocrit	(Pries et al., 1990)
$\eta^{(plasma)}$	4.0×10^{-6} kPa s	Plasma viscosity	(Pries et al., 1990)
$p^{(min)}, p^{(max)}$	0, 90 kPa	Boundary pressure	
$t_{TC}^{(uo)}$	100 h	TC survival time under hypoxia	(Yu et al., 2002)
$t_{TC}^{(prol)}$	10 h	TC proliferation time	
$t_{EC}^{(sprout)}$	40 h	Sprout generation time	
$t_{EC}^{(dil)}$	20 h	Vasodilation time	(Döme et al., 2002)
$t_{EC}^{(migr)}$	1 h	Sprout extension time	(Nehls et al., 1998)
$r^{(init)}$	5 μm	Initial vessel radius	
$r^{(stable)}$	20 μm	Stable vessel radius	(Döme et al., 2002)
$r^{(max)}$	30 μm	Max vessel radius	(Döme et al., 2002)
$s^{(max)}$	20 h	Sprout extension limit	(Nehls et al., 1998)
$l^{(spr)}$	30 μm	Inter-sprout-site distance	(Döme et al., 2002)
$f^{(c,max)}$	0.5 Pa	Peak critical shear force	
$p^{(c,max)}$	0.01	Peak collapse probability	

For the cases in which experimental data are available a reference is given. The other cases are based on educated guesses and the sensibility of the model with respect to variations of these values was studied.

O₂ levels, indicated by a small bright band surrounding the low oxygen region. Simultaneously the radius of the central vessels increases. This initial remodeling creates a disturbance in the almost homogeneous global flow also causing long range O₂-field variations due to the coupling via the hematocrit. Apparently the O₂/hematocrit increase dominates regions close to the central diagonal axis where most blood enters/leaves the tumor. Thereby asymmetrical growth is induced showing that despite neovascularization O₂ supply is the limiting factor for TC proliferation. When the tumor grows over the highly vascularized region, vessels begin to collapse. Vessels in the vicinity of tumor cells are continuously exposed to growth factors and thus increase their radius up to $r^{(max)}$. In regions void of vessels, tumor cells die after $t_{TC}^{(uo)}$, due to the lack of oxygen. As expected ca. 100 μm wide cuff remain alive around few surviving vessels.

Despite the star like structure of the network, which is clearly an artifact of the unrealistic flow boundary conditions, we can reproduce general tumor-network features in agreement with the rest of the literature (Holash et al., 1999a, b; Bartha and Rieger, 2006; Döme et al., 2002). Fig. 4 gives a quantitative analysis of the dynamical evolution. The curves are averaged over 20 runs, with different random number generator seeds but otherwise identical parameters. Statistical fluctuations are of the order of 10%, growing toward the tumor center. Fig. 4(f) shows how the tumor density varies with distance r to the center of the system. The tumor periphery moves outward linearly with a speed of $2 \mu\text{m}/\text{h} = 2\Delta r/t_{TC}^{(prol)}$. The factor 2 is typical for Eden growth (Eden, 1961). Fig. 4(a) shows the average microvascular radius (MVR). Since tumor vessels are always enclosed by TCs that produce GF, the radius grows everywhere inside the tumor at a constant rate. At a fixed location this means that as soon as the tumor is grown over it, the radius increases linearly until the threshold $r^{(max)}$ is reached. Hence a plateau is observed when the spatial variations at a fixed time are considered. Fig. 4(b) shows the MVD and agrees with the pictures in Fig. 3 regarding the compartmentalization of the system. There is a region of high MVD which coincides with the TC density drop. Inside the tumor, the MVD drops to 1/4 of the original MVD, since only few vessels survive the collapse process. In Fig. 4(d) it can be seen that the wall shear stress drops by almost two orders of magnitude, even below the critical collapse force $f^{(c,max)} = 1 \text{ Pa}$. Considering that the support of the band where vessels collapse due to solid pressure is $\delta^{(fc)} = 1 \text{ mm}$ broad, this means that vessels collapse in a narrow shell in the tumor periphery. Hence, altering the rules for the collapse process, leads to different MVDs and network structures as evident in Section 3.4. The drastic reduction in shear stress stems from equally drastic reduction in pressure gradients. In contrast to flow and shear stress, the pressure gradients assume near constant values after the drop at the tumor boundary. Hence, near the tumor center, the vessel radius dependence which is $r(v)^4$ and $r(v)$ for the blood flow rate and shear stress, respectively is responsible for variations of the latter

properties. Fig. 4(e) shows the radial oxygen variations, which are strongly correlated to the MVD variations. Naturally the O₂ level drops in the tumor center. The average value in the tissue is $\langle c_o \rangle = 0.275$. In the highly vascularized zone it increases by 30%. In contrast to our previous work the O₂ increase is not proportional to the MVD due to the O₂ dependent source strength.

Quantitatively our results agree well with the morphological data provided in Döme et al. (2002). They analyzed human malignant melanoma spatially divided into three regions: (i) the tumor center, (ii) the tumor periphery—a 100 μm wide band of tumor immediately adjacent to the invasive edge, and (iii) the peritumoral host tissue—a 200 μm wide band of host tissue immediately adjacent to the periphery. It was found that for tumors larger than 1.5 mm the MVD in (i) drops to 25% of the MVD in normal skin. In (iii) the MVD reaches values up to two times the normal MVD. In terms of radii, the MVR grows from ≈ 8 to $\approx 30\text{--}35 \mu\text{m}$ in the center, at day 15, and remains constant. From day 12 on the MVR in (ii) and (iii) also remains constant, and grows from (iii) to (ii) to (i).

Boxcounting analysis: The concept of a fractal dimension is often used to characterize differences between normal vasculature and tumor vasculature (Baish and Jain, 2000). One commonly used method to estimate fractal dimension is box-counting, which is carried out by superimposing a grid with box diameter l on the fractal object and counting the number of boxes n which overlap the object. The self similar nature of true fractal object leads to a power law relationship between box count and box size with the fractal dimension d_f as exponent:

$$n(l) \propto l^{-d_f}. \quad (13)$$

d_f is usually extracted by a linear fit in a log–log plot. However in experiments one can usually only measure l over two orders of magnitude. Furthermore natural objects (or rather photographs thereof) are usually not perfectly fractal i.e. box-counting plots exhibit non-constant slopes. Therefore even a small constant regime is often considered sufficient to speak of a fractal dimension (or more truthfully named box-counting dimension); see the discussion in Chung and Chung (2001a, b). Therefore what we mean in following with “fractal dimension” is the number that we obtained by the procedure described below and which is analogous to the way in which this number is extracted from the analysis of experimental data (Gazit et al., 1995; Baish and Jain, 2000; Chung and Chung, 2001a, b).

We did box-counting for the tumor as well as for different parts of the vessel network at the time $t = 1000 \text{ h}$. At this time the diameter of the tumor is ca. 5 mm. Vessels are treated as ideal line segments, and overlapping boxes are visited by a digital differential analyzer algorithm (Glassner, 1994). TC occupied locations were treated as points. Boxes with size L were shifted by $\max\{L/10 \mu\text{m}, 16\}^2$ different offsets equidistantly distributed in $[0, L]^2$, and the minimum box-count was taken. The fractal dimension is then estimated as average over the

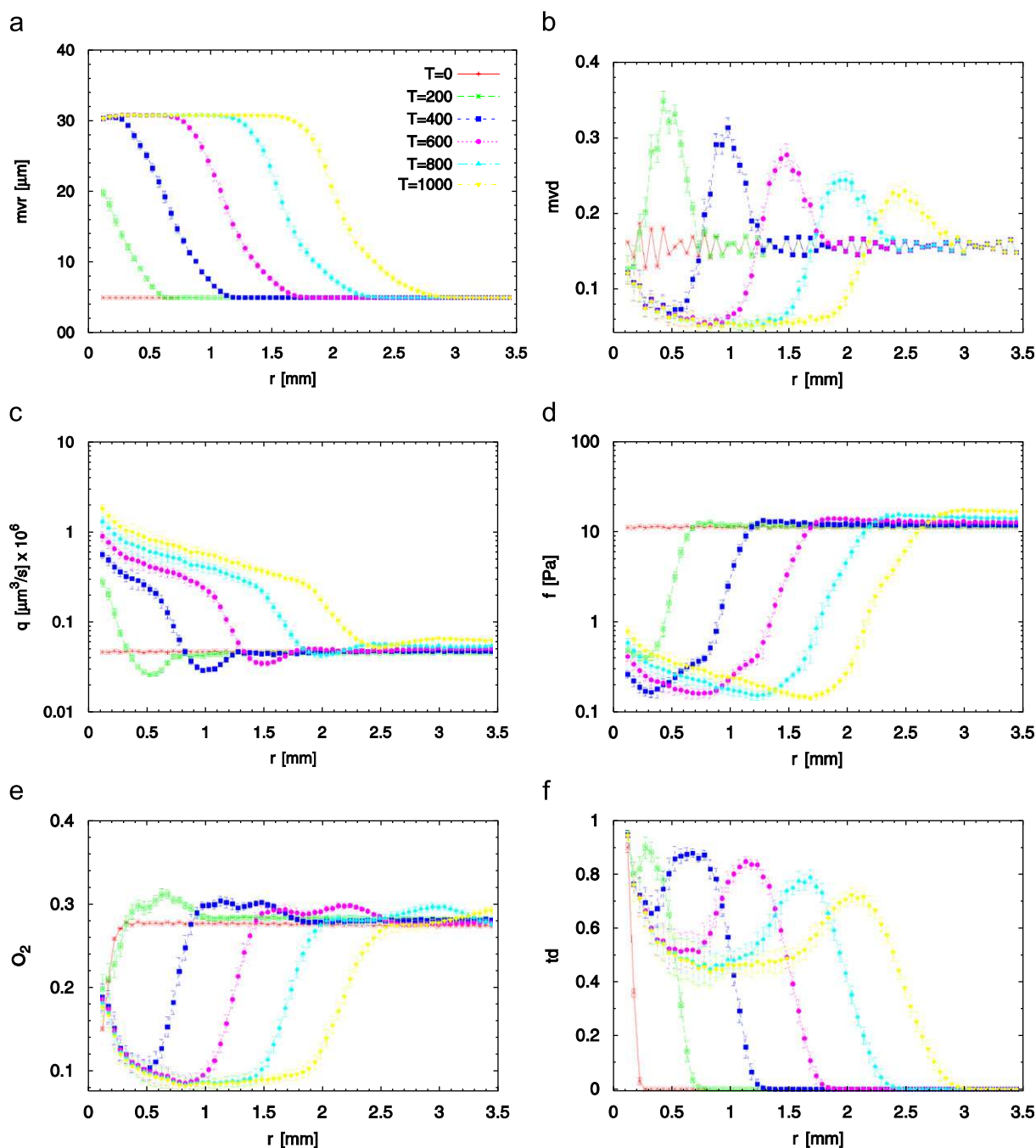


Fig. 4. Various dynamic variables in dependence on the radial distance r to the tumor center: (a) Shows the vessel radius. It decreases with the distance to the tumor, whereas at a fixed distance to the tumor center it increases with time. (b) Shows the microvascular vascular density (MVD) dependence. The MVD is high at the tumor boundary, and low in the tumor center. The maximum value decreases with time due to the asymmetry of the tumor. (c) The flow rate increases by more than an order of magnitude inside the tumor. Whereas (d) shows that the shear force decreases by almost two orders of magnitude. (e) The oxygen level follows roughly the same shape as the MVD. Due to implicitly defined source strengths, the increase in high-MVD regions is much less than simply proportional. (f) Shows the tumor density. One can see that the tumor radius increases linearly in time, as expected according to the eden rule. The density drop eventually becomes less pronounced due to the asymmetric growth.

local slopes of the log–log plot, which are first estimated by least-squares fits of 17 points around the respective pivots. The averaging is done over a suitable range, i.e. a regime with constant slope if available and between 200 and 1000 μm otherwise. Indicated errors represent root mean square deviations from the mean local slope. Hence, a large value would indicate a less fractal object.

The mean fractal dimension of the vasculature was estimated over three regions as indicated in Fig. 5. The center of the tumor, for which $\langle d_f \rangle(C) = 1.59 \pm 0.02$ was obtained. This central region reaches up to a boundary region (B), a 400 μm wide band along the perimeter, centered at the invasive edge. The width of the band is chosen deliberately according to the growth factor radius,

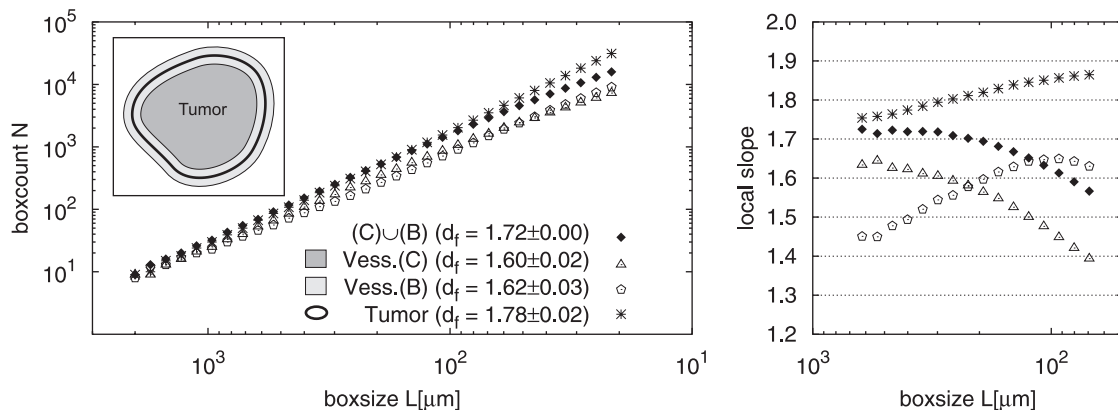


Fig. 5. Fractal dimension analysis of the base case tumor via boxcounting. Left: Boxsize vs. boxcount logarithmic plots. (C) denotes the vessel network in the tumor center region. This fills the space up to a $200\mu\text{m}$ wide band centered at the invasive edge around the tumor (B) . $(C) \cup (B)$ contains all vessels in the union of region (C) and (B) . “Tumor” denotes the viable regions of the tumor. Right: Local slopes of the curves on the left.

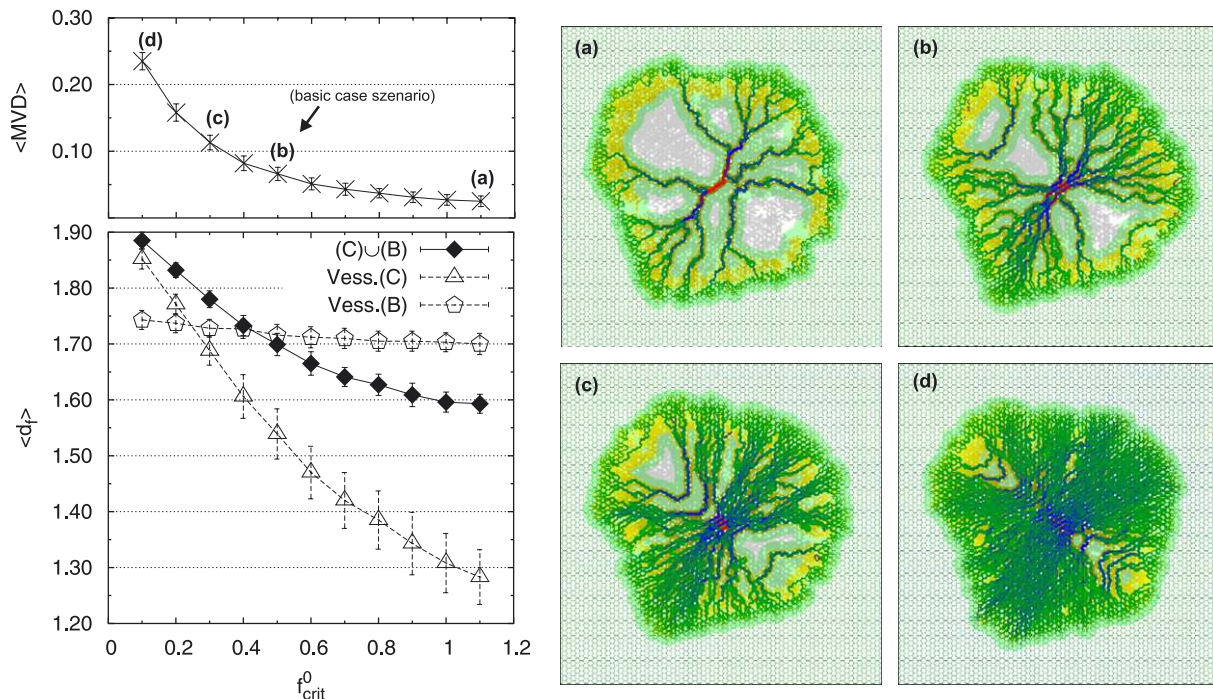


Fig. 6. Fractal dimension in dependence on critical shear stress. Left: In analogy to Fig. 5, (B) denotes a $200\mu\text{m}$ wide band around the invasive edge, (C) the central region, and $(B \cup C)$ the entire tumor vasculature. The MVD is averaged over 20 tumors and over a disc with $r = 1.6\text{mm}$. The data were generated by running simulations with $f_{\text{crit}}^{(c, \text{max})}$ ranging from 0.1 to 1.1 Pa. Right: Four configurations are shown with critical shear forces $f_{\text{crit}}^{(c, \text{max})} = 1.1, 0.5, 0.3, 0.1$ Pa. The labels on the left figure correspond to these configurations. The fractal dimension ranges from 1.61 to 1.82.

such that the exclusively angiogenesis dominated remodeling is captured. There $\langle d_f \rangle(B) = 1.63 \pm 0.03$ was obtained. The fractal dimension of the complete tumor vasculature turned out to be $\langle d_f \rangle(C \cup B) = 1.71 \pm 0.01$, and that of the tumor $\langle d_f \rangle(\text{Tumor}) = 1.78 \pm 0.02$. These values are lower than those reported in Bartha and Rieger (2006) for the simplified model, but are closer to the value $d_f = 1.81 \pm 0.04$ found experimentally for carcinoma (Gazit et al., 1995; Baish and Jain, 2000).

Fig. 5 also shows that the local slopes for the tumor and its vasculature are very similar for box-sizes greater $350\mu\text{m}$. This can be explained by considering that all tumor vessels have cuffs of viable TCs around themselves

with a diameter of ca. $200\mu\text{m}$ - twice the oxygen diffusion radius. Further away from vessels no living TCs exist. Therefore in the large box limit ($L \gg 200\mu\text{m}$) vessels and TCs will touch mostly the same boxes and thus yield similar fractal dimensions.

3.3. Parameter variations

Further experiments reveal that the fractal dimension of the tumor vasculature is apparently not a universal constant. Multiple simulations were performed where the maximum critical shear force ranges from 0.1 to 1.1 Pa, producing tumors with decreasing internal MVD. Fig. 6

shows the results. The fractal dimension of the boundary $\langle d_f \rangle(B)$ remains constant around 1.68, whereas the dimension of the complete vasculature $\langle d_f \rangle(B \cup C)$ ranges from 1.61 to 1.83. Naturally $\langle d_f \rangle(B)$ is a lower bound because it corresponds to the case where no internal vessels are present. With increasing density the dimension is dominated by the internal vasculature. The dimension of the tumor follows that of the vasculature for reasons already discussed.

In order to study the relation to conventional random bond percolation, simulations were performed with critical shear stresses ten times higher than normal $f^{(c,max)} = 5 \text{ Pa}$. At normal values for the collapse probability $p^{(c,max)} = 0.01$, this would remove all vessels almost instantly when the tumor grows over them. As shown in Fig. 7 there is however a sharp transition at $p^{(c,max)} = 0.001$ from the absence of vessels in the center to configurations where no vessels collapse at all. Note that the high value essentially inhibits the shear force stabilization mechanism which means that collapses are purely random and uncorrelated with flow. Visually this can be seen by the absence of the imposed flow direction. As a consequence all central vessels had the same probability to collapse by the end of the simulation, namely the probability to collapse until the stable radius is reached. Therefore the results here are in agreement with conventional percolation theory as described in the discussion Section 5.

3.4. Simplifications

In the following the effect of several simplifications toward the model discussed in Bartha and Rieger (2006) are discussed: replacing the viscosity term with a constant or purely radius dependent value; settings the vessel collapse probability and critical shear force to step functions; generating perfused sprouts instantly; and setting the oxygen source strength constant.

Blood viscosity: To compare the effect of different models for blood viscosity, we set the blood-oxygen content constant to the initial hematocrit value: $c_o^{(B)} = H^{(0)} = 0.45$. Consequently, this removes the large scale variations in the oxygen field and thus produces symmetric tumors. With this modification multiple simulation runs were performed with

- (i) the original viscosity model including hematocrit and blood phase separation;
- (ii) a viscosity term which was derived from *in vitro* data (Gödde and Kurz, 2001) and which depends only on the vessel radius $\eta = \eta^{(plasma)} \eta^{(rel)}(r)$. (see Fig. 8);
- (iii) the vessel viscosity set to the constant blood plasma viscosity. $\eta = \eta^{(plasma)}$.

The result is shown in Fig. 9. While the cases (ii) and (iii) do not differ significantly, the tumor MVD in (i) is ca.

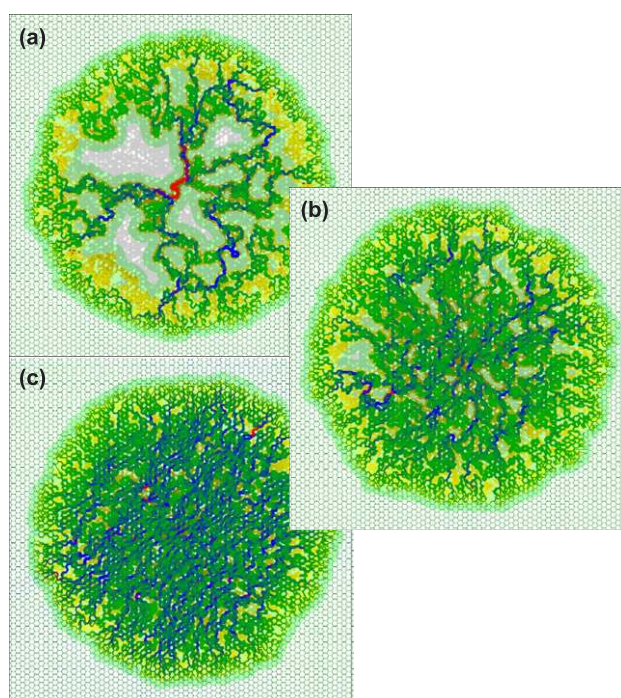
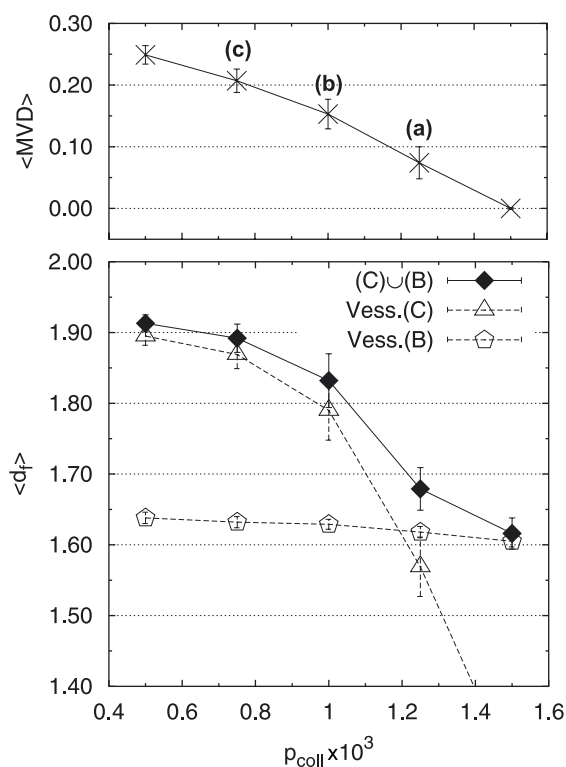


Fig. 7. Fractal dimension for tumors with uncorrelated vessel collapses. Left: (B) denotes a $200 \mu\text{m}$ wide band around the invasive edge, (C) the central region, and $(B \cup C)$ the entire tumor vasculature. Fractal dimension estimates for the three regions are shown, where $p^{(c,max)}$ ranges from 0.5×10^{-3} to 1.5×10^{-3} . Furthermore critical shear force and collapse probability were set constant within the tumor with $p^{(c)}$ as indicated $f^{(c,max)}$ was set very high to 5 Pa in order to reduce shear force correlation of collapses to an insignificant amount. Right: Three configurations are shown with $p^{(c,max)} = 1.25, 1.00, 0.75 \times 10^{-3}$ for (a),(b),(c) respectively.

two times lower than in (ii),(iii). This is unexpected but we think the following is a plausible explanation: The viscosity in (i) rapidly decreases by 50% from $r = 5$ to $20 \mu\text{m}$, i.e. from outside to inside the tumor, whereas it changes less drastically in (ii) and (iii). The total flow into the tumor is generally limited by the flow resistance of the surrounding network. Let us assume a prescribed constant in-flow $Q =$

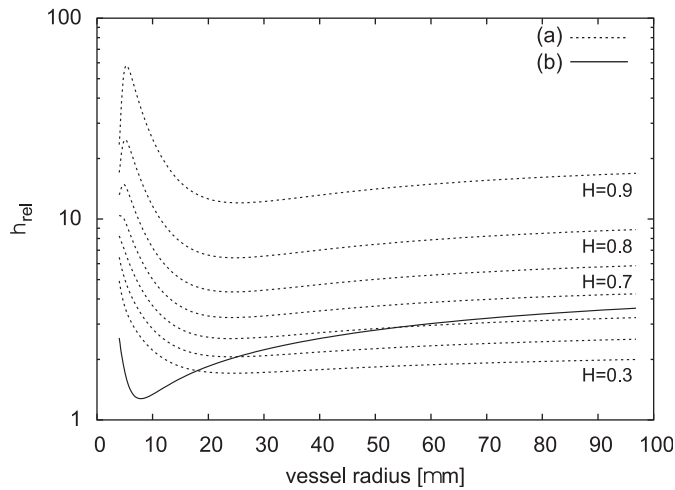


Fig. 8. Plot of the relative viscosity as a function of the vessel radius: (a) according to the formula derived in Pries et al. (1994), evaluated for hematocrit values $H = 0.3$ – 0.9 ; (b) data derived from in vitro measurements—see Gödde and Kurz (2001). Used here for the simplified model without hematocrit.

$Nq \propto Nf r^3 / \eta$ which has to be supported by N vessels threading the tumor. Thereby assuming homogeneous flow-rate q , radius r , and shear force f . Let us further assume that f is identical to $f^{(c,max)}$. Then it is easy to see that the number of remaining vessels is proportional to the viscosity η .

Increasing the critical shear stress from 0.5 to $f^{(c,max)} = 1.0 \text{ Pa}$ drops the MVD back to the level of the base-case at the cost of increased flow rate and shear stress in the vessels. Fig. 9 shows respective averaged curves. Apparently there is no fundamental change in vessel morphology. This is also reflected by fractal dimension analysis where the mean dimensions only differ at most by 3%. Thus it is reasonable to assume that for the purpose of morphological studies an effective constant blood viscosity—ca. twice the plasma viscosity—can be used.

Vessel collapse: In the base-case both the collapse probability $p^{(c)}$ and the critical shear force $f^{(c)}$ are modulated by the function g_1 which introduces an explicit location dependency. In the following we present two cases with differently designed functions which might be equally well suited models. With $p^{(c)}$, we refer to the collapse probability of unstable ($f < f^{(c)}$ and $r < r^{(stable)}$) normal perfused vessels.

- (i) Denotes the base-case where g_1 has a torus-like profile, as shown in Section 2.2. And where $p^{(c)}$ is additionally multiplied by a vessel-radius dependent term.

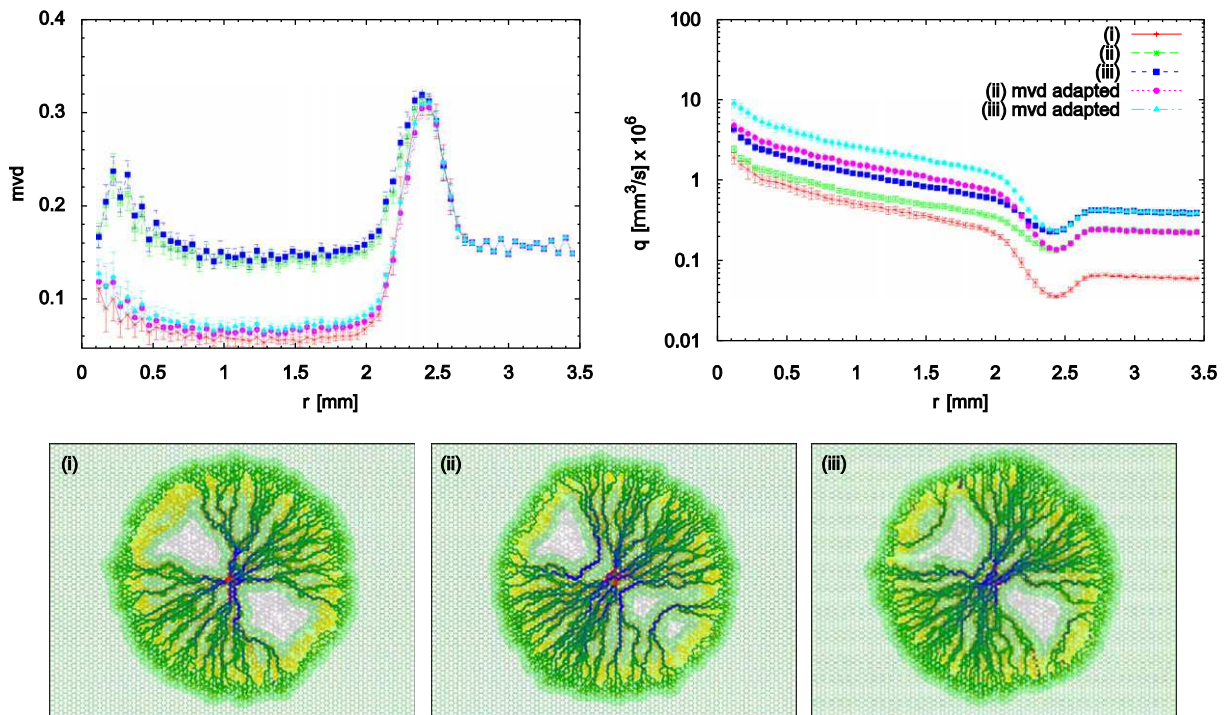


Fig. 9. Comparison of viscosity functions. Top: Shown are radial MVD and flow rate curves for different viscosity models and parameters at $t = 1000$. “adapted mvd” denotes data where the critical shear force has been tuned such that the MVD matches that of the original model. Bottom: Shown are snapshots of tumors of the adapted configurations. (i) Denotes the original flow model. All the simulation runs here where done with the oxygen field unaffected by the blood hematocrit content (ii) uses radius-only dependent viscosity formula of, Gödde and Kurz (2001) and (iii) assumes a constant value.

- (ii) $f^{(c)}$ and $p^{(c)}$ assume constant values within the tumor and zero outside.

$$f^{(c)}(a, \mathbf{x}) = f^{(c)}(\phi, x) = f^{(c, \max)} \cdot \theta(x_T(\phi) - x), \tag{14}$$

$$p^{(c)}(a, \mathbf{x}) = p^{(c)}(\phi, x) = p^{(c, \max)} \cdot \theta(x_T(\phi) - x) \cdot \theta(r^{(stable)} - r_a), \tag{15}$$

where θ is the step function, x is the distance to the center, ϕ the polar angle and r_a the vessel radius. Beside the dependence on the distance to the tumor, the linear dependence on r_a has also been replaced by a step function, such that the collapse probability becomes 0 instantly once $r_a \geq r^{(stable)}$. Without changes to other parameters this results in decreased central MVD. Therefore $f^{(c, \max)} = 0.25$ Pa is chosen, which is 1/2 of the normal value. $p^{(c, \max)} = 0.01$ is left unchanged. In the latter case no significant difference to the base case scenario could be observed. Radial curves differ at worst by 10% and the mean fractal dimension is also in agreement within the error bounds.

- (iii) $f^{(c)}$ decays from $f^{(c, \max)}$ at the center of the tumor to 0 at the invasive edge. For $p^{(c)}$ the simple form from (ii) is chosen.

$$f^{(c)}(a, \mathbf{x}) = f^{(c)}(\phi, x) = f^{(c, \max)} \cdot \max\{0, 1 - x/x_T(\phi)\}, \tag{16}$$

$$p^{(c)}(a, \mathbf{x}) = p^{(c)}(\phi, x) = p^{(c, \max)} \cdot \theta(x_T(\phi) - x) \cdot \theta(r^{(stable)} - r_a). \tag{17}$$

In this case the original parameters work fine: $f^{(c, \max)} = 0.5$ Pa and $p^{(c, \max)} = 0.01$. Fig. 10 shows that compared to (i) and (ii) a smoother transition from the high-MVD boundary to the tumor center with low MVD is obtained. In an experiment not shown here this effect was enhanced by setting $p^{(c)}(a) \propto \max\{0, 1 - r_a/r^{(stable)}\}$. Further on, peripheral MVD has slightly increased since collapse events happen now closer to the center where the critical shear force threshold is high enough. Being directly correlated to the MVD other measurements such as oxygen level or tumor density exhibit similar behavior. The mean fractal dimension of the tumor vasculature is $\langle d_f \rangle = 1.80$.

Sprout migration: In analogy to our previous work, we also checked the results when “sprouts” instantly extend to the next vessel, possibly creating a perfused loop.

This simplified sprout model works as follows: Starting at a parent vessel, sites along a straight path are checked for a destination vessel. As before, the direction is determined by the local GF gradient at the starting site. A vessel connection is added, provided that all conditions for sprout generation—such that it has to be outside the tumor—are fulfilled for the starting site, and that the

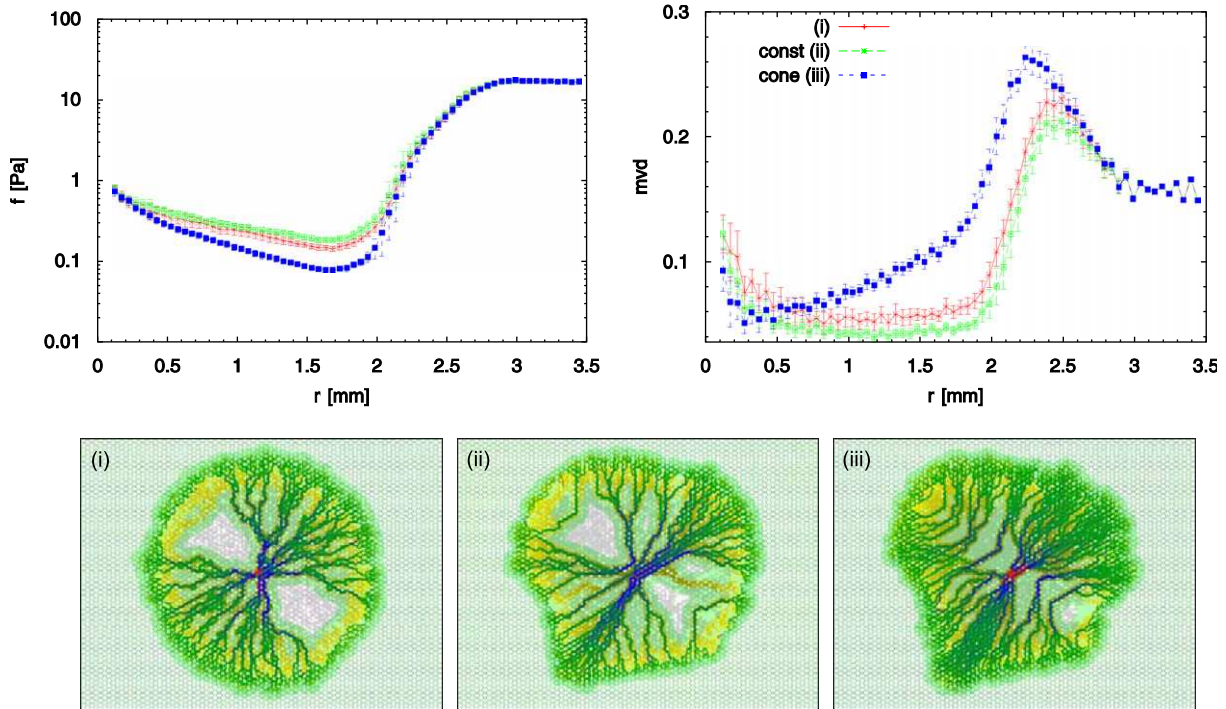


Fig. 10. Comparison of different dependencies of $p^{(c)}$ and $f^{(c)}$ on local system properties. Top: row shows mean shear force and vessel density by radial distance at $t = 1000$, (i) is the basic case model, (ii) has positive constant values for $p^{(c)}$ and $f^{(c)}$ inside the tumor, with the exception that $p^{(c)} = 0$ for $r \geq r^{(stable)}$ and (iii) has a linear decay from $f^{(c)} = f^{(c, \max)}$ at $r = 0$ to 0 at the invasive edge. Notice how the MVD decreases much smoother toward the center. Bottom: shows snapshots of sample tumors.

destination site has less than three incident vessels. The resulting tumor's boundary regions exhibit ca 70% the MVD of the full model's tumors. Apparently the stronger requirements for vessel creation limit the degrees of freedom for the system's evolution. For example in the original model there is the possibility that two sprouts grow simultaneously and form a perfused wedge when they meet inside a hexagon. MVD correlated data vary accordingly, but otherwise no fundamental changes could be observed.

Oxygen field computation: Solving the O_2 diffusion equation with implicit source strengths can become expensive, in particular in three dimensions. Therefore we also performed simulations using a simplified model. Instead of solving $\Delta c_o - \kappa c_o + \alpha(c_o^{(B)} - c_o) = 0$, we do now consider

$$\Delta c_o(\mathbf{x}) - \kappa^{(M)} c_o + \alpha c_o^{(B)} = 0, \quad (18)$$

where the coefficient κ equals the tissue consumption $\kappa^{(M)}$, disregarding the tumor. The occurrence of $c_o(\mathbf{x})$ is omitted in the source term which means that O_2 is produced at a fixed rate. (18) could be efficiently solved by a Greens-function approach, in analogy to our solution of the GF distribution. In the present case, q_0 is simply a prefactor that scales the field values globally, and it is chosen to get the mean O_2 $\langle c_o \rangle = 0.2$. The tumor proliferation threshold remains at the original value $\theta_o^{(prot)} = 0.29$.

As a consequence the O_2 level increase from normal MVD to high MVD is overestimated by ca. 50%. Fig. 11 shows snapshots from two runs at $t = 1000$ h.

- (i) shows a snapshot from the full model. To facilitate comparisons the effect of hematocrit on O_2 has been disabled, i.e. $c_o^{(B)} = H^{(0)}$;
- (ii) shows a snapshot from the simplified model. As can be seen the tumor grows slower and develops an elliptical shape. Here TCs produce GF only if $c_o(\mathbf{x}) < \theta_o^{(prot)}$. Due to the higher O_2 level, the outer band where TCs are allowed to proliferate—and do not produce GF—is almost as wide as the GF radius. Therefore the GF influence region—indicated by a bright green background—does not reach as far into the tissue as in (i), leading to slower vessel generation and thus slower tumor growth. Depending on parameters, the growth of the tumor may even come to halt in the beginning of the evolution when the O_2 level increases above $\theta_o^{(prot)}$ for all TCs in the nucleus. In the full model no reasonable parameter set allows such an increase in O_2 and therefore this behavior has never been observed;
- (iii) shows snapshots from the simplified model—modified so that TCs always produce GF. Naturally the GF influence zone now has the largest possible extend, leading to continuous neovascularization and virtually undisturbed Eden-like tumor growth. Overestimating

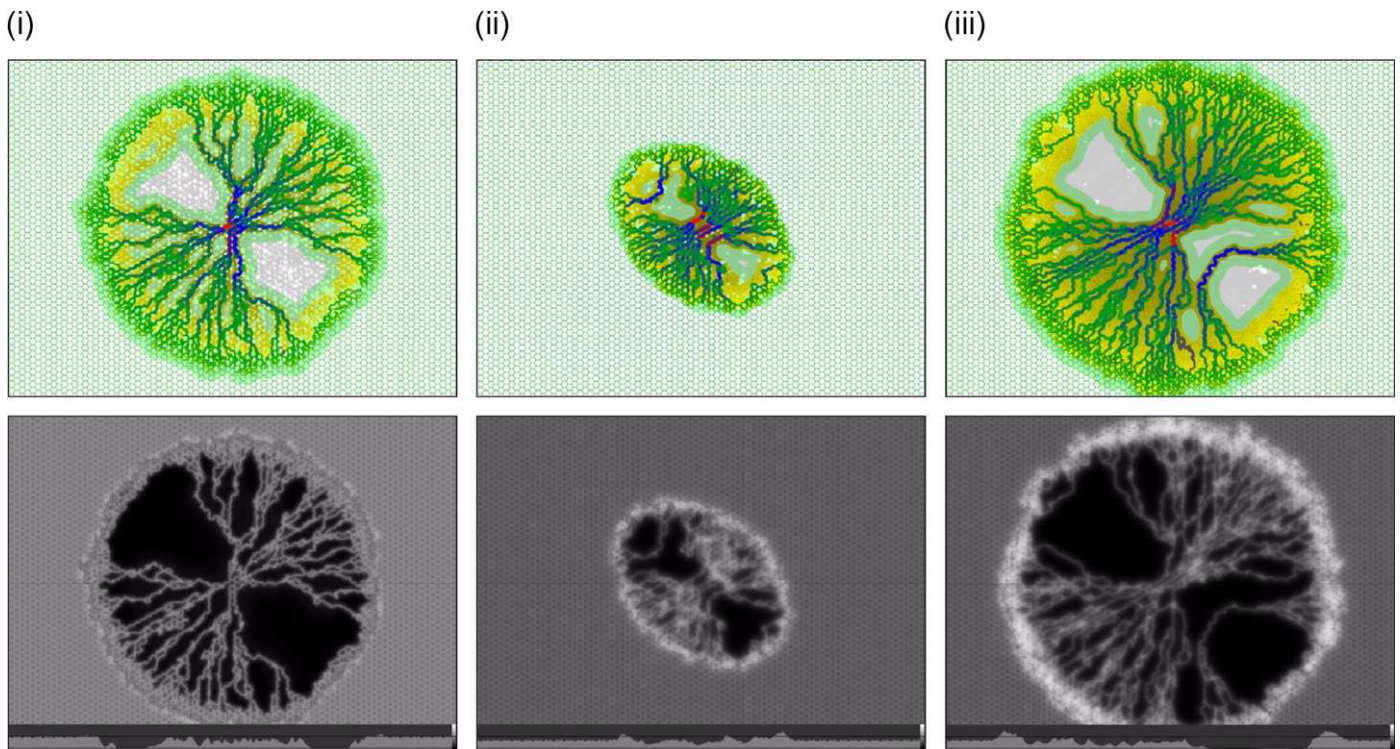


Fig. 11. Comparison of different oxygen and proliferation models. The top row shows vessel, tumor, gf-influence configurations. The lower row shows associated oxygen fields and central cross section, (i) is the full O_2 model for $c_o^{(B)} = H^{(0)} = const$, (ii) is the simplified O_2 model with constant source strength, (iii) is the simplified model (ii) with the addition that TC always produce GF.

the O₂ levels also the effect of making the model more robust regarding the choice of the TC proliferation threshold $\theta_o^{(prol)}$. This leads to the observations that tumor (iii) is denser than tumor (i) and grows slightly faster. The O₂ level in (i) increases by mere 10% at the high MVD periphery, leaving not much choice for $\theta_o^{(prol)}$ because at low values TCs can proliferate quickly along the original vessels which can create holes as seen in Fig. 11 (i). At high values the tumor might not proliferate at all.

Simplifications combined: Measurements from tumors with simplifications combined are shown in Fig. 12. In these simulations blood viscosity is set constant $\eta = \eta^{(plasma)}$, collapse probability and shear force are also set constant according to (14), oxygen computations are done with the simplified model from (18), and all TCs produce GF. Parameters, $f^{(c,max)}$ and $p^{(c,max)}$ in particular, are equal to the settings in the full model simulations. To get better estimates for data near the invasive edge, it is compared to the basic model without hematocrit affecting oxygen levels $c_o^{(B)} = H^{(0)}$.

All modifications combined lead to changes in many measurements. Most of which have already been discussed in the examples above. For example the almost 10-fold increase in flow rate due to reduced viscosity, increased oxygen in high MVD regions due to constant source strengths, faster and denser tumor growth due to better

oxygen supply. Not observable before is an apparent difference in vessel morphology. Note the tendency to form compact straight bundles of 3–8 vessels. Vessels in snapshots of the basic case—denoted (i) here, see Fig. 3 for instance do not seem to have this property, instead those exhibit many small weakly perfused loops and cross-links. Radial curves (ii) seem to reflect this also by an overall increase in shear force. Most likely weakly perfused vessels in (i) survive long enough until the relatively thin ring of high collapse probability has moved further outwards. If so they can contribute to the shear force measurement such that the mean values are lowered. Fractal dimension analysis also indicates different morphological features. The mean vasculature dimension has increased to $\langle d_f \rangle = 1.77$, although the central MVD has not increased significantly. Fig. 12 also shows results from box-counting analysis of a single sample tumor. Over a small range the local slope reaches peak values of ca. 1.82.

4. Drug flow modeling

This section discusses modeling, and results, of simulated drug flow through the tumor vasculature. The mathematical model for drug flow is based on McDougall et al. (2002), where it was demonstrated how the concentration profile of a tracer substance flowing through a vascular network can be tracked. The drug flow model is designed on top of the already established network model.

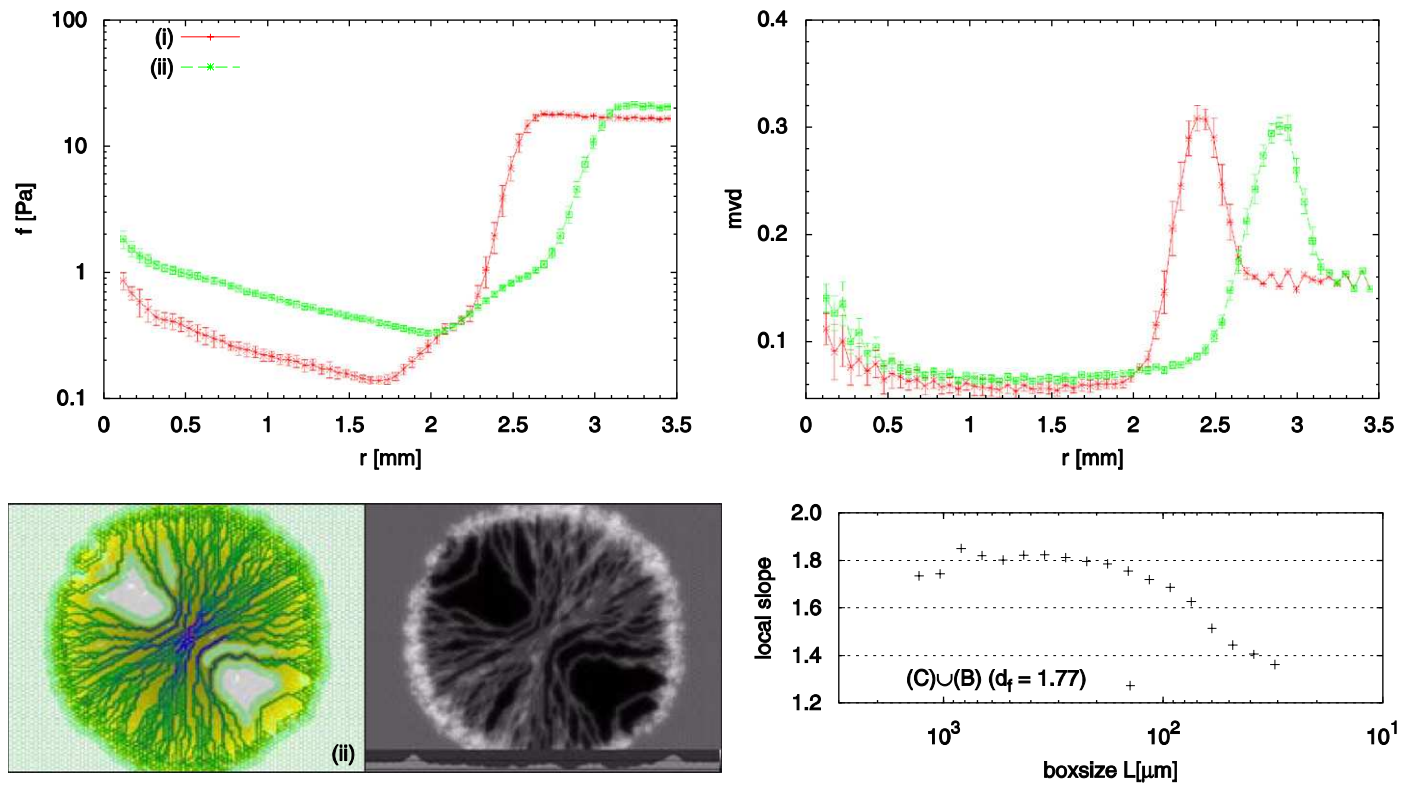


Fig. 12. Measurements from simulations with simplified viscosity, oxygen computations and vessel collapse model. Top row shows radial curves for shear force and MVD, (i) is the original model and (ii) the simplified version. The bottom row shows snapshots on the left. The right-hand side shows local slopes from boxcounting analysis for the complete tumor vasculature.

Hemodynamic parameters, such as flow rate are precomputed (taken over from the results of the tumor simulation). The network is completely static during the simulation, which is reasonable as the drug injection does not last longer than one hour. An iterative algorithm first propagates drug mass from vessels to downstream nodes, followed by a second pass where drug is distributed among the outflow vessels. Thereby mass conservation is strictly enforced. One such iteration corresponds to a certain time-step δt . A detailed description is given in the following.

4.1. Model definition

First, node tuples (i, j) which identify vessels now reflect the flow direction by requiring that $p_i \geq p_j$. Geometric and hydrodynamic properties q, l, r, p have meanings as before and their values are static. With I_i and O_i we denote the inflow- and outflow-vessels attached to a node i . In addition to the ideal pipe-flow model, a number of further assumptions are made: Drug is moved downstream with the average flow velocity $v = q/[\pi r^2]$ neglecting radial velocity differences. For each vessel, the simulation tracks a single drug-containing cylindrical subsection. Let $u \in [0, l]$ be its start at the upstream end, measured along the central vessel axis. The downstream end is given by $d \in (u, l]$. The occupied volume is thus $V = (d - u)\pi r^2$, and it is assumed that the drug mass m inside this volume is always homogeneously distributed at the concentration m/V . Thus the description of the concentration profile inside a vessel segment is limited to a single square pulse. This does not appear to be a problem, but when necessary, segments can be subdivided to gain a suitable resolution.

For each time step δt the following is done: First, for each vessel $a = (i, j)$ which has drug $m > 0$ drug is moved downstream by the distance Δx . Let $t' = t + \delta t$, then:

$$\Delta x = q/[\pi r^2]\delta t,$$

$$u^{t'} = u^t + \Delta x,$$

$$d^{t'} = d^t + \Delta x.$$

The volume is then pruned at the end of the vessel, and the lost drug mass is accounted to the attached node. This means if $d > l$ and $u < l$ the drug propagation into the nodes is as follows:

$$\Delta m = m^t/V \cdot [d^{t'} - l]\pi r^2,$$

$$m^{t'} = m^t - \Delta m,$$

$$m_j^{t'} = m_j^t + \Delta m,$$

$$d^{t'} = l.$$

If the time step is large enough it can happen that a vessel is completely drained of drug $u^{t'} > l$. Care must be taken that state variables are kept consistent. Instead of the steps above, all mass is transferred to the node: $\Delta m = m^t$, and the drug start and end variables are reset to $u^{t'} = d^{t'} = 0$.

In a second stage it is looped over all nodes $i \in N$ that have drug $m_i > 0$. This drug is now propagated further downstream into connected vessels. At boundary nodes, drug may be introduced by adding the contribution $\Delta m = (\sum_{a \in O} q_a - \sum_{a \in I} q_a)C^{(in)}\delta t$ from the in-flowing blood volume. The distribution at branching points assumes perfect mixing, i.e. the nodal drug mass is split among outflow vessels proportional to the blood volume that flows into a vessel. Let Q be the total out-flowing volume: $Q = \max[\sum_{a \in O_i} q_a, \sum_{a \in I} q_a]$. This formal description respects that the correct value has to be computed for boundary nodes where Kirchhoff's law is violated due to exchange with the environment. For internal nodes Q is of course equal to $\sum_{a \in O_i} q_a$. Then for all vessels $a \in O_i$ drug mass is updated according to

$$m_a^{t+1} = m_a^t + q_a/Q \cdot m_i^t.$$

Furthermore u_a is set to 0, because drug just entered at the upstream vessel junction. Once again care must be taken to ensure a consistent system state at the end of the iteration. In our implementation the downstream drug end must move forward to $d_a^{t+1} = q_a/[\pi r_a^2] \cdot \delta t$ if the vessel was empty. Note that in this case it has also been $d_a^t = 0$. The time step δt must be chosen carefully to ensure that the location of the drug remains consistent with the network structure. During a time step drug can only move as far as the length of a vessel. Therefore it must be ensured that the in-flowing blood volume $q\delta t$ is less than the volume of the vessel: $q\delta t < l\pi r^2$. The largest possible δt is thus

$$\delta t = \min_{a \in V} \left\{ \frac{l_a \pi r_a^2}{q_a} \right\}. \quad (19)$$

Drug uptake by the tumor is not considered here. It was incorporated in McDougall et al. (2006) in a very crude way: Drug was instantly removed once it reached the tumor. This is not feasible here, since the goal is to study the concentration inside tumor and see if there are spots that are unlikely to be supplied by sufficient drug. It should be possible with some more numerical effort to include a diffusion process through the vessel wall in the line of the O_2 concentration computations presented before. But for simplicity and the lack of experimental data this has not been done yet. As a consequence the intravascular drug concentration here can only predict an upper bound to the real concentration.

4.2. Results

Here we discuss results for two configuration types: (i) the base-case (Fig. 3); (ii) nearly shear force uncorrelated systems with $p^{(c,max)} = 0.001$ and $f^{(c,max)} = 0.5$ (Fig. 7).

In both cases first a preprocessing step was applied. Vessels outside a circular region were removed, such that a band of approximately 1 mm width remained around the tumor. Doing so ensures that drug arrives evenly at the invasive edge, which would not be the case if the network spreads over the entire rectangular domain. Fig. 13 shows

the flow velocity which is of the order of 0.5 mm/s. Regular capillary networks have high flow resistances and do not support increased flows inside the tumor. On the contrary, the dilation causes slower velocity, due to the preservation of mass (Fig. 14). Thereby (i) and (ii) show similar behavior. Simulations were done with injection durations $t^{(in)}$ ranging from 2 to 60 s. The injected concentration was always set to $C^{(init)} = 1$. Fig. 15 shows a sequence of concentration profiles for the hexagonal lattice base-case (i) and $t^{(in)} = 60$ s. Drug enters at the bottom left boundary, and flows toward the tumor. The concentration at the drug “front” shows an increasingly smooth transition. That is because at branching points, the front does not arrive through all inflow vessel simultaneously. Thus drug containing blood is mixed with “clean” blood, decreasing the concentration in out-flowing blood. After 60 s tumor vessels are almost completely saturated with drug. A prolonged injection would keep the system in a fully saturated steady state. The second half of the sequence shows how blood flows out of the tumor after the injection ends.

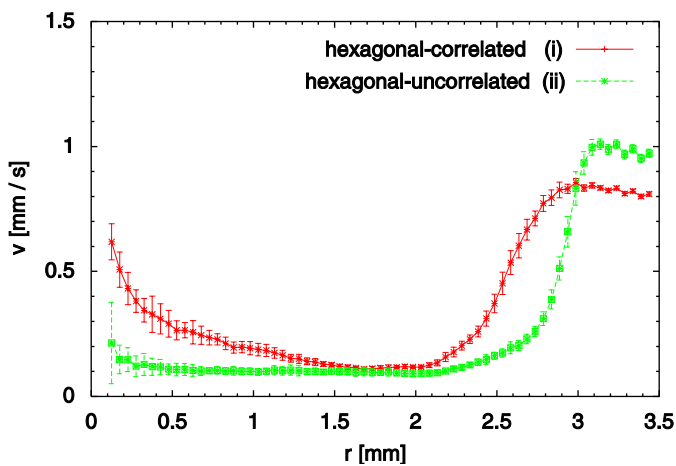


Fig. 13. Radial measurement of the mean flow velocity $v = q/[\pi r^2]$. (i) denotes the base-case (ii) a shear force uncorrelated system with random collapses (Fig. 7).

For shorter injection times, flow results naturally give a similar picture (no image sequence shown here). A compact short burst of approximate length $vt^{(in)}$ flows unhampered in diagonal direction through the tumor. However, the maximum concentration can be significantly decreased due to the mentioned mixing effects. For example in the extreme case where $t^{(in)} = 2$ s, the number of vessels where the concentration $C > 0.5$ is reduced to 30%.

Fig. 16 shows averaged measurements of case (i). The plot on the left indicates the percentage of vessel network length that was exposed to a drug concentration greater than the value on the x-axis. The data are given for injection times $t^{(in)} = 10, 20, 30$ s. For the 30 s injection, 90% of the vascular network was exposed to the maximum possible drug concentration $C^{(init)} = 1$, while all vessels were exposed to at least a concentration of $C = 0.9$. This simply reflects that the systems was nearly saturated with drug, which is also evident by the snapshots.

The right plot in Fig. 16 shows the percentage of vessel network length for which the concentration was larger than a threshold C_t for a total period greater than the value indicated on the x-axis. The data is again given for several injection times. For $C_t = 0.5$ and $t^{(in)} = 60$ s the curve has a step function profile, whereby the drop occurs at $t = 60$ s. This point in time corresponds in good agreement to the duration in which the high concentration “pulse” passes through the tumor. The concentration at a fixed location increases (decreases) smoothly over time before (after) the plateau of saturation. This means that the lower the concentration threshold, the longer the exposure times. Therefore curves for lower thresholds show “tails” beyond the saturation period. Prolonging the injection interval by Δt would increase the time where the system is in a saturated steady state, thus shifting the exposure time curves uniformly by Δt to the right. This is clear since the time that the system remains in steady state is irrelevant. The curves for $t^{(in)} = 10$ and 30 s show the effect very well that the drop is simply shifted to the end of the injection period, thereby preserving the trails.

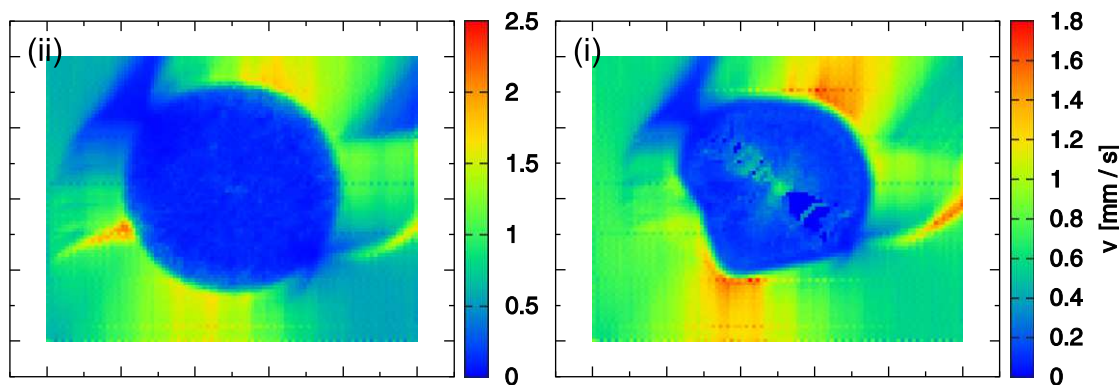


Fig. 14. Spatial distribution of the blood flow velocity for (i) the base-case scenario (Fig. 3) and (ii) the shear force uncorrelated case (Fig. 7b). Both plots show an average over 20 simulation runs at time step $t = 1000$ h, the represented area being 12×10 mm². Compared to normal tissue, the flow velocity is reduced in the tumor. The flow increases in (i) toward the center due to the star like structure with fewer vessels there.

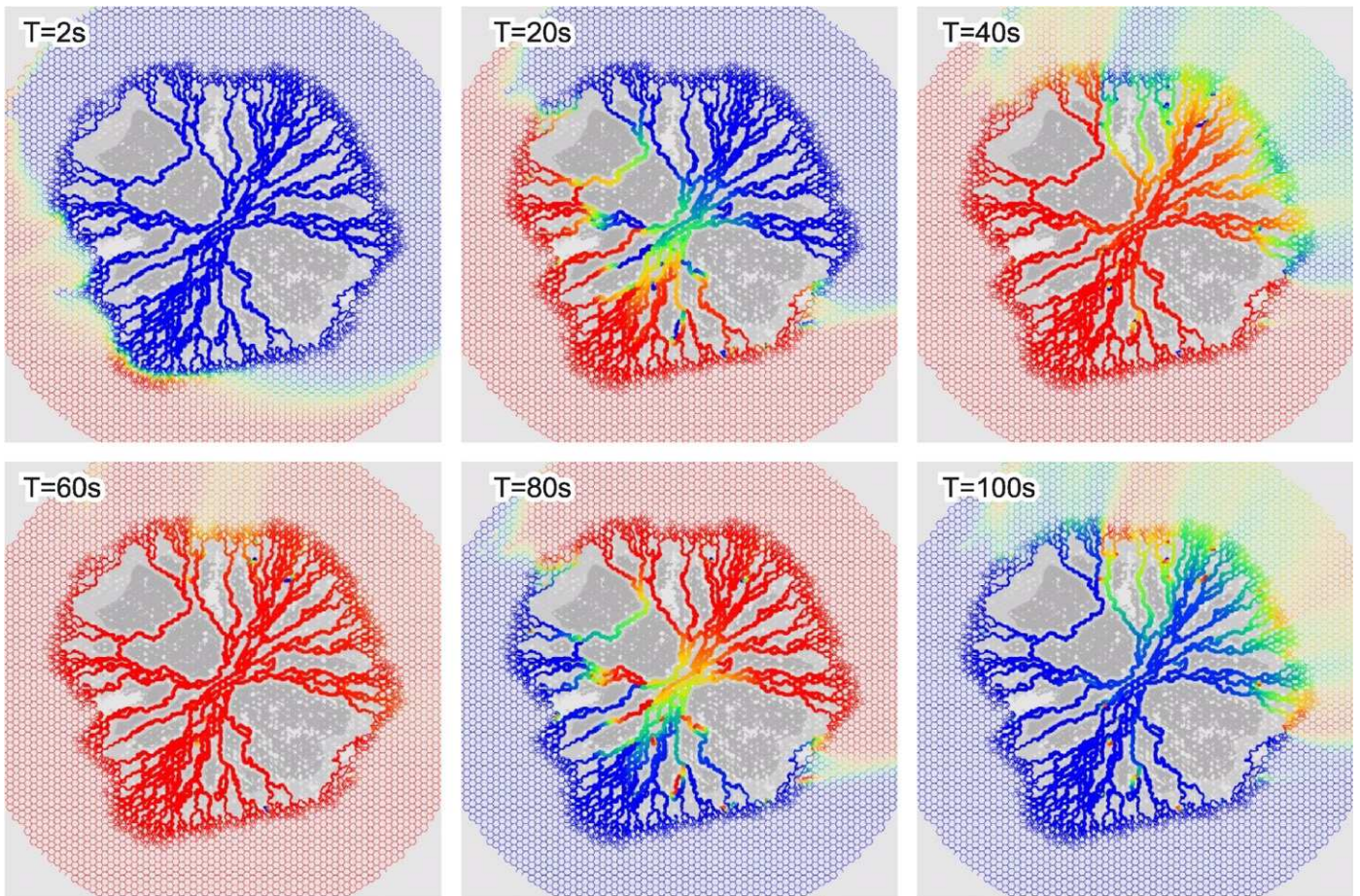


Fig. 15. Concentration profiles for an injection of $t^{(in)} = 60$ s into the hexagonal base-case vasculature (i). The color code ranges from red at $C = 1$ over yellow and green to blue at $C = 0$. Light gray area represents viable tumor tissue, darker gray represents dead tissue. Drug reaches the invasive edge within the first 2 s. At the middle of the sequence, the tumor becomes saturated with drug, except for a few tiny spots. Note how the concentration drops gradually in most vessels as an effect of mixing with “clean” blood.

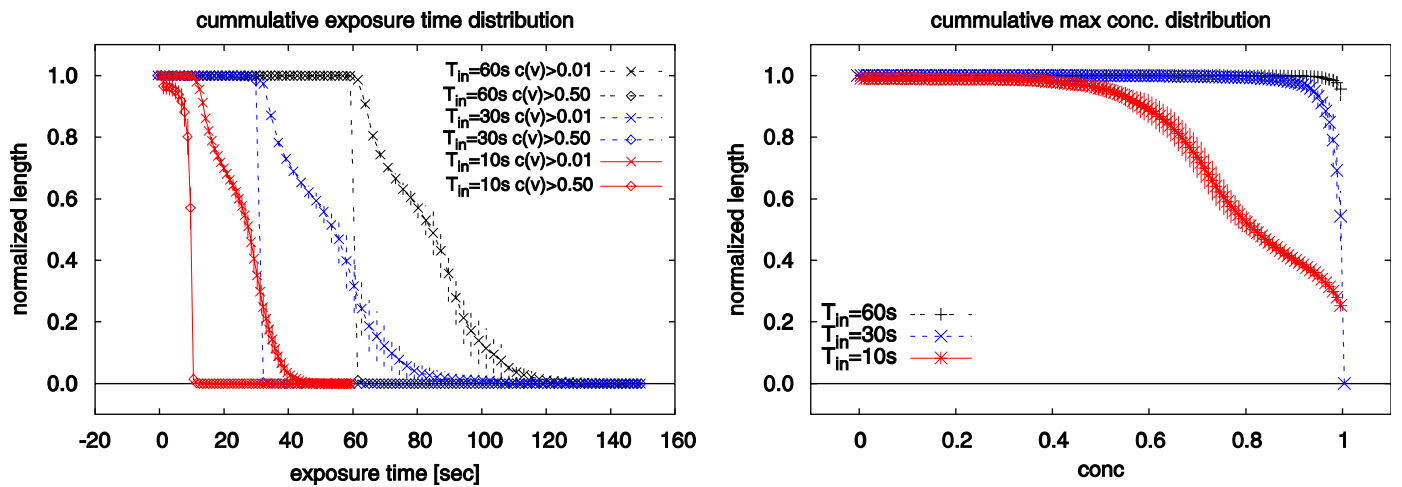


Fig. 16. Quantitative measurements of the base-case (i) for various $t^{(in)}$. Right: The plot indicates the percentage of vessel network length that was exposed to a drug concentration greater than the value on the x -axis. When the system has time to reach a steady state all vessels become exposed to $C(v) = 1$, thus producing a constant line in the plot. Left: The plot shows the percentage of vessel network length for which the concentration was larger than C_l for a total period of more than indicated on the x -axis. The steep drops occur at the end of the injection duration. Naturally the mean time where vessels are exposed to $C > 0$ is on the order of $t^{(in)}$ plus the time it takes to clear the tumor of drug, depending on the vascular morphology and flow rates.

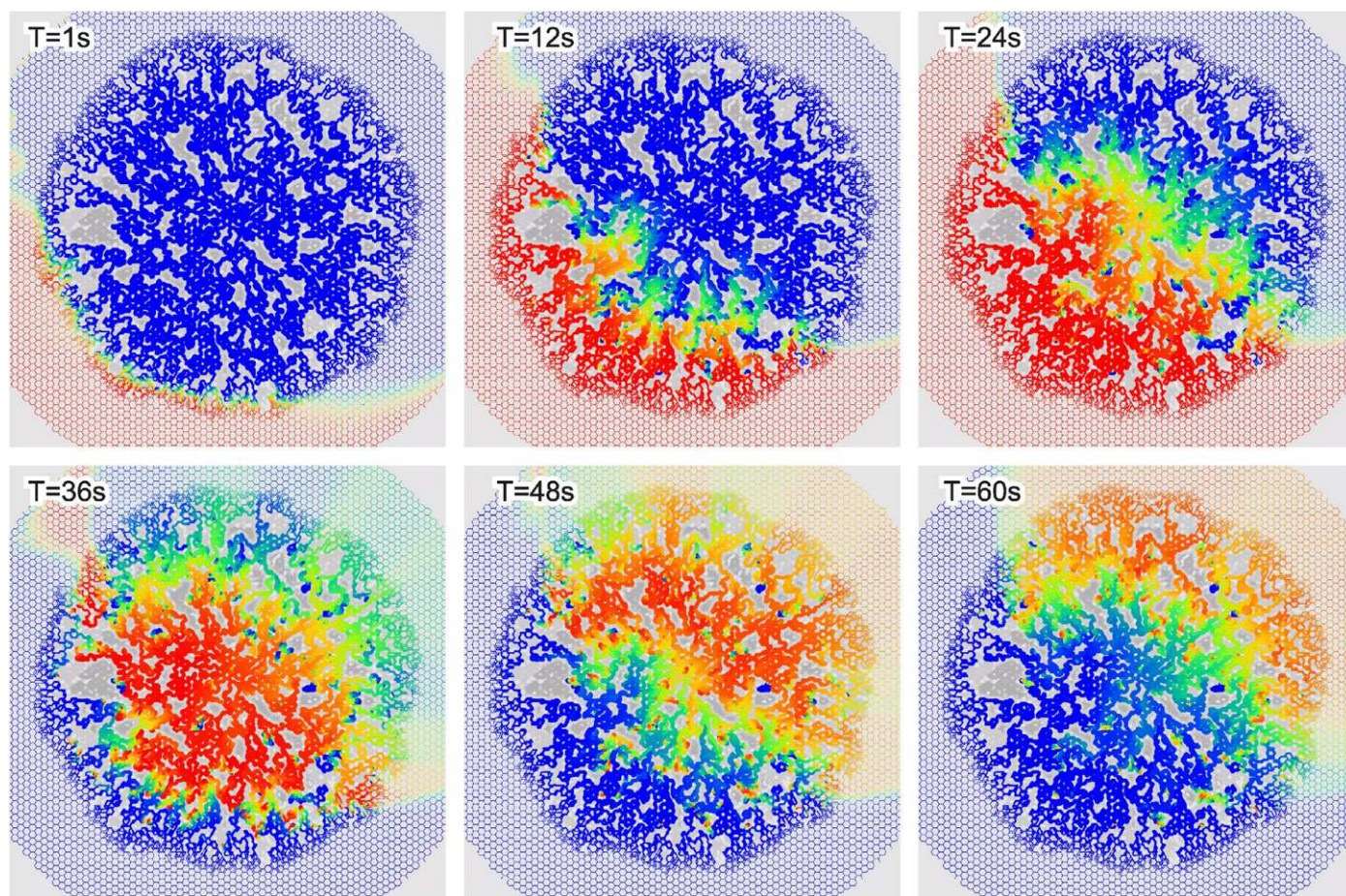


Fig. 17. Concentration profiles for an injection of $t^{(in)} = 60$ s into the hexagonal shear force uncorrelated vasculature (ii). The morphology created by random collapses inside the tumor exhibits more poorly perfused loops than any other vasculatures. As can be seen a few vessels have not been reached by the injected drug during the whole simulation period. The qualitative behavior is otherwise in good agreement with the run presented in Fig. 15.

Plots for the uncorrelated case analogous to Fig. 16 are not shown here because they are qualitatively as well as quantitatively very similar but exhibit a few unreachable loops. This is reflected in a smoother drop in the maximum concentration curve: ca. 80% of the vasculature had a concentration greater than 0.8. The exposure time plot showed slightly smoother drops at the injection times and a longer trail but is otherwise identical to Fig. 16.

Fig. 17 show concentration profile sequences for the remaining cases. Most remarkable in the uncorrelated case (ii) is the occurrence of small unreachable loops. It can happen when vessels survive which are oriented perpendicular to the global pressure gradient given by the boundary conditions. Flow rates in these loops are consequently drastically reduced.

5. Discussion

We have shown that the basic predictions of the model introduced in Bartha and Rieger (2006) are very robust against different sophistication levels of mathematical modeling that we investigated: The base case scenario, in which model parameters are chosen to the best agreement

with experimental data for melanoma (Döme et al., 2002), the tumor compartmentalizes after a short time into three regions: A well vascularized peritumoral plexus with an MVD that is 2–3 fold larger than the normal tissue MVD, a well perfused peritumoral region and a necrotic core with low MVD and only a few thick vessels threading the tumor, which are covered by a ca. 100 μm thick cuff of tumor cells. Oxygen levels are therefore extremely low in the tumor vessel. The fractal properties of tumor vasculature are substantially different from the normal vasculature, with estimates for the fractal dimension that are lower than that of the normal capillary network. Their characteristics have their origin in the vessel collapse processes and therefore also depend sensibly on collapse probability and critical shear force. Concerning the hydrodynamic blood flow patterns our model shows substantially reduced pressure gradients and shear flow in the tumor vasculature, although the blood flow rate is increased in the extremely thick vessels in the tumor center. The tumor radius grows linearly in time, which is natural as long as TC proliferation is confined to the tumor surface region and no growth inhibition effects, like solid stress, are incorporated.

These are robust features that are characteristic for the model we have studied here *and* for the simplified model of Bartha and Rieger (2006). A few differences between the two versions occur only on a smaller scale.

Calculating oxygen sources implicitly, i.e. driven by concentration gradients between blood and tissue, instead of assuming a constant source strength as in Bartha and Rieger (2006), have the following effect: Surface TCs can proliferate in the original vasculature while cells behind the invasive edge now suffer from hypoxia due to increased metabolic demand inside the tumor. They are thus secreting GFs to induce angiogenesis. If the oxygen threshold for proliferation is of the order of the average tissue- O_2 levels ($\theta_o^{(prol)} \approx \langle c_o \rangle$), the model predicts a strong dependency on the micro-scale O_2 variations and therewith also on local vascular morphology. The model with explicit sources is more stable with respect to the proliferation threshold, since the O_2 level increases rather drastically in highly vascularized regions. However, by choosing suitable parameters, the vascular morphology of the model we studied here and the simplified version with constant source strength can be matched. Therefore to study the global features of tumor vasculature the crude approximations to O_2 diffusion fields may be used, in particular in numerically more challenging situations such as 3d simulations (Lee et al., 2006).

Progressively simplified blood flow computations alone have shown limited effects, mainly changes in the flow rates up to one order of magnitude could be observed within the tumor. Additional modifications of the collapse rules influenced the shape of the vascular network visibly, (Fig. 10.(ii) vs. Fig. 12.(ii)), but still the simplified model for blood flow can be used. Also the incorporation of the blood phase separation effect does not appear of significance for vascular morphology. When blood oxygen levels are allowed to vary proportional to hematocrit, the model predicts asymmetric growth depending on local hematocrit levels. Therefore if this aspect is to be neglected, performing computations according to Pries et al. (1994) with a constant hematocrit $H_0 = 0.45$ appears to be a good compromise.

Inserting completely new perfused vessels rather than generating migrating sprouts that eventually join to target vessels does not lead to substantial changes. The latter model version merely leaves more degrees of freedom for forming circulated loop. In two dimensions the space to grow in is confined between the initial vessels. Therefore incorporating a randomized sprout migration dynamics becomes relevant in a three dimensional model, where it is not a priori clear that sprouts migrating in a random direction hit a target vessel in a reasonable distance. Here chemoattractants and the size of the growth cone (i.e. extension of filopodia in real sprouts) become essential model features.

Concerning our drug flow simulations we have demonstrated that drug flows relatively well through all of the networks. Even in the extreme case—the uncorrelated

system—an infusion time of the order of a few minutes is sufficient to saturate the vasculature with drug. Therefore our model predicts that blood-borne drug transport to and into tumors that grow within a homogeneously vascularized tissue is not limited by the particular morphology of tumor vasculature. Considering the underlying mechanisms that are responsible for this morphology in our model (and in real tumors) it is plausible that drug reaches (nearly) all parts of the vasculature: Shear force correlated vessel collapse naturally leads to elimination of weakly perfused vessels. In the case of random collapses, pressure gradients are still sufficient to drive blood through the vessels, but an order of magnitude slower.

In related work concerning modeling of tumor induced angiogenesis, McDougall et al. (2006) found that the morphology of tumor vasculature plays a crucial role in drug delivery and that changes to key system parameters could have big impact on the structure of the vasculature. The origin of this discrepancy with our conclusion lies in the different model assumption. As outlined in the introduction, they consider a strictly avascular tumor, where sprouts migrate toward the tumor, but are not allowed to enter it. The resulting vessel networks exhibit extremely high connectivity close to the tumor surface, however the involved angio-adaptation mechanisms lead to vasodilation of comparably few pathways. Depending on the model parameters, the number of high-throughput vessels, and their distance to the tumor varies sufficiently to lead to uptake rates which vary by several orders of magnitude.

In contrast to this we study here a type of tumors like melanoma, which are primarily vascularized by co-option rather than vessel ingrowth (Döme et al., 2002, 2007). For them, as we have demonstrated, a blood-borne “delivery problem” does not exist. This does however not automatically imply that drug reaches all tumor cells since neither drug transport through the tumor tissue nor drug uptake have been addressed (Minchinton and Tannock, 2006). Regarding tissue transport it is known that the difference between interstitial fluid pressure (IFP) and microvascular pressure (MVP) is low due to vessel leakiness. Since convective transport is driven by pressure differences, high IFP could pose a barrier to drug delivery (Hassid et al., 2006). On the other hand, leakiness and MVP-IFP gradients could lead to premature release predominantly in locally restricted regions around vessels where blood enters the tumor. Vessels in the outflow regions would thus be depleted of drug. Locally released drug would then be transported by IFP gradients out of the tumor. Furthermore drugs usually consist of large macromolecules. Their low diffusibility through the vessel wall and generally lower diffusibility than O_2 could lead to situations where sufficient O_2 reaches certain TCs to let them remain viable, but not enough drug reaches them to kill them off due to the lower diffusion radius. Thus we conclude that much more than the vessel morphology, processes like transportation out of the vessels through

convection and diffusion seem to be a key factor in successful drug delivery.

In future work it would be useful to study the remodeling of an arterio-venous network. Getting access to a realistic initial network is likely to pose a hard problem in particular if it must be artificially created. Further aspects to assess are interstitial fluid transport and O_2 release with associated intravascular O_2 decrease. Finally, vessel collapse and regression dominate the network remodelling process of the vasculature in the tumor center. In addition to anti-angiogenic factors solid stress is assumed to play a pivotal role in these processes. Therefore it would be highly desirable to incorporate an appropriate description of the dynamic evolution of solid stress in the tumor and its surrounding tissue to go beyond the phenomenological treatment of vessel collapse that we used in the model that we have presented in this work.

References

- Alarcon, T., Byrne, H.M., Maini, P.K., 2003. A cellular automaton model for tumour growth in inhomogeneous environment. *J. Theor. Biol.* 225, 257–274.
- Anderson, A.R.A., Chaplain, M.A.J., 1998. Continuous and discrete mathematical models of tumor-induced angiogenesis. *Bull. Math. Biol.* 60, 857–900.
- Baish, J.W., Jain, R.K., 2000. Fractals and cancer. *Persp. Cancer Res.* 60, 3683–3688.
- Bartha, K., Rieger, H., 2006. Vascular network remodeling via vessel cooption, regression and growth in tumors. *J. Theor. Biol.* 241, 903–918.
- Betteridge, R., Owen, M.R., Byrne, H.M., Alarcon, T., Maini, P.K., 2006. The impact of cell crowding and active cell movement on vascular tumour growth. *Networks and Heterogeneous Media* 1, 515–535.
- Breward, C.J., Byrne, H.M., Lewis, C.E., 2003. A multiphase model describing vascular tumour growth. *Bull. Math. Biol.* 65, 609–640.
- Briggs, W.L., Henson, V.E., McCormick, S.F., 2001. A Multigrid Tutorial. The Society for Industrial and Applied Mathematics (SIAM).
- Bru, A., Albertos, S., Subiza, J.L., Lopez, J., Garcia-Asenjo, Bru, I., 2003. The universal dynamics of tumor growth. *Biophys. J.* 85, 2948–2961.
- Byrne, H.M., Chaplain, M.A.J., 1995. Mathematical models for tumour angiogenesis: numerical simulations and nonlinear wave solutions. *Bull. Math. Biol.* 57, 461–486.
- Byrne, H.M., Alarcon, T., Owen, M.R., Webb, S.D., Maini, P.K., 2006. Modelling aspects of cancer dynamics: a review. *Philos. Trans. R. Soc. London Ser. A* 364, 1563–1578.
- Carmeliet, P., Jain, R.K., 2000. Angiogenesis in cancer and other diseases. *Nature* 407, 249–257.
- Chaplain, M.A.J., McDougall, S.R., Anderson, A.R.A., 2006. Mathematical modelling of tumor-induced angiogenesis. *Annu. Rev. Biomed. Eng.* 8, 233–257.
- Chung, H.-W., Chung, H.-J., 2001a. Fractals and cancer. *Cancer Res.* 60, 3683–3688 (Correspondence to: J.W. Baish, R.K. Jain).
- Chung, H.-W., Chung, H.-J., 2001b. Fractals and cancer. *Cancer Res.* 61, 8347–8351 (Correspondence to: J.W. Baish, R.K. Jain).
- Cormen, T.H., Leiserson, C.E., Rivest, R.L., Stein, C., 1990. *Introduction to Algorithms*. Chapter 23.4: Topological Sort. MIT Press/McGraw-Hill, Cambridge, MA/New York, pp. 485–488.
- Davis, T., 2004. Algorithm 832: UMFPAK, an unsymmetric-pattern multifrontal method. *ACM Transactions on Mathematical Software* 30, 196–199.
- Dimmeler, S., Zeiher, A.M., 2000. Endothelial cell apoptosis in angiogenesis and vessel regression. *Circ. Res.* 87, 434–439.
- Döme, B., Paku, S., Somlai, B., Tímár, J., 2002. Vascularization of cutaneous melanoma involves vessel co-option and has clinical significance. *J. Pathol.* 197, 355–362.
- Döme, B., Hendrix, M.J.C., Paku, S., Tóvári, J., Tímár, J., 2007. Alternative vascularization mechanisms in cancer pathology and therapeutic implications. *J. Pathol.* 170, 1–15.
- Drasdo, D., Höhme, S., 2005. A single-cell-based model of tumor growth in vitro: monolayers and spheroids. *Phys. Biol.* 2, 133–147.
- Eden, M., 1961. In: Neyman, J. (Ed.), *Proceedings of the Fourth Berkeley Symposium on Mathematics and Probability*. University of California Press, Berkeley, pp. 223–240.
- Erber, R., Eichelsbacher, U., Powajbo, V., Korn, T., Djonov, V., Lin, J., Hammes, H.-P., Grobholz, R., Ullrich, A., Vajkoczy, P., 2006. EphB4 controls blood vascular morphogenesis during postnatal angiogenesis. *EMBO Journal*, 25 628–641.
- Fung, Y.C., 1993. *Biomechanics*. Springer, New York.
- Gazit, Y., Berk, D.A., Michael Leunig, L.T.B., Jain, R.K., 1995. Scale-invariant behavior and vascular network formation in normal and tumor tissue. *Phys. Rev. Lett.* 75, 2428–2431.
- Gerhardt, H., Golding, M., Frutinger, M., Ruhrberg, C., Lundkvist, A., Abramsson, A., Jeltsch, M., Mitchell, C., Alitalo, K., Shima, D., Betsholz, C., 2003. VEGF guides angiogenic sprouting utilizing endothelial tip cell filopodia. *J. Cell Biol.* 161, 1163–1177.
- Gimbrone, M.A., Cotran, R.S., Leapman, S.B., Folkman, J., 1974. Tumor growth and neo-vascularization: an experiment model using the rabbit cornea. *J. Nat. Cancer Inst.* 52, 413–427.
- Glassner, A.S. (Ed.), 1994. *Graphics Gems I (Chapter II.8)*. Digital Line Drawing. Academic Press, New York.
- Gödde, R., Kurz, H., 2001. Structural and biophysical simulation of angiogenesis and vascular remodeling. *Dev. Dyn.* 220, 387–401.
- Hassid, Y., Furman-Haran, E., Margalit, R., Eilam, R., Degani, H., 2006. Noninvasive magnetic resonance imaging of transport and interstitial fluid pressure in ectopic human lung tumors. *Cancer Res.* 66, 4159–4166.
- Holash, J., Maisonpierre, P.C., Compton, D., Boland, P., Alexander, C.R., Zagzag, D., Yancopoulos, G.D., Wiegand, S.J., 1999a. Vessel cooption, regression, and growth in tumors mediated by angiopoietins and VEGF. *Science* 284, 1994–1998.
- Holash, J., Wiegand, S., Yancopoulos, G., 1999b. New model of tumor angiogenesis: dynamic balance between vessel regression and growth mediated by angiopoietins and VEGF. *Oncogene* 18, 5356–5362.
- Iyer, N.V., Kotch, L.E., Agani, F., Leung, S.W., Laughner, E., Wenger, R.H., Gassmann, M., Gearhart, J.D., Lawler, A.M., Yu, A., Semeza, G.L., 1998. Cellular and developmental control of O-2 homeostasis by hypoxia-inducible factor 1 alpha. *Genes Dev.* 12, 149–162.
- Ji, J.W., Tsoukias, N.M., Goldman, D., Popel, A.S., 2006. A computational model of oxygen transport in skeletal muscle for sprouting and splitting modes of angiogenesis. *J. Theor. Biol.* 241, 94–108.
- Lee, D.-S., Bartha, K., Rieger, H., 2006. Flow correlated percolation during vascular remodelling in growing tumors. *Phys. Rev. Lett.* 96, 058104-1–058104-4.
- Levine, H.A., Sleeman, B.D., Nilsen-Hamilton, M., 2001. Mathematical modeling of the onset of capillary formation initiating angiogenesis. *J. Math. Biol.* 42, 195–238.
- Lowengrub, J.S., Frieboes, H.B., Wise, S., Zheng, X., Macklin, P., Bearer, E., Cristini, V., 2007. Computer simulation of glioma growth and morphology. *NeuroImage* 37, 59–70.
- Mantzaris, N.V., Webb, S., Othmer, H.G., 2004. Mathematical modeling of tumor-induced angiogenesis. *J. Math. Biol.* 49, 111–187.
- McDougall, S.R., Anderson, A.R.A., Chaplain, M.A.J., Sherratt, J.A., 2002. Mathematical modelling of flow through vascular networks: implications for tumor-induced angiogenesis and chemotherapy strategies. *Bull. Math. Biol.* 64, 673–702.
- McDougall, S.R., Anderson, A.R.A., Chaplain, M.A.J., 2006. Mathematical modelling of dynamic adaptive tumour-induced angiogenesis: clinical implications and therapeutic targeting strategies. *J. Theor. Biol.* 241, 564–589.
- Minchinton, A.I., Tannock, I.F., 2006. Drug penetration in solid tumours. *Nat. Rev. Cancer* 6, 583–592.

- Nehls, V., Herrmann, R., Hühnen, M., 1998. Guided migration as a novel mechanism of capillary network remodeling is regulated by fibroblast growth factor. *Histochem. Cell Biol.* 109, 319–329.
- Paku, S., 1998. Current concepts of tumor-induced angiogenesis. *Pathol. Oncol. Res.* 4, 62–75.
- Plank, M.J., Sleeman, B.D., 2003. A reinforced random walk model of tumour angiogenesis and anti-angiogenic strategies. *Math. Med. Biol.*, 20135–20181.
- Plank, M.J., Sleeman, B.D., 2004. Lattice and non-lattice models of tumour angiogenesis. *Bull. Math. Biol.* 66, 1785–1819.
- Preziosi, L. (Ed.), 2003. *Cancer modelling and simulation*. In: Preziosi, L. (Ed.), *Mathematical and Computational Biology*, vol. 3. Chapman & Hall/CRC Press, London/Boca Raton.
- Pries, A.R., Secomb, T.W., Gaehtgens, P., Gross, J.F., 1990. Blood flow in microvascular networks. Experiments and simulation. *Circ. Res.* 67, 826–834.
- Pries, A.R., Secomb, T.W., Gessner, T., Sperandio, M.B., Gross, J.F., Gaehtgens, P., 1994. Resistance to blood flow in microvessels in vivo. *Circ. Res.* 75, 904–915.
- Pries, A.R., Secomb, T.W., Gaehtgens, P., 1998. Structural adaptation and stability of microvascular networks: theory and simulations. *Am. J. Physiol. Heart Circ. Physiol.* 275, 349–360.
- Sansone, B.C., Scalerandi, M., Condat, C.A., 2001. Emergence of taxis and synergy in angiogenesis. *Phys. Rev. Lett.* 87, 128102.
- Secomb, T.W., Hsu, R., Park, E.Y.H., Dewhurst, M.W., 2004. Green's function methods for analysis of oxygen delivery to tissue by microvascular networks. *A. Biomed. Eng.* 32, 1519–1529.
- Sun, S.Y., Wheeler, M.F., Obeyesekere, M., Patrick, C.W., 2005. A deterministic model of growth factor-induced angiogenesis. *Bull. Math. Biol.* 67, 313–337.
- Tong, S., Yuan, F., 2001. Numerical simulations of angiogenesis in the cornea. *Microvasc. Res.* 61, 14–27.
- Yu, J.L., Rak, J.W., Coomber, B., Hicklin, D.J., Kerbel, R.S., 2002. Effect of p53 status on tumor response to antiangiogenic therapy. *Science* 295, 1526–1528.
- Zheng, X., Wise, S.M., Cristini, V., 2005. Nonlinear simulation of tumor necrosis, neo-vascularization and tissue invasion via an adaptive finite-element/level-set method. *Bull. Math. Biol.* 67, 211–259.



Vascular remodelling of an arterio-venous blood vessel network during solid tumour growth

M. Welter^a, K. Bartha^b, H. Rieger^{a,*}

^a Theoretische Physik, Universität des Saarlandes, PF 151150, 66041 Saarbrücken, Germany

^b Department of Medical Biochemistry, Semmelweis University, Budapest, Hungary

ARTICLE INFO

Article history:

Received 20 December 2007

Received in revised form

26 February 2009

Accepted 3 April 2009

Available online 14 April 2009

Keywords:

Cancer

Tumour growth

Angiogenesis

Vascular networks

Blood flow

Computer simulation

ABSTRACT

We formulate a theoretical model to analyze the vascular remodelling process of an arterio-venous vessel network during solid tumour growth. The model incorporates a hierarchically organized initial vasculature comprising arteries, veins and capillaries, and involves sprouting angiogenesis, vessel cooption, dilation and regression as well as tumour cell proliferation and death. The emerging tumour vasculature is non-hierarchical, compartmentalized into well-characterized zones and transports efficiently an injected drug-bolus. It displays a complex geometry with necrotic zones and “hot spots” of increased vascular density and blood flow of varying size. The corresponding cluster size distribution is algebraic, reminiscent of a self-organized critical state. The intra-tumour vascular-density fluctuations correlate with pressure drops in the initial vasculature suggesting a physical mechanism underlying hot spot formation.

© 2009 Elsevier Ltd. All rights reserved.

1. Introduction

Tumours can grow to a size of approximately 1–2 mm³ before their metabolic demands are restricted due to the diffusion limit of oxygen and nutrients. In order to grow beyond this size, the tumour switches to an angiogenic phenotype and induces the development of new blood vessels mainly via sprouting angiogenesis, i.e. the formation of new vessels from pre-existing vasculature. This process is regulated by a variety of pro- and anti-angiogenic factors and is regarded as a prerequisite for further outgrowth of the tumour (Carmeliet and Jain, 2000). However, it has been suggested that many tumours can also grow in an avascular stage, mainly in well-vascularized tissue like brain and lung (Wesseling et al., 1994; Holmgren et al., 1995; Pezzella et al., 1997). Tumour cells (TCs) can grow along existing vessels without evoking an angiogenic response. This process was defined as vessel-cooption.

It was already proposed in Thompson et al. (1987) that tumours acquire their vasculature by incorporation of host tissue capillaries. The first detailed study of vessel cooption was published in Holash et al. (1999a), where it was found that 1 or 2 weeks after implantation of C6 glioma cells in a rat brain the small tumours were already well vascularized with vessels that had characteristics of normal brain vessels. After 4 weeks, blood vessels had undergone a dramatic regression without any

compensatory angiogenic response. In the centre of the tumour, tumour cells were organized around the few functional vessels and massive tumour cell death was detected. In the tumour periphery, in contrast, a robust angiogenic response was observed. Vessel cooption has now been observed in different tumour types like human melanoma (Döme et al., 2002), neuroblastoma (Kim et al., 2002), and ovarian cancer (Zhang et al., 2003); it can persist during the entire period of tumour growth and it can even represent the only source for nutrients in angiogenesis-independent tumour growth (Sakariassen et al., 2006).

From these experimental observations the anatomy of solid, vascularized tumour grown within in a vascularized tissue displays a characteristic compartmentalization into essentially three regions (Holash et al., 1999a; Döme et al., 2002): (i) the highly vascularized tumour perimeter with a micro-vascular density (MVD) that is substantially higher than the MVD of the surrounding normal tissue, (ii) the well-vascularized tumour periphery with dilated blood vessels and a tortuous vessel network topology, and (iii) a poorly vascularized tumour centre with large necrotic regions threaded by only a few very thick vessels that are surrounded by a cuff of viable tumour cells. Thus, during tumour growth the original, hierarchically organized arterio-venous blood vessel network has been remodelled into a completely different compartmentalized morphology. Several microscopic phenomena on the cellular level have been identified to be involved in this remodelling process:

(1) *Angiogenic sprouting*: Up-regulation of pro-angiogenic factors in tumour-cells (like vascular endothelial growth factor, VEGF, and other growth factors) can create additional vessels via

* Corresponding author. Tel.: +49 681 302 3969; fax: +49 681 302 4899.
E-mail address: h.rieger@mx.uni-saarland.de (H. Rieger).

sprouting angiogenesis in some regions of the tumour, most frequently in its perimeter (Carmeliet and Jain, 2000). (2) *Vessel regression*: The maintenance of incorporated mature microvessels depends on the survival of endothelial cells (ECs) and their survival is intimately tied to their local microenvironment and, in particular, to the presence of pericytes, survival promoting cytokines, and extracellular matrix (ECM) proteins. The major molecular players that control this process are angiopoietins and VEGF (Holash et al., 1999a). Angiopoietin-1 (Ang-1) promotes EC survival and tumour vessel maintenance, whereas angiopoietin-2 (Ang-2) negatively interferes with these agonistic signals by blocking the Ang-1 receptor Tie-2 (Maisonpierre et al., 1997; Holash et al., 1999b; Scharpfenecker et al., 2005). In coopted blood vessels Ang-2 is up-regulated, causing the destabilization of their capillary walls, i.e. the detachment of pericytes from the endothelial tube (Holash et al., 1999b). Once ECs are separated from pericytes, they become particularly vulnerable resulting in the regression of destabilized vessels. (3) *Vessel dilation*: The vascularization program of the pro-angiogenic phenotype can be switched from sprouting angiogenesis to circumferential growth in the interior of the tumour. This switch is mediated by the guidance molecules EphB4 (and its ligand ephrinB2), both expressed by ECs of malignant brain tumours (Erber et al., 2006), which acts as a negative regulator of blood vessel branching and vascular network formation, and also reduces the permeability of the tumour vascular system via activation of the Ang-1/Tie-2 systems at the endothelium/pericyte interface.

The potential morphological consequence of these processes is (1) the increase of micro-vascular density (MVD) at the tumour perimeter (via up-regulation of VEGF and other growth factors), (2) vessel regression in the interior of the tumour (via up-regulation of Ang-2 and mechanical forces) and (3) vessel dilation and stabilization in the tumour centre (via VEGF and EphB4). The complex interplay of these three mechanisms with the architecture and blood flow organization of the original vasculature and a growing invasive tumour is the topic of this paper. By formulating and analyzing a mathematical model involving these features we will get insight into how they and their interplay affect morphological characteristics of the emerging tumour vasculature. Among these characteristics are the size, shape, MVD and blood flow distribution of the different compartments of the tumour (perimeter, periphery and centre), geometric properties of the tumour vasculature like the statistics and distribution of the spatial inhomogeneities and “hot spots” (regions of increased MVD and blood flow, Pahernik et al., 2001) within the tumour and drug transport along the intra-vascular blood flow.

In recent work (Bartha and Rieger, 2006; Lee et al., 2006; Welter et al., 2008) the issue of vascular remodelling in a growing tumour by the three basic mechanisms—angiogenic sprouting, vessel regression and dilation—was addressed in a model that comprised a regular capillary grid as initial vascular network. The compartmentalization of the tumour as well as other global features, like the time and radius dependencies of average MVD, tumour cell density, vessel radius and blood flow characteristics were predicted in good agreement with experimental data, but local characteristics, like a single hot spot in the centre and a general bias in the flow direction, could be attributed to the special topology of the initial network. In this paper we consider a more realistic arterio-venous vascular network as initial vasculature and study the effect it has on the emerging tumour vasculature.

In well-vascularized tissue the average inter-capillary distance is 50–100 μm , in highly vascularized tissue like brain even less (depending on the oxygen demand and the resulting diffusion length), implying the importance of the incorporation of the

original vasculature into a model for tumour-induced angiogenesis. This vasculature is organized in a hierarchical way, in which an arterial and a venous tree are interdigitated by capillaries. Oxygen and other nutrients are distributed into the surrounding tissue by the lowest level capillaries, the two trees representing their supply and drainage system. The MVD, given by the average inter-capillary distance, is homogeneous in one kind of tissue to provide a homogeneous oxygen and nutrient supply, but the two interdigitating hierarchical trees form a spatially very inhomogeneous blood vessel network. Consequently the vascular remodelling process in a growing tumour will also be spatially inhomogeneous: sprouting angiogenesis occurs mainly from capillaries and venules, higher level arteries protected by a thick layer of pericytes are more stable and regress later or not at all, regression of higher level arteries has fatal consequences for the whole arterial sub-tree below it, newly formed vessels between arteries and veins could act as shunts redirecting huge amount of blood, etc.

1.1. Previous modelling

Mathematical modelling of tumour angiogenesis has been an active research area in the recent years, but there has been little work on the role of vessel cooption and regression. Since the early work of Balding and McElwain (1985), many models of the process of capillary formation in response to a tumour-derived growth factor have been constructed. Examples include Chaplain and Stuart (1993), Chaplain et al. (1995), Byrne and Chaplain (1995) and Holmes and Sleeman (2000). These models are macroscopic in that they deal with continuous quantities, such as endothelial cell density, via a system of partial differential equations. One disadvantage of this modelling approach is its inability to capture microscopic features of the process, such as vessel branching and looping and the morphological properties of the emerging capillary network.

Several researchers have therefore formulated discrete, or microscopic, models of tumour angiogenesis. These often contain a stochastic element and model at the level of the individual cell, see, for example Stokes and Lauffenburger (1991) and Turner and Sherratt (2002). Anderson and Chaplain (1998) derived a discrete model for EC movement in angiogenesis via a discretization of a continuous model. Here tip-cells located at discrete lattice points are assigned probabilities to migrate to adjacent lattice points within the next time-step. These probabilities account for chemotactic, haptotactic, and diffusive contributions corresponding to a continuum formulation. Capillaries are represented as masked points on the grid and probabilistic branching rules depend on the sprout age, VEGF concentration and EC density. An extension to three dimensions is presented in Chaplain (2000).

The blood flow in capillary networks has been modelled in Godde and Kurz (2001), McDougall et al. (2002), Stephanou et al. (2005) and McDougall et al. (2006) and then extended to describe the dependence of vessel remodelling on blood pressure and shear stress (Godde and Kurz, 2001; Bartha and Rieger, 2006; Lee et al., 2006; Stephanou et al., 2006; Welter et al., 2008). Recently discrete agent-based models for tumour-induced angiogenesis were coupled to models of tumour growth (Zheng et al., 2005; Bartha and Rieger, 2006; Lee et al., 2006; Frieboes et al., 2007; Welter et al., 2008; Wise et al., 2008; Macklin et al., 2008). A growing tumour coopting the vessels of the normal tissue was considered with a pre-existing static capillary network without angiogenesis or regression in Alarcon et al. (2003) and Betteridge et al. (2006) and with a fully dynamic capillary network in Bartha and Rieger (2006), Lee et al. (2006), Welter et al. (2008) and Owen et al. (2008).

1.2. Present model

1.2.1. Arterio-venous vasculature

To study and quantify these effects during vascular remodeling during tumour growth we employ and extend a mathematical model for a two-dimensional arterio-venous blood vessel network that has been presented in Gødde and Kurz (2001). Here we restrict our study to a two-dimensional situation, but it can straightforwardly be extended to three dimensions (to be published). The model generates stochastically an arterio-venous network with physiologically realistic parameters (Gødde and Kurz, 2001). By varying the number and location of sources and sinks the global topology of the network can be adopted to different situations for the initial nucleus of the tumour—e.g. close to a major artery or vein or far away from major vessels. At each branching point the vessel radius decreases according to Murray's law (Murray, 1926), each vessel represents a pipe with given radius within which blood flows according to Hagen–Poiseuille with a radius-dependent effective viscosity. Boundary conditions that imprint and define the blood flow in the network are the blood pressure values within the roots of the arterial and venous trees. The vessels represent the sources of the diffusion determined oxygen/nutrient concentration field, surrounding cells represent its sinks.

1.2.2. Sprouting angiogenesis

This arterio-venous network serves as the initial vasculature for our model of remodelling by a growing tumour. Depending on the local oxygen concentration tumour cells represent the sources of the diffusion determined VEGF concentration field, which triggers either the generation of tip-cells for angiogenic sprouting from existing vessels outside or at the periphery of the tumour, or the circumferential growth inside the tumour. In contrast to vessel in-growth models as in Anderson and Chaplain (1998) tip-cells are not dominantly generated by branching of existing tip-cells but by sprouting from vessels of the original network. This tip-cell generation from existing vessels is initiated by the activation of VEGF receptors with subsequent up-regulation of the delta-like-4 (Dll4) ligand in one EC (Liu et al., 2003), and the Dll4-mediated activation of Notch1 receptors in the neighbouring EC (Sainson et al., 2005; Williams et al., 2006). This lateral inhibition leads to an alternating pattern of cell fates in capillary walls under the influence of VEGF and results in a separation of one to two non-tip-cells between each tip-cell. The underlying negative feedback-loop involving VEGF receptors, Dll4 and Notch has been analyzed theoretically in Bentley et al. (2008), our model only incorporates the resulting pattern for tip-cell generation along existing vessels exposed to elevated concentrations of VEGF.

The subsequent migration, branching and anastomosis of angiogenic sprouts was recently modelled in a detailed way (Bauer et al., 2007; Milde et al., 2008), involving besides VEGF matrix metalloprotease (MMP) and the filamentous structure of the extracellular matrix. In our model tip-cells migrate in the direction of a sufficiently large VEGF gradient (chemotaxis), otherwise randomly. The path they describe is supposed to be filled with stalk cells forming a lumen and finally, once the tip-cell hits another vessel (anastomosis), a functional vessel carrying blood flow. These assumptions are analogous to previous work (McDougall et al., 2002, 2006; Stephanou et al., 2005), but some details differ: (1) Due to the pre-existing vasculature vessels typically migrate only 50–100 μm before the filopodia of the tip-cell extending up to 20–30 μm into the surrounding tissue in all directions (Gerhardt et al., 2003) touch another vessel. Therefore directional clues are not as important here as in pure vessel in-growth models. (2) Tip-cells migrate maximally 100–150 μm and

in case they did not make successful contact with another vessel, they retreat (Nehls et al., 1998). (3) Tip-cell branching is not included, but we allow for tip-cell generation along the sprout and the newly formed vessel, which mimics branching.

1.2.3. Vessel dilation and regression

Inside the tumour the VEGF concentration is generally still high but angiogenic sprouting is replaced by circumferential growth due to the up-regulation of EphB4 in the ECs forming the walls of coopted vessels (Erber et al., 2006). The molecular mechanisms for this up-regulation are unknown but apparently contact with tumour cells is necessary. Therefore we incorporate this switch to circumferential growth by a dependence upon the contact time of ECs with tumour cells.

In an analogous way we model the effect of an up-regulation of Ang-2 in coopted vessels, which has been analyzed theoretically in Plank et al. (2004) and which leads to vessel destabilization and regression: an increasing contact time of vessels with tumour cells, implying an increasing residence time within the tumour, leads to a higher collapse probability of tumour vessels. The collapse probability is also correlated with the origin of the vessel (artery, vein or capillary) and the shear force exerted by the blood flow upon the vessel walls. It is conceivable that mechanical forces in the form of solid stress exerted by the expanding tumour also influence the collapse of coopted vessels. This can in principle be included into the model along the lines described in Frieboes et al. (2007), Wise et al. (2008) and Macklin et al. (2008) but we choose here a stochastic approach: the tumour region with the potentially largest stress is the periphery due to the highest proliferation rate and because the necrotic centre consists of liquidized biological matter that generates a homogeneous interstitial fluid pressure, which is thus not able to sustain solid stress. Thus with increasing distance of a vessel from the tumour boundary not only its contact time with tumour cells increases (up-regulating Ang-2) but also the mechanical stress acting upon it. Hence the collapse probability of a coopted vessel increases with increasing distance from the tumour boundary (and with decreasing shear force).

1.2.4. Tumour model

Our focus in this work is the vascular remodelling process, which we assume to be dominantly dependent on where vessels are located, how stable they are (i.e. from which level in the arterio-venous tree they originate), how long they have been in contact with tumour cells and how well they are perfused. Therefore we choose a simplified representation of the growing tumour: proliferation of tumour cells takes place, if sufficient oxygen/nutrients are present and if there is available space. This captures the most essential features of experimental (Brú et al., 2003) and theoretical (Drasdo and Höhme, 2005) observations that proliferation of tumour cells is confined to the outer rim of an avascular tumour. Since in our model for vascular tumour growth proliferation depends on oxygen and since the oxygen concentration is highest close to vessels, tumour cells proliferate preferentially along vessels, which is commonly observed in aggressive tumours growing in vascularized tissue. We do not include migration of the tumour cells, but this can easily be incorporated into the model together with cell–cell adhesion and mechanical stresses (Ambrosi and Preziosi, 2002; Byrne and Preziosi, 2003; Breward et al., 2003; Frieboes et al., 2007; Wise et al., 2008; Macklin et al., 2008). Finally tumour cells die when they were underoxygenated for a specific time interval.

1.2.5. Scope and outline of this paper

The questions that we address with the model that we formulate are: What is the fate of the well-organized hierarchical

structure of an arterio-venous vessel network when it is co-opted and remodelled by an aggressively growing tumour? What are the geometrical characteristics of the emerging tumour vasculature and what are the potential mechanisms leading to spatial inhomogeneities or hot spots? And what are the global blood flow patterns and the drug transport performance of the tumour vasculature? Since we will be interested in the large scale properties of the vasculature of tumours with a size up to 5–10 cm, we will have to omit some of the mechanical and/or chemical aspects incorporated into other tumour-angiogenesis models that neglect the structure of the initial vasculature, and use a simplified, stochastic modelling approach instead.

This paper is organized as follows: in the next section the model is defined, including the method to construct an arterio-venous initial network. In the model definition we restrict ourselves to the mathematical formulation and refer to the introductory Sections 1.2.1–1.2.4 for the supporting biological observations and experimental literature. Section 3 presents the results for global properties for a choice of parameters that is guided by experimental data for melanoma (Döme et al., 2002). These results include a discussion of the emerging morphologies; radial distributions of vessel density, vessel radius, tumour density, flow rates, shear forces, vessel statistics, parameter dependencies, spatial inhomogeneities, and drug flow. Section 4 concludes the paper with a summary of the main results and a discussion.

2. Mathematical model

The model represents tumour cells and vessels as discrete elements which occupy lattice sites and bonds, respectively, on a two-dimensional triangular lattice (Fig. 1). Tumour and vessel network interact predominantly via a growthfactor (GF) and an oxygen concentration (O_2) field. Most of the mathematical definitions follow closely (Welter et al., 2008) apart from the arterio-venous initial network.

2.1. Definition of the system state

2.1.1. Tumour

Each lattice site of the space occupied by the tumour is identified with one TC. A lattice site which was occupied by a tumour cell in the past represents necrotic tissue, otherwise

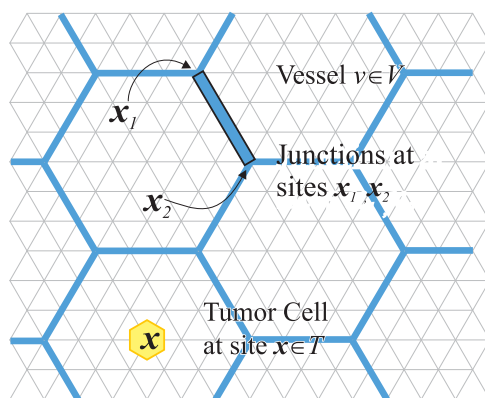


Fig. 1. Illustration of the discrete configuration space of the model: all discrete elements are aligned with the underlying triangular lattice shown in the background. Blue bars represent single vessels which occupy lattice bonds. One vessel is highlighted by a black frame, its junctions to other vessels are denoted by x_1, x_2 . Each tumour cell (TC) occupies one lattice sites. A single TC is depicted as a yellow hexagon. (For interpretation of the references to colour in this figure legend, the reader is referred to the web version of this article.)

unoccupied sites represent normal tissue. The lattice constant of $10\mu\text{m}$ is of the order of the typical size of a cell so that the identification of cells with sites is meaningful.

2.1.2. Vessel network

The vasculature is modelled as a network of connected ideal tubes that run along the bonds of the lattice. Its topology of which can be described by a graph, in which edges are identified with vessel segments. Graph nodes thereby occupy sites of the lattice. Due to the two-dimensionality of the model we allow individual vessels and TCs to occupy the same space within the lattice, since otherwise disconnected structures arise. In a three-dimensional model set-up this construction is not necessary. All elements (TCs, vessels, nodes) have physiological parameters associated with them—for instance vessel radius r —which define their internal state and which will be introduced below.

2.1.3. Blood flow

To compute the flow rate q of each vessel segment, the shear force f exerted on the vessel walls, and the blood pressure p , we adopt the approach widely used in the literature (Gödde and Kurz, 2001; Betteridge et al., 2006; McDougall et al., 2006): a system of linear equations is derived from Poiseuille's law and mass balance equations for the nodes, which is solved numerically to obtain the blood pressure for each node. At arterial/venous supply/drain boundary-nodes we set the pressure to fixed values. To account for the complex non-Newtonian fluid behaviour we use a vessel radius and hematocrit (red blood cell fraction)-dependent viscosity term (Pries et al., 1994). For simplicity we neglect the phase-separation effect and assume a constant hematocrit of 0.45 which is the average in humans.

2.1.4. Oxygen

The O_2 concentration field denoted as c is defined as the solution of the stationary (i.e. time-independent) diffusion equation $\nabla^2 c - \gamma_c c + \alpha_c (c^{(B)} - c) = 0$, where γ_c is a tissue-dependent consumption rate, $c^{(B)}$ the blood O_2 level and α_c the source strength incorporating local vascular area-fraction and wall permeability. It is solved numerically once per time step (see below), with no-flux boundary conditions on the lattice of the discrete system. We restrict ourselves to the stationary solution of the O_2 -diffusion equation since the relaxation time of the O_2 concentration to adapt to source/sink changes is of the order of seconds whereas changes of the tumour or vasculature configuration occur on the time scale of hours. We further assumed that oxygen uptake is non-saturated so that a linear consumption term makes sense. In the presence of the high tumour demand this simplification is justified. We assume that all vessels have equal oxygen content and also contribute equally to tissue, i.e. α_c and $c^{(B)}$ assume constant values of model parameters at vessel sites.

Under physiological conditions only the thinnest capillaries release oxygen into the surrounding tissue, but in our two-dimensional situation also higher order vessels have to release O_2 because otherwise large scale depressions of the O_2 concentration would occur around large vessels due to the lack of capillaries, which would unrealistically confine tumour growth. This construct is again necessary due to the two-dimensionality of our model, in three dimensions the space around large vessels van still be filled with capillaries. We also implemented a three-dimensional version of the model, where only capillaries are a source of O_2 . It turns out that the results are the same as in the present model in two space dimensions with also larger capillaries emitting O_2 (Welter et al., unpublished).

We also neglect variations of the O_2 level within the vessels, assuming these variations are small over the length of a O_2

releasing capillary. In previous work (Welter et al., 2008) we compared simulation results for models with constant and varying hematocrit and found differences only on a micro-scale but not in large scale characteristics.

2.1.5. Growthfactor

Analogous to the O_2 field we define the equation for the GF field denoted g . In practice it is calculated as the superposition of contributions from underoxygenated tumour cells, which are characterized by $c < c_{TC}^{(prol)}$, where $c_{TC}^{(prol)}$ is a model parameter. Each of these cells generates a GF distribution which decays linearly as $(1 - x/R_g)$ with the distance x up to the GF diffusion radius R_g . This is a simplification based on assumption that GF has a limited diffusion range similar to oxygen and that it is secreted at a constant rate.

2.2. Definition of the dynamical processes

The dynamical evolution of the system is described as a stochastic process in which elements can be removed or added and their internal state can be changed according to rates that depend on the current system state. In practice we implemented an iterative scheme where update rules that correspond to the processes described below are applied sequentially for each time step of length $\Delta t = 1$ h. A rate thus translates into a probability $p = \Delta t/\tau$ for a specific transition to happen within the time step of length Δt , where τ is the mean time between transition events. With our parameter choices, the probabilities are sufficiently small such that this approach is a reasonable approximation to a continuous stochastic process.

The microscopic biological observations for the following basic model assumptions were discussed in the introduction in Section 1.2, including the experimental citations.

TC Proliferation: (see Section 1.2.4) New TCs occupy empty neighbour sites of the existing tumour with probability $\Delta t/t_{TC}^{(prol)}$ if the local O_2 level is above the hypoxia threshold parameter $c_{TC}^{(prol)}$. The parameter $t_{TC}^{(prol)}$ is the mean proliferation time (Fig. 2a).

TC Death: (see Section 1.2.4) TCs are removed if the local O_2 level is less than the necrosis threshold $c_{TC}^{(death)}$ for longer than the time $t_{TC}^{(uo)}$, where $c_{TC}^{(death)}$ and $t_{TC}^{(uo)}$ are system parameters. For simplicity potential variations among different TC genotypes are neglected (Fig. 2b).

Angiogenic sprouting: (see Section 1.2.2) Sprouting can be initiated by the generation of tip-cells at sites on the vessel network depending on several factors:

- (1) (VEGF dependence of tip-cell generation): The local GF concentration must be non-zero (for simplicity the sprouting probability is independent of the concentration value).
- (2) (Alternating pattern of tip-cell and non-tip-cell in the vessel walls): There is no sprouting from the next $l^{(spr)}$ sites in the vicinity of existing branching points.
- (3) (Switch from angiogenic sprouting to circumferential growth, see Section 1.2.3): When the tumour grows over a particular vessel-occupied site, sprouting is prohibited for this site after the delay time $t_{EC}^{(switch)}$.

If these conditions are fulfilled a new vessel segment may be added with probability $\Delta t/t_{EC}^{(sprout)}$, where the parameter $t_{EC}^{(sprout)}$ is the mean time to extend a sprout by the length of a lattice-bond. The direction along the steepest GF gradient is taken. During the following time steps more bonds are added—one per step with probability $\Delta t/t_{EC}^{(sprout)}$. For simplicity the direction from the initial bond is retained. On contact a branching point is created fusing the vessels and terminating the sprouting behaviour. Otherwise the extension of the sprouts is limited by the amount of time $t_{EC}^{(migr)}$, after which sprouts become inactive and count as normal (unperfused) vessels (Fig. 2c, d).

Vessel collapse: (see Section 1.2.3) We account for varying vessel stability by a “degree-of-maturation” variable w , which is initialized with the thickness of healthy vessel walls (see parameter section). w decreases continuously inside the tumour with the rate k_w . Vessels remain stable while w is larger than 0. In addition, collapses are correlated with shear stresses f on the

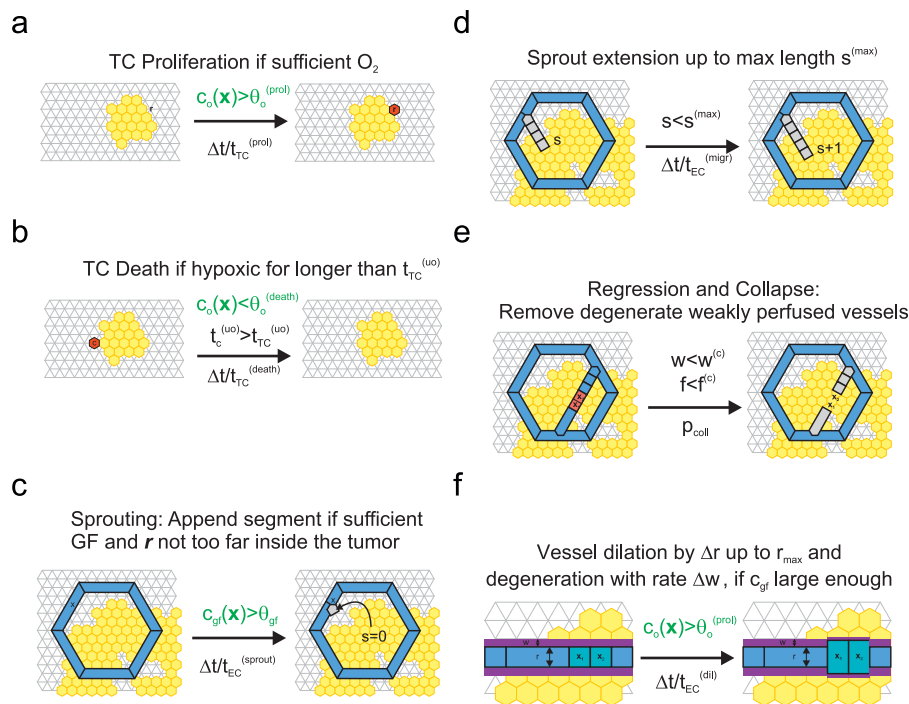


Fig. 2. Sketch of the dynamical processes in the model: (a) TC proliferation, (b) TC death, (c) sprout formation, (d) sprout migration, (e) vessel regression and removal, (f) dilation and wall degradation. See text for details.

vessel wall: if f is larger than the threshold parameter $f^{(coll)}$ vessels remain stable. Otherwise vessels are removed with probability $p^{(coll)} = \Delta t/t_{EC}^{(death)}$, where $t_{EC}^{(death)}$ is the mean survival time. Sprouts are an exception to the above mechanisms (Fig. 2e).

Vessel dilation: (see Section 1.2.3) After a vessel segment switched to circumferential growth (see angiogenic sprouting) the vessel radius r increases with the rate k_r if the local GF concentration is non-zero and $r < r^{(max)}$ (Fig. 2f).

2.3. Arterio-venous tree construction

Vasculature in real tissue exhibits a tree like structure. Few thick arteries branch out into arteriolar microvessels. Terminal branches are connected to the capillary bed, a dense network consisting of thin vessels where most of the exchange with the surrounding tissue happens. Further upstream blood is collected in venules which fuse into thick veins. The design goal of such a structure is to provide a sufficient supply of nutrients to all regions of the tissue, while minimizing the energy necessary to maintain the circulation.

Gödde and Kurz (2001) presented a method to grow and remodel vascular trees stochastically according to probabilistic rules that depend on local system properties. The simultaneous construction of arterial and venous trees makes their approach well suited for generating an initial vasculature for our tumour model.

Its basis is the growth of random arterial and venous trees on a lattice, under exclusion of already occupied sites. This is followed by stochastic shear stress guided remodelling at the tree leaves. Thereby weakly perfused leaves regress while strongly perfused leaves can grow. The vessel radii are computed by “Murray’s Law” (Murray, 1926) from prescribed radii of the leaves. This eventually leads to a well-perfused space filling network with a relatively homogeneous capillary density distribution.

We provide the algorithmic details in the Appendix. Parameters are given there as well as in the parameter section below. Figs. 3a and 5 show the results used as input for our tumour model described above in Section 2.2.

While it is highly non-trivial to synthesize vascular networks that are realistic in every way possible, our initial networks exhibit reasonable hierarchical structures, spatial distributions of the capillaries, and good agreement with the flow-data of the original paper (Fig. 8).

2.4. Parameters

In order to observe typical features of the tumour-network morphology we have to simulate a sufficiently large area. The construction of the initial vasculature is carried out on a much coarser lattice because it is inherent to the algorithm that ca. 50% of the bonds are occupied with vessels. Therefore the resulting microvascular density is primarily a function of the lattice constant l_{coarse} . Based on the MVD for human skin (ca. 100 vessels per mm^2 cross-sectional area) and the MVD in the regular lattice cases (Bartha and Rieger, 2006; Welter et al., 2008), we set l_{coarse} to 60 μm . The a priori capillary radii are 4 μm for arterioles and 5 μm for venules, respectively. The radii of the vascular tree roots depend on the branching pattern. Because of this variation the blood pressure p at each root node is determined as a function of the vessel radius r : $p(r) = 0.133(18 + 72/(1 + \exp((r + 21 \mu\text{m})/16 \mu\text{m})))$ kPa, where r is negated for arterial vessels. It is based on the data in Pries et al. (1995), and results in average values of 2.4 kPa in vein (on average 88 μm radius) and 10 kPa in arteries (on average 52 μm radius).

Table 1
Model parameters of the base case.

Parameter	Value	Description
L	1200	Lattice size
l	10 μm	Lattice const
l_{coarse}	60 μm	Lattice const. (tree constr.)
$c^{(B)}$	0.45	Blood oxygen level
α_c	0.002 $1/\mu\text{m}^2$	O ₂ source coefficient
γ_c (normal)	$1/90^2$ $1/\mu\text{m}^2$	O ₂ consumption. coeff
γ_c (tumor)	$1/50^2$ $1/\mu\text{m}^2$	
R_g	200 μm	Growthfactor diffusion range
$t_{EC}^{(switch)}$	24 h	Sprouting/dilation switch delay
$t_{EC}^{(sprout)}$	5 h/10 μm	Sprout extension time
$t_{EC}^{(migr)}$	100 h	Sprout activity duration
$l^{(spr)}$	20 μm	Sprout sites minimum separation
$r^{(sprout)}$	4 μm	Initial sprout vessel radius
k_r	0.4 $\mu\text{m}/\text{h}$	Vessel dilation rate
$r^{(max)}$	25 μm	Maximum dilation radius
$t_{TC}^{(prol)}$	10 h	TC proliferation time
$t_{TC}^{(w)}$	100 h	Hypoxic TC survival time
$f^{(coll)}$	1 Pa	Critical wall shear stress
$t_{EC}^{(death)}$	10 h	Unstable vessel survival time
k_w	0.04 $\mu\text{m}/\text{h}$	Dematuration (w) rate
$c_{TC}^{(death)}$	0.03	TC hypoxia O ₂ threshold
$c_{TC}^{(prol)}$	0.3	TC proliferation O ₂ threshold
	88 ± 21 μm	Venous tree root radius
	52 ± 14 μm	Arterial tree root radius
	2.4 ± 0.1 kPa	Venous tree root blood pressure
	10 ± 1 kPa	Arterial tree root blood pressure

Blood pressures and radii of the root nodes are stated as averages ± deviations over all configurations (see text).

In the following we define the parameters for a base case scenario for the tumour model (see Table 1). The size of the lattice is 1200×1200 sites, with the lattice constant $l = 10 \mu\text{m}$ ($\approx 12 \times 10 \text{mm}^2$ since it is a triangular lattice).

The initial tumour is an Eden-grown cluster of 1000 cells and 300 μm in diameter. We set the TC proliferation time $t_{TC}^{(prol)}$ to 10 h, the viability time under hypoxia $t_{TC}^{(w)}$ to 100 h, and the apoptosis time to 2 h, the O₂-threshold for proliferation $c_{TC}^{(prol)}$ to $0.3 \approx 0.9(c)$ and the threshold for extreme underoxygenation $c_{TC}^{(death)}$ to $c_{TC}^{(prol)}/10$.

We set angiogenesis related parameters as follows: sprout extension time (mean waiting time between additions of new lattice bonds to a sprouting vessel) $t_{EC}^{(sprout)}$ to 5 h, sprout viability time $t_{EC}^{(migr)}$ to 100 h (estimated from figures in Nehls et al. (1998)), sprouting site separation distance $l^{(spr)}$ to 20 μm , the initial sprout radius $r^{(sprout)}$ to 4 μm , the delay until the switch to circumferential growth happens $t_{EC}^{(switch)}$ to 24 h, the circumferential growth rate k_r to 0.4 $\mu\text{m}/\text{h}$, the maximum radius $r^{(max)}$ to 25 μm and the growth factor diffusion range R_g to 200 μm (estimated from morphological data by Döme et al. (2002)).

Parameters related to vessel regression are as follows: we set the critical shear force $f^{(coll)}$ deliberately to 1 Pa which is 10% of the average shear stress, and the mean waiting time for regression $t_{EC}^{(death)}$ to 10 h which applies for uncirculated as well as degenerate vessels ($w \leq 0$). We had to estimate the dematuration rate k_w from the presentation by Holash et al. (1999a). It is set to 0.04 $\mu\text{m}/\text{h}$, resulting in regression delays from 93 h (4 μm vessels) to 625 h (50 μm vessels). The maturation variable for the original vasculature and new sprouts is initialized with an estimate for the wall thickness (Pries et al., 2005).

The O₂-diffusion parameters are chosen so that the field becomes dimensionless, the diffusion range is ca. 100 μm , the O₂ level in the middle of two vessels drops to ca. 50% of the peak values. These are typical observations in Carmeliet and Jain (2000)

and Torres Filho et al. (1994). Our respective values are $0.002 \text{ 1}/\mu\text{m}^2$ for α_c , $1/90^2 \mu\text{m}^2$ for γ_c in normal tissue and $1/50^2 \mu\text{m}^2$ in tumour tissue. An upper bound for the concentration is the blood oxygen level $c^{(B)}$ which we set to 0.45. The choice can be arbitrary

because c scales linearly with $c^{(B)}$. We refer for a full discussion to Welter et al. (2008).

3. Results

The model predicts the dynamical evolution of the global morphology consistent with experiments and our previous results as explained in the introduction.

Fig. 3a shows a sample system in its initial state. The vessel network was generated by first laying out stems of the trees manually, and then starting the random growth process with branching points on each site on the stems. This is described in detail in the Appendix. The layout of the stems is indicated in the top right corner of Fig. 3. Their lengths and locations are sampled from uniform distributions. The approach was motivated by the observation that vasculatures exhibit relatively thick straight vessels down to a certain level in the hierarchy as can be seen in photos from the CAM (Mironov et al., 1998), or in recent 3d vascular imaging (Cassot et al., 2006) experiments.

Fig. 3b–d display snapshots at successive times. Initially the tumour O_2 consumption leads to decreased O_2 levels inside the nucleus and consequently enables vascular remodelling via growthfactor production of the TCs. The sprouting process first creates a dense capillary plexus which provides more oxygen and facilitates tumour growth. Vessel collapses begin after a few days ($t = 200 \text{ h}$). Small capillaries can collapse immediately under bad perfusion while thicker vessels survive longer due to their stability, i.e. large w , independent on blood flow until they become unstable. The network is thus progressively remodelled, predominantly within a thin band around the tumour boundary. The sparse network left in the centre remains static except for a few collapses of isolated threads.

The final configuration is displayed in Fig. 4a. A magnified view on the boundary region of the tumour is shown in Fig. 4b. The resulting network morphologies show the typical high-MVD periphery and low-density centre. The remaining internal vessels form short-cuts between arteries and veins which touch the tumour surface. This is a consequence of the dilation that all vessels undergo in the tumour. The short-cuts consist of neovasculature as well as parts of the initial vasculature. Beside isolated threads we frequently observe regions where vessels are densely clustered.

The configurations shown in Fig. 5 were generated from alternate layouts of the vascular stems which are illustrated again in the top right corner. The stems represent the sources and drains of the arterio-venous networks. Biologically they correspond to different arrangements of the number and location of the main arteries and veins in the original blood vessel network in the neighbourhood of the tumour nucleus. The

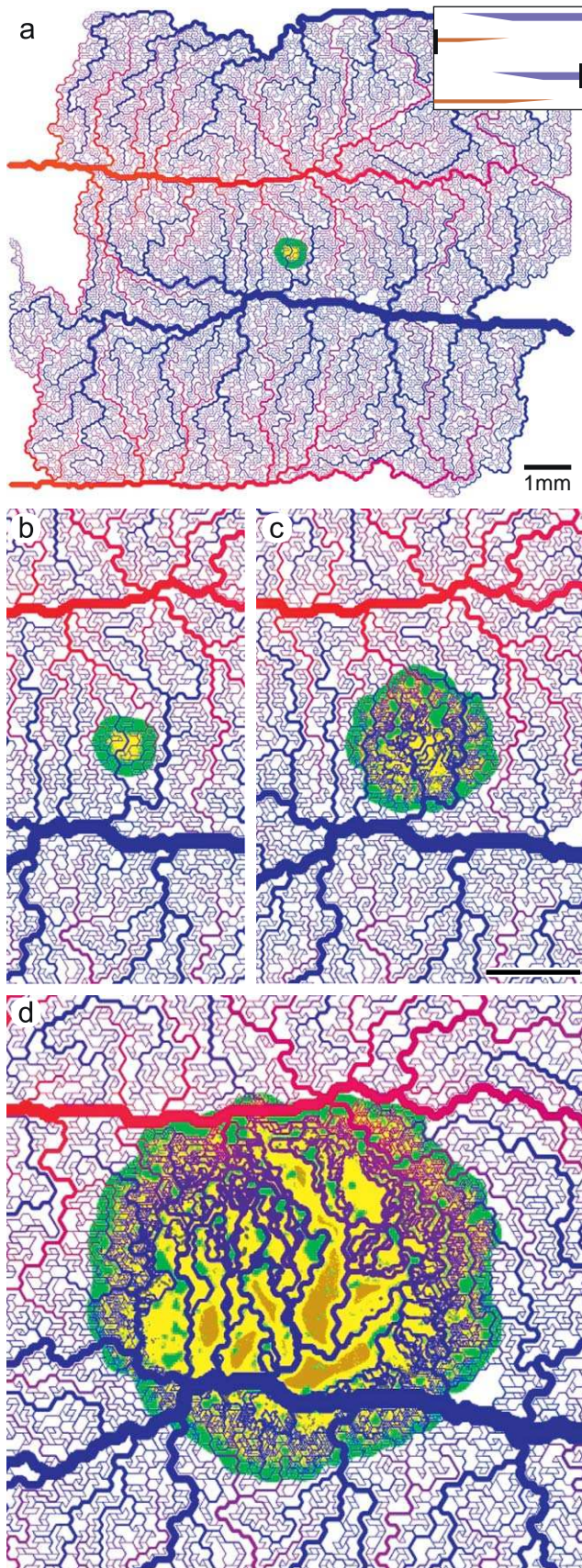


Fig. 3. (a) Snapshot of the initial model configuration. Arteries are red and veins blue. Their radius originates from the construction algorithms (Section 2.3), depending on the network topology and a priori capillary radii. The colour code of the resulting networks shows the blood pressure distribution from 12 (red) to 0 kPa (blue). The small yellow area in the system centre is the tumour nucleus initialized by Eden growth to a maximum of 1000 TCs. Necrotic tumour tissue which appears on the other figures has a dark yellow colour. The background in normal tissue/extracellular matrix is coloured green where the growthfactor (GF) concentration can cause angiogenesis. The inset shows the layout of the vascular tree stems which serve as starting locations for the network generation algorithm. The lengths (indicated by wedge shaped part of the bars) and positions (indicated by the two black vertical bars) of these stems are drawn from uniform distributions. (b)–(d) Snapshots of the model evolution at times 0, 200, 600 h. The vessel network is progressively remodelled, resulting in the typical morphology with high peripheral MVD, dilated vessels, low central MVD with many isolated threads, cuffs of viable TCs around them, and necrotic tissue in non-vascularized zones. (For interpretation of the references to colour in this figure legend, the reader is referred to the web version of this article.)

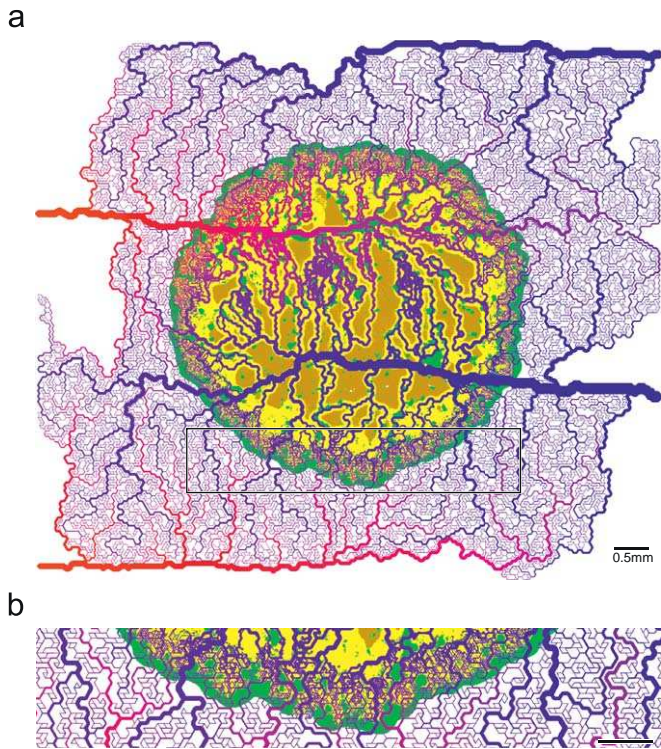


Fig. 4. (a) Final model configuration at $t=1200$ h resulting from continued expansion from the states depicted in Fig. 3. Typical features of solid tumour growth are retained. Now the tumour has also coopted a major artery and a vein. It is apparent that in between an increased number of well-conducting pathways have formed which serve as arterio-venous short-cuts. These originated from neovasculature as well as original capillaries which both have undergone circumferential growth and thus carry high blood throughput. The formation of clusters with increased local MVD, preferably close to the artery, is also evident. (b) Magnified view of the invasive edge that shows in detail how the vasculature is remodelled. Alternating with very high MVD on small scale, there are “holes” of the size of the intervascular distance in normal tissue. This is an effect of prohibiting sprouts from arteries, which would otherwise fill the holes, leading to a homogeneous vascular density. Behind the peripheral zone, the MVD drops rapidly. One can further see a few isolated dilated vessels directly connected to arterioles/venules in healthy tissue beyond the invasive edge.

result of the stochastic arterio-venous tree generation based on the different source and drain locations is shown in the top row. They look morphologically quite different, (a) displays a large artery close to the tumour nucleus, (b) a large vein, and in (c) is the tumour equally distant from major arteries and veins. However, the density of capillaries, the MVD, is identical for all three configurations.

Starting with these different initial networks the final tumour vasculature predicted by our model is depicted in the bottom row of Fig. 5. Obviously they differ in the local MVD configuration: in (d) the MVD is large in a central region (a hot spot), in (e) and (f) it is low. We conclude that differences in the original vasculature lead to differences in the arrangement of spatial inhomogeneities within the tumour (hot spots, necrotic regions), which will be discussed below. But the global compartmentalization pattern is identical for all three configurations, as can be seen from the radial distributions.

3.1. Radial distributions

Fig. 6 shows various quantities averaged over concentric annuli centred around the tumour centre. The stochastic construction of the initial vasculatures can leave the periphery unoccupied, but the vascularized regions exhibit a homogeneous MVD by design

and have no holes. We run 10 Monte-Carlo simulations for each of the four basic layouts discussed above. We rejected configurations that were too small to support tumour growth till the end at $t=1200$ h.

MVD and TC density are computed as the fraction of occupied sites within a shell. Hemodynamic properties are averaged over occupied bonds only. MVD and vessel-radius show the typical compartmentalization that has been observed in melanoma (Döme et al., 2002) and glioma (Vajkoczy and Menger, 2000). We have discussed and compared our data extensively in earlier papers Bartha and Rieger (2006) and Welter et al. (2008).

Briefly, Döme et al. (2002) reported MVD and vessel radius in three distinct regions: the central region, a $100\mu\text{m}$ wide peripheral band just behind the invasive edge, a $200\mu\text{m}$ wide peritumoural region outside the invasive edge. In the central region, they found 25% MVD of normal tissue, and up to 200% in the peritumoural region. The vessel perimeter grows linearly from $50\mu\text{m}$ and assumes a plateau at $200\mu\text{m}$ by day 15.

In contrast to our simulation on a regular vascular network, flow rates and shear force now show a plateau similar to the vessel radius. Previously the fixed pressure gradient along the boundaries of the regular (rectangular or hexagonal) networks leads to unrealistic star shaped morphologies, directing all blood flow through the centre. Hierarchical initial networks do not lead to these artifacts. The axial blood pressure gradient dp/dl which is not shown here decreases monotonically towards the centre by more than one order of magnitude. The blood flow rate q is proportional to $r^4 dp/dl$ and increases on average towards the centre beyond a small local minimum at the invasive edge. Thus the r^4 dependency of the radius outweighs the pressure drop. The shear force dependency is $r dp/dl$ which leads to a decrease towards the centre.

3.2. Vessel statistics

Fig. 7 shows scatter plots of hemodynamic variables against the vessel radius r , which are in good agreement with those obtained in Gödde and Kurz (2001). The plots combine samples throughout the vasculature (tumour and surrounding vessels) from all runs (at $t=800$). At this time a sufficient number of samples from the initial vasculature are available with negligible boundary effects.

We generally observe that the variance of the flow related parameters increases drastically towards the capillaries. This might be an artifact of our initial network construction, but averaged quantities display physiologically sound characteristics.

The dilation of internal tumour vessels leads to samples clustered at the maximum radius and one observes increased fluctuations at this particular radius. In particular vessels that connect arteries and veins at the tumour surface and thread through the tumour interior have blood pressure values in between the respective extremal values. In contrast, most non-dilated vessels which are obviously located in the outer rim fall in the same parameter ranges as normal vessels.

A few capillaries exhibit significantly lowered flow rates and velocities. Fig. 8, containing a spatial representation of the flow-rates, shows that the weakly perfused vessels are exclusively located in the tumour perimeter. As in this figure we observed that central vessels generally transport as much blood as equally thick vessels in normal vasculature. In Section 3.5 we show how this impacts the transport of drugs.

3.3. Parameter dependencies

We analyzed variations of all major model parameters extensively in Bartha and Rieger (2006) and Welter et al. (2008).

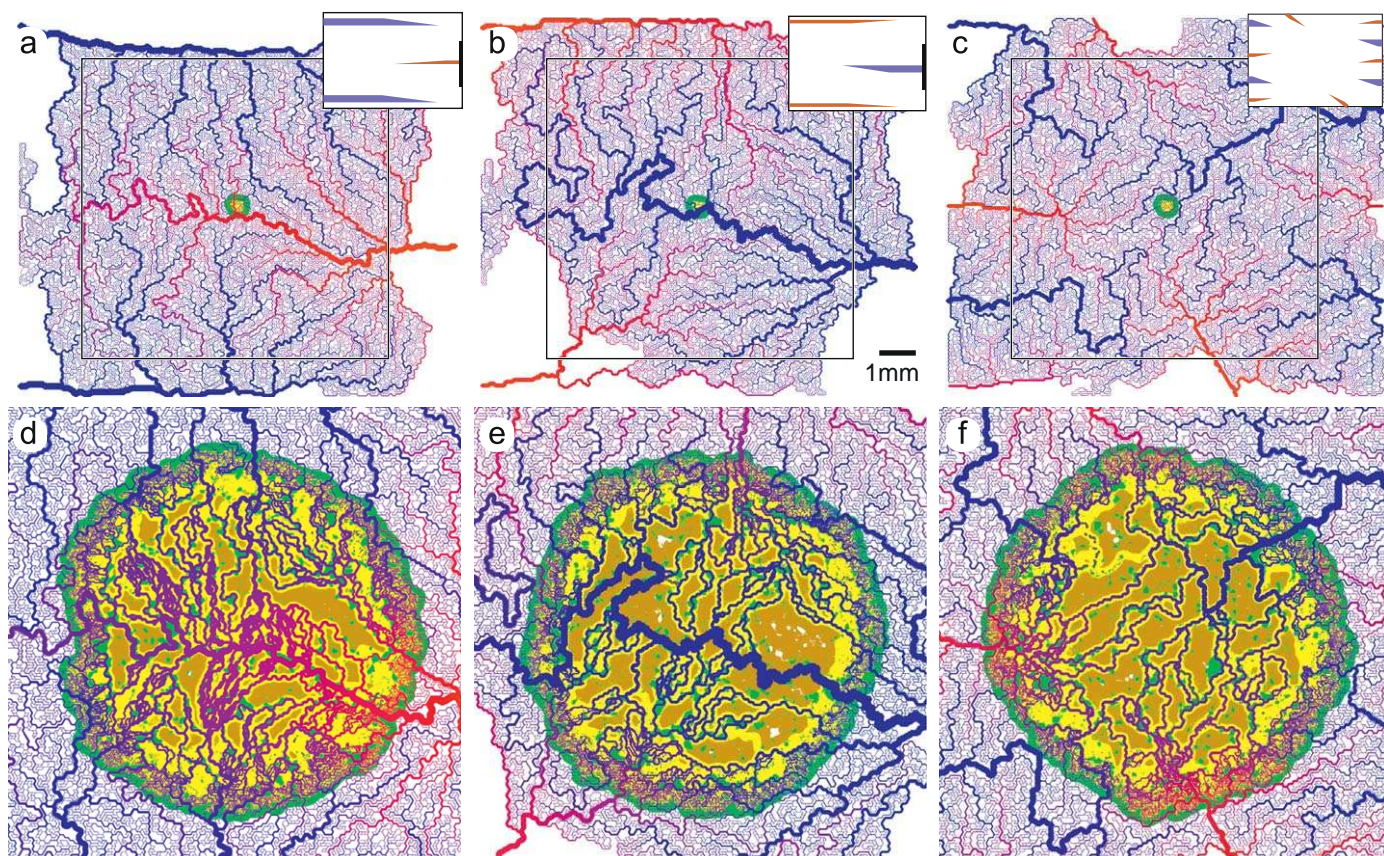


Fig. 5. (a)–(c) Initial vessel networks generated from different layouts as depicted analogous to the inlets in Fig. 3. (d)–(f) Final model configurations emerging from the networks above. The formation of local vessel clusters is clearly visible in the central region in (d), but not so in (e) and (f). In the latter increased MVD can be observed in a few locations close to the tumour boundary. In our reasoning, varying blood pressure differences between neighbouring vessels in the normal vasculature causes a highly inhomogeneous shear stress distribution in the tumour periphery. Thus the varying degree of stability leads to these clusters.

It was found that model predictions are very robust against variations and also details of the mathematical modelling. The effects of most parameter variations are obvious: the TC proliferation time $t_{TC}^{(prol)}$ mainly determines the expansion rate of the tumour provided the oxygen level c in the original vasculature is sufficiently above the proliferation threshold $c_{TC}^{(prol)}$. Otherwise growth can be slowed down depending on the rate at which peripheral vasculature is created and its final density (MVD). The latter is regulated by the sprout migration rate $1/t_{EC}^{(migr)}$ and minimum distance between branching points $l^{(spr)}$. The blood flow characteristics play an important role for the internal tumour MVD. The higher the shear stresses f (or the lower the associated threshold value $f^{(coll)}$) the more vessels will survive. We have identified a mechanism that leads to a lower bound for the MVD: when vessels collapse their blood volume is directed through the remaining vessels, increasing their flow rate and shear stress, thus stabilizing them. With the addition of the arterio-venous network the temporal evolution of the MVD depends on the vessel dematuration rate k_w . Once the tumour has grown over the peripheral plexus there is a delay until the maturity value w of vessels has decreased to 0. Together with the mean survival time $t_{TC}^{(death)}$ of degenerate vessels this delay causes the high-MVD rim to reach into the tumour by a certain width proportional to the delay time. Moreover the number of surviving thick arterioles and venules depends critically on the dematuration rate. If it is high these vessels will collapse early if it is low they may never collapse during the time of observation (1200 h).

The large shear force variations among capillaries in the original vasculature poses the question whether an absolute threshold for the collapse criterion is appropriate. Therefore we

also checked the result of setting the probability $p^{(coll)}$, with which unstable vessels collapse, proportional to the relative deviation from the initial shear stress f_{init} ($p^{(coll)} \propto 1.0 - (f/f_{init})/f^{(coll)}$ for $f/f_{init} < f^{(coll)}$) instead of using an absolute threshold. This leads to decreased global MVD fluctuations among the simulation runs and also to increased local homogeneity, but does not change the model behaviour qualitatively.

In the present model variant, vessels can collapse any time after degradation ($w \leq 0$), depending on shear stress. It is, however, also an option to restrict collapses to the tumour rim. For example, it has been suggested that the death of tumour cells releases solid pressure from near vessels that is otherwise exerted by the tumour (Griffon-Etienne et al., 1999). Moreover, in previous papers we assumed the existence of a stable radius, preventing collapses in the centre where vessel radii are larger. Indeed, the EphB4 signalling mechanism which induces circumferential growth also leads to reduced leakiness, tightened EC junctions and endothelium/pericyte interaction (Erber et al., 2006), making an actual stability improvement plausible. Therefore we altered the model, assuming unconditionally stable internal vessels, by choosing collapse probability $p_{ring}^{(coll)}$ which takes on $p^{(coll)}$ only inside a band of width $l_{ring}^{(coll)}$ centred at the invasive edge, and which is zero otherwise. The result depends strongly on the time vessels spent in the collapse region, given implicitly by $l_{ring}^{(coll)}$ divided by the radial expansion velocity of the tumour. If this time is of the order of the survival time inside the tumour a transition occurs towards a highly vascularized centre, shown in Fig. 9 and analyzed in detail in Bartha and Rieger (2006) and Welter et al. (2008). Moreover $p_{ring}^{(coll)}$ causes less fluctuations with respect to initial networks because more of the initially thick vessels can

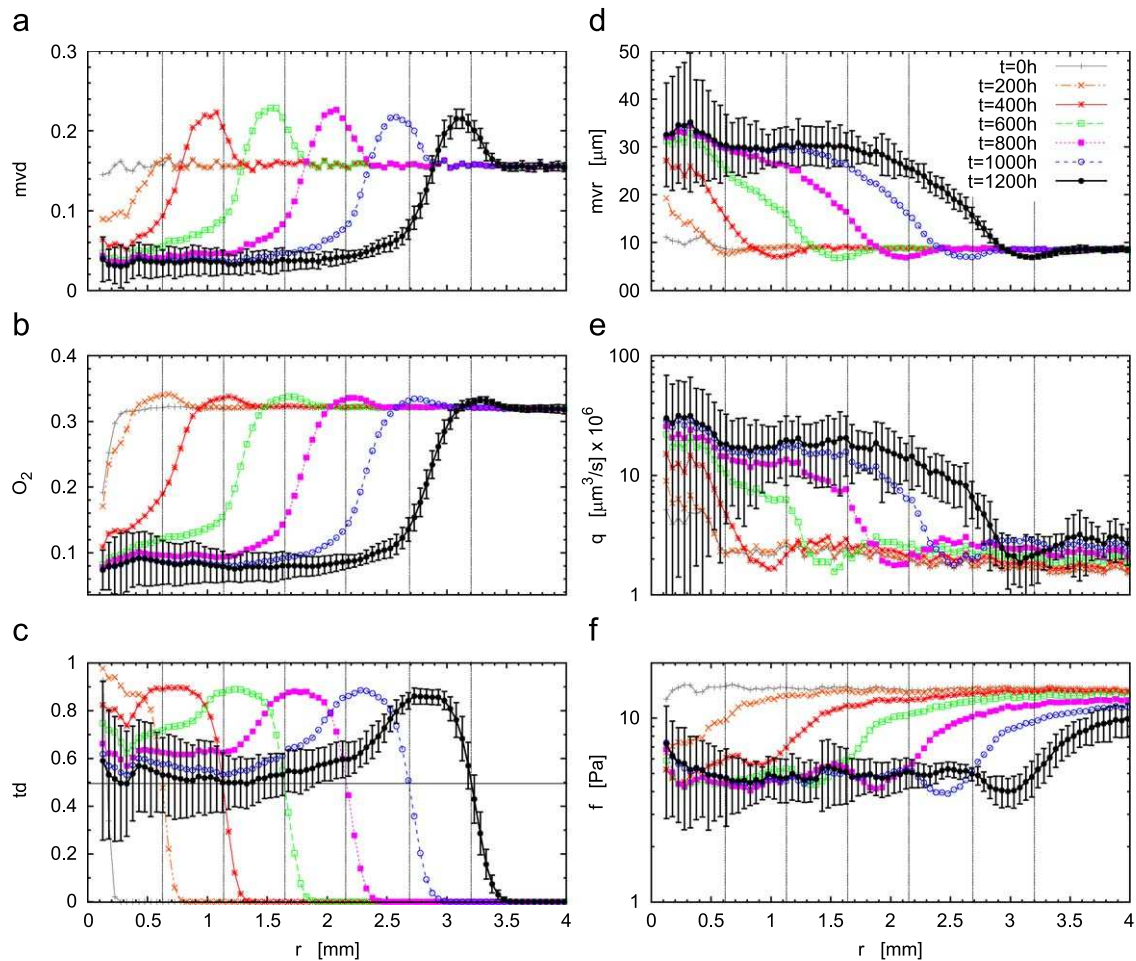


Fig. 6. Radial distributions of hydrodynamic and morphological variables of the base case simulations. The radius r here denotes the distance from the tumour centre. One data point represents an average over a concentric $50\ \mu\text{m}$ wide shell, and over 40 runs: (a) shows the MVD, (b) the O_2 level and (c) the TC density, (d) the vessel radius, (e) the flow rate and (f) the shear force. The latter three are given as the average over actually occupied sites within a shell, instead of over all sites. For $t = 1200\ \text{h}$ also the root mean square deviations are indicated as error bars.

provide a backbone which never collapses due to $w > 0$ while being in the collapse ring.

3.4. Spatial inhomogeneities

Qualitatively one can already see that the location of highly vascularized zones in the tumour is connected to the location of the thicker vessels. They occur frequently where an artery is close to a vein, or vice versa, since an increased number of vessels survive in between. This can be seen clearly in Fig. 4 but it is also apparent in other configurations (Fig. 5). Qualitatively we can explain those hot spots through blood pressure gradients that arise in the tumour vasculature when short-cuts between nearby arteries and veins are formed. Major vessels can thereby act as stable backbones with very high or low blood pressure. Close proximity of two or more such vessels implies high shear stresses in the intermediate capillary bed and thus increased stability. Moreover the shear stress in arteries is normally larger than in veins. This asymmetry apparently leads to hot spot formation preferably close to the arterial branches.

This motivates the following quantitative analysis where intervascular “blood pressure” gradients of the original vasculature are related to the tumour MVD: first we compute a field $p(\mathbf{x})$ as solution to the Laplace equation $\nabla^2 p = 0$ subject to the boundary

condition that p is set to the blood pressure at vessel sites. Thus p interpolates the blood pressure between adjacent vessels. Then, for a given region, we obtain the spatial average of the gradient $\|\nabla p\|$ at $t = 0\ \text{h}$ and plot it against an estimate for the tumour MVD at $t = 1200\ \text{h}$.

The main plot of Fig. 10 shows the MVD versus $\langle \|\nabla p\| \rangle$ over entire tumours with one data point per simulation run. The correlation coefficient is usually very large ≈ 0.9 for this global measurement. Analogously we analyzed single tumour instances where the average is taken locally over randomly distributed discs with $150\ \mu\text{m}$ radius. The inset shows the resulting distribution of one such measurement. The correlation coefficients of which vary between 0.2 and 0.4. Since a single collapse event can cause long-ranged regressions of adjacent network sections, it is plausible that local measurements only show weak correlations. Moreover since the vascular blood pressure at boundary vessels is prescribed based on their radius, only the location of initial vessels leads to the variety of emerging tumour morphologies.

Fig. 11 shows intermediate data which stems from the simulation run shown in Fig. 4. The bottom image (Fig. 11c) shows the site occupation by the vessel network. It is easy to identify the tumour network by its typical structure. In Fig. 11a, where $\|\nabla p\|$ is displayed, one observes that indeed the local gradients are stronger in the area close to the major artery in the top half, than close to the vein in the lower half. The snapshots (b)

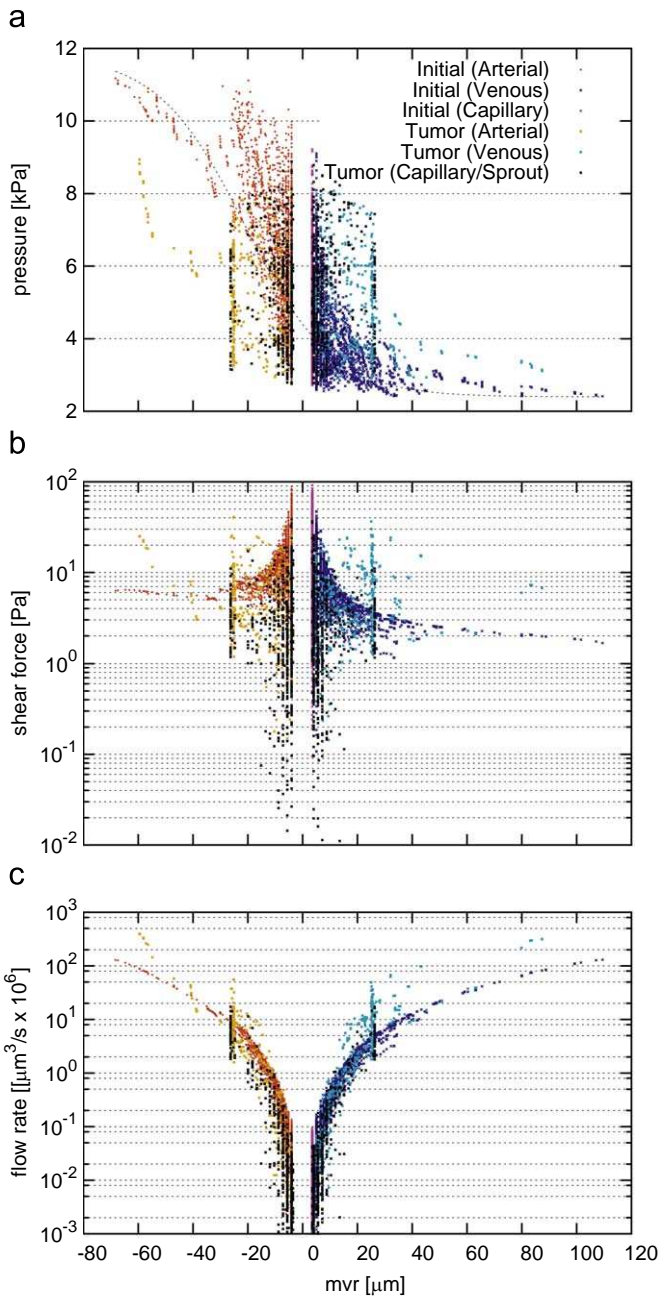


Fig. 7. Scatter plot showing hydrodynamic variables of a single simulation run plotted against the vascular radius. Each data point is a sample from uniformly distributed locations over the entire network. Samples from arteries are red and plotted with negative radius, capillaries are pink, veins are blue, all drawn from the original vasculature at $t=0$ h. Black dots represent samples from the tumour vasculature of base case at $t=1000$ h. Since tumour vessels have no hierarchical organization, these points were put with probability 1/2 on one side or the other. (For interpretation of the references to colour in this figure legend, the reader is referred to the web version of this article.)

and (d) on the right column show respective averages of the left-hand side data. These distributions show the behaviour that zones with elevated $\langle \|\nabla p\| \rangle$ are also probable locations of high MVD.

We further quantify the spatial inhomogeneities by probability distributions for local MVD (Fig. 12a), necrotic region size (b) and hot spot size (c). The distributions are determined by histograms of the respective local samples, combined from 40 runs. The MVD is estimated as the fraction of occupied sites within boxes (250 μm in size) of a regular grid. The plot displays two peaks. One large peak at low MVD ≈ 0.07 which decays algebraically

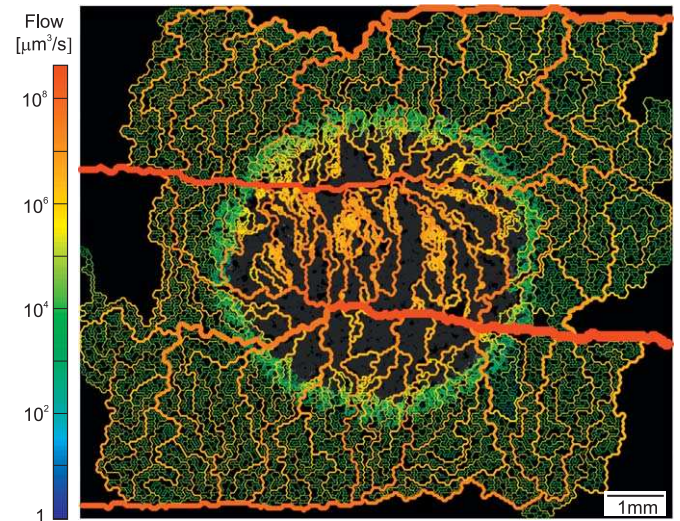


Fig. 8. Flow rate distribution in the vessel network shown in Fig. 4 with a logarithmic scale. The flow rate here is the blood volume per time through the vessel cross-section, not to be misunderstood as the blood flow per tissue volume. In our results dilated tumour internal vessels usually exhibit high flow rates like in this instance. If one would measure in/outflow per tissue volume element as in dynamic MRT measurements one would observe hot spots located at the respective high-MVD zones.

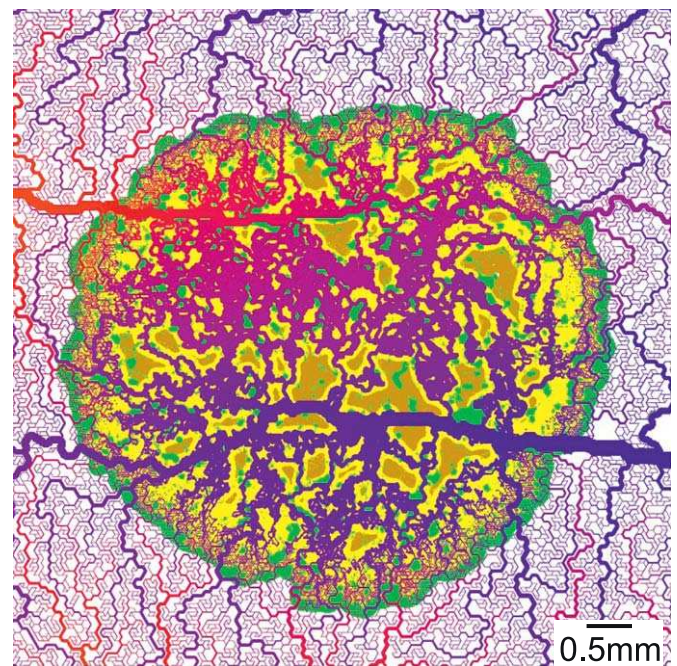


Fig. 9. Final configuration at $t=1200$ h of a simulation run using an alternate vessel collapse rule where vessel collapses are restricted to a thin band (here 400 μm in width) around the invasive edge. The new collapse probability $p_{ring}^{(coll)}$ equals $p^{(coll)}$ modulated with a window-function which depends on the distance to the tumour centre (see text). In this instance, parameters are such that the mean survival time of unstable vessels is of the order of the time they spend in the “collapse region”. This puts the random collapse process in a dominant role over the maturity variable. The system is near a transition to a fully vascularized tumour. The parameter set is the same as in the base case, except for the critical shear force $f^{(coll)}$ which is set to 3 Pa, instead of 1 Pa.

with exponent ~ 1.4 and a smaller peak at MVD ≈ 0.45 . The latter originates from the high-MVD zone in the tumour periphery. Not included is a peak which appears at MVD = 0 due to large non-vascularized regions. The necrotic-region size distribution shows the probability to find a cluster of dead TCs with a given cell

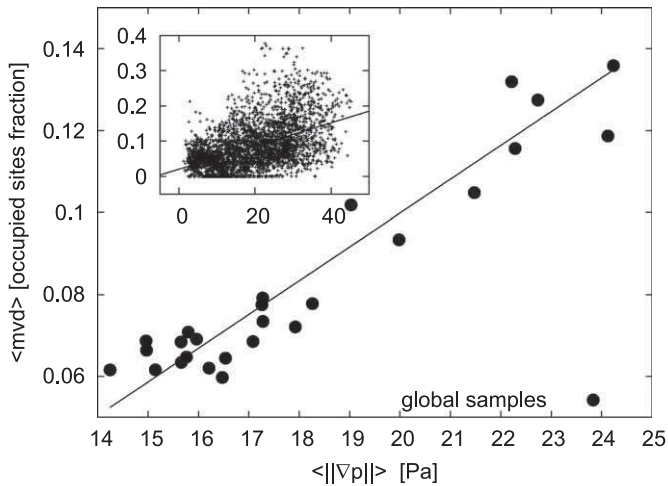


Fig. 10. Vascular density versus the mean pressure gradient ($\|\nabla p\|$) originating from the blood pressure differences between neighbouring vessels (see text). In the main plot data points stem from different runs of the base case, whereby the averages are taken over the entire tumour interiors (excluding the vascularized boundary region) at $t = 1200$ h. The inset displays data for a single tumour, where the averaging is done locally over a small disc with radius $150 \mu\text{m}$ (see Fig. 11).

count. The hot spot size distribution plots the probability to find a cluster with a certain number of sites where the local MVD is larger than a threshold (here 0.15). Both of the latter distributions exhibit purely algebraic decay also with the exponent ~ 1.4 .

3.5. Drug transport

To analyze the effectiveness of blood-borne drug transport to a tumour and its distribution inside a time-dependent concentration profile over the vasculature is propagated according to the local blood flow rates. A corresponding mathematical model was presented (McDougall et al., 2002) for a pure vessel-in-growth capillary network, originating from a single parent vessel. It was predicted that large amounts of drug bypasses the tumour, varying by an order of magnitude depending on parameters. We adopt this method to check whether there are similar obstacles to successful drug delivery inherent to the tumour vascular networks, predicted by our model.

The starting point is a given configuration for the vasculature with precomputed variables for flow, flow velocity, vessel length, and radius. In addition, a mass parameter m is now associated with each vessel describing the amount of drug in the blood

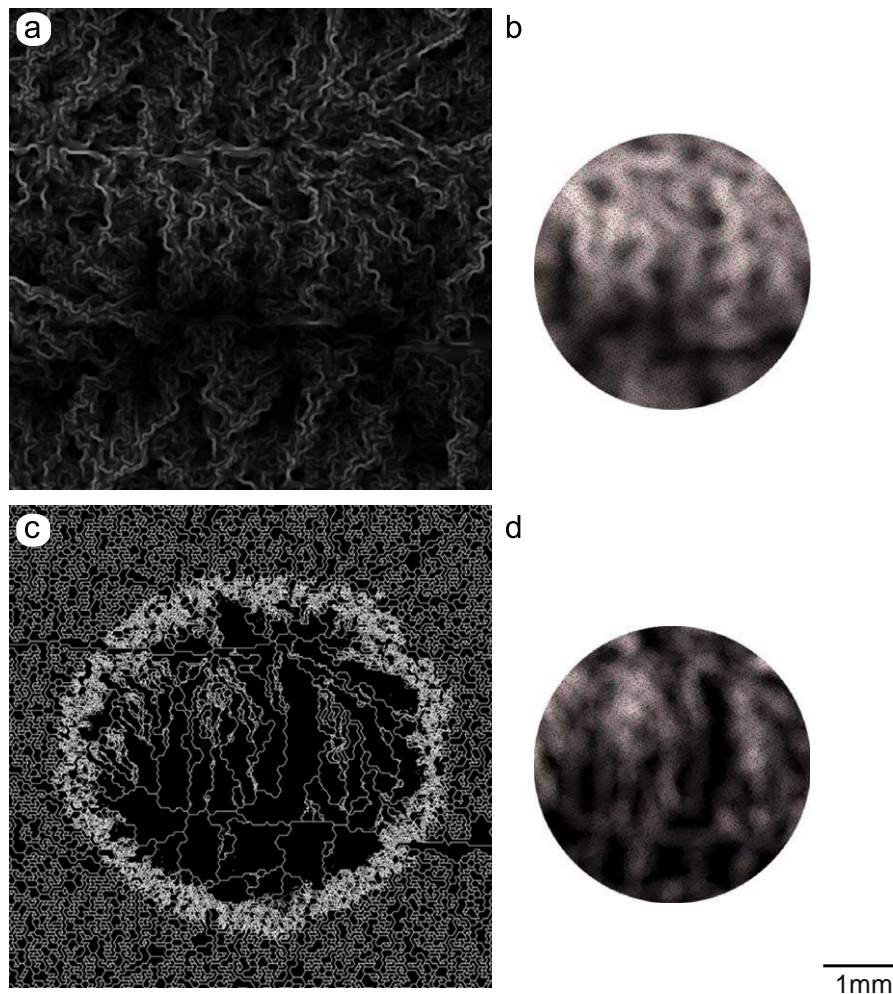


Fig. 11. Demonstration of the intermediate data that lead to the plots in Fig. 10: (a) shows the local magnitude of the gradient $\|\nabla p\|$ (see text). To correlate the MVD locally with $\|\nabla p\|$, mean values were computed at randomly distributed locations, each by averaging over a $150 \mu\text{m}$ radius disc; (b) shows these samples, such that space closest to some data point is filled with a grey scale value proportional to $\|\nabla p\|$; (c) shows the site occupation of the vasculature; (d) shows an estimate for the local vascular density. Value ranges are 0–45 (black to white) for $\|\nabla p\|$ and 0–0.4 for the MVD.

volume contained in the vessel. The mass content m is deterministically updated in successive time steps as follows: first the drug amount flowing out of vessels is determined and added to respective node-mass variables. Under the assumption of perfect mixing, the nodal masses are then redistributed into further downstream vessel. Thereby mass conservation is strictly enforced. A detailed description can be found in Welter et al. (2008) and McDougall et al. (2002). The most severe limitation of this model is that there is no exchange with extra-vascular space and therefore also no uptake by the tumour.

The results in the following were obtained with a continuous injection into our base case vasculatures. From $t = 0$ on, blood with solute drug at conc. $C^{(init)} = 1$ flows into the vasculature which is initially filled with “clean” blood. The flow rates are of the order of mm/s, which is sufficient to saturate 80–100% of the vessels within seconds, depending on the network configuration.

Fig. 13 shows a sequence of snapshots over 6 s. Drug enters the system via the arteries and flows downstream with a sharp transition at the drug/clean interface. When vessels merge in

upstream direction mixing with clean blood occurs so that the concentration profile smooths out in the veins. After 20 s nearly full saturation is achieved. Dilatation of internal tumour vessels and direct connections to feeding arterioles lead to comparably fast filling with drug. The torturous structure and the redirection of blood flow through shot-cuts, away from the capillary bed, leads to decreased flow rates in the periphery. Figs. 7c and 8 show such vessels with low flow rates of the order of $10^3 \mu\text{m}^3/\text{s}$, corresponding to velocities of the order of $10 \mu\text{m}/\text{s}$. The average flow velocity over all vessels in the original network is $\sim 1.8 \text{ mm}/\text{s}$. Consequently we frequently observe regions which take significantly longer to be filled.

Quantitative analysis of drug efficiency impact is only possible to a limited degree due to the lack of tumour uptake modelling. Moreover even few surviving TCs can grow a new tumour mass. Nonetheless we measured statistics for the total amount of drug in the vasculature. Fig. 14a shows the fractional length of the tumour vessel network for which the maximum drug concentration was larger than indicated on the c -axis. After 20 s,

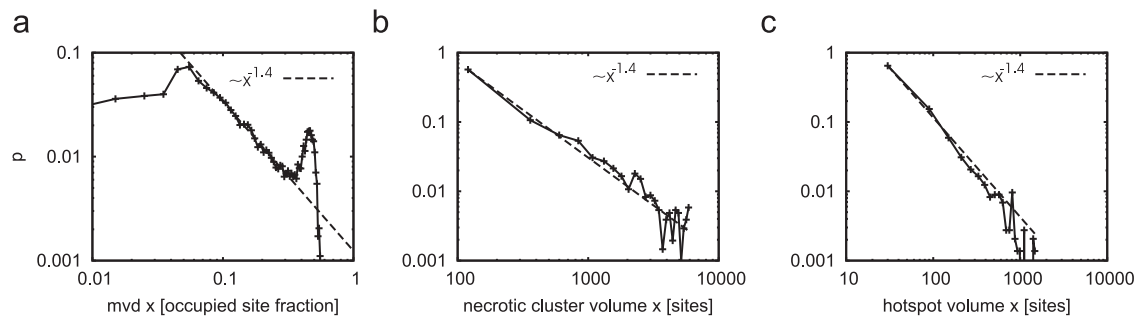


Fig. 12. Probability distributions in log–log plots, for (a) the local MVD, given as the local average over $250 \mu\text{m}$ wide boxes, (b) the volume of necrotic tissue clusters, defined as the number of sites in connected components of dead tissue, (c) the volume of vessel hot spot areas, defined as the connected components of regions where the local MVD exceeds a threshold (0.15). The distributions are generated by binning observed values in histograms over 40 simulation runs (at $t = 1200 \text{ h}$). We note that the distributions show algebraic decay. In this instance in particular with the same exponent with an error of 2%.

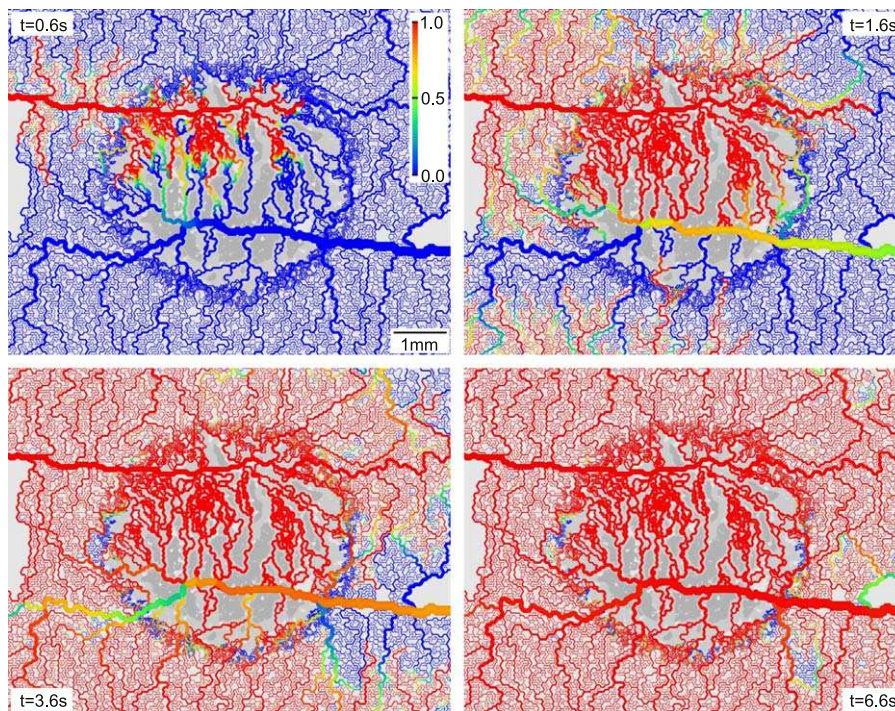


Fig. 13. Snapshots of the drug-flow simulation using the basic configuration (Figs. 3 and 4) at $t = 1000 \text{ h}$. The colour code shows the drug concentration as indicated on the gradient bar. A high drug concentration reaches most parts of the vasculature after a few seconds. In the $T = 6.6 \text{ s}$ snapshots a few vessels in the boundary region are not yet perfused. The time until drug saturates the complete vasculature is of the order of minutes. We can observe this behaviour generally for all resulting networks.

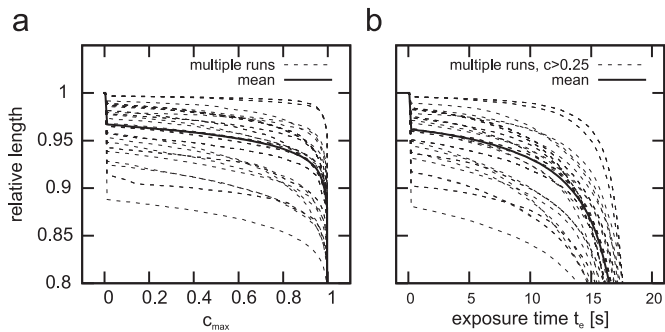


Fig. 14. (a) Fraction of total tumour network length that has been exposed to a drug concentration larger than the indicated concentration c_{max} (at $t = 20$ s of the drug simulation). The black line represents the average over 40 runs with different networks. (b) Fraction of total tumour network length that has been exposed to a drug concentration larger than 0.25 for longer than indicated time t_e . The black line represents the average over 40 runs with different networks. Like in Fig. 15, tumour networks from the base case at $t = 1000$ h were used.

on average $94 \pm 3\%$ of the vasculature had been exposed to a drug concentration of at least 80%. For higher concentrations the curve decreases drastically. The curve at $c = 0$ shows that $4 \pm 3\%$ had not been drug perfused at all. In absolute numbers the latter corresponds to 15 ± 12 mm. Fig. 14b shows the fractional length of the tumour vessel—network for which the concentration was larger than the threshold $c = 0.25$ for a total duration greater than indicated on the x-axis as t_e . This measurement was also done at $t = 20$ s, thus the exposure time cannot be longer than that. It shows that large parts, say $93 \pm 4\%$, of the vasculature had been exposed to 50% drug concentration longer than 10 s. Considering the flow rates/velocities mentioned above one can expect the remaining few millimetres to be drug perfused within a time frame of minutes.

4. Conclusion

4.1. Summary

In this paper we formulated a hybrid cellular automaton model to analyze the vascular remodelling process of an arterio-venous vessel network during solid tumour growth. It is based on the modelling approach described in Bartha and Rieger (2006), Lee et al. (2006) and Welter et al. (2008) and extends it by incorporating a hierarchically organized initial vasculature comprising arteries, veins and capillaries. The model involves sprouting angiogenesis, vessel cooption, dilation and regression as well as tumour cell proliferation and death.

The model predicts that the tumour vasculature emerging from the interplay of these processes is non-hierarchical and compartmentalized into a highly vascularized tumour perimeter, a tumour periphery with large vessels density and dilated vessels and a central region containing necrotic regions with a low microvascular density threaded by extremely dilated vessels. This tumour compartmentalization is therefore independent of the initial vasculature, as has been conjectured on the basis of results for models involving a grid-like initial blood vessel network (Bartha and Rieger, 2006; Lee et al., 2006; Welter et al., 2008). Blood-borne drug transport along the tumour vasculature also turns out to be efficient, the reason for it being the dominant regression of vessels with low shear-forces leaving only those that are well perfused.

One consequence of the arterio-venous initial vasculature, which is absent for grid-like starting networks, is the emergence of short-cuts or “shunts” and concomitantly an increased blood flow through the tumour vasculature. There are experimental studies which agree with this prediction: in Sahani et al. (2005) perfusion parameters in rectal cancer were measured via computer tomography where consistently increased blood flow is reported by approximately a factor of two compared to normal tissue. It was argued that angiogenesis facilitates the creation of arterio-venous shunts which bypass the capillary network. The same mechanism is at work in our model: thick arterioles and venules provide a well-conducting support structure around the tumour. Since the total pressure difference between the tree roots is fixed, the transported blood volume is given by the total flow resistance of entire vascular tree. Dilation of a few vessels forming a path between the tree roots can remove bottlenecks formed by thinner vessels. The creation of new vessels thereby promotes arterio-venous short-cuts, or shunts, through multiple partly disjoint paths. After vessel dilation this leads to a decreased total flow resistance, which implies an increased blood flow through the tumour vasculature when compared with the initial vasculature. This is in contrast to grid-like initial networks, where the total flow resistance is dominated by the network outside the tumour (Bartha and Rieger, 2006; Welter et al., 2008) and the flow cannot increase via the dilation of tumour internal vessels.

Another consequence of an arterio-venous initial vasculature is the emergence of isolated highly vascularized clusters connected by thick vessels within the tumour vasculature. These “hot spots” are also observed in real tumours (Pahernik et al., 2001). Already by a visual comparison of the starting network with the final tumour vasculature one observes that hot spots form more frequently in those regions where the starting network contained predominantly arteries. An analysis of the correlations between various local hydrodynamic quantities of the original network (blood pressure, blood pressure gradient, blood flow) and the local MVD in the tumour vasculature revealed a significant correlation between local blood pressure gradients of the original arterio-venous network and the most probable locations of hot spots in the tumour vasculature. This is plausible since a high pressure gradient within the vessels implies a high shear force exerted by the blood on the vessel walls, which stabilizes the vessel against collapse and therefore leads to an increased vessel survival probability when the tumour has grown over this region. We note that in our model this hydrodynamic mechanism plays a dominant role in the hot spot formation, whereas potential local variations in pro- and anti-angiogenic effectors within the tumour were not involved but could also play a role in this process. It should be possible to check the model predictions experimentally by implanting a tumour nucleus into healthy tissue, whose vasculature has been analyzed before implantation.

We also find that the emerging spatial inhomogeneities in the tumour vasculature are organized in a complex way: the probability distribution of local MVD values as well as the probability distribution of the hot spot volume (defined as the size of connected clusters of regions with MVD larger than the original MVD) has an algebraic tail with exponent ~ 1.4 . Also the size distribution of the connected clusters of necrotic tumour regions showed an algebraic tail (again with exponent ~ 1.4). These power laws are reminiscent of a self-organized critical state (Jensen, 1998), for which the absence of a typical length scale (over which for instance size distributions would decay exponentially) is characteristic, like in a stochastic dilution process at the percolation threshold or a flow-correlated percolation process (Lee et al., 2006).

4.2. Discussion

We summarize briefly what biological insights we can extract from our work. (a) The experimentally observed compartmentalization of the tumour vasculature (Holash et al., 1999a; Döme et al., 2002) is independent of the initial vasculature and a consequence of the basic mechanisms that we identified: (1) the existence of an original vasculature, (2) angiogenic sprouting in the tumour perimeter, (3) blood flow correlated vessel regression and (4) a switch from angiogenic sprouting to circumferential growth within the tumour. If the latter is absent, thick vessels will be rare, leading to increased shear flow and concomitantly to increased stability of the tumour vessels—thus altering the compartmentalization. In addition we predict that (b) blood-borne drug transport is efficient through a tumour vasculature in which vessel regression is blood flow correlated—experimentally observed deficiencies in drug delivery must have other reasons. And (c) the experimentally observed hot spots or MVD inhomogeneities of the tumour vasculature are correlated with the blood pressure gradients of the original vasculature.

Potential experimental tests for these predictions are: (i) if it would be possible to experimentally switch off circumferential growth or prevent vessel collapse the model predicts a different compartmentalization of the tumour vasculature, which could be analyzed experimentally with immunohistology; (ii) intravital microscopy with fluorescently labelled drug proteins or nanoparticles could be used to check the model predictions on blood-borne drug transport; (iii) again using intravital microscopy the local blood pressure in the original vasculature could be analyzed before implanting subcutaneously a small (radius < 2 mm) tumour spheroid. Then the emerging spatial inhomogeneities of the tumour vasculature could be correlated with the spatially resolved blood pressure in the original vasculature.

In this work we were mainly interested in the morphological transformation of an arterio-venous initial vasculature by a growing tumour. Our intention was to characterize the complex geometry of the emerging networks and to identify the basic initial conditions and processes determining the emerging vessel network. There have been attempts to utilize such geometric characteristics of the tumour vasculature (like the fractal dimension) as a diagnostic tools in cancer research (Baish and Jain, 2000), but the purpose of our present work was not to extend these ideas. Rather, the messages that we intended to deliver were simply: (1) the initial vasculature is an important determinant of the tumour vessel network morphology and (2) the complex geometry and characteristic spatial inhomogeneities of the tumour vasculature emerges already from a few basic processes which we described here phenomenologically with stochastic rules.

Obviously one can pose the question, in how far our results depend upon our stochastic modelling approach. This describes certain processes on a coarser scale than *ab-initio* calculations (Frieboes et al., 2007; Bauer et al., 2007; Wise et al., 2008; Milde et al., 2008). For instance rather than calculating the solid stress within the tumour explicitly and incorporating it, among other factors, into the vessel collapse probability we use the prediction of continuum mechanical models for tumour growth (see, e.g. Breward et al., 2003) that solid stress is largest in the strongly proliferating periphery of the tumour and increase the collapse probability correspondingly in this region. Or rather than modelling adhesion forces between different cell species (ECs and tumour cells) and providing tumour cells with the capability to migrate, we do not involve migration and allow proliferation only when space and nutrients are available. Although we restricted ourselves in this paper to a parameter regime that leads almost exclusively to circular tumours a significantly enhanced nutrient

demand of the tumour cells can also produce protrusions along the major vessels. Obviously, from a puristic modelling point of view it would be desirable to replace the phenomenological stochastic rules by deterministic processes involving solid stress, cell–cell adhesion and cell motility. But we think that we described the *effect* of these aspects on a sufficiently large scale correctly such that the main message (see above) will not change by a more detailed modelling, which is underway (to be published).

Besides these mechanical aspects there are important biochemical processes that we also modelled phenomenologically: (1) Instead of incorporating the negative feedback-loop involving VEGF receptors, Dll4 and Notch that restricts tip-cell generation during angiogenic sprouting (Bentley et al., 2008) we simply employed a rule, by which tip-cells can only be generated every 2nd or 3rd vessel segment (corresponding roughly 2–3 EC lengths). Such a rule is necessary when the initial vasculature is ubiquitous as in our model since otherwise the presence of VEGF generates tip-cells in an uncontrolled fashion. (2) Instead of modelling angiogenic sprout migration and branching involving matrix metalloproteases and collagen fibres (Bauer et al., 2007; Milde et al., 2008) we used commonly accepted stochastic rules (Anderson and Chaplain, 1998). The ubiquity of original vessels in our model diminishes the importance of the migration and branching process per se, since the intercapillary distances are rather short, which is different from models without initial vasculature. (3) We omitted an explicit mathematical description of the up-regulation of Ang-2 in ECs of coopted vessels within the tumour in Plank et al. (2004), but confined ourselves to describe only its destabilizing effect behind the tumour progression front. (4) Similarly we did not model explicitly the up-regulation of EphB4 in tumour vessels that triggers the switch of the tumour vascularization program from angiogenic sprouting to circumferential growth but incorporated this switch with a heuristic rule.

Our intention in connection with the aspects 1–4 was to demonstrate that they have important consequences for the global morphology of the emerging tumour vasculature, and not to formulate a detailed *ab-initio* model for it. The simplifications were mainly motivated by computational tractability considerations for large scale simulations, in particular when transferring the model into a three-dimensional environment. In any case we would like to stress that if one would endeavour to implement a simulation environment that is expected to predict the growth of a particular tumour type in a specific tissue these aspects must be incorporated. In particular the geometry and characteristics of the initial vasculature has to be taken into account, which is missing in almost all existing tumour growth models. Not only the morphology of the emerging tumour vasculature is completely different in vessel-in-growth models (Anderson and Chaplain, 1998; Zheng et al., 2005; Frieboes et al., 2007; Wise et al., 2008; Milde et al., 2008) when compared with our results, but also their blood flow characteristics and their determinants for blood-borne drug transport are completely different (McDougall et al., 2002, 2006).

Hence the question remains, in which situations (or for what tumour types in which tissue) a vessel-in-growth model might be sufficient or whether the initial vasculature has to be taken into account. One has to consider that living tissue is always vascularized and that intercapillary distances for any tissue range from 50 to 150 μm . It appears therefore highly improbable that a tumour nucleus resides more than 200 μm away from the next capillary, and once it starts to grow parts of it will penetrate vascularized tissue. A pure vessel-in-growth situation is therefore only realized under artificial circumstances like in animal models (Gimbrone et al., 1974), and represents possibly a good approximation in cases where the tumour grows asymmetrically on a

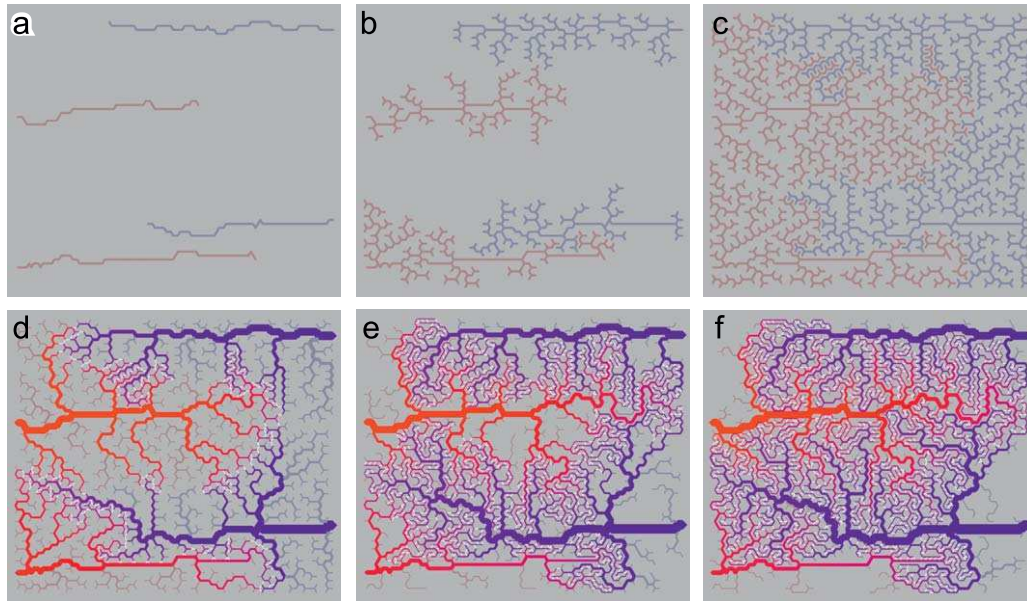


Fig. 15. Sketch of the construction method of vascular trees. The snapshots show a sample system, three times smaller than those needed for the simulation runs, during the growth stages. Arteries are shown in reddish tones, veins in blue. A dim colour indicates that no blood flow takes place. A saturated colour means that the vessel is perfused: (a) shows initial vessel chains randomly placed within specified bounds, (b) shows an intermediate configuration during the first stage where tripod elements are randomly attached to the tree tips, (c) shows the result of this stage, in (d) connecting capillaries (colour coded white) have been added as well as all vessel radii determined and blood flow computed. In between the perfused branches many other branches were unable to connect to their opposing type. Moreover the capillary distribution is concentrated half way between the major vessels, (e) shows an intermediate snapshot of the subsequent optimization stage. Remodelling at the tree tips takes place based on the shear stress distribution. Weakly perfused vessels are removed, leaving space for growing heavily perfused vessels. Eventually this leads to a homogeneous capillary distribution in a well perfused network (f). (For interpretation of the references to colour in this figure legend, the reader is referred to the web version of this article.)

vascularized tissue sheet and extends perpendicularly into non-tissue region, as for instance in the dorsal skinfold chamber. In all other situations, in particular when tumours grow completely within well-vascularized tissues, an appropriate description of the surrounding tissue blood vessel network needs to be taken into account.

As we have mentioned before we have already generalized our model to a three-dimensional situation. Most aspects of the model can be transferred in a straightforward manner (Lee et al., 2006), only the construction of a three-dimensional arterio-venous network poses a non-trivial technical problem (to be published). We will also model O_2 release with associated intravascular O_2 decrease and replace the current discrete representation of tumour cells by a continuum description involving mechanical stress, tumour cell migration and cell–cell adhesion. For the study of drug-delivery within tumours in addition to blood-borne drug transport also extravasation and the interstitial fluid transport has to be incorporated into the model.

Appendix A

In this Appendix the construction of vascular trees is described.

The construction is based upon a small set of prescribed vascular stems from which arterio-venous trees will be grown. The basic structural element for this process is a tripod consisting of three vessel segments arranged in 120° angles. These tripods are appended successively at randomly chosen sites, either at the leafs of the growing trees or on the starting vessels. Thereby overlap with already occupied sites/bonds is forbidden, and so the process continues until there are no more valid configurations where tripods could be added. The resulting network consists of at least two binary trees with at least one arterial and one venous side (Fig. 15b, c).

To compute blood flow vessel radii must be known. “Murray’s Law” (Murray, 1926) relates the radius of a parent vessel a_r to the radii of branches b_r, c_r . $a_r^\alpha = b_r^\alpha + c_r^\alpha$, where $\alpha = 2.7$ is a realistic value as used by Gödde and Kurz (2001). The radii of the tree leaves are set to $4\ \mu\text{m}$ for arteries, and $5\ \mu\text{m}$ for veins. Thus all other radii can be computed in a recursive algorithm which visits a vessel once its descendants have been processed.

To get a complete network, for each lattice bond a “capillary” vessel is added ($3.5\ \mu\text{m}$ radius) if it connects an arterial tree with a venous tree, if less than three vessels will connect to the nodes, and if all connected vessels fulfil $r < 20\ \mu\text{m}$.

Fig. 15d illustrates a sample configuration at this point before the second stage, in which the network is optimized by an iterative remodelling process. This consists of radius computation, capillary creation, flow rate and shear force computation, capillary removal, and the actual remodelling sweep, until the system reaches a steady state. Our remodelling sweep works as follows: an event type $E \in \text{growth, death}$ is drawn randomly for each segment according to the respective weights w_g, w_d . Relating these to shear stress f such that w_g is monotonically increasing and w_d is monotonically decreasing leads to expansion in well-perfused branches while non-perfused branches regress and make room for further growth. The details of the f dependence are not crucial. A linear mapping $\tilde{f} := (f - f_{\min}) / (f_{\max} - f_{\min})$ of the interval between the extremal values f_{\min} and f_{\max} over the vasculature usually suffices. Moreover we add a constant “offset” w_0 to both weights. This reduces the rate at which uncirculated vessels regress. And secondly it adds fluctuation to prevent deadlocks in high shear stress regions. Thus the final weights are $w_g = \tilde{f} + w_0$, $w_d = 1 - \tilde{f} + w_0$. Tree vessels are then traversed in random order.

An event E may take place but it can be rejected. This would be the case for the death of a segment in the middle of the tree since removal is restricted to the tree leaves. Growth happens at the downstream end of a vessel, not limited to leaves. It is rejected if there are already two daughter branches, or if the vessel radius

$r > 50 \mu\text{m}$, or trivially if there are no unoccupied lattice sites. Else one of the admissible configurations is randomly picked. Beside tripods we also allow single vessel to be added. This facilitates growth into regions where bottlenecks evolved due to close proximity of two or more major vessels. Fig. 15e shows an intermediate step during stage. And Fig. 15f shows the final configuration.

References

- Alarcon, T., Byrne, H., Maini, P., 2003. A cellular automaton model for tumour growth in inhomogeneous environment. *J. Theor. Biol.* 225, 257–274.
- Ambrosi, D., Preziosi, L., 2002. On the closure of mass balance models for tumor growth. *Math. Models Meth. Appl. Sci.* 12, 737–754.
- Anderson, A.R.A., Chaplain, M.A.J., 1998. Continuous and discrete mathematical models of tumor-induced angiogenesis. *Bull. Math. Biol.* 60, 857–900.
- Baish, J.W., Jain, R.K., 2000. Fractals and cancer. *Pers. Cancer Res.* 60, 3683–3688.
- Balding, D., McElwain, D.L.S., 1985. Mathematical modelling of tumor-induced capillary growth. *J. Theor. Biol.* 114, 53–73.
- Bartha, K., Rieger, H., 2006. Vascular network remodeling via vessel cooption, regression and growth in tumors. *J. Theor. Biol.* 241, 903–918.
- Bauer, A.L., Jackson, T.L., Jiang, Y., 2007. A cell-based model exhibiting branching and anastomosis during tumor-induced angiogenesis. *Biophys. J.* 92, 3098–3104.
- Bentley, K., Gerhardt, H., Bates, P.A., 2008. Agent-based simulation of notch-mediated tip cell selection in angiogenic sprout initialisation. *J. Theor. Biol.* 250, 25–36.
- Betteridge, R., Owen, M.R., Byrne, H.M., Alarcon, T., Maini, P.K., 2006. The impact of cell crowding and active cell movement on vascular tumour growth. *Netw. Hetero. Media* 1, 515–535.
- Breward, C.J., Byrne, H.M., Lewis, C.E., 2003. A multiphase model describing vascular tumour growth. *Bull. Math. Biol.* 65, 609–640.
- Brú, A., Albertos, S., Subiza, J.L., Lopez, J., García-Asenjo, Brú, I., 2003. The universal dynamics of tumor growth. *Biophys. J.* 85, 2948–2961.
- Byrne, H.M., Chaplain, M.A.J., 1995. Mathematical models for tumour angiogenesis: numerical simulations and nonlinear wave solutions. *Bull. Math. Biol.* 57, 461–486.
- Byrne, H.M., Preziosi, L., 2003. Modeling solid tumor growth using the theory of mixtures. *Math. Meth. Biol.* 20, 341–366.
- Carmeliet, P., Jain, R.K., 2000. Angiogenesis in cancer and other diseases. *Nature* 407, 249–257.
- Cassot, F., Lauwers, F., Fouard, C., Prohaska, S., Lauwers-Cances, V., 2006. A novel three-dimensional computer-assisted method for a quantitative study of microvascular networks of the human cerebral cortex. *Microcirculation* 13, 1–18.
- Chaplain, M.A.J., Stuart, A.M., 1993. A model mechanism for the chemotactic response of endothelial cells to tumour angiogenesis factor. *IMA J. Math. Appl. Med. Biol.* 10, 149–168.
- Chaplain, M.A.J., Giles, S.M., Sleeman, B.D., Jarvis, R.J., 1995. A mathematical model for tumour angiogenesis. *J. Math. Biol.* 33, 744–770.
- Chaplain, M.A., 2000. Mathematical modeling of angiogenesis. *J. Neurooncol.* 50, 37–51.
- Döme, B., Paku, S., Somlai, B., Tímár, J., 2002. Vascularization of cutaneous melanoma involves vessel co-option and has clinical significance. *J. Path.* 197, 355–362.
- Drasdo, D., Höhme, S., 2005. A single-cell-based model of tumor growth in vitro: monolayers and spheroids. *Phys. Biol.* 2, 133–147.
- Erber, R., Eichelsbacher, U., Powajbo, V., Korn, T., Djonov, V., Lin, J., Hammes, H.-P., Grobholz, R., Ullrich, A., Vajkoczy, P., 2006. EphB4 controls blood vascular morphogenesis during postnatal angiogenesis. *EMBO* 25, 628–641.
- Frieboes, H.B., Lowengrup, J.S., Wise, S., Zheng, X., Macklin, P., Bearer, E., Cristini, V., 2007. Computer simulation of glioma growth and morphology. *NeuroImage* 37, 59–70.
- Gerhardt, H., Golding, M., Fruttiger, M., Ruhrberg, C., Lundkvist, A., Abramsson, A., Jeltsch, M., Mitchell, C., Alitalo, K., Shima, D., Betsholtz, C., 2003. VEGF guides angiogenic sprouting utilizing endothelial tip cell filopodia. *J. Cell Biol.* 161, 1163–1177.
- Gimbrone, M.A., Cotran, R.S., Leapman, S.B., Folkman, J., 1974. Tumor growth and neovascularization: an experiment model using the rabbit cornea. *J. Nat. Cancer Inst.* 52, 413–427.
- Gödde, R., Kurz, H., 2001. Structural and biophysical simulation of angiogenesis and vascular remodeling. *Dev. Dyn.* 220, 387–401.
- Griffon-Etienne, G., Boucher, Y., Brekken, C., Suit, H.D., Jain, R.K., 1999. Taxane-induced apoptosis decompressed blood vessels and lowers interstitial fluid pressure in solid tumors: clinical implications. *Cancer Res.* 59, 3776–3782.
- Holash, J., Maisonpierre, P.C., Compton, D., Boland, P., Alexander, C.R., Zagzag, D., Yancopoulos, G.D., Wiegand, S.J., 1999a. Vessel cooption, regression, and growth in tumors mediated by angiopoietins and VEGF. *Science* 284, 1994–1998.
- Holash, J., Wiegand, S., Yancopoulos, G., 1999b. New model of tumor angiogenesis: dynamic balance between vessel regression and growth mediated by angiopoietins and VEGF. *Oncogene* 18, 5356–5362.
- Holmes, M.J., Sleeman, B.D., 2000. A mathematical model of tumour angiogenesis incorporating cellular traction and viscoelastic effects. *J. Theor. Biol.* 202, 95–112.
- Holmgren, L., O'Reilly, M.S., Folkman, J., 1995. Dormancy of micrometastases: balanced proliferation and apoptosis in the presence of angiogenesis suppression. *Nat. Med.* 1, 149–153.
- Jensen, H.J., 1998. Self-Organized Criticality: Emergent Complex Behavior in Physical and Biological Systems. Cambridge University Press, Cambridge.
- Kim, E.S., Serur, A., Huang, J., Manley, C.A., McCrudden, K.W., Frischer, J.S., et al., 2002. Potent VEGF blockade causes regression of coopted vessels in a model of neuroblastoma. *Proc. Natl. Acad. Sci.* 99, 11399–11404.
- Lee, D.S., Bartha, K., Rieger, H., 2006. Flow correlated percolation during vascular remodeling in growing tumors. *Phys. Rev. Lett.* 96, 058104-1–058104-4.
- Liu, Z.J., Shirakawa, T., Li, Y., Soma, A., Oka, M., Dotto, G.P., Fairman, R.M., Velazquez, O.C., Herlyn, M., 2003. Regulation of Notch1 and Dll4 by vascular endothelial growth factor in arterial endothelial cells: implications for modulating arteriogenesis and angiogenesis. *Mol. Cell Biol.* 23, 14–25.
- Maisonpierre, P.C., Suri, C., Jones, P.F., Bartunkova, S., Wiegand, S.J., Radziejewski, C., Compton, D., McClain, J., Aldrich, T.H., Papadopoulos, N., Daly, T.J., Davis, S., Sato, T.N., Yancopoulos, G.D., 1997. Angiopoietin-2, a natural antagonist for Tie2 that disrupts in vivo angiogenesis. *Science* 277, 55–60.
- Macklin, P., McDougall, S., Anderson, A.R.A., Chaplain, M.J., Cristini, J., 2008. Multiscale modelling and nonlinear simulation of vascular tumour growth. *J. Math. Biol.* 58, 765–798.
- McDougall, S.R., Anderson, A.R.A., Chaplain, M.A.J., 2006. Mathematical modelling of dynamic adaptive tumour-induced angiogenesis: clinical implications and therapeutic targeting strategies. *J. Theor. Biol.* 241, 564–589.
- McDougall, S.R., Anderson, A.R.A., Chaplain, M.A.J., Sherratt, J.A., 2002. Mathematical modelling of flow through vascular networks: implications for tumour-induced angiogenesis and chemotherapy strategies. *Bull. Math. Biol.* 64, 673–702.
- Milde, F., Bergdorf, M., Koumoutsakos, P., 2008. A hybrid model for three-dimensional simulations of sprouting angiogenesis. *Biophys. J.* 95, 3146–3160.
- Mironov, V., Little, C., Sage, H. (Eds.), 1998. Vascular Morphogenesis: In Vivo, In Vitro, In Monte. Birkhäuser, Boston.
- Murray, C.D., 1926. The physiological principle of minimum work: the vascular system and the cost of blood volume. *Proc. Natl. Acad. Sci. USA* 12, 207–214.
- Nehls, V., Herrmann, R., Hühnen, M., 1998. Guided migration as a novel mechanism of capillary network remodeling is regulated by basic fibroblast growth factor. *Histochem. Cell Biol.* 109, 319–329.
- Owen, M.R., Alarcon, T., Maini, P.K., Byrne, H.M., 2008. Angiogenesis and vascular remodelling normal and cancerous tissues. *J. Math. Biol.* 58, 689–721.
- Pahernik, S., Griebel, J., Botzlar, A., Gneiting, M., Dellian, M., Goetz, A.E., 2001. Quantitative imaging of tumour blood flow by contrast-enhanced magnetic resonance imaging. *Brit. J. Canc.* 85, 1655–1663.
- Pezzella, F., Pastorino, U., Tagliabue, E., Andreola, S., Sozzi, G., Gasparini, G., et al., 1997. Non-small-cell lung carcinoma tumor growth without morphological evidence of neo-angiogenesis. *Am. J. Path.* 151, 1417–1423.
- Plank, M.J., Sleeman, B.D., Jones, P.F., 2004. Lattice and non-lattice models of tumour angiogenesis. *Bull. Math. Biol.* 66, 1785–1819.
- Pries, A.R., Reglin, B., Secomb, T.W., 2005. Remodeling of blood vessels: responses of diameter and wall thickness to hemodynamic and metabolic stimuli. *Hypertension* 46, 725–731.
- Pries, A.R., Secomb, T.W., Gessner, T., Sperandio, M.B., Gross, J.F., Gaehtgens, P., 1994. Resistance to blood flow in microvessels in vivo. *Circ. Res.* 75, 904–915.
- Pries, A.R., Secomb, T.W., Gaehtgens, P., 1995. Design principles of vascular beds. *Circ. Res.* 77, 1017–1022.
- Sahani, D.V., Kalva, S.P., Hamberg, L.M., Hahn, P.F., Willett, C.G., Saini, S., Mueller, P.R., Lee, T.Y., 2005. Assessing tumor perfusion and treatment response in rectal cancer with multisection CT: initial observations. *Radiology* 234, 785–792.
- Sainson, R., Aoto, J., Nakatsu, M.N., Holderfield, M., Conn, E., Koller, E., Hughes, C.C.W., 2005. Cell-autonomous Notch signalling regulates endothelial cell branching and proliferation during vascular tubulogenesis. *FASEB J.* 19, 1027–1029.
- Sakariassen, P.Ø., Prestegarden, L., Wang, J., Skaftnesmo, K.O., Mahesparan, R., Molthoff, C., Sminia, P., Sundlisaeter, E., Misra, A., Tysnes, B.B., Chekenya, M., Peters, H., Lende, G., Kalland, K.H., Øyan, A.M., Petersen, K., Jonassen, I., van der Kogel, A., Feuerstein, B.G., Terzis, A.J., Bjerkvig, R., Enger, P.Ø., 2006. Angiogenesis-independent tumor growth mediated by stem-like cancer cells. *Proc. Natl. Acad. Sci.* 103, 16466–16471.
- Scharpfenecker, M., Fiedler, U., Reiss, Y., Augustin, H.G., 2005. The Tie-2 ligand angiopoietin-2 destabilizes quiescent endothelium through an internal autocrine loop mechanism. *J. Cell. Sci.* 118, 771–780.
- Stephanou, A., McDougall, S.R., Anderson, A.R.A., Chaplain, M.A.J., 2005. Mathematical modeling of flow in 2D and 3D vascular networks: applications to anti-angiogenic and chemotherapeutic drug strategies. *Math. Comput. Model.* 41, 1137–1156.
- Stephanou, A., McDougall, S.R., Anderson, M.A.J., 2006. Mathematical modeling of the influence of blood rheological properties upon adaptive tumor-induced angiogenesis. *Math. Comput. Model.* 44, 96–123.
- Stokes, C.L., Lauffenburger, D.A., 1991. Analysis of the roles of microvessel endothelial cell random motility and chemotaxis in angiogenesis. *J. Theor. Biol.* 152, 377–403.
- Thompson, W.D., Shiach, K.J., Fraser, R.A., McIntosh, L.C., Simpson, J.G., 1987. Tumours acquire their vasculature by vessel incorporation, not vessel ingrowth. *J. Path.* 151, 323–332.

- Torres Filho, I.P., Leunig, M., Yuan, F., Intaglietta, M., Jain, R.K., 1994. Noninvasive measurement of microvascular and interstitial oxygen profiles in a human tumor in SCID mice. *Proc. Natl. Acad. Sci. USA* 91, 2081–2085.
- Turner, S., Sherratt, J.A., 2002. Intercellular adhesion and cancer invasion: a discrete simulation using the extended Potts model. *J. Theor. Biol.* 216, 85–100.
- Vajkoczy, P., Menger, M.D., 2000. Vascular microenvironment in gliomas. *J. Neurooncol.* 50, 99–108.
- Welter, M., Bartha, K., Rieger, H., 2008. Emergent vascular network inhomogeneities and resulting blood flow patterns in a growing tumor. *J. Theor. Biol.* 250, 257–280.
- Wesseling, P., van der Laak, J.A., de Leeuw, H., Ruiters, D.J., Burger, P.C., 1994. Quantitative immunohistological analysis of the microvasculature in untreated human glioblastoma multiforme. Computer-assisted image analysis of whole-tumor sections. *J. Neurosurg.* 81, 902–909.
- Williams, C.K., Li, J.-L., Murga, M., Harris, A.L., Tosato, G., 2006. Up-regulation of the Notch ligand delta-like 4 inhibits VEGF induced endothelial cell function. *Blood* 107, 931–939.
- Wise, S.M., Lowengrup, J.S., Frieboes, H.B., Cristini, V., 2008. Three-dimensional multispecies nonlinear tumor growth—I model and numerical method. *J. Theor. Biol.* 253, 524–543.
- Zhang, L., Yang, N., Park, J.W., Katsaros, D., Fracchioli, S., Cao, G., et al., 2003. Tumor-derived vascular endothelial growth factor up-regulates angiopoietin-2 in host endothelium and destabilizes host vasculature, supporting angiogenesis in ovarian cancer. *Cancer Res.* 63, 3403–3412.
- Zheng, X., Wise, S.M., Cristini, V., 2005. Nonlinear simulation of tumor necrosis, neo-vascularization and tissue invasion via an adaptive finite-element/level-set method. *Bull. Math. Biol.* 67, 211–259.

Physical determinants of vascular network remodeling during tumor growth

M. Welter and H. Rieger^a

Theoretical Physics, Saarland University, 66041 Saarbrücken, Germany

Received 11 February 2010

Published online: 6 July 2010 – © EDP Sciences / Società Italiana di Fisica / Springer-Verlag 2010

Abstract. The process in which a growing tumor transforms a hierarchically organized arterio-venous blood vessel network into a tumor specific vasculature is analyzed with a theoretical model. The physical determinants of this remodeling involve the morphological and hydrodynamic properties of the initial network, generation of new vessels (sprouting angiogenesis), vessel dilation (circumferential growth), vessel regression, tumor cell proliferation and death, and the interdependence of these processes via spatio-temporal changes of blood flow parameters, oxygen/nutrient supply and growth factor concentration fields. The emerging tumor vasculature is non-hierarchical, compartmentalized into well-characterized zones, displays a complex geometry with necrotic zones and “hot spots” of increased vascular density and blood flow of varying size, and transports drug injections efficiently. Implications for current theoretical views on tumor-induced angiogenesis are discussed.

1 Introduction

Tissues in living organisms need a persistent supply with oxygen and other nutrients provided by the vascular blood flow through the vessel network threading the tissue. Fast proliferating cells in a growing tumor have an increased oxygen/nutrient demand, for which reason tumors usually cannot grow beyond a size of $1\text{--}2\text{ mm}^3$ without modifying the original vasculature. This modification, comprising a substantial increase of microvascular density in the growth zone of the tumor, is denoted as angiogenesis, the creation of new blood vessels from existing ones [1].

The emerging tumor vasculature is in many respects different from the hierarchically organized arterio-venous blood vessel network in normal tissues. The expected increase in microvascular density (MVD) is usually observed in the periphery of the tumor, whereas the morphology of the vasculature in the tumor center is characterized by decreased MVD, dilated vessels, and regions of necrotic tumor tissue [2–5]. The resulting tumor-specific capillary network is very heterogeneous, composed of dense and void regions, and has geometric properties different from normal arterio-venous or normal capillary networks.

Besides pro- and anti-angiogenic molecular factors, mechanical, hydrodynamical and collective processes must be involved in the process that transforms or remodels the original arterio-venous blood vessel network into a tumor-specific vasculature. In this paper we want, with the help of a theoretical model, to address the physical determinants of the dynamical evolution, final morphology and

blood flow properties of a tumor blood vessel network. We hypothesize that co-option of existing vessels and vessel regression, besides angiogenic sprouting and vessel dilation, are essential processes that determine the geometric and hydrodynamic properties of the tumor vasculature.

The study of theoretical models of tumor growth has a long and multifaceted history (for recent reviews, see [6, 7] and references therein). Earlier work focusing on tumor-induced angiogenesis can roughly be divided into three categories: 1) continuum models without a proper representation of a blood vessel network and blood flow [8–12]; 2) hybrid models with a fixed vessel network geometry and a dynamically evolving tumor [13–15]; and 3) hybrid models with a fixed tumor (as a source of a diffusing growth factor) and a dynamically evolving tumor vasculature starting from a single parent vessel far away from the growth factor source [16–19].

The latter models are also denoted as vessel-ingrowth models since the whole tumor vasculature grows from outside towards the tumor surface. Subsequent work was still inspired by these vessel-in-growth models [20–24]: although in these studies the tumor also evolved dynamically, focusing on a detailed analysis of the interactions between tumor and host tissue, all new vessels started to grow from one or more parent vessels in a non-physiologically far distance from the tumor. The remodeling process that transforms the original arterio-venous vasculature of the host tissue into a tumor-specific vessel network has not been addressed with this Ansatz, which is the topic of the work that we present in this paper.

^a e-mail: h.rieger@mx.uni-saarland.de

In recent work [25–27], see also [28], the issue of vascular remodeling in a growing tumor by the three basic mechanisms —angiogenic sprouting, vessel regression and dilation— was addressed in a model that comprised a regular capillary grid as initial vascular network. The compartmentalization of the tumor as well as other global features, like the time and radius dependences of average MVD, tumor cell density, vessel radius and blood flow characteristics, were predicted in good agreement with experimental data, but local characteristics, like a single hot spot in the center and a general bias in the flow direction, could be attributed to the special topology of the initial network. In this paper we consider a more realistic three-dimensional arterio-venous vascular network as initial vasculature and study the effect it has on the emerging tumor vasculature. It is based on a simplified two-dimensional model that was studied in [29].

In well-vascularized tissue the average inter-capillary distance is 50–100 μm , in highly vascularized tissue like brain even less (depending on the oxygen demand and the resulting diffusion length), implying the importance of the incorporation of the original vasculature into a model for tumor-induced angiogenesis. This vasculature is organized in a hierarchical way, in which an arterial and a venous tree are interdigitated by capillaries. Oxygen and other nutrients are distributed into the surrounding tissue by the lowest-level capillaries, the two trees representing their supply and drainage system. The MVD, given by the average inter-capillary distance, is homogeneous in one kind of tissue to provide a homogeneous oxygen and nutrient supply, but the two interdigitating hierarchical trees form a spatially very inhomogeneous blood vessel network. Consequently the vascular remodeling process in a growing tumor will also be spatially inhomogeneous: sprouting angiogenesis occurs mainly from capillaries and venules, higher-level arteries protected by a thick layer of pericytes are more stable and regress later or not at all, regression of higher level arteries has fatal consequences for the whole arterial sub-tree below it, newly formed vessels between arteries and veins could act as shunts redirecting huge amount of blood, etc.

With this background we want to analyze the transformation of the well-organized hierarchical structure of an arterio-venous vessel network when it is co-opted and remodeled by an aggressively growing tumor. We are interested in the geometrical characteristics of the emerging tumor vasculature and the potential mechanisms leading to spatial inhomogeneities or hot spots. And we will study the global blood flow patterns and the drug transport performance of the tumor vasculature. The paper is organized as follows: In the next section the model is defined, including the method to construct an arterio-venous initial network. Section 3 presents the results for global properties for a choice of parameters that is guided by experimental data for melanoma [4,5]. These results include a discussion of the emerging morphologies; radial distributions of vessel density, vessel radius, tumor density, flow rates, shear forces, etc., vessel statistics, parameter dependencies, spatial inhomogeneities, and drug flow. Section 4

concludes the paper with a summary of the main results and a discussion.

2 Model definition

An arterio-venous network serves as the initial vasculature for our model of remodeling by a growing tumor. Depending on the local oxygen concentration, tumor cells represent the sources of the diffusion determined growth factor (GF) concentration field, which triggers either the generation of tip cells for angiogenic sprouting from existing vessels outside or at the periphery of the tumor, or circumferential growth within the tumor (for potential molecular mechanisms for this switch in the angiogenic program within the tumor, see [30]). In contrast to vessel in-growth models as in [16], tip cells are not dominantly generated by branching of existing tip cells but by sprouting from vessels of the original network. Lateral inhibition leads to a minimum spatial distance in a vessel segment between individual tip cell generation events [31].

Tip cells migrate in the direction of a sufficiently large GF gradient (chemotaxis), otherwise randomly. The path they describe is supposed to be filled with stalk cells forming a lumen and finally, once the tip cell hits another vessel (anastomosis), a functional vessel carrying blood flow is formed. Due to the pre-existing vasculature, vessels typically migrate only 50–100 μm before the filopodia of the tip cell extending up to 20–30 μm into the surrounding tissue in all directions [32] touch another vessel. Therefore directional cues are not as important here as in pure vessel in-growth models. And tip cells migrate maximally 100–150 μm and in case they did not make successful contact with another vessel, they retreat [33].

Inside the tumor, vessels destabilize and regress (for the potential molecular determinants of this destabilization, see [2,3]). In our model an increasing contact time of vessels with tumor cells, implying an increasing residence time within the tumor, leads to a higher collapse probability of tumor vessels. The collapse probability is also correlated with the origin of the vessel (artery, vein or capillary) and the shear force exerted by the blood flow upon the vessel walls [34].

2.1 Configuration space

The model consists of a discrete representation of the vasculature and continuum models for a non-specific growth factor concentration g , oxygen concentration o and tumor-cell density c .

The vasculature can be described as a graph where edges represent vessel segments and nodes represent branching points, respectively. This graph is embedded in a regular cubic lattice with the lattice constant Δl , which means that the nodes are located at the lattice sites and edges are coincident with the lattice edges. Vessels and nodes are dynamically created and destroyed over time. In Addition they have attached biophysical properties which can also vary over time.

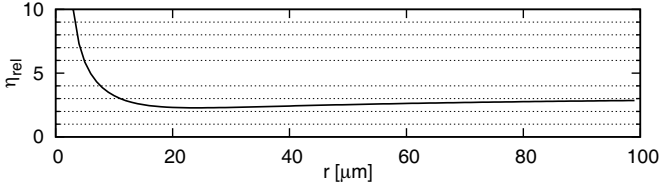


Fig. 1. Relative viscosity η_{rel} as a function of the vessel radius r . The actual viscosity is the viscosity of blood plasma $\eta = 4 \cdot 10^{-6}$ kPa s $\times \eta_{\text{rel}}$. The shape of η_{rel} was obtained from a best fit of experimental *in vitro* data [37]. η_{rel} is also a function of the hematocrit H . For simplicity, we assumed that $H = 0.45$, the average in humans.

2.2 Blood flow

To compute blood flow, vessels are treated as a network of pipes with radius r , volume flow rate q and wall shear force f . q is determined by Poiseuille's law *i.e.* $q \propto r^4 / \eta(p_1 - p_2)$ given the hydrostatic pressure difference $p_1 - p_2$ at the attached nodes. The viscosity η is radius dependent, following [37], see fig. 1. For simplicity under the assumption of a homogeneous hematocrit of 0.45. As boundary condition the pressure is fixed at the arterial and venous roots of the vascular trees. Together with the mass conservation, *i.e.* inflow equal outflow rates at the nodes, we obtain a sparse linear equation system which is solved numerically.

2.3 Tumor cell density

Here we introduce a continuum model for the tumor cell density $c(\mathbf{r}, t)$. Under stress-free conditions without cell proliferation and death, the tumor cell density is $c^{(\text{norm})}$, which we assume to be $1/10 \mu\text{m}^3$, reflecting a typical lateral size of tumor cells of $10 \mu\text{m}$. The dynamical evolution of the tumor cell density in the presence of cell proliferation and death is assumed to be given by a reaction-diffusion equation

$$\partial c / \partial t = -\nabla \cdot J + c^+ + c^-, \quad (1)$$

where J is the tumor cell flux and c^+ and c^- are source and sink terms describing cell proliferation and death, respectively.

In the following c^+ , c^- and J are defined: We assume that tumor cells need sufficient oxygen to proliferate, which means that the local oxygen concentration o must exceed the threshold $o_{TC}^{(\text{prol})}$, else $c^+ = 0$. Moreover we assume that a maximum packing density $c^{(\text{max})}$ exists where cells are compressed so that they cannot proliferate further. We use the simplest expression to reflect that

$$c^+ = 1/t_{TC}^{(\text{prol})} c \left(1 - \frac{c}{c^{(\text{max})}}\right) \quad \text{if } o \geq o_{TC}^{(\text{prol})} \quad \text{else } 0, \quad (2)$$

where $t_{TC}^{(\text{prol})}$ is the mean proliferation time of unconstrained cells. Furthermore we assume that cells undergo apoptosis with the constant death rate $1/t_{TC}^{(\text{death})}$ if the local oxygen level o drops below $o_{TC}^{(\text{death})}$. The model includes

this by the definition of c^- ,

$$c^- = -1/t_{TC}^{(\text{death})} c \quad \text{if } o < o_{TC}^{(\text{death})} \quad \text{else } 0. \quad (3)$$

For simplicity, interaction with the resulting cellular debris is neglected. In the following the cell flux J is defined. We assume that cells migrate only in response to compression. Therefore a phenomenological ‘‘solid pressure’’ P is introduced. Its equation of state depends on the cell density c as follows: Below the density $c^{(\text{norm})}$ cells are not compressed, thus feel no forces, thus we set $P = 0$ for $c \leq c^{(\text{norm})}$. Else we define P as linear function which is zero for $c = c^{(\text{norm})}$ and increases to $P = 1$ for $c = c^{(\text{max})}$. In the style of Darcy's law, momentum terms in the equations of motion are neglected so that the cell migration speed is proportional to the driving force, which means that

$$J = -Dc\nabla P, \quad (4)$$

where D is an additional mobility constant. The cell density cannot exceed $c^{(\text{max})}$ since there are no external forces and $c^+ \rightarrow 0$ for $c \rightarrow c^{(\text{max})}$ even though P remains finite.

In the general framework of such a model it would be possible to add cell-cell adhesion. In this case one would consider volume fractions of other species, *e.g.*, normal tissue and necrotic tissue which interact via a free energy potential. See [21] and the references therein. The result is an effective surface tension force. Combined with expansive forces which drive the tumor rim outward, it can cause a fingering instability. In our simpler model where we have omitted such forces, tumor cells move diffusively opposed to their density gradient. Since tissue oxygenization is homogeneous on a coarse scale, this results in approximately spherically growing tumors. Biologically our model corresponds to a situation where tumor cells adhere to each other as much as to other cells. Also the tumor can expand without significant resistance from the surrounding tissue. We can justify this considering that i) not all tumors exhibit fingering instabilities, ii) we consider small tumor of less than 1 cm diameter and iii) pH level changes can happen that kill normal cells.

Below we compare our results with experimental data from melanoma. To accommodate the model to this specific tumor type, which can extend through multiple skin layers from the surface to muscle tissue, it would be straight forward to include inhomogeneous and/or anisotropic environments. We would expect this to trigger a different front shape of the growing tumor. However we think—as is the case with a ‘‘fingering’’ tumor—that the characteristics of the blood vessel network which we are interested would be invariant with respect to such additions.

In order to identify necrotic regions, we record the maximum local TC density over time. If the current TC density is zero and there were TCs in the past, we consider the location to be necrotic. On the basis of the rest of our framework, there are no forces that would impose interesting dynamics on the shape of necrotic regions. Thus we use this crude approximation.

The equations are discretized with a simple explicit finite-volume scheme on a cubic grid with $30 \mu\text{m}$ grid cell

size. We compute the fluxes through the cell faces separately. Knowing the fluxes, $\nabla \cdot J$ in (1) is discretized using a convective upwind scheme. To ensure stability, the time step for the integration is 0.1 h, whereas the updates of the rest of the system (see below) are done in 1 h steps.

2.4 Oxygen concentration field

The time scale for oxygen diffusion to reach a stationary state is of the order of seconds whereas the timescale for tumor cell proliferation, tip cell migration and endothelial cell proliferation is of the order of hours. Therefore we use for the oxygen concentration the quasi-static solution o of the diffusion equation, which adopts instantaneously any change in the source (vessels) and sink (tumor cells) configuration,

$$0 = \nabla^2 o - \gamma_o o + \alpha_o (o^{(B)} - o), \quad (5)$$

where γ_o is a consumption rate coefficient, $o^{(B)}$ the blood O_2 level and α_o a source coefficient. γ_o is a linear combination of the tissue specific constants $\gamma_o^{(\text{norm})}$, $\gamma_o^{(\text{tum})}$ and $\gamma_o^{(\text{necro})} = 0$, for normal tissue, tumor tissue and necrotic regions, respectively. The definition of the density parameters implies that the necrotic areas inside the tumor do not consume oxygen. The factor α_o determines the amount of extravasated oxygen per concentration difference at the vessel wall. It is defined as permeability times wall surface area per concentration and tissue volume. For simplicity it assumes a constant value for all blood circulated vessels. $o^{(B)}$ is the oxygen concentration in blood plasma, for which local variations are also neglected.

The coefficients γ_o and α_o comprise the diffusion constant and therefore it does not appear in (5). We estimate γ_o based on the diffusion range R_o of oxygen around isolated vessels found in tumors. Therefore we use that a delta peak as source distribution generates an exponentially decaying radial profile $\exp(-x/\sqrt{\gamma_o})$. Thus R_g is of the order of $1/\sqrt{\gamma_o}$. The parameter $o^{(B)}$ is determined such that, given γ_o , the concentration between vessels is ca. 50% of the concentration at the vessel wall.

2.5 Growth factor concentration field

The growth factor concentration g is computed by a Greens' function-like method. Underoxygenized tumor cells, which means that locally $o < o_{TC}^{(\text{prol})}$, produce growth factor at a constant rate. It diffuses through the tissues and degrades with a constant rate. Therefore each source cell produces an exponentially decaying distribution. Thus we can write g as

$$g(\mathbf{x}) = \int d^3 \mathbf{x}' G(\|\mathbf{x}' - \mathbf{x}\|) \theta(o_{TC}^{(\text{prol})} - o(\mathbf{x}')) c(\mathbf{x}'), \quad (6)$$

where θ is the Heaviside step function. For simplicity we define $G(x) \propto \max(0, 1 - x/R_g)$ as a linearly decaying normalized function which vanishes at $x = R_g$, where R_g is a ‘‘diffusion range’’ and limits the region where angiogenesis is induced.

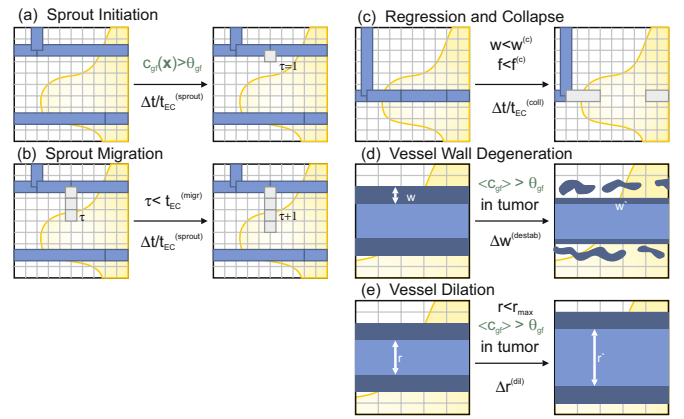


Fig. 2. (Colour on-line) Sketch of the vessel network remodeling processes. Initial/final states are shown to the left/right of the arrow with the rate parameter below and essential preconditions above the arrow. Vessel segments are shown as blue bars, the tumor is depicted as yellow mass and the underlying lattice is illustrated in the background. (a) A new sprout is generated by potentially splitting an existing segment, adding a node and adding the new sprout segment. (b) A sprout is extended by adding further segments to its tip. (c) Vessel regression is modeled by removal of respective segments. This can disrupt blood flow, leaving non-circulated vessels which are depicted in gray. (d) Vessel walls degenerate within the tumor due to detachment of support cells. This is modeled by a decreasing maturation parameter and depicted here as decreasing wall strength and surrounding debris. (e) Within the tumor vessels dilate. See text for details.

2.6 Vessel network remodeling dynamics

The evolution of the network is subject to three stochastic processes: sprout initiation, sprout migration and collapse as well as continuous wall degeneration and vessel dilation (fig. 2). The definition of these processes closely follows the definition in [29], where 2d networks are considered. Therefore we only give a brief description here and refer in particular for the biological motivation of the details to [29].

Sprout initiation: A new vessel segment can be added with probability $\Delta t/t_{EC}^{(\text{sprout})}$ at any location on the network if the local growth factor concentration is non-zero, the distance to the next branching point is less than $l^{(\text{spr})}$ and the time spent within the tumor is less than $t_{EC}^{(\text{switch})}$. ‘‘Within the tumor’’ is defined as $\langle c \rangle > c^{(\text{norm})}/2$ averaged over the segment. The new segment occupies an edge on the lattice (length Δl) and points in the direction of the largest growth factor increase.

Sprout migration: Those segments are tagged as sprouts, which means that further segments can be attached with probability $\Delta t/t_{EC}^{(\text{sprout})}$, extending the original sprout. Sprouts can also spawn sub-sprouts like normal vessels can. They are, however, excluded from the collapse, degeneration and circumferential

growth mechanisms. Sprout vessels are untagged and become normal vessels if the tip fuses with another vessel such that blood can flow, or if their respective lifetime variable τ , which every sprout has attached, has reached its predefined maximum $t_{EC}^{(\text{migr})}$. If the tip fuses with another sprout without creating a conducting branch, it remains tagged as sprout.

Wall degeneration: The structural support provided by the cell layers surrounding the endothelial cells is represented by the wall stability variable w . For new vessels and the original vasculature it is initialized with the wall thickness of healthy vessels, see [29]. For vessels inside the tumor its value decreases at the constant rate Δw until zero.

Vessel collapse: A segment can be removed with probability $\Delta t/t_{EC}^{(\text{coll})}$ if its wall stability variable w is zero and the wall shear stress f is below the threshold $f^{(\text{coll})}$.

Vessel dilation: The vessel radius r increases at the constant rate k_r if $r < r^{(\text{max})}$, the average growth factor concentration over the segment is non-zero and if the time spent within the tumor is larger than $t_{EC}^{(\text{switch})}$.

Per time step ($\Delta t = 1$ h), a Monte Carlo sweep is done per stochastic process and all continuous variables and fields are advanced in time. The parameter values that we use throughout the paper are given in table 1 (references to physiological data are given in [25, 27, 29]).

The model is stable with respect to parameters, since our observables vary smoothly with parameter deviations. For brevity we omit an analysis here. In our previous papers [25, 27] we have discussed variations for 2d models which are also relevant for the present study.

2.7 Arterio-venous tree construction

The vasculature in real tissue exhibits a tree-like structure. Few thick arteries branch out into arteriolar microvessels. Terminal branches are connected to the capillary bed, a dense network consisting of thin vessels where most of the exchange with the surrounding tissue happens. Further upstream blood is collected in venules which fuse into thick veins. The design goal of such a structure is to provide a sufficient supply of nutrients to all regions of the tissue, while minimizing the energy necessary to maintain the circulation.

In [35] a method was presented to construct representations of vascular trees stochastically according to probabilistic rules that depend on local system properties. The construction of the blood vessel network is based on the stochastic remodeling of a collection of binary trees. Each tree represents either an arterial or a venous branch. Analogous to the definition of the tumor growth model, the tree edges coincide with the edges of a cubic lattice, and have associated hydrodynamic properties. The remodeling is executed in successive sweeps where tree leaves are

Table 1. List of parameter values used for all simulations.

Parameter	Value	Description
N	800	Lattice size
Δl	10 μm	Lattice constant
Δl_V	60 μm	Lattice constant (tree construction)
D	300 $\mu\text{m}^2/\text{s}$	TC mobility
$c^{(\text{norm})}$	1/(10 $\mu\text{m})^3$	Normal cell density
$c^{(\text{max})}$	2/(10 $\mu\text{m})^3$	Maximum cell density
$o^{(B)}$	1	Blood oxygen level
α_o	0.004/ μm^2	O ₂ source coefficient
$\gamma_o^{(\text{norm})}$	1/(100 $\mu\text{m})^2$	O ₂ consumption coefficient by normal cells
$\gamma_o^{(\text{tum})}$	2/(100 $\mu\text{m})^2$	O ₂ consumption coefficient by tumor cells
R_g	200 μm	Growth factor diffusion range
$t_{EC}^{(\text{switch})}$	24 h	Sprouting/Dilation switch delay
$t_{EC}^{(\text{sprout})}$	5 h/10 μm	Sprout extension time
$t_{EC}^{(\text{migr})}$	100 h	Sprout activity duration
$l^{(\text{spr})}$	20 μm	Sprout sites minimum separation
$r^{(\text{sprout})}$	4 μm	Initial sprout vessel radius
k_r	0.4 $\mu\text{m}/\text{h}$	Vessel dilation rate
$r^{(\text{max})}$	25 μm	Maximum dilation radius
$t_{TC}^{(\text{prol})}$	10 h	TC proliferation time
$t_{TC}^{(\text{uo})}$	100 h	Hypoxic TC survival time
$f^{(\text{coll})}$	2 Pa	Critical wall shear stress
$t_{EC}^{(\text{coll})}$	20 h	Unstable vessel survival time
Δw	0.05 $\mu\text{m}/\text{h}$	Dematuration (w) rate
$o_{TC}^{(\text{death})}$	0.01	TC hypoxia O ₂ threshold
$o_{TC}^{(\text{prol})}$	0.1	TC proliferation O ₂ threshold

removed or extended depending on the wall shear stress in the parent edge. Thereby moves that would result in overlapping nodes are rejected. The initial configuration is generated by first placing tree roots randomly at the boundary sites of the lattice, followed by random growth until the lattice is filled. Blood flow is computed between remodeling sweeps. Prior to that, the individual trees are connected by ‘‘capillary’’ edges, which are temporarily added between leaves of opposing type. For brevity we refer the reader to the appendix of [29], where the procedure is described in detail for a triangular 2d lattice. The difference to the cubic 3d case considered here lies in the number and location of root nodes and the pieces appended at nodes where growth happens. Here we chose initial locations of the root nodes randomly according to a uniform distribution over the system domain faces. Arterial and venous types are selected in alternating order. A new location is rejected if it is closer than $N\Delta l/10$ to either another root or an edge of the system domain. The

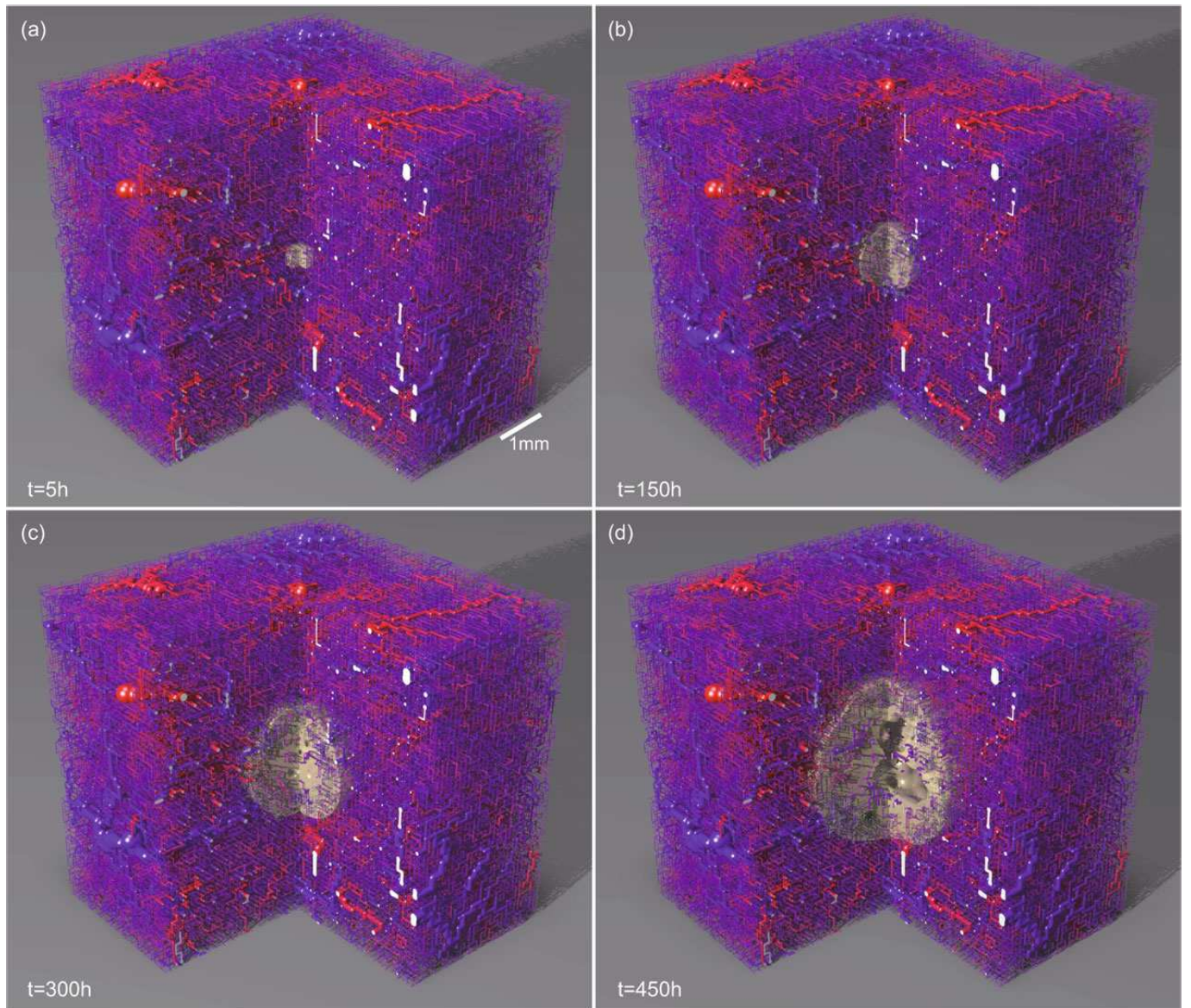


Fig. 3. Visualization of the vessel and tumor configuration generated by a simulation of the model at different times. A cut through the cubic simulation volume is shown. The vessels are depicted as cylinders which are color coded by their blood pressure (blue = 0 kPa; red = 12 kPa). Non-circulated vessels are shown in gray. The spheroid in the center shows the isosurface where the tumor cell density equals 50% of the normal packing density $c^{(norm)}$.

growth pieces are selected from three planar configurations: a single edge, a \vdash shape consisting of three edges, and a \sqcap shape consisting of five edges. The latter two should approximate the more realistic Y shapes in real vasculatures. Among all admissible configurations and orientations, one is randomly picked.

While it is highly non-trivial to synthesize vascular networks that are realistic in every way possible, our initial networks exhibit reasonable hierarchical structures, spatial distributions of the capillaries, and agreement with the flow data in [35] and the experimental references therein. Figure 6 shows analogous plots which can be used for comparison. They are discussed with respect to the tumor network in sect. 3.2.

3 Results

In fig. 3 we show snapshots of the dynamical evolution of the tumor and vessel network configuration at successive times. Initially the tumor O_2 consumption leads to decreased O_2 levels within the nucleus and consequently enables vascular remodeling via growth factor production of the TCs. The sprouting process first creates a dense capillary plexus which provides more oxygen and facilitates tumor growth. Vessel collapses begin after a few days ($t = 200$ h). Small capillaries collapse immediately under bad perfusion while thicker vessels survive longer due to their stability, *i.e.* large w , independent of blood flow until they become unstable. The network is thus progressively

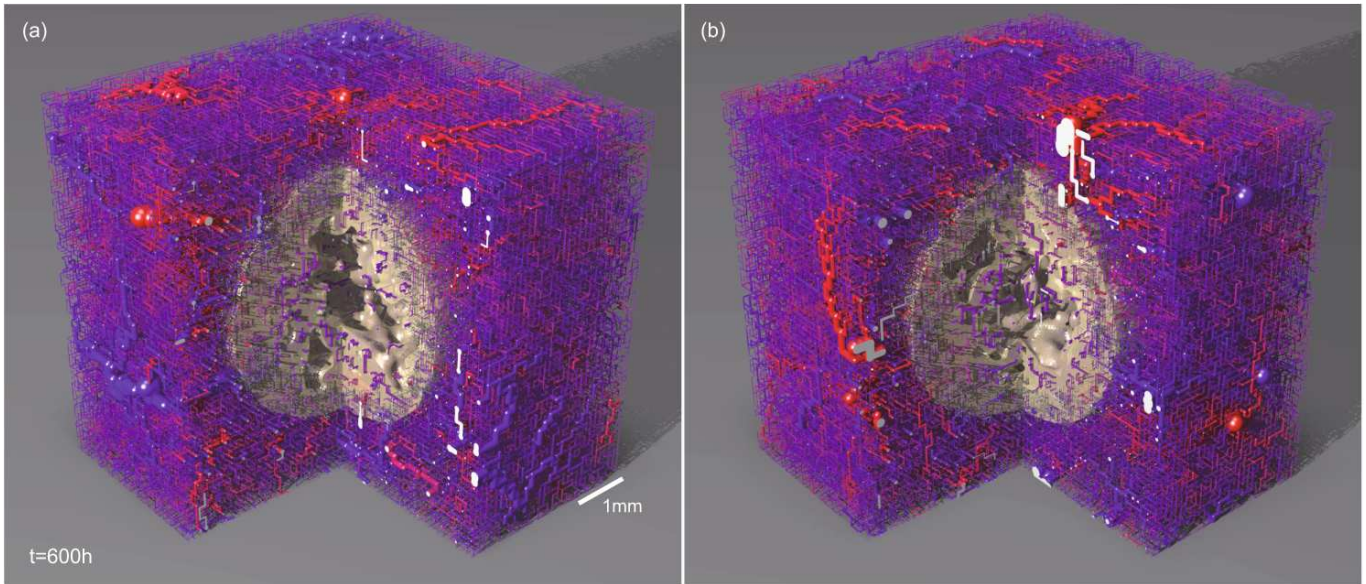


Fig. 4. Left: final configuration (at time $t = 600$ h) of the simulation run shown in fig. 3. Right: for comparison a final configuration resulting from a simulation run that started with a different initial arterio-venous network. Generally one observes that the MVD behind the tumor rim is increased due to a large number of sprouting vessels. Most of them are not viable because they cannot form blood circulated circuits, in addition also many original capillaries regress. The tumor becomes interspersed with a few isolated, dilated vessels. The lack of oxygen in non-perfused regions leads to the empty (necrotic) regions in the center.

remodeled, predominantly within a thin band around the tumor boundary. The sparse network left in the center remains static except for few collapses of isolated threads.

The resulting network morphologies shown in fig. 4 display the typical high-MVD periphery and low-density center. The remaining internal vessels form short-cuts between arteries and veins which touch the tumor surface. This is a consequence of the dilation that all vessels undergo in the tumor. The short-cuts consist of neovasculture as well as parts of the initial vasculature.

Starting with different initial arterio-venous networks yields different final configurations, as shown in fig. 4, but their global characteristics, as quantified by the radial distribution functions analyzed in the next subsections, do not vary significantly.

The tumor masses grow approximately spherically. After a short initial phase their radius increases linearly, since proliferation is predominantly restricted to the boundary where sufficient space and oxygen is available. The cell density profiles c exhibit steep slopes at the invasive edges, dropping from $c^{(\text{norm})}$ to zero. In the tumor interior c fluctuates between zero and $c^{(\text{max})}$, depending on oxygenization.

3.1 Radial distributions

Figure 5 shows the tumor density (in all panels), average vessel radius (panel a), microvascular density (MVD, panel b), oxygen concentration (panel c), blood flow rate through the vessels (panel d), vessel wall shear force (panel e) and growth factor concentration (panel f) as a function

of the radial distance r from the tumor center for different times. The data are averaged over 50 simulation runs with different initial networks and over concentric spherical shells centered around the tumor center. The microvascular density (MVD) is defined as the volume fraction occupied by the vessels. The quantities which are associated with vessel segments (radius, flow, shear force) are averaged over the number of vessel-occupied lattice sites within the respective shells.

In each panel the radial tumor density at the appropriate times is represented by broken lines: it facilitates the comparison of various features of the vessel quantities with the tumor extension. The peak in the radial tumor density indicates the boundary of the tumor (stochastic fluctuations within the shells as well as from sample to sample cause the finite width of this step). Since the individual curves are for equidistant times, it is clear from the linear shift of the peak density that the tumor radius grows linearly in time. Behind the peak, at smaller distances r from the center, the tumor density drops monotonously, reflecting the emergence of necrotic zones in the tumor center.

The MVD in panel (b) of fig. 5 has a peak in the peritumoral region, *i.e.* outside of the tumor at a distance slightly larger than the peak of the tumor density. It is 1.5 to 2 times higher than the normal MVD (plateau value at large distances). Inside the tumor (at small distances) the MVD drops monotonously to zero (at long enough times), again reflecting the emergence of the necrotic core.

Correlated with the peak in the MVD is a small peak in the oxygen concentration (panel (c) of fig. 5), and a dip in the average vessel radius (panel (a)), the average flow

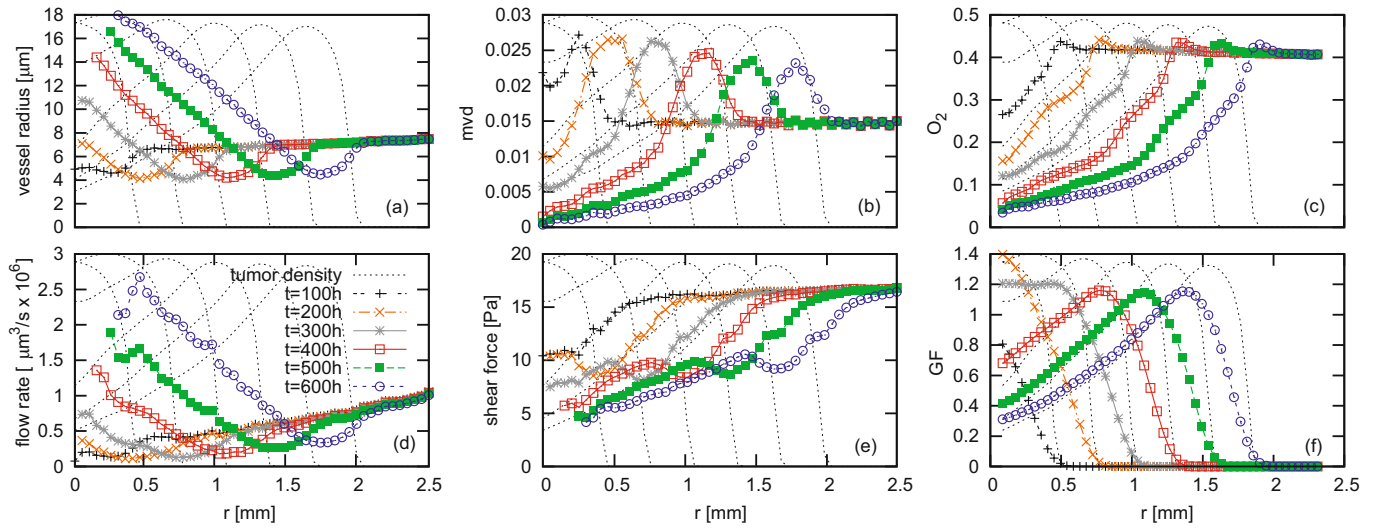


Fig. 5. Results for (a) vessel radius, (b) microvascular density (MVD), (c) oxygen concentration, (d) blood flow rate through the vessels, (e) vessel wall shear force, and (f) growth factor concentration as a function of the radial distance from the tumor center for different times (see lower left panel for legend). The broken lines indicate the radial tumor density at the times corresponding to the other data shown.

rate (panel (d)), and the average shear force (panel (e)): The peak in the MVD in the peritumoral region reflects the presence of many new capillaries, which increase the oxygen supply but simultaneously decrease the average vessel radius since capillaries have minimum radius. Furthermore, since the average blood flow that is supplied by the arterio-venous network is approximately constant, this flow has to be distributed over 50–100% more microvessels in the tumor perimeter, which induces a reduction in average flow rate and shear force.

Within the tumor (*i.e.* for distances smaller than the location of the peak of the MVD) the vessel radius increases monotonously with decreasing distance from the tumor center (panel (a) of fig. 5), which is the effect of the switch from angiogenic sprouting to circumferential growth within the tumor. The axial blood pressure gradient within the vessels, dp/dl , which is not shown here, decreases monotonically with decreasing distance from the tumor center by more than one order of magnitude. Although the pressure gradient decreases, the average blood flow rate (q , panel d) within the vessels increases towards the tumor center, since it is proportional to the 4th power of the vessel radius R , $q \propto R^4 dp/dl$. The average shear force f is proportional to the 1st power of R , $f \propto R dp/dl$, therefore it decreases with decreasing distance from the center.

The average oxygen concentration (panel c) decreases rapidly towards the tumor center and drops below the GF production threshold $o_{TC}^{(prol)} = 0.1$ (relative to normal oxygen) at approximately the same distance $r_{low\ oxy}$, where the growth factor concentration (GF, panel f) displays a peak. This peak is therefore not at the same position as the peak of the tumor density. For distances smaller than the “underoxygenization radius” $r < r_{low\ oxy}$, all tumor

cells produce GF and the shape of the GF concentration *versus* distance r is identical with the tumor density.

MVD and vessel radius show the typical compartmentalization that has been observed in melanoma [4,5] and glioma [36]: For instance in [4] the MVD and vessel radius were measured in three distinct regions of human and mouse melanoma: the central region, a 100 μm wide peripheral band just behind the invasive edge, a 200 μm wide peritumoral region outside the invasive edge. In the central region, they found a MVD that was reduced to 25% of the MVD of normal tissue, and increased up to 200% in the peritumoral region. They found that the vessel perimeter grew linearly from 50 μm to a plateau at 200 μm by day 15.

In contrast to our results for regular vascular networks [25–27], flow rates and shear force now show a plateau similar to the vessel radius. In [25–27] the fixed pressure gradient along the boundaries of the regular (rectangular or hexagonal) networks led to unrealistic star-shaped morphologies, directing all blood flow through the center. The hierarchical initial networks that we consider here do not have these artifacts and display a physiologically realistic morphology.

3.2 Vessel statistics

Figure 6 shows scatter plots of hemodynamic variables against the vessel radius r , which are in good agreement with those obtained in [35]. The plots combine samples throughout the full vasculature from all runs at $t = 400$ h.

We generally observe that the variance of the flow-related parameters increases drastically towards the capillaries. This might be an artifact of our initial network construction, but averaged quantities display physiologically sound characteristics.

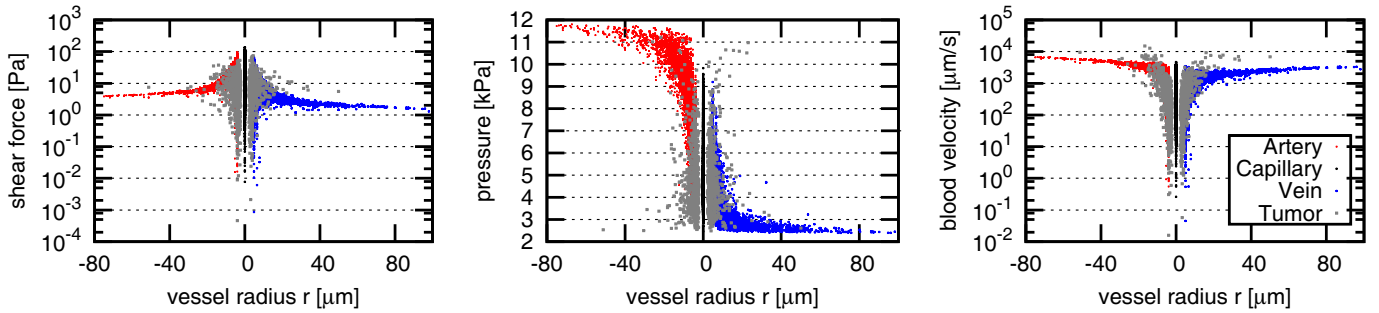


Fig. 6. (Colour on-line) Scatter plots of vessel-related hydrodynamic quantities —shear force, pressure, and blood velocity— against the vessel radius r (each dot corresponding to one vessel). Red dots (to the left with negative radius for better visibility) correspond to arteriolar vessels, blue dots (to the right) to venous vessels, black dots (at $r = 0$) to capillaries, gray dots to tumor vessels. The latter are randomly plotted on either side (arteriole or venous) because they do not exhibit a clear hierarchical distinction. The plot combines samples uniformly distributed over the full vasculatures of all simulation runs at $t = 400$ h.

The blood pressure plot shows that the tumor vessels tend to exhibit low blood pressure. The few larger tumor vessels ($r > 10 \mu\text{m}$), however, show a more uniform distribution. The velocity plot shows that these vessels have high blood flow rates, whereas the average for capillaries is about one order of magnitude lower. Both observations support the view that tumor-internal vessels form short-circuits between arteries and veins intruding into the tumor rim. Responsible for this is the vasodilation mechanism which acts on all tumor vessels and decreases their flow resistance.

Compared to hierarchical 2d networks [29], flow parameters are distributed similarly. However, a few details are apparent. i) The sigmoidal shape of the pressure distribution seems to be more pronounced. ii) The shear force in the arteries decreases for large r whereas it increases for the 2d networks. iii) In fig. 7 of ref. [29] one could observe tumor vessels which have reached the maximum dilation radius and exhibit flow parameters spanning over several orders of magnitude. We think that i) and ii) can be attributed to the three dimensionality of the system which enables different initial network geometries to emerge. iii) is the result of the shorter simulation time, since most tumor vessels might not reach the maximum dilation radius.

3.3 Fractal dimension

The vascular tumor network is extremely inhomogeneous and has geometric, in particular fractal, properties that are very different from normal vasculature [38]. The concept of a fractal dimension is often used to characterize differences between normal vasculature and tumor vasculature [38,39].

One commonly used method to estimate fractal dimension is box-counting, which is carried out by superimposing boxes of size ϵ arranged as a regular grid on the fractal object and counting the number of boxes N_ϵ which overlap the object. The self-similar nature of true fractal object leads to the power law $N_\epsilon \propto \epsilon^{-D_f}$, where N_ϵ is the number of overlapping boxes. D_f is usually extracted by a linear fit in a log-log plot. However in experiments one can usu-

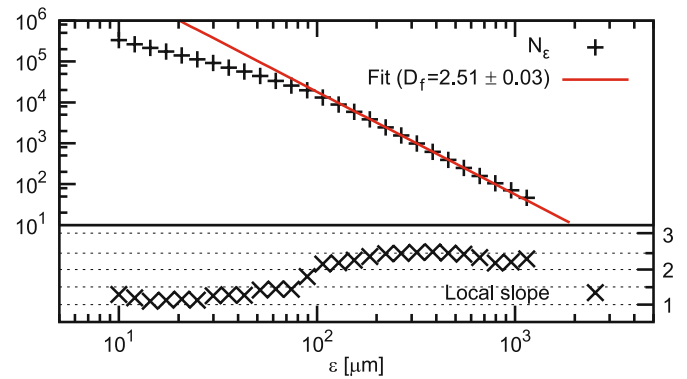


Fig. 7. Top: log-log plot of the box counts N_ϵ against the box size ϵ for the determination of the fractal dimension of the tumor vasculature of one final system. For the intersection with the boxes, the vessels were approximated as lines. An estimate for the fractal dimension is obtained from the best fit to $N_\epsilon \propto \epsilon^{-D_f}$. Bottom: the data represent the (negative) local slopes of the data points for N_ϵ in the log-log plot above.

ally measure ϵ at most over two orders of magnitude. Furthermore natural objects (or rather photographs thereof) are usually not perfectly fractal *i.e.* box-counting plots exhibit non-constant slopes. Therefore even a small constant regime is often considered sufficient to speak of a fractal dimension (or more truthfully named box-counting dimension); see the discussion in [41]. Therefore what we mean in the following with “fractal dimension” is the number that we obtained by the procedure described below and which is analogous to the way in which this number is extracted from the analysis of experimental data [38,39,41].

For the application of the box-counting procedure, our vessel networks are approximated as a collection of line segments. For the measurement of the tumor network we discard segments which are not within the tumor (“within the tumor” is where $\langle c \rangle > c^{(\text{norm})}/2$, see sect. 2.6). Our data for $\log(N_\epsilon)$ as a function of $\log(\epsilon)$ do not follow a straight line as one would expect if $N_\epsilon \propto \epsilon^{-D_f}$ but are slightly bended, see upper panel of fig. 7. From the data we can extract the local slopes and plot them as a function of ϵ as done in the bottom panel of fig. 7. At small box

sizes the local slopes are close to -1 , reflecting the fact that in the analysis we assumed the vessel segments to be 1-dimensional objects. For larger box sizes the local slopes start to reflect the network geometry (rather than the geometry of individual vessels) and we can consistently identify a small plateau at $D_f \approx 2.5$, which we take as our estimate for the fractal dimension of the vessel network: $D_f = 2.5 \pm 0.03$ on average. This is in very good agreement with the value obtained earlier for regular cubic initial networks (in 3d) $D_f = 2.52 \pm 0.05$ [26].

In [26] it was hypothesized that the fractal properties of the emerging tumor vasculature are independent of the initial (3d) blood vessel network. Our present finding that D_f of the tumor vasculature for a 3d arterio-venous initial network is close to D_f for 3d regular initial networks supports this hypothesis.

We also checked the non-capillary parts of the initial network and obtained with equally well matching fits $\langle D_f \rangle = 1.46$ for arteries, $\langle D_f \rangle = 1.51$ for veins, and $\langle D_f \rangle = 1.64$ for both combined, which is close to the estimate for real arterio-venous subcutaneous vascular networks [39].

Moreover, in [25,26] we identified the basic mechanism responsible for the fractal properties of the tumor vasculature as the stochastic, blood flow correlated removal of vessels via vessel collapse and regression, denoted as flow correlated percolation (see also [42]).

3.4 Spatial inhomogeneities and hot spots

“Hot spots” are regions of increased blood flow within the tumor. It is possible to compare our results at least qualitatively with clinical imaging of tumor blood flow using tomography techniques, *e.g.* [43]. Therefore we generated maps of local average flow velocities $\langle v \rangle = \frac{1}{|C|} \int_C v(\mathbf{x}) d\mathbf{x}$, where C is a small subvolume, $v(\mathbf{x}) = q/\pi r^2$ is the flow velocity at locations within a vessel and zero everywhere else, and q denotes the flow rates of the respective vessels. The integral is evaluated stochastically. An example is shown in fig. 8. Analogous to imaging experiments, we can find regions of zero flow and so-called hot spots with high velocities. Unperfused regions coincide with necrotic regions by design of our model. Likewise, hot spots are identified by vessels threading the tumor. Since the tumor vessels have high flow rates and are dilated, even one such vessel can show up as a “hot spot”. Our model thus supports the hypothesis raised in [43] that hot spots are due to highly conductive arterio-venous shortcuts.

In 2d [29], one could observe the formation of dense vessel clusters accompanying the predominant isolated strings of surviving vessels in the tumor center. It could be shown that these clusters are more likely to form in regions with high hydrodynamic pressure differences between neighboring vessels. A map of these pressure differences can be constructed by determining the solution of the Laplace equation for a pressure field $p(\mathbf{r})$ defined on the space between the vessels with the boundary condition that $p(\mathbf{r})$ is identical to the blood pressure inside the vessel at location \mathbf{r} . Thus, the field $p(\mathbf{r})$ interpolates the

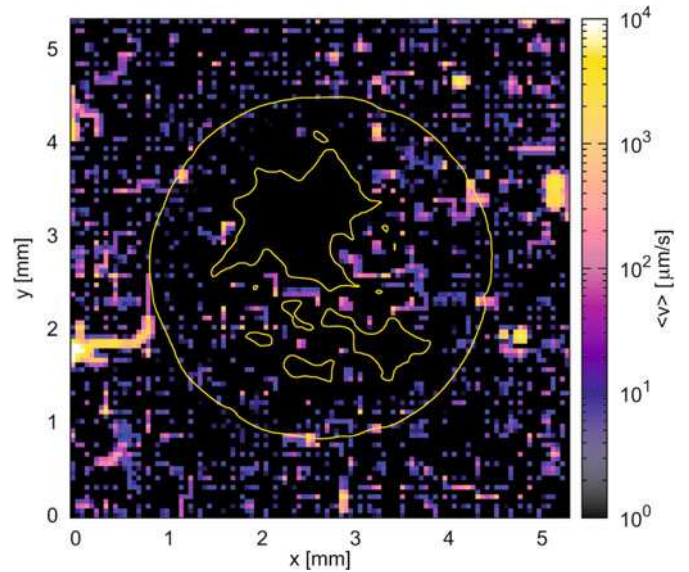


Fig. 8. (Colour on-line) Local flow velocity distribution in a slice through a tumor vasculature. The yellow line shows the $c^{(\text{norm})}/2$ isocontour of the tumor cell density. The plotted quantity is the blood flow velocity averaged over $(50 \mu\text{m})^3$ grid cells. The resulting image is reminiscent of MRI blood flow studies and shows regions with low flow and hot spots. Since we did not incorporate the interstitial flow, the distribution is zero where vessels are absent.

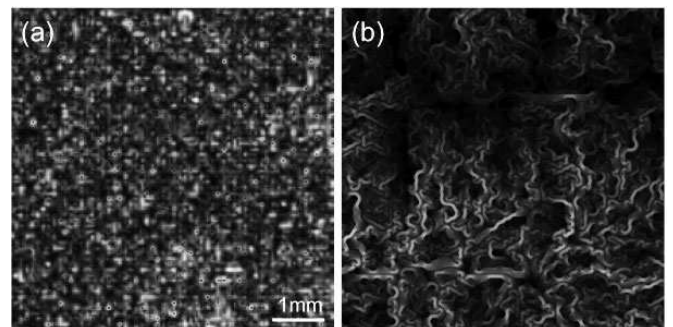


Fig. 9. Local values of $|\nabla p|$ are shown, where $p(\mathbf{r})$ is a continuous field which interpolates the blood pressure between neighboring vessels of an initial network configuration. (a) Shows a slice through the center of a 3d system considered here and (b) shows the result for a 2d network obtained in [29]. While in (b) large-scale fluctuations can lead to dense clusters of internal tumor vessels, (a) is comparably homogeneous and the tumor networks consist of isolated strings in the tumor interior.

pressure between vessels. The (local) gradient magnitude $|\nabla p|$ of this map for the original vasculature shows positive correlation with the (local) microvascular density in the emerging tumor vasculature in 2d [29].

However, dense vessel clusters observed in 2d [29] are absent in the tumor vasculature emerging from the 3d arterio-venous networks considered here. Concomitantly the pressure (gradient) fields for the 3d initial networks considered here are more homogeneous, except on a very short scale between neighboring vessels. Figure 9 demonstrates this by a comparison of the pressure gradient $|\nabla p|$

for (a) a 3d initial network and (b) a 2d network. The spatial variation of the pressure gradient $|\nabla p|$ is determined by the geometry of the initial vessel network, which again depends on the precise location of the roots of the arterial and venous trees (sources and sinks) and the details of the construction algorithm. We think it would be possible to construct an arterio-venous initial network in 3d, where results would resemble those reported for 2d in [29], see fig. 9(b), but we have not checked this yet.

4 Drug transport

To analyze the effectiveness of blood-borne drug transport to a tumor and its distribution inside, a time-dependent concentration profile over the vasculature is propagated according to the local blood flow velocities. A corresponding mathematical model was presented [17] for a pure vessel-in-growth capillary network, originating from a single parent vessel. We adopted this method to check whether there are similar obstacles to successful drug delivery inherent to the tumor vascular networks.

The starting point is a given configuration for the vasculature with precomputed variables for flow, flow velocity, vessel length, and radius. In addition, a mass parameter m is associated with each vessel describing the amount of drug in the blood volume contained in the vessel. The mass content m is deterministically updated in successive time steps as follows: First the drug amount flowing out of vessels is determined and added to corresponding node mass variables. Under the assumption of perfect mixing, the nodal masses are then redistributed into further downstream vessel. Thereby mass conservation is strictly enforced. A detailed description can be found in [27,17]. The most severe limitation of this model is that there is no exchange with extravascular space and therefore also no uptake by the tumor.

The results in the following were obtained with continuous injections into the final tumor networks. Initially the networks are filled with “clean” blood. Extravasation of drug is neglected.

When drug is inserted simultaneously through all arterial inlets, it is distributed very rapidly over the whole network. Within the order of several seconds the network is saturated with the maximum drug concentration. To illustrate that, fig. 10 shows a sequence of snapshots over 5 seconds. At the tumor border, where the MVD is high and the network contains many loops, there may be tiny regions (ca. $100\ \mu\text{m}$ diameter) that take an order of magnitude longer to fill. Note also that the dilated tumor vessels through the center conduct very well and act as short-circuits between arteries and veins. The outer regions of the system where the network remains normal can also transport drug towards the tumor periphery. Therefore the tumor as a whole is well perfused.

In [17,18] it was predicted that large amounts of drug bypass the tumor, varying by an order of magnitude depending on parameters. Drug bypassing also occurs naturally in our model since all vessels (original and tumor) are perfused with drug after ca. 5 s (see fig. 10). This is

independent of the details of the vasculature be it from healthy or pathological tissue: whenever one wants to hit a specific region of the vascularized tissue with a blood-borne drug, one has to inject it into a high-level artery which also branches into parts outside the target region. The more relevant question therefore is: How long, during an injection of length δt , are all target vessels exposed to a drug concentration larger than a predefined threshold? For realistic situations the question “how much drug volume” bypasses the tumor is somewhat ill-defined, since the answer depends on the level of the arterial tree one injects the drug in.

We analyzed how long tumor vessels are exposed to a drug concentration larger than a predefined minimum drug level c_{thres} and show the result in fig. 11. It confirms the former visual impression that drug perfusion is fast: For instance, in our 30 s simulation time over 90% of the vessel network was exposed to at least $c = 0.5$ for at least 25 s, and 99% for at least 15 s. Also the curves for $c_{\text{thres}} = 0.5$ and 0.01 nearly match, from which one can conclude that drug advances through the network with a sharp front, exposing vessels “on contact” instantly to high drug concentrations.

Although we consider here continuous drug infusions, a bolus injection of fixed drug volume or limited time should be extremely short (less than 5 seconds) in order to be distinguishable from a continuous infusion due to the speed at which drug is transported. Therefore our predictions are also relevant for bolus injections longer than 5 seconds.

Qualitatively the results for drug flow reported here agree with those for 2d arterio-venous networks [29]. A notable difference is that in 2d the tumor networks can disrupt the flow in larger regions ($\gg 100\ \mu\text{m}$ diameter) than here, which also extend into sections of the original network. This is because the initial network configurations considered in [29] have fewer pathways to major feeding vessels. Therefore blood flow to aforementioned regions passes through the comparably badly conducting tumor boundary, resulting in low flow rates.

We remain with our conclusion that experimentally observed deficiencies in drug delivery must have other reasons, and these most probably lie within the characteristics of extravasation of drug and interstitial fluid transport within the tumor, which we did not include into the present version of our model.

5 Discussion

In this paper we formulated a hybrid cellular automaton model to analyze the vascular remodeling process of three-dimensional arterio-venous vessel networks during solid tumor growth. The model involves sprouting angiogenesis, vessel co-option, dilation and regression as well as tumor cell proliferation and death. It predicts that the tumor vasculature emerging from the interplay of these processes is non-hierarchical and compartmentalized into a highly vascularized tumor perimeter, a tumor periphery with large vessel density and dilated vessels and a central region containing necrotic regions with a low microvascular density

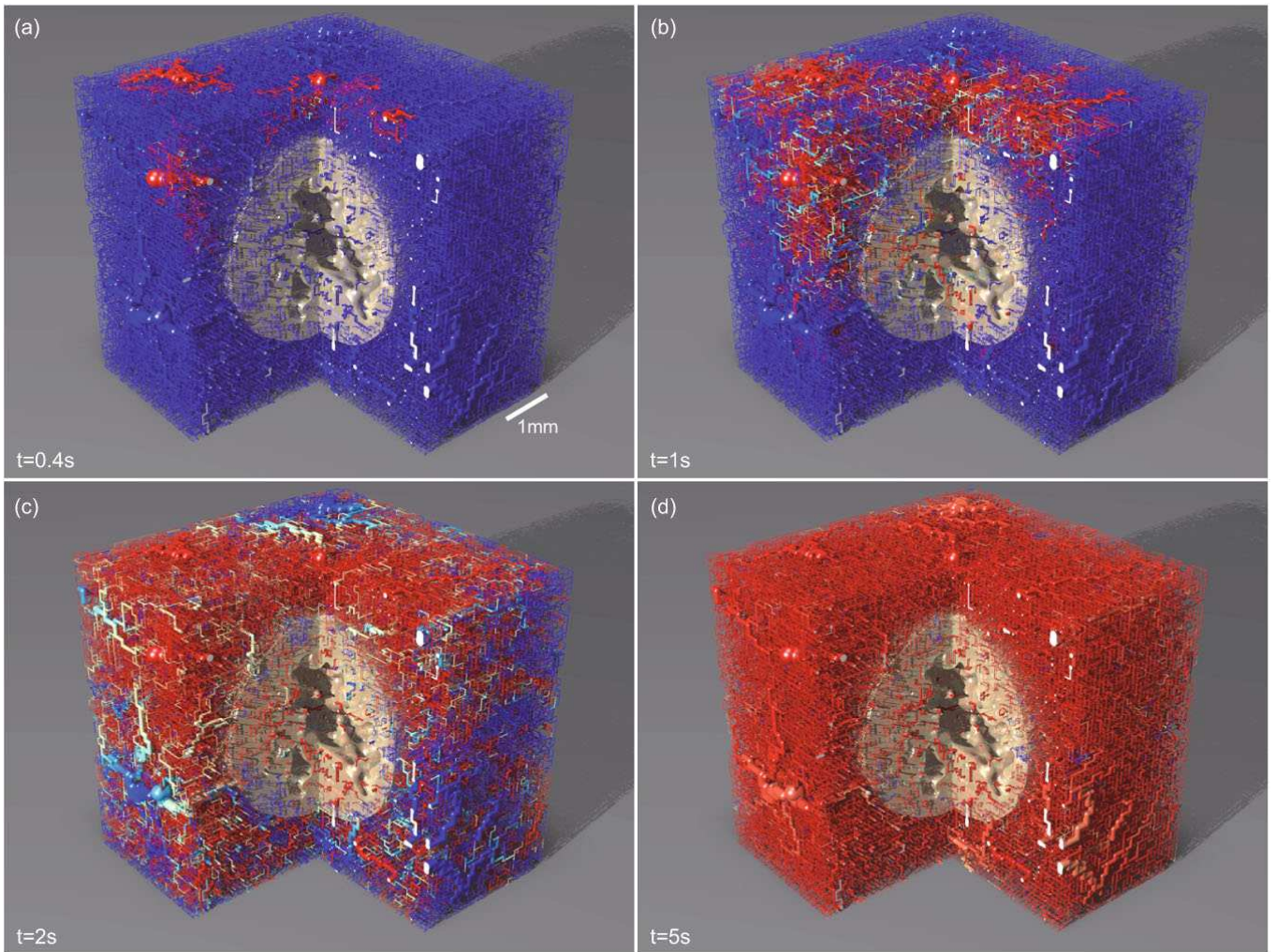


Fig. 10. (Colour on-line) Snapshots of a drug flow simulation in a tumor vessel network produced by our model. The color code shows the dimensionless concentration (red: 1; blue: 0). The drug is injected with the initial concentration 1 at the arterial root nodes. The transport is very effective. Already after 5s the vasculature is almost completely saturated.

threaded by extremely dilated vessels. This is a general feature of the remodeling process of the normal vasculature into the tumor vasculature in the model, and we propose this to hold also for *in vivo* tumor: none of the initial characteristics of the original vessel network survives this process. In this work this proposition was demonstrated for a 3d arterio-venous initial network, and analogous observations have been made for 2d arterio-venous initial networks [29] and for regular networks consisting of capillaries of equal diameter arranged in a regular grid with a given MVD, in 2d [25] and 3d [26]. Once the tumor grows over it, it gets transformed into a compartmentalized network with irregularly arranged dilated vessels and a decreasing MVD from the tumor periphery to the tumor center, resulting in an inhomogeneous oxygen distribution.

5.1 Comparison with earlier work in 2d and 3d

Before more general conclusions are discussed, we highlight some notable differences and similarities of the re-

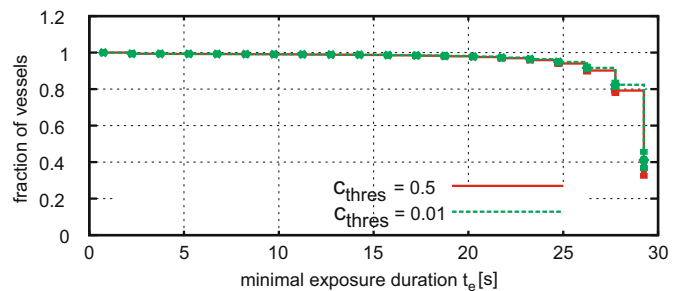


Fig. 11. Exposure durations: A point in the diagram means that a certain fraction of the vessel network is exposed to a drug concentration larger than C_{thres} for a duration longer than t_e . Simulation time: 30s.

sults of our model systems. The global morphology of the vascular tumor networks, as reflected by measurements of radial distributions of various parameters agrees qualitatively very well in all of our model versions. Quantitative differences arise primarily in the flow rate distributions

since these depend strongly on the network morphology. Moreover, the vessel statistics of arterio-venous initial networks agrees very well in 2d [29] and 3d (fig. 6), and also with [35] from where we adopted the initial network construction method.

Concerning the emerging tumor vessel network morphology, significant differences to the results reported here exist for regular initial networks [25–27]. In these studies a linear blood pressure gradient was imposed as a boundary condition which drives blood from from one corner of the simulation domain to the opposite corner. This aligns surviving tumor vessels in the flow direction, and can even impose artifacts where vessels converge to a singular point in the center of the tumor. These artifacts are absent in hierarchical arterio-venous initial networks studied in this paper and in [29]. Resulting tumor networks are isotropic, but may not be homogeneous. One can divide them into sections which consist of dense clusters of capillaries and on the other hand vessels which thread the tumor as isolated strings. We can attribute their relative occurrence to the morphological details of the initial networks—location of major feeding/draining vessels in particular.

Analysis of the fractal dimension D_f (see below) can give valuable insight into the fundamental mechanism of the emergence of the specific tumor network morphology. In all of our model systems the value for D_f agrees reasonably well with the value of the fractal dimension of the critical percolation cluster in site percolation, either in 2d [25, 29] or in 3d, [26] and this study.

Lastly, our simulations show that drug transport is much more efficient for arterio-venous networks than for regular (capillary) networks [27]. The latter case is not a very realistic choice for transport studies, since it lacks the fast pathways provided by arteries and veins. For grid-like initial capillary networks it takes ca. 60 seconds for drug to travel from one end of the system to the other. Arterio-venous networks, in contrast, both in 2d and 3d, lead to the saturation of 90% network with drug, including the tumor section, within ca. 6s. There are isolated regions where vascular remodeling cuts off high-level arterial/venous vessels and redirects flow through the weakly conducting neo-vasculature in the tumor boundary. This leads to locally decreased flow rates, so that drug delivery is an order of magnitude slower. This effect is more pronounced in 2d than in 3d.

5.2 Conclusion

We propose that vessel collapse and local blood flow characteristics have to be correlated via the local shear stress. If the collapse events would occur independently from one another with some probability p , a fundamental law in percolation theory [44] predicts that either the interior of the tumor is completely filled (*i.e.* does not contain large connected necrotic regions) or it is completely void up to a small boundary region—except for one special value for the parameter p , the percolation threshold p_c . We confirmed this scenario by testing different model variants containing uncorrelated collapse events. The existence of

a model parameter like the collapse probability that has to be fine-tuned to a special value in order to reproduce vessels that thread the whole tumor would obviously be unsatisfactory. Only if we correlated the vessel collapse with the shear stress, the model predicts a realistic vascular network morphology that is robust against parameter variations. The basic mechanism for this robustness is the redirection of the flow after collapse events into still intact vessels resulting in an increased shear stress in the remaining vessels and thus a drastically reduced collapse probability. Shear stress rather than blood flow as a hemodynamic criterion for vessel stability appears to be plausible, since the endothelial cells in the vessel wall have information about the shear stress but probably less about the total flow. We checked that a correlation of vessel collapses with the blood flow also leads to unrealistic network morphologies in which only a few vessels survive within the whole tumor (*i.e.* a tumor periphery with increased MVD is completely missing). The reason for this is the dependence of the flow from the fourth power of the vessel radius. This leads to a strong variation of the flow between vessels of only slightly different radius, implying the survival of only the thickest vessels if collapse is correlated with the flow.

The emerging tumor vasculature has a complex geometry and a fractal dimension¹ different from the initial arterio-venous network. It has been suggested [38, 39] that the origin of the fractal architecture of tumor vasculature might be based on an underlying invasion percolation process [45, 46] due to inhomogeneities in the growth supporting matrix. Since our theoretical model does not involve any such matrix inhomogeneities, we propose that it is rather the flow-correlated percolation process that determines the fractal properties of the tumor vasculature. A commonly accepted view for a large class of tumors like melanoma [4, 5], also shared by our theoretical approach, is that neo-vascularization mainly occurs at the tumor perimeter and a drastic reduction of vessel density occurs in the interior of the tumor. Within such a scenario it appears unlikely that the fractal properties attained during growth in the periphery, independent of having characteristics of invasion percolation or not, survive the random dilution process in the tumor center.

Our drug flow simulations demonstrated that drug flows relatively well through all of the networks and an infusion time of the order of a few seconds is sufficient to saturate the vasculature with drug. Therefore, without further refinements, the model predicts that drug efficiency is not limited by the transportation process through the vasculature. Considering the model mechanisms which lead to the tumor vasculature, it is plausible that drug reaches (nearly) all parts of the vasculature: Shear force correlate vessel collapse naturally leads to elimination of weakly perfused vessels. In the case of random collapses, pressure

¹ *Fractal dimension* denotes here the number that one obtains by a box-counting procedure and does not intend to imply that the tumor vasculature, neither *in vivo* nor *in silico*, represents a mathematical fractal, or a good physical realization of a mathematical fractal.

gradients are still sufficient to drive blood through the vessels, but an order of magnitude slower.

In [18] it was found that the morphology of tumor vasculature plays a crucial role in drug delivery and that changes to key system parameters could have a big impact on the structure of the vasculature. The origin of this discrepancy with our conclusion lies in the different model assumption: In [18] a strictly avascular tumor was considered, where sprouts migrate towards the tumor, but are not allowed to enter it. These networks exhibit extremely high connectivity close to the tumor surface but the involved angio-adaptation mechanisms lead to vasodilation of comparably few pathways. Depending on the model parameters the number of high-throughput vessels and their distance to the tumor varies sufficiently to lead to uptake rates which vary by several orders of magnitude.

In contrast to this we study here a type of tumor like melanoma, which are primarily vascularized by co-option rather than vessel ingrowth [4,5]. For them, as we have demonstrated, a blood-borne “delivery problem” does not exist. This does however not automatically imply that drug reaches all tumor cells since neither drug transport through the tumor tissue nor drug uptake have been addressed [47]. Regarding tissue transport it is known that the difference between interstitial fluid pressure (IFP) and microvascular pressure (MVP) is low due to vessel leakiness. Since convective transport is driven by pressure differences, high IFP could pose a barrier to drug delivery [48]. On the other hand, leakiness and MVP-IFP gradients could lead to premature release predominantly in locally restricted regions around vessels where blood enters the tumor. Vessels in the outflow regions would thus be depleted of drug. Locally released drug would then be transported by IFP gradients out of the tumor. Furthermore drugs usually consist of large macromolecules. Their low diffusibility through the vessel wall and generally lower diffusibility than oxygen could lead to situations where sufficient oxygen reaches certain TCs to let them remain viable, but not enough drug reaches them to kill them off due to the lower diffusion radius. Thus we conclude that, to a higher degree than the vessels morphology, processes like transportation out of the vessels through convection and diffusion seem to be key factors in successful drug delivery. It is straightforward to include and analyze these mechanisms into the model presented here.

References

1. P. Carmeliet, R.K. Jain, *Nature* **407**, 249 (2000).
2. J. Holash *et al.*, *Science* **284**, 1994 (1999).
3. J. Holash, S.J. Wiegand, G.D. Yancopoulos, *Oncogene* **18**, 5356 (1999).
4. B. Döme, S. Paku, B. Somlai, J. Tímár, *J. Path.* **197**, 355 (2002).
5. B. Döme, M.J.C. Hendrix, S. Paku, S., J. Tóvári, J. Tímár, *J. Path.* **170**, 1 (2007).
6. P. Tracqui, *Rep. Prog. Phys.* **72**, 056701 (2009).
7. J.S. Lowengrub, H.B. Friboes, F. Jin, Y.-L. Chuang, X. Li, P. Macklin, S.M. Wise, V. Cristini, *Nonlinearity* **23**, R1 (2010).
8. D. Balding, D.L.S. McElwain, *J. Theor. Biol.* **114**, 53 (1985).
9. M.A.J. Chaplain, A.M. Stuart, *IMA J. Math. Appl. Med. Biol.* **10**, 149 (1993).
10. M.A.J. Chaplain, S.M. Giles, B.D. Sleeman, R.J. Jarvis, *J. Math. Biol.* **33**, 744 (1995).
11. H.M. Byrne, M.A.J. Chaplain, *Bull. Math. Biol.* **57**, 461 (1995).
12. M.J. Holmes, B.D. Sleeman, *J. Theor. Biol.* **202**, 95 (2000).
13. T. Alarcon, H. Byrne, P. Maini, *J. Theor. Biol.* **225**, 257 (2003).
14. R. Betteridge, M.R. Owen, H. Byrne, T. Alarcon, P. Maini, *Netw. Hetero. Media* **1**, 515 (2006).
15. M.R. Owen, T. Alarcon, P. Maini, H. Byrne, *J. Math. Biol.* **58**, 689 (2008).
16. A.R.A. Anderson, M.A.J. Chaplain, *Bull. Math. Biol.* **60**, 857 (1998).
17. S.R. McDougall, A.R.A. Anderson, M.A.J. Chaplain, J.A. Sherratt, *Bull. Math. Biol.* **64**, 673 (2002).
18. S.R. McDougall, A.R.A. Anderson, M.A.J. Chaplain, *J. Theor. Biol.* **241**, 564 (2006).
19. A. Stephanou, S.R. McDougall, A.R.A. Anderson, M.A.J. Chaplain, *Math. Comput. Model.* **41**, 1137 (2005).
20. X. Zheng, S.M. Wise, V. Cristini, *Bull. Math. Biol.* **67**, 211 (2005).
21. H.B. Friboes, J.S. Lowengrub, S. Wise, X. Zheng, P. Macklin, E. Bearer, V. Cristini, *NeuroImage* **37**, 59 (2007).
22. S.M. Wise, J.S. Lowengrub, H.B. Friboes, V. Cristini, *J. Theor. Biol.* **253**, 524 (2008).
23. P. Macklin, S. McDougall, A.R.A. Anderson, M.J. Chaplain, V. Cristini, J. Lowengrub, *J. Math. Biol.* **58**, 765 (2008).
24. J. Wu, Q. Long, S.X. Xu, A.R. Padhani, *J. Biomech.* **42**, 712 (2009).
25. K. Bartha, H. Rieger, *J. Theor. Biol.* **241**, 903 (2006).
26. D.S. Lee, K. Bartha, H. Rieger, *Phys. Rev. Lett.* **96**, 058104-1 (2006).
27. M. Welter, K. Bartha, H. Rieger, *J. Theor. Biol.* **250**, 257 (2008).
28. A. Shirinifard, J.S. Gens, B.L. Zaitlen, N.J. Poplawski, M. Swat, *PLoS ONE* **4**, e7190 (2009).
29. M. Welter, K. Bartha, H. Rieger, *J. Theor. Biol.* **259**, 405 (2009).
30. R. Erber *et al.*, *EMBO* **25**, 628 (2006).
31. K. Bentley, H. Gerhardt, P.A. Bates, *J. Theor. Biol.* **250**, 25 (2008).
32. H. Gerhardt *et al.*, *J. Cell Biol.* **161**, 1163 (2003).
33. V. Nehls, R. Herrmann, M. Hünken, *Histochem. Cell. Biol.* **109**, 319 (1998).
34. S. Dimmeler, A.M. Zeiher, *Circ. Res.* **87**, 434 (2000).
35. R. Gödde, H. Kurz, *Dev. Dyn.* **220**, 387 (2001).
36. P. Vajkoczy, M.D. Menger, *J. Neurooncol.* **50**, 99 (2000).
37. A.R. Pries, T.W. Secomb, T. Gessner, M.B. Sperandio, J.F. Gross, P. Gaehtgens, *Circ. Res.* **75**, 904 (1994).
38. J.W. Baish, R.K. Jain, R.K., *Cancer Res.* **60**, 3683 (2000).
39. Y. Gazit, D.A. Berk, L.T.B. Michael Leunig, R.K. Jain, *Phys. Rev. Lett.* **75**, 2428 (1995).
40. J.W. Baish, R.K. Jain, *Nat. Med.* **4**, 984 (1998).
41. H.-W. Chung, H.-J. Chung, *Cancer Res.* **61**, 8347 (2001).
42. R. Paul, *Eur. Phys. J. E* **30**, 101 (2009).
43. S. Pahernik, J. Griebel, A. Botzlar, T. Gneiting, M. Brandl, M. Dellian, A.E. Goetz, *Brit. J. Canc.* **85**, 1655 (2001).

44. D. Stauffer, A. Aharony, *Introduction to Percolation Theory*, 2nd edition (Taylor & Francis, London, 1992).
45. L. Furuberg, J. Feder, A. Aharony, T. Jossang, Phys. Rev. Lett. **61**, 2117 (1988).
46. A.P. Sheppard, M.A. Knackstedt, W.V. Pinczewski, M. Sahimi, J. Phys. A **32**, L521 (1999).
47. A.I. Minchinton, I.F. Tannock, Nat. Rev. Canc. **6**, 583 (2006).
48. Y. Hassid, E. Furman-Haran, R. Margalit, R. Eilam, H. Degani, Cancer Res. **66**, 4159 (2006).



Interstitial Fluid Flow and Drug Delivery in Vascularized Tumors: A Computational Model

Michael Welter, Heiko Rieger*

Theoretical Physics, Saarland University, Saarbrücken, Germany

Abstract

Interstitial fluid is a solution that bathes and surrounds the human cells and provides them with nutrients and a way of waste removal. It is generally believed that elevated tumor interstitial fluid pressure (IFP) is partly responsible for the poor penetration and distribution of therapeutic agents in solid tumors, but the complex interplay of extravasation, permeabilities, vascular heterogeneities and diffusive and convective drug transport remains poorly understood. Here we consider—with the help of a theoretical model—the tumor IFP, interstitial fluid flow (IFF) and its impact upon drug delivery within tumor depending on biophysical determinants such as vessel network morphology, permeabilities and diffusive vs. convective transport. We developed a vascular tumor growth model, including vessel co-option, regression, and angiogenesis, that we extend here by the interstitium (represented by a porous medium obeying Darcy's law) and sources (vessels) and sinks (lymphatics) for IFF. With it we compute the spatial variation of the IFP and IFF and determine its correlation with the vascular network morphology and physiological parameters like vessel wall permeability, tissue conductivity, distribution of lymphatics etc. We find that an increased vascular wall conductivity together with a reduction of lymph function leads to increased tumor IFP, but also that the latter does not necessarily imply a decreased extravasation rate: Generally the IF flow rate is positively correlated with the various conductivities in the system. The IFF field is then used to determine the drug distribution after an injection via a convection diffusion reaction equation for intra- and extracellular concentrations with parameters guided by experimental data for the drug Doxorubicin. We observe that the interplay of convective and diffusive drug transport can lead to quite unexpected effects in the presence of a heterogeneous, compartmentalized vasculature. Finally we discuss various strategies to increase drug exposure time of tumor cells.

Citation: Welter M, Rieger H (2013) Interstitial Fluid Flow and Drug Delivery in Vascularized Tumors: A Computational Model. PLoS ONE 8(8): e70395. doi:10.1371/journal.pone.0070395

Editor: Timothy W. Secomb, University of Arizona, United States of America

Received: January 28, 2013; **Accepted:** June 18, 2013; **Published:** August 5, 2013

Copyright: © 2013 Welter, Rieger. This is an open-access article distributed under the terms of the Creative Commons Attribution License, which permits unrestricted use, distribution, and reproduction in any medium, provided the original author and source are credited.

Funding: Funding: University, Deutsche Forschungsgemeinschaft. The funders had no role in study design, data collection and analysis, decision to publish, or preparation of the manuscript.

Competing Interests: The authors have declared that no competing interests exist.

* Email: h.rieger@mx.uni-saarland.de

Introduction

Cancer is a complex disease which involves phenomena across different scales from the molecular genetic level to the tissue as a whole. Cancerous cells of solid tumors have undergone mutations all of which combined lead to cancer [1]. These involve a dysfunctional control of proliferation, the ability to survive under low nutrient conditions and the stimulation of increased vascularization through angiogenesis [2]. This leads to an advantage in the competition over space and nutrients whereby cancer cells are also able to evade the immune systems which would otherwise kill malfunctioning cells. Solid tumors grow as compact masses. In order to grow larger than a few millimeters they must acquire additional nutrient supply through a blood vessel network. In response to inadequate supply cells produce signaling substances called growth factors which diffuse through the tissue and stimulate sprouting of new blood vessels from preexisting host vessels (angiogenesis). In tumors this angiogenic activity is located within a few hundred micrometers from the tumor rim. Fueling further growth, the resulting neovasculature is progressively co-opted together with the original blood vessels by the expanding tumor mass while also pushing the neovascularization zone further into normal tissue. Chemical signaling by the tumor is however abnormal, leading to chaotic non-hierarchical vascular organiza-

tion. Behind the invasive edge, angiogenic activity ceases. Further proliferation of endothelial cells instead leads to circumferential growth and dilated tumor vessels. Also vessel walls degenerate via detachment of structural support cells like pericytes and smooth muscle cells. In conjunction with decreased blood flow rates vessels become prone to collapse leading to large unvascularized regions. Some surviving vessels thread the tumor, distal to which the tumor tissue becomes necrotic due to the lack of nutrients. As a whole such a typical tumor vasculature is characterized by tortuous vessels, chaotic connectivity and heterogeneous distribution as well as a compartmentalization into a zone with high micro-vascular density (MVD) near the invasive edge and a rapid density drop towards the center.

The interstitial fluid (IF), which is a solution that bathes and surrounds the human cells and originates from blood plasma extravasating from capillaries through pores and intercellular clefts in the vessel wall, plays an important role in the development and treatment of tumors. Due to degenerate walls many tumor vessels are leaky leading to a stronger coupling of the interstitial fluid pressure (IFP) with the blood pressure. This leads to an interstitial hypertension which can be elevated up to the blood pressure. The resulting decreased pressure difference across vessel walls is believed pose a barrier to drug delivery due to decreased convective trans-vascular transport or even back-flow [3–8].

Moreover functional lymphatics which would normally drain the superfluous fluid are absent in most tumors aggravating the IFP increase [2]. As a result the IFP profile assumes a plateau in the center of the tumor and drops off rapidly across the boundary. This gradient drives a strong outward directed convective flow at around $0.1 \mu\text{m/s}$. Signaling chemicals or tumor cells can therewith be transported into normal tissue or into lymphatics, promoting invasive behavior and metastatization [8,9]. Indeed high IFP is associated with a negative prognosis. High IFP also has negative implications for chemotherapeutic treatment. Through the outward convection, drug may be removed from the peripheral regions.

Mathematical modeling of interstitial fluid flow and delivery was first approached in a radially symmetric geometry with homogeneously distributed source and sink terms using a porous media model for the interstitial flow velocity [3]. This predicted in agreement with experimental results an elevated IFP profile and the corresponding velocity profile. Convective (drug) extravasation was virtually limited to a small peripheral region. Later, extensions were developed using explicit representations of the blood vessel network in two dimensions. In [10] individual vessels were arranged as rectangular grid and their blood pressure was coupled to the IFP at their lattice sites, including the effect of fluid loss through the vessel walls. A similar approach was taken in [11] but with a tumor vasculature which was generated from in-growth from two parent vessels. Except for [3] these studies did not consider drug transport. Recently, simulations of IF flow and drug transport were conducted based on imaging data from real tissues [12]. An analysis of biophysical parameters governing the distribution of the local drug concentration was performed in [13] primarily focusing on the effects of varying tissue permeabilities for diffusing drugs. The modeling incorporated a tumor vasculature, realistic tumor lesions and cellular uptake and binding. However convective transport was neglected. In [14] a model was introduced in which interstitial fluid interacts with a growing tumor, also incorporating a vascular network that evolves dynamically from an initial capillary grid. IFF and hence convective transport of macro-molecules depend crucially on the spatial distribution and strength of IF sources and sinks within the tumor, which are determined by the spatial arrangement of blood vessels together and their local blood pressure. Even when lymphatics are absent within the tumor, leaky vessels with low blood pressure represent also sinks for IFF inducing non-trivial flow patterns inside the tumor with unexpected effects for the convective transport of macro-molecules. It is clear that the predictive power of a computational model for IFF and drug delivery depends critically on the physiological relevance of the underlying model for the tumor vasculature. In the present paper we present for the first time a IFF and drug delivery study with a realistic, hierarchically organized arteriovenous initial vasculature, circumferential growth of tumor vessels and IF back flow into tumor vessels.

In earlier work we developed a mathematical model for vascularized tumor growth which involved an initial vasculature [15,16] arranged as a grid and updating rules representing angiogenesis, dilation and collapse. More recently, it was extended with an arteriovenous initial vasculature where quite realistically few arteries and veins branch out in a tree-like manner down to the lowest level where they are connected by capillaries [17–19]. Using this framework, biophysical aspects of tumor blood flow and the spatial distribution of tumor blood vessel were analyzed but it did not involve the IF explicitly nor the presence of drugs.

In this paper we want to compute the interstitial fluid pressure and flow within a tumor and use this information to predict drug

delivery within the tumor and its various dependencies on physiological parameters. These parameters include the blood vessel network morphology as opposed to simplified vasculature models, blood flow characteristics, blood pressure, permeabilities of the vessel walls, the interstitium and lymphatic walls, the mass of drug particles, i.e. the ratio of convection vs. diffusion. The tumor phenotype that we consider is a vascularized solid tumor for example a melanoma or glioma which grow in their natural environment in a human host with characteristic features as described above. Samples of such tumors were studied experimentally in [20,21,32].

One particular question is how far an elevated IFP is an obstacle to drug delivery. The general consensus is that elevated IFP reduces the convective flux through the vessel walls, due to the lowered pressure difference. However, our results indicate that this does not necessarily need to be true and that the relation between IFP and IFF is more complex, also involving vessel wall and tissue conductivity. Moreover our model predicts Peclet numbers (ratio of diffusion to convection) of the order of 1 in the tumor periphery. There the IF flow is largest and almost perpendicular to the boundary into normal tissue. Hence neither diffusion nor convection can be neglected. Finally our model also allows to study extreme cases like the delivery of very heavy drug particles, which are transported purely by convection. Their distribution is harder to predict than for a highly diffusive drug since it is dependent on long range transport along chaotic IF flow patterns which are eventually governed by vascular morphology.

This paper is organized as follows: Our mathematical model is defined in the next section. We first define the representation of the vessel network followed by remodeling rules during tumor growth and the procedure to construct the initial network. Then we define continuous parts, including the representation of tissue, modeling of tumor growth, IF flow, chemical concentration fields involved in tumor growth and finally drug transport. Finally a brief overview of our numerical implementation and a derivation of parameters are given. The subsequent results section comprises a discussion of a typical base case including a brief presentation of results obtained from tumor growth simulations and an in-depth analysis of IF flow and drug delivery. After that various other cases are analyzed before the paper is finally concluded.

Model

The model has been developed for simulations in three dimensions in Cartesian space. It is a hybrid model with discrete (vessels) and continuous parts (everything except vessels), see Figure 1 for an illustration. Continuous distributions are defined in the spatial domain Ω that we choose to be a cubic box. Discrete vessels are defined on a face centered cubic (FCC) lattice \mathbb{L} , which has 60° branching angles between parent and child branches. Varying branching angles would require modeling the vessel network in continuous space, which is computationally much more demanding but would not change the large scale morphology of the resulting network. Ω overlaps with \mathbb{L} and both are centered at the origin. The lateral size of \mathbb{L} is 8 mm and that of Ω is 4.5 mm. The size of \mathbb{L} is chosen to be larger to reduce boundary effects. Ω is initially filled with normal tissue and contains a small tumor nucleus located in its center.

We study IF flow and drug delivery for static tumor configurations. This means the tumor growth is simulated up to a specific time without explicit involvement of IF or modeling effects of drugs. Then IFP and IF flow are computed, and finally the spatiotemporal distribution of the drug concentration with the tumor frozen in time. A coupling would be interesting in the

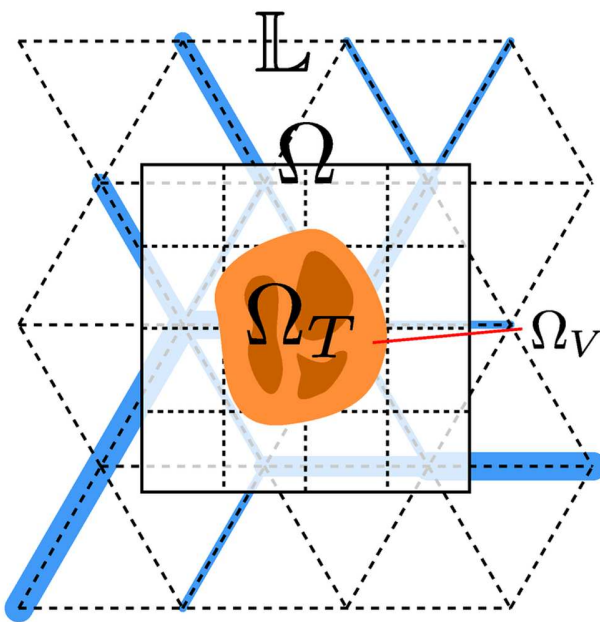


Figure 1. Illustration of the model components. \mathbb{L} denotes the lattice on which edges can be occupied with vessel segments. A few exemplary segments are shown as blue bars. \mathbb{L} coexists with Ω which denotes the region over that continuum equations are defined. The tumor region Ω_T is indicated in yellow. The darker tone indicates necrotic regions. Viable regions, denoted Ω_V are brighter. doi:10.1371/journal.pone.0070395.g001

context of studying various therapeutic protocols, which we defer to forthcoming publications.

Blood Vessel Network

Let $\mathbb{V} = \{\{v\}, \{n\}\}$ be the graph which formally describes vessels (edges) $\{v\}$ and junctions (nodes) $\{n\}$. Vessels coincide with bonds from \mathbb{L} , starting at one site of \mathbb{L} and ending at another. They can span multiple bonds but must be straight. Each vessel carries biophysical properties like radius or blood flow. We will introduce them as needed.

Blood flow is an essential part of our model. For vessels we compute the flow rate q_v (volume through its cross-section per time) and shear stress on the vessel wall f_v and the blood pressure p_v at the endpoints. The indices are dropped in the following. We assume ideal pipe flow within the vessels, obeying Hagen-Poiseuille’s law

$$q = \frac{\pi r^4 \Delta p}{8 \eta l}$$

$$f = \frac{r \Delta p}{2 l},$$

where Δp is the pressure difference between the vessel ends, l is the vessel length, η the blood viscosity and r the vessel radius. η is composed of the blood plasma viscosity $4 \cdot 10^{-6}$ kPa s times the relative viscosity $\eta_r(r, H)$ which is a function of the hematocrit H and the radius. For η_r we use a formula based on in vivo experimental data [22]. For simplicity, we assume that $H = 0.45$, the average in the human body. Mass conservation at each node requires that the flow rates of attached vessels sum to zero:

$\sum_v q_v = 0$ (Kirchhof’s law). Together with appropriate boundary conditions a system of linear equations for the nodal pressures arises which is solved numerically. As boundary condition the pressure is fixed at the arterial and venous roots of the vascular trees. These boundary pressures are determined as function of the vessel radius, also guided by experimental data [23] (see Supplement S1 (1)). Note that we do not incorporate the extravasated fluid into the mass balance, which is justified since, as we will demonstrate in the results section, the amount of extravasated liquid is orders of magnitudes smaller than the total vascular blood flow. In the rest of the paper q and f will denote the absolute value of the flow and shear force within a vessel - above they carried a sign.

Blood vessel network remodeling, the process in which the hierarchically structured initial network is reorganized by the growing tumor is defined by a set of stochastic and continuous processes which model angiogenesis, dilation, degeneration and collapse. They are implemented as updating rules which are applied consecutively in each time step. As a result, vessels are created, deleted or they change their properties. These rules are adopted straight forward from the 2d case [18] and presented here again for completeness.

Our time stepping scheme advances the vessel network in fixed steps of width Δt . Assuming that the frequency of a stochastic event is determined by a rate parameter k we approximate the probability for its occurrence in one time step as $p = k \Delta t$. We chose Δt sufficiently small such that $p < 1$. The time evolution of continuous processes described by differential equations of first order in time is handled by Euler’s method with time step Δt . In the following we describe the individual vascular remodeling processes that are incorporated into our model, for an illustration of these processes (see Supplement S1).

Sprout initiation models the event when endothelial cells (ECs) leave the parent vessel in order to grow a new sprout. It is a stochastic process that adds new vessel segments to the existing network. Lattice sites occupied by the existing network are visited in random order and at each of these sites a new segment is attached with probability $\Delta t / t_{EC}^{(sprout)}$ provided that the following conditions are met: the growth factor concentration is non-zero, the distance to the next branching point is larger than $l^{(spr)}$ and the time spent within the tumor is less than $t_{EC}^{(switch)}$. The new segments are created along neighboring lattice edges where the growth factor gradient is maximal and where no other vessels are already present. A vessel is tagged as “within the tumor” if at least one of the endpoints is within the tumor, which is true where the level set function $\theta(x) < 0$ (see below). Vessels also have a property which can tag them as sprouts and tell for how long they have been sprouts. We denote this “life-time as sprout” as τ .

Sprout migration is the process in which initial sprout vessels continue to grow. The probability is $\Delta t / t_{EC}^{(sprout)}$ for vessels which are tagged as sprout. A growth event is realized by appending a vessel segment along a single lattice edge in the same direction as the existing sprout. Sprout vessels are untagged and become normal vessels if the tip fuses with another vessel such that blood can flow or if their $\tau > t_{EC}^{(migr)}$, where $t_{EC}^{(migr)}$ is a parameter which defines the maximal sprout growth time. If the tip fuses with another sprout without creating a conducting branch then it remains tagged as sprout. Sprout initiation can also start from sprouts which emulates tip splitting as observed in-vivo and in-vitro. Sprouts are excluded from the collapse, degeneration and circumferential growth mechanisms.

Wall degeneration models the detachment and disintegration of cell layers and membranes around the vessel lumen. Therefore

we implement the property w which reflects the vessel wall thickness for normal vessels, and continuously decreases for tumor vessels with the rate Δw until zero. For values smaller than e.g. the size of an EC, w becomes an abstracted representation of the stability and tightness which the remaining EC layer provides. w is initialized (sprouts and initial vessels) with the wall thickness of real healthy vessels in dependence on their radius [24] (see Supplement S1).

Vessel collapse models pinch off of blood flow and complete disintegration of the vessel. It is a stochastic process where a vessel can be removed with probability $\Delta t/t_{EC}^{(coll)}$ under the condition that its wall stability variable $w < w_{(coll)}$ and its wall shear stress $f < f^{(coll)}$. Thereby $r^{(max)}$, $t_{EC}^{(switch)}$, $t_{EC}^{(coll)}$, $w_{(coll)}$ and $f^{(coll)}$ are model parameters. Recently the Ang-Tie system was modeled in a similar context [25]. This is straight forward to include in future work. Here we model the effects of it, rather than the system directly.

Vessel dilation models the switch to circumferential growth within the tumor [21]. During circumferential growth the vessel radius increases continuously with the rate Δr . The requirement is hereby that $r < r^{(max)}$, the average growth factor concentration over the segment is non-zero and the time spent within the tumor is larger than $t_{EC}^{(switch)}$.

Initial Blood Vessel Network Construction

To our knowledge there are no data sets from real networks available that cover a few millimeters of tissue and represent the complete vasculature including micro vessels in a form which is convertible to a “network of pipes” as required for our modeling purposes. Therefore we decided to generate it algorithmically. Our aim is to maximize the lattice occupation with a network which exhibits a hierarchical topology and homogeneously distributed capillaries.

A well known method is constraint constructive optimization (CCO) [26] in which a tree is grown by successively adding branch segments at locations given by some optimality criterion e.g. minimal total surface area. The constraints are that there is no geometrical overlap of the branch segments and that new segments must reach certain previously unperfused tissue blocks. The radii at branching points r_b, r_c behave according to Murray’s law [27] $r_a^\alpha = r_b^\alpha + r_c^\alpha$, where r_a is the radius of the parent branch and α is an exponent. α has been found to range between 2.55 and 3. The latter is a common choice which is also taken here.

In [28] a method was presented in which vascular trees on a lattice are stochastically grown and remodeled. This has the advantage of being relatively simple and being capable of building connected networks comprising arteries, capillaries and veins, whereas in CCO one typically has “dangling” terminal branches where capillaries should connect to. In [18] we adopted this method in order to obtain initial networks for 2d simulations. Later we applied it on a cubic lattice [19] and here we apply it on a FCC lattice. An illustration of the steps can be found in Supplement S1.

The initial network construction is based on a relatively coarse lattice with a lattice constant that corresponds to the mean intercapillary distance $\tilde{h}_L = 80\mu m$. After the construction of the network on the coarser network it has to be mapped on the finer lattice with $\tilde{h}_L = 10\mu m$ for use in the subsequent simulation. FCC lattices can be subdivided not unlike cubic lattices, meaning that sites and edges of the coarse lattice coincide with site and edges on the fine lattice. The tedious details are omitted here.

The construction is initialized by placing nodes which serve as roots for the trees onto boundary sites of the lattice. The type of these nodes is either arterial or venous, placed in alternating order.

The subsequent construction is then carried out in two stages. In stage one, trees are grown by a stochastic process in which “structural elements” are successively appended to one of the current tree leafs. As structural element we take either single vessels or a Y-shaped aggregate of three vessels. The element, its orientation and the leaf are determined by randomly (see Supplement S1). Eventually the lattice is filled but arterial and venous side are not interdigitating sufficiently to yield a homogeneous capillary distribution.

This is corrected in a second remodeling stage. Capillaries are temporarily inserted in-between neighboring arterial and venous terminals. We set the capillary radii to $4\mu m$. Radii of terminal branches are set to $4.5\mu m$ for arteries and $5\mu m$ for veins. Radii of higher level vessels are determined by Murray’s law. As a result an intermediate functional vascular tree is obtain for which blood flow is computed. Shear-stress dependent growth and shrinkage is carried out by stochastic removal and attachment of vessels from or to terminal branches. High shear-stress means higher probability to grow and vice versa. The idea originates from the observation that high shear stress indeed promotes vessel survival and stability [29]. We repeat this stage until the number of capillaries reaches a plateau. Trees can potentially grow from each of the root nodes. A few of these trees establish themselves while most of them regress and disappear.

For this paper we extended the algorithm from [18,19] with an “outer” loop producing increasingly fine resolved networks in a hierarchical fashion. This effectively reduces the tortuosity of major vessels. The first level (coarsest network) is constructed as described above. Then the lattice is refined, halving the lattice spacing and doubling the number of sites in each direction. Arteriovenous trees are kept in place and capillaries are discarded. Each vessel segment now occupies two lattice bonds. The lattice spacing is then reset to its former value. Hence, the spatial extend and segment lengths are effectively doubled. Now the random growth and remodeling steps are executed as above, where the previous terminal nodes now serve as new roots. This up-scaling and growth procedure is repeated a preset number of times. The results shown here were generated from a $25 \times 31 \times 31$ base lattice and 2 up-scaling steps.

The Continuum Model for Tissue

Our tissue model is based on the framework developed in [30] which describes the tissue as a mixture of various tissue constituents. A mathematical model is formulated in terms of smoothed fields of quantities such as density, velocity, stress, etc. Several constituents can coexist at one material point due to smoothing. Assuming incompressibility, one can describe the composition in terms of volume fractions with the constraint that the fractions sum up to one at every point in space. For brevity, we just give the final set of equations. A derivation can be found in [30], see also [31]. The result is a system of partial differential equations of the diffusion convection reaction type.

First, let us denote tissue constituents and their volume fractions:

- ϕ_T : tumor cells
- ϕ_N : normal cells
- ϕ_D : necrotic cells
- $\phi = \phi_T + \phi_N + \phi_D$
- m : ECM
- $l = 1 - \phi - m$: interstitial fluid

Tumor cells and normal cells are immiscibly separated by the interface $\partial\Omega_T(t)$, where $\Omega_T(t)$ is the tumor region.

$$\phi = \begin{cases} \phi_T + \phi_D, & \text{in } \Omega_T, \\ \phi_N + \phi_D, & \text{in } \Omega \setminus \Omega_T \end{cases}$$

This is analogous to immiscible liquids, where cell-cell adhesion forces correspond to the atomic forces in the liquids. We assume however that the adhesion forces are very weak, which allows us to neglect the surface tension term which would normally appear in the momentum balance equation. It will be included in future work.

All ϕ constituents move with the same velocity field v_ϕ which is driven by the gradient of a solid pressure (the isotropic component of the stress tensor) p_ϕ . It is based on the assumption that inertia is dominated by friction against a rigid ECM through which cells flow like a liquid through a porous medium. Therefore we have

$$v_\phi = -K_\phi \nabla(\phi p_\phi) \tag{1}$$

$$\frac{\partial \phi}{\partial t} + \nabla \cdot (\phi v_\phi) = Q_\phi \tag{2}$$

$$\frac{\partial \phi_D}{\partial t} + \nabla \cdot (\phi_D v_\phi) = Q_D \tag{3}$$

$$\dot{x} \cdot n = v_\phi \cdot n, \text{ for } x \in \partial \Omega_T, \tag{4}$$

where (1) is the condensed momentum balance, K_ϕ is a mobility constant and Q_ϕ and Q_D are source terms to be defined below. Note that this set of equations is applicable to tumors that have a clearly delineated rim as for instance rat C6 gliomas and human glioblastomas [21], human malignant melanoma [20], leiomyomata [32], etc. It is not valid for non-solid cancers like Leukemia and highly invasive tumors which do not have such a clearly delineated rim.

The motion of $\partial \Omega_T$ is formally defined by (4). In practice we use the level set method [33] to represent Ω_T and $\partial \Omega_T$ and introduce an auxiliary field $\theta(x)$ which gives the closest distance to $\partial \Omega_T$. It is signed so that $\theta(x) < 0$ for $x \in \Omega_T$. Over time it evolves according to the advection equation

$$\frac{\partial \theta}{\partial t} + v_\phi \cdot \nabla \theta = 0. \tag{5}$$

We can now define $\phi_T = (1 - \Theta_h(\theta))(\phi - \phi_D)$ and $\phi_N = \Theta_h(\theta)(\phi - \phi_D)$, where h is the lattice spacing of the numerical grid (see below) Θ denotes a smoothed Heaviside step function with width (see Supplement S1).

For the pressure we take

$$p_\phi(\phi) = \max[E(\phi - \tilde{\phi}_0), 0].$$

For simplicity and the lack of better knowledge we use a linear elastic law with elastic modulus E . Also, we assume that cells do not exert pressure upon each other when ϕ is less than the volume fraction in a fully relaxed state $\tilde{\phi}_0$.

The source terms are composed of contributions from T, N and D as follows

$$Q_\phi = Q_N^+ + Q_N^- + Q_T^+ + Q_T^- + Q_N^x + Q_T^x,$$

$$Q_D = -Q_T^x - Q_N^x,$$

where Q_α^\pm stands for proliferation and apoptosis of phase α and Q_α^x stands for necrosis.

We assume proliferation depends on packing density [34], i.e. volume fraction ϕ , and on available nutrients c_o . Cells do not proliferate in regions with high density where apoptosis reduces the density towards the so called homeostatic (equilibrium) density $\phi_{0,\alpha}$. At $\phi = \phi_{0,\alpha}$, and for sufficiently high c_o , apoptosis and proliferation rates cancel so that the net production rate $Q_\alpha^+ + Q_\alpha^-$ vanishes. Moreover Q_α^+ varies linearly with $\phi - \phi_{0,\alpha}$. Under low nutrient conditions proliferative activity stops, i.e. $Q_\alpha^+ = 0$ for $c_o < \zeta^+$, where ζ^+ is a threshold parameter. Consequently, apoptosis and possibly necrosis reduce the cell density. The difference between these events is that apoptosis leaves no debris as cells are deconstructed in an orderly fashion, i.e. the respective cellular material vanishes. Necrosis occurs under very low nutrient conditions if $c_o < \zeta^x < \zeta^+$, where ζ^x is also a threshold parameter. The fraction of cells undergoing necrosis is transferred to ϕ_D via the rates Q_α^x . In total this behavior is summarized in the following formulas:

$$Q_\alpha^+ = \phi_\alpha \max[\min[\frac{\gamma_\alpha^+}{\sigma_\phi}(\phi_{0,\alpha} - \phi) + \gamma_\alpha^-, \gamma_\alpha^+ \Theta(c_o - \zeta^+)], 0]$$

$$Q_\alpha^- = -\phi_\alpha \gamma_\alpha^-$$

$$Q_\alpha^x = -\phi_\alpha \gamma_\alpha^x (1 - \Theta(c_o - \zeta^x)),$$

for $\alpha = T, N$, where γ_α^+ , γ_α^- and γ_α^x are constant rate coefficients (proliferation, apoptosis and necrosis), σ_ϕ determines the sensitivity to density variations and Θ is the Heaviside function. Note, the use of “min” in conjunction with the Heaviside function. It limits the proliferation rate by either γ_α^+ or 0 (no proliferation) depending on nutrients.

Interstitial Fluid Flow

IF is commonly modeled as a liquid within a porous medium, e.g. [11,12,14,35]. We follow this approach and assume that cells and ECM collectively constitute the porous medium. Here we consider only stationary states, with a static tumor and a rigid medium, thus $\partial l / \partial t = 0$. Mass balance for the IF fraction l requires that

$$\nabla \cdot (lv_l) = Q_l, \tag{6}$$

with its velocity v_l and source distribution Q_l . Neglecting inertia terms one obtains the momentum balance equation

$$0 = \nabla \cdot \mathbf{T}_l + \mathbf{f}_l, \tag{7}$$

where \mathbf{T}_l is the stress tensor of the liquid, $(\mathbf{V})_{ij} = \partial T_{ij} / \partial x_j$ and f_l an interaction force with the other constituents. We use the results in

[31] and [30] where constitutive relations for $\underline{\mathbf{T}}_l$ and f_l were obtained for the case of a solid-fluid mixture. Assuming that the interstitial fluid is an ideal inviscid liquid, its stress tensor consists only of the contribution from the interstitial fluid pressure p_i or in the following just p .

$$\underline{\mathbf{T}}_l = -lp\underline{\mathbf{I}} \tag{8}$$

The interaction force is defined in such a way that we later obtain a variant of Darcy's law

$$f_l = -\frac{1}{K_l}\mathbf{v}_l + p\nabla l. \tag{9}$$

The first term represents friction with cells and ECM fibers, where K_l is a tissue dependent permeability coefficient. Substitution of equations (8) and (9) in (7) yields a variant of Darcy's law

$$\mathbf{v}_l = -lK_l\nabla p, \tag{10}$$

which leads to an elliptic equation for the pressure

$$-\nabla \cdot (l^2 K_l \nabla p) = Q_l. \tag{11}$$

Note that $l^2 K_l$ is the classical conductivity of the porous medium. We define $K_l = K_l(\theta)$ so that it smoothly interpolates between parameter values for tumor $K_{l,T}$ and normal tissue $K_{l,N}$. $K_{l,T}$ and $K_{l,N}$ are chosen so that the conductivity in the bulk assumes experimentally determined values. Note that l is almost constant distal to the tumor boundary and varies over a small value range since $\phi \in [0.5, 0.6]$.

The source term is composed of contributions from the vessel network Q_{lv} and lymphatic sinks Q_{ll} so that $Q_l = Q_{lv} + Q_{ll}$. Both are determined by the flux across the channel walls. For vessels, this flux is driven by the pressure difference $p_v - p_i$ and an osmotic contribution $\sigma[\pi_v - \pi_i]$ (Starlings equation) [36]. For lymphatics we assume an analogous relation but neglect osmosis due to the lack of data.

$$Q_{lv} = L_l^{(v)} S/V(p_v - p_i - \sigma[\pi_v - \pi_i]) \tag{12}$$

$$Q_{ll} = L_l^{(L)} S^{(L)}/V(p_L - p_i), \tag{13}$$

where p_L is the lymphatic pressure, $L_l^{(v)}$ and $L_l^{(L)}$ are permeabilities, S/V and $S^{(L)}/V$ are the channel surface area densities per volume and π_i and π_v denote the so called oncotic pressures. σ , the reflection coefficient, is a tissue specific value.

The standard approach for modeling exchange with vessels on a small scale would use boundary conditions at the vessel walls, while tessellating the surrounding space with a fine grained mesh. However this would make the large length scale which we are interested in inaccessible due to the size (we have of the order of 10^6 vessel segments). Instead we integrate the flux approximately over the vessel surfaces within each numerical grid cells and add it as source term. An approximation inherent to this method is that the space covered by the vasculature is not excluded from the interstitial space.

Hence (12) is not applied in this exact form. The source flux is implemented as superposition of smoothed delta functions δ_ϵ (see Supplement S1). Their locations y are generated from a stochastic uniform sampling of the surfaces of the cylindrical pipes which make up the vessel network. We write this formally as $y \in v$, where v symbolizes a vessel. For a numerical grid cell with index i and center x_i , Q_{lv} then becomes

$$(Q_{lv})_i = \sum_v \sum_{y \in v} c_i^{v,y} (p_v(y) - p_i - \sigma[\pi_v - \pi_i]) \tag{14}$$

$$c_i^{v,y} = \delta_h(x_i - y) L_l^y S^{v,y} / h^3,$$

where h is the grid spacing, L_l^y the wall permeability, $S^{v,y}$ is the area corresponding to a sample on v , and $p_v(y)$ is the blood pressure in v at position y , linearly interpolated between the nodes.

Different degrees of vessel leakiness are incorporated based on the maturity state w . We assume that w reflects the vessel wall thickness for sufficiently large vessels and that the wall's resistance $(L_l^y)^{-1}$ increases proportionally to the wall's thickness. This eventually leads us to

$$(L_l^y)^{-1} = \max \left\{ (\lambda_{l,T})^{-1}, \frac{(\lambda_{l,N})^{-1}}{w_{(init)}(r=5\mu m)} w^v \right\}, \tag{15}$$

where $\lambda_{l,T}$ and $\lambda_{l,N}$ are experimentally determined permeabilities for capillaries in tumor and normal tissue, respectively, and $w_{(init)}(r)$ is a formula based on experimental data [24] from which we obtain the physiologically normal thickness of the vessel wall depending on the radius (see Supplement S1 (2)). For small w the identification with the wall thickness breaks down and it becomes a mere abstract quantity inversely related to the amount of leakiness. In order to obtain realistic permeabilities for tumor vessels as well, we are therefore free to bound L_l^y from above by $\lambda_{l,T}$.

Lymphatics on the other hand are modeled as continuous sink distribution, where their surface area $S^{(L)}$ depends on the tissue type via θ analogous to K_l and moreover $L_l^{(L)}$ and p_L are assumed to be constant. Hence we can use (13) directly in the numerical implementation.

Chemical Concentration Fields

The basis for the description of dissolved chemicals is the following diffusion convection reaction equation which determines the evolution of the concentration $c^{(\alpha)}$ in constituent α [30].

$$\frac{\partial \alpha c^{(\alpha)}}{\partial t} + \nabla \cdot (\alpha c^{(\alpha)} \mathbf{v}_\alpha) = \nabla \cdot (\alpha D_c^{(\alpha)} \nabla c^{(\alpha)}) + Q_c^{(\alpha)}, \tag{16}$$

where $D_c^{(\alpha)}$ are effective diffusion constants (assumed to be scalar) and $Q_c^{(\alpha)}$ a source term. For nutrients and growth factors, we approximate the concentration as the equal in all phases $c^{(\alpha)} \equiv c$ under the assumption that the exchange among constituents is very fast. Then, summation of (16) over all α gives

$$\frac{\partial c}{\partial t} + \nabla \cdot (c \mathbf{v}_c) = \nabla \cdot (D_c \nabla c) + Q_c \tag{17}$$

$$\mathbf{v}_c = \phi \mathbf{v}_\phi + l \mathbf{v}_l + m \mathbf{v}_m,$$

where D_c is the composite effective diffusion coefficient, and v_c the composite velocity of the mixture. In the following we will use subscripts to c to denote specific chemical species: c_o denote nutrients, c_g are growth factors. For drug we distinguish concentrations in two different compartments $s_i : = c_{d,i}$ for which $i = 1, 2$ denote the extra- and intra cellular space, respectively.

Nutrients are represented by the most prominent one, namely oxygen with its concentration c_o . The time scale on which c_o relaxes after changes is negligible, of the order of seconds, and thus c_o is assumed to be always in a quasi stationary state, instantaneously adapting to changes in the system. Convection is neglected due to the dominance of diffusion. Consequently we obtain

$$0 = D_o \nabla^2 c_o - \gamma_o^- c_o + L_o S / V (c_o^v - c_o), \quad (18)$$

where we already replaced Q with a particular form of the source term: The second term represents consumption with the tissue dependent rate γ_o^- . The third term represents the diffusive flux across the vessel wall, which we treat analogous to the interstitial fluid source term (14), only L_l^v is replaced by L_o^v , and p_v by the blood oxygen concentration c_o^v . Since we already assumed that the hematocrit is constant over the whole vasculature, we further assume for simplicity that the oxygen concentration c_o^v also constant over the perfused parts and zero in unperfused vessels.

Growth factors are collectively represented as a single diffusible species with its concentration c_g . A prominent representative is VEGF which is over expressed in under-oxygenated tumor cells. We assume a constant production rate by tumor cells in locations where $c_o < \zeta^+$ and that it diffuses, binds and degrades everywhere equally. Instead of solving a diffusion equation we use a simpler and faster approximation based on a Green's function approach: every source site generates a linearly decaying contribution to c_g with the cutoff or diffusion radius R_g . Thus we have

$$c_g(x) = \int d^3 x' G(|x' - x|) \phi_t(x') \Theta(\zeta^+ - c_o(x')) \quad (19)$$

where we define $G(x) \propto \max(0, 1 - x/R_g)$, with a normalization constant so that $\int G(|x|) = 1$. Note that consequently, by definition of the angiogenesis rules, sprouting occurs within R_g of oxygen deprived TCs and a c_g gradient arises along which sprouts are oriented.

Transport and uptake of drug is modeled as diffusion advection process in the interstitial fluid and sequestration into the cell constituent. We distinguish between the concentrations s_1 in the IF and s_2 within cells as average over the solvent volume. The tissue volume average reads $s = s_1 l + s_2 \phi$ with the volume fractions l and ϕ as defined above. Following (16), we define specialized mass balance equations as

$$l \frac{\partial s_1}{\partial t} + \nabla \cdot (s_1 l v_l) = \nabla \cdot (l D_s \nabla s_1) + Q_{s_1} + Q_{12} \quad (20)$$

$$\phi \frac{\partial s_2}{\partial t} = -Q_{12}, \quad (21)$$

where Q_{12} is the exchange rate between the two compartments, Q_{s_1} the source contributions from vessels and lymphatics and D_s the diffusion coefficient in the IF. For a simple derivation of Q_{12} , we assume the total flux of molecules across the cell-fluid interface

area S within some volume V has the form $J = S(\tilde{k}_{21}s_2 - \tilde{k}_{12}s_1)$ with the rate constants \tilde{k}_{ij} which model the combined effect of diffusion through the cell membrane and intracellular binding and unbinding. We write S in terms of the single cell volume V_c and surface area S_c as $S = l \phi V S_c / V_c$, assuming that only the fraction l of the cell surface is in contact with the IF. Then we obtain with $k_{ij} = \frac{S_c}{V_c} \tilde{k}_{ij}$

$$Q_{12} = J/V = \phi l (k_{21}s_2 - k_{12}s_1). \quad (22)$$

Furthermore the contributions from vascular and lymphatic exchange are given by

$$Q_{s_1} = Q_{lv}^+ s^v - (Q_{lv}^- + Q_{ll}^-) s_1 + L_s^v S / V l (s^v - s_1), \quad (23)$$

where S has the original meaning of vessel surface area again. The diffusive permeability L_s^v is defined exactly like L_l^v in (14) and (15) with correspondingly exchanged subscripts including the permeabilities of tumor vessels $\lambda_{s,T}$ and normal capillaries $\lambda_{s,N}$. Q_{lv}^+ stands for extravasated fluid volume per mixture volume carrying the concentration s^v which is the concentration within the vessels. We assume that s^v is homogeneous over the whole network but time dependent where the dependency is given as closed formula e.g. an exponential decay after a hypothetical injection at $t = 0$. Q_{lv}^- stands for fluid uptake by vessels. Analogously Q_{ll}^- for uptake through lymphatic. Since these terms represent flow out of the interstitial space, they are multiplied by s_1 in order to obtain the respective solute flux. We could define a Q_{ll}^+ for symmetry but in practice fluid always flows into lymphatics, never in the opposite direction. We treat $Q_{l\beta}^\pm$ analogously to $Q_{\beta\beta}$, for $\beta = l, v$ in (12) and (13) with the exception that only contributions are added where the blood or lymphatic pressure is larger (+) or lower (-) than the IF pressure. Indeed $Q_{lv}^+ + Q_{lv}^- + Q_{ll}^+ + Q_{ll}^- = Q_l$.

Numerical Implementation

Solutions to partial differential equations are computed by finite difference schemes on a regular uniform staggered grid [37]. Numerical values for concentrations, volume fractions, etc. are defined on grid cells, while velocities and fluxes are defined on faces. The grid spacing h is $30 \mu m$ which corresponds approximately to two to three tissue cells. The diffusion terms are discretized by standard 9 point centered difference stencils. All system of linear equations are solved with (algebraic multigrid - if needed) preconditioned conjugate gradient method. Specifically, we use the solvers in [38]. Advection terms are treated by a central scheme for conservation laws [39]. In the time, the operator splitting technique [37] allows treatment of various sub-systems separately, i.e. sub-systems are advanced one by one, always using the newest available state. The cell volume fractions ϕ and ϕ_D are updated simultaneously with the 2nd order improved Euler method. The level set function θ is updated likewise. The vessel network is updated in 1 hour steps. In these periods for ϕ, ϕ_D and θ smaller sub-steps must be taken the length of which is dictated by the stability conditions of the time integration methods. In practice these steps are about $0.02h$ wide. Sometimes θ must be "redistanced" in order to restore the distance function property $|\nabla \theta| = 1$. The WENO method presented in [40] works very well for our purposes. The computation of c_g and c_o as well as redistancing are not performed every step. We determine the time between updating these fields by the time it takes tissue cells to cross a numerical grid cell and also by the time scale of the source

term, which gives the time $\min(h/v_\phi, (\partial Q_\phi/\partial t)^{-1})$, where we take the minimum over space and time since the last update. The numerical solution of the drug concentrations s_1 and s_2 is carried out using the central advection scheme [39] and the improved Euler method.

Parameters

A list of parameters for our base case system can be found in tables 1 and 2. The sprouting parameters $t_{EC}^{(sprout)}$ and $t_{EC}^{(migr)}$ are estimated from in-vitro endothelial cell (EC) migration experiments in [41]. It is known that angiogenesis is inhibited in ECs near existing branching points. For this $l^{(spr)} = 20\mu m$ seem reasonable, which are about two nearby ECs. The vessel dilation rate Δr and maximal radius $r^{(max)}$ was extracted from [21] where the spatial compartmentalization of human melanoma was described. The wall thickness w is initialized at $t=0$ depending on the vessel radius (see Supplement S1 (2)) guided by experimental data [24]. The wall degradation rate was estimated from [21] based on tissue section at increasing stages of tumor progression. We simply observed how long it takes until the supporting wall structures of a vessel with a certain radius are removed. For the critical collapse shear stress $f^{(coll)}$ we assumed that it is a low percentage of the average shear stress within the system, also guided by comparison of predicted vascular density levels with data from [20].

The oxygen level in our model is dimensionless and normalized to 1 which is the level within vessels. We divide the diffusion equation (18) by D_o . Hence it is left to determine the quotients with the consumption rates $\gamma_{o,\alpha}^-/D_o$ and vessel permeability $\lambda_{o,\alpha}/D_o$ for $\alpha = N, T$. For this purpose we use that the penetration depth (i.e. the length scale on which the solution decays around vessels) in tumor tissue is about $100\mu m$ and can be expressed as $\sqrt{D_o/\gamma_{o,T}^-}$. We assume that $\gamma_{o,T}^- = 4\gamma_{o,N}^+$. The precise number is arbitrary and non-crucial but reflects that tumor cells have a higher oxygen consumption rate leading to decreased tissue oxygen levels. We then tuned $\lambda_{o,N}/D_o$ so that the oxygen level in normal tissue is above ca. 1/2. For simplicity we assume that the permeabilities in tumor and normal tissue are equal $\lambda_{o,T} = \lambda_{o,N}$.

We assume that tumor and tissue cells have the same fastest possible proliferation rate (γ_N^+ and γ_T^+) of once per day. The time to live for normal cells is assumed to be 10 days after which they undergo apoptosis, yielding γ_N^- . Tumor cells have acquired mutations which enable them to circumvent the apoptotic mechanisms. Therefore we set $\gamma_T^- = 0$. Cells under severe hypoxia are assumed to die off relatively quickly within 48 h (γ_T^x and γ_N^x) and become necrotic tissue.

The oxygen threshold below which cells become necrotic is $\zeta^x = 0.03$. Cells stop proliferating when the oxygen level is below $\zeta^+ = 0.3$ which is ca. 60% of the lowest level in normal tissue. Since only tumor cells are ever exposed to low oxygen levels, we also do not distinguish between tumor and normal tissue here.

Our cell volume fractions reflect a high-density prototypical tissue. We assume that tumor cells have become less sensitive to solid pressure from nearby cells and so their homeostatic level is 0.6 ($\phi_{0,T}$) while it is 0.4 ($\phi_{0,N}$) for normal cells. Here we follow [34], where the idea for this pressure regulated proliferation originated. A similar model was also employed in [42] but with different parameters.

Parameters for interstitial fluid flow and drug transport are summarized in table 2. The permeability coefficients $K_{l,\alpha}$ and $\lambda_{l,\alpha}$ as well as osmosis parameters π_i , π_v and σ are obtained from [35] and the references therein. Where the actual permeability is

provided, e.g. $l^2 K_l$, we compute the coefficient by dividing with the typical $l \approx 0.2$ in the respective tissue. For lymphatics we assume a wall permeability ($L_j^{(L)}$) which is of the same order of magnitude as for capillaries ($\lambda_{l,N}$). The lymphatic surface area per volume ($S_N^{(L)}/V$) is estimated by assuming that there is a grid-like network with a channel every $100\mu m$ and a radius of $10\mu m$. We leave the tumor without lymphatics ($S_T^{(L)} = 0$), since these are absent or dysfunctional in tumors (see [5] and the references therein).

The drug distribution model is guided by experimental data on the pharmacokinetics of Doxorubicin, which has been used for a

Table 1. Model Parameters: Tumor Growth.

Parameter	Value	Unit	Description
n_l	(825,990,961)		Lattice size
h_l	10	μm	Lattice spacing
n_Ω	(150,150,150)		Lattice size
$h_\Omega \equiv h$	30	μm	Lattice spacing
	500	μm	Initial tumor diameter
$t_{EC}^{(switch)}$	24	h	Circumferential growth switch delay
$t_{EC}^{(sprout)}$	0.5	$\mu m/h$	Sprout extension speed
$t_{EC}^{(migr)}$	100	h	Sprout activity duration
$l^{(spr)}$	20	μm	Sprout sites minimum separation
$r^{(sprout)}$	4	μm	Initial sprout vessel radius
Δr	0.4	$\mu m/h$	Vessel dilation rate
$r^{(max)}$	25	μm	Maximum dilation radius
$f^{(coll)}$	2	Pa	Critical wall shear-stress
$t_{EC}^{(coll)}$	20	h	Unstable vessel survival time
Δw	-0.05	$\mu m/h$	Vessel wall degradation (w) rate
m	0.2		ECM fraction
$\tilde{\phi}_0$	0.4		Relaxed cell fraction
$K_\phi E$	510 ³	$\mu m^2/h$	Cell mobility \times elastic modulus
γ_T^+	1/24	h^{-1}	Tumor cell proliferation rate
γ_N^+	1/24	h^{-1}	Normal cell proliferation rate
γ_T^-	0	h^{-1}	Tumor cell apoptosis rate
γ_N^-	1/240	h^{-1}	Normal cell apoptosis rate
γ_T^x	1/48	h^{-1}	Tumor cell necrosis rate
γ_N^x	1/48	h^{-1}	Normal cell necrosis rate
σ_ϕ	0.2		Cell pressure sensitivity
$\phi_{0,T}$	0.6		Homeostatic tumor cell fraction
$\phi_{0,N}$	0.4		Homeostatic normal cell fraction
ζ^+	0.3		Oxygen threshold for proliferation
ζ^x	0.03		Oxygen threshold for necrosis
$\gamma_{o,T}^-/D_o$	80 ⁻²	μm^{-2}	Oxygen consumption rate in tumor
$\gamma_{o,N}^-/D_o$	200 ⁻²	μm^{-2}	Oxygen consumption rate in normal tissue
$\gamma_{o,D}^-/D_o$	200 ⁻²	μm^{-2}	Oxygen consumption rate in necrotic tissue
λ_o/D_o	0.04	μm^{-2}	Vessel permeability to oxygen
R_g	200	μm	Growth factor diffusion range

List of parameters for tumor growth.
doi:10.1371/journal.pone.0070395.t001

Table 2. Model Parameters: Interstitial Fluid and Drug.

$K_{l,N}$	20	$\mu\text{m}^2\text{kPa}^{-1}\text{s}^{-1}$	Normal tissue permeability coeff.
$K_{l,T}$	20	$\mu\text{m}^2\text{kPa}^{-1}\text{s}^{-1}$	Tumor tissue permeability coeff.
$K_{l,D}$	200	$\mu\text{m}^2\text{kPa}^{-1}\text{s}^{-1}$	Necrotic tissue permeability coeff.
p_L	-0.5	kPa	Lymphatic fluid pressure
$S_N^{(L)}/V$	0.01	μm^{-1}	Lymphatic surface area per volume in normal tissue
$S_T^{(L)}/V$	0		Lymphatic surface area per volume in tumor tissue
$L_l^{(L)}$	0.02	$\mu\text{mkPa}^{-1}\text{s}^{-1}$	Lymphatic wall permeability
$\sigma_{l,N}$	0.85		Osmotic reflection coefficient in normal tissue
$\sigma_{l,T}$	0		Osmotic reflection coefficient in tumor tissue
π_v	2.7	kPa	Vessel oncotic pressure
π_i	1.33	kPa	Interstitial oncotic pressure
$\lambda_{i,T}$	1	$\mu\text{mkPa}^{-1}\text{s}^{-1}$	Tumor vessel wall permeability
$\lambda_{i,N}$	0.01	$\mu\text{mkPa}^{-1}\text{s}^{-1}$	Normal capillary wall permeability
D_s	16	$\mu\text{m}^2/\text{s}$	Drug diffusion coefficient
$\lambda_{s,N}$	0.1710^3	$\mu\text{m}/\text{s}$	Vessel permeability to drug in normal tissue
$\lambda_{s,T}$	1710^3	$\mu\text{m}/\text{s}$	Vessel permeability to drug in tumor tissue
k_{12}	0.1	s^{-1}	Drug transport rate, extra-to intracellular
k_{21}	0.001	s^{-1}	Drug transport rate, intra-to extracellular

List of parameters for interstitial fluid flow and drug delivery.
doi:10.1371/journal.pone.0070395.t002

long time to treat various cancers. For the diffusion coefficient D_s and exchange rates k_{ij} we follow [13] who presented a similar model with additional cellular compartments. The diffusion constant stems from [43] where it was estimated as ca. $1000\mu\text{m}^2/\text{min}$, which we use as well. Given an isolated system with two compartments and transition rates k_{12} and k_{21} , the steady state concentration ratio equals the ratio of the rates. In experiments with cell cultures [44], intra-cellular to medium ratios of ca. 100 were observed. It seems reasonable to associate k_{12} , the cell uptake rate with diffusion through the vessel wall. In [13] this rate was estimated as 5.4min^{-1} . Thus we simply use $k_{12} = 10^{-2}\text{s}^{-1}$ and $k_{21} = 10^{-4}\text{s}^{-1}$. Note that k_{21} is close to the estimated lysosomal release rate which is also the slowest rate in the model proposed in [13], so this may be identified as bottleneck for release. It remains to determine the vascular permeabilities. We estimate these based on the diffusivity in plasma. As an approximation we write the permeability of a planar sheet of thickness L as D/L , where D is the diffusion constant. We take $180\mu\text{m}^2/\text{s}$ for D in plasma and we identify $L = 10\mu\text{m}$ with the thickness of the capillary wall. We assume that drug only diffuses through the gaps between endothelial cells (ECs). Assuming that in very leaky tumor vessels, there would be a circular gap with $1.5\mu\text{m}$ radius per EC [35], we arrive at the fraction of gaps over the vessel surface $G = 0.017$, assuming $10^2\mu\text{m}^2$ per EC, thus $\lambda_{s,T} = DG/L$. Assuming the difference between tumor and normal capillaries is due to leakiness, we determine $\lambda_{s,N}$ by requiring that the ratios are equal: $\lambda_{s,N}/\lambda_{s,T} = \lambda_{l,N}/\lambda_{l,T}$.

Results

Tumor Growth

Snapshots from a simulation are displayed in Figure 2. We performed 15 simulation runs, producing 15 final states which differ in their initial blood vessel networks (and the seeds for the

random number generator used for the stochastic events during the simulation). For a video visualizing the spatiotemporal evolution of the model see Supplements S14 and S14.

Initially, the tumor is prepared as a small sphere in which the tissue consists of tumor cells instead of normal cells. We define the distance function θ at $t = 0$ as the signed distance from the sphere boundary. The tumor is located in the center of the simulation box and has a radius of 0.5 mm. Increased oxygen consumption leads to decreased oxygen levels within the tumor which leads to expression of growth factors which again stimulates angiogenesis within R_g . Eventually blood-perfused neovasculature raises the oxygen level in the tumor periphery and enables further tumor growth. The first snapshot in Figure 2 shows the system after 100 h. At this point the system is in a state displaying the typical compartmentalization into high micro vascular density (MVD) rim, decreasing MVD toward the tumor center, isolated vessels threading the tumor, necrotic regions associated with unvascularized regions and tumor proliferation confined to its rim. The tumor continues to grow by vascularizing and pushing into the surrounding tissue, leaving a torturous chaotic tumor network behind. The final snapshot is taken at $t = 700$ h where the tumor has reached the edge of the continuum domain Ω . Its final radius is ca. 2.5 mm. By design of the tumor-vessel interactions similar observations were reported in earlier work in [15], [16], [18], where much simpler tumor models were used. See also Figure 3 where important system variables as a function of the distance from the invasive edge θ are shown.

To generate these plots we sorted data points based on their spatial position into bins, or shells surrounding the invasive edge according to their θ value. The width of the bins is $30\mu\text{m}$. Unless stated otherwise, we computed the averages of the binned values for each simulation run. The plotted data displays the means and standard deviations of the ensemble, not the spatial fluctuations. Spatial fluctuations can be seen in the map plots and are analyzed

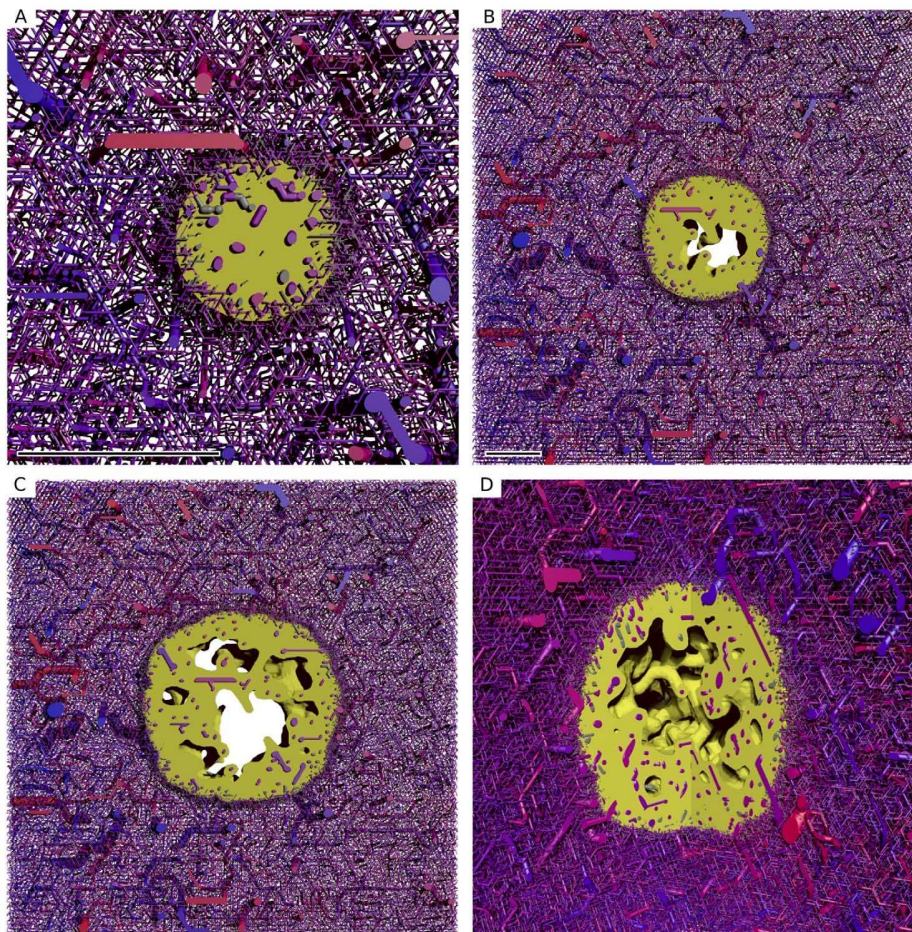


Figure 2. Snapshots from the simulation of a growing tumor. (A) to (C) depict $400\mu\text{m}$ thick slices through the origin. The scale bar indicates 1mm . (A) is a close-up. (B) and (C) have the same scale. The snapshots are taken after 100 h, 400 h, 700 h. (D) shows the same time as (C) from a different point of view where a quadrant was cut out. The boundary to the viable tumor mass is rendered as solid yellow surface. Necrotic regions appear as void spaces within the tumor. The blood vessel network is rendered as collection of cylinders, color coded by blood pressure. Red is high (arteries), and blue is low (veins).
doi:10.1371/journal.pone.0070395.g002

in more detail only for the distribution of drug. Note that we may define averages over (parts of the) vessel network formally as line integrals over the vessel center lines divided by the total length of respective parts. In practice we generate sampling points on center-lines and sort these into bins as we do with numerical grid values. This is applied e.g. in Figure 3B (vessel radius).

The predictions described above are in good agreement with experimental data from [20] and [21] for human melanoma xenografts and gliomas respectively. Our new continuum model describes tissue more realistically by the incorporation of actual host tissue cells, cell motility and cell-cell adhesion. We will report a more detailed analysis of the resulting morphological aspects elsewhere.

Interstitial Fluid Flow

Pressure, velocity and source terms were computed numerically for the final tumor configurations at $t = 700\text{ h}$. For the IF flow studies we assumed that the tumors are static from this time on. Generally the motion of the IF is coupled to the motion of the other tissue constituents since “empty” spaces are filled with the IF. However in our case the velocity of the fluid is orders of

magnitude larger than the velocity of cells, for which reason we can neglect these interactions.

Figure 4 shows slices through simulation data of one sample. Figure 4A displays the vessel volume fraction θ_v . The data are generated by superposition of smoothed delta functions which are distributed stochastically within the cylindrical volumes comprising the network edges. In Figure 4C we plotted the source term Q_I which is the IF volume flowing in or out of the interstitial space per volume and time. By definition, lymphatics are absent within the tumor, thus therein the only sources and sinks are blood vessels, which appear as lengthy blobs with positive (extravasation) or negative (uptake) contributions. Uptake is possible since the blood pressure can also be lower than the local IFP. At the tumor rim we see a significant amount of fluid being taken up, since there is a strong outward flux from the tumor which is absorbed into lymphatics and potentially also into parts of the neovascular plexus.

The IFP profile is elevated within the tumor and decays rapidly over its boundary. See Figure 4D and Figure 5A. The peak pressure in the tumor center is ca 6 kPa (45 mmHg). Outside it is 0.5 kPa (3.75 mmHg). We set the lymphatic pressure to -0.5 kPa , and the average blood pressure is ca 6.25 kPa (47 mmHg). In

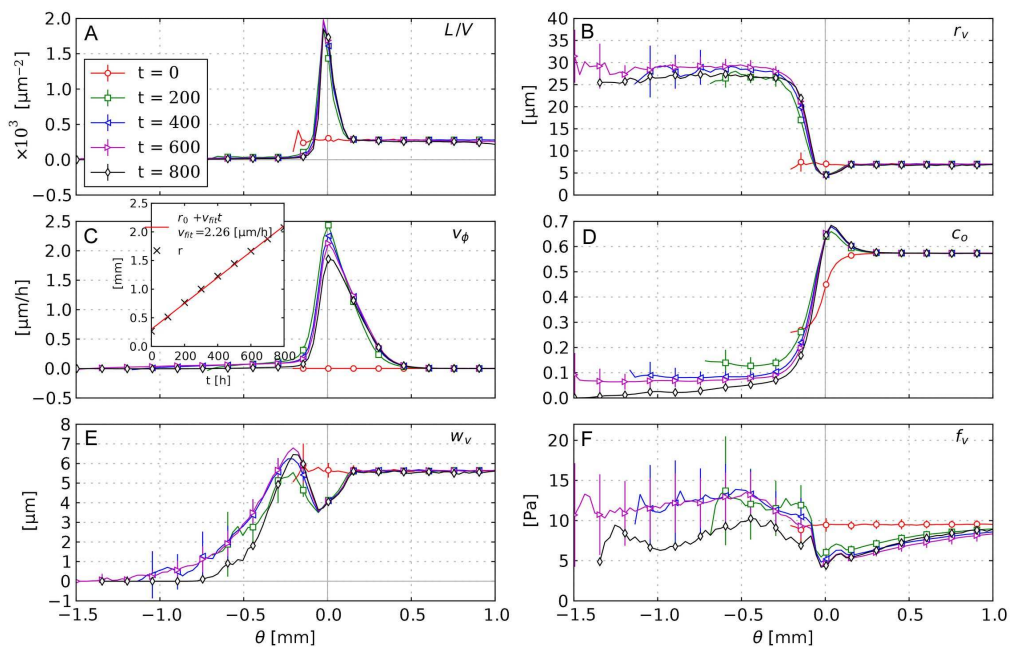


Figure 3. Radial distributions of biophysical properties in the tumor growth model. (A) MVD, (B) vessel radius, (C) cell velocity, (D) oxygen, (E) wall thickness, (F) wall shear stress. The distributions are plotted vs. the distance from the tumor surface θ . Each data point corresponds to the average over a small θ -interval. The errorbars indicate the standard deviation among different simulation runs (see text). The inset in (C) shows the approximate radius of the tumor and a linear fit. This radius is determined by averaging the distance from the origin over numerical grid cells where $-h < \theta < h$.
doi:10.1371/journal.pone.0070395.g003

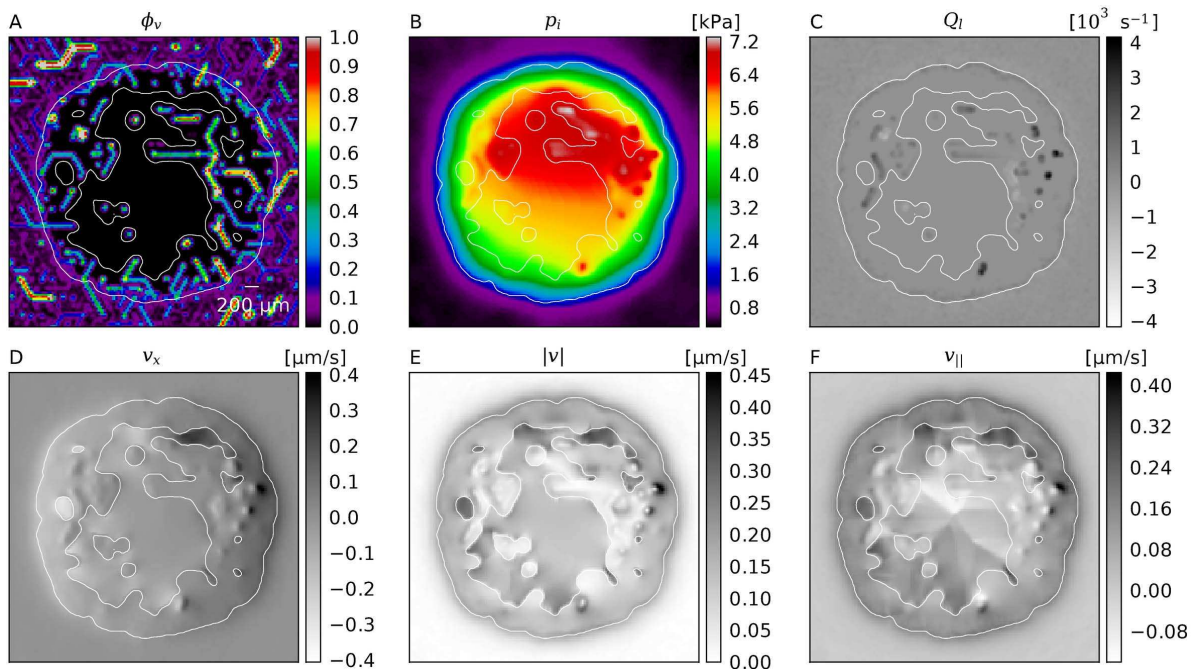


Figure 4. Snapshots of interstitial fluid flow quantities. (A) Vessel volume fraction, (B) IFP, (C) Fluid source term, (D) x-component of the IF velocity, (E) Magnitude of the IF velocity, (F) Projection of IF velocity onto the outward direction, i.e. onto the gradient of θ . The plots were generated from 2d slices through the center of a typical simulation result from the base case. The contour line indicates the boundary of the viable tumor mass. The internal regions consist of necrotic tissue, while the outer area is normal host tissue.
doi:10.1371/journal.pone.0070395.g004

models using pure capillary networks a pressure range from 15 to 25 mmHg is commonly either directly set or imposed via boundary conditions, e.g. in [10,12,14,15]. In the presence of higher level arteries (as in our model) a much higher IFP can be observed, because of the elevated pressure in arteries and connected vessels. Mean in vivo tumor IFPs are reported in [35] from 0 to 5 kPa (38 mmHg) for various tumor types. Most tumors exhibit a high degree of heterogeneity, with deviations from the mean of 100%. The elevated IFP has a finite “penetration depth” into normal tissue (see below). Beyond that the IFP appears relatively homogeneous. Fine grained fluctuations are introduced by fluctuations of the capillary surface area per grid cell.

The order of magnitude of the interstitial fluid velocity is considered to be 0.1 to 1 $\mu\text{m/s}$ [4,45–47]. In particular, it is found to be highest close to the tumor boundary where the pressure gradient is steepest, leading to a strong outward flux. Our results, shown in Figure 4A and Figure 5B are in agreement with this experimental observation. The velocity peak in the region is at 0.2 $\mu\text{m/s}$.

Furthermore the velocity patterns in our data show a significant amount of fluid being transported in between tumor vessels. In Figure 4D this can be directly observed. For the whole ensemble we measured the outward projection of the velocity vector

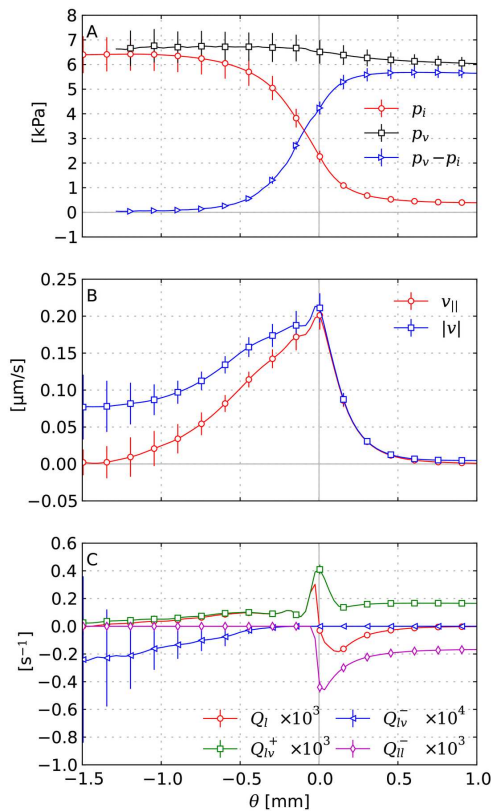


Figure 5. Radial distributions of interstitial fluid flow quantities. (A) IFP, blood pressure and the pressure drop across the vessel wall. (B) IF velocity: $|v|$ plots the magnitude and $v_{||}$ the projection onto the direction of the shortest path to the tumor boundary $v_i \nabla \theta / |\nabla \theta|$, respectively. (C) The total fluid source term Q_I as well as contributions to it which are: extravasation Q_{lv}^+ , uptake by vessels Q_{lv}^- and uptake by lymphatics Q_{ll}^- . Each data point corresponds to the average over a small θ -interval. The error bars indicate the standard deviation among different simulation runs (see text). doi:10.1371/journal.pone.0070395.g005

$v_{||} \equiv v_i \nabla \theta / |\nabla \theta|$ together with the velocity magnitude $|v| \equiv |v_i|$, which are plotted in Figure 5. Spatial distributions from one simulation can be seen in Figure 4E and F. Within the tumor center, $v_{||}$ vanishes whereas $|v|$ decreases to ca. 0.05 $\mu\text{m/s}$. This means that the flow becomes increasingly isotropic toward the center, where the IF apparently flows in between isolated tumor vessels instead of to the tumor boundary. This flow is more than an order of magnitude faster than IFF in normal tissue.

In the tumor periphery fluid uptake by lymphatics is significantly increased compared to normal tissue further away (Figure 5C, Q_{ll}^-) because since lymphatic vessel are absent in the tumor, the extravasated fluid must cross the tumor boundary to be absorbed in normal tissue. The determining equation for the IF pressure p , and the equations for oxygen and growth factors, have a structure like $\nabla^2 u - cu = r$, for some constant c , dependent variable $u(x)$ and arbitrary distribution $r(x)$. For this equation any local change in r causes an exponentially decaying disturbance in u . The length scale of the decay is $1/\sqrt{c}$. Since $c = L_i^{(L)} S^{(L)} / V (K_i l^2)^{-1}$ for the IFP, we see a “penetration depth” of 98 μm .

Furthermore, in addition to the fluid that originates from the tumor interior, we find that the neovascular plexus extravasates a huge amount of fluid (Figure 5C, Q_{lv}^+). The collective surface area of these vessels is large due to the amount of vessels, they are very permeable and the $p_v - p_i$ difference is relatively large, so this is not surprising but it has implications for the escape of tumor cells from the rim into the lymphatic system, and subsequently metastasis.

At this point we should discuss the validity of our approximation that neglects the loss of blood plasma from the vasculature due to extravasation. Apart from the study of IF flow this approximation is standard but in particular for tumor blood flow the coupling through leaky thread-like vessels it is a more severe simplification, where one would ideally solve for the IFP and blood pressure simultaneously and fully coupled. To clarify this we first determined the fraction of extravasated fluid relative to the total vascular blood flow into the tumor. To be precise we computed

$$Q_I^{+(rel)} = \frac{\int_{\Omega_T} Q_{lv}^+ dx}{\sum_{v \in \mathbb{V} \cap \partial \Omega_T} q_v},$$

where $\mathbb{V} \cap \partial \Omega_T$ symbolizes the set of all vessels which intersect $\partial \Omega_T$ with blood flow directed into the tumor. We obtain $Q_I^{+(rel)} = 4 \pm 1.6 \cdot 10^{-4}$ over our base case states, which suggest that a fully coupled solution would not differ significantly from our solution. For completeness, the absolute values are presented in Table 3.

Moreover, we estimate the length scale over which IFP coupling would cause a decrease of the blood pressure along a single isolated vessel. For this purpose let $q(x)$ be the flow rate as volume per time through a blood vessel with the axial coordinate x . It is determined by $q = -A p'$, i.e. Poiseuille’s law, where $'$ denotes the derivative with respect to x , A a conductivity constant and $p = p(x)$ the blood pressure. The fluid loss through the gaps of the vascular walls is the derivative of q , i.e. $q' = B(p_i - p)$, whereby we have incorporated the osmosis contribution $\sigma(\pi_v - \pi_i)$ into an effective blood pressure p . B is defined as $B = 2\pi r L_i^y$, where L_i^y is the wall permeability constant. p_i denotes the interstitial pressure.

If we now assume that $p_i \equiv const$, we can easily derive a characteristic length scale λ over which p approaches p_i . By combining the above equations, we solve for $p(x)$ and obtain $p(x) = \exp(x/\lambda)C_1 + \exp(-x/\lambda)C_2 + C_3x + C_4$, where

Table 3. Tumor volume, blood flow and interstitial fluid sources.

$ \Omega_T $	$2.72 \pm 0.04 \cdot 10^{10}$	μm^3	Tumor volume
$ \Omega_T / \Omega $	0.286 ± 0.004		Fractional tumor volume
$\sum_{v \in V \cap \partial\Omega_T} q_v$	$7.7 \pm 3.4 \cdot 10^9$	$\mu\text{m}^3 \text{s}^{-1}$	Blood flow through tumor boundary
$\int_{\Omega_T} Q_i^+ dx$	$2.5 \pm 0.3 \cdot 10^6$	$\mu\text{m}^3 \text{s}^{-1}$	IF influx (tumor)
$\int_{\Omega_T} Q_i^- dx$	$-1.3 \pm 1 \cdot 10^5$	$\mu\text{m}^3 \text{s}^{-1}$	IF uptake (tumor)
$\int_{\Omega_N} Q_i^+ dx$	$1.16 \pm 0.06 \cdot 10^7$	$\mu\text{m}^3 \text{s}^{-1}$	IF influx (normal)
$\int_{\Omega_N} Q_i^- dx$	$-1.40, \pm 0.08 \cdot 10^7$	$\mu\text{m}^3 \text{s}^{-1}$	IF uptake (normal)
$Q_i^{+(rel)}$	$4 \pm 1.6 \cdot 10^{-4}$		Ratio of IF extravasation to blood flow.

$|\Omega_T|$ and the quantities involving Q were computed by numerical integration, i.e. summation over grid cells, weighted by $\Theta(\theta)$ or $1 - \Theta(\theta)$ as required by the respective region. Tumor blood flow was computed by summing q_v over vessels where (i) the sign of θ changes between the endpoints, (ii) blood flow is directed into the tumor, which is straight forward to check based on the nodal blood pressures and θ . Of course, mass is preserved, i.e. inflow and outflow are equal (in particular since we neglect extravasated fluid). Also due to mass conservation, the IF uptake in normal tissue is slightly higher than influx because flux from the tumor is absorbed as well. Uptake within the tumor is low due to the lack of lymphatics. $Q_i^{+(rel)}$ is the ratio of $\sum_{v \in V \cap \partial\Omega_T} q_v$ to $\int_{\Omega_T} Q_i^+ dx$, indicating that only a very small fraction of the blood plasma which is entering the tumor is lost into the tumor interstitium.
doi:10.1371/journal.pone.0070395.t003

C_1, C_2, C_3 and C_4 are constants which must be determined by boundary conditions. For λ one obtains $\lambda = \sqrt{A/B}$ i.e. the root of the ratio of flow to wall conductivity. Note that for $\lambda \rightarrow \infty$ one can recover the standard Poiseuille's law. Based on our model parameters, the order of magnitude of λ is estimated to lie within 10^3 to $10^6 \mu\text{m}$, depending on the vessel. Actual measured values are shown in Figure 6D. Within the tumor λ is actually longer than the system size. For capillaries λ may be around 1 mm, which is still much longer than the length of typical capillaries. The value of λ for major normal vessels is similar to tumor vessels. Other relevant variables namely B , q' and q are shown in Figure 6A, B, and C, respectively. In spite of the simplifications used we think this justifies the uncoupled evaluation of the interstitial fluid flow.

In the following we further comment on blood flow and extravasation. In silico data for $B = 2\pi r L_i^v$ in Figure 6A shows a 20 fold increase from normal tissue to tumor tissue. Remarkably we can distinguish between an increase of r and L_i^v . The clustering with short ramp-up is associated with initially thin vessels which dilate to the maximal radius $r^{(max)}$. Their permeability L_i^v increases simultaneously and eventually hits its upper bound $\lambda_{i,T}$. A plateau of maximal B forms where r and L_i^v reached their bounds which is here about $250 \mu\text{m}$ behind the tumor boundary. The lower ramp corresponds to thicker vessels, too thick to dilate (because $r > r^{(max)}$), but for which L_i^v increases.

The flow rate q , shown in Figure 6C, displays a clear distinction between tumor and normal tissue as do most other variables. In the tumor center it is more uniform and orders of magnitude higher than in normal tissue. q varies with the radius like r^4 , thus dilated vessels provide very well conducting pathways acting as arteriovenous shunts. Most of the data points in normal tissue stem from capillaries which have respectively slow flow rates. Going up the vascular hierarchy, we find increasing flow rates beyond those of tumor vessels and of course less vessels. In the neovascular plexus close to the tumor boundary we observe lower-than-normal

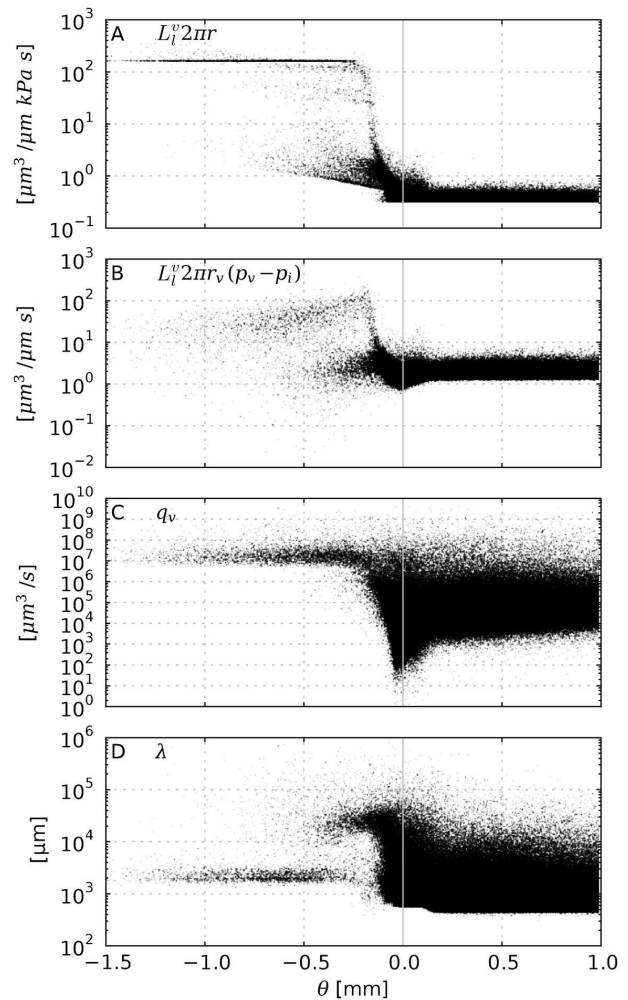


Figure 6. Radial scatter plots of properties related to (trans-)vascular flow. (A) the vessel wall permeability multiplied by the circumference $L_i^v 2\pi r$, (B) the transvascular flow $L_i^v 2\pi r (p_v - p_i)$, which is the fluid volume that flows through the vessel wall per vessel length and time. (C) the flow rate of vessels q_v , i.e. the blood volume per time that flows through the cross section. (D) an approximate length scale over which p_v decays toward p_i (see text). Data points stem from uniformly distributed sampling points on the vascular networks of 15 simulation runs.
doi:10.1371/journal.pone.0070395.g006

flow rates, which is plausible since the blood volume is distributed over more vessels, which implies slower flow velocities in order to satisfy mass conservation. See also our results and discussion in [18].

The flow rate through the vessel wall q' , shown in Figure 6B, correlates well with the wall permeability B weighted by the vessel circumference. Its magnitude within the tumor is about an order of magnitude larger than in normal tissue. This contradicts the common hypothesis that increased interstitial pressure hinders fluid extravasation. However, the permeability increase dominates the decreased IF pressure difference, which is only halved within the tumor compared to normal tissue.

Drug Transport

Here we analyze the spatiotemporal evolution of the concentration distribution s of some substance over the time frame of 96

hours. s was computed numerically according to (20) based on the data from previous simulations of tumor growth and interstitial fluid flow. Thereby the tumor is considered static and the IF flow is in a stationary state. Normally a tumor would grow further during this time frame. However since we do not model pharmacodynamics (i.e. cell killing) it seems reasonable to make this simplification. Parameters for our base case are derived from data for Doxorubicin, a commonly used chemotherapeutic drug. Assume that initially the tissue is “clean” i.e. without drug. A bolus injection into the hosts body is modeled by the time varying blood plasma concentration $s^v(t)$. For an injection we take the exponential function $s^v(t) = \exp(-t/t_{sv})$ with the time scale $t_{sv} = 1$ h. Our results are presented with unit-less normalized concentrations for which $s^v(0) = 1$.

The distribution of Doxorubicin is usually observed in vivo with the aid of fluorescence imaging, e.g. in [43,44,48]. Typically one observes exponentially decaying concentration profiles around tumor vessels, at least during the first few hours. Eventually drug is distributed relatively evenly. When the blood is cleared of drug, molecules diffuse back into the blood stream and so the concentration near vessels decreases again. The overall drug level decreases over the course of a few days until all drug is cleared from the tissue.

Our simulations results agree well with this observation. To illustrate this, Figure 7 shows the spatiotemporal evolution of the concentration s in a sequence of snapshots. The data are taken from one of the 15 systems we considered as the base case. See Supplement S16 for a video.

Upon closer inspection of these figures and comparison with Figure 4 A it becomes apparent that some vessels are not releasing drug. The explanation is that close to the tumor rim we have two classes of vessels with comparable radii but different permeabilities: (i) Mature vessels stemming from arterioles or venules which release little drug and (ii) dilated capillaries. Toward the tumor center these differences vanish due to wall degeneration.

In Figure 8A drug concentrations are plotted as average $\langle s \rangle_\theta$ against θ in the same way as Figure 3, i.e. as average over shells of constant θ . Initially these drug profiles show a strong similarity with the profiles of the vessel volume fraction which is also plotted. Both have a peak at the tumor rim and decay into the tumor to

significantly lower levels than in normal tissue. Of course, we expected such a correlation, because the “bulk” transvascular flux is proportional to the vessel surface area. This proportionality also implies a faster drug uptake by diffusion once blood is cleared from drug. Therefore one might naively expect that the tumor rim is cleared fastest of drug, afterwards normal tissue, and finally the tumor center. The actual result at $t = 96$ h is different, namely that the profile is relatively flat and monotonously increasing into normal tissue. Following the discussion below, it is clear that convection fulfills a significant contribution to transport, moving drug outwards and flattening the profile. This is studied in more detail considering a diffusion dominated system in the the case (iii) (see below).

The ratio of convection to diffusion is quantifiable by the Peclet number which is defined as $Pe_L = LV/D$, where L is a characteristic length, V the velocity and D the diffusion constant. $Pe_L > 1$ means that transport is convection dominated and $Pe_L < 1$ means diffusion domination. It depends on L , so we analyze our system by determining L while requiring that $Pe_L = 1$ whereby we denote respective L as $L_{dc} = D/V$. The mean over the tumor $\langle L_{dc} \rangle_T$ is $150 \pm 4 \mu m$. This practically the same length as the diffusion range of oxygen, i.e. the distance from drug sources (vessels) up to which viable tumor cells are present. Hence diffusion and convection are predicted to be equally relevant. In contrast L_{dc} is two orders of magnitude larger within normal tissue which means that transport to spaces in-between capillaries is strongly diffusion dominated (see Supplement S13 Figure 1A for a spatial L_{dc} map).

In Figure 8B the mean drug concentration $\langle s \rangle_\rho$ is shown against the distance from tumor vessels ρ . The profiles were generated exactly like the plots against θ by defining ρ as the (signed) distance from the region where the vessel volume fraction $\phi_v > 0.01$ which captures all vessels. Another interpretation of ρ is a penetration depth into the cuffs surrounding vessels and further into necrotic regions. It shows that over the first few hours $\langle s(\rho) \rangle$ is very well fitted by an exponential decay function $\propto \exp(\rho/\rho_0(t))$. Where the length scale ρ_0 is approximately $30 \mu m$, which is in good agreement with [43,44,48]. During the 3 to 24 hours period the exponential behavior vanishes. Thereby the level at the “tail” increases while the level in vascularized regions

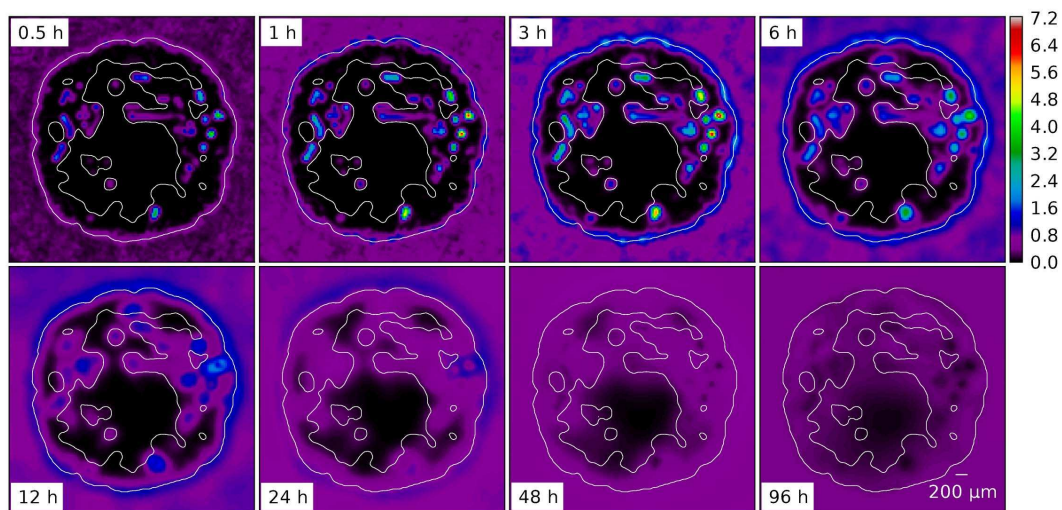


Figure 7. Series of snapshots of the rug distribution s of a typical base case system. Times and length scale are as indicated. The contour delineates the viable tumor mass. doi:10.1371/journal.pone.0070395.g007

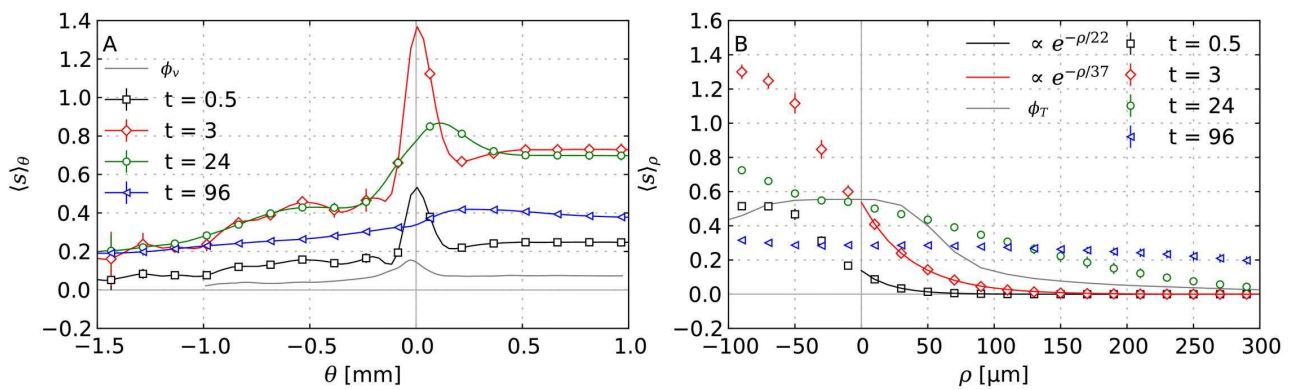


Figure 8. Profiles of drug concentrations at different times. (A) radial distributions of the drug concentration vs. θ similar to Figure 5. (B) the same concentration distributions are plotted vs. the distance ρ from nearby vessels. ϕ_v and ϕ_T show the profiles of the volume fractions of vessels and tumor cells, respectively. Early on, the concentration plots in (B) can be fitted with an exponential in agreement with experimental data as given in the legend. Each data point corresponds to the average over a small θ or ρ -interval, where ρ is the distance from vascularized regions similar to θ (see text). The error bars indicate the standard deviation of the ensemble. doi:10.1371/journal.pone.0070395.g008

decrease. After 48 hours the profile is almost flat within the local fluctuations at about 30% of the peak value at 30 min.

For the further analysis and quantification of drug delivery we have to introduce an appropriate metric that represents the time-independent spatial distribution of drug doses. Quantities which commonly enter pharmacodynamical models are the maximal concentration over time and the area under curve (AUC) which is the time integral of the concentration. Even in the case of Doxorubicin, which has been known for a long time, models using either one have emerged, see e.g. the discussion in [49]. Mathematically those quantities correspond to the $\|\cdot\|_\infty$ and $\|\cdot\|_1$ norms (over time), respectively. $\|f\|_1$ can be bounded by $\|f\|_\infty \leq \|f\|_1 \leq t\|f\|_\infty$ where f is a proper function and t is the observation duration. This bound is of course not very strict so it seems justified to consider both. We use intracellular concentrations since we assume that drug has to enter the cell to e.g. bind to DNA in order to be efficacious. Our denotations are ICMAx for $\|s_2\|_\infty$ and ICAUC for $\|s_2\|_1$.

As expected we find the highest values near tumor vessels from where it decreases into the unvascularized (necrotic) regions further away, see Figure 9A and B. ICMAx and ICAUC are qualitatively similar and also display strong similarities with early concentration distributions at ca. $t = 3$ h. ICMAx is comparably sharp and in fact approximately s/ϕ at $t = 3$ h. The extracellularly dissolved drug is negligible since its concentration is two orders of magnitude lower. Hence, $s \approx \phi s_2$. Obviously ICMAx is very sensitive to the high initial drug levels, whereas ICAUC gives more weight to later smoother distributions and thus appears more blurry. Their penetration depth is about $200\mu\text{m}$ so the whole viable tumor mass obtains significant (meaning non-zero) contributions. The ratio of local maximum to minimum for the AUC is $23 \pm$ whereas it is 122 ± 2 for ICMAx. In Figure 9C and D, ensemble averages of ICMAx and ICAUC are plotted as radial distributions together with the vessel volume fraction. The correlations are obvious and can be explained by the same reasoning as for the time-dependent concentration distributions. The displayed compartmentalization in decreasing exposure towards the center and peripheral peak is qualitatively retained for most of the parameter variations except for extreme cases with drastically increased interstitial transport rates such as case (v) (see below).

Variations

In this section we discuss a number of physiologically relevant variations of the base case scenario. We consider the following cases separately:

- (i) Heavier drug particles.
- (ii) Prolonged infusions.
- (iii) Neglected Convection.
- (iv) Vascular permeability.
- (v) Hydraulic conductivity of interstitium.
- (vi) Amount of normal lymphatics.
- (vii) Tumor lymphatics.

For all cases we produced the corresponding data shown in Figures 3, 4, 5, 6, 7, 8, and 9. They are compiled in Supplements S2, S3, S4, S5, S6, S7, S8, S9, S10, S11, and S12. Videos visualizing the spatiotemporal evolution of the concentration distributions in cases (i), (ii) and (iii) are provided as Supplements S17, S18 and S19.

Below we discuss the physiological implications of these results. In Figure 10 we present a comparison of the mean $\langle \cdot \rangle_\xi$ and standard deviation (STD) $\text{std}_\xi(\cdot)$ of the ICAUC and ICMAx distributions. ξ stands for a region over which mean and STD are taken. V denotes the viable tumor where $\phi_i > 0.5$, TB the boundary where $-250\mu\text{m} \leq \theta \leq 0$ and TI the interior where $\theta < -250\mu\text{m}$. This serves as an assessment of drug delivery efficiency. Higher mean, and smaller STD (i.e. less spatial fluctuations) means better delivery. Histograms representing actual probability density functions for ICAUC and ICMAx are shown in comparison in Supplement S13.

(i) Heavier drug particles. In this case we consider a drug with a molecular weight of 10^5g/mol . This corresponds to the application of viruses or nano particles as delivery system, which we realize by the adjustment of diffusion related parameters, namely $\lambda_{s,N}, \lambda_{s,T}, D_s$ and k_{ij} . For a particle performing Brownian motion, the diffusion constant scales with $1/\sqrt{m}$ of the particle mass m . Hence we scale those parameters by $\sqrt{540/10^5}$, where 540g/mol is the molecular weight of Doxorubicin from the base case. This leads to a strongly convection dominated transport where L_{dc} is of the order of $1\mu\text{m}$.

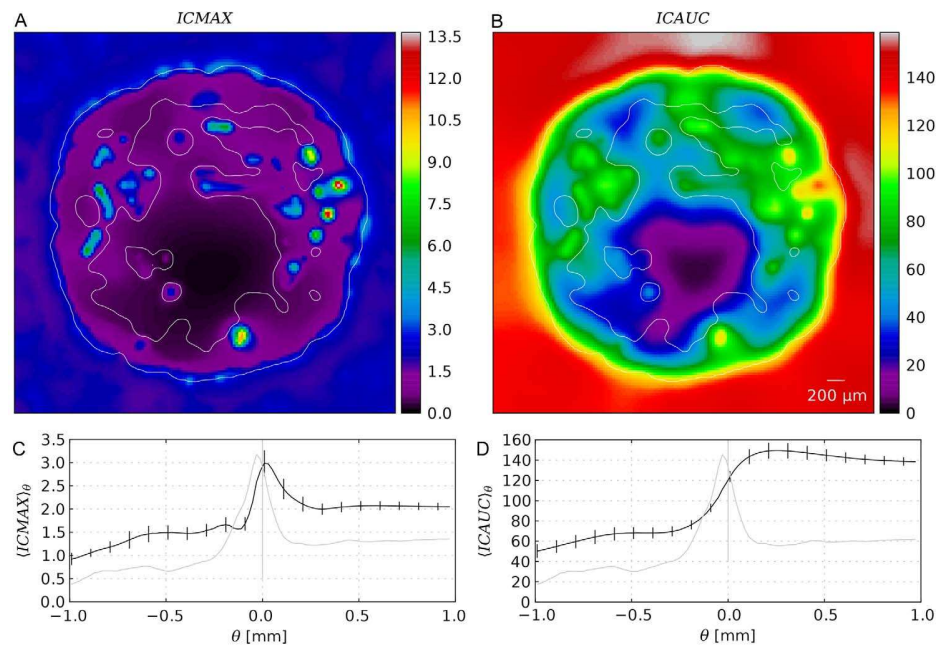


Figure 9. Spatial distributions of drug exposure metrics. (A) Snapshot of the intracellular maximal concentration ICMAX, and (B) snapshot of the time integrated concentration ICAUC from a typical simulation result from the base case. The contours delineate the viable tumor mass. (C) and (D) Plots of ICMAX and ICAUC from the base case as ensemble averaged (15 systems) radial distributions (black) similar to Figure 5. In addition, the vessel volume fraction is plotted as well (grey). doi:10.1371/journal.pone.0070395.g009

We see that for heavy particles the IF flow clearly dominates the drug distribution as seen in Figure 11 (see also Supplement S2, and the video provided in Supplement S17). As a result the tumor contains many small, isolated regions where a small amount of drug is delivered. This is reflected by the PDFs ($\bar{p}(\text{ICMAX})$, $\bar{p}(\text{ICAUC})$) which are broader and lower values are more common. Interestingly, the p_{auc} distribution completely changes from bell shaped to almost box shaped, see Supplement S13 Figure 2. The mean values $\langle \text{ICMAX} \rangle_V$ and $\langle \text{ICAUC} \rangle_V$ decrease by ca. 50% which can be expected due to the decreased transvascular diffusivity.

(ii) Prolonged infusions. Chemotherapy often follows a complicated schedule with several prolonged infusions, which is important to avoid toxicity to normal tissue. The basic idea is that drug given in low concentrations accumulates in the tumor, whereas the concentration in normal tissue remains tolerable. As a simple case we consider the administration of a prolonged infusion. In (ii)a during a 24 h period and in (ii)b continuously during 96 h. The ICMAX and ICAUC distributions, are surprisingly similar to the base case (see Supplements S3, S4 and the video Supplement S18). The difference lies in the scale. The average concentration $\langle s \rangle_T$ increases approximately linearly in time for as long as the infusion is active.

That means even by the end of our simulation at $t = 96$ h the tumor is far from saturated. We expect this to occur when influx equals removal of drug. Assuming that $s_2/s_1 = k_{12}/k_{21}$ in a quasi steady state the time scale for a purely diffusing particle to move 1 mm can be estimated via the diffusion law $\langle x \rangle^2 = Dt$ as 1700 h, which is a reasonable estimate for the saturation time scale. Note that our results likely overestimate concentrations and underestimate the speed of the transport due to the lack of saturable cellular components.

(iii) Neglected Convection. This case serves to gain insight in the role of convective transport of drug through the interstitium.

For this purpose the convective term in (20) was neglected. Figure 12 shows that initially ($t = 1/2$ and $3h$) this case is indistinguishable from the base case. But later, $\langle s \rangle_\theta$ profiles remain peaked within the tumor, leading to significantly increased peripheral drug concentrations. In fact the average concentration in the center remains nearly constant up to a ca. $250\mu\text{m}$ wide peripheral shell (see also Supplement S5, and the video Supplement S19). Thus, convection has the effect of “flattening” the profile apparently by driving additional drug into the neovascularized rim where it is reabsorbed once the blood stream is cleared of drug.

In the following cases (vi), (v), (iv) and (vii) we analyze the effect of varying permeabilities. In [3] it was shown that the IFP profile depends only on the ratio of vascular to interstitial hydraulic conductivity. Here we have spatially varying coefficients but the same scaling law is expected. Nonetheless we vary both parameters since their effect on the velocity and thus drug transport is different. Beside the IFP it seems appropriate to consider the actual flow through the tumor. We quantify this by the mean values $\langle \cdot \rangle_T$ of the following components of the source term in (12): $\langle Q_I \rangle_T$ measures the amount of fluid that must leave the tumor through its boundary in interstitial space. $\langle Q_I^+ \rangle_T$ is the amount of extravasated fluid since vessels are the only sources. $\langle Q_I^- \rangle_T$ is the amount of fluid taken up by vessels or lymphatics. Note that $\langle Q_I^- \rangle_T$ is typically an order of magnitude less than $\langle Q_I^+ \rangle_T$, which is clear since there should be very little back flow into vessels. Their response to parameter variations is shown in Figure 13.

(iv) Vascular permeability. We vary $\lambda_{i,T}$ between 1/1000 and 10 times the b.c. value for leaky tumor vessels. Note that this does not simply scale all permeabilities (i.e. L_i^v) equally, rather $\lambda_{i,T}$ is the cutoff for L_i^v which increases up to this value for $w \rightarrow 0$ (see (15)). Also note the conductivity of normal capillaries is $\lambda_{i,N} = 1/100\lambda_{i,T}(b.c.)$.

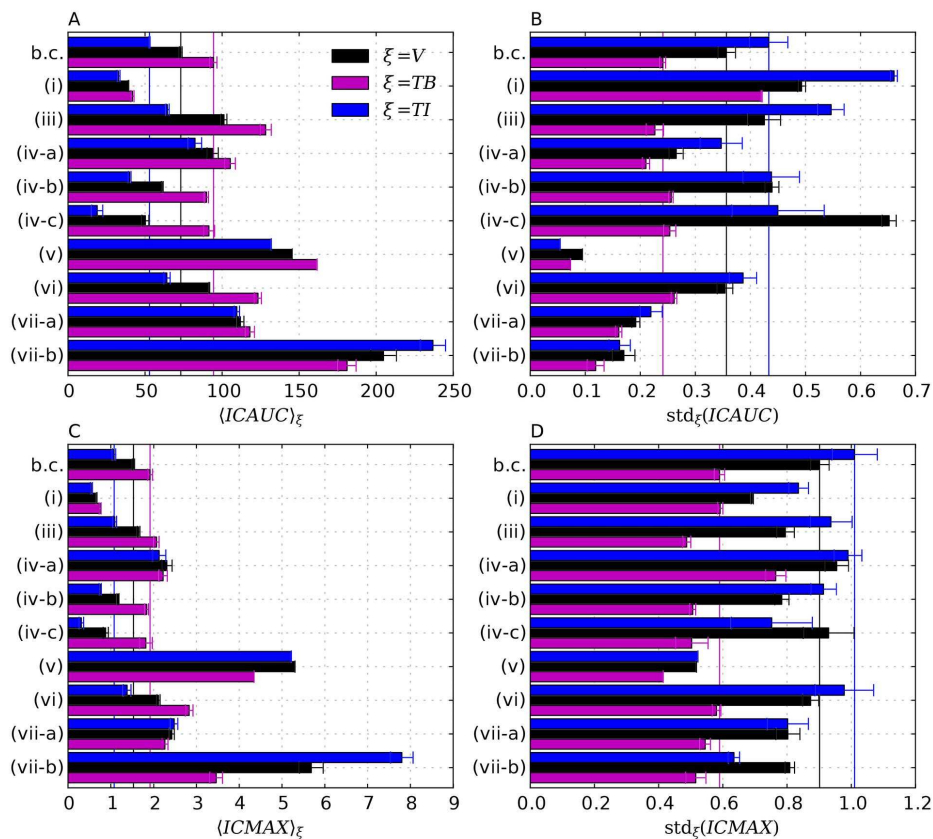


Figure 10. Comparison of the means and STDs of the probability distribution functions (PDFs) of ICMAx and ICAUC. These quantities are presented for different regions, where each region is associated with its own PDF using ξ as index, where V stands for the viable tumor mass, TB for tumor boundary and TI for tumor interior (see text). Spatial mean, indicated by brackets (or STD, indicated by *std*) are first computed for all systems in the ensemble and then averaging over the ensemble. The error bars show respective deviations from the average within the ensemble. The meaning of the case labels is as follows: (b.c.) base case, (i) heavier drug particles, i.e. molecular mass increased by a factor of $2 \cdot 10^3$. (iii) neglected interstitial convection, (iv) tumor vascular permeability scaled by a factor of 10 (a), 1/10 (b), and 1/100 (c), (v) hydraulic conductivity of interstitium scaled by a factor of 10, (vi) amount of normal lymphatics scaled by a factor of 10, (vii) presence of 10% (a) and 100% of the normal lymphatics amount in the tumor. Note that (ii) (prolonged infusions) are not shown due to the scale. doi:10.1371/journal.pone.0070395.g010

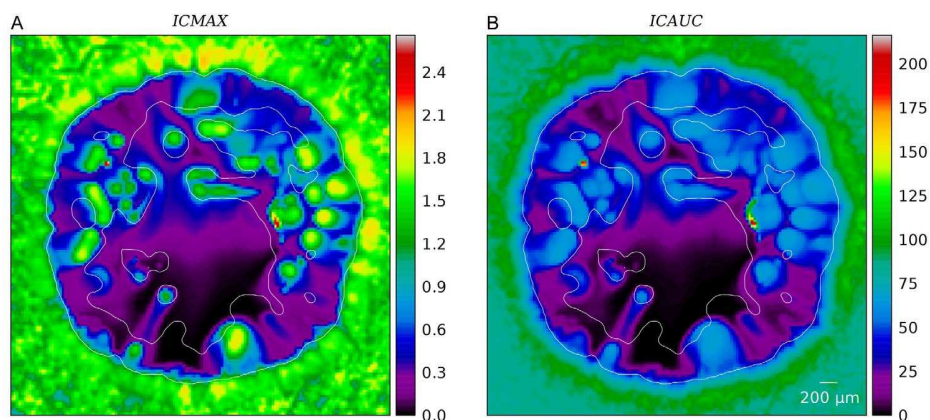


Figure 11. Spatial distributions of (A) ICMAx and (B) ICAUC for the case (i). Here 10^4 times heavier drug particles are considered which renders diffusive transport insignificant (see text). The presentation is analogous to Figure 9 of the base case. doi:10.1371/journal.pone.0070395.g011

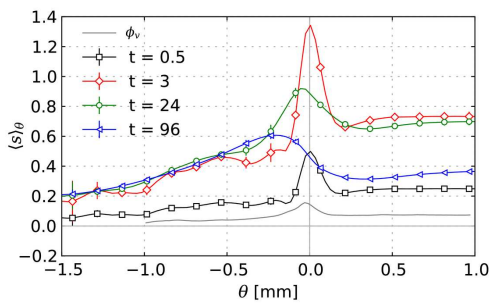


Figure 12. Drug concentrations in the case (vii) where convective transport was neglected. Results are presented as averaged profiles plotted vs. θ as in Figure 8. doi:10.1371/journal.pone.0070395.g012

Increasing $\lambda_{l,T}$ has little effect on the IFP and IFV profile since the IFP already approaches rapidly the blood pressure, see Figure 14 A. The plots of the source terms (Figure 13 A show that for increasing permeabilities most of the little additional flow is reabsorbed into vessels ($\langle Q_l^- \rangle_T$). The flow that crosses the boundary is insignificantly altered. For lower permeabilities the uptake $\langle Q_l^- \rangle_T$ decreases much more rapidly than the influx $\langle Q_{lv}^+ \rangle_T$. The latter varies weakly within one order of magnitude over the whole $\lambda_{l,T}$ range, implying that the hydraulic resistance of other components, i.e. interstitium and lymphatics limits the flow. Interestingly, setting $\lambda_{l,T}$ to the level of normal vessels is not enough to lower the IFP to a normal level. It is only reduced by about 50%. Further reduction to $1/1000\lambda_{l,T}$ (b.c.) yields near zero IFP (≈ 0.1 kPa) but an outward gradient persists.

Predictions for drug delivery were made for $\lambda_{l,T} = 10, 1/10$ and $1/100\lambda_{l,T}$ of the base case. See Figure 10 (iv)-A to C (see also Supplements S6, S7 and S8, respectively). In conjunction with $\lambda_{l,T}$ we also varied the diffusive permeability $\lambda_{s,T}$ by the same factor. The mean ICMAX and ICAUC level in Ω_{TB} are invariant since this regions exhibits rather normal vessels since leakiness increases gradually toward the center. In the interior, $\langle \text{ICMAX} \rangle_{TI}$ and $\langle \text{ICAUC} \rangle_{TI}$ increase with the permeability as

expected. Here too, for (iv)-A we find ICMAX levels in the tumor which are comparable to normal tissue.

(v) Hydraulic conductivity of interstitium. The base case considers a dense tissue which implies a low conductivity due to the dependence on the available interstitial volume. Sparser tissues were estimated to be orders of magnitude more permeable [50]. To analyze such a situation we scale the tissue permeability coefficient $K_{l,\alpha}$ up to 100 times simultaneously for $\alpha = N$ and T . For brevity, α is omitted in the following. Increasing K_l alone produces unrealistic results where the IFP within normal tissue rises well above 0. Hence the lymphatic permeability $L_l^{(L)}$, was also increased by the same factor.

With increasing K_l we observe a decreasing IFP which drops to ca. 1/7 of the base case value for a 100 times increase of K_l , as shown in Figure 14B. The IFV decreases sub-proportionally, up to a factor of 20. Interestingly, the region where most fluid is extravasated shifts from close to the boundary to the tumor center. Concomitantly one finds a shift of the peak in the $v(\theta)$ toward the tumor center and less back flow through vessels as compared to the base case as indicated by lowered $\langle Q_l^- \rangle_T$. For the total flow $\langle Q_l \rangle_T$ we can identify two regimes: Up to a 10 times increase we see an approximately linear variation, and for larger K_l a logarithmic behavior.

Drug delivery is analyzed for an increase of K_l by a factor of 10, where we additionally upscale the diffusion constant D_s by the same amount (see Supplement S9 for additional figures). This is rather ad-hoc but based on the assumption that the free volume fraction and the amount of ECM components varies, on which the effective diffusion constant and IF permeability linearly depend on as a first order approximation. As a result we obtain a significantly more homogeneous ICMAX and ICAUC distributions. See the comparison Figure 10B,C-(v) vs. (b.c.). The effect is most drastic for ICAUC but also the ICMAX fluctuations over Ω_{TB} are significantly reduced. Remarkably, the tumor interior now shows higher drug concentrations (Figure 10A-(v)) than the exterior. The fact that the drug delivery to the interior is comparable to normal tissue is surprising since permeabilities were adjusted also for normal tissue not just the tumor.

(vi) Amount of normal lymphatics. The lymphatic system is not well documented due to the lack of specific markers for its

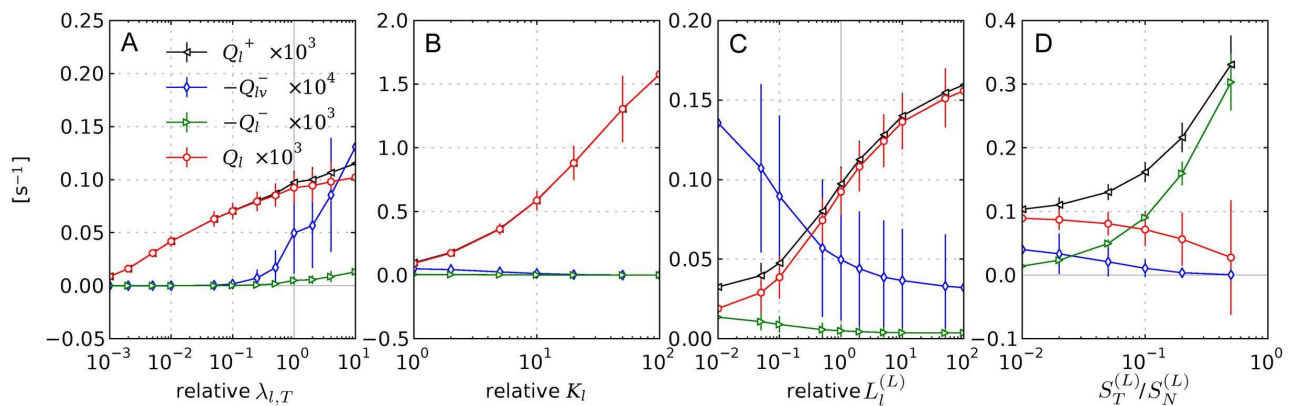


Figure 13. Mean fluid source rates over the whole tumor in dependence on varying parameters. Q with its sub and super scripts refer to contributions to the source term as defined in (12), (23). The plotted mean values are defined simply as ensemble averages of the spatial means over the tumor. The error bars show the standard deviations within the ensemble. The subplots depict the following cases: (A) Variation of the upper vessel wall permeability bound $\lambda_{l,t}$ (case (iv)). (B) Variation of the interstitial permeability coefficient K_l (case (v)). (C) Variation of the lymphatic wall permeability in normal tissue (case (vi)). (D) Variation of the lymphatic density in the tumor given as fraction of the normal tissue lymphatic density $S_T^{(L)}/S_N^{(L)}$ (case (vii)). Except for in (D) the ordinate scale is relative to the base case. doi:10.1371/journal.pone.0070395.g013

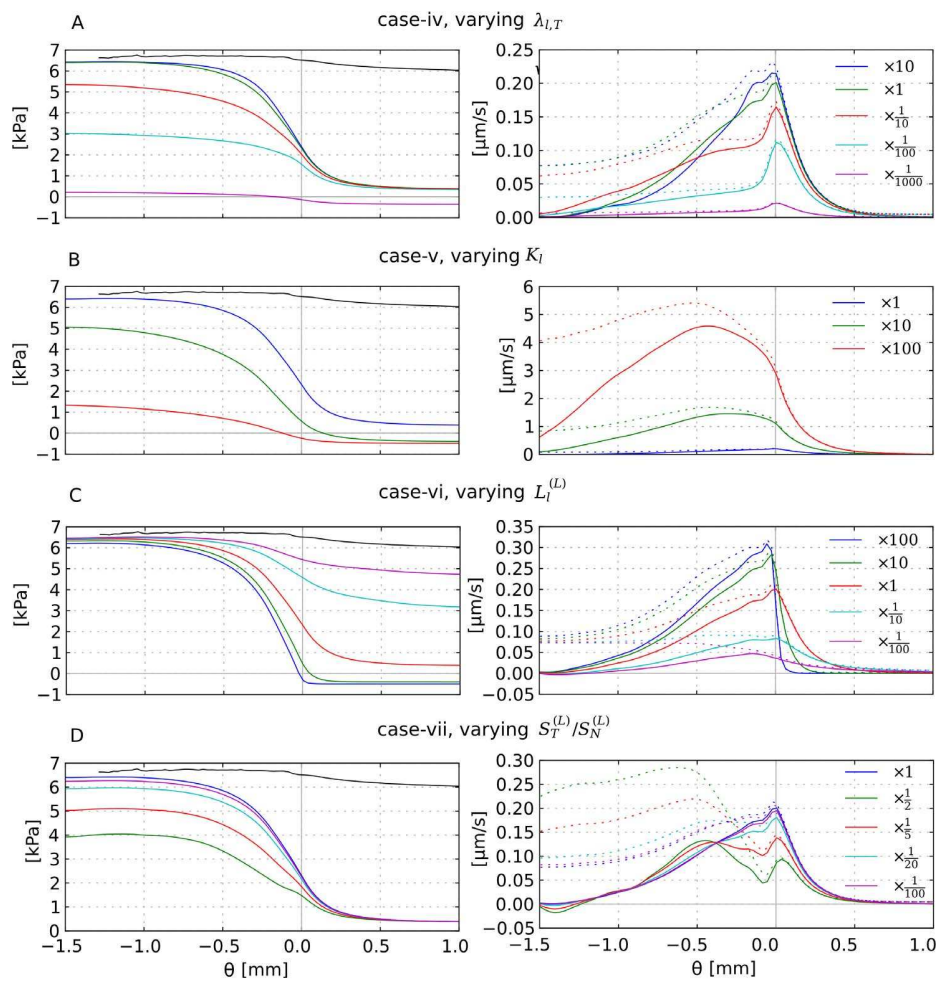


Figure 14. Radial distributions as result of parameter variations. Left: IFP, right: IFF, averaged over 15 system analogous to Figure 5. The relative deviation from the original base case parameter values is given in the figure legends, except in (D). The considered cases are as indicated in the sub-figure heading: (A) Variation of the upper vessel wall permeability bound $\lambda_{i,T}$ (case (iv)). (B) Variation of the interstitial permeability coefficient K_i (case (v)). (C) Variation of the lymphatic wall permeability $L_i^{(L)}$ in normal tissue (case (vi)). (D) Variation of the amount of tumor lymphatics $S_T^{(L)}/S_N^{(L)}$, where the legend shows $S_T^{(L)}/S_N^{(L)}$ directly (case (vii)). doi:10.1371/journal.pone.0070395.g014

channel walls. In our parameter determination we assumed that it has a similar capacity as the capillary bed. Moreover tumors can induce lymph angiogenesis similar to normal angiogenesis [9] thereby increasing the amount of lymphatics nearby. Hence we consider variations of the source term coefficient $L_i^{(L)}S^{(L)}/V$ from 100 to 1/100 times the base case (b.c.) value.

As discussed above, the IFP has a “penetration depth” across the tumor boundary which is proportional to $\sqrt{K_{i,N}l^2/L_i^{(L)}S^{(L)}}$ and indeed we see a variation of this magnitude in the radial profile. Moreover with increasing $L_i^{(L)}S^{(L)}/V$ the IFP drops asymptotically to the lymphatic pressure p_L , which can be explained by the analogy of an electrical resistor. A $L_i^{(L)}S^{(L)}/V$ decrease on the other hand drives the IFP in unrealistically high. The central tumor IFP is thereby relatively invariant to these parameter changes, see Figure 14C. The IF velocity varies according to the gradient across the boundary and can be increased by up to 50% in the extreme case. The global flow $\langle Q_i \rangle_T$ increases by about the same magnitude. The average back

flow $\langle Q_{iv} \rangle_T$ decreases insignificantly within the error bars. On the other hand for low $L_i^{(L)}S^{(L)}/V$ more back flow is observed, which is reasonable since the uptake capacity of lymphatics is decreased.

For drug transport we only consider the case with a factor of 10. Qualitatively the ICMAX and ICAUC distributions appear similar to the base case (figures are provided in Supplement S10). The increased flow apparently leads to higher drug levels all over the tumor, but the effect is strongest in the TB region. Spatial fluctuations are also insignificantly changed. Thus we can conclude that the delivery slightly improved. Given that the fluid transport rate $\langle Q_i \rangle$ increased by 50% this is surprising since case (i) demonstrated that a larger convection-diffusion ratio can have a negative effect.

(vii) Tumor lymphatics. In this hypothetical case we assume that functional lymphatics exist within the tumor. We model this by a non-zero lymphatic sink coefficient $L_i^{(L)}S^{(L)}/V$ as a fraction of the coefficient in normal tissue. This differs from taking a higher tissue conductivity by the assumption of the underlying channel

organization. The latter case implies a grid like structure whereas the former implies a hierarchical structure where exchange takes place over the thinnest channels analogously to blood vessel network. Those lymphatic capillaries can be expected to exhibit approximately equal blood pressure over the whole tissue. Hence the use of homogeneously distributed sinks with lymphatic pressure p_L .

Resulting IFPs and IFV plots are shown in Figure 14D. As can be seen an increasing presence of lymphatics “pulls” down the IFP to p_L . The outward velocity component $v_{||}$ decreases proportionally as can be expected based on the IFP gradient. But the actual velocity magnitude $|v|$ increases with the amount of lymphatics. This can be expected as well since the velocity field is increasingly superimposed by flow away from vessels to nearby locations where fluid is absorbed. This is also reflected by increasing transvascular flow $\langle Q_{I+} \rangle_T$, decreased flow across the boundary, $\langle Q_I \rangle_T$ and the back flow $\langle Q_{Iv}^- \rangle_T$ as shown in Figure 13C.

We computed the drug transport for systems with (a) 0.1 and (b) 1 times the normal lymphatics (see Supplements S11 and S12, respectively). What we would expect is that the changed flow patterns (directed away from vessels) facilitate the delivery to more distant regions. As Figure 10A and B-(vii) show this is indeed the case. Even in (a) a significant improvement is achieved. The ICMAX and ICAUC levels in the rather unrealistic case (b) are increased dramatically. This must also be attributed to leaky tumor vessels. Thereby spatial fluctuations are either unchanged (std, ICMAX) or significantly reduced std, (ICAUC).

Discussion

Based upon an extension of our model for remodeling of tumor vasculature introduced in [15,16,18,19] we studied interstitial fluid flow (IFF) and drug transport.

Since the spatial details of IFF depends crucially the spatial arrangement of blood vessels and their blood pressure we considered, for the first time, a model for IFF and drug transport that involves a realistic arteriovenous initial vascular network evolving dynamically with the tumor. As a result tumor vessels are connected to a wide variety of original host vessels - from capillaries to ca. 50 μm arterioles and veins. Blood flow is determined for the whole system including the whole remaining host vasculature which comprises not only a single parent vessels but many vessels covering the entire simulation domain. It should be emphasized that an arteriovenous initial vasculature produces blood flow patterns and blood pressure fields that differs substantially from grid-like arrangements [15,18]: the latter usually have a fixed blood pressure gradient direction imposed upon them which can also (unrealistically) impose a preferred direction on tumor vessel growth and skew the IFP distribution. For a tumor blood vessel network emerging from an arteriovenous initial vasculature we obtain much higher blood flow rates through individual vessels due to arteriovenous shunts and circumferential growth, and more irregular (spatial) blood pressure distributions. Due to transvascular coupling these circumstances are also relevant for the IFP, IFF and drug transport.

A first remarkable result is that in spite of an expected IFP plateau within the tumor IFF does not cease and still allows for substantial convective transport, which is opposite to the currently prevailing view [3–9] that states that increased IFP poses a barrier to successful drug delivery within tumors. The physical explanation is simply that it is misleading to consider the pressure drop along the vessel wall alone as the driving force for IFF - in principle the complete network of hydraulic resistors has to be taken into account to obtain reliable predictions. Qualitatively it is

sufficient to bear in mind that for IFF the tumor is series of resistors with a fixed potential outside the tumor (the lymphatics of healthy tissue) - decreasing one resistor, for instance by increasing the permeability of the vessel walls, generally *increases* the flow, in spite of the lower potential drop along the decreased resistor.

Another interesting result is that heavy macro-molecules are still distributed more or less evenly into viable areas in the tumor perimeter in spite of a pronounced outward IFP gradient there, which one could naively expect to remove drug before an efficacious dose is achieved. The reason is IFF between tumor internal vessels, that transports macro-molecules convectively from leaky high pressure vessels through the tumor tissue into neighboring low pressure vessels. In the following we discuss our results quantitatively in detail.

It is already established that leaky tumor vessels and lack of tumor lymphatics lead to a drastically increased hydraulic pressure of the interstitial fluid (IFP) in the tumor and that the resulting gradient drives fluid out of the tumor with a velocity of 0.1 to 1 $\mu\text{m/s}$ [4,51] and our results agree with these experimental observations very well. Our model predictions of the central IFP is ca. 6 kPa, which is at the upper limit of experimentally observed values. This value is also higher than in normal capillaries due to the coupling with higher level arterioles in which the blood pressure is naturally higher. The vessel walls of arteries and veins within the tumor become leaky [21] and thus increase their conductivity, which means tighter coupling between IFP and blood pressure which as a result causes the IFP to approach the level of nearby arteries or veins. Indeed, the predicted mean pressure difference between blood and interstitium vanishes towards the tumor center. Local fluctuations produce flow into, out of and in-between vessels which is not necessarily directed outwards. The outward component of the velocity vector dominates in the tumor periphery. Around the tumor perimeter we find a thin layer where where the fluid is absorbed into lymphatics. Absorption into blood vessels frequently occurs deep inside the tumor. It should be noted that the fluctuations among samples are very large, about 100%. Consequently, depending on their location in the microenvironment, seemingly by chance some tumors could be more likely to metastasize through the blood stream than others of the same kind. Although the transvascular flow of tumor vessels is elevated by an order of magnitude compared to normal capillaries, we estimated that only a small fraction of the order of 0.01 percent of the blood flow which enters the tumor is lost into the interstitium. The biophysical factors upon this ratio depends are the vascular morphology and the permeability of vessel walls, interstitium, and lymphatics. Here, dilated vessels and arteriovenous shunts lead generally to elevated flow rates (q) in tumor vessels. Note that q depends strongly on the vessel radius r , i.e. $q \propto r^4$.

In addition to the base case we considered scenarios in which the conductivities of vessel walls, lymphatics and the interstitium are varied individually. We observe universally that the influx through vessels, and therewith the IFF through the tumor, increases with the conductivity. The sensitivity to these changes is rather low, even for variations of several orders of magnitude. Lower IFP does thereby not correlate with increased flow. For example the reduction of IFP can be achieved by increasing the tissue conductivity or decreasing the vessel wall conductivity. In the first case the IFF is increased while in the second it is decreased. This relationship between IFF and conductivity can be easily understood on the basis of analogy of our flow equations with an electrical network of ohmic resistors: As an extreme idealization let us consider a linear chain of three resistors, representing the walls of the tumor vasculature, the interstitium

and lymphatic walls, whereby the potentials are fixed at the ends. Then of course the current is determined by the total resistance and the voltage drop over one resistor grows with its resistance. An increase of the first resistor (decrease of vessel wall conductance) as well as decrease of the second resistor (increase of tissue conductivity) both imply a lower voltage drop at the second resistor (lower IFP). But the current (the IFF) decreases in the 1st case and increases in the 2nd.

We quantify the local exposure to drug with the help of both the time integrated intracellular concentration (denoted as ICAUC for intracellular area under curve) as well as the maximal concentration (denoted as ICMAX for intracellular maximal concentration), which we consider separately. Our model predicts that on a large scale, drug delivery is compartmentalized similar to the vasculature. Let us subdivide the system into concentric shells with increasing distance from the invasive edge and consider averaged quantities over such shells. Close to the invasive edge we typically find an exposure peak, the location of which is not exactly aligned with the MVD peak due to outward convection. Towards the tumor center the decreasing vessel density leads to a sharp drop down to a plateau at a certain lower bound which is for our base case ca. 50% of the level at the tumor periphery. The height of this plateau depends on various factors including extravasation rate, transport rate through the interstitium, but predominantly vessel density.

The tumor center is threaded by many isolated vessels, and our model predicts exponentially decaying concentration gradients around them in agreement with experimental results e.g. [43,48]. Over longer time scales of many hours to days, the initial distributions smear out akin to the behavior of freely diffusing particles, and also decrease globally due to reabsorption. The magnitude of these time scales depend on the transport rates, cellular uptake and binding dynamics.

Although we did not study it in detail, we want to stress that cellular uptake and retention dynamics also govern the total amount of extravasated drug to a certain extent because the faster the uptake rate, the lower the interstitial concentration, the larger transvascular gradients which drive diffusive fluxes and counteract re-absorption by convection.

It has been suspected for over a decade that IFF could wash out drug from the tumor. Our model predicts this effect but as drastic in magnitude as expected. Simulation runs in which convective transport was neglected show that a ca. 2.5 times higher drug concentration is retained in the periphery whereas the radial profile of the time-independent exposure measures (ICAUC, ICMAX) merely exhibit a smoother decay from periphery to center. In the opposite extreme case of non-diffusing particles under normal convection the the interstitial flow causes sufficient flux to achieve significant drug delivery which is on a coarse scale comparable to the base case. Here we do however observe islands in the viable tumor region where no drug is delivered, implying that such tumor fragments could remain viable after treatment. In cases with diffusion, at least small amounts of drug are delivered.

Different tissue types as well as the effect of therapies that improve drug delivery can be described within the model by changing various permeability constants. We varied diffusion constants simultaneously with conductive constants by the same factors as first approximation to hypothetical changes e.g. of the intercellular channel geometry. As a result, global exposure levels and the amount of extravasated fluid correlate well with these permeabilities as well as with each other. Unfortunately relative local fluctuations, i.e. the STD over space of ICAUC and ICMAX are not correlated with these variations, making them unsuited as basis for achieving are uniform efficacy or dose.

Within the biologically relevant parameter space of which we only considered a small part, analysis of other cases will certainly lead to additional insight. For example in [14] tumor interstitium and capillary permeabilities ($K_{I,T}$ and $\lambda_{I,T}$ in terms of our model) were varied simultaneously, leading to a flattened tumor IFP profile for increasing permeability. From such observations in an experimental setting one could draw conclusions about the nature of the tumor tissue.

With this in mind a tumor therapy that comprises a treatment that solely reduces the vessel leakiness appears not to be effective. A currently frequently discussed alternative is to improve the efficacy of drugs by turning the ill-formed tumor vasculature normal again [52] by pharmacological means during or before a conventional therapy. A step in this direction is obviously to reduce the leakiness of tumor vessels. However, our simulations predict an actual reduction of the global ICAUC and ICMAX levels while their relative fluctuations may even increase. On the other hand increased permeability leads to significantly improved delivery in the tumor center. Unfortunately this case is unlikely to be a therapeutic goal since it could increase the direct exposure of the blood stream to tumor cells increasing the chance of tumor cells entering it. A good treatment strategy would be to prioritize the maintenance, or fabrication of a dense tumor vasculature, rather than exclusively tightening the leaks in the already sparse vasculature. If a tumor is detected early enough the vasculature could thus be kept intact and deliver drugs effectively, simply due to the amount of functional capillaries, even though their walls are expected to conduct drug worse than leaky walls.

Vascular targeting therapies that take the opposite direction namely that aim to destroy the remaining tumor vasculature completely exists hand have proven to be promising, see e.g. [53]. A common problem in therapy is that tumor cell in vivo are more resistant to treatment than cell cultures. Many factors are involved but not all are purely of genetic nature. For example the lack of oxygen plays an important role for the development of radiation resistance. Or the drug delivery through the sparse tumor vasculature is insufficient, which is supported by our model prediction that the drug concentrations in the tumor are much lower than in normal tissue. If cells in the interior were killed indirectly by vascular targeting, a viable shell around the boundary would remain which could be effectively treated conventionally due to the better vascularization. It is plausible that the removal of the inner tumor vessels would lead to a reduction of the IFP and thereby lower IFF across the boundary. As our results show, the absence of this peripheral flow can improve the drug exposure of the boundary significantly potentially leading to better treatment in combination with vascular targeting.

Interestingly, the ICMAX and ICAUC levels increase with the interstitial permeability, lymphatic permeability, or when providing the tumor with a fraction of surviving lymphatics. In addition to that and perhaps more importantly, drug concentrations become more homogeneous as well. This effect is much more prominent for ICAUC than for ICMAX, where for the former the spatial STD decreases from over 0.4 to ca. 0.2. With a 10 times increased interstitial conductivity the ICAUC distribution even becomes completely smooth over the whole tumor at levels higher than in normal tissue. Unfortunately, in those cases the IFF is also increased which would likely increase the shedding of TCs into lymphatics, not to mention the danger of having TCs in direct contact with tumor lymphatics. Hence, despite significantly improved delivery the parameters above are certainly not a useful therapeutic target.

The final ICMAX and ICAUC distributions for continuous infusions are hardly distinguishable from the bolus case except for the scale. The reason is that the time scale to achieve a stationary

state (estimated ca. 1700 h) is much longer than the infusion periods (24 h and 96 h) which we tried. For Doxorubicin cellular uptake is relatively fast (of the order of minutes) and release is slow (of the order of hours), hence the local concentrations are in a steady state where most of the drug is arrested in cells, lowering the effective transport rates. It can be expected that drugs with low uptake rates perform better in this respect.

Supporting Information

Supplement S1 Further details on the model.
(PDF)

Supplement S2 Supplemental figures for case i.
(PDF)

Supplement S3 Supplemental figures for case ii-a.
(PDF)

Supplement S4 Supplemental figures for case ii-b.
(PDF)

Supplement S5 Supplemental figures for case iii.
(PDF)

Supplement S6 Supplemental figures for case iv-a.
(PDF)

Supplement S7 Supplemental figures for case iv-b.
(PDF)

Supplement S8 Supplemental figures for case iv-c.
(PDF)

Supplement S9 Supplemental figures for case v.
(PDF)

Supplement S10 Supplemental figures for case vi.
(PDF)

Supplement S11 Supplemental figures for case vii-a.
(PDF)

Supplement S12 Supplemental figures for case vii-b.
(PDF)

Supplement S13 Supplemental figures.
(PDF)

Supplement S14 Video of a growing tumor in silico. A quarter of the system is cut out to open the view into the interior. The presentation is analogous to Figure 2, i.e. the yellow mass depicts the viable tumor. Void spaces within the tumor are necrotic regions. The blood vessel network is color coded by blood pressure. Red is high (arteries), and blue is low (veins).
(AVI)

Supplement S15 Video of a growing tumor in silico. Here we visualized a ca. 200 μm thick slice through the center of the system. The presentation is analogous to Figure 2, i.e. the yellow mass depicts the viable tumor. Void spaces within the tumor are necrotic regions. The blood vessel network is color coded by blood pressure. Red is high (arteries), and blue is low (veins).
(AVI)

Supplement S16 Video of the drug concentration distribution for the base case.
(AVI)

Supplement S17 Video of the drug concentration distribution for case i.
(AVI)

Supplement S18 Video of the drug concentration distribution for case ii-b.
(AVI)

Supplement S19 Video of the drug concentration distribution for case iii.
(AVI)

Author Contributions

Conceived and designed the experiments: MW HR. Performed the experiments: MW. Analyzed the data: MW. Wrote the paper: MW HR.

References

- Hanahan D, Weinberg RA (2000) The hallmarks of cancer. *Cell* 100: 57–70.
- Carmeliet P, Jain R (2000) Angiogenesis in cancer and other diseases. *Nature* 407: 249–257.
- Jain RK, Baxter LT (1988) Mechanisms of heterogeneous distribution of monoclonal antibodies and other macromolecules in tumors: significance of elevated interstitial pressure. *Cancer Res* 48: 7022–7032.
- Jain RK (1999) Transport of molecules, particles, and cells in solid tumors. *Annu Rev Biomed Eng* 1: 241–263.
- Heldin CH, Rubin K, Pietras K, Ostman A (2004) High interstitial fluid pressure - an obstacle in cancer therapy. *Nat Rev Cancer* 4: 806–813.
- Minchinton AI, Tannock IF (2006) Drug penetration in solid tumours. *Nat Rev Cancer* 6: 583–592.
- Hassid Y, Furman-Haran E, Margalit R, Eilam R, Degani H (2006) Noninvasive magnetic resonance imaging of transport and interstitial fluid pressure in ectopic human lung tumors. *Cancer Research* 66: 4159–4166.
- Shieh AC, Swartz MA (2011) Regulation of tumor invasion by interstitial fluid flow. *Phys Biol* 8: 015012.
- Swartz MA, Lund AW (2012) Lymphatic and interstitial flow in the tumour microenvironment: linking mechanobiology with immunity. *Nat Rev Cancer* 12: 210–219.
- Baish JW, Netti PA, Jain RK (1997) Transmural coupling of fluid flow in microcirculatory network and interstitium in tumors. *Microvasc Res* 53: 128–141.
- Wu J, Xu S, Long Q, Collins MW, Konig CS, et al. (2008) Coupled modeling of blood perfusion in intravascular, interstitial spaces in tumor microvasculature. *J Biomech* 41: 996–1004.
- Zhao J, Salmon H, Sarntinoranont M (2007) Effect of heterogeneous vasculature on interstitial transport within a solid tumor. *Microvasc Res* 73: 224–236.
- Sinek JP, Sanga S, Zheng X, Frieboes HB, Ferrari M, et al. (2009) Predicting drug pharmacokinetics and effect in vascularized tumors using computer simulation. *J Math Biol* 58: 485–510.
- Wu M, Frieboes HB, McDougall SR, Chaplain MA, Cristini V, et al. (2013) The effect of interstitial pressure on tumor growth: Coupling with the blood and lymphatic vascular systems. *Journal of Theoretical Biology* 320: 131–151.
- Bartha K, Rieger H (2006) Vascular network remodeling via vessel cooption, regression and growth in tumors. *J Theor Biol* 241: 903–918.
- Lee D, Rieger H, Bartha K (2006) Flow correlated percolation during vascular remodeling in growing tumors. *Physical Review Letters* 96: 058104-1-058104-4.
- Welter M, Bartha K, Rieger H (2008) Emergent vascular network inhomogeneities and resulting blood flow patterns in a growing tumor. *J Theor Biol* 250: 257–280.
- Welter M, Bartha K, Rieger H (2009) Vascular remodelling of an arterio-venous blood vessel network during solid tumour growth. *J Theor Biol* 259: 405–422.
- Welter M, Rieger H (2010) Physical determinants of vascular network remodeling during tumor growth. *Eur Phys J E Soft Matter* 33: 149–163.
- Döme B, Paku S, Somlai B, Timár J (2002) Vascularization of cutaneous melanoma involves vessel cooption and has clinical significance. *The Journal of Pathology* 197: 355–362.
- Holash J, Maisonpierre PC, Compton D, Boland P, Alexander CR, et al. (1999) Vessel cooption, regression, and growth in tumors mediated by angiopoietins and vegf. *Science* 284: 1994–1998.
- Pries AR, Secomb TW, Gessner T, Sperandio MB, Gross JF, et al. (1994) Resistance to blood flow in microvessels in vivo. *Circ Res* 75: 904–915.
- Pries A, Secomb T, Gachtgens P (1995) Design principles of vascular beds. *Circulation Research* 77.
- Pries AR, Reglin B, Secomb TW (2005) Remodeling of blood vessels: responses of diameter and wall thickness to hemodynamic and metabolic stimuli. *Hypertension* 46: 725–731.
- Gevertz JL, Torquato S (2006) Modeling the effects of vasculature evolution on early brain tumor growth. *J Theor Biol* 243: 517–531.
- Schreiner W, Buxbaum P (1993) Computer-optimization of vascular trees. *Biomedical Engineering, IEEE Transactions on* 40: 482–491.

27. Murray C (1926) The physiological principle of minimum work: The vascular system and the cost of blood volume. In: Proc Natl Acad Sci USA. volume 12, 207–214.
28. Gödde R, Kurz H (2001) Structural and biophysical simulation of angiogenesis and vascular remodeling. *Developmental Dynamics* 220: 387–401.
29. Dimmeler S, Zeiher AM (2000) Endothelial cell apoptosis in angiogenesis and vessel regression. *Circulation Research* 87: 434–439.
30. Preziosi L, Tosin A (2009) Multiphase modelling of tumour growth and extracellular matrix interaction: mathematical tools and applications. *J Math Biol* 58: 625–656.
31. Rajagopal KR, Tao L (1995) *Mechanics of mixtures*. World scientific Singapore.
32. Walocha JA, Litwin JA, Miodoński AJ (2003) Vascular system of intramural leiomyomata revealed by corrosion casting and scanning electron microscopy. *Hum Reprod* 18: 1088–1093.
33. Sethian JA (1996) *Level Set Methods*. Cambridge University Press. URL <http://visinfo.zib.de/EVlib/Show?EVL-1996-149>.
34. Chaplain MA, Graziano L, Preziosi L (2006) Mathematical modelling of the loss of tissue compression responsiveness and its role in solid tumour development. *Math Med Biol* 23: 197–229.
35. Jain RK, Tong RT, Munn LL (2007) Effect of vascular normalization by antiangiogenic therapy on interstitial hypertension, peritumor edema, and lymphatic metastasis: insights from a mathematical model. *Cancer Res* 67: 2729–2735.
36. West J (2012) *Respiratory physiology: the essentials*. Lippincott Williams & Wilkins.
37. LeVeque RJ (2007) Finite difference methods for ordinary and partial differential equations - steady-state and time-dependent problems. SIAM. URL <http://www.cc-securehost.com/SIAM/OT98.html>.
38. Heroux MA, Bartlett RA, Howle VE, Hoekstra RJ, Hu JJ, et al. (2005) An overview of the Trilinos project. *ACM Transactions on Mathematical Software* 31: 397–423.
39. Kurganov A, Tadmor E (2000) New high-resolution central schemes for nonlinear conservation laws and convection–diffusion equations. *Journal of Computational Physics* 160: 241–282.
40. Jiang GS, Peng D (2000) Weighted ENO schemes for Hamilton-Jacobi equations. *SIAM Journal on Scientific computing* 21: 2126–2143.
41. Nehls V, Herrmann R, Hühnen M (1998) Guided migration as a novel mechanism of capillary network remodeling is regulated by fibroblast growth factor. *Histochem Cell Biol* 109: 319–329.
42. Basan M, Risler T, Joanny JF, Sastre-Garau X, Prost J (2009) Homeostatic competition drives tumor growth and metastasis nucleation. *HFSP J* 3: 265–272.
43. Lankelma J, Dekker H, Luque FR, Luyckx S, Hoekman K, et al. (1999) Doxorubicin gradients in human breast cancer. *Clin Cancer Res* 5: 1703–1707.
44. Zheng JH, Chen CT, Au JL, Wientjes MG (2001) Time- and concentration-dependent penetration of doxorubicin in prostate tumors. *AAPS PharmSci* 3: E15.
45. Leu AJ, Berk DA, Yuan F, Jain RK (1994) Flow velocity in the superficial lymphatic network of the mouse tail. *Am J Physiol* 267: H1507–1513.
46. Chary SR, Jain RK (1989) Direct measurement of interstitial convection and diffusion of albumin in normal and neoplastic tissues by fluorescence photobleaching. *Proc Natl Acad Sci USA* 86: 5385–5389.
47. Dafni H, Israely T, Bhujwala ZM, Benjamin LE, Neeman M (2002) Overexpression of vascular endothelial growth factor 165 drives peritumor interstitial convection and induces lymphatic drain: magnetic resonance imaging, confocal microscopy, and histological tracking of triple-labeled albumin. *Cancer Res* 62: 6731–6739.
48. Primeau AJ, Rendon A, Hedley D, Lilje L, Tannock IF (2005) The distribution of the anticancer drug Doxorubicin in relation to blood vessels in solid tumors. *Clin Cancer Res* 11: 8782–8788.
49. El-Kareh AW, Secomb TW (2005) Two-mechanism peak concentration model for cellular pharmacodynamics of Doxorubicin. *Neoplasia* 7: 705–713.
50. Levick JR (1987) Flow through interstitium and other fibrous matrices. *QJ Exp Physiol* 72: 409–437.
51. Fukumura D, Jain RK (2007) Tumor microenvironment abnormalities: causes, consequences, and strategies to normalize. *J Cell Biochem* 101: 937–949.
52. Jain RK (2005) Normalization of tumor vasculature: an emerging concept in antiangiogenic therapy. *Science* 307: 58–62.
53. Siemann DW, Horsman MR (2009) Vascular targeted therapies in oncology. *Cell Tissue Res* 335: 241–248.

S1 Details of the model

Illustrative figures

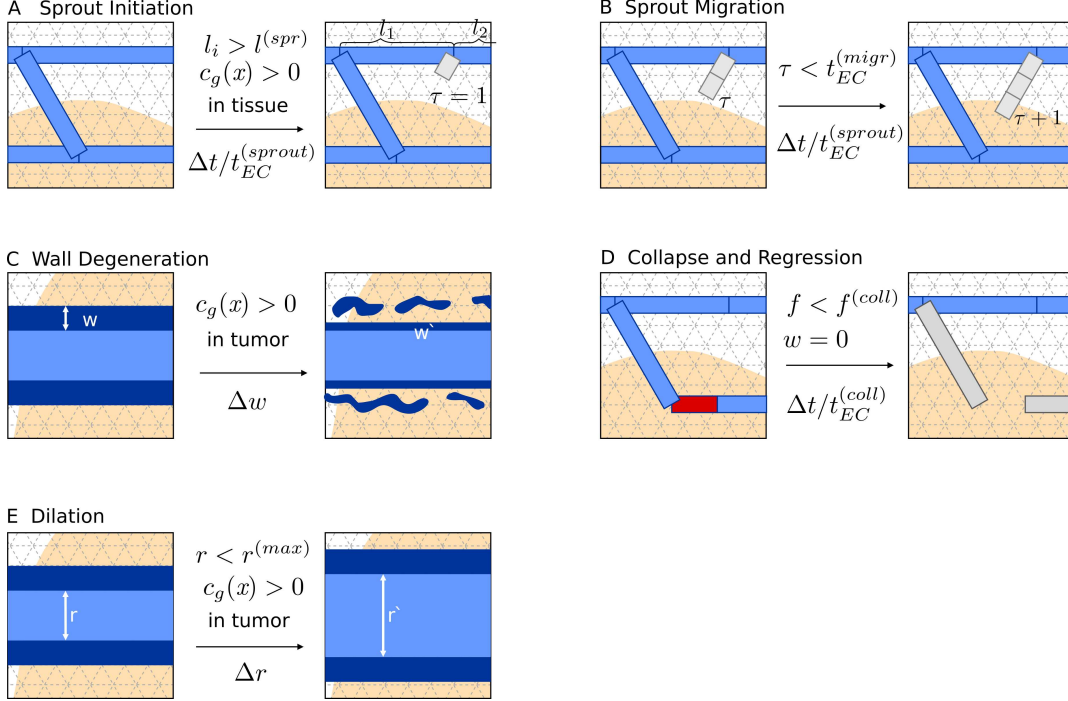


Figure 1: **Illustration of the vessel network remodeling processes.** The contents of the boxes display exemplified states of the vessel network. The vessel segments are shown as blue boxes if perfused with blood, else they are in a gray shade. Dark-blue borders (in C and E) represent vessel walls of varying thickness. The presence of a tumor is hinted at by the light orange region. The state transitions go from left to right as indicated by the arrows whereby the rate parameter is denoted below- and essential preconditions above the arrows, respectively. The note “in tissue” or “in tumor” refers to the location of a segment, see text for the precise definitions these conditions. In (A) a new sprout is generated. In this instance the preexisting segment is split at the branching point. Subsequently a new sprout segment is added with its life-time counter τ initialized to 1. l_i denote the distances to neighboring branching points. Since vessels can be chained together without branching points it is in general required to traverse such chains until $l_i > l^{(spr)}$ or a branching point is found. (B) depicts the further extension of the sprout from (A). It has already been extended to two segments and a third segment is appended. The lengths of sprout segments are always exactly one lattice bond. τ is inherited from the parent segment and incremented by 1 for all sprouts once per remodeling sweep. (C) depicts the degradation of the vessel walls with the rate Δw . Though w is defined as an abstract measure, it can be related to the wall thickness as shown here. w' stands for the value at the next time step, i.e. using Euler’s method $w' = w + \Delta t \Delta w$. In (D) an unstable vessel is removed, representing occlusion of blood flow and complete disintegration. Such event is assumed to happen only to vessels with maximally degenerate walls and low wall shear-stresses. Previously attached vessels can become dead ends which means blood cannot circulate through them any more. Such segments are identified by the biconnected component graph-algorithm [1] and excluded from blood flow computations. Since these vessels trivially have $f < f^{(coll)}$, they can collapse easily, resulting in a long ranged effect. (E) depicts the dilation of tumor vessels. The new radius after one time step is $r' = r + \Delta t \Delta r$.

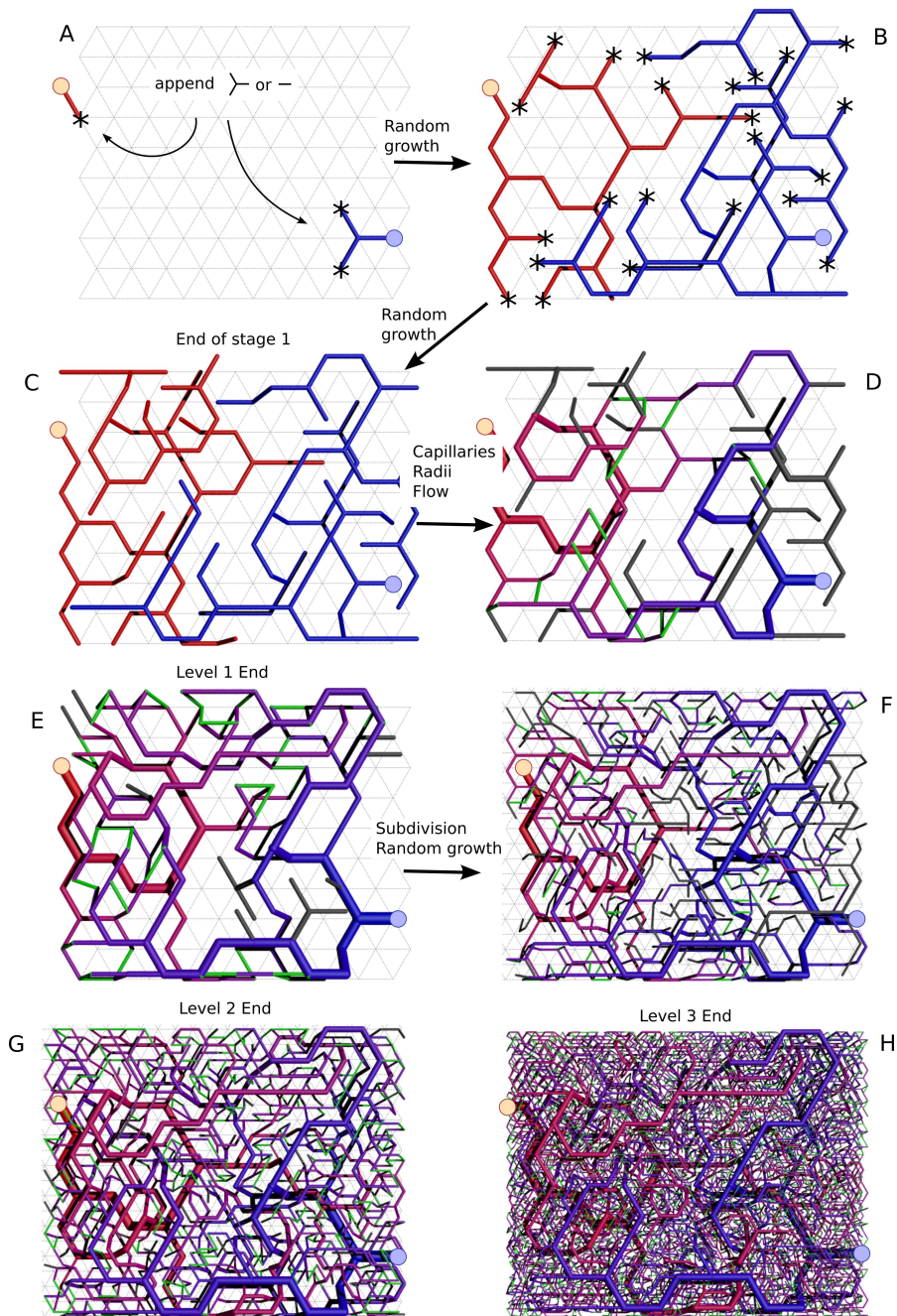


Figure 2: **Sketch of the vessel network generation algorithm.** For illustration we display subsequent actual configurations from a run on a $10 \times 10 \times 2$ lattice. The background mesh depicts the $z = 0$ layer of lattice. The color code for the vessels generally shows arteries in red and veins in blue. If blood flow data is available (D to H) the blood pressure is mapped to a red-blue gradient. The two circles (see A) display the location of the root nodes. Here are just two, but for our other results we placed them in alternating order at all boundary sites of the lattice. (A) shows the state after two growth iterations. Stars indicate the open ends where further elements can be appended (also in B). (B) shows the state during the random growth process. (C) shows the state at the end of the random growth process. Further additions would cause overlap which is forbidden. In (D) capillaries were added, radii computed and blood flow computed. Unperfused branches are displayed in dark gray. Capillaries are green. (E) displays the state after shear-stress based remodeling. (F) shows the network on a lattice which was upscaled once, doubling the number of sites and the length of the original vessel segments to span over two lattice bonds. Previous tips served as starting points for random growth as in A to C. This was followed by determination of radii, generation of capillaries, and computation of blood flow as in C to D. (G) shows the result from (F) after remodeling. Here perfused capillaries are well distributed. (H) shows the final state after an additional up-scaling step.

Initial blood vessel network construction

Random growth: The addition of a new element q at a tree tip is determined by probability weights w_q for all possible additions q . Specifically, we must consider the type and orientation of a new element. Additions resulting in overlap with the existing network are forbidden. Also we allow only additions in the forward direction. For non-admissible configurations we set $w_q = 0$, else we set $w_q = \cos(\varphi)$, where φ denotes the angle between the element and the parent branch. A specific element for addition is then picked according to the probabilities generated from the normalized weights $p_q = w_q / (\sum_q w_q)$.

Remodeling: In addition to the selection of the growth direction we must determine for each site on the network whether a new element is attached, a segment is removed, which is only possible at tree tips or if no changes are made. For these cases the following probability weights for growth w_g , regression, w_d and idleness w_i are given

$$\begin{aligned} w_g &= f/f_{max} \\ w_d &= 1 - f/f_{max} \\ w_i &= \infty \text{ if } f = 0 \text{ and not } N(\mathbf{x}), \text{ else } 0, \end{aligned}$$

where N is a boolean indicator function which maps to true if and only if there are perfused vessels within the range of $3\tilde{h}_L = 240\mu m$, f is the shear stress and f_{max} is the maximal stress over all of the tree tips. The probabilities for an event are given by the normalized weights as above, as well as the probabilities for the element type and its orientation. Against this background we wrote $w_i = \infty$ in the symbolic meaning that it yields $p_g = 0, p_d = 0, p_i = 1$.

Pressure radius relation

The root nodes of the trees have fixed blood pressures as boundary condition. Their value is determined by an empirical formula which was fit to Fig. 5 in [2].

$$\begin{aligned} r' &= r \text{ for a vein, else } -r \\ A1 &= 89, A2 = 18, r_0 = -21, \Delta r = 16 \\ P &= 0.133[A2 + (A1 - A2)/(1 + \exp((r' - r_0)/\Delta r))] \end{aligned} \quad (1)$$

in units of μm for the radius r and kPa for the pressure P . For our typical networks this yields pressures from ca 2.5 to 12 kPa, where the radii of the root vessels are ca. $100 \mu m$.

Radius wall-thickness relation

Initially the vessel wall thickness $w(t=0) = w^{(init)}$ must be well defined. Guided by [3], we use

$$w_{(init)} = 2r(0.65 - 0.2 \log(2r)), \quad (2)$$

depending on the vessel radius r . Sprouts are also created with $w = w_{(init)}$.

Smoothed Heaviside and Dirac Delta functions

We adopt sin/cosine based formulas commonly used in level set and immersed boundary methods, see e.g. [4, 5].

$$\begin{aligned} \delta_\epsilon(x) &= \frac{1}{\epsilon} \begin{cases} \frac{1}{2}(1 + \cos(\frac{\pi x}{\epsilon})) & \text{if } |x| \leq \epsilon, \\ 0 & \text{otherwise} \end{cases} \\ \delta_\epsilon(\mathbf{x}) &= \delta_\epsilon(\mathbf{x}_0)\delta_\epsilon(\mathbf{x}_1)\delta_\epsilon(\mathbf{x}_2). \end{aligned} \quad (3)$$

In addition to the convergence to the ‘‘sharp’’ Dirac delta it has the nice properties that it is continuous and has limited support. The smoothed Heaviside function is the integral over $\delta_\epsilon(x)$ and reads

$$\Theta_\epsilon(x) = \begin{cases} 0 & \text{if } x \leq -\epsilon, \\ \frac{1}{2}[1 + \frac{x}{\epsilon} + \frac{1}{\pi} \sin(\frac{\pi x}{\epsilon})] & \text{if } |x| < \epsilon, \\ 1 & \text{otherwise} \end{cases} .$$

References

- [1] Hopcroft J, Tarjan R (1973) Algorithm 447: Efficient algorithms for graph manipulation. *Commun ACM* 16: 372–378.
- [2] Pries A, Secomb T, Gaehtgens P (1995) Design principles of vascular beds. *Circulation Research* 77.
- [3] Pries AR, Reglin B, Secomb TW (2005) Remodeling of blood vessels: responses of diameter and wall thickness to hemodynamic and metabolic stimuli. *Hypertension* 46: 725–731.
- [4] Sethian JA (1996) *Level Set Methods*. Cambridge University Press. URL <http://visinfo.zib.de/EVlib/Show?EVL-1996-149>.
- [5] Peskin CS (2002) The immersed boundary method. *Acta Numerica* 11: 479–517.

Computational analysis of tumor oxygenation, vascular remodeling and blood flow with applications to breast cancer.

Michael Welter¹, Thierry Fredrich¹, Herbert Rinneberg², Heiko Rieger^{1,*},

1 Theoretical Physics, Saarland University, Saarbrücken, Germany

2 Division of Medical Physics and Metrological Information Technology, Physikalisch Technische Bundesanstalt PTB Berlin, Germany

* E-mail: h.rieger@mx.uni-saarland.de

Abstract

The oxygenation of tumor tissue is in general very heterogeneous, not only spatially inhomogeneous in one tumor but also varying strongly among different individuals with the same kind of cancer, where the average blood oxygen saturation can be lower or larger than the surrounding tissue. This wide variation of tumor oxygenation must be related to corresponding heterogeneities in the underlying blood vessel network, which again could be used as diagnostic markers in cancer treatment. Unfortunately the spatial resolution of non-invasive oxygen measurements techniques as tissue optics or MRI is too low to allow for even an approximate reconstruction of the underlying vessel network, which itself is hardly accessible experimentally. Therefore computational models for tumor vascularization, blood flow and oxygenation are needed as a tool to interpret the available data. In this paper we present such a computational model for trans-vascular oxygen transport in tumor blood vessel networks formed by vascular remodeling via cooption, angiogenesis, and regression. A specially adopted numerical procedure allows the computation of the intra- and extravascular partial oxygen pressure distribution of macroscopic tumor tissue regions of sizes up to 1 cm^3 . Spatial inhomogeneities in the extra-vascular partial oxygen pressure distribution can be related to different tumor compartments characterized by varying capillary densities and blood flow characteristics. We calculated regional blood volume rBV, average hemoglobin concentration c_{HB} , and average blood oxygenation Y in tumors and their surrounding normal tissue. In addition, the relation between average blood oxygenation and hemoglobin concentration was determined. The results qualitatively reproduced published experimental data obtained for a cohort of 87 breast cancer patients. We show that the wide range of blood oxygenation data from above to below normal tissue can be related to strong variations in the location and morphology of high caliber vessels threading the tumor.

Author Summary

Blood vessel networks supply all parts of the body with oxygen, but also nourish growing tumors, which in return remodel the existing tissue vasculature via angiogenesis, vessel cooption and regression. The emerging tumor vasculature characteristics are in many respects very different from normal tissues, lacking a hierarchical arterio-venous organization and being spatially highly inhomogeneous, resulting also in spatially inhomogeneous oxygenation with hypoxic and hyperoxic regions. Tissue oxygenation and regional blood volume and flow can be measured non-invasively and it would be highly desirable to infer from the obtained data tumor vascularization characteristics, which are important for cancer diagnosis and therapy. Unfortunately the spatial resolution of these non-invasive techniques is very restricted so that computational models are needed to interpret the oxygenation and blood flow data. In this paper we present such a computational model and apply it to experimental data from breast cancer patients obtained with optical mammography and MRI.

Introduction

Tumor Oxygenation and Experimental Methods

Adequate supply of tissue with oxygen and nutrients critically depends on the structure and function of its vasculature. For tumors to grow beyond 2 *mm* in size, new vasculature must develop, i.e. angiogenesis must occur [1]. The vasculature of solid tumors, however, is known to differ distinctly from that of surrounding normal tissue. Whereas vasculature in normal tissue is arranged in a hierarchy of arteries, arterioles, capillaries, venules and veins and grows under tight control of inter-capillary distances, tumor vasculature develops in a chaotic manner without such control, leading to spatial vascular heterogeneity. In solid tumors necrotic regions, and regions of low microvessel density (MVD) may occur, whereas tumor blood vessels are more abundant at the tumor-host interface [2]. Tumor vessels are known to be immature, fragile, tortuous, dilated, to form (large diameter) arterio-venous shunts and often it is even difficult to distinguish arterioles and venules, i.e. the classification of tumor vessels as arterioles, capillaries and venules is no longer adequate [2, 3, 4, 5, 6, 7]. In addition, tumor vessels exhibit high permeability to macromolecules [3]. The structurally abnormal tumor vasculature results in spatially and temporally heterogeneous blood flow, affecting tissue oxygenation (acute or perfusion-limited hypoxia). From intravital dorsal window microscopy on tumor models it is known that blood flow through tumor capillaries is frequently sluggish and at times may even be stationary and reverse direction. It follows that blood flow through tumors may not follow a constant unidirectional path. In addition, red blood cell (RBC) flux varies greatly among tumor vessels, many tumor vessels do not carry RBCs but contain plasma only [2, 3, 4, 6, 8]. Furthermore, tissue solid pressure, generated by proliferating cancer cells, may compress tumor blood vessels thus reducing or impairing blood flow [9, 10, 11]. Tumor cells separated from nearby capillaries beyond the diffusion limit of oxygen suffer from chronic (diffusion-limited) hypoxia. Hypoxic tumor cells are known to be resistant to ionizing radiation, since oxygen is needed to stabilize radiation-induced DNA defects and, in addition, are considered to be resistant to some anticancer drugs. Therefore, tumor hypoxia is associated with poor prognosis, because it causes resistance to standard therapies and promotes more aggressive phenotypes [12, 13].

Because of their limited spatial resolution present-day non-invasive imaging techniques used in clinical practice do not allow to visualize tumor vasculature, blood flow and distributions of e.g. oxygen and nutrients at the capillary and cellular level, despite the diagnostic relevance, e.g. of *MVD* and the presence of hypoxic tumor cells. Therefore, computational modeling is an appropriate tool to analyze the relations between experimentally measurable characteristics of tumor vasculature and oxygenation.

Tissue oxygenation has been measured in human tumors by oxygen polarography using needle electrodes [14]. However, needle techniques are invasive and suffer from sampling errors. In this way oxygen partial pressures were found to be highly heterogeneous in tumors with median oxygen pressures below that of the host tissue. More importantly, tumors often exhibit hypoxic regions with oxygen partial pressures below 10 *mmHg*. Today, non-invasive positron emission tomography (PET) is employed clinically to image oxygenation status of tumor tissue [15]. The radio-labeled hypoxia imaging agent ¹⁸F-fluoromisonidazole (¹⁸F-MISO), e.g., freely diffuses in tissue after intravenous injection and extravasation from the vasculature. However, it is immobilized by binding to intracellular macromolecules in viable tumor cells that are located in areas with oxygen partial pressures below 10 *mmHg*, thus indicating hypoxia. In order to deduce ¹⁸F-MISO concentrations from measured tissue activity curves, modeling of concentrations of the radio-labeled imaging agent and of oxygen in tumor tissue is required [16, 17, 18]. Previously, PET together with the steady state ¹⁵O₂ inhalation method were used to measure cerebral metabolic rate of oxygen consumption CMRO₂ and oxygen utilization, i.e. the oxygen extraction fraction OEF in normal brain tissue [19]. This method had also been applied to human breast [20] and brain tumors [21, 22]. However for tumors this method is considered not to be accurate because homogeneous compartment models used to analyze the PET data do not take into account the inherent perfusion heterogeneity of tumors [23]. Dynamic PET measurements following application of a diffusible tracer allow to quantitatively deduce perfusion (blood flow *rBF*) of normal tissue and tumors. For example, perfusion of normal breast tissue and of breast tumors was measured by intravenous application of a bolus of H₂¹⁵O or inhalation of C¹⁵O₂ that is converted to H₂¹⁵O in the lungs [24, 25]. Furthermore, blood volume is obtained from PET measurements using C¹⁵O, or ¹¹CO that irreversibly bind to

hemoglobin.

Measurements of intravascular oxygen concentrations being complementary to extravascular tissue oxygenation measurements can be carried out by a variety imaging methods. There are several methods based on magnetic resonance imaging (MRI) that are sensitive to blood oxygen saturation in brain tissue ([26, 27]. Quantitative blood oxygen level dependent MRI (qBOLD-MRI) exploits magnetic field perturbations close to blood vessels originating from paramagnetic deoxy-hemoglobin. Such magnetic field perturbations increase the relaxation rate $1/T_2^*$ of water, obtained from gradient echo images. Based on a mathematical model of magnetization in each voxel, qBOLD-MRI was used to measure blood oxygen saturation in brain tumors and in contralateral healthy brain tissue of a tumor model [28]. While good spatial resolution is achieved, a number of parameters other than blood oxygen saturation affect the measured proton relaxation rate $1/T_2^*$, e.g. macroscopic field inhomogeneities and blood volume rBV , requiring additional MRI measurements to reliably deduce blood oxygen saturation. Blood volume can be inferred by measuring the water relaxation rates $1/T_2^*$ before and after application of a superparamagnetic blood pool contrast agent [28, 29]. Traditionally, T_2^* -weighted dynamic contrast enhanced MRI following application of a bolus of low-molecular weight paramagnetic contrast agent (e.g. Gd-DTPA) has been used to estimate perfusion from gradient echo images taken at high temporal resolution [30]. More recently cerebral perfusion was measured quantitatively by arterial spin labeling (ASL) followed by fast MRI techniques [31, 32]. Arterial spin labeling generates a bolus of magnetically tagged intravascular water in the artery feeding the tissue. The magnetically tagged water is then imaged in the capillaries and brain tissue of the imaging plane selected. Perfusion is deduced quantitatively from signal intensities of images with and without ASL applied.

In vivo tissue optical spectroscopy extending from the red to near infrared (NIR) spectrum allows to measure absorption by deoxy-hemoglobin (HbD) and oxy-hemoglobin (HbO) and hence to deduce blood oxygen saturation. Optical mammography [33, 34, 35] has been developed over the past one to two decades and a large body of data on concentrations c_{HbD} and c_{HbO} in normal breast tissue and breast tumors has been collected from many patients [36, 37, 38]. Mostly, the breast is slightly compressed between two glass plates and transmittance of laser radiation through the tissue is measured with the photon source at selected positions. Because of light scattering, photon trajectories through the (slightly compressed) breast are much (about 5 times) longer compared to the geometrical distance between photon source and detector, i.e. between the point of entry and point of exit of the photons, resulting in high sensitivity towards absorption. The transmitted photons sample a banana-shaped volume of the tissue with spatially varying optical properties. Assuming the host tissue and the tumor to have homogeneous but different optical properties, absorption and scattering properties of tumors and surrounding host tissue can be determined separately. Alternatively, methods have been developed to reconstruct the tissue absorption and scattering coefficients in 3D, provided transmittance of laser radiation is measured over a sufficient range of projection angles. Because of light scattering, optical mammograms obtained by diffuse optical imaging generally have poor spatial resolution.

The analysis of optical mammograms generally showed total hemoglobin concentration c_{Hb} , c_{HbD} , c_{HbO} to be larger in breast tumors compared to their host tissue by a factor of 3.5 on average. This observation can qualitatively be explained by a larger blood volume in tumors compared to the host tissue. Average blood oxygen saturation $c_{HbO}/c_{Hb} = Y$ in tissue, on the other hand, reflects the balance between vascular flux of oxygen that enters the tissue, i.e. oxygen supply, and oxygen flux from the vascular network into tissue, reflecting oxygen demand. Besides total hemoglobin concentration, blood oxygen saturation is thus another parameter characterizing the tumor and host vascular networks. Average blood oxygen saturation in breast tumors was observed to be both larger or smaller than that of their host tissue [37, 38]. Tumor tissue is - at least in parts - hypoxic, thereby increasing the intravascular-extravascular gradient of partial oxygen pressure and hence transvascular flux of oxygen into tumor tissue. Likewise blood flow, i.e. perfusion rBF , was measured by PET in breast tumors to be mostly above that of normal tissue amounting rBF in tumors to be larger by a factor 5 on average. Actually, the balance between oxygen supply and demand may have diagnostic value for therapy control. Recently it was reported [14] that breast cancer patients who underwent neoadjuvant chemotherapy before surgery and who were subsequently not classified as complete responders by immuno-histochemistry (non-pCR), tended to initially exhibit tumor blood oxygenation below that of the host tissue. On the other hand, patients

who were ranked as pathological complete responders (pCR) exhibited on average the same blood oxygen saturation in tumor and host tissue.

In this paper we simulate average blood oxygen saturation in normal breast tissue and breast tumors using two different models. Within a simple three-compartment model, taking into account concentrations of oxygen bound to hemoglobin, of oxygen dissolved in plasma and in tissue we calculate average blood oxygen saturation as a function of the ratio $\kappa = P_{O_2} S\rho O / rBF$ of permeability rate constant over regional blood flow for selected partial oxygen pressures in tissue. Alternatively the dependence of average blood oxygen saturation on the ratio of oxygen demand and supply, i. e. on the oxygen extraction fraction OEF is simulated. The computational model, on the other hand, tries to solve an ill-posed inverse problem, i.e. to determine vascular networks of normal breast tissue and of breast tumors that are consistent with experimental data on regional blood volume rBV and average blood oxygen saturation Y obtained previously from a cohort of 87 breast cancer patients [37]. For this purpose we algorithmically construct 3D vasculature of normal tissue and tumors following methods developed by us previously [39]. Because of its stochastic nature each growth process produces a different vascular network of the host and tumor tissue. The growth of the tumor results in vascular remodeling via vessel co-option, angiogenesis, and vessel regression. The bulk of tissue, excluding the vascular network, is considered as consisting of two homogeneous parts, an expanding sphere of tumor tissue, and the surrounding normal breast tissue. In this paper we extended our computational model to simulate oxygen supply and consumption. Taking each vessel segment as oxygen line source with a strength given by its transvascular oxygen flux, oxygen diffusion and consumption in tissue are calculated, yielding partial oxygen pressure distribution in tissue and blood oxygen saturation in the vascular network. Only stationary solutions are sought, ignoring transient variations of blood flow through tissue as discussed above. For each vascular network generated our model allows us to calculate biophysical and metabolic quantities, e.g. vascular (blood) volume rBV , microvessel density MVD , surface density, i.e. vessel surface per unit volume of tissue $S\rho$, perfusion rBF , total hemoglobin concentration, c_{Hb} , average blood oxygen saturation Y , oxygen extraction fraction OEF and metabolic rate of oxygen consumption MRO_2 in host and tumor tissue. By comparing calculated parameters with experimental data, algorithmically generated vascular structures of host and tumor tissue can be optimized. Furthermore a first step is taken to elucidate the relationship between vascular morphology and oxygen delivery in tumor specific networks. Although our model is generally applicable, e.g. to PET measurements using ^{18}F -MISO to detect tumor hypoxia and to qBOLD-MRI data to deduce blood oxygen saturation in brain tumors, in this paper we restrict ourselves to optical mammography.

Computational models allowing for oxygen diffusion in tissue

Krogh et al. [40] published a theoretical analysis of oxygen delivery in a piece of muscle tissue based on densely packed, parallel tissue cylinders each with a blood vessel running along its center line. Since each vessel was assumed to supply oxygen to its own cylinder only, the problem is reduced to that of a single cylinder. The diffusion-reaction equation for partial oxygen pressure in tissue is solved analytically assuming radial symmetry and neglecting diffusion along the cylinder orientation. In addition, blood is taken as homogeneous hemoglobin solution and intravascular radial gradients of oxygen partial pressure were neglected [41].

The current literature contains a large body of work on improved Krogh models which take the granular nature of blood into account by incorporating detailed modeling of convective and diffusive processes in and around red blood cells (RBCs), as well as hydrodynamic and mechanical aspects of RBCs. These improved models play an important role for the development of network transport models since they can be used to derive effective radial mass transport coefficients of oxygen, but a full review of all related work is beyond the scope of this paper. We restrict ourselves to references [42, 43, 44, 45, 46] the results of which were used in this work and refer for further reference to [41].

The detailed solution of three dimensional transport models for vascular tubes is prohibitively expensive for entire networks. Instead the problem is commonly approximated as piecewise one-dimensional advection on a segment by segment basis. Moreover the assumption of parallel tissue cylinders is unjustified in general and in particular for tumor networks due to their varying MVD and chaotic connectivity. In the literature regarding the simulation of tumor growth [39, 47, 48, 49, 50, 51, 52, 53, 54, 55, 56, 57, 58, 59, 60], the vascular oxygen distribution is universally assumed to be either homogeneous or proportional to the hematocrit for simplicity and efficiency reasons.

However, models, where this assumption had not been made, were used extensively to study given static networks in muscle fibers, various animal model tissues and also tumor networks of limited extent. Relevant literature will be reviewed below.

Goldman et al. [61] developed a computational model to determine oxygen distributions within a small blood vessel network and the surrounding tissue. Their model simulates the blood vessel network as interconnected perfused pipes (Poiseuille flow) and accounts for convective oxygen transport by the blood stream. This network is coupled to interstitial space (i.e. tissue) via boundary conditions which relate the radial transvascular oxygen flux at each point on the vessel surface with the PO₂ gradient at the respective location in tissue. In order to determine the tissue PO₂ level, a diffusion equation had to be solved which was handled numerically by finite differencing methods. While being accurate, the method of transvascular coupling requires fine resolution of the numerical grid to resolve the PO₂ gradients around the vascular walls. Indeed, the authors considered a tissue block of length 400 μm discretized into 200 grid points, compared to a typical capillary radius of 3 μm . The authors and co-workers published several follow-up papers [62, 63, 64, 65, 66] studying various scenarios and pathological alterations of the vascular network of a muscle fiber. The limitation to relatively small systems has, however, remained.

Hsu and Secomb [67] conceived a different computational approach based on Green's functions which was later improved upon [68]. An advantage of their method is fast convergence and the elegant handling of transvascular coupling, alleviating the need for excessively fine tessellation for boundary conditions. The model was applied to analyze tissue oxygen distributions from a small 3D tumor network comprising a few dozen segments only [68, 69]. However, due to the long ranged Green's function, the method is difficult to apply to large systems. Recently Secomb et al. published their source code [70]. Using their code, we succeeded in computing oxygen distributions for small systems of up to 1 mm^3 but further increase of the system size to 1 cm^3 , which we require, incurs an infeasible computational cost, both in time and memory.

Recently Secomb's Green's function method [68] was applied to models of cranial blood vessel networks [71, 72]. Safaeian et al. were particularly interested in the structure of cranial blood vessel networks and the effects caused by an occlusion of blood flow. The blood supply of the cranial cortex is organized in a two-dimensional top layer and a sub-surface bulk. The top layer contains arterial and venous trees, from the ends of which arterioles proceed vertically down into the bulk. After some distance these arterioles branch out into a very dense and rather tortuous capillary plexus. Safaeian et al. mimic this structure with a simplified artificially generated network.

Beard [73] developed a computational framework for solute transport in vascular networks. The general idea is similar to the aforementioned work where advective transport through a network is coupled with diffusion based transport in a tissue domain. The diffusion equation is discretized by a finite volume/difference approach, and source terms corresponding to the surface area of nearby vessels are added locally. This is also the idea behind our method applied in this paper. However, oxygen-hemoglobin binding dynamics were neglected.

If less detailed knowledge about the oxygen distribution is acceptable, a single-vessel model can provide useful insight. He et al. [74] developed a model to predict the heating of a tumor in a human breast by laser irradiation and the consequential alteration of the oxygen supply. In this model, perfusion data is derived from flow through single vessels and in turn fed back into the heat transport equation. It incorporates an elastic vessel wall, thermal expansion and pulsatile flow. The average tissue oxygen level is determined based on a Krogh cylinder model. A shortcoming of this model, as with the standard Krogh model, is the neglect of the complex flow patterns within tumor networks since only one tube acts as representative for all vessels.

Several works [16, 17, 18, 75, 76] consider (tumor) tissue oxygenation with the help of models where variations of the vascular oxygen content are neglected and vessels which are sources of oxygen are represented by point sources in two dimensions or lines in three dimensions. The spatial distribution of these sources [75] was generated according to probability distributions for intercapillary distances. Various scenarios were analyzed for hypoxic/normoxic conditions. Espinoza et al. [76] used a particle based numerical calculation [77] (lattice-free discretization) and placed discretization sites coincident with vascular oxygen sources. The oxygen level at these sites was set to fixed values analogous to traditional Dirichlet boundary conditions. Predictive models have gained importance since the development of tracer substances which accumulate in hypoxic tissue and can be used to derive the oxygen status of tumors. Kelly used a probability density function

derived from empirical MVD distributions to statistically generate vascular maps in 2D. These vascular maps were then used to calculate the steady state oxygen distribution in tissue besides the binding kinetics of the radio-tracer [17] F-miso. Skeldon et al. [16] first analyzed simplifying assumptions for theoretical computations of tissue oxygen distributions, and then considered the distribution of this tracer at a previously computed two-dimensional map of the local PO₂.

Lagerlöf et al. [78] considered the effect of varying degrees of hypoxia on radio sensitivity. To this end they obtained a voxelized three dimensional representation of a real vasculature from microscopy data, taken on an excised animal tumor. Tissue images were binarized, matched and resampled according to a numerical grid over which the PO₂ distribution was computed. Sites occupied by vessels were kept constant. Very recently this group published a study [79] on an idealized 3D vascular structure of a tumor, consisting of equidistant parallel vessels. Oxygen is transported by blood flow from the inlets to the ends of the vessel tree, while being able to diffuse from vessels into surrounding tissue voxels. The authors studied the effect of longitudinally decreasing blood oxygen saturation on the predicted radiation sensitivity.

Within the framework of our computational model we algorithmically construct 3d vascular networks of normal tissue and tumor tissue to reflect the various breast carcinomas of a patient cohort. Subsequently, besides geometric and hemodynamic properties intravascular and tissue oxygen concentrations are simulated. Previously, the 3d vascular network of tumors grown in tumor models were reconstructed from high resolution imaging data [80, 81]. Recently, Stamatelos et al. [7] reconstructed the 3d vascular architecture of a human breast cancer xenograft model of size 280 mm³ from micro-computed tomography (μ -CT) data taken ex-vivo. While geometric and hemodynamic properties of the reconstructed vascular network were simulated, distributions of intravascular and tissue oxygen concentrations or of other solutes were not considered. To our knowledge it has not been attempted yet to apply a theoretical model with a realistic tumor vasculature, e.g. vasculature obtained from that of the host tissue by vascular remodeling to explain the experimentally observed blood oxygen saturation and hemoglobin content in tumors [37, 38] and their relation to the vascular structure of the tumor. In order to explain the oxygen saturation variability observed among a cohort of breast cancer patients, it seems necessary to incorporate the vascular oxygen concentration as a model variable and the change thereof due to transvascular exchange. In particular, it is not sufficient to approximate the oxygen concentration as being strictly proportional to the hematocrit for instance because this assumption yields a constant saturation by definition $Y = c_{HbO}/c_{Hb}$, i.e., for such models, Y is an input parameter. Moreover, the typical tumor vasculature compartmentalization only manifests itself for tumors of a certain size, typically larger than 1 mm diameter, which current methods are not well suited for due to computational expenses.

Compartment models for brain vascular and tissue oxygenation

Compartment models have long been used to simulate tracer kinetics, new developments of such models and their application to MRI have recently been reviewed [82]. Valabregue et al. [83] used a three compartment brain model comprising oxygen bound to hemoglobin, oxygen dissolved in plasma and in brain tissue to simulate the dependence of cerebral metabolic rate of oxygen consumption $CMRO_2$ and of oxygen extraction fraction OEF on perfusion rBF , both under dynamic and stationary conditions. These authors applied their model to calculate relative signal changes based on the BOLD effect, measured by human functional magnetic resonance imaging (fMRI) following execution of motoric, visual or neurological tasks. Hayashi et al. [84] used the same compartment model, yet neglected the brain tissue oxygen pool to analyze the $CMRO_2$ - rBF relationship assuming various pathophysiologic brain conditions such as ischemia, hypoxia, anemia, or hypo- and hyper-capnic CBF variations. More recently, Jespersen and Ostergaard have extended the three-compartment model by including transit time heterogeneity [85]. Rather than considering a single vascular tube together with a well defined vascular transit time as previous authors, Jespersen et al. assumed a Krogh-like arrangement of parallel capillaries and a distribution of single capillary transit times. The authors investigated the impact of transit time distribution on oxygen extraction and metabolic rate of oxygen consumption in normal brain tissue. However, the three compartment model had never been applied before to simulate average blood oxygen saturation Y in normal tissue and tumors. Although average blood oxygen saturation Y will likewise be affected by transit time heterogeneity, consideration of transit time heterogeneity is beyond the scope of the present paper.

Experimental data from optical mammography

The present paper frequently refers to the results on hemoglobin concentrations c_{Hb} and average blood oxygen Y of breast tumors and surrounding normal breast tissue obtained from a cohort of 87 breast cancer patients using optical mammography [37]. For the sake of readability, we reproduce the relevant figures. See Fig. 1 and Fig. 2.

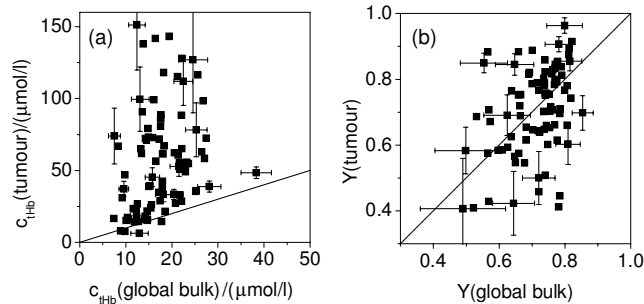


Figure 1. Physiological parameters of tumors versus those of corresponding healthy breast tissue for 87 patients: (a, left) total hemoglobin concentration c_{tHb} ; (b, right) blood oxygen saturation Y . Reproduced from Ref. [37, Fig. 3a,b], by permission of IOP Publishing. All rights reserved.

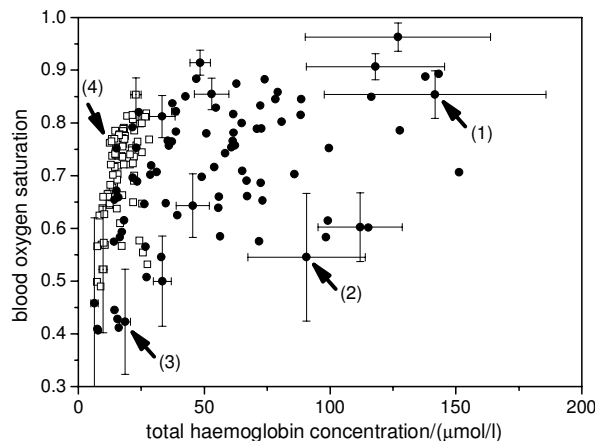


Figure 2. Blood oxygen saturation versus total hemoglobin concentration: Error bars [37, cf. Fig.3a,b] on tumor data correspond to uncertainties of tumor radius a_T and location z_T along compression direction, besides statistical contributions, error bars on healthy breast tissue data reflect statistical uncertainties only. Reproduced from Ref. [37, Fig. 5], by permission of IOP Publishing. All rights reserved.

Models

In the following section we explain the theoretical model employed here. This model has been used in the literature before [67, 68] but for clearness we review it here again in detail. Further below we present our attempt to solve the fully coupled equations for vascular and tissue PO₂ distributions efficiently. Finally a simple homogeneous three-compartment model of blood oxygenation is presented and approximate analytic solutions are considered.

Blood Oxygen

The concentration of oxygen dissolved in blood plasma or in tissue is proportional to the oxygen partial pressure (PO₂), i.e. $c_p = \alpha P$ and $c_t = \alpha_t P_t$, where P , P_t are the oxygen partial pressures in

plasma and tissue, respectively, and α , α_t the oxygen solubilities. Conventionally, the partial pressures are measured in *mmHg* and solubilities in *ml O₂/ml/mmHg*, yielding the oxygen concentrations expressed as oxygen gas volume at standard conditions (STP 0°C, 1 bar) per unit volume of plasma or tissue. In blood, oxygen, besides being dissolved in plasma, is bound to hemoglobin. Up to 4 molecules of oxygen can be bound per hemoglobin molecule. The chemical equilibrium between dissolved oxygen and oxygen-carrying hemoglobin depends on the number of oxygen molecules bound to hemoglobin, and the reaction is sufficiently fast, that the equilibrium state needs to be considered only. The cooperativity of oxygen-hemoglobin binding leads to the well-known oxygen dissociation curve [86], that can be approximated by the Hill equation [41]

$$S(P) = \frac{P^n}{P^n + P_{S50}^n}, \quad (1)$$

where $S(P)$ is the blood oxygen saturation, P_{S50} denotes the partial pressure at 50% saturation and n is the Hill exponent (see Table 1). Consequently, the total blood oxygen concentration, denoted by c , is the sum of the concentrations of dissolved and bound oxygen.

$$c = c_p + c_b = \alpha P + Hc_0S(P), \quad (2)$$

where H is the hematocrit, i.e. the volume fraction of red blood cells, and c_0 denotes the concentration of oxygen per unit volume of red blood cells (RBCs) at maximal saturation (s. Table 1).

Oxygen Transport within a Single Vascular Cylindrical Tube

The intravascular PO₂ variation along the longitudinal axis of a cylindrical vascular tube is described by $P(x)$, where x is the spatial coordinate. Following [67], we make the zeroth order approximation that the variation of PO₂, hematocrit, and flow velocity in the radial direction within vascular tubes are negligible. This approximation reduces the problem to advection in one dimension. Radial transport, i.e. transvascular oxygen exchange is accounted for by the addition of suitable mass transfer terms (see below). Hence, the product of the oxygen concentration with the blood flow rate yields the oxygen flux ι representing the total amount of oxygen at any given point that flows per unit time through the tubes cross-sectional area

$$\iota(P) = qc(P). \quad (3)$$

While blood flows along the vessel, some oxygen is continuously lost through the vessel wall. The respective transvascular flux density j_{tv} is given in units of amount of oxygen per lumen surface area and time. It causes a change in the longitudinal oxygen flux, which is expressed as

$$\frac{d\iota}{dx} = q \left[Hc_0 \frac{dS}{dP} \frac{dP}{dx} + \alpha \frac{dP}{dx} \right] = -2\pi r j_{tv}(x), \quad (4)$$

where the second expression is just the evaluation of $d\iota/dx$, and r is the vessel radius. Reordering yields the derivative of P

$$\frac{dP}{dx} = \frac{-2r\pi j_{tv}(x)}{q \left[Hc_0 \frac{dS}{dP} + \alpha \right]}. \quad (5)$$

For simplicity only losses due to diffusion are considered. This is certainly a good approximation for normal vessels because oxygen is a light molecule and has a proportionately high diffusion speed. Its diffusion constant in water is ca. $2 \cdot 10^3 \mu\text{m}^2/\text{s}$. Walls of tumor vessels, on the other hand, are leaky e.g. for plasma which is why a significant convective transport is plausible. Interstitial fluid velocities of up to $v = 1 \mu\text{m}/\text{s}$ have been reported near tumor vessels [90, 91, 92, 93]. In order to judge whether diffusive or convective transport in tissue is dominant, we calculated the Peclet number $P_e = vL/D$ which relates advective transport rate to diffusive transport rate over a certain

Table 1. Oxygen transport parameters

Symbol	Unit	Value	Ref/Note
n		2.7	[45]
P_{S50}	$mmHg$	27	[45]
α	$ml O_2 ml^{-1} mmHg^{-1}$	$3.1 \cdot 10^{-5}$	[45] (a)
α_t	$ml O_2 ml^{-1} mmHg^{-1}$	$2.8 \cdot 10^{-5}$	[45] (a)
c_0	$ml O_2 / ml$	0.5	[87] (b)
D_t	$\mu m^2 / s$	2410	[45]
D_p	$\mu m^2 / s$	2750	[45]
$P_{M50}(normal)$	$mmHg$	4	(c)
$P_{M50}(tumor)$	$mmHg$	2	(c)
$M_0(normal)$	$\mu l O_2 ml^{-1} min^{-1}$	3.7	(d)
$M_0(tumor)$	$\mu l O_2 ml^{-1} min^{-1}$	14.8	(d)
γ	$\mu m^3 O_2 \mu m^{-2} s^{-1} mmHg^{-1}$	0.0057 – 0.0208	(e)
$H^{(BC)}$		0.45	
$P_e^{(BC)}$	$mmHg$	100	[88] (f)
$\Delta P^{(BC)}$	$mmHg / \mu m$	1	[88] (f)
$P_0^{(BC)}$	$mmHg$	55	[88] (f)
h_v	μm	4	
h	μm	40	

Shows parameters for throughout all simulations except case METAB where $M_0(tumor)$ is picked at random for each simulation. (a) Assuming 22.4 l/mol under normal conditions. (b) Computed as the product of the hemoglobin binding capacity 1.34 ml O₂/g and the hemoglobin mass per RBC volume 0.34 g/ml. (c) Literature [66, 68, 76, 89] values for M_{P50} range from 1 to 4 mmHg. M_{P50} represents a threshold below which cells become hypoxic. We lowered M_{P50} in tumor tissue by a factor of 1/2 because cancer cells are generally associated with a resistance to hypoxia. (d) A consumption rate for physiological conditions amounting to $3.7 \cdot 10^{-3} ml O_2 ml Tissue^{-1} min^{-1}$ was estimated from perfusion rates (rBF), assuming an oxygen extraction fraction of 0.4 [24, 25]. The reference [19] refers to the cerebral oxygen consumption. See also Table.2. For tumors we assumed an four fold increased consumption M_0 . (e) The first value is obtained for $r = 60\mu m$ and the latter for $r = 3\mu m$. (f) The PO₂ at the inlet vessels is prescribed in dependence on the vessel radius r according to (12). For the lack of a better source, we used intra-vascular PO₂ measurements from rat brains [88] as reference.

distance L . A reasonable L is $100\mu m$, corresponding to typical intercapillary separations, yielding $P_e = 1/20$. It follows that the transport is diffusion dominated.

Intravascular radial oxygen transport is in itself a complex problem. To make transvascular oxygen flux workable, the mass transfer coefficient (MTC) γ is introduced that relates the transvascular oxygen flux density with the PO₂ difference between the plasma and tissue partial oxygen pressure P and P_t .

$$j_{tv}(x) = \gamma \cdot (P(x) - P_t(x)). \quad (6)$$

Since vessels are represented as lines, we also assume that P_t is constant over the entire circumference. Note that $\gamma 2\pi r = K^{-1}$, where K is the radial transport resistance used in [46, 67, 68]. The MTC depends on several factors like tube radius, oxygen saturation, RBC shape [41] and vessel morphology [94]. We consider a radius dependency according to a simple fit model, based on empirical data for radial oxygen transfer in vascular tubes [43, 44, 45]:

$$\gamma(r) = \frac{D_p \alpha_p}{r} p_2 (1 - \exp(-r/p_1)), \quad (7)$$

where p_1 and p_2 are fit parameters and D_p and α_p are oxygen diffusion coefficient and solubility in blood plasma. This form provides a good fit to the MTC obtained from Nusselt numbers nu [44,

Fig. 14] according to the relationship $\gamma = nuD_p\alpha_p/r$ [41]. We calibrated p_1 and p_2 with several test cases of vascular tubes from theoretical [45] and experimental data [43] oxygen saturation S , by the end of the tubes, gives a good fit (s. S1 Appendix). In this way we obtain $p_1 = 7.2 \mu m$ and $p_2 = 4$. A straight forward fit of [44, Fig. 14] yields $p_2 = 4.7$, but we found that the former value of p_2 gives better agreement when blood oxygen saturation increases caused by uptake through an external medium [43, Fig. 3], with negligible impact on other cases.

Blood Flow and Hematocrit in Vascular Networks

The vascular network is represented by a graph where edges represent vessel segments each connected to two nodes, whereas nodes may be attached to one to three vessel segments. Following the work of Pries et al. [95] we calculated blood pressure p at each node as well as blood flow rate q and hematocrit H associated with each vessel segment. A direction is imposed on each vessel segment according to its blood flow direction. The primary unknowns are the nodal pressures and segment hematocrits. The hematocrit, i.e. the fractional volume of red blood cells (RBCs) in blood may differ between various vessel segments due to phase separation.

The flow rates are given by Hagen-Poiseuilles law for flow through pipes $q = \pi r^4 \Delta p / (8\eta l)$, where r denotes the radius of the segment, l its length, η the (apparent) blood viscosity, and Δp the difference of the blood pressure at both nodes the vessel segment is attached to. Mass conservation demands at each non-boundary node that

$$\sum_{i \in \mathbb{I}} q_i = \sum_{j \in \mathbb{O}} q_j \quad (8)$$

$$\sum_{i \in \mathbb{I}} H_i q_i = \sum_{j \in \mathbb{O}} H_j q_j, \quad (9)$$

where the sets \mathbb{I} and \mathbb{O} contain the adjacent up- and downstream vessels depending on the current node. In contrast to the Ref. [95] we use pressure boundary conditions (BCs) where p at root nodes is set to a fixed value $p(\text{root}) = p^{(BC)}(r)$ depending on the radius and the type of vessel (artery or vein) (s. Eq. (1) in S5 Appendix). Eq. (8) and BCs lead to a system of linear equations, the solution of which yields the nodal pressures. The system is very large, of the order of 10^6 unknowns. We found that the Conjugate Gradient algorithm with the Multilevel (ML) preconditioner from the Trilinos software library [96] solves it efficiently.

The apparent blood viscosity in microvessels varies with r and H (Fahraeus-Lindqvist effect) and is expressed by decomposing it into $\eta = \eta_{\text{plasma}} \eta_{\text{rel}}(r, H)$, where η_{plasma} is the viscosity of pure blood plasma and $\eta_{\text{rel}}(r, H)$ is known as relative viscosity. We implemented the η_{rel} formula from more recent work Pries et al. [97] where η_{rel} is based on in vivo data. For brevity we refer to the original publication for the expression for η_{rel} .

Furthermore RBCs at arterial bifurcations tend to flow into the faster perfused branch (phase separation effect) resulting in an uneven hematocrit distribution across the network. Pries et al. [95] devised a phenomenological formula which describes the hematocrit H in the downstream branches of a bifurcation as a function of q and r of all adjacent vessels. For details we refer to [95]. With the help of this formula we compute the RBC flow qH in down stream vessels of arterial bifurcations, i.e. where one vessels splits into two downstream vessels. On the other hand, venous bifurcations have only one downstream branch where H is determined by (9). Our initial vascular network, representing the vascular network of normal tissue, contains by default only bifurcations and the trivial case of two adjacent vessels. The tumor growth model [39] on the other hand was modified, rejecting sprout connections to other vessels that resulted in junctions with more than three vessels attached. The hematocrit over the entire network can thus be computed with a simple depth-first search graph traversal algorithm [98] starting from the venous ends and determining the downstream H while backtracking.

The ansatz to solve this coupled system of equations is iterative. In each iteration, the nodal pressures are computed using the results for the vessel segment hematocrit of the previous iterations, followed by the computation of the hematocrit with new flow rates. Details can be found in [95].

Oxygen in Vascular Networks

The ansatz to determine the PO2 across the vascular network is similar to the method followed for calculating the distribution of hematocrit. First we consider the distribution at an arbitrarily selected node. Let P_i for $i \in \mathbb{I}$ be the PO2 at downstream ends of adjacent inlet vessels. Then P_j for $j \in \mathbb{O}$ at the upstream ends of outlet vessels are to be determined. The main assumption made is that RBCs flowing into the junction instantly assume a common equilibrium partial pressure \tilde{P} , that by definition equals the PO2 at all outlets $P_j = \tilde{P}$ for $j \in \mathbb{O}$. \tilde{P} is determined with the help of the oxygen mass balance

$$\sum_{i \in \mathbb{I}} q_i (c_0 S(P_i) H_i + \alpha P_i) = \tilde{t} = \sum_{j \in \mathbb{O}} q_j (c_0 S(\tilde{P}) H_j + \alpha \tilde{P}), \quad (10)$$

where the left hand side is known and provides the total oxygen flux \tilde{t} at the node under discussion. The right hand side is rearranged as

$$\tilde{t} = \left[\sum_{i \in \mathbb{O}} H_i q_i \right] c_0 S(\tilde{P}) + \left[\sum_{i \in \mathbb{O}} q_i \right] \alpha \tilde{P}, \quad (11)$$

where quantities in brackets are known RBC, and blood, flow rates. Eq. (11) was solved numerically for \tilde{P} using a bisection search. At inlet (root) nodes, boundary conditions (BCs) must be specified. We use Dirichlet BCs where $P = P^{(BC)}$ is given according to a curve $P^{(BC)}(r)$ depending on the arteriolar radius.

$$P^{(BC)}(r) = \min(P_0^{(BC)} + \Delta P^{(BC)} r, P_c^{(BC)}). \quad (12)$$

For the parameter values of $P_0^{(BC)}, \Delta P^{(BC)}, P_c^{(BC)}$ see Table 1.

The determination of PO2 across the entire network can be defined procedurally with the help of the depth-first search graph traversal [98] analogous to the propagation of hematocrit. Starting from venous root nodes, the network is traversed towards the upstream ends. Let us consider a given node while backtracking. P is known at the upstream ends of adjacent inlet vessels, and according to (5) the down-stream P is determined. Hence, (11) provides P for further backtracking downstream. This procedure holds under the caveat that j_{tv} is known, which is addressed below.

Oxygen in Tissue

The oxygen concentration in tissue, denoted $c_t(\mathbf{y})$, as a function of position \mathbf{y} , is determined by the solution of the following steady state diffusion equation, considering a cubic domain $\Omega = (0, L)^3$ with lateral size L and Neumann boundary conditions.

$$D_t \nabla^2 c_t - M + Q = 0 \quad (13)$$

$$\nabla c_t \cdot \mathbf{n} = 0 \text{ on } \partial\Omega, \quad (14)$$

where M is the oxygen consumption rate and the last term Q represents the oxygen exchange with vessels. With the help of the solubility α_t this equation is rewritten in terms of the partial pressure P_t .

$$\alpha_t D_t \nabla^2 P_t - M + Q = 0 \quad (15)$$

$$\nabla P_t \cdot \mathbf{n} = 0 \text{ on } \partial\Omega, \quad (16)$$

where the symbols $Q = Q(P_t, \mathbf{y})$ and $M = M(P_t)$ are redefined as functions of P_t . They emerge from their former versions by simple scaling of their arguments by α_t .

We model consumption according to the well-known Michaelis-Menten (MM) model [41]. The MM model takes into account that cells consume oxygen up to a maximal rate M_0 even at high (excess) oxygen availability, and that consumption must drop to zero when the local oxygen partial pressure drops to zero. M is consequently defined as

$$M(P) = M_0 \frac{P}{P + P_{M50}}, \quad (17)$$

where the subscript for P has been dropped. The partial pressure at which M equals 50% of its maximal rate M_0 is denoted by P_{M50} . $M(P)$ increases monotonously and approaches M_0 asymptotically. The advantage of the MM model over zero-or first order kinetics is a realistic description of hyper-and hypoxic situations.

To find the vascular contribution Q , representing sources and drains, we follow [67] where line-like sources are embedded into the volume (tissue) with a magnitude equal to j_{tv} . Symbolically written, this corresponds to

$$Q(\mathbf{y}) = \sum_{v \in \mathbb{V}} \int_v 2\pi r j_{tv}(\mathbf{x}, r) \delta(\mathbf{x} - \mathbf{y}) dx, \quad (18)$$

where the summation is taken over all vessels and the integration along their center lines. δ is the Dirac delta distribution and j_{tv} is given in (6,7).

Numerical Solution

The equation for the vascular oxygen distribution (5,11) together with the diffusion equation for tissue (15) form a complicated non-linear system of equations with the partial pressures values as unknowns. The only practical way to treat this is through a numerical solution.

Previously a similar approach to ours was followed by Beard [73] who distributes the exchange flux with vessels to nearby sites of a discretization grid of the tissue domain. We justify this approach with a formulation based on a Finite Element Method (FEM) and in contrast to [73] also include hemoglobin binding dynamics. As a result we obtain a sparse system of equations which is efficiently solved by an iterative scheme.

The principal idea of the FEM is to seek an approximate solution within a finite dimensional vector space V that is spanned by basis functions φ_i . Various choices are possible, e.g. Fourier bases, but the common approach is to introduce a grid and organize the φ_i such that their contribution is centered around a corresponding grid site \mathbf{x}_i , requiring that $\varphi_i(\mathbf{x}_i) = 1$ and $\varphi_i(\mathbf{x}_j) = 0$ for $i \neq j$. Here the choice falls for simplicity on piecewise linear (P1) tensor product bases which are defined on a regular cubic grid. Then φ_i reads

$$\begin{aligned} \tilde{w}(x) &= \max(0, 1 - |x|/h) \\ w(\mathbf{x}) &= \tilde{w}(x_0)\tilde{w}(x_1)\tilde{w}(x_2) \\ \varphi_i(\mathbf{y}) &= w(\mathbf{y} - \mathbf{x}_i), \end{aligned}$$

where h is the lattice constant and $\mathbf{y} = (y_0, y_1, y_2)$ and likewise \mathbf{x} in three dimensions. Incidentally evaluation of a function $f(\mathbf{y}) = \sum f_i \varphi_i(\mathbf{y})$ with some coefficients f_i is equivalent to a (tri-) linear interpolation of the coefficients between grid sites that are nearest to \mathbf{y} . Hence, let the tissue PO2 be an element of V such that

$$P_t = \sum_j P_{t,j} \varphi_j. \quad (19)$$

At this point it is advisable to proceed with the treatment of the vascular system. It is by definition already represented as discrete collection of segments but these are implicitly further subdivided by the integration points that are introduced for the solution of the axial transport equation (5) (see below). We impose an equidistant subdivision with the constant step length

$h_v = 10\mu m$. In general, the last point needs to coincide with the end of the vessel. For our choice of h_v this holds true because our networks are generated on a lattice, the constant of which is a multiple of, or equal to, $10\mu m$. We also evaluated more general cases with smaller h_v for increased accuracy but found that this produces no significantly different results.

In the following the index k, l is used for points on the vessel network whereas i, j index sites on the tissue grid. Now it is convenient to introduce vector and matrix notations. Hence let coefficient vectors be denoted in bold face, such that $\mathbf{P}_t = \{P_{t,i}\}$ and $\mathbf{P} = \{P_k\}$. And let further linear operators (matrices) be denoted in bold face underlined $\underline{\cdot}$.

The solution procedure relies on an outer iteration where the tissue degrees of freedom $\{P_{t,i}\}$ and the vessel degrees of freedom $\{P_k\}$ are updated in alternating order. This can be written with the aid of two functions $\mathbf{F}(\mathbf{P}, \mathbf{P}_t)$ and $\mathbf{F}_t(\mathbf{P}, \mathbf{P}_t)$ determining \mathbf{P} and \mathbf{P}_t from the last known quantities. An iteration variable n is introduced denoting the current step number. This is not to be confused with n in the Hill-equation (1).

for $n = 1, 2, 3, \dots$

$$\mathbf{P}^{(n+1)} = \mathbf{F}(\mathbf{P}_t^{(n)}) \quad (20)$$

$$\mathbf{P}_t^{(n+1)} = \mathbf{F}_t(\mathbf{P}^{(n+1)}, \mathbf{P}_t^{(n)}) \quad (21)$$

while $\|\mathbf{P}_t^{(n+1)} - \mathbf{P}_t^{(n)}\|_\infty > \epsilon$ and $\|\mathbf{P}^{(n+1)} - \mathbf{P}^{(n)}\|_\infty > \epsilon$,

where $\|\cdot\|_\infty$ denotes the maximum norm. We set the initial guess for tissue $\mathbf{P}_t^{(1)}$ to $P_{root,max}/2$ on all grid points. \mathbf{P} needs no initial value since it is entirely determined by \mathbf{P}_t . The iteration is stopped when the change between the updates becomes less than ϵ , where we consider $\epsilon = 0.1mmHg$ to be small enough. Usually 200 to 400 iterations are needed for convergence, when applied to our tumor networks.

Evaluation of \mathbf{F} : The vascular tree is traversed down stream as explained. At each vessel, first the upstream PO2 is determined according to (11) or according to the boundary condition (12) if it is an inlet node .

Then (5) is integrated with the implicit Euler method [99]. Explicit methods are not well suited to the problem since their stability requirements [99] lead to a step size $h_v < const \cdot q$. Since many tumor vessels are slowly perfused this would lead to sub micro meter steps, incurring a prohibitive performance penalty. Note that the representation of P_t as superposition of basis functions readily provides a means to obtain its function value for the r.h.s of (5). Since the bases φ_i have a small support this can be efficiently implemented. Moreover storage of all P_k values is not required. Instead we perform required operations ‘‘on the fly’’ when the vascular PO2 is computed in \mathbf{F} . This means we either record oxygen exchange contributions for P_t into the system matrix (35) or compute observables for final output. It is sufficient to just store P_k at the upstream end of each vessel which is just \tilde{P} from (11).

Evaluation of \mathbf{F}_t : Our approach for the solution of the diffusion equation (15) can be derived from the Galerkin method, where in brief, the general idea is as follows. First, the standard scalar product over the space of integrable functions over Ω is introduced $(f, g) = \int f g d\mathbf{x}$. Furthermore instead of the true solution, an approximation within the vector space V is searched for. This solution is defined as $f \in V$ for which the residual R after evaluation of the differential equation w.r.t. f is minimal, i.e. we look for $f \in V$ such that $(R, R) = min$. Here P_t takes the role of f and we have

$$R = \alpha_t D_t \nabla^2 P_t - M(P_t) + Q(P_t). \quad (22)$$

It can be shown that minimization of $\|R\|$ is equivalent to finding the P_t where R is orthogonal to V

$$(R, \varphi_i) = 0 \quad \forall i. \quad (23)$$

Eventually this results in an equation per grid site i in the unknowns $\{P_{t,i}\}$. The l.h.s. of (23) decomposes into the summands

$$\alpha_t D_t(\nabla^2 P_t, \varphi_i) \quad (24)$$

$$(M(P_t), \varphi_i) \quad (25)$$

$$(Q(P_t), \varphi_i), \quad (26)$$

for which algebraic expressions are needed.

The benefit of considering a finite element formulation lies in the straight forward treatment of the transvascular exchange Q with its the Dirac delta. Also FEM makes it straight forward to use higher order elements for better accuracy. Here however we use P1 elements. Moreover, it has been shown that the FEM discretization with the P1 basis can be made to look identical to the standard finite difference discretization. (See e.g [100].) The trick is to perform the integration in (\cdot, \cdot) according to the trapezoidal rule. Performing the integration using the trapezoidal rule, one indeed obtains for a smooth enough function g that

$$(g, \varphi_i) \approx h^3 g(\mathbf{x}_i), \quad (27)$$

i.e. obtaining g sampled at the grid point i which equals g_i if $g = \sum_i g_i \varphi_i$. Likewise one obtains for a sufficiently smooth function f

$$(\nabla^2 f, \varphi_i) \approx h^3 [\underline{\Delta}_h \mathbf{f}]_i + \text{boundary terms}, \quad (28)$$

where

$$(\underline{\Delta}_h \mathbf{f})_i = \sum_{j \in \text{Neighbors of } i} (f_j - f_i)/h. \quad (29)$$

$\underline{\Delta}_h$ is the discrete Laplacian [99] known from finite differences. Neighbors of i denotes the 6 nearest grid neighbors. At the boundaries we modify $\underline{\Delta}_h$ to account for the missing neighbors [99]. The consumption term $M(P_t)$ is expanded to first order around the oxygen level from the last step. Following the above rationale, it is evaluated per grid point which yields

$$\frac{1}{h^3} (M, \varphi_i) \approx M(P_{t,i}^{(n)}) + M'(P_{t,i}^{(n)}) [P_{t,i}^{(n+1)} - P_{t,i}^{(n)}], \quad (30)$$

where $'$ denotes the first derivative. More conveniently in matrix notation and with dropped super scripts, we write

$$\mathbf{MA} + \mathbf{MB} \mathbf{I} P_t, \quad (31)$$

where \mathbf{I} denotes the identity, and

$$MA_i = M(P_{t,i}^{(n)}) - M'(P_{t,i}^{(n)}) P_{t,i}^{(n)} \quad (32)$$

$$MB_i = M'(P_{t,i}^{(n)}) \quad (33)$$

The last contribution is derived by expanding (26). For better readability, the super scripts are dropped again. Also the dependence of r and γ on the current vessel v is implied but for readability not indicated.

$$\begin{aligned} (Q(P_t), \varphi_i) &= \int_{\Omega} \sum_{v \in \mathbb{V}} \int_v 2\pi r j_{tv} \delta(\mathbf{x} - \mathbf{y}) \varphi_i(\mathbf{y}) dx d\mathbf{y} \\ &= \sum_{v \in \mathbb{V}} \int_v 2\pi r j_{tv} \varphi_i(\mathbf{x}) dx \\ &= \sum_{v \in \mathbb{V}} \int_v 2\pi r \gamma [P(\mathbf{x}) - P_t(\mathbf{x})] \varphi_i(\mathbf{x}) dx \\ &= \left[\sum_{v \in \mathbb{V}} \int_v 2\pi r \gamma P(\mathbf{x}) \varphi_i(\mathbf{x}) dx \right] + \left[\sum_j \sum_{v \in \mathbb{V}} \int_v 2\pi r \gamma P_{t,j} \varphi_j(\mathbf{x}) \varphi_i(\mathbf{x}) dx \right] \end{aligned} \quad (34)$$

The expression given in (34) approximates the total volume rate of oxygen that extravasates from the entire vascular system into the tissue volume associated with the basis function φ_i . Now the integral over the vessel network is approximated with a Riemann sum based on the integration points $\{P_k\}$ from step (20). Each integration point k represents a finite length segment $\Delta x_k = h_v$ except at the end points of each segment where $\Delta x_k = h_v/2$. In order to achieve good accuracy, we require $h_v \ll h$. Else, the integration kernel $2\pi\gamma\varphi_i$ or $2\pi\gamma\varphi_i\varphi_j$ will be under-sampled. This limitation could be removed to some degree by interpolation of the numerical solution of $P(x)$, decoupling it from the integration quadrature formula. From (34) one obtains for the total volume rate of extravasated oxygen per cell volume

$$\frac{1}{h^3}(Q(P_t), \varphi_i) \approx \underbrace{\sum_k \frac{\Delta x_k 2\pi r}{h^3} \gamma P_k \varphi_i(\mathbf{x}_k)}_{\mathbf{QA}_i} + \sum_j P_{t,j} \left[\underbrace{\sum_k \frac{\Delta x_k 2\pi r}{h^3} \gamma \varphi_j(\mathbf{x}_k) \varphi_i(\mathbf{x}_k)}_{\mathbf{QB}_{ij}} \right]. \quad (35)$$

The factor $\Delta x_k 2\pi r / h^3$ is intuitively understood as vessel surface area per cell volume. Finally, the completely assembled system of equations reads

$$[\alpha_t D_t \Delta_h - \mathbf{MBI} + \mathbf{QB}] P_t = \mathbf{MA} - \mathbf{QA}. \quad (36)$$

It is easy to see that this is a sparse symmetric system. The Laplacian gives rise to 6 off-diagonal entries. The operator \mathbf{QB} gives rise to 26 off-diagonal entries corresponding to the nearest and second nearest grid neighbors. For points which are spaced further apart, φ_i and φ_j have no overlap so their product in (35) becomes zero.

In order to improve the efficiency we approximate $P_t(\mathbf{x}_k)$ with the value from the current site $P_{t,i}$. This approximation is justified physically since the oxygen diffusion length considerably exceeds the lattice spacing h . Consequently, \mathbf{QB} is diagonalized such that the new version, now denoted $\tilde{\mathbf{QB}}$, reads

$$\tilde{\mathbf{QB}}_{ij} = \sum_k \frac{\Delta x_k 2\pi r}{h^3} \gamma \varphi_i(\mathbf{x}_k) \delta_{ij}. \quad (37)$$

This is a sparse linear system where the only off-diagonal terms stem only from the Laplacian, removing the off-diagonal entries corresponding to the second nearest neighbors. We solved these systems with an algebraic multigrid method (Trilinos ML [96]). We found the difference between the $\tilde{\mathbf{QB}}$ and \mathbf{QB} solutions negligible.

Homogeneous Three-Compartment Model of Blood Oxygenation

Before simulating various biophysical variables using artificial vascular networks of normal and tumor tissue, we calculate blood oxygen saturation Y in breast tissue and breast tumors within a simple model consisting of the three compartments oxygen dissolved in plasma, oxygen bound to hemoglobin and oxygen dissolved in tissue surrounding a cylindrical blood vessel of radius r and length l . By comparing calculated average blood oxygenation with experimental data published previously, blood oxygenation of breast tumors and associated normal breast tissue is analyzed for oxygen extraction fraction OEF , the ratio of oxygen extravasation rate constant over blood flow rate $P_{O_2} S \rho / rBF$ and the metabolic rate of oxygen consumption MRO_2 that serve as reference for the computational model described above. The compartment model was used previously to simulate metabolic rates of oxygen consumption of normal brain tissue [83, 85].

In contrast to the previous sections, oxygen concentration in tissue is assumed to be uniform, i.e. with respect to oxygen, tissue is well mixed and hence diffusion of oxygen in tissue is not taken into account. Furthermore, rather than considering a network of blood vessels, oxygen concentration is calculated along a single vessel, representing the total vascular length of the network. We approximate Eq. (5) together with Eq.(6) as

$$\frac{dc_p(\xi)}{d\xi} = -\frac{\gamma(r)}{\alpha} \frac{2\pi rl}{q} \frac{c_p(\xi) - \bar{c}_t}{\left[1 + \frac{Hc_0}{\alpha} \frac{dS}{dP}\right]}. \quad (38)$$

The longitudinal variable has been normalized to the vessel length, $\xi = x/l$, i.e. $0 \leq \xi \leq 1$, $c_p(\xi) = \alpha P(\xi)$ is the concentration of oxygen dissolved in plasma, $\bar{c}_t = \alpha_t \langle P_t \rangle$ the average oxygen concentration in tissue, and $\alpha = \alpha_t$ was assumed. Eq.(38) can be rewritten for the oxygen concentration in blood $c = c_p + c_b$ yielding

$$\frac{dc(\xi)}{d\xi} = -\kappa \{c_p(\xi) - \bar{c}_t\}, \quad (39)$$

where $c_b(\xi) = Hc_0S(\xi)$ is the concentration of oxygen bound to hemoglobin, $S(\xi)$ the blood oxygen saturation, $\kappa = P_{O_2}S\rho/rBF$ is the ratio of the oxygen extravasation rate constant $P_{O_2}S\rho$ over the blood flow rate rBF , and $S\rho$ is the surface area per unit volume of tissue. Formally, in Eq.(38) $2\pi rl/|\Omega|$ and $q/|\Omega|$ were replaced by $S\rho$ and rBF , respectively. Alternatively, $\kappa = P_{O_2}S\rho(rBV)^{-1}MTT$ may be expressed in terms of the regional blood volume rBV and the product of the oxygen extravasation rate constant $P_{O_2}S\rho$ and the mean transit time MTT . Setting $c_p(\xi) = \beta(S)c_b(\xi)$ with

$$\beta(S) = \frac{\alpha P_{50}}{c_0 H \cdot S} \left(\frac{S}{1-S} \right)^{1/n}$$

Eq. (39) is reformulated as

$$\frac{dc(\xi)}{d\xi} = -\kappa \left\{ \alpha P_{50} \left(\frac{c(\xi)}{c_0 H - c(\xi)} \right)^{1/n} - \bar{c}_t \right\}, \quad (40)$$

where the small contribution of dissolved oxygen to the total oxygen concentration has been neglected on the right hand side of Eq.(40). From the solution $c(\xi)$ of Eq.(40), obtained for assumed values of κ , \bar{c}_t and the arterial oxygen concentration $c(0) = c_0 H \cdot S(0)$, the oxygen saturation $S(\xi)$, and the concentration of dissolved oxygen $c_p(\xi)$ along the vessel axis, as well as the oxygen extraction fraction $OEf = 1 - S(1)/S(0)$ are derived. Furthermore, the average blood oxygen saturation $Y = \int_0^1 S(\xi)d\xi$ and the average concentration $\bar{c}_p = \int_0^1 c_p(\xi)d\xi$ of oxygen dissolved in plasma are calculated.

In tissue optics [36, 37, 38] and MRI [28], however, average blood saturation Y is measured rather than the oxygen extraction fraction proper. Furthermore, integrating Eq.(39) along the vessel axis yields for the transvascular oxygen flux per unit volume of tissue $rJ_{tv} \equiv J_{tv}/|\Omega| = P_{O_2}S\rho \{ \bar{c}_p - \bar{c}_t \}$. Assuming stationary conditions, the metabolic rate of oxygen consumption equals the transvascular oxygen flux per unit volume of tissue, i.e. $MRO_2 = rJ_{tv}$. Hence with κ , \bar{c}_t and $c(0)$ selected, the ratio $MRO_2/rJ_{in} = OEf$ of the metabolic rate of oxygen consumption over oxygen flux $rJ_{in} = c(0) \cdot rBF$ is determined, entering the vascular network per unit volume of tissue. Adopting additionally a value for the perfusion rBF , the metabolic rate of oxygen consumption MRO_2 and the extravasation constant $P_{O_2}S\rho$ are deduced.

For a qualitative discussion, illustrating the dependence of Y on $P_{O_2}S\rho/rBF$ and \bar{c}_t , we use the simple Renkin-Crone model, that neglects cooperativity of oxygen binding to hemoglobin, i.e. the dependence $\beta(S)$ on saturation, thus considering a fixed position on the oxyhemoglobin dissociation curve. Then Eq. (39) is rewritten as

$$\frac{dc(\xi)}{d\xi} = -\kappa_{eff} \{c(\xi) - \bar{c}_t/\beta\} \quad (41)$$

where $\kappa_{eff} = P_{eff}S\rho/rBF = \beta P$ and $\beta \ll 1$ was used. Eq. (41) is readily integrated to yield the average blood saturation

$$Y = \left\{ S(0) - \frac{\bar{c}_t}{c_0 H \beta} \right\} \frac{1 - \exp(-\kappa_{eff})}{\kappa_{eff}} + \frac{\bar{c}_t}{c_0 H \beta}. \quad (42)$$

Within this approximation, average blood oxygen saturation Y varies as $\{1 - \exp(-k_{eff})\}/k_{eff}$ and experiences a shift towards higher values at finite tissue oxygen partial pressures. A maximal loss of oxygen from the vasculature to tissue is simulated by setting $\bar{c}_t = 0$, i.e. when neglecting the backflow of oxygen from the tissue to the vascular system, as supposed by the Renkin-Crone model. In this case, Eq.(42) represents a lower limit for the average blood oxygen saturation Y . For $k_{eff} \ll 1$, i.e. for low extravasation constant $P_{eff}S\rho$ or high blood flow rBF (permeability limited case) average blood oxygen saturation Y approaches $S(0)$, independently of the average blood oxygen concentration \bar{c}_t in tissue. For $\kappa_{eff} \gg 1$, i.e. for high extravasation constant $P_{eff}S\rho$ or low perfusion rBF (flow-limited case) average blood oxygenation Y increases linearly with $1/\kappa_{eff}$.

While the simple Renkin-Crone model provides some physical insight, for a quantitative discussion of the results of the compartment model, Eq. (40) needs to be integrated numerically [83]. In addition, the permeability coefficient P_{O_2} is a lumped parameter, that does not represent the true capillary permeability $\gamma(r)/\alpha$, but implicitly depends on the mass transfer coefficient γ and on the distribution of tissue partial oxygen pressure and therefore depends on its average $\langle P_t \rangle$ (s. Eq. (14) in S2 Appendix) We note in passing that the apparent oxygen extraction fraction $OE_{app} = 1 - Y/S(0)$ always falls below the oxygen fraction OE proper, apart from the trivial case $OE = 0$. Furthermore, the metabolic rate of oxygen consumption, normalized to the extravasation rate constant $P_{O_2}S\rho$ is equal to the difference between the average plasma \bar{c}_p and tissue \bar{c}_t oxygen concentrations. In contrast, no such relation exists for the average blood oxygen saturation Y which roughly follows \bar{c}_p as given by the Hill equation, at least in the range of tissue oxygen saturations considered in this paper. Stationary models of oxygen transport in a single vascular tube that do not assume perfect tissue oxygen mixing and therefore account for diffusion of oxygen in tissue [43, 45] allowing for longitudinally decreasing tissue oxygen partial pressure. In contrast Eq.(39) causes $dc(\xi)/d\xi$ to tend to zero, when the plasma oxygen concentration $c_p(\xi)$ approaches the constant tissue oxygen concentration \bar{c}_t . In this case oxygen flux from plasma to tissue is balanced by the reverse flux from tissue to plasma and no net exchange of oxygen takes place further downstream. When $c_p(\xi = 1) = \bar{c}_t$, the maximal oxygen extraction fraction is reached, given by

$$OE_{max} = 1 - \left\{ \frac{1}{1 + (P_{50}/P_t)^n} + \frac{\alpha P_t}{H c_0} \right\} \{S(0)[1 + \beta(S(0))]\}^{-1}$$

where the small contributions of dissolved oxygen at $c(0)$ and $c(1)$ have been taken into account. Hence, for a selected tissue oxygen partial pressure P_t there is an upper limit $MRO_{2,max}$ to the metabolic rate of oxygen consumption, corresponding to OE_{max} . At sufficiently large ratios $\kappa = P_{O_2}S\rho/rBF$ the transvascular oxygen flux per unit volume of tissue, i.e. the product $P_{O_2}S\rho(\bar{c}_p - \bar{c}_t)$ tends towards $MRO_{2,max}$ apart from the small contributions of dissolved oxygen to $MRO_{2,max}$. Actually, in this situation, the predominant drop of intravascular oxygen concentration from its initial value at $\xi = 0$ occurs at positions $\xi < 1$. The meaning of the permeability coefficient P_{H_2O} of water and the limitations of the Renkin-Crone model used to derive blood flow from dynamical PET data were discussed by [101].

Results

Predictions of Compartment Model and Comparison with Experimental Data

Besides arterial oxygen concentration, two parameters, i.e. the ratio κ and the tissue concentration \bar{c}_t enter the compartment model. Therefore, experimental data on two parameters, e.g. average oxygen saturation Y and metabolic rate of oxygen consumption MRO_2 are needed to define the model and to calculate other biophysical parameters. From experimental data on average blood oxygen saturation Y the associated parameters $P_{O_2}S\rho/rBF$, the average intravascular partial oxygen pressure $\langle P \rangle$ and the OE can be deduced, provided \bar{c}_t is known or assumed. Provided perfusion

rBF is known in addition, the metabolic rate $P_{O_2}S\rho$ and the metabolic rate of oxygen consumption MRO_2 can be calculated.

The median blood oxygen saturations of 87 breast tumors and of their surrounding normal breast tissue were found to be the same within error limits $Y_{tum,median} \approx Y_{norm,median} = 0.73$ [37]. Using this value we have calculated corresponding oxygen extraction fraction OEF and ratio of the oxygen extravasation rate constant over perfusion $P_{O_2}S\rho/rBF$ for various tissue oxygen partial pressures P_t between $P_t = 0$ and $P_t = 37 \text{ mmHg}$ (s. Table 2). By imposing the constraint $Y = Y_{exp} = 0.73$ the ratio κ and tissue oxygen concentration \bar{c}_t are no longer independent parameters, but implicitly dependent on each other, e.g. $\kappa = \kappa(\bar{c}_t)$. Together with the published median blood flow rates $rBF_{tum,median}$, $rBF_{norm,median}$, the extravasation rate constants $P_{O_2}S\rho$ and metabolic rates of oxygen consumption MRO_2 were additionally deduced for tumors and normal breast tissue. As can be seen from Table 2, the difference between the average oxygen concentration in plasma and tissue decreases with increasing tissue oxygen partial pressure, whereas the ratio $\kappa = P_{O_2}S\rho/rBF$ increases by about a factor of 10 within the range of tissue oxygen partial pressures considered to yield the same average tissue blood oxygen Y . The oxygen extraction fraction OEF drops from 0.41 at $P_t = 0$ to 0.26 at $P_t = 37 \text{ mmHg}$, i.e. the saturation $S(\xi = 1)$ is higher at the higher tissue oxygen pressure (s. Fig.1 in S3 Appendix). Correspondingly, the metabolic rate of oxygen consumption decreases from 5.2 to $3.4 \mu\text{lO}_2/\text{ml tissue}/\text{min}$ for normal breast tissue. The reported value of $MRO_2 = 4.5 \mu\text{lO}_2/\text{ml tissue}/\text{min}$ for normal breast tissue falls well within the range of calculated rates (s. Tab. 2) [20]. At the same tissue oxygen partial pressure P_t , the metabolic rates of oxygen consumption of tumors are five times higher in tumors than in normal breast tissue because of the higher perfusion in breast tumors, provided average blood oxygen saturation Y and arterial oxygen concentration is the same in both cases. From steady state PET measurements after $^{15}\text{O}_2$ inhalation the metabolic rate of oxygen consumption for breast tissue was deduced to be $MRO_2 = 6.6 \mu\text{lO}_2/\text{ml tissue}/\text{min}$. This value is considerably lower than the range $19 - 26 \mu\text{lO}_2/\text{ml tissue}/\text{min}$ of metabolic rates deduced from the median value $Y_{tum,median} = 0.73$ assuming an arterial oxygen concentration of $c(0) = 0.214 \text{ ml O}_2/\text{ml blood}$. However, the PET result was challenged [23], because tumor heterogeneity precludes the method of data analysis used by Beaney et al. [20].

The computational model assumes partial pressure dependent metabolic rates of oxygen consumption $M = M(P_t)$ (s. Eq. (17), Table 1) with different parameters M_0 and P_{M50} chosen for normal breast tissue and breast tumors. Within the range of tissue partial oxygen pressures P_t considered by the compartment model (s. Table 2) the metabolic rates $M = M(P_t)$ of oxygen consumption ($0 - 3.36 \mu\text{l O}_2/\text{ml tissue}/\text{min}$, normal breast tissue, $0 - 14.1 \mu\text{l O}_2/\text{ml tissue}/\text{min}$, breast tumor) generally fall below the values for MRO_2 listed in Table 2 for normal tissue and breast tumors. Using the published median blood flow rates $rBF_{tum,median}$, $rBF_{norm,median}$ the corresponding values for the oxygen extraction fraction OEF are lower compared to the results listed in Table 2. Correspondingly, the range of average blood oxygen saturation ($0.77 \leq Y_{norm} \leq 0.95$, $0.80 \leq Y_{tum} \leq 0.95$) are above the median value $Y_{tum,median} \approx Y_{norm,median} = 0.73$.

The compartment model allows to derive the conditions, when average blood oxygen saturation Y_{tum} falls above or below Y_{norm} of the surrounding normal breast tissue. In Fig. 3 we have plotted blood oxygen saturation Y , calculated by numerically integrating Eq. (40) for constant tissue oxygen partial pressures of $c_t = 0, 5, 15, 30, 45 \text{ mmHg}$ versus the ratio of blood flow rate over extravasation rate constant $1/\kappa = rBF/P_{O_2}S\rho$ as suggested by the approximate expression of the Crone Renkin model (s. Eq. (42)). At $c_t = 0$, oxygen extravasation is maximal, because there is no backflow of oxygen from the tissue to the vascular system. Therefore, the bottom curve ($c_t = 0$) represents a lower limit for blood oxygen saturation. Finite tissue oxygen concentrations, on the other hand, decrease the loss of oxygen to tissue by extravasation and cause shifts towards higher saturation values Y . To discuss conditions when Y_{tum} falls above or below Y_{norm} we choose the partial oxygen pressures for normal breast tissue and tumors to be $P_{t,norm} = 15 \text{ mmHg}$ and $P_{t,tum} = 5 \text{ mmHg}$ respectively. Previously invasive needle measurements of tissue oxygen tension by oxygen polarography were carried out on 16 breast cancer patients at a large number of breast positions [14]. Generally, broad distributions of partial oxygen pressures were observed in normal breast tissue and tumors with median values of $P_{t,median} = 65 \text{ mmHg}$ and $P_{t,median} = 30 \text{ mmHg}$, and lower bounds of $P_{t,min} = 12.5 \text{ mmHg}$ and $P_{t,min} = 0 - 2.5 \text{ mmHg}$ for normal breast tissue and breast tumors, respectively. The partial pressures chosen presently for normal breast tissue and breast carcinoma are

close to these lower bounds. Since tissue oxygen partial pressure of a particular breast tumor is likely to be lower than oxygen pressure in the surrounding normal breast tissue, $Y(c_{t,tum})$ is larger than $Y(c_{t,normal})$, provided the shift in blood oxygen saturation of normal breast tissue due to higher tissue oxygen concentration $c_{t,normal}$, is at least compensated for by a higher value of $(rBF/P_{O_2}S\rho)_{tum}$ compared to $(rBF/P_{O_2}S\rho)_{norm}$, e.g. by larger blood flow rBF_{tum} or lower oxygen extravasation rate constant $(P_{O_2}S\rho)_{tum}$, otherwise the opposite holds true. The former condition is illustrated in Fig. 3 for the maximal blood oxygen saturation $Y_{max,normal} = 0.85$ observed experimentally in normal breast tissue within the patient cohort of the clinical study [37]. In this case, $Y_{max,normal} < Y(c_{t,tum})$ for $0.037 < (rBF/P_{O_2}S\rho)_{tum}$ (s. Fig. 3, vertical dashed line). Tumor volumes with rather few, yet fairly large blood vessels are likely to exhibit high blood flow rates rBF_{tum} resulting in blood oxygen saturation values above that of normal breast tissue ($Y_{norm} < Y_{tum}$). The opposite situation occurs, when tumor perfusion is lower ($rBF_{tum} < rBF_{norm}$) and extravasation rate constant is higher $(P_{O_2}S\rho)_{norm} < (P_{O_2}S\rho)_{tum}$ compared to normal breast tissue. For example, tumors with a well developed plexus of blood vessels may exhibit reduced values of $(rBF/P_{O_2}S\rho)_{tum}$, resulting in average blood oxygenation tum norm $Y_{tum} < Y_{norm}$. Regional blood volume rBV of tumors is known to be almost exclusively larger than that of normal breast tissue. It is likely that surface area per volume of tissue $S\rho_{tum}$ also increases besides blood volume in cases of a well developed plexus. Furthermore, solid pressure present in tumors may compress blood vessels reducing blood flow. It is therefore conceivable, that tumors with $Y_{tum} < Y_{norm}$ can be associated with networks of enhanced surface area per unit volume of tissue, and/or reduced blood flow. Furthermore, although the median of blood flow rates in breast tumors $rBF_{tum,median} = 0.3 \text{ ml blood/ml tissue/min}$ is 5 times that of normal breast tissue ($rBF_{norm,median} = 0.06 \text{ ml blood/ml tissue/min}$), there is some overlap of the rBF_{tum} and rBF_{norm} ranges ($0.08 \leq rBF_{tum} \leq 0.9 \text{ ml blood/ml tissue/min}$, versus $0.03 \leq rBF_{norm} \leq 0.17 \text{ ml blood/ml tissue/min}$) indicating that $rBF_{tum} < rBF_{norm}$ may occur [24, 25].

The minimal and maximal blood oxygen saturations Y_{min}, Y_{max} observed experimentally [37, Fig.3b] (reproduced in Fig. 1) for normal tissue ($Y_{min} = 0.49, Y_{max} = 0.85$) and tumor tissue ($Y_{min} = 0.41, Y_{max} = 0.91$) are indicated in Fig. 3 by short-dashed and dash-dotted horizontal lines, respectively. For the partial oxygen pressures $P_{t,normal} = 15 \text{ mmHg}$, and $P_{t,tum} = 5 \text{ mmHg}$ chosen, these boundaries are converted to the $rBF/P_{O_2}S\rho$ ranges $0.27 \cdot 10^{-2} \leq rBF/P_{O_2}S\rho \leq 3 \cdot 10^{-2}$ (normal tissue, s. vertical short-dash lines) and $0.34 \cdot 10^{-2} \leq rBF/P_{O_2}S\rho \leq 0.1$ (tumor tissue, vertical dash-dotted lines). Both ranges overlap, reflecting the observation that Y_{tum} may fall below and above Y_{norm} [37, Fig. 3b]. We consider a position on the diagonal of Fig. 3b of [37], corresponding to $Y_{tum,0} = Y_{norm,0} = Y_0$. Moving along the vertical line $Y_{norm} = Y_0 = \text{constant}$ to a position in the upper triangle of Fig. 3b with $Y_{tum} > Y_{tum,0}$ we may write in first approximation

$$Y_{tum} - Y_{tum,0} = \frac{\partial Y}{\partial \kappa} \Big|_{\kappa_{tum,0}; \bar{c}_{t,tum,0}} (\kappa_{tum} - \kappa_{tum,0}) + \frac{\partial Y}{\partial \bar{c}_t} \Big|_{\kappa_{tum,0}; \bar{c}_{t,tum,0}} (\bar{c}_{t,tum} - \bar{c}_{t,tum,0}). \quad (43)$$

Note, that $\partial Y / \partial \bar{c}_t > 0$ whereas $\partial Y / \partial \kappa < 0$. For the right hand side to be positive, at least one of the terms should be positive and outweigh the other term, in case it is negative. For example, for higher perfusion $rBF_{tum} > rBF_{tum,0}$ and lower rate constant of extravasation $P_{O_2}S\rho_{tum} < P_{O_2}S\rho_{tum,0}$ the ratio $\kappa_{tum} < \kappa_{tum,0}$ results in higher average oxygen saturation, provided tissue oxygen concentration only moderately decreases ($\bar{c}_{t,tum} < \bar{c}_{t,tum,0}$) or even increases, i.e. the tumor tissue is only moderately more hypoxic or even less hypoxic. An increase in vessel radius leads to enhanced rBF , rather few vessels with fairly large radii to a smaller vascular surface area per unit volume of tissue $S\rho$ and hence to a reduced rate constant for extravasation, while a lower metabolic rate of oxygen consumption in tissue tends to lead to higher tissue oxygen concentrations. Conversely when $\kappa_{tum} > \kappa_{tum,0}$ due to reduced perfusion or higher rate constant of extravasation the oxygen concentration in tissue needs to increase sufficiently $\bar{c}_{t,tum} > \bar{c}_{t,tum,0}$ for $Y_{tum} > Y_{tum,0}$ to hold true.

Roughly speaking the upper triangle of Fig 3b of Ref. [37] predominantly corresponds to well perfused tumors $(rBF)_{tum} > (rBF)_{norm}$ or tumors with low extravasation rate constants $P_{O_2}S\rho_{tum} < P_{O_2}S\rho_{norm}$ that are only moderately more hypoxic or even less hypoxic. The opposite holds true for the lower triangle, encompassing tumors with higher ratio κ i.e. lower perfusion or higher rate of extravasation as well as lower tissue oxygen concentration. It follows that average blood oxygen saturation Y reflects structural properties of the vasculature, its hemodynamics and

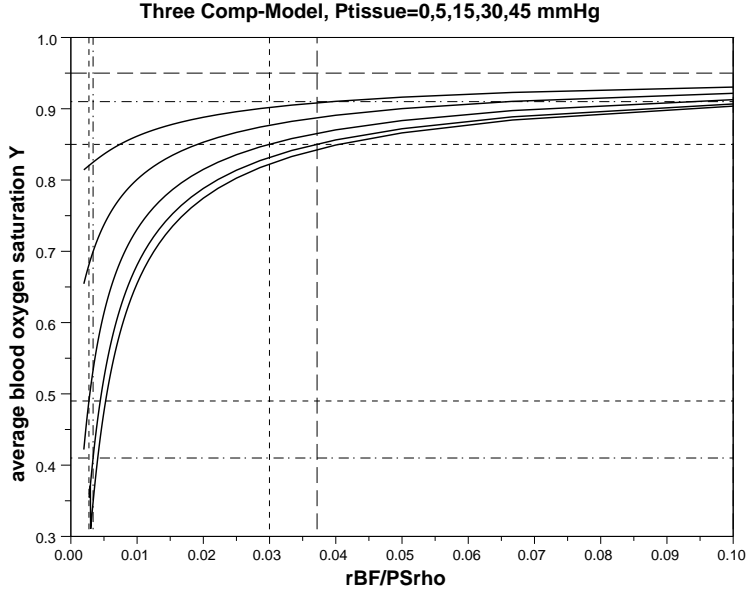


Figure 3. Blood oxygen saturation Y calculated by numerical integration of Eq. (39) for constant tissue oxygen partial pressures of 0, 5, 15, 30 and 45 $mmHg$ (bottom to top). Y is plotted versus ratio $1/\kappa = rBF/PS\rho$ of blood flow rate over oxygen extravasation rate constant. For $1 \ll rBF/PS\rho$, the saturation Y approaches the value of the blood oxygen saturation $S(0) = 0.95$ at input (horizontal dashed line). The bottom curve corresponds to zero tissue oxygen pressure ($P_t = 0$) representing the lower limit for the average blood oxygen saturation. Assuming oxygen partial pressures of $P_t = 15 mmHg$ (third curve from bottom) and $P_t = 5 mmHg$ (second curve from bottom) for normal tissue and tumor tissue respectively, blood oxygen saturation $Y(tumor)$ of breast tumors with $0.037 < rBF/PS\rho$ (s. dashed vertical line) exceeds that of normal tissue $Y(normal)$ while the opposite is true for $rBF/PS\rho < 0.037$. In the former case tumors fall into the upper triangle of [37, Fig. 3b], while the lower triangle contains tumors with $rBF/PS\rho < 0.037$. The minimal and maximal blood oxygen saturation Y_{min}, Y_{max} observed experimentally [37, Fig. 3a] for normal tissue (short-dashed horizontal lines $Y_{min} = 0.49$, $Y_{max} = 0.85$) and tumor tissue (dash-dotted lines, $Y_{min} = 0.41$, $Y_{max} = 0.91$) are also indicated in Fig. 3. These boundaries are converted into the ranges $0.27 \cdot 10^{-2} \leq rBF/PS\rho \leq 3 \cdot 10^{-2}$ (normal tissue, s. vertical short-dashed lines) and $0.34 \cdot 10^{-2} \leq rBF/PS\rho \leq 0.1$ (tumor tissue, vertical dash-dotted lines) for $rBF/PS\rho$.

metabolic properties of the tissue investigated. Besides relating blood oxygen saturation Y to the ratio $1/\kappa = rBF/P_{O_2}S\rho$ of perfusion over extravasation rate constant (s. Fig. 3) we calculated Y as a function of the ratio $MRO_2/rJ_{in} = OEF$ of the metabolic rate of oxygen consumption over the (arterial) oxygen flux $rJ_{in} = c(0) \cdot rBF$ entering the vascular network per unit volume of tissue for selected values of the tissue oxygen partial pressure P_t (s. Fig. 4). Fig. 4 provides another way to compare Y_{tum} to Y_{norm} . At constant tissue partial oxygen pressure P_t , average blood oxygen saturation Y monotonously decreases with increasing oxygen extraction fraction OEF . Furthermore, at constant OEF average blood oxygen saturation Y decreases with increasing tissue partial oxygen pressure P_t . Likewise, at constant average blood oxygenation Y oxygen extraction fraction OEF decreases with increasing P_t . These trends are also evident from Fig.1 and Fig.2 in S3 Appendix, illustrating blood oxygen saturation $S(\xi)$ along the vessel axis for selected tissue partial oxygen pressures P_t and constraints $Y = const$ and $OEF = const$, respectively. Thus, data falling into the upper triangle of Fig. 3b of Ref. [37] correspond to cases ($Y_{tum} > Y_{norm}$) for which the ratio of oxygen demand over oxygen supply is smaller for tumors compared to the surrounding normal tissue, $(MRO_2/rJ_{in})_{tum} < (MRO_2/rJ_{in})_{norm}$ apart from shifts of the oxygen extraction fraction OEF due to different oxygen partial pressures in normal breast tissue and breast tumors. Conversely, data appearing in the lower triangle of Fig. 3b of Ref. [37] ($Y_{tum} < Y_{norm}$) correspond to tumors with $(MRO_2/rJ_{in})_{norm} < (MRO_2/rJ_{in})_{tum}$ apart from OEF shifts due to different tissue oxygen partial pressures in tumors and normal breast tissue.

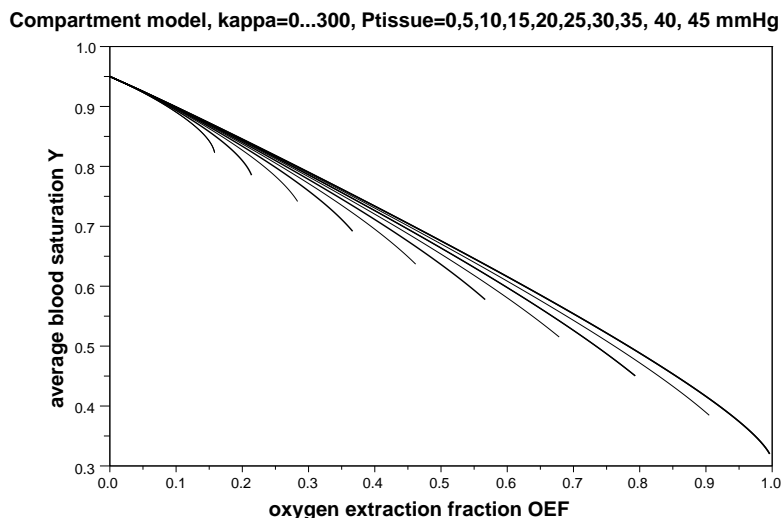


Figure 4. Simulated average blood oxygen saturation Y versus oxygen extraction fraction OEF for selected partial oxygen pressures $P_t = 0, 5, 10, 15, 20, 25, 30, 35, 40 \text{ mmHg}$ (from top to bottom), corresponding to $\kappa = P_{O_2}S\rho/rBF$ varying between $\kappa = 0$ and $\kappa = 300$.

We have plotted average blood oxygen saturation Y measured in normal breast tissue (Fig. 5) and breast tumors (Fig. 6b) by optical mammography versus regional blood volume. The data in Fig. 5 and 6 are exactly the same as the data in Fig. 5a of Ref. [37], reproduced in Fig. 2, however plotted versus rBV rather than hemoglobin concentration c_{Hb} and separately for normal and tumorous breast tissue. Hemoglobin concentrations $c_{Hb} = c_{Hb,blood}rBV$ were converted to regional blood volume assuming an average of $c_{Hb,blood} = 140 \text{ g Hb/l blood}$. Furthermore, average blood oxygen saturation Y calculated for selected tissue partial oxygen pressures P_t are also included in Fig. 5 and 6. For this purpose $1/\kappa = rBF/P_{O_2}S\rho$ was converted to $rBV = P_{O_2}S\rho \cdot MTT/\kappa$ taking the product $P_{O_2}S\rho \cdot MTT$ from the values $P_{O_2}S\rho$ listed in Table 2 together with median values of the regional blood volume $rBV = 0.008 \text{ ml blood/ml tissue}$ (from $c_{Hb} = 17.3 \mu\text{mol/l}$ [37], normal breast tissue) and $rBV = 0.0244 \text{ ml blood/ml tissue}$ (from $c_{Hb} = 53 \mu\text{mol/l}$ [37], breast tumors) together with the published median values for rBF_{norm} and rBF_{tum} (s.above). The products $P_{O_2}S\rho \cdot MTT$ derived in this way depend to some extent on tissue oxygen partial pressure (cf. Table 2). For Fig. 5 and 6 we selected the values $P_{O_2}S\rho \cdot MTT = 1$ (normal breast tissue) and $P_{O_2}S\rho \cdot MTT = 3$

(breast tumors), respectively, derived at $P_t = 20 \text{ mmHg}$. Despite some data scatter, Fig. 5 and 6 clearly exhibit the low threshold behavior. Data appearing above the lower threshold ($P_t = 0$) interpreted as reflecting finite tissue oxygen concentrations, i.e. indicating tissue oxygen status. In addition, reduced values of $P_{O_2}S\rho$, resulting in smaller losses of oxygen to the tissue environment, and shorter mean transit times MTT result in higher average blood oxygen saturation. Of course, the low threshold behavior is also visible in Fig. 5a of Ref. [37], reproduced in Fig. 2. Although we focus on results of optical mammography, we point out the striking similarity between Fig. 5a of Ref. [37] relating to measurements taken on a cohort of breast cancer patients and Fig. 4 of Ref. [28] showing blood oxygen saturation Y versus blood volume fraction rBV of a large number of voxels of normal brain tissue and of a brain tumor in a particular tumor model, deduced from MRI measurements. Compared to the optical data, the MRI measurements are taken at considerably higher spatial resolution, resulting in many more data, clearly showing the lower threshold of Y and the many data above it.

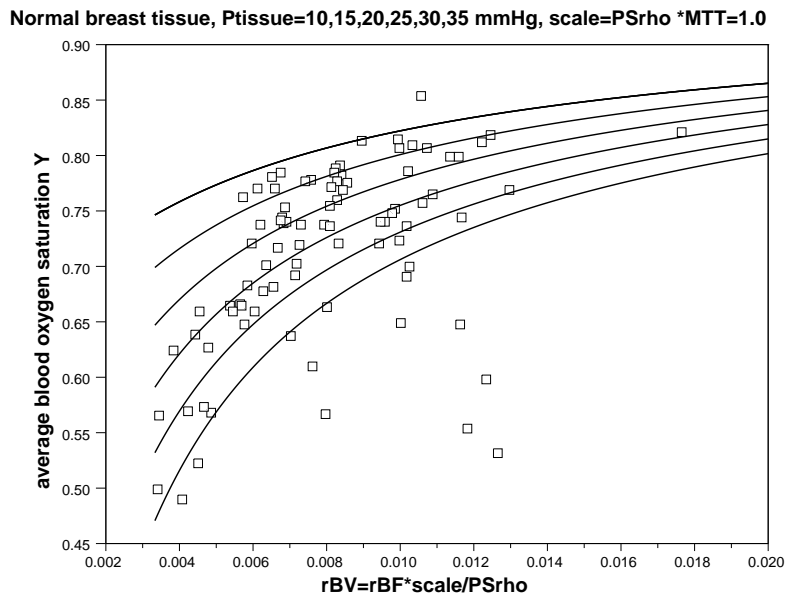


Figure 5. Experimental (open symbols) and calculated (solid lines) average blood oxygen saturation Y in normal breast tissue of 87 breast tumor patients (cf. Fig. 6) versus regional blood volume [37, Fig. 5]. Solid lines correspond to oxygen partial pressures $P_t = 10, 15, 20, 25, 30, 35 \text{ mmHg}$ (from bottom to top). Experimental values for regional blood volume rBV were deduced from measured hemoglobin concentrations c_{Hb} , theoretical values $rBV = P_{O_2}S\rho \cdot MTT/\kappa$ were obtained scaling $1/\kappa$ with $P_{O_2}S\rho \cdot MTT = 1$ (s. text).

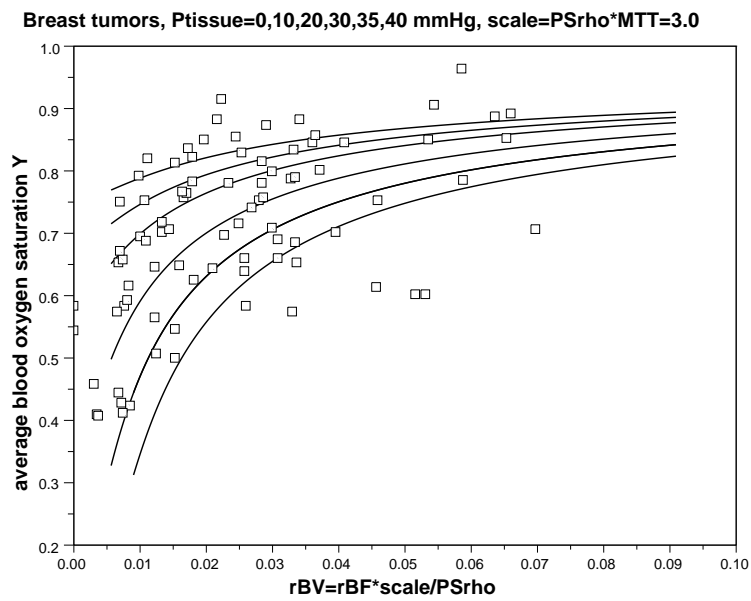


Figure 6. Experimental (open symbols) and calculated (solid lines) average blood oxygen saturation Y of 87 breast tumors versus regional blood volume [37, Fig. 5]. Solid lines correspond to oxygen partial pressures $P_t = 10, 15, 20, 25, 30, 35$ mmHg (from bottom to top). Experimental values for regional blood volume rBV were deduced from measured hemoglobin concentrations c_{Hb} , theoretical values $rBV = P_{O_2} S \rho \cdot MTT / \kappa$ were obtained scaling $1/\kappa$ with $P_{O_2} S \rho \cdot MTT = 3$ (s. text).

Table 2. Oxygen consumption and extravasation rate computed by the compartment model

$P_t / mmHg$	OEF	$rBF/PS\rho$	$PS\rho / ml O_2/ml/min$ ($rBF_{tum} = 0.06/min$)	$PS\rho / ml O_2/ml/min$ ($rBF_{tum} = 0.3/min$)	$MRO_2 / \mu l O_2/ml/min$ ($rBF_{norm} = 0.06/min$)	$MRO_2 / \mu l O_2/ml/min$ ($rBF_{tum} = 0.3/min$)
0	0.407	0.015	4.04	20.2	5.2	26.1
5	0.401	0.013	4.52	22.6	5.15	25.6
10	0.393	0.012	5.16	25.8	5.05	25.3
15	0.385	0.010	6.0	30.2	4.94	24.7
20	0.373	0.008	7.3	36.4	4.79	23.9
25	0.357	0.006	9.25	46.2	4.58	22.9
30	0.332	0.005	13.2	66.0	4.26	21.3
35	0.289	0.003	23.8	118.9	3.71	18.6

This table shows the dependence of oxygen extraction fraction OEF , ratio of blood flow rate over extravasation rate constant $1/\kappa$, extravasation rate constant $PS\rho$, metabolic rate of oxygen consumption MRO_2 on partial oxygen pressure P_t in tissue using average blood oxygen saturation $Y_{norm} = Y_{tum} = 0.73$ (median). $c_{in} = c_0 H \cdot S_{in} = 0.214 ml O_2/ml blood$, $H = 0.45 ml RBC/ml blood$, $S_{in} = S(0) = 0.95$, $OEF_{app} = 1 - Y/S_{in} = 0.232$, median blood flow rate for normal breast tissue and breast tumors [24, 25]

Artificial Blood Vessel Networks Representing Normal Breast Tissue

Ideally, one would start from digitized 3D blood vessel networks of each breast patient to simulate hemodynamic properties, as well as intravascular and extravascular oxygen concentrations in tumor and surrounding normal tissue. Although 3D vascular networks of tumors grown in tumor models can be generated from μ -CT data [80, 81], such techniques are not applicable to humans. Therefore, 3D vascular trees are algorithmically constructed, following methods previously applied to model vasculature in melanomas and gliomas [39, 55, 56, 57, 58, 59]. The model employed in this paper is described in detail in Ref. [39], representing an extension of the model used in [102] which is based on wall shear stress guided random growth of interdigitating vascular trees on a lattice.

For the sake of readability we briefly review the model and refer the reader to the supplemental material S1 of Ref. [39]. Simulations are performed on a cubical domain with lateral length of $L = 8 \text{ mm}$. At first a 3D network is constructed, representing the blood vessel network in a section of normal tissue, i.e. the host. Starting from arterial and venous root nodes, located at boundary sites of the face centered cubic lattice used to carry the vascular network, vessel segments of different shape (linear, tripod) are statistically appended along several possible directions. This process is continued until further addition of vessel segments causes segments to overlap, assumed to be forbidden. Subsequently nearby open ends at terminal branches of the arterial and venous trees generated in this way are (temporarily) connected by (straight) vessel segments representing capillaries. Radii of capillaries, of arterial and venous terminal segments are set to $2.5 \mu\text{m}$, $2.5 \mu\text{m}$ and $3.8 \mu\text{m}$, respectively, whereas radii of parent segments are determined from Murray's law, i.e. $r_c^\alpha = r_a^\alpha + r_b^\alpha$ with r_c being the radius of the parent vessel, r_a , r_b the radii of the two downstream vessels and $\alpha = 3$ has been selected. Blood flow through the temporary network is calculated, including shear wall stress of segments. With the capillaries removed additional vessel segments are stochastically attached to or removed from terminal branches with probability based on wall shear stress. The entire process is continued until the number of capillaries reaches a plateau. Eventually the whole lattice is filled with a reasonably realistic arteriovenous network, the lattice constant $h_{(gen)}$ being the determinant of MVD. $h_{(gen)} = 130 \mu\text{m}$ has been selected.

In Fig. 7 nine different root node geometries are shown used to generate vascular networks of normal breast tissue and of tumors. The resulting vascular networks depend strongly on root node geometry chosen. For each root node geometry 10 vascular networks (10 network realizations) were grown, differing among each other because of the statistical nature of the growth process. Thus a total of 90 different vascular networks were generated representing normal breast tissue.

Artificial Tumor Blood Vessel Networks

Starting from one of the 90 vascular networks representing normal tissue the associated tumorous vessel network is formed by vascular remodeling via cooption, angiogenesis, and regression. For this purpose a small sized spherical tumor ($R_{tumor}(t=0) = 250\mu\text{m}$), the radius of which grows at constant speed $v_{tumor} = 2 \mu\text{m}/h$, is placed initially at the center of the simulation domain. During fixed time intervals Δt the vasculature within the tumor is modified by the following biological processes at prescribed probabilities [39, 58]:

- (i) Angiogenic sprouting: In normal tissue, lattice sites occupied by vessels, i.e. sites, have a chance (probability $\Delta t/t_{EC}^{(sprout)}$) to spawn a sprout segment on an adjacent lattice bond provided the site is close enough to the tumor, i.e. within the growth factor diffusion distance R_g rather than requiring the growth factor concentration to be sufficiently high, as previously postulated [55]. Furthermore, no other branching points must be nearby, i.e. within the distance of $l^{(spr)}$. Vessels within the tumor sphere, switch to circumferential growth (s. below).
- (ii) Sprout growth: sprouting vessels have a chance (probability $\Delta t/t_{EC}^{(sprout)}$) to be extended by another lattice bond. Sprouts have a total lifetime of $t_{EC}^{(migr)}$. When sprouts hit an existing vessel during their lifetime, they fuse by anastomosis and form a functional vessel carrying blood. Otherwise sprouts are prone to collapse after their lifetime.
- (iii) Circumferential growth: vessels switch from sprouting to circumferential growth after their residence time $t_{EC}^{(switch)}$ within the tumor. After switching to circumferential growth we assume

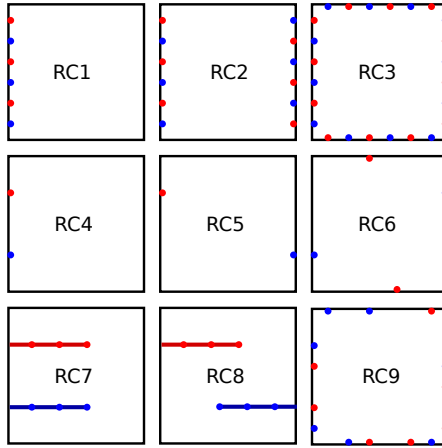


Figure 7. Illustration of vascular tree configurations: Schematic views from above on simulation cubes indicate vascular tree root locations for configurations denoted RC1 to RC9. In RC1 to RC3 boundary sites are occupied in alternating order either with arterial or venous nodes. In RC1 only one face of the simulation cube is used, in RC2 two opposing sides are used and in RC3 four faces are used. In RC4, RC5 and RC6 we place nodes at 33% and 66% of the length of the cube faces diagonals on the diagonals. As before, one, two and four faces are used, where in total only two (RC4, RC5) and four nodes (RC6) are placed. In RC7 and RC8 we first create fixed parent vessels protruding along the x-axis to 60% of the cube length into the interior. On each site occupied by these parent vessels a regular root node is created for further growth. Flow boundary conditions are specified at the actual inlets and outlets at the cube boundaries. In RC9 each boundary site of the lattice is occupied with a root node with probability p_{root} . Before a network is created, p_{root} is drawn equally distributed between 0 and 1, however a configuration is only accepted if there is at least one arterial and one venous node.

that each endothelial cell ($10 \times 10 \mu m^2$ surface area) at the inner wall to duplicate every $t_{EC}^{(prol)}$ hours leading to an increase of vascular radius r . We impose an upper limit on the radius ($r^{(max)}$) after which circumferential growth stops.

- (iv) Degradation of vessel wall stability: vessels possess a wall stability value w as an abstract measure of the state of degeneracy of their vessel wall. The stability measure w is initialized relating it to the wall thickness of healthy vessels [39, Suppl.1, Eq.(2)]. The wall stability of tumor vessels decreases over time at the rate Δw until zero. Once zero, vessels are allowed to collapse and regress (see below).
- (v) Vessel collapse and regression: If the wall shear stress f of a segment falls below a threshold ($f^{(coll)}$) and $w = 0$, then the segment is removed from the network at probability $p^{(coll)}$, representing collapse, occlusion and complete regression. In this study we set $p^{(coll)}$ to 1, making collapses deterministic.

These processes are implemented in time-discrete steps Δt during which the network morphology is modified. For this purpose the simulation sweeps over all vessels and makes alterations accordingly. Since vessel collapse and regression can take place provided shear stress falls below a lower threshold, blood flow and hence shear stress are updated after each time interval Δt . The simulation growth process was deliberately stopped at $t = 600 h$ when the tumor diameter had grown to ca. $3 mm$ to minimize boundary effects which would occur if the tumor was allowed to grow to the size of the simulation box.

Some of the processes modifying tumor vasculature, such as sprout initiation and growth of sprouts, vessel dilation and vessel wall degeneration depend on the presence of growth factors in tumor tissue, such as vascular endothelial growth factor VEGF. In previous work [39, 55, 56, 57, 58, 59] therefore incorporated a concentration field for growth factors in tumorous tissue produced by tumor cells. Modification of the existing vasculature required vascular endothelial growth factor concentration to be sufficiently high. In the present paper, however, this growth factor concentration

field is omitted. Instead we define another concentric (growing) sphere with a slightly larger radius $R_{tumor}(t) + R_g$, where the parameter R_g reflects the VEGF diffusion distance, i.e. the distance the growth factor diffuses, before its concentration drops to insignificant levels due to degradation and binding. Within the sphere of radius $R_{tumor}(t) + R_g$, the aforementioned processes, e.g. angiogenic sprouting, can take place, as if there was sufficiently a high concentration of growth factors. This considerable simplification of the growth process is justified because results obtained in this way are consistent with the predictions of more complex models. Also, proliferation in solid tumors is confined to the outer rim due to competition for space and nutrients leading to a constant expansion rate of the tumor radius. However, some very aggressive brain tumors are known to exhibit morphological instabilities leading to fingering growth patterns but we have no indication that this applies to breast tumors.

The vasculature obtained at the end of the tumor growth process ($t = 600 h$) represents the tumor specific network together with modifications of the normal vasculature occurring at the tumor-normal tissue interface. Generally, we take the starting network at $t = 0$ with the initial small tumor inserted ($R_{tumor} = 250\mu m$) to represent normal breast tissue. For each of the 90 network realizations at $t = 0$ we calculated blood flow, hematocrit distribution and intravascular and tissue oxygen PO2 distributions according to Sec. ‘Models’. Parameters related to oxygen transport (s. Table 1) are to a large extent taken from [45], compiled from various sources, not specifically for breast tissue. In order to qualitatively reproduce experimental data obtained from 87 patients, i.e. in order to account for biological variability, each of the 90 tumor network realizations ($t = 600 h$) was evaluated for blood flow, hematocrit and oxygen concentration in blood and tissue. In the following we discuss three different scenarios denoted BASE, CMPR and METAB. Cases BASE and METAB use the same tumor vascular networks ($t = 600 h$), but differ in their assumptions made to calculate tissue metabolic rate of oxygen consumption variables. CMPR, on the other hand, augments the processes that cause remodeling of the tumor vasculature by accounting for vascular compression by solid pressure, leading to tumor vascular networks at $t = 600 h$ that differ from the networks of the scenarios BASE and METAB.

Case BASE

This is our base case with parameters for growth of breast tumor vasculature listed in Table 3. Blood flow, hematocrit distribution, blood and tissue oxygen concentrations were calculated using each of the 90 realizations of tumor vasculature ($t = 600 h$) together with parameters related to oxygen transport given in Table 1. It should be noted that Michaelis-Menten parameters for tumor tissue were assumed to be $M_0(tumor) = 4 \cdot M_0(normal)$ and $R_{M50}(tumor) = 0.5 \cdot R_{M50}(normal)$. Compared to melanomas changes in the tumor growth parameters (s. Table 3) include $l^{(spr)}$, governing the MVD near the tumor rim, $f^{(coll)}$, and $r^{(max)}$ determining the central MVD and rBV . Other parameters such as the sprouting time $t_{EC}^{(sprout)}$, and vessel wall degradation rate Δw are unaltered. Interestingly, our value for $f^{(coll)}$ falls within the order of magnitude of physiological wall shear stress in human veins (ca. $1 Pa$), which is about one order of magnitude lower than in arteries [103]. Consistent with previous results, we obtain highly compartmentalized networks that comprise a central core with low MVD and highly vascularized peripheral shell of a few hundred micrometer thickness, see Fig. 8. The arterio-venous organization is lost, and the remaining high caliber vessel protruding into and through the tumor are connected with a chaotic network of dilated capillaries. The aforementioned processes causing vascular remodeling via cooption, angiogenesis, and regression favor either growth of vessels up to the limit $r^{(max)}$ or complete regression. It turns out that the tumor vasculature of scenario BASE is unsuited to explain some of the experimental data, in particular the correlation plot Y_{tum} versus Y_{norm} . Since average blood oxygen saturation Y is the RBC-volume-weighted average of blood oxygen saturation taken over all vessel segments (s. S2 Appendix), high caliber vessels predominantly contribute to Y . Likewise, because high caliber vessels criss-cross the central tumor volume, oxygen supply exceeds oxygen demand and average blood oxygen saturation values of tumors generally fall above those of corresponding normal breast tissue.

Table 3. List of parameters for tumor growth

Parameter	Value	Unit	Description
$R_{tumor}(t=0)$	250	μm	Initial tumor radius
v_{tumor}	2	$\mu m/h$	Tumor radius expansion rate
R_g	200	μm	Growth factor diffusion range
$t_{EC}^{(switch)}$	12	h	Circumferential growth switch delay
$t_{EC}^{(sprout)}$	2	h	Time between sprouting events
$t_{EC}^{(migr)}$	50	h	Sprout activity duration
$l^{(spr)}$	80	μm	Sprout sites minimum separation
$t_{EC}^{(prol)}$	144	h	Endothelial cell proliferation time
$r^{(sprout)}$	2.6	μm	Initial sprout vessel radius
$r^{(max)}$	14	μm	Maximum dilation radius
$p^{(coll)}$	1		Vessel collapse probability
Δw	0.05	$\mu m/h$	Vessel stability (w) decrease rate
$f^{(coll)}$	0.25	Pa	Critical wall shear stress
$h_{(tumor)}$	10	μm	Lattice constant of tumor growth simulation
$h_{(gen)}$	130	μm	Lattice constant of initial network generation

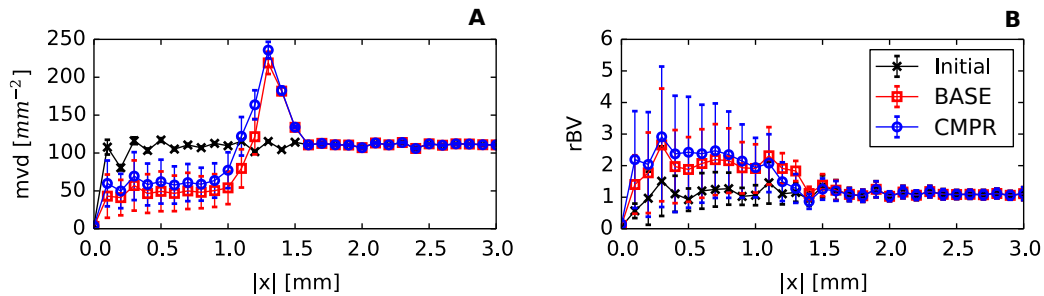


Figure 8. Radial distributions of the microvascular density, MVD , and the relative blood volume, rBV . The simulation box was divided in $100 \mu m$ thick concentric shells over which the regional MVD and rBV were determined to obtain radial profiles depending on the distance from the center $|x|$. Plotted is the ensemble mean of these profiles, where the error bars display the standard deviation (STD). As can be seen, a compartmentalization into varying degrees of vascularization and vasodilation exist which is typical for Melanoma [104] and Glioma [105]. We assume that these features are also present in breast tumors. The STD of MVD further shows that the MVD of the tumor core is below normal in most realizations of the ensemble which conforms to our expectations for tumors. For cases BASE and CMPR, both of which are shown, we require the mean values to be similar since we want to study the effect of additional fluctuations alone (see case CMPR). Oscillations are an artifact of the confinement of the vessels to a lattice.

Case CMPR: Vascular compression

We explored the effect of compression of tumor vessels during tumor growth by extravascular stress on simulated average blood oxygen saturation Y_{tum} based on the final $t = 600 h$ tumor vasculature. Compression of tumor vessels will change the relation of Y_{tum} and the blood oxygen saturation of the surrounding normal breast tissue Y_{norm} obtained from the corresponding vascular network at $t = 0$. Elevated interstitial fluid pressure (IFP) is known to be a hallmark of tumors [10], primarily caused by the increased leakiness of tumor vessels and the lymph drain being impaired in solid tumors. Yet the precise mechanisms by which extravascular pressure compresses tumor vessels are still under debate [106, 107]. The uncontrolled proliferation and growth of tumor cells within a restricted volume generates extravascular solid stress. Solid stress accumulates within the tumor volume through an increase in tumor cell density and hyperproduction of interstitial matrix molecules such as collagen and hyaluronan [9, 10, 11]. Collagen fibers are resistant to tensile stress whereas hyaluronan resists compression thus transferring stress on tumor vessels. On the other hand water-loaded hyaluronan can be considered to be part of the relative immobile fluid phase of the interstitial fluid, contributing to IFP apart from contributions of the freely mobile fluid phase. Furthermore, solid stress can be exerted on the tumor volume by the surrounding normal tissue. It was estimated that solid stress becomes significant for tumor volumes larger than $0.065 mm^3$, corresponding to a sphere of $R_{tumor} = 250 \mu m$ [108]. A detailed simulation of solid stress during progression of the tumor is beyond the scope of the present paper. Therefore we assume that all vessels of the tumor vasculature experience compression during the growth process, i.e. a reduction of their radius by a constant factor. The fundamental difference to the case BASE is that in this way high-caliber vessels experience a reduction in radius, which cannot be achieved by the previous model that predicts either growth or complete removal of vessels. Hence we introduce a new “compressed” vessel radius, denoted \tilde{r} which enters the blood flow and oxygen computation. We consider a function $\psi(|\mathbf{x}|)$ of the spatial coordinate \mathbf{x} that represents the magnitude of compression relative to the base radius, depending on the distance from the tumor center $|\mathbf{x}|$. Therefore we define $\tilde{r} = \psi \cdot r$. We let ψ describe a linear transition between full compression of magnitude $1 - \xi_{cpr}$, in the tumor center and zero in normal tissue. Thus, vascular radii \tilde{r} within the tumor, with the exception of a small transition zone of width w_{cpr} , are reduced relative to r by a factor of ξ_{cpr} .

$$\psi(x) = \begin{cases} \xi_{cpr} & \text{for } x < R - w_{cpr} \\ 1 & \text{for } x > R + w_{cpr} \\ \xi_{cpr} - \frac{x - R + w_{cpr}}{2w_{cpr}} \cdot (\xi_{cpr} - 1) & \text{else,} \end{cases} \quad (44)$$

where R is the radius of the tumor and w_{cpr} is $200 \mu m$ in our simulations. We assume that varying degrees of compression are present in the tumors of the patient cohort due to phenotypical differences from tumor to tumor or differences in the micro environment of the host. Therefore a new ξ_{cpr} was drawn for each simulation from a uniform distribution over the interval between 0.5 and 1. The lower bound of 0.5 was deliberately chosen since it appears to be the lower bound of what was reported for experiments, i.e. relief of stress resulted in two times increase of vessel diameters [109].

Case METAB: Variation of tumor oxygen consumption rate

In contrast to case CMPR scenario, METAB uses the identical tumor vascular networks as case BASE. However, rather than selecting the same maximal oxygen consumption rate M_0 for all tumors as in scenario BASE we consider variations of the maximal tumor oxygen consumption rate M_0 among various tumors reflecting phenotypical differences. In this way we probe the impact of tumor tissue oxygen consumption versus tumor vascular restructuring on intra-and extravascular oxygen distributions. Therefore, $M_0 / (ml O_2/ml/min)$ is drawn from a lognormal distribution with $\mu = \log(0.0149)$ and $\sigma = 0.3$ on a tumor by tumor basis, yielding a median M_0 identical to case BASE (s. Table 2) and a standard deviation of 32% of the median. The oxygen consumption rate of normal tissue is kept at its original value (Table 2). Furthermore oxygen partial pressures P_{M50} were kept unchanged.

Results of the computational model

We calculated various biophysical variables for the initial network at $t = 0$ and for the cases BASE, CMPR and METAB at $t = 600 h$. Values listed in Table 4 represent averages (means) over the results of all 90vascular networks, including standard deviations. Explicit formulas for these parameters are given in S2 Appendix. It should be kept in mind that for most biophysical variables results corresponding to a particular vascular network represent (weighted) averages taken over all segments of the network (s. S2 Appendix). For comparison we list in Table 4 experimental and some theoretical results taken from the literature.

The microvascular density MVD is measured microscopically by counting the number of microvessels per area of a tissue microscopic slide. It is a quantity not easy to simulate. Therefore we take the simulated length density L_D , i.e. the total length of the vascular network divided by the tissue volume as measure for MVD (s. S2 Appendix). This definition yields at least the correct dimension and is identical to the number of vessels per cross-sectional area in case of a Krogh-like arrangement of parallel vessels. When comparing experimental MVD data and simulated length densities L_D it should be kept in mind that both parameters are not identical. In a large portion of the experimental literature on breast tumors, the MVD is obtained from well vascularized areas, so called hot-spots. Dhakal et al. [111] reported densities between $15\text{-}348 \text{ mm}^{-2}$ with a mean of 88 mm^{-2} . Hot-spots are predominantly found near the tumor rim, but apparently not exclusively. Fernandez-Guinea et al. [112] reported MVD values from tumor centers which are somewhat lower $0\text{-}157 \text{ mm}^{-2}$ with a median of 20 mm^{-2} . We obtain a whole-tumor average of $133 \pm 18 \text{ mm}^{-2}$ (case CMPR, s. Table 4) which includes a significant contribution of the rim. The prediction of the MVD of the central part of the tumor agrees with this data. Microvessel density MVD of normal breast tissue is reproduced accurately.

The regional vessel volume rBV denotes the volume fraction of tissue occupied by vessels. Additionally, the relative venous volume $vrBV$, i.e. the total volume occupied by venules and venes over the total blood volume is given in case of normal tissue. Because the classification of vessel segments of the tumor vasculature into arterioles, capillaries and venules no longer applies, the latter quantity is meaningless in case of tumors. Tissue hemoglobin concentration c_{Hb} is the product of mean corpuscular hemoglobin concentration ($MCHC$) and regional RBC volume $rRBCV$ (s. S2 Appendix). Assuming homogeneous hematocrit, tissue hemoglobin concentration is given by $c_{Hb} = MCHC \cdot H \cdot rBV$. Thus, using experimentally measured hemoglobin concentrations of normal breast tissue ($c_{Hb} = 17.3 \text{ } \mu\text{mol/l}$ [37]), and of tumors ($c_{Hb} = 53 \text{ mol/Hb}$ [37]), we estimate the vascular volume fraction to be $rBV = 0.008$ (normal breast tissue) and $rBV = 0.0244$ (breast tumors) assuming a hemoglobin molar mass of 64.5 kg/mol and hemoglobin concentration in blood $c_{Hb,blood} = 14 \text{ g/dl}$ (women, normal range: $12\text{-}16 \text{ g/dl}$) corresponding to $MCHC = 311 \text{ g/l}$ hemoglobin per RBC volume and $H = 0.45$.

Results on hemoglobin concentration of normal breast tissue and breast tumors obtained by a number of groups using optical mammography scatter by about a factor of two [37], resulting in an upper limit of $rBV = 0.016$ for normal breast tissue and a range of $rBV = 0.01\text{-}0.06$ for tumors. Beaney [21] obtained distinctly larger rBV estimates for normal breast tissue ($rBV = 0.034$) and breast tumors ($rBV = 0.043$), derived from PET measurements using the steady state $^{15}\text{O}_2$ inhalation technique. Note, however, that the rBV values reported by Beaney [21] for breast tumors, have to be considered as unreliable since the compartment model used to analyze the PET data is inaccurate for heterogeneous tissue [23]. For comparison, in normal human brain regional blood volume was determined from PET measurements to be $rBV = 0.038 \pm 0.007$ [19]. Using MRI and a brain tumor animal model yielded $rBV = 0.026 \pm 0.003$ (normal brain tissue) and $rBV = 0.053 \pm 0.006$ (brain tumor) [28]. Our simulated regional vessel volume of normal breast tissue and breast tumors (case CMPR) are consistent with experimental breast data, simulated rBV of breast tumors was found to be larger than rBV of normal breast tissue as observed experimentally. For breast tissue, we deduce a venous fraction of the total blood volume fraction $vrBV/rBV = 68\%$ (s. Table 4) in fair agreement with MRI data in normal human brain (77%) [119]. Vessel segments contribute to the tissue hemoglobin concentration c_{Hb} according to their blood hemoglobin concentration, weighted by their fractional volume. Likewise, vessel segments contribute to the tissue oxy-hemoglobin concentration $c_{Hb,O}$ (deoxy-hemoglobin concentration $c_{Hb,D}$) according to their average blood oxy-hemoglobin concentration (average blood deoxy-hemoglobin concentration), again weighted by their fractional volume. In order to simulate c_{HbO} or c_{HbD} average

Table 4. Simulation results of the computational model and experimental data.

Symbol	Unit	Initial	Exp/Lit.	BASE	CMPR	METAB	Exp/Lit.
MVD	mm^{-2}	111 ± 0	115 ± 8 [110]	112 ± 19	133 ± 18	112 ± 19	88 [111]
							20 [112] (a)
rBV	%	0.983 ± 0.105	-	1.94 ± 0.63	1.81 ± 0.86	1.94 ± 0.63	2.7 ± 1.6 [37]
							4.3 ± 1.3 [21] (b)
f	Pa	4.21 ± 1.12	$0.1 - 2$ [103]	3.15 ± 0.95	2.63 ± 0.7	3.15 ± 0.95	-
r	μm	4.07 ± 0.07	-	5.94 ± 0.4	5.21 ± 0.98	5.94 ± 0.4	-
$S\rho$	mm^{-1}	2.84 ± 0.04	-	4.21 ± 0.96	4.39 ± 1.14	4.21 ± 0.96	-
$S\rho/rBV$	μm^{-1}	0.292 ± 0.029	-	0.224 ± 0.026	0.266 ± 0.055	0.224 ± 0.026	0.165 [7] (c)
rBF	$ml\ g^{-1}\ min^{-1}$	0.053 ± 0.0139	0.06 [24]	1.6 ± 1.27	1.24 ± 1.34	1.6 ± 1.27	0.32 [24]
			0.056 ± 0.014 [25]				0.19 ± 0.1 [21]
			0.04 ± 0.01 [21]				0.29 ± 0.17 [25]
			0.028 ± 0.017 [113]				
rBF_{scaled}	$ml\ g^{-1}\ min^{-1}$	-	-	0.123 ± 0.042	0.0911 ± 0.0507	0.123 ± 0.042	(d)
$\langle S_{in} \rangle_q$		0.958 ± 0.018	0.98 [114] (e)	0.888 ± 0.062	0.833 ± 0.1	0.888 ± 0.063	-
rJ_{in}	$\mu l\ O_2\ ml^{-1}\ min^{-1}$	11.6 ± 3.2	-	331 ± 266	249 ± 282	331 ± 265	-
\dot{j}_{tv}	$nl\ O_2\ cm^{-2}\ min^{-1}$	122 ± 1	600 [115] (f)	238 ± 20	202 ± 17	242 ± 58	-
MRO_2	$\mu l\ O_2\ ml^{-1}\ min^{-1}$	3.32 ± 0.07	4.5 [21]	12.5 ± 1.3	12.1 ± 1.6	12.7 ± 3.3	6.6 [21]
			33 ± 5 [19] (g)				
OEF		0.336 ± 0.098	0.65 ± 0.1 [21]	0.0678 ± 0.0497	0.109 ± 0.088	0.0677 ± 0.0515	0.23 ± 0.08 [21]
c_{Hb}	$\mu mol/l$	23.6 ± 2.6	17.3 ± 6.2 [37]	47.4 ± 14.4	43.1 ± 19.5	47.4 ± 14.4	53 ± 32 [37]
			16 ± 4 [38]				70 ± 35 [38]
Y		0.703 ± 0.098	0.74 ± 0.14 [37]	0.807 ± 0.096	0.733 ± 0.14	0.807 ± 0.097	0.72 ± 0.14 [37]
			0.74 ± 0.09 [38]				0.71 ± 0.10 [38]
P	$mmHg$	38.6 ± 6.1	-	44.9 ± 11.3	34.3 ± 12.6	44.9 ± 11.7	-
P_t	$mmHg$	36.3 ± 6.1	30 [116]	34.8 ± 13.8	28.7 ± 13.5	34.9 ± 14.3	30 [14]
			65 [14]				
			$40 - 50$ [117] (h)				

Shows averages and standard deviations taken over 90 initial networks ($t = 0\ h$) and tumors ($t = 600\ h$) for cases BASE, CMPR and METAB. We compiled experimental literature data in the columns ‘Exp/Lit.’ for normal (left) and tumor tissue (last col.), respectively. (a) The computed values are actually the line density L_D . The experimental values given are medians of histological MVD [111, 112]. (b) rBV estimated from c_{Hb} assuming $2.18\ \mu mol/l$ hemoglobin in blood [37]. Data from [21] was obtained by PET of human breasts. Note that PET data from [21] for tumor tissues are considered unreliable (see text). (c) Obtained from digitized animal model tumor network obtained by μ -CT. (d) rBF_{scaled} is the initial tissue rBF scaled by the ratio of the rBF values for the iso-volumetric tumor sphere at $t = 0$ and $t = 600\ h$ (see text). (e) Oxygen saturation of human arterial blood at sea level. (f) Obtained by oxygen micro-electrode measurement in rat brains [115]. (g) Ref. [19] refers to human brain MRO_2 . See also Table 1. (h) Obtained from human skin tissue [118], peritumoral skin tissue [116] and muscle tissue in breast tumor-bearing rats [117].

for each vessel segment blood oxygenation has to be known. The simulated average blood oxygen saturation $Y = c_{HbO}/c_{Hb}$ of normal breast tissue agrees well with experimental data. The same holds true for tumor average blood oxygen saturation simulated within the compression model (case CMPR).

Besides the vascular surface area per unit volume of tissue, i.e. vascular surface density $S\rho = S_D$, Table 4 lists the vessel surface to vessel volume ratio $S/V = S\rho/rBV$. For tumor vasculature (case CMPR) we find $S/V = 0.27 \mu m^{-1}$ close to the value for normal breast tissue ($S/V = 0.29 \mu m^{-1}$). This modest decrease is ultimately explained by the low maximal dilation radius $r^{(max)} = 14 \mu m$, leading to an average vascular diameter r only $2 \mu m$ above the average radius in initial networks. Naturally, S/V is proportional to $1/r$, i.e. for a single vessel, but in general the trend for lower surface area to volume ratios for increasing radii still holds true. A contributing factor is the peripheral plexus of thin and densely packed vessel (high S/V), part of which is included in the tumor volume. Stamatelos [7] reported a surface to volume ratio of $S/V = 0.17 \mu m^{-1}$ for a breast tumor model.

The regional blood flow, rBF , i.e. perfusion, is given by the total blood flow q entering a selected tissue volume Ω per regional volume $|\Omega|$ (s. S2 Appendix). To obtain perfusion of the entire system rBF_{norm} over all arterial root nodes and divide by the volume of the simulation box $|\Omega| = L^3$. For a partial volume such as a small spherical tumor inside a tissue cuboid some caution must be taken. For example, considering a Krogh-like arrangement of parallel vessels crossing the entrance face A of a tissue cuboid corresponding to total blood flux q_{tot} and surface flux density q_{tot}/A , the perfusion of a cross-sectional slice with volume $V_{slice} = A \cdot \Delta x$ inside the tissue and oriented parallel to the entrance face A is proportional to $1/\Delta x$. Likewise, at constant surface flux density the perfusion of a small spherical volume inside a tissue cuboid scales as tumor $1/R$. In order to compare simulated tumor regional blood flow with experimental perfusion data for breast tumors with typical volumes of several cm^3 we normalize total flux $q_{sph,tum}(t = 600 h)$ of the small spherical ($R_{tumor} \approx 1.5 mm$) tumor to the total flux $q_{sph,norm}(t = 0)$ of the isovolumetric spherical volume of normal tissue at the center of the simulation box. The scaled tumor perfusion is then given by $rBF_{scaled} = rBF_{norm} \cdot q_{sph,tum}(t = 600 h)/q_{sph,norm}(t = 0)$. The total flux $q_{sph,tum}$, and $q_{sph,norm}$ are obtained by summing blood flow q over those vessels that penetrate the surface of the sphere and have a blood flow direction into the spherical tissue volume. In addition, Table 4 lists the regional blood flow of the small spherical tumor $rBF = q_{sph,tum}/|\Omega_{sph}|$. Previously, a general decrease of total tumor blood flow normalized to tumor weight was seen for human breast cancer xenografts ranging from $0.5 m/g/min$ at $m_{tumor} = 0.4 g$ down to $0.025 ml/g/min$ at $m_{tumor} = 8g$ [120]. On the other hand dynamical PET measurements ($^{15}O_2$) on 37 breast cancer patients yielded $rBF = 0.06 ml/g/min$ (mean, normal tissue, range $0.03 - 0.17 ml/g/min$) and $rBF = 0.32 ml/g/min$ (mean, tumor, range $0.08 - 0.9 ml/g/min$) [24]. Nearly the same results were obtained by [25]. Our results for normal breast tissue (range: $0.032 - 0.064 ml/ml/min$) agree well with experimental data. The simulated mean perfusion (range: $0.13 - 7.5 ml/g/min$) of the small ($0.014 cm^3$) spherical tumors is higher by about a factor of 5 compared to the clinical results, whereas the scaled perfusion (case CMPR) is lower by a factor 1/2.

The global ensemble average of simulated PO2 of normal tissue and tumor tissue amounts to $36 \pm 6 mmHg$ and $29 \pm 13 mmHg$, respectively. Polarographic PO2 measurements at a large number of sites in normal breast tissue and breast tumors of 15 patients yielded median PO2 values of $65 mmHg$ and $30 mmHg$, respectively [14]. None of the measurements in normal breast tissue fell below $12.5 mmHg$, whereas in almost 40 tissue areas with partial oxygen pressures between 0 and $2.5 mmHg$ were detected. The simulated PO2 value of tumor tissue (case CMPR) exactly reproduces the experimental result, the coincidence possibly being fortuitous, considering the skewed histogram of measured partial oxygen pressures. Since the distribution of measured partial oxygen pressures in normal breast tissue is rather broad, simulated and measured tissue partial oxygen pressures in normal tissue can be considered to agree.

The computational model assumes tissue metabolic rate of oxygen consumption to follow a Michaelis-Menten relation and takes the maximal rate M_0 and half-pressure R_{M50} as input. In particular, maximal rate M_0 in tumor tissue was assumed to be four times larger than in normal breast tissue, whereas half-pressure R_{M50} of normal breast tissue was adopted to be twice that of breast cancers. Since (average) partial oxygen pressure in normal and tumorous breast tissue were simulated to be considerably higher than the assumed half-pressures R_{M50} , the simulated

metabolic rates $MRO_2 = 3.25 \mu\text{O}_2/\text{ml}/\text{min}$ (normal tissue) and $MRO_2 = 12.1 \mu\text{O}_2/\text{ml}/\text{min}$ (breast tumor, case CMPR) are essentially determined by the assumed parameters of the Michaelis-Menten relation. From PET measurements based on the steady-state $^{15}\text{O}_2$ inhalation technique, Beaney [21] reported $MRO_2 = 4.5 \mu\text{O}_2/\text{ml}/\text{min}$ and $MRO_2 = 6.6 \mu\text{O}_2/\text{ml}/\text{min}$ for normal breast tissue and breast tumors, respectively. The latter value had been challenged because of tumor inhomogeneity [23]. Within the framework of the three compartment model (s. Table 1 in S3 Appendix) we estimate metabolic rate of oxygen consumption to range between $MRO_2 = 3.5 - 5.2 \mu\text{O}_2/\text{ml}/\text{min}$ (normal tissue) and $MRO_2 = 8.9 - 14.3 \mu\text{O}_2/\text{ml}/\text{min}$ (breast tumor), using for the average blood oxygen saturation $Y_{exp} = 0.74$ (normal) and $Y_{exp} = 0.72$ (breast tumors) [37]. $S_{in} = 0.958$ and $S_{in} = 0.833$ of the average arterial saturation for normal and tumorous tissue, respectively, given in Table 4. The quoted ranges of the metabolic rates of oxygen consumption correspond to the range $0 \leq P_t \leq 37 \text{ mmHg}$ of tissue partial oxygen pressures assumed by the compartment model. Simulated and experimental metabolic rates agree well, For comparison we note that for normal human brain PET measurements yielded $CMRO = 33 \pm 5 \mu\text{O}_2/\text{ml}/\text{min}$ [19].

It was discussed in Sec. ‘Predictions of Compartment Model and Comparison with Experimental Data’, that average blood oxygen saturation is (negatively) correlated with oxygen extraction fraction $OEF = J_{tv}/J_{in} = (J_{in} - J_{out})/J_{in}$, where J_{tv} is the total transvascular oxygen flux into tissue, in J (J_{out}) the total vascular influx (efflux) into the vasculature (leaving the vasculature) of the tissue volume considered. For the whole simulation box, J_{in} and J_{out} are determined by summing oxygen flux qc over all root arteries or veins, respectively. For the tumor, we sum qc over vessels penetrating the tumor surface with a flow direction into or out of the tumor. For normal breast tissue and breast tumors (case CMPR) we obtain the result $OEF = 0.34 \pm 0.1$ and $OEF = 0.11 \pm 0.09$, respectively. Within the framework of the compartment model we estimate oxygen extraction fraction both of normal breast tissue and breast tumors to fall into the range $OEF = 0.26 \pm 0.41$, depending on partial oxygen pressure in tissue. Oxygen extraction data on normal breast tissue and breast tumors are scarce. Beaney [21] reported the oxygen extraction fraction of normal breast tissue to be $OEF = 0.65 \pm 0.1$. This result seems to be rather high considering the oxygen extraction of normal human brain measured by PET to be $OEF = 0.44 \pm 0.06$ [19]. Using the steady state $^{15}\text{O}_2$ inhalation technique almost the same oxygen extraction fractions were measured for breast tumors ($OEF = 0.23 \pm 0.08$, [21]) and brain tumors ($OEF = 0.22 \pm 0.04$, [22]), however the same reservations remain concerning inadequate data analysis because of tissue heterogeneity. Our simulations predict for breast tumors (case CMPR) oxygen extraction fractions of $OEF = 0.11 \pm 0.09$, an estimate likely to be too low. Since $MRO_2 = c_{Hb,blood} S_{in} \cdot rBF \cdot OEF$, where S_{in} is the arterial blood oxygenation of the vessels penetrating the surface of the spherical tumor, overestimation of the tumor regional blood flow will cause an underestimation of the oxygen extraction fraction OEF , since the metabolic rate of oxygen consumption is essentially fixed by the input parameters of the model. In other words, since tum in $OEF = MRO_2 \cdot rJ_{in}$ overestimation of the oxygen influx into the tumor reduces the estimated oxygen extraction fraction. In addition, Table 4 lists the oxygen influx J_{in} and average transvascular oxygen flux density j_{tv} , where we write j_{tv} informally for the average over the network length (s. S2 Appendix).

In the following we illustrate results obtained for selected root node geometries. Fig. 9 corresponds to case CMPR, root node geometry RC9 and shows partial oxygen pressure (PO2) distributions of blood vessels, P , and of tissue, P_t , as well as corresponding blood oxygen saturations S . Typical features of tumor vasculatures are visible such as heterogeneity, compartmentalization, a highly vascularized rim, a sparsely vascularized center and the loss of hierarchical organization. Other cases (BASE, METAB) and root node geometries exhibit similar looking distributions of PO2 and blood oxygen saturation of normal tissue and tumor periphery. On the other hand the vascularization of the tumor center can be clearly visibly lower or higher than the example shown, which is accompanied with varying degrees of oxygenation. The compartmentalization is also evident in the average radial profile of the microvascular density, MVD , and regional blood volume, rBV , shown Fig. 8. We made sure that in good approximation cases BASE and CMPR exhibited similar radial MVD and rBV profiles. This requirement is critical since we aim to analyze the effect on blood oxygen saturation Y by varying the compression factors ξ_{cpr} among the ensemble of 90 tumor vascular networks, while retaining agreement with experimental data on MVD and rBV . Let us now consider details of the oxygen distribution as for instance shown in Fig. 9C. Immediately obvious, we see severe hypoxia at the tumor center due the sparse vasculature there. As one would expect, P_t is highest near vessels

and falls off over a scale of 100 to 200 μm into non-vascularized spaces. Tumor vessels in the central region of the tumor, significantly vary in their oxygen content. Some vessels, carry highly saturated blood, in particular when connected to nearby arterioles. When isolated vessels thread the tumor over distances of several hundred micrometers, blood oxygen saturation S visibly decreases to the point where vessels are completely depleted of oxygen. The tissue PO2 near such vessels appears to follow this trend, i.e. it also decreases. Remarkably, the (neo)vascular plexus around the tumor rim is dominated by severe oxygen deprivation, too. Evidently, vessels that are underoxygenated do not penetrate far into the tumor, but those vessels which advance towards the tumor center carry normal amounts of oxygen. As Fig. 10 shows, underoxygenation of the rim results from the accompanying low hematocrit, leading to reduced oxygen capacity and fast oxygen depletion. On average, at the tumor center the hematocrit is elevated by 17%, whereas in the periphery hematocrit amounts on average to 66% only of the baseline normal tissue (data not shown), according to radial profiles analogous to Fig. 8.

We compare the results of our oxygen model with tumor growth models that assume for simplicity constant intravascular oxygen concentration. To this end we modified our model, omitting the propagation of oxygen through the vascular network. A map of the resulting oxygen distribution is shown in Fig. 11, where we assumed a constant intravascular partial oxygen pressure P equal to the ensemble mean of 39 $mmHg$ as it is obtained from the full model. An obvious qualitative difference is the absence of long ranged P_t variations in normal tissue. Instead, fine grained fluctuations in-between neighboring vessels are much more apparent. Moreover, the P_t level along the surviving tumor vessels is nearly constant so that the P_t distribution can approximately be described by a function of the distance to the closest vessel alone. The neglect of varying hematocrit leads to overestimation of P_t in the peripheral region (see above). Naturally, this simplified model implies constant tissue oxygen saturation Y , and thus does not allow to analyze experimental data on blood oxygen saturation in normal and tumorous tissue.

Furthermore our model predicts mean tissue concentrations of hemoglobin c_{Hb} , oxyhemoglobin c_{HbO} , deoxy-hemoglobin c_{HbD} and, therefore, mean blood oxygen saturation Y in tissue at least in qualitative agreement with optical mammography data [37, 38]. In analogy to the experimental papers [37, Fig. 3a,b and 5a], [38, Fig. 3a,b], we produced Figs. 12, 13 and 14 for cases BASE, CMPR, and METAB, respectively. In these figures, one data point shows the result of a single simulation based on a selected root node configuration identified by colored symbols (s. Fig. 7). The $c_{Hb}(tumor)-c_{Hb}(normal)$ correlations simulated for cases BASE, CMPR and METAB (s. Fig. 12A, Fig. 13A) qualitatively agree well with the experimentally observed ones [37, Fig. 3a] and [38, Fig. 3a]. On the other hand only for case CMPR the simulated $Y(tumor)-Y(normal)$ correlations (s. Fig. 13B) shows the blood oxygen saturation in tumor tissue to fall both above and below that of the corresponding host tissue, whereas cases BASE and METAB yield tumor blood oxygen saturations essentially to be always larger than host tissue. For the simulated $Y(tumor)-Y(normal)$ plots it makes virtually no difference choosing the initial tissue at time $t = 0$ or the tissue surrounding the final tumor as reference. Since Y is the RBC-volume weighted average of blood oxygen saturation taken over all vessel segments, dilated tumor vessel, prevailing in case BASE (s. discussion above) will dominantly contribute to Y , in particular when high blood flow rates and hence high oxygen input flux cause their blood oxygen saturation to be high.

Variation of M_0 in case METAB affects transvascular oxygen flux J_{tv} and therefore oxygen extraction fraction. Since average blood oxygen saturation Y is (negatively) correlated with OEF , blood oxygen saturation Y of tumors is lowered, provided oxygen extraction fraction is increased by selecting a higher maximal metabolic rate M_0 (s. Fig. 14A). However, since simulated J_{tv}/J_{in} tumors is rather low, i.e. oxygen influx is rather large compared to transvascular oxygen flux and the variations of M_0 applied are not sufficient to lower Y (tumor) below Y (normal). Likewise, compressing tumor vessels will reduce oxygen influx and hence increase oxygen extraction. Because of the negative correlation of blood oxygen saturation Y with oxygen extraction fraction, average blood oxygen saturation will decrease with increasing compression, i.e. at lower compression factors ξ_{cpr} , as long as average blood oxygen saturation is sufficiently far from saturation. These conclusions are immediately evident from Fig. 14D. Different initial vessel configurations give rise to a spread among Y for a given ξ_{cpr} (or M_0).

Figs. 12C, 13C and 14C illustrate the correlation between blood oxygen saturation Y and total hemoglobin concentration. In each case (BASE, CMPR, METAB) good agreement with

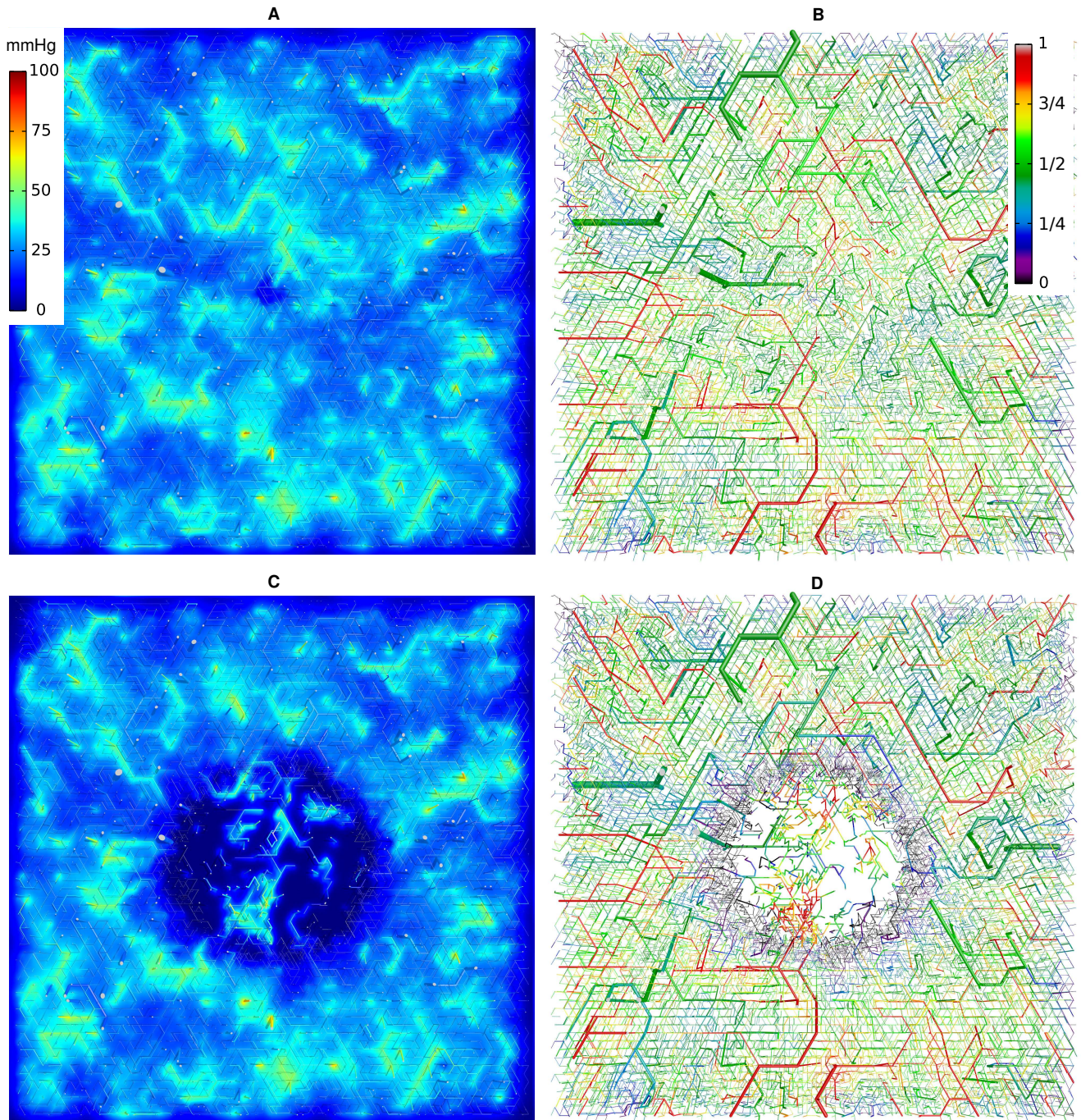


Figure 9. Blood oxygen saturation and oxygen partial pressure corresponding to case CMPR, root node configuration RC9. The left column (A,C) shows the PO₂ of vessels, P and of tissue, P_t in a slice through the center of the simulation domain. The camera is looking vertically onto the horizontal cutting plane so that the whole lateral extent of 8 mm is shown. The vessel network is visualized as a collection of cylinders that have been truncated 100 μm above and below the central plane. The resulting cross sectional areas are light grey. Otherwise the color code indicates the PO₂, P , of vessels and P_t of tissue, respectively. In the right column (B,D), only the network is shown color coded by saturation S . The top row (A,B) shows the initial state at $t=0$. The bottom row (C,D) shows the final state after $t = 600 h$.

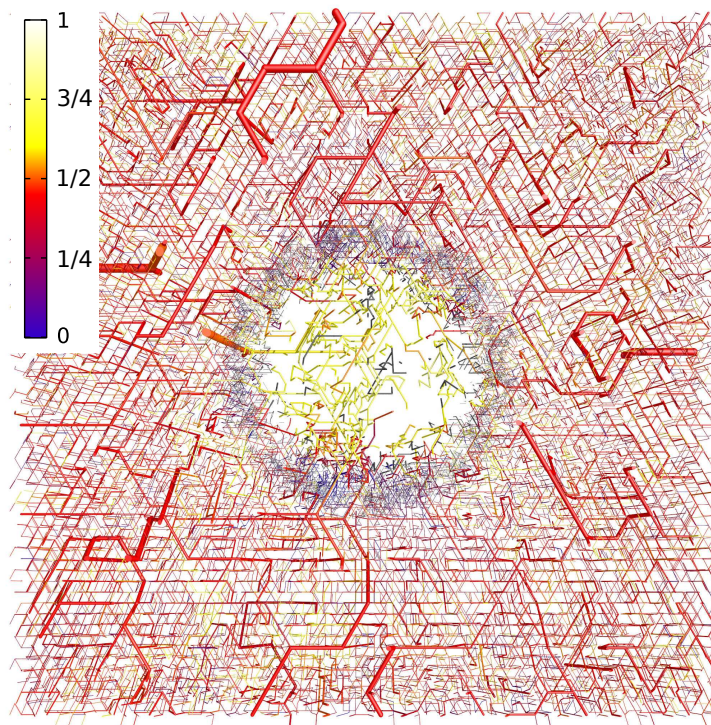


Figure 10. Hematocrit distribution corresponding to Fig. 9D, showing the same slice of the vessel network, but color coded for H . Our blood flow model includes the phase separation effect which leads to a severe reduction of the hematocrit in the peripheral tumor network and an elevated hematocrit in the vessels at the tumor center.

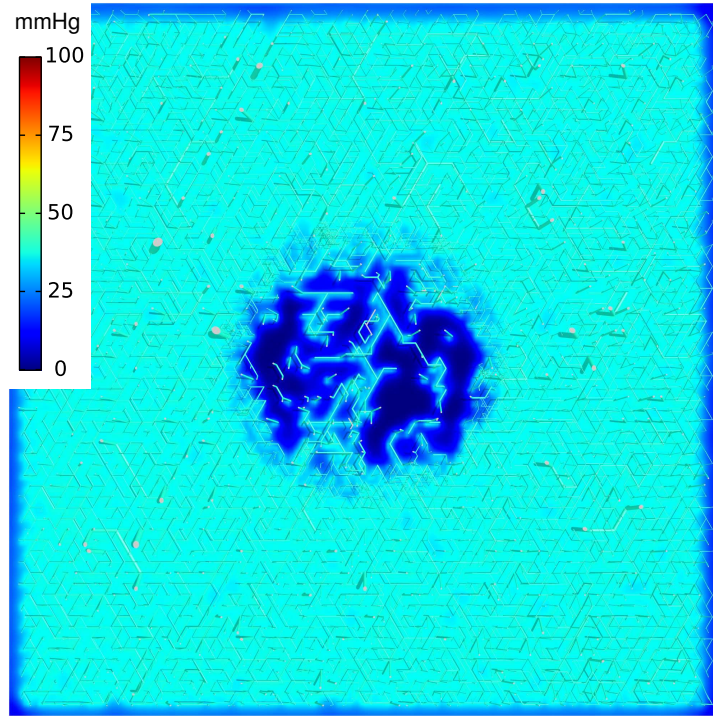


Figure 11. Tissue oxygen distribution at constant vascular PO₂: This figure shows a visualization of the network depicted in Fig. 9 but with blood PO₂ held constant, and only the tissue PO₂ map was computed. The value of the blood PO₂ was chosen to equal the prediction of the ensemble mean of blood PO₂ of normal tissue, amounting to 39 *mmHg* .

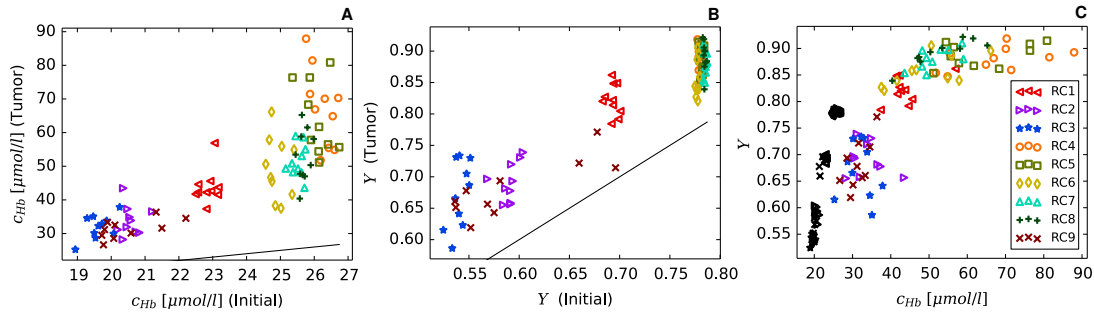


Figure 12. Hemoglobin concentrations and tissue oxygen saturations (Case BASE): Each data point corresponds to a different simulation run, where the color code indicates the type of initial network configuration (see text). Figure A displays the hemoglobin concentration c_{Hb} of tumor tissue versus c_{Hb} in normal tissue. The depiction in (B) shows analogously the tissue oxygen saturation Y . (C) shows Y against c_{Hb} where tumor (colored) and normal tissue (black) are both shown as different point sets. Black lines in (A) and (B) have slope 1 and serve as visual guides, i.e. a symbol underneath them corresponds to a tumor where the quantity considered is less than in normal tissue. Consistent with experimental results on hemoglobin concentration in normal breast tissue and breast tumors [37, Fig.3a] hemoglobin concentration c_{Hb} and hence regional blood volume rBV in tumors is predicted to be always larger than that of surrounding normal breast tissue. However, contrary to experimental data [37, Fig.3b] average blood oxygen saturation Y in tumors is predicted to be always larger than in normal breast tissue (base line).

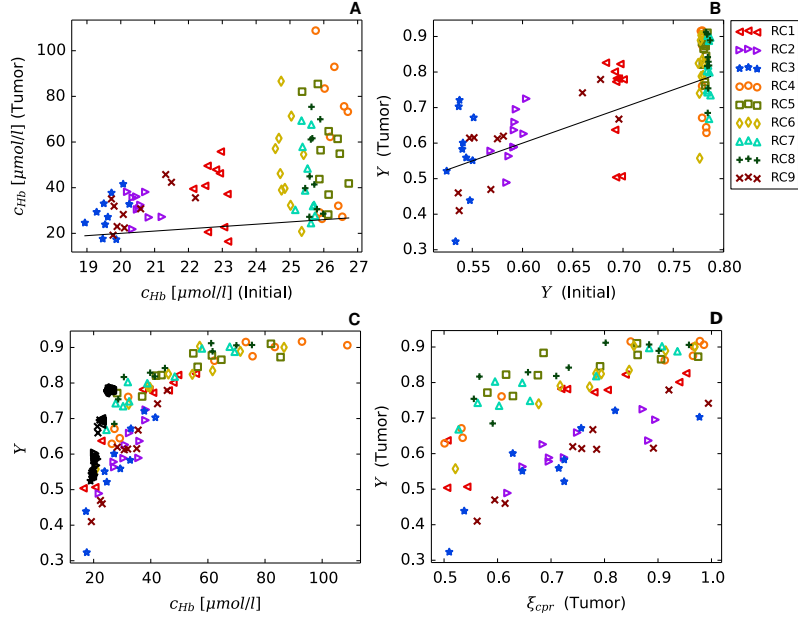


Figure 13. Hemoglobin concentrations and tissue oxygen saturations (Case CMPR): This figure is the analog of Fig. 12, but for case CMPR. Each simulation was performed with a different factor ξ_{cpr} according to which the radii of all tumor vessels were scaled so that the variation across the ensemble is increased and blood flow through some of the high caliber tumor vessels is impaired. In addition, panel (D) shows the Y dependence on ξ_{cpr} .

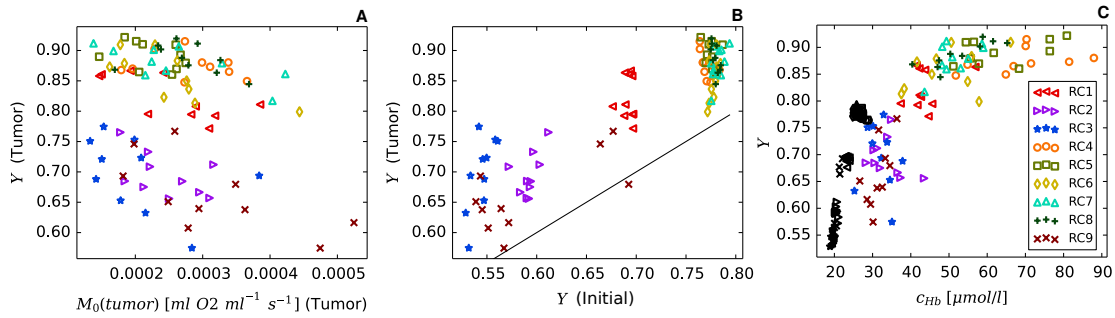


Figure 14. Hemoglobin concentrations and tissue oxygen saturations (Case METAB): This figure is the analog of Fig. 12 for case METAB. Here, each simulation was performed with a different tumor oxygen consumption rate parameter M_0 , distributed according to a lognormal distribution. In this case, c_{Hb} is identical to case BASE, therefore panel (A) shows instead the dependence of Y on M_0 . Panels (B) and (C), show plots of c_{Hb} and Y as in the previous figures. The impact on the tumor Y is more moderate compared to case CMPR.

experimental results is obtained [37, Fig. 5a]. The figures show the limiting behavior of average blood oxygen saturation, yet data above the lower limit of Y at selected hemoglobin concentration c_{Hb} are missing. Fig. 15A,C illustrates that perfusion rates rBF correlate positively with tissue hemoglobin concentration c_{Hb} in both tumor and normal tissue, and therefore with vessel volume rBV . Indeed, the correlation of Y versus c_{Hb} and Y versus rBF look qualitatively similar (data not shown). Configurations RC4 through RC8 yield particularly high perfusion rates. This must be related to the number of arterial inlets (venous outlets) of which only two to four are involved for these geometries

In contrast, root node geometries RC1, RC2, and RC3 contain root nodes on all sites on one or several faces of the simulation cuboid (see Fig. 7). In order to obtain good agreement of Y versus c_{Hb} correlations with Grose et al. [37], data points of all configurations RC1 through RC9 are required. In particular RC4 through RC8 contribute high c_{Hb} and Y . Evidently these configurations exhibit a large vessel volume rBV , hence high c_{Hb} . This apparent contradiction can be explained by the network construction algorithm. Since vessel radii are governed by Murray's law, the radii of root vessels grow the larger, the more expansive the supplied (or drained) tree is. This is clear because for $0 < \text{Murray-}\alpha < \infty$ vessel radii become larger at each bifurcation from leafs to the top.

In S4 Appendix we show for perfect binary trees, that the regional blood volume rBV decreases according to a power law with growing number of roots nodes, provided that the total number of vessels is kept constant. Variation of the root radii and blood volume rBV causes increased perfusion in two ways. First, the flow resistance of the entire vascular tree decreases with increasing rBV . Thus, provided a fixed blood pressure difference, the perfusion rBF increases with rBV . Secondly, the blood pressure differential between arterial and venous sides increases with root radii according to the blood pressure-radius relation (Eq. (1) in S5 Appendix) for $p^{(BC)}(r)$. Since $p^{(BC)}$ is used as pressure boundary-condition at root nodes, perfusion increases with the pressure differential depending on r . Consequently, given other parameters such as permeabilities fixed, an increased perfusion rBF leads to an increase in Y until saturation (s. Sec. 'Predictions of Compartment Model and Comparison with Experimental Data').

Fig. 15D and Fig. 15F correlate vascular surface to volume ratios for normal tissue and tumors respectively. In either case, the ratio decreases with increasing regional blood volume rBV , probably due to the presence of larger vessels at higher fractional blood volumes. As can be seen from Fig. 15E vascular surface to volume ratios of tumors are mostly smaller than those of normal tissue. In contrast, vascular surface density $S\rho$ increases with increasing regional blood volume both for normal breast tissue and tumors. Vascular surface density is seen to be higher than that of normal breast tissue. Finally we compare oxygen extraction fractions for normal (Fig. 15J) and tumorous (Fig. 15K) tissue. Since metabolic rate of oxygen consumption MRO_2 is essentially an input in both cases and intravascular oxygen concentration at input is nearly constant, $OEF = MRO_2/c_{in}/rBF$ plotted versus rBF follows a hyperbola, as can be seen from Fig. 15J (normal tissue) and Fig. 15L (tumor).

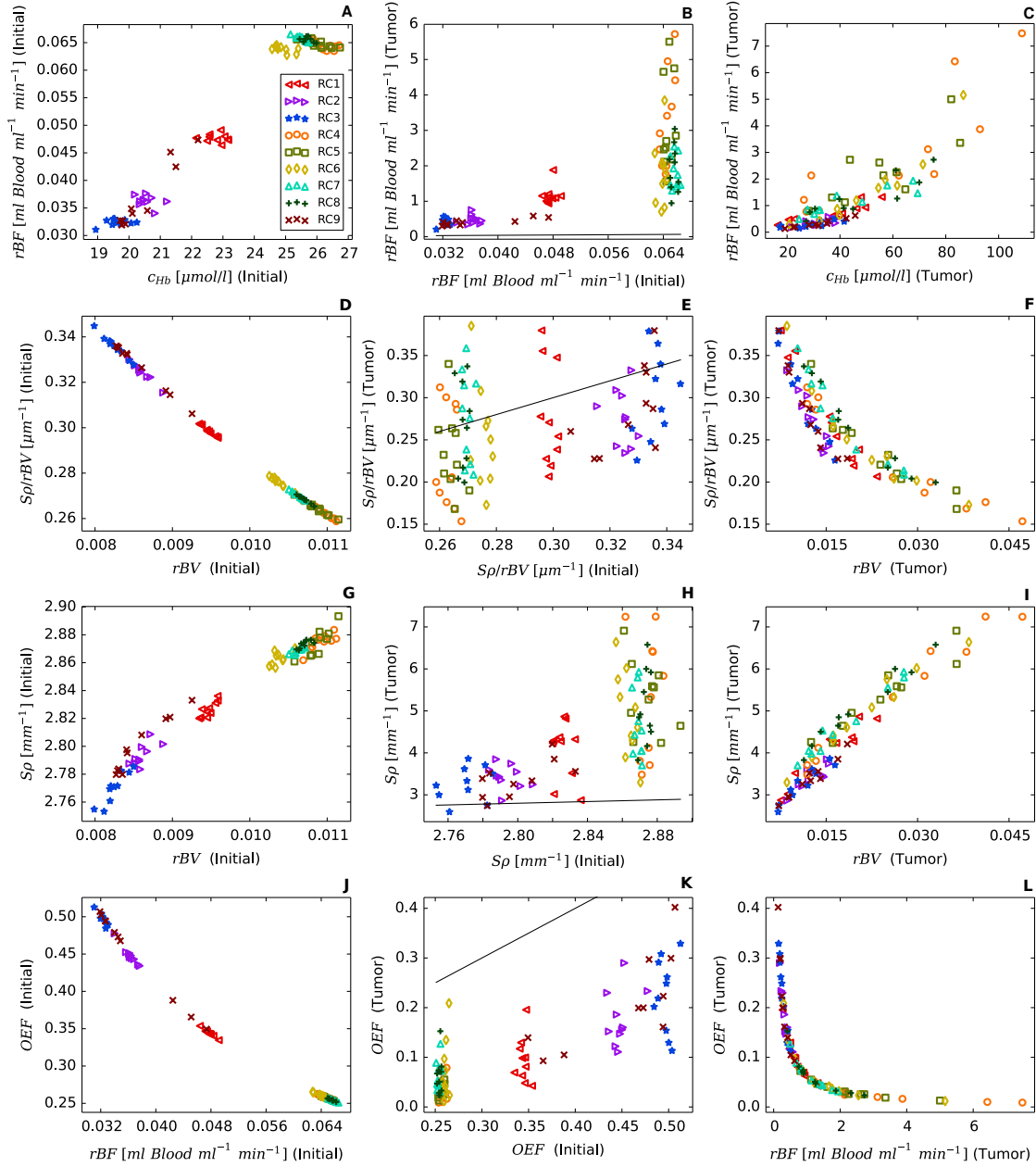


Figure 15. Other biophysical quantities (Case CMPR): Like in previous scatter plots, each data point corresponds to a single simulation. The symbol code shows the root nodes configuration according to the legend in (A). Correlations for initial tissue ($t = 0$) and tumor tissue ($t = 600 h$) are shown in the left column (A,D,G,J) and right column (C,F,I,L), respectively. Correlations for normal vs. tumor tissue are shown in the center column (B,E,H,K). Perfusion rates rBF increase with hemoglobin concentration c_{Hb} due to increasing vascular volume. The correlation of rBF (Tumor) vs. rBF (Initial) exhibits virtually the distribution of c_{Hb} correlations of Fig. 13A. In (D), (F): Vascular surface to volume ratio decreases with increasing regional vascular volume due to increasing vascular radii. E compares vascular surface to volume ratio of tumors with corresponding normal tissue. In (G, H, I): Surface density increases with increasing regional blood volume. Tumor surface density is seen to be higher than that of normal breast tissue. In (J, K, L): Oxygen extraction of tumors is below that of normal tissue because of higher regional blood flow.

Discussion

Discussion of Results of the Network Model

We simulated intravascular and extravascular distributions of partial oxygen pressure arising in artificial, algorithmically generated, tumor blood vessel networks and networks of surrounding normal tissue. The model takes the blood vessel network, tissue oxygen consumption rates and the radius of the tumor as input besides biophysical parameters such as arterial blood pressure, hematocrit, and arterial blood oxygen saturation and computes stationary oxygen partial pressure maps (PO₂) for the network and tissue. Our computational method the iteration of the solution of sparse matrix equations, avoiding the costly inversion of dense equations which arise from the Green's functions method [68]. Our method also allows for under resolved numerical grids discretizing the tissue domain, where PO₂ gradient boundary conditions at vessel walls [41] cannot be used since the diameter of vascular lumens can be smaller than the grid constant and thus completely contained inside a grid cell. The present work uses a tissue cuboid of about 0.5cm^3 and a tumor radius of 1.5mm , still significantly below tissue volumes probed experimentally. In particular, we compared regional blood volume rBV or total hemoglobin concentration c_{Hb} and average blood oxygen saturation $Y = c_{HbO}/c_{Hb}$ of tumors and associated normal networks. Furthermore the dependence of average blood oxygen saturation Y on regional blood flow rBF and on rBV or c_{Hb} was simulated separately for tumor and normal tissue. We focused on breast tumors and normal breast tissue guided by metabolic and morphological experimental data. From optical mammography studies [37, 38] taken on a large cohort (n=87, n=32) of breast cancer patients it was concluded that tissue hemoglobin concentration c_{Hb} in tumors almost exclusively exceeds that in corresponding normal breast tissue, whereas average blood oxygen saturation Y in tumors was seen to be higher or lower than blood oxygen saturation in surrounding normal breast tissue. Besides such correlations of biophysical or metabolic parameters between tumor and surrounding normal breast tissue it was observed that in tumors high hemoglobin concentration was correlated with high average blood oxygen saturation.

Our simulations of distributions of intravascular and extravascular partial oxygen pressures aim at underpinning the experimental observations with artificially generated vascular networks of tumors and associated normal tissue, i.e. we attempt to solve an illposed inverse problem. Our previous model of tumor vessel remodeling (case BASE), developed to account for the vasculature of growing melanomas, qualitatively explains all experimental observations of optical mammography, apart from cases with tumor average blood oxygen saturation lower than that of normal breast tissue. The higher hemoglobin concentration generally observed in tumors compared to surrounding normal tissue is simply a consequence of circumferential growth of tumor blood vessels, outweighing vascular regression. A moderate vasodilation is sufficient because vessel volume grows proportional to r^4 . Furthermore, regional blood flow rBF was simulated to be well to moderately correlated with hemoglobin concentration c_{Hb} and therefore with regional blood volume rBV , a result obtained both for tumors and normal tissue. Thus the correlation of high hemoglobin concentration with high average blood oxygen saturation observed experimentally reflects low oxygen extraction at high blood flow rates.

However, cases with average blood oxygen saturation in tumors below normal breast tissue require a modification of the tumor vascular growth process. Using our previous model of tumor vessel remodeling (case BASE) the average blood oxygen saturation was calculated in tumors to be exclusively higher than in surrounding normal tissue. Our method to simulate tumor vasculature had been developed previously based on morphologic data (MVD) of melanomas. It is therefore not too surprising that addition of data on average blood oxygen saturation Y depending on metabolic characteristics of tumor tissue besides vascular structure and hemodynamics, i.e. on oxygen demand and oxygen supply, may require modifications of the vascular growth model. In this paper we tentatively assume for these cases that tumor blood vessels are compressed during growth by solid pressure known to be elevated in solid tumors (case CMPR). Each of the 90 tumor vessel networks is subject to a different, statistically selected degree of compression, mimicking phenotypical differences among breast cancer patients, yet keeping the ensemble average of MVD , and rBV the same as for case BASE. In this way average blood oxygen saturation Y of about half of the tumors fell below that of surrounding normal tissue. However, there are some drawbacks with this extension of our vascular growth model. The compression of tumor blood vessels by a randomly selected degree effectively

amounts to reducing the maximal radius $r^{(max)}$ reached by circumferential growth on average. On the one hand the value of $r^{(max)} = 14\mu m$ selected is already rather small considering that we expect some degree of vasodilation to occur. On the other hand, reducing $r^{(max)}$ leads to skewed balance between microvessel density MVD and regional blood volume rBV which we currently consider as adequate. Alternatively using the original tumor vessel networks of case BASE we calculated blood oxygen saturation in tumors assuming different (maximal) metabolic rates of oxygen consumption in each case simulating phenotypical differences between cancer patients (case METAB). The ensemble average of the metabolic rate of oxygen consumption MRO_2 was kept the same as in case BASE. Despite differences in metabolic rates of oxygen consumption among the 90 tumors, blood oxygen saturation of all tumors were calculated to be higher than in surrounding normal tissue. Although allowance for compression of tumor vessels by solid pressure enables us to qualitatively explain experimental data on blood oxygen saturation in tumor and surrounding normal tissue, we cannot exclude other modifications of growth processes leading to vascular remodeling in tumors.

All of our tumor networks exhibit typical features like chaotic connectivity, a sparsely vascularized tumor center, a highly vascularized tumor rim and vasodilation. Variations of vessel networks from tumor to tumor are introduced by the vascular microenvironments in which the tumors grow. To this end we arbitrarily adopted nine root node geometries, differing in location and number of arterial (venous) inlet (outlet) vessels. Starting from each root node geometry ten normal vascular networks were grown which, too, differed among each other because of the statistical nature of the growth process. Using the total of 90 normal vascular networks we demonstrated that the specific arrangement of host vessels prior to tumor growth can play a significant role for the outcome of tumor vascular remodeling. Depending on the root node geometry, drastic variations in microvascular density MVD at the tumor center, regional blood volume rBV and perfusion rBF were observed. The same parameters are subject to fluctuations over the initial networks, yet to a much lesser extent. In earlier work [57, 58] such variations were explained by the interplay of shear stress controlled vessel survival and the location of former arterioles and veins within the tumor. When arteries (arterioles) and veins (venules) are coopted in close proximity by the tumor, angiogenesis is likely to produce arterio-venous shunts that are very stable due to high shear stress caused by high blood flow rate associated with large blood pressure gradients across the shunts. Such shunts can form clusters with high transport capacity. Since the rate of change of the oxygen concentration along the vessel axis is inversely proportional to blood flow rate q , it follows that tumors with many such arterio-venous shunts will exhibit low oxygen extraction and therefore high average blood oxygen saturation Y . Hence, tumors with clusters of high-caliber vessels threading the tumor are associated with cases for which average blood oxygen saturation was found to exceed that of surrounding normal breast tissue. Recently it was proposed that defective signaling along the tumor microvasculature to avoid excessive flow through shunts is a primary cause of local hypoxia in tumors [121].

In our simulations we take the phase separation effect into account, i.e. RBCs at bifurcations prefer to flow into the more strongly perfused branch [95, 122]. Accordingly our simulated hematocrit distributions show a redirection of red blood cells (RBCs) into central tumor vessels. These redirected RBCs are lacking in the peripheral capillary plexus, drastically decreasing its oxygen carrying capacity, resulting in fast oxygen depletion to hypoxia inducing levels which could drive further invasive behavior in real tumors.

When setting the intravascular PO2 constant our maps of PO2 in tissue obtained suggest that the simplified model is suitable to produce qualitative results when features like necrotic regions, and oxygen concentration at the outer rim are of interest but exact numbers on oxygen availability are secondary. Many tumor growth models make this approximation for reasons of computational cost and simplicity. A model variant of intermediate complexity might consider an oxygen source strength proportional to the hematocrit which better captures the oxygen distribution in the periphery but overestimates the oxygen concentration around central tumor vessels compared to the simple constant source approximation. The latter variant has also found application e.g. in [50, 57].

Discussion of Results of the Compartment Model

The three-compartment model provides a complementary approach to simulate blood oxygen saturation in tissue. The model considers a single vessel representing the total length of the vascular network together with a homogeneous tissue compartment of constant partial oxygen pressure. Hence no information on vascular structure and distribution of oxygen concentration in tissue

can be obtained. In reality, biophysical and metabolic parameters entering the model represent averages taken over the vessel network and tissue volume. Input parameters are hematocrit H and arterial blood oxygen saturation $S(0)$, regional blood flow rBF and hence oxygen flux J_{in} into the vasculature per unit volume of tissue. Other relevant parameters are the extravasation rate constant $P_{O_2}S\rho$, the transvascular oxygen flux $J_{tv}/|\Omega| = MRO_2$ per unit volume of tissue, i.e. the metabolic rate of oxygen consumption, and (average) partial oxygen pressure P_t in tissue. Average blood oxygen saturation Y plotted versus the ratio $rBF/P_{O_2}S\rho$ for selected partial oxygen pressures P_t immediately explains the experimentally observed dependence of average blood oxygenation Y in tumor tissue versus hemoglobin concentration c_{Hb} . The computational model has shown regional blood flow rBF to be correlated with hemoglobin concentration c_{Hb} , thus the experimental plot Y versus c_{Hb} and the simulated dependence Y versus $rBF/P_{O_2}S\rho$ can be compared, apart from a scaling of the horizontal axis. The lower limit of average blood oxygen saturation Y at constant ratio $rBF/P_{O_2}S\rho$ or at constant hemoglobin concentration c_{Hb} corresponds to the maximal transvascular oxygen flux into tissue, i.e. maximal oxygen loss at minimal partial oxygen pressure in tissue. Data on average blood oxygen saturation Y appearing above the limiting curve $Y = Y(rBF/P_{O_2}S\rho)$ are interpreted as corresponding to higher oxygen partial pressures P_t in tissue. The computational model likewise reproduces the limiting curve of average blood oxygenation versus hemoglobin concentration in tumors, yet it fails to account for data with higher blood oxygen saturation corresponding to lower oxygen losses from the vasculature to tissue, a fact presently not understood. The compartment model allows to interpret the correlation between blood oxygen saturation Y in tumors and surrounding normal breast tissue. Tumors with ratios $P_{O_2}S\rho/rBF$ smaller (larger) than that of surrounding normal tissue exhibit higher (lower) average blood oxygen saturation than normal tissue, provided average oxygen partial pressures in tumor and normal surrounding tissue are the same, otherwise shifts of blood oxygen saturation with partial oxygen pressure have to be taken into account. Equivalently, average blood oxygen saturation in tumors is higher (lower) when the ratio $MRO_2/J_{in} = OEF$, i.e. the ratio of oxygen demand over oxygen supply is smaller (higher) than in surrounding normal tissue, apart from shifts due to different partial oxygen pressures in tissue.

The same argument explains why case METAB did not achieve blood oxygen saturation Y of some tumors to fall below that of normal breast tissue despite higher (maximal) metabolic rates of oxygen consumption. Because of high regional blood flow in tumors, i.e. high oxygen supply, the increases in metabolic rates of oxygen consumption, i.e. oxygen demand, were not large enough to increase oxygen extraction fraction sufficiently. Likewise, compression of tumor vasculature during growth (case CMPR) was carried out keeping the ensemble average of regional blood volume rBV to be the same as in case BASE. Therefore, a fraction of the tumor vascular networks of the ensemble correspond to lower rBV while others are associated with higher regional blood volumes. Since regional blood volume and regional blood flow are correlated, tumors with lower regional blood flow and hence lower oxygen supply lead to lower blood oxygen saturation Y , provided Y is far enough from saturation.

Limitations and Outlook

Although we explained salient features of the experimentally observed correlations of hemoglobin concentration and blood oxygen saturation between tumorous and corresponding normal breast tissue (inter-vascular-network correlations) as well as the dependence of average blood oxygenation on hemoglobin concentration for normal breast tissue and tumors (intra-vascular-network correlations) our computational and compartment models have significant limitations. The compartment model used to calculate average blood oxygenation should be extended to include a distribution of vascular segment transit times. Our computational model did not exploit all experimental information available from optical mammography on a cohort of 87 patients. Hemoglobin (c_{Hb}), oxy- and deoxy-hemoglobin (c_{HbO} , c_{HbD}) concentrations, exhibit log-normal distributions, with tumors generally showing broader distributions compared with normal breast tissue. In future, such prior knowledge should be included as input for simulations.

A significant limitation of the computational model is the small size of the spherical tumors embedded in the simulation domain, making a comparison of simulated data with experimental results to some extent uncertain, notably for regional blood flow. Also, the vascular structure of cm sized tumors might be different from the mm -sized tumors that were simulated. In future, efforts

should aim at simulating larger vascular networks of normal and tumorous tissue. Moreover, for the sake of simplicity we considered vascular networks to be embedded into homogeneous tissues in our present paper, a simplification being questionable in case of tumors.

Presently our computational method based on a uniform grid is inaccurate due to poor convergence with lattice spacing h . As pointed out in [123], optimal convergence of the solution of elliptic partial differential equations with Dirac source terms can be achieved by adaptive meshes, concentrating discretization points near the source contributions. This insight should be taken into account in future work in order to improve the accuracy the method.

Available anatomical information should be used to generate realistic geometries of feeding arteries (arterioles) and draining veins (venules), rather than arbitrarily creating geometric patterns of root nodes as in this paper. Alternatively, following [82] a possible remedy to this problem might be to exclude root node geometries that result in unrealistic values of biophysical variables, e.g. unreasonably low or high perfusion rates. Indeed network types RC1, RC2, RC3 and RC9 exhibit regional blood flows rBF which agree much better with experimental data than other root node geometries.

More fundamentally, although elevated interstitial fluid pressure is a hallmark of tumors, and unhindered fluid communication between blood and interstitial space is supposed, [124] we neglected the enhanced extravasation of liquid from the vascular network to the interstitial compartment. Elevated interstitial fluid pressure affects blood flow by lowering the intravascular pressure gradient, that may even lead to stasis. Due to the hyperpermeability of tumor vasculature towards e.g. plasma proteins, hemoconcentration occurs resulting in an increase in apparent viscosity [125]. Presently, this modification of tumor blood rheology is not taken into account in our paper. In addition, we did not consider local disturbances, such as partial or complete (temporary) pinch-offs of tumor vessels or local plasma leakage, causing high local blood viscosity, resulting in shunting away blood flow from some parts of the vasculature. Only steady state solutions, e.g. of blood flow distribution and average blood oxygen saturation were calculated, although blood flow in tumor vasculature is known to be sluggish and chaotic, sometimes even reversing directions.

Overall compression of tumor blood vessels by tissue internal pressures was found to be one mechanism to explain low average blood oxygen saturations in tumors. However, other biological processes may cause tumor blood vessels to shrink and such processes cannot be excluded. No attempt was made to simulate pressure of liquid and solid tissue components, other than an oversimplified ad-hoc radius reduction by a constant factor (Case CMPR). Furthermore, pressure applied externally to the breast during optical mammography should be included into such simulations.

Future efforts should clarify to what extent the various approximations made affect the simulation of average blood oxygenation. To our knowledge our present paper is the first attempt to correlate blood oxygen saturation of human tumors with artificial tumor vascular networks, blood flow and transvascular oxygen flux, i.e. metabolic rate of oxygen consumption. We expect our computational and compartment models to find applications to analyses of clinical data obtained by PET, MRI, biomedical optics and hybrid techniques such as photoacoustics, probing tissue vascularization and oxygenation.

Supporting Information

S1 Appendix

Oxygen Mass Transfer Coefficient In this supplemental material we will review simulation results in comparison with literature references and our calibration procedure of the mass transfer coefficient γ .

S2 Appendix

Explicit Formulas for Relevant Biophysical Quantities The simulation of tumor growth and oxygen PO₂ distributions in blood and tissue yields vascular flow rates q_v , hematocrit H_v , oxygen partial pressure P at discrete points on vessel axes, and tissue partial oxygen pressure P_t . In this section explicit formulas of other derived biophysical quantities are provided.

S3 Appendix

Compartment Model. Longitudinal oxygen saturation variation of single vessels obtained from the compartment model at fixed average saturation level or fixed oxygen extraction.

S4 Appendix

Regional Blood Volume of Confined Perfect Binary Trees. In this section we derive an approximative relation between the number of root nodes and the regional blood volume, provided that the total number of vessels is held constant. Here we assume that all vascular trees are perfect binary trees.

S5 Appendix

Blood Pressure Radius Relation. The formula for the boundary value of the blood pressure $p^{(BC)}$ is provided.

References

1. Folkman J. Tumor angiogenesis: therapeutic implications. *N Engl J Med.* 1971 Nov;285(21):1182–1186.
2. Nagy JA, Chang SH, Dvorak AM, Dvorak HF. Why are tumour blood vessels abnormal and why is it important to know? *Br J Cancer.* 2009 Mar;100(6):865–869.
3. Carmeliet P, Jain R. Angiogenesis in cancer and other diseases. *Nature.* 2000;407:249–257.
4. Dewhirst MW, Cao Y, Moeller B. Cycling hypoxia and free radicals regulate angiogenesis and radiotherapy response. *Nat Rev Cancer.* 2008 Jun;8(6):425–437.
5. Jain RK. Normalization of tumor vasculature: an emerging concept in antiangiogenic therapy. *Science.* 2005 Jan;307(5706):58–62.
6. Neri D, Bicknell R. Tumour vascular targeting. *Nat Rev Cancer.* 2005 Jun;5(6):436–446.
7. Stamatelos SK, Kim E, Pathak AP, Popel AS. A bioimage informatics based reconstruction of breast tumor microvasculature with computational blood flow predictions. *Microvasc Res.* 2014 Jan;91:8–21.
8. Gillies RJ, Schornack PA, Secomb TW, Raghunand N. Causes and effects of heterogeneous perfusion in tumors. *Neoplasia.* 1999 Aug;1(3):197–207.
9. Chauhan VP, Stylianopoulos T, Boucher Y, Jain RK. Delivery of molecular and nanoscale medicine to tumors: transport barriers and strategies. *Annu Rev Chem Biomol Eng.* 2011;2:281–298.
10. Padera TP, Stoll BR, Tooredman JB, Capen D, di Tomaso E, Jain RK. Pathology: cancer cells compress intratumour vessels. *Nature.* 2004 Feb;427(6976):695.
11. Stylianopoulos T, Martin JD, Chauhan VP, Jain SR, Diop-Frimpong B, Bardeesy N, et al. Causes, consequences, and remedies for growth-induced solid stress in murine and human tumors. *Proc Natl Acad Sci USA.* 2012 Sep;109(38):15101–15108.
12. Brown JM, Wilson WR. Exploiting tumour hypoxia in cancer treatment. *Nat Rev Cancer.* 2004 Jun;4(6):437–447.
13. Harris AL. Hypoxia—a key regulatory factor in tumour growth. *Nat Rev Cancer.* 2002 Jan;2(1):38–47.
14. Vaupel P, Schienger K, Knoop C, Hockel M. Oxygenation of human tumors: Evaluation of tissue oxygen distribution in breast cancers by computerized O₂ tension measurements. *Cancer Research.* 1991;51(12):3316–3322.

15. Padhani AR, Krohn KA, Lewis JS, Alber M. Imaging oxygenation of human tumours. *Eur Radiol.* 2007 Apr;17(4):861–872.
16. Skeldon AC, Chaffey G, Lloyd DJ, Mohan V, Bradley DA, Nisbet A. Modelling and detecting tumour oxygenation levels. *PLoS ONE.* 2012;7(6):e38597.
17. Kelly CJ, Brady M. A model to simulate tumour oxygenation and dynamic [18F]-Fmiso PET data. *Phys Med Biol.* 2006 Nov;51(22):5859–5873.
18. Monnich D, Troost EG, Kaanders JH, Oyen WJ, Alber M, Thorwarth D. Modelling and simulation of [18F]fluoromisonidazole dynamics based on histology-derived microvessel maps. *Phys Med Biol.* 2011 Apr;56(7):2045–2057.
19. Ito H, Kanno I, Kato C, Sasaki T, Ishii K, Ouchi Y, et al. Database of normal human cerebral blood flow, cerebral blood volume, cerebral oxygen extraction fraction and cerebral metabolic rate of oxygen measured by positron emission tomography with 15O-labelled carbon dioxide or water, carbon monoxide and oxygen: a multicentre study in Japan. *Eur J Nucl Med Mol Imaging.* 2004 May;31(5):635–643.
20. Beaney RP, Lammertsma AA, Jones T, McKenzie CG, Halnan KE. Positron emission tomography for in-vivo measurement of regional blood flow, oxygen utilisation, and blood volume in patients with breast carcinoma. *Lancet.* 1984 Jan;1(8369):131–134.
21. Beaney RP. Positron emission tomography in the study of human tumors. *Semin Nucl Med.* 1984 Oct;14(4):324–341.
22. Leenders KL. PET: blood flow and oxygen consumption in brain tumors. *J Neurooncol.* 1994;22(3):269–273.
23. Lammertsma AA, Jones T. Low oxygen extraction fraction in tumours measured with the oxygen-15 steady state technique: effect of tissue heterogeneity. *The British Journal of Radiology.* 1992;65(776):697–700.
24. Mankoff DA, Dunnwald LK, Gralow JR, Ellis GK, Charlop A, Lawton TJ, et al. Blood flow and metabolism in locally advanced breast cancer: relationship to response to therapy. *J Nucl Med.* 2002 Apr;43(4):500–509.
25. Wilson CB, Lammertsma AA, McKenzie CG, Sikora K, Jones T. Measurements of blood flow and exchanging water space in breast tumors using positron emission tomography: a rapid and noninvasive dynamic method. *Cancer Res.* 1992 Mar;52(6):1592–1597.
26. Christen T, Bolar DS, Zaharchuk G. Imaging brain oxygenation with MRI using blood oxygenation approaches: methods, validation, and clinical applications. *AJNR Am J Neuroradiol.* 2013;34(6):1113–1123.
27. An H, Liu Q, Eldeniz C, Lin W. Absolute oxygenation metabolism measurements using magnetic resonance imaging. *Open Neuroimag J.* 2011;5:120–135. Suppl. 1-M8.
28. Christen T, Lemasson B, Pannetier N, Farion R, Remy C, Zaharchuk G, et al. Is T2* enough to assess oxygenation? Quantitative blood oxygen level-dependent analysis in brain tumor. *Radiology.* 2012 Feb;262(2):495–502.
29. Christen T, Ni W, Qiu D, Schmiedeskamp H, Bammer R, Moseley M, et al. High-resolution cerebral blood volume imaging in humans using the blood pool contrast agent ferumoxytol. *Magn Reson Med.* 2013 Sep;70(3):705–710.
30. Ostergaard L. Principles of cerebral perfusion imaging by bolus tracking. *J Magn Reson Imaging.* 2005 Dec;22(6):710–717.
31. Buxton RB, Frank LR, Wong EC, Siewert B, Warach S, Edelman RR. A general kinetic model for quantitative perfusion imaging with arterial spin labeling. *Magn Reson Med.* 1998 Sep;40(3):383–396.

32. Wolf RL, Detre JA. Clinical neuroimaging using arterial spin-labeled perfusion magnetic resonance imaging. *Neurotherapeutics*. 2007 Jul;4(3):346–359.
33. Taroni P. Diffuse optical imaging and spectroscopy of the breast: a brief outline of history and perspectives. *Photochem Photobiol Sci*. 2012 Feb;11(2):241–250.
34. Grosenick D, Moesta KT, Moller M, Mucke J, Wabnitz H, Gebauer B, et al. Time-domain scanning optical mammography: I. Recording and assessment of mammograms of 154 patients. *Phys Med Biol*. 2005 Jun;50(11):2429–2449.
35. Taroni P, Torricelli A, Spinelli L, Pifferi A, Arpaia F, Danesini G, et al. Time-resolved optical mammography between 637 and 985 nm: clinical study on the detection and identification of breast lesions. *Phys Med Biol*. 2005 Jun;50(11):2469–2488.
36. Choe R, Konecky SD, Corlu A, Lee K, Durduran T, Busch DR, et al. Differentiation of benign and malignant breast tumors by in-vivo three-dimensional parallel-plate diffuse optical tomography. *J Biomed Opt*. 2009;14(2):024020.
37. Grosenick D, Wabnitz H, Moesta KT, Mucke J, Schlag PM, Rinneberg H. Time-domain scanning optical mammography: II. Optical properties and tissue parameters of 87 carcinomas. *Phys Med Biol*. 2005 Jun;50(11):2451–2468.
38. Spinelli L, Torricelli A, Pifferi A, Taroni P, Danesini G, Cubeddu R. Characterization of female breast lesions from multi-wavelength time-resolved optical mammography. *Phys Med Biol*. 2005 Jun;50(11):2489–2502.
39. Welter M, Rieger H. Interstitial fluid flow and drug delivery in vascularized tumors: a computational model. *PLoS ONE*. 2013;8(8):e70395. Available from: <http://dx.doi.org/10.1371/journal.pone.0070395>.
40. Krogh A. The number and distribution of capillaries in muscles with calculations of the oxygen pressure head necessary for supplying the tissue. *J Physiol (Lond)*. 1919 May;52(6):409–415.
41. Goldman D. Theoretical models of microvascular oxygen transport to tissue. *Microcirculation*. 2008 Nov;15(8):795–811.
42. Nair PK, Hellums JD, Olson JS. Prediction of oxygen transport rates in blood flowing in large capillaries. *Microvasc Res*. 1989 Nov;38(3):269–285.
43. Nair PK, Huang NS, Hellums JD, Olson JS. A simple model for prediction of oxygen transport rates by flowing blood in large capillaries. *Microvasc Res*. 1990 Mar;39(2):203–211.
44. Hellums JD, Nair PK, Huang NS, Ohshima N. Simulation of intraluminal gas transport processes in the microcirculation. *Ann Biomed Eng*. 1996;24(1):1–24.
45. Moschandreou TE, Ellis CG, Goldman D. Influence of tissue metabolism and capillary oxygen supply on arteriolar oxygen transport: a computational model. *Math Biosci*. 2011 Jul;232(1):1–10.
46. Safaeian, N . Computational Modelling of Capillaries in Neuro-vascular Coupling: A Thesis Presented for the Degree of Doctor of Philosophy in Mechanical Engineering at the University of Canterbury, Christchurch, New Zealand. University of Canterbury; 2012.
47. Alarcon T, Byrne HM, Maini PK. A cellular automaton model for tumour growth in inhomogeneous environment. *Journal of Theoretical Biology*. 2003;225:257–274.
48. Byrne HM, Owen MR, Alarcon T, Murphy J, Maini PK. MODELLING THE RESPONSE OF VASCULAR TUMOURS TO CHEMOTHERAPY: A MULTISCALE APPROACH. *Mathematical Models and Methods in Applied Sciences*. 2006;16(supp01):1219–1241.
49. Byrne HM, Alarcon T, Owen MR, Webb SD, Maini PK. Modelling aspects of cancer dynamics: a review. *Phil Trans R Soc*. 2006;364:1563–1578.

50. Owen MR, Alarcon T, Maini PK, Byrne HM. Angiogenesis and vascular remodelling in normal and cancerous tissues. *J Math Biol.* 2009 Apr;58(4-5):689–721.
51. Bauer AL, Jackson TL, Jiang Y. A cell-based model exhibiting branching and anastomosis during tumor-induced angiogenesis. *Biophys J.* 2007 May;92(9):3105–3121.
52. Zheng X, Wise SM, Cristini V. Nonlinear simulation of tumor necrosis, neo-vascularization and tissue invasion via an adaptive finite-element/level-set method. *Bull Math Biol.* 2005;67:211–259.
53. Macklin P, McDougall S, Anderson AR, Chaplain MA, Cristini V, Lowengrub J. Multiscale modelling and nonlinear simulation of vascular tumour growth. *J Math Biol.* 2009 Apr;58:765–798.
54. Frieboes HB, Lowengrub JS, Wise S, Zheng X, Macklin P, Bearer EL, et al. Computer simulation of glioma growth and morphology. *Neuroimage.* 2007;37 Suppl 1:59–70.
55. Bartha K, Rieger H. Vascular network remodeling via vessel cooption, regression and growth in tumors. *J Theor Biol.* 2006;241:903–918. Available from: <http://www.sciencedirect.com/science/article/pii/S0022519306000373>.
56. Lee DS, Rieger H, Bartha K. Flow correlated percolation during vascular remodeling in growing tumors. *Physical Review Letters.* 2006;96:0581041–0581044. Available from: <http://link.aps.org/doi/10.1103/PhysRevLett.96.058104>.
57. Welter M, Bartha K, Rieger H. Emergent vascular network inhomogeneities and resulting blood flow patterns in a growing tumor. *J Theor Biol.* 2008 Jan;250(2):257–280. Available from: <http://www.sciencedirect.com/science/article/pii/S0022519307004584>.
58. Welter M, Bartha K, Rieger H. Vascular remodelling of an arterio-venous blood vessel network during solid tumour growth. *J Theor Biol.* 2009 Aug;259(3):405–422. Available from: <http://www.sciencedirect.com/science/article/pii/S0022519309001635>.
59. Welter M, Rieger H. Physical determinants of vascular network remodeling during tumor growth. *Eur Phys J E Soft Matter.* 2010 Oct;33(2):149–163. Available from: <http://dx.doi.org/10.1140/epje/i2010-10611-6>.
60. Rieger H, Welter M. Integrative models of vascular remodeling during tumor growth. *Wiley Interdisciplinary Reviews: Systems Biology and Medicine.* 2015;7(3):113–129. Available from: <http://dx.doi.org/10.1002/wsbm.1295>.
61. Goldman D, Popel AS. Computational modeling of oxygen transport from complex capillary networks. Relation to the microcirculation physiome. *Adv Exp Med Biol.* 1999;471:555–563.
62. Goldman D, Popel AS. A computational study of the effect of capillary network anastomoses and tortuosity on oxygen transport. *J Theor Biol.* 2000 Sep;206(2):181–194.
63. Goldman D, Bateman RM, Ellis CG. Effect of sepsis on skeletal muscle oxygen consumption and tissue oxygenation: interpreting capillary oxygen transport data using a mathematical model. *Am J Physiol Heart Circ Physiol.* 2004 Dec;287(6):H2535–2544.
64. Goldman D, Bateman RM, Ellis CG. Effect of decreased O₂ supply on skeletal muscle oxygenation and O₂ consumption during sepsis: role of heterogeneous capillary spacing and blood flow. *Am J Physiol Heart Circ Physiol.* 2006 Jun;290(6):H2277–2285.
65. Tsoukias NM, Goldman D, Vadapalli A, Pittman RN, Popel AS. A computational model of oxygen delivery by hemoglobin-based oxygen carriers in three-dimensional microvascular networks. *J Theor Biol.* 2007 Oct;248(4):657–674.
66. Fraser GM, Goldman D, Ellis CG. Comparison of generated parallel capillary arrays to three-dimensional reconstructed capillary networks in modeling oxygen transport in discrete microvascular volumes. *Microcirculation.* 2013 Nov;20(8):748–763.

67. Hsu R, Secomb TW. A Green's function method for analysis of oxygen delivery to tissue by microvascular networks. *Mathematical Biosciences*. 1989;96(1):61 – 78.
68. Secomb TW, Hsu R, Park EYH, Dewhirst MW. Green's Function Methods for Analysis of Oxygen Delivery to Tissue by Microvascular Networks. *Annals of Biomedical Engineering*. 2004;32(11):1519–1529.
69. Secomb TW, Hsu R, Dewhirst MW, Klitzman B, Gross JF. Analysis of oxygen transport to tumor tissue by microvascular networks. *Int J Radiat Oncol Biol Phys*. 1993 Feb;25(3):481–489.
70. Secomb TW; 2014. Available from: <http://www.physiology.arizona.edu/people/secomb/greens>.
71. Safaeian N, Sellier M, David T. A computational model of hemodynamic parameters in cortical capillary networks. *J Theor Biol*. 2011 Feb;271(1):145–156.
72. Safaeian N, David T. A computational model of oxygen transport in the cerebrocapillary levels for normal and pathologic brain function. *J Cereb Blood Flow Metab*. 2013 Oct;33(10):1633–1641.
73. Beard DA. Computational framework for generating transport models from databases of microvascular anatomy. *Ann Biomed Eng*. 2001 Oct;29(10):837–843.
74. He Y, Shirazaki M, Liu H, Himeno R, Sun Z. A numerical coupling model to analyze the blood flow, temperature, and oxygen transport in human breast tumor under laser irradiation. *Comput Biol Med*. 2006 Dec;36(12):1336–1350.
75. Dasu A, Toma-Dasu I, Karlsson M. Theoretical simulation of tumour oxygenation and results from acute and chronic hypoxia. *Phys Med Biol*. 2003 Sep;48(17):2829–2842.
76. Espinoza I, Peschke P, Karger CP. A model to simulate the oxygen distribution in hypoxic tumors for different vascular architectures. *Med Phys*. 2013 Aug;40(8):081703.
77. Degond P, Mas-Gallic S. The Weighted Particle Method for Convection-Diffusion Equations. Part 1: The Case of an Isotropic Viscosity. *Mathematics of Computation*. 1989;53(188):485–507.
78. Lagerlöf JH, Kindblom J, Cortez E, Pietras K, Bernhardt P. Image-based 3D modeling study of the influence of vessel density and blood hemoglobin concentration on tumor oxygenation and response to irradiation. *Med Phys*. 2013 Feb;40(2):024101.
79. Lagerlöf JH, Kindblom J, Bernhardt P. The impact of including spatially longitudinal heterogeneities of vessel oxygen content and vascular fraction in 3D tumor oxygenation models on predicted radiation sensitivity. *Med Phys*. 2014 Apr;41(4):044101.
80. Kim E, Stamatelos S, Cebulla J, Bhujwala ZM, Popel AS, Pathak AP. Multiscale imaging and computational modeling of blood flow in the tumor vasculature. *Ann Biomed Eng*. 2012 Nov;40(11):2425–2441.
81. Kim E, Cebulla J, Ward BD, Rhie K, Zhang J, Pathak AP. Assessing breast cancer angiogenesis in vivo: which susceptibility contrast MRI biomarkers are relevant? *Magn Reson Med*. 2013 Oct;70(4):1106–1116.
82. Sourbron SP, Buckley DL. Tracer kinetic modelling in MRI: estimating perfusion and capillary permeability. *Phys Med Biol*. 2012 Jan;57(2):1–33.
83. Valabregue R, Aubert A, Burger J, Bittoun J, Costalat R. Relation between cerebral blood flow and metabolism explained by a model of oxygen exchange. *J Cereb Blood Flow Metab*. 2003 May;23(5):536–545.

84. Hayashi T, Watabe H, Kudomi N, Kim KM, Enmi J, Hayashida K, et al. A theoretical model of oxygen delivery and metabolism for physiologic interpretation of quantitative cerebral blood flow and metabolic rate of oxygen. *J Cereb Blood Flow Metab.* 2003 Nov;23(11):1314–1323.
85. Jespersen SN, Ostergaard L. The roles of cerebral blood flow, capillary transit time heterogeneity, and oxygen tension in brain oxygenation and metabolism. *J Cereb Blood Flow Metab.* 2012 Feb;32(2):264–277.
86. Zubieta-Calleja G, Paulev PE. 15. In: *New Human Physiology*. Paulev-Zubieta; 2015. .
87. Pittman RN. Regulation of tissue oxygenation. In: *Colloquium Series on Integrated Systems Physiology: From Molecule to Function*. vol. 3. Morgan & Claypool Life Sciences; 2011. p. 1–100.
88. Yaseen MA, Srinivasan VJ, Sakadzic S, Radhakrishnan H, Gorczynska I, Wu W, et al. Microvascular oxygen tension and flow measurements in rodent cerebral cortex during baseline conditions and functional activation. *J Cereb Blood Flow Metab.* 2011;31:1051–1063.
89. Kirkpatrick JP, Brizel DM, Dewhirst MW. A mathematical model of tumor oxygen and glucose mass transport and metabolism with complex reaction kinetics. *Radiat Res.* 2003 Mar;159(3):336–344.
90. Jain RK. Transport of molecules, particles, and cells in solid tumors. *Annu Rev Biomed Eng.* 1999;1:241–263.
91. Leu AJ, Berk DA, Yuan F, Jain RK. Flow velocity in the superficial lymphatic network of the mouse tail. *Am J Physiol.* 1994;267(4 Pt 2):H1507–1513.
92. Chary SR, Jain RK. Direct measurement of interstitial convection and diffusion of albumin in normal and neoplastic tissues by fluorescence photobleaching. *Proc Natl Acad Sci USA.* 1989;86:5385–5389.
93. Dafni H, Israely T, Bhujwala ZM, Benjamin LE, Neeman M. Overexpression of vascular endothelial growth factor 165 drives peritumor interstitial convection and induces lymphatic drain: magnetic resonance imaging, confocal microscopy, and histological tracking of triple-labeled albumin. *Cancer Res.* 2002;62(22):6731–6739.
94. Coppola, G and Caro, C. Oxygen mass transfer in a model three-dimensional artery. *Journal of The Royal Society Interface.* 2008;5(26):1067–1075.
95. Pries A, Secomb T, Gaehtgens P, Gross J. Blood flow in microvascular networks. Experiments and simulation. *Circulation Research.* 1990;67:826–834.
96. Heroux MA, Bartlett RA, Howle VE, Hoekstra RJ, Hu JJ, Kolda TG, et al. An overview of the Trilinos project. *ACM Transactions on Mathematical Software.* 2005;31(3):397–423.
97. Pries AR, Secomb TW, Gessner T, Sperandio MB, Gross JF, Gaehtgens P. Resistance to blood flow in microvessels in vivo. *Circ Res.* 1994 Nov;75(5):904–915.
98. Thomas H Cormen RLR Charles E Leiserson, Stein C. 22.3. In: *Introduction to Algorithms*, third edition. The MIT Press; 2009. .
99. LeVeque RJ. Finite difference methods for ordinary and partial differential equations - steady-state and time-dependent problems. *SIAM*; 2007.
100. Knabner P, L A. *Numerik partieller Differentialgleichungen*. Springer Verlag; 2000.
101. Lorthois S, Duru P, Billanou I, Quintard M, Celsis P. Kinetic modeling in the context of cerebral blood flow quantification by $H_2^{15}O$ positron emission tomography: the meaning of the permeability coefficient in Renkin-Crone’s model revisited at capillary scale. *J Theor Biol.* 2014 Jul;353:157–169.

102. Gödde R, Kurz H. Structural and Biophysical Simulation of Angiogenesis and Vascular Remodeling. *Developmental Dynamics*. 2001;220:387–401.
103. Ando J, Yamamoto K. Flow detection and calcium signalling in vascular endothelial cells. *Cardiovasc Res*. 2013 Jul;99(2):260–268.
104. Döme B, Paku S, B S, Tímár. Vascularization of cutaneous melanoma involves vessel co-option and has clinical significance. *The Journal of Pathology*. 2002;197(3):355–362.
105. Holash J, Maisonpierre PC, Compton D, Boland P, Alexander CR, Zagzag D, et al. Vessel Cooption, Regression, and Growth in Tumors Mediated by Angiopoietins and VEGF. *Science*. 1999;284:1994–1998.
106. Chauhan VP, Boucher Y, Ferrone CR, Roberge S, Martin JD, Stylianopoulos T, et al. Compression of pancreatic tumor blood vessels by hyaluronan is caused by solid stress and not interstitial fluid pressure. *Cancer Cell*. 2014 Jul;26(1):14–15.
107. DelGiorno KE, Carlson MA, Osgood R, Provenzano PP, Brockenbough JS, Thompson CB, et al. Response to Chauhan et Al.: interstitial pressure and vascular collapse in pancreas cancer-fluids and solids, measurement and meaning. *Cancer Cell*. 2014 Jul;26(1):16–17.
108. Stylianopoulos T, Martin JD, Snuderl M, Mpekris F, Jain SR, Jain RK. Coevolution of solid stress and interstitial fluid pressure in tumors during progression: implications for vascular collapse. *Cancer Res*. 2013 Jul;73(13):3833–3841.
109. Griffon-Etienne G, Boucher Y, Brekken C, Suit HD, Jain RK. Taxane-induced apoptosis decompresses blood vessels and lowers interstitial fluid pressure in solid tumors: clinical implications. *Cancer Res*. 1999 Aug;59(15):3776–3782.
110. Viacava P, Naccarato AG, Bocci G, Fanelli G, Aretini P, Lonobile A, et al. Angiogenesis and VEGF expression in pre-invasive lesions of the human breast. *J Pathol*. 2004 Oct;204(2):140–146.
111. Dhakal HP, Bassarova A, Naume B, Synnestvedt M, Borgen E, Kaaresen R, et al. Breast carcinoma vascularity: a comparison of manual microvessel count and Chalkley count. *Histol Histopathol*. 2009 Aug;24(8):1049–1059.
112. Fernandez-Guinea O, Alvarez-Cofino A, Eiro N, Gonzalez LO, del Casar JM, Fernandez-Garcia B, et al. Low microvascular density at the tumor center is related to the expression of metalloproteases and their inhibitors and with the occurrence of distant metastasis in breast carcinomas. *Int J Clin Oncol*. 2013 Aug;18(4):629–640.
113. Carp SA, Selb J, Fang Q, Moore R, Kopans DB, Rafferty E, et al. Dynamic functional and mechanical response of breast tissue to compression. *Opt Express*. 2008 Sep;16(20):16064–16078.
114. Marieb EN, Hoehn K. *Human Anatomy & Physiology*. Pearson; 2013.
115. Sharan M, Vovenko EP, Vadapalli A, Popel AS, Pittman RN. Experimental and theoretical studies of oxygen gradients in rat pial microvessels. *J Cereb Blood Flow Metab*. 2008 Sep;28(9):1597–1604.
116. Hartmann P, Mirtolouei R, Untersberger S, Ziegler W, Hermann Z, Richtig E, et al. Non-invasive imaging of tissue PO₂ in malignant melanoma of the skin. *Melanoma Res*. 2006 Dec;16(6):479–486.
117. Ito M, Yang DJ, Mawlawi O, Mendez R, Oh CS, Azhdarinia A, et al. {PET} and Planar Imaging of Tumor Hypoxia With Labeled Metronidazole. *Academic Radiology*. 2006;13(5):598 – 609.
118. Spence VA, Walker WF. Tissue oxygen tension in normal and ischaemic human skin. *Cardiovasc Res*. 1984 Mar;18(3):140–144.

119. An H, Lin W. Cerebral venous and arterial blood volumes can be estimated separately in humans using magnetic resonance imaging. *Magn Reson Med*. 2002 Oct;48(4):583–588.
120. Vaupel P, Fortmeyer HP, Runkel S, Kallinowski F. Blood flow, oxygen consumption, and tissue oxygenation of human breast cancer xenografts in nude rats. *Cancer Res*. 1987 Jul;47(13):3496–3503.
121. Pries AR, Hopfner M, le Noble F, Dewhirst MW, Secomb TW. The shunt problem: control of functional shunting in normal and tumour vasculature. *Nat Rev Cancer*. 2010 Aug;10(8):587–593.
122. Pries AR, Ley K, Claassen M, Gaehtgens P. Red cell distribution at microvascular bifurcations. *Microvasc Res*. 1989 Jul;38(1):81–101.
123. D’Angelo C. Finite Element Approximation of Elliptic Problems with Dirac Measure Terms in Weighted Spaces: Applications to One- and Three-dimensional Coupled Problems. *SIAM Journal on Numerical Analysis*. 2012;50(1):194–215.
124. Jain RK, Tong RT, Munn LL. Effect of vascular normalization by antiangiogenic therapy on interstitial hypertension, peritumor edema, and lymphatic metastasis: insights from a mathematical model. *Cancer Res*. 2007;67(6):2729–2735.
125. Jain RK, Stylianopoulos T. Delivering nanomedicine to solid tumors. *Nat Rev Clin Oncol*. 2010 Nov;7(11):653–664.

S1 Appendix

Oxygen Mass Transfer Coefficient

In this supplemental material we will review simulation results in comparison with literature references and our calibration procedure of the mass transfer coefficient γ . In order to determine γ we constructed the phenomenological formula

$$\gamma(r) = \frac{D_p \alpha_p}{r} p_2 (1 - \exp(-r/p_1)), \quad (1)$$

with free parameters p_1 and p_2 based on experimental and computed data for Nusselt numbers nu [1, 2] of capillaries and arterioles (see Fig. 1). The Nusselt number is related to the mass transfer coefficient by $nu = 2r\gamma/D_p^{-1}\alpha_p^{-1}$, where r is the radius, D_p the oxygen diffusion constant in plasma and α_p the solubility constant, i.e. nu is a non-dimensional permeability coefficient. Using aforementioned data we obtained initial guesses of parameters p_1 and p_2 of Eq. (1). However, we also pursued the idea to fit the results of our model, i.e. the partial oxygen pressure in vascular tubes, to experimental data and precise calculations [3, 2]. This way we also take systematic discretization errors into account.

To this end, the common setting considered is a 4 mm long perfused vascular tube embedded in a block of a medium through which oxygen can diffuse. In brief, some details are as follows, The theoretical model [2] incorporates a multi-layered vascular tube as source of oxygen and a surrounding infinite tissue with a homogeneous background representing oxygen release from the capillary plexus. We augmented the tissue diffusion equation (15) accordingly by adding the source term $\kappa - P_{t,i}\kappa/P^*$, where $\kappa = 0.625 mmHg$ and $\kappa/P^* = 30$. Other parameter which are already present in our model were readily adopted. The flow rate q poses an exception since it was not provided directly. We determined it according to [2, (A6)] using the velocity profile coefficients in the appendix. The simulation box was made large enough that the radial P_t profile can assume the asymptotic value (42 mmHg) determined by κ and M_0 . Nair et al. [3] considered a configuration where a vascular tube is surrounded by a block of rubber which is in contact with air with a specific oxygen partial pressure. Two variants of this exist. One where oxygen rich blood releases oxygen [3, Fig. 2] and another where oxygen depleted blood takes up oxygen [3, Fig. 3]. In the former case the PO2 of the air is kept at 168 mmHg and the blood PO2 at the inlet is 0. Vice versa for the latter case. In either case, gas exchange happens through the surrounding rubber block. We realized this by Dirichlet boundary conditions and by setting the consumption rate $M_0 = 0$. The faces perpendicular to the longitudinal axis were imposed with no-flux conditions. The system size was set according to the reported half-thickness of the block as 4 mm \times 80 μm \times 80 μm . Our data is produced with a spatial resolution of $h = 20 \mu m$. We compare the blood oxygen saturation S at the end of the vascular tubes with the reference values from [3, 2] as shown in Fig. 2. It was not possible to obtain good agreement in all the cases, in particular for vascular oxygen uptake (plus in Fig. 2). In order to obtain the result shown, we used $p_2 = 4$. The best fit to aforementioned Nusselt numbers ($p_2 = 4.7$) resulted in a worse fit for vascular oxygen uptake and little change else.

Secomb [4] recently published the software that produced the results for the theoretical studies [5, 6] using a Green's function method. We compared it against our results in several cases for single vessels as well as vessel networks, although not to the size that we require (s. Sec. 'Computational models allowing for oxygen diffusion in tissue'). The deviations are generally of the magnitude $\pm 10 mmHg$ depending on the location on the network. An example of our results is shown in Fig. 3.

Poor convergence of the solution with the grid constant h is a significant source of error in our method. Convergence tests with respect to the grid constant h show sublinear convergence as shown in Fig. 4 where we plotted vascular and tissue oxygen partial pressures in a single vascular tube for different grid constants. Extrapolating, we again expect an error of the order of 10 mmHg by the end of the vessels, depending on q and S . The reason for poor convergence is the singular nature of the oxygen source term (18) in the tissue oxygen diffusion equation, i.e. the use of the Dirac- δ function. It was shown [7] that optimal convergence is obtained by using locally refined meshes. In future work it will be mandatory to improve the accuracy.

It is possible to arrive at inconsistent solutions when the iteration of (20) and (21) has not sufficiently converged. Then the amount of oxygen extracted from the network will not be the same as

the amount consumed by tissue. Hence, in order to check for conservation of mass we determined the total transvascular oxygen flux J_{tv} , the total consumption $J_{cons} = \int_{\Omega} M(P_t)$ and consider the error $e_{tv} = (J_{tv} - J_{cons})/J_{tv}$. We also check the mass conservation error in the vasculature due to the numerical integration of P and determine $e_v = (J_{in} - J_{out} - J_{tv})/J_{in}$, where J_{in} and J_{out} are the influx and efflux through root nodes. We found both errors to be less than 1% at the point where further iteration does not change the solution any more.

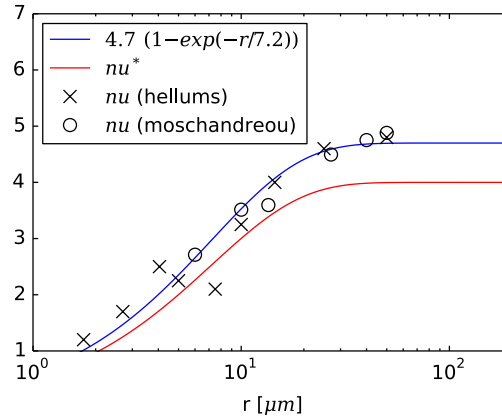


Figure 1. Nusselt numbers: The dimensionless Nusselt number nu describes the oxygen flux through the vessel wall in proportion to difference between the average intravascular PO2 and the PO2 at the wall. The designations of the legend are as follows: nu^* denotes the Nusselt number used in our simulations, whereas $nu(hellums)$ and $nu(moschandreou)$ denote experimental [1] and theoretical data [2, Fig. 6]. In future a saturation dependence should be added, but here we only included the radius dependence and assumed a constant saturation of $S \approx 0.9$. The blue line is a best fit to aforementioned data. For nu^* , the prefactor is 4 instead of 4.7 in the best fit.

References

- [1] J. D. Hellums, P. K. Nair, N. S. Huang, and N. Ohshima. Simulation of intraluminal gas transport processes in the microcirculation. *Ann Biomed Eng*, 24(1):1–24, 1996.
- [2] T. E. Moschandreou, C. G. Ellis, and D. Goldman. Influence of tissue metabolism and capillary oxygen supply on arteriolar oxygen transport: a computational model. *Math Biosci*, 232(1): 1–10, Jul 2011.
- [3] P. K. Nair, N. S. Huang, J. D. Hellums, and J. S. Olson. A simple model for prediction of oxygen transport rates by flowing blood in large capillaries. *Microvasc. Res.*, 39(2):203–211, Mar 1990.
- [4] Timothy W. Secomb, 2014. URL <http://www.physiology.arizona.edu/people/secomb/greens>.
- [5] Timothy W. Secomb, Richard Hsu, Eric Y. H. Park, and Mark W. Dewhirst. Green’s function methods for analysis of oxygen delivery to tissue by microvascular networks. *Annals of Biomedical Engineering*, 32(11):1519–1529, 2004.
- [6] Safaeian, N. *Computational Modelling of Capillaries in Neuro-vascular Coupling: A Thesis Presented for the Degree of Doctor of Philosophy in Mechanical Engineering at the University of Canterbury, Christchurch, New Zealand*. University of Canterbury, 2012.
- [7] Carlo D’Angelo. Finite element approximation of elliptic problems with dirac measure terms in weighted spaces: Applications to one- and three-dimensional coupled problems. *SIAM Journal on Numerical Analysis*, 50(1):194–215, 2012.

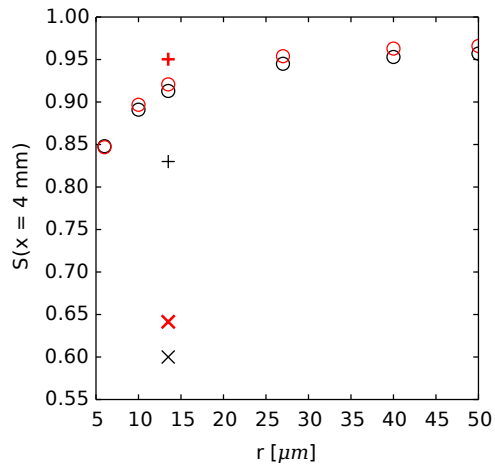


Figure 2. Result of mass transfer coefficient calibration: We considered a single 4 mm long vascular tube embedded in a passive medium through which oxygen can diffuse. We computed the blood oxygen saturation S at the end of the vascular tube $x = 4 \text{ mm}$ (red) under various conditions (see text), in particular varying vascular radii r . Literature data of more sophisticated capillary models for equivalent cases [2, Fig. 4] (\circ), [3, Fig. 2] (\times), and [3, Fig. 3] (+) are shown as black symbols. We aimed to chose the mass transfer coefficient γ for good agreement with this data.

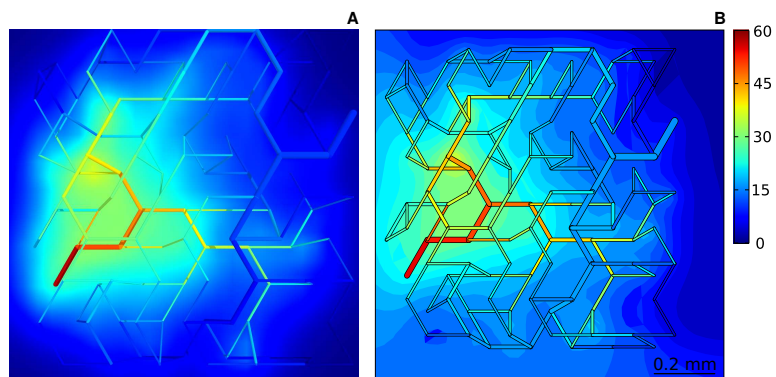


Figure 3. Comparison with Green's function method: (A) shows the oxygen partial pressure PO_2 distribution produced by our program. (B) shows the distribution produced by the software by Secomb [4]. The solution of vascular PO_2 distribution P is layered on top of a slice through the tissue oxygen PO_2 distribution P_t . The same input, a small artificial network, was used in both cases. Although the solutions appear qualitatively similar, there are differences of ca. 10 mmHg.

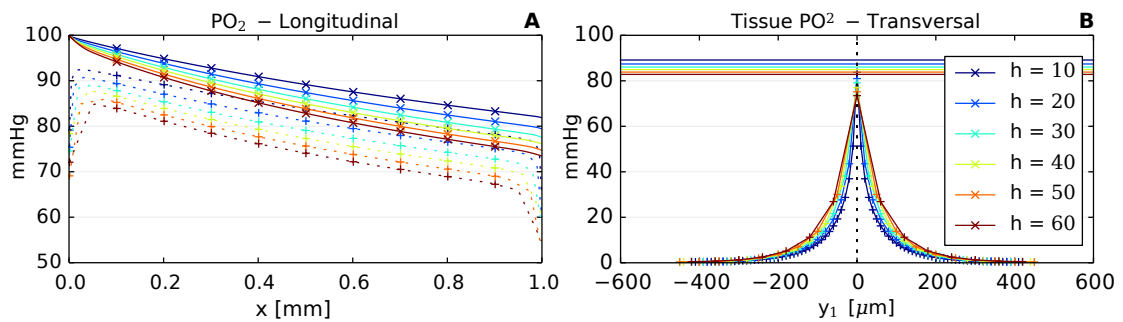


Figure 4. Convergence test w.r.t. grid constant h . We consider a small simulation volume with a single vessel of length 1 mm inside. Vascular (P , crosses) and tissue (P_t , pluses) oxygen partial pressure PO₂ distributions are shown. The development of P and P_t (dotted line) along the vessel center axis is displayed in (A). In (B) we plotted the transversal profile of P_t , i.e. perpendicular to the vessel axis along the spatial coordinate y_1 at a point half way between the ends of the vessel. The horizontal lines indicate the vascular PO₂ at this point. For smaller h the curves lie somewhat further apart, indicating sub-linear convergence, i.e. if the error to the true solution was linear in h we would observe a constant spacing between curves.

S2 Appendix

Explicit Formulas for Relevant Biophysical Quantities

After vascular networks of normal tissue and tumor were constructed, distributions of hematocrit in vascular networks and oxygen concentrations in vascular networks and tissue are calculated, yielding for each vessel segment $v \in \mathbb{V}$ e.g. radius r_v , length l_v , hematocrit H_v , blood flow q_v , blood oxygen saturation $S_v(0)$ and oxygen concentration at vessel entrance $c_v(0)$, average blood oxygen saturation Y_v . Using this information, the following averages are calculated, pertaining to the tissue volume Ω .

Length density :

$$L_D = \frac{1}{|\Omega|} \sum_{v \in \mathbb{V}} l_v, \quad (1)$$

taken as measure for microvessel density MVD .

Regional blood volume :

$$rBV = \frac{1}{|\Omega|} \sum_{v \in \mathbb{V}} \pi r_v^2 l_v \quad (2)$$

Vascular surface area per unit volume of tissue :

$$S\rho = \frac{1}{|\Omega|} \sum_{v \in \mathbb{V}} 2\pi r_v l_v, \quad (3)$$

where S is the vascular surface area per gram tissue and ρ tissue density.

Regional blood flow :

$$rBF = \frac{1}{|\Omega|} \sum_{v \in \text{In}\partial\Omega} q_v = \frac{1}{|\Omega|} \sum_{v \in \text{Out}\partial\Omega} q_v, \quad (4)$$

where $\text{In}\mathbb{V}$ ($\text{Out}\mathbb{V}$) denote set of all vessel segments penetrating surface $\partial\Omega$ with blood flow pointing inwards (outwards).

Hemoglobin concentration :

$$c_{Hb} = MCHC \cdot rRBCV = \frac{MCHC}{|\Omega|} \sum_{v \in \mathbb{V}} \pi r_v^2 l_v H_v \quad (5)$$

with mean corpuscular hemoglobin concentration $MCHC$, regional RBC volume $rRBCV$.

Oxyhemoglobin concentration :

$$c_{HbO_2} = \frac{MCHC}{|\Omega|} \sum_{v \in \mathbb{V}} \pi r_v^2 l_v H_v \frac{1}{l_v} \int_v S_v(x) dx \quad (6)$$

and an analogous expression for the deoxyhemoglobin concentration c_{HbD} , replacing $\frac{1}{l_v} \int_v S_v(x) dx$ by $1 - \frac{1}{l_v} \int_v S_v(x) dx$.

Blood oxygen saturation :

$$Y = \frac{c_{HbO}}{c_{Hb}} = \sum_{v \in \mathbb{V}} \left\{ \frac{\pi r_v^2 H_v l_v}{\sum_{u \in \mathbb{V}} \pi r_u^2 l_u H_u} \frac{1}{l_v} \int_v S_v(x) dx \right\}, \quad (7)$$

where Y is the RBC-volume-weighted average of blood oxygen saturation taken over all vessel segments.

Length-weighted average blood oxygen saturation :

$$\langle S \rangle = \sum_{v \in \mathbb{V}} \frac{l_v}{\sum_{u \in \mathbb{V}} l_u} \frac{1}{l_v} \int_v S_v(x) dx \quad (8)$$

Average partial oxygen pressure in blood :

$$\langle P \rangle = \sum_{v \in \mathbb{V}} \frac{l_v}{\sum_{u \in \mathbb{V}} l_u} \frac{1}{l_v} \int_v P(x) dx, \quad (9)$$

where the average concentration of dissolved oxygen in blood is given by $\bar{c}_p = \alpha \langle P \rangle$.

Average tissue partial oxygen pressure :

$$P_t = \frac{1}{|\Omega|} \int_{\Omega} P_t(\mathbf{x}) d^3x, \quad (10)$$

where the average oxygen concentration in tissue is given by $\bar{c}_t = \alpha_t \langle P_t \rangle$.

Metabolic rate of oxygen consumption :

$$MRO_2 = \frac{1}{|\Omega|} \int_{\Omega} M(P_t(\mathbf{x})) d^3x, \quad (11)$$

where M is the Michaelis-Menten relation (17).

Total transvascular oxygen flux :

$$J_{tv} = \sum_{v \in \mathbb{V}} 2\pi r_v \gamma(r_v) \int_v \{P(x) - P_t(x)\} dx, \quad (12)$$

and corresponding regional transvascular oxygen flux $rJ_{tv} = J_{tv}/|\Omega|$.

Average transvascular oxygen flux density :

$$\langle j_{tv} \rangle = \frac{1}{\sum_{u \in \mathbb{V}} l_u} \sum_{v \in \mathbb{V}} \gamma(r_v) \int_v \{P(x) - P_t(x)\} dx, \quad (13)$$

i.e. the average transvascular oxygen flux density is the length weighted average over the mean oxygen flux density of all vessel segments; note that $S\rho \langle j_{tv} \rangle \neq \frac{J_{tv}}{|\Omega|} = MRO_2$.

Oxygen permeability : from $J_{tv}/|\Omega| = P_{O_2} S\rho \{\bar{c}_p - \bar{c}_t\}$ one obtains

$$P_{O_2} = \frac{MRO_2}{\langle S\rho \rangle \{\bar{c}_p - \bar{c}_t\}} = \frac{1}{|\Omega|} \frac{\sum_{v \in \mathbb{V}} 2\pi r_v \gamma(r_v) \int_v \{P(x) - P_t(x)\} dx}{\langle S\rho \rangle \{\alpha \langle P \rangle - \alpha_t \langle P_t \rangle\}} \quad (14)$$

Oxygen flux entering vascular network :

$$J_{in} = \sum_{v \in \mathbb{I} \cap \partial\Omega} q_v \{c_0 H_v S_{in,v} + \alpha P_{in,v}\}, \quad (15)$$

with $P_{in,v} = P_v^{(BC)}$ and $S_{in,v}$ given by the Hill equation. The corresponding regional influx is $rJ_{in} = J_{in}/|\Omega|$.

Oxygen flux leaving vascular network :

$$J_{out} = \sum_{v \in \mathbb{O} \cap \partial\Omega} q_v \{c_0 H_v S_{out,v} + \alpha P_{out,v}\} \quad (16)$$

Oxygen extraction fraction :

$$OEF = \frac{J_{in} - J_{out}}{J_{in}}. \quad (17)$$

S3 Appendix

Compartment Model

For comparison with results obtained by the computational model (s. Table 4 in the main paper) we estimated metabolic rates of oxygen consumption MRO_2 and oxygen extraction fraction OEF within the framework of the computational model, using the following model (input) parameters:

- RBC oxygen carrying capacity: $c_0 = 0.50 \text{ ml } O_2/\text{ml RBC}$ (s. Table 1)
- hematocrit: $H = 0.45$ (s. Table 1)
- Hill exponent: $n = 2.7$ (s. Table 1)
- blood oxygen partial pressure at half saturation: $P_{S50} = 27 \text{ mmHg}$ (s. Table 1)
- oxygen solubility (plasma): $3.1 \cdot 10^{-5} \text{ ml } O_2/\text{ml}/\text{mmHg}$ (s. Table 1)
- measured average blood oxygen saturation: $Y_{exp} = 0.74$ (normal), $Y_{exp} = 0.72$ (tumor) [1].
- arterial blood oxygen saturation: $S_{in} = 0.958$ (normal, s. Table 4), $S_{in} = 0.833$ (tumor, s. Table 4)
- perfusion: $rBF = 0.06 \text{ ml blood}/\text{ml}/\text{min}$ (normal), $rBF = 0.30 \text{ ml blood}/\text{ml}/\text{min}$ (tumor) [2, 3]

Table 1. Metabolic rate of oxygen consumption and oxygen extraction fraction as function of assumed tissue oxygen partial pressure

P_t <i>mmHg</i>	MRO_2 (normal) $\mu\text{l } O_2/\text{ml}/\text{min}$	OEF (normal)	MRO_2 (tumor) $\mu\text{l } O_2/\text{ml}/\text{min}$	OEF (tumor)
0	5.15	0.398	14.30	0.254
5	5.08	0.393	14.18	0.252
10	4.99	0.386	14.02	0.249
15	4.88	0.377	13.81	0.246
20	4.74	0.366	13.51	0.240
25	4.54	0.351	13.04	0.232
30	4.25	0.328	12.24	0.218
35	3.76	0.291	10.44	0.186
37	3.45	0.267	8.91	0.159

References

- [1] D. Grosenick, H. Wabnitz, K. T. Moesta, J. Mucke, P. M. Schlag, and H. Rinneberg. Time-domain scanning optical mammography: II. Optical properties and tissue parameters of 87 carcinomas. *Phys Med Biol*, 50(11):2451–2468, Jun 2005.
- [2] C. B. Wilson, A. A. Lammertsma, C. G. McKenzie, K. Sikora, and T. Jones. Measurements of blood flow and exchanging water space in breast tumors using positron emission tomography: a rapid and noninvasive dynamic method. *Cancer Res.*, 52(6):1592–1597, Mar 1992.
- [3] D. A. Mankoff, L. K. Dunnwald, J. R. Gralow, G. K. Ellis, A. Charlop, T. J. Lawton, E. K. Schubert, J. Tseng, and R. B. Livingston. Blood flow and metabolism in locally advanced breast cancer: relationship to response to therapy. *J. Nucl. Med.*, 43(4):500–509, Apr 2002.

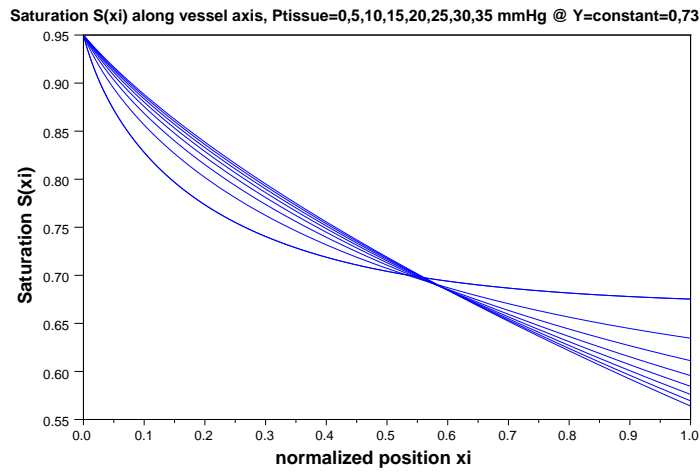


Figure 1. Vascular blood oxygen saturation $S(\xi)$ along vessel axis ($0 \leq \xi \leq 1$) for fixed average blood oxygenation $Y = 0.73$, assuming $S(0) = 0.95$ and tissue oxygen partial pressures of $P_t = 0, 10, 15, 20, 25, 30, 35 \text{ mmHg}$ (from bottom to top at $\xi = 1$); intersection caused by constraint $Y = \text{constant}$ results in decrease of oxygen extraction fraction OEF with increasing tissue oxygen pressure.

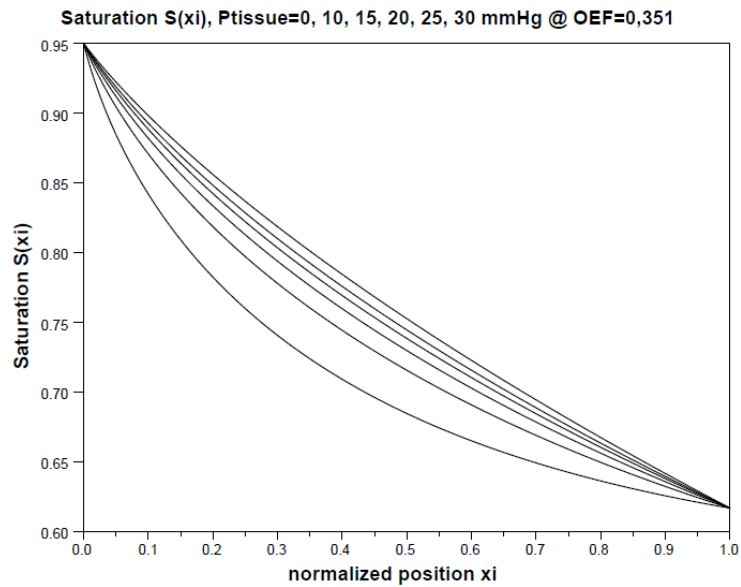


Figure 2. Vascular blood oxygen saturation $S(\xi)$ along vessel axis ($0 \leq \xi \leq 1$) for fixed oxygen extraction fraction $OEF = 0.351$, assuming $S(0) = 0.95$ and tissue oxygen partial pressures of $P_t = 0, 10, 15, 20, 25, 30 \text{ mmHg}$ (from top to bottom).

S4 Appendix

Regional Blood Volume of Confined Perfect Binary Trees

In this section we derive an approximative relation between the number of root nodes R and the regional blood volume rBV , provided that the total number of vessels M is held constant, i.e. all vascular trees are confined to the simulation box Ω and adhere to a fixed vascular density. Naturally R is also the number of trees. We assume that all vascular trees are perfect binary trees, i.e. tree levels from $k = 0$ at the top to $k = n - 1$ at capillary (leaf) level have the maximum number of vessels 2^k . Furthermore we assume that trees are equal in the number of vessels (connections) N . Hence $M = N \cdot R$ is split to equal parts between trees. There is no distinction between arterial and venous tree, and capillaries are neglected. For given number of levels (depth) n , a tree has $N = \sum_{k=0}^{n-1} 2^k$ connections. This is a geometric series for which holds in general

$$\sum_{k=0}^{n-1} q^k = \frac{q^n - 1}{q - 1}, \quad (1)$$

for some q . N can therefore be written as $N = 2^n - 1$, from which we obtain the depth

$$n = \log_2(N + 1), \quad (2)$$

Let further the radii at a bifurcation be given by Murray's law, i.e. $r_c^\alpha = r_a^\alpha + r_b^\alpha$. Since a and b are the same, we have $r_c = 2^{1/\alpha} r_{a=b}$, or in relation to the tree level k , we have the radius at level k

$$r_k = 2^{(n-1-k)/\alpha} r_{n-1}, \quad (3)$$

where r_{n-1} is the capillary radius. Now let's estimate the volume of the tree TV , provided equal vessel lengths l . By summing over tree levels we obtain

$$TV = l\pi \sum_{k=0}^{n-1} 2^k r_k^2, \quad (4)$$

since each level has 2^k vessels of radius r_k . Replacing r_k by Eq.(3) we obtain

$$TV = \pi r_0^2 l \cdot 2^{(n-1)2/\alpha} \sum_{k=0}^{n-1} 2^{k(1-2/\alpha)}. \quad (5)$$

This is again a geometric series which is rewritten with the help of Eq.(1) and $q = 2^{1-(2/\alpha-1)}$ to remove the sum. Furthermore without loss of generality we set $\pi r_0^2 l = 1$. After some basic algebra, the result is

$$TV = \frac{2^n - 2^{(2/\alpha)n}}{2 - 2^{2/\alpha}} \quad (6)$$

$$= \frac{(N + 1) - (N + 1)^{2/\alpha}}{2 - 2^{2/\alpha}}, \quad (7)$$

where in the second line we further used that $2^n = N + 1$. Now to satisfy the constraint that the total number of vessels taken over all trees is constant M , we substitute $N = M/R$, using the number of trees R . For brevity we set the volume of the simulation box $|\Omega| = 1$ without loss of generality. Thus we obtain the total regional volume of all trees rBV

$$rBV = \frac{TVR}{|\Omega|} \quad (8)$$

$$= M \frac{1 + \frac{R}{M} - \frac{R}{M} \left(\frac{M}{R} + 1\right)^{2/\alpha}}{2 - 2^{2/\alpha}}. \quad (9)$$

The denominator $2 - 2^{2/\alpha}$ is a positive increasing function of α that vanishes for $\alpha = 2$ and which asymptotically approaches 1 for $\alpha \rightarrow \infty$. It can be shown that the nominator is a decreasing

function in R , which is well approximated for small $R/M \ll 1$ by $1 - (R/M)^{(1-2/\alpha)}$. In the edge case where $\alpha = 2$ we still obtain a decreasing function by calculating the limit of $\alpha \rightarrow 2$ for Eq.(6). In that case it is logarithmic with $rBV = \frac{1}{2}(R + M) \log_2(M/R + 1)$.

Murray's α determines how much parent vessel radii grow at bifurcations. In the limit of $\alpha \rightarrow \infty$, Murray's law selects the radius of the thicker child vessel as the radius of the parent vessel. This means all radii become equal, and indeed $rBV(\alpha \rightarrow \infty) = M$ is obtained from Eq.(9). As we would intuitively expect, the dependence on R is eliminated. For realistic $2 \leq \alpha \leq 3$, the dependence on R cannot be removed. Moreover we can consider the case where all vessels are root vessels, i.e. $R = M$. Then again $rBV = M$ is obtained, which is clear since then again all vessels have equal radii. In actual simulations the assumption of perfect and equally sized trees does not hold, i.e. frequently, small branches are generated. Moreover, even if all lattice boundary sites are occupied with root nodes, only a small fraction of them grow to vascular trees of significant size. Most of them regress to a single starting node without any connections. Despite that, we observe a clear trend of decreasing rBV with increasing R .

S5 Appendix

Blood Pressure Radius Relation

We first fit a curve to blood pressure data of rat mesentery [1]. Then we scaled the curve (adjusting $A1$ and $A2$) so that physiological blood pressures [2, Fig. 19.6] are obtain in venules and arterioles, thus obtaining for the blood pressure boundary condition

$$p^{(BC)}(r) = [A2 + (A1 - A2)/(1 + \exp((r' - r_0)/\Delta r))], \quad (1)$$

where $r' = r$ for a vein, else $-r$, and $A1 = 89 \text{ mmHg}$, $A2 = 18 \text{ mmHg}$, $r_0 = -21\mu\text{m}$, $\Delta r = 16\mu\text{m}$.

References

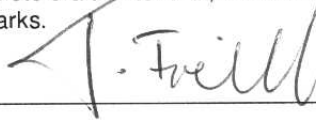
- [1] A.R. Pries, T.W. Secomb, and P. Gaehtgens. Design principles of vascular beds. *Circulation Research*, 77(1017-1022), 1995.
- [2] E.N. Marieb and K. Hoehn. *Human Anatomy & Physiology*. Pearson, 2013. ISBN 9780321743268.

Part III

**Demarcation from the work of the
co-authors**

Demarcation from the work of the co-authors

The author of this thesis, Michael Welter, developed scientific goals and questions to be answered in the Refs. [WBR08; WBR09; WR10; WR13; Wel+] together with the coauthors in collaborative effort. Subsequent model development, computer implementation, design of the experiments, calculations, and analysis of the results were performed by the first author alone, with the exceptions that Fredrich carried out the comparison with the Green's functions method [s. Wel+, Appendix S1, Fig. 3], and Rinneberg developed and analyzed the homogeneous compartment model [s. Wel+, "Homogeneous Three-Compartment Model of Blood Oxygenation"]. Rieger, Bartha and Rinneberg acted as supervisors giving inspiration through discussions and criticism. For the publication manuscripts, the Welter delivered the presentation of results, comprising figures and tables and other data. The co-authors supplied an introduction and discussion for the earlier papers [WBR08; WBR09]. Welter wrote drafts of other sections, or in case of the later papers [WR10; WR13; Wel+] he wrote a complete draft. After that, the coauthors revised the manuscript for better readability and additional remarks.



Signature Coauthor

References

- [WBR08] M. Welter, K. Bartha, and H. Rieger. "Emergent vascular network inhomogeneities and resulting blood flow patterns in a growing tumor". In: *J. Theor. Biol.* 250.2 (Jan. 2008), pp. 257–280.
- [WBR09] M. Welter, K. Bartha, and H. Rieger. "Vascular remodelling of an arterio-venous blood vessel network during solid tumour growth". In: *J. Theor. Biol.* 259.3 (Aug. 2009), pp. 405–422.
- [Wel+] M. Welter et al. "Relation between tumor oxygenation, vascular remodeling, and blood flow: a computational model with applications to breast cancer."
- [WR10] M. Welter and H. Rieger. "Physical determinants of vascular network remodeling during tumor growth". In: *Eur Phys J E Soft Matter* 33.2 (Oct. 2010), pp. 149–163.
- [WR13] M. Welter and H. Rieger. "Interstitial fluid flow and drug delivery in vascularized tumors: a computational model". In: *PLoS ONE* 8.8 (2013), e70395.

Demarcation from the work of the co-authors

The author of this thesis, Michael Welter, developed scientific goals and questions to be answered in the Refs. [WBR08; WBR09; WR10; WR13; Wel+] together with the coauthors in collaborative effort. Subsequent model development, computer implementation, design of the experiments, calculations, and analysis of the results were performed by the first author alone, with the exceptions that Fredrich carried out the comparison with the Green's functions method [s. Wel+, Appendix S1, Fig. 3], and Rinneberg developed and analyzed the homogeneous compartment model [s. Wel+, "Homogeneous Three-Compartment Model of Blood Oxygenation"]. Rieger, Bartha and Rinneberg acted as supervisors giving inspiration through discussions and criticism. For the publication manuscripts, the Welter delivered the presentation of results, comprising figures and tables and other data. The co-authors supplied an introduction and discussion for the earlier papers [WBR08; WBR09]. Welter wrote drafts of other sections, or in case of the later papers [WR10; WR13; Wel+] he wrote a complete draft. After that, the coauthors revised the manuscript for better readability and additional remarks.



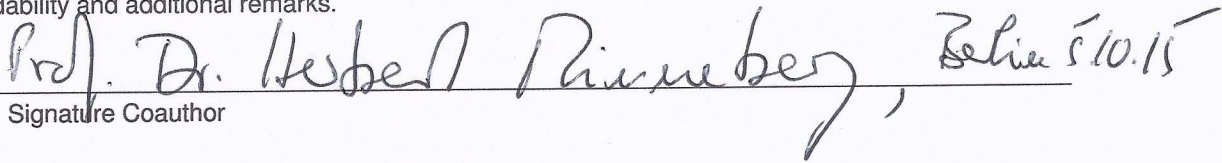
Signature Coauthor

References

- [WBR08] M. Welter, K. Bartha, and H. Rieger. "Emergent vascular network inhomogeneities and resulting blood flow patterns in a growing tumor". In: *J. Theor. Biol.* 250.2 (Jan. 2008), pp. 257–280.
- [WBR09] M. Welter, K. Bartha, and H. Rieger. "Vascular remodelling of an arterio-venous blood vessel network during solid tumour growth". In: *J. Theor. Biol.* 259.3 (Aug. 2009), pp. 405–422.
- [Wel+] M. Welter et al. "Relation between tumor oxygenation, vascular remodeling, and blood flow: a computational model with applications to breast cancer."
- [WR10] M. Welter and H. Rieger. "Physical determinants of vascular network remodeling during tumor growth". In: *Eur Phys J E Soft Matter* 33.2 (Oct. 2010), pp. 149–163.
- [WR13] M. Welter and H. Rieger. "Interstitial fluid flow and drug delivery in vascularized tumors: a computational model". In: *PLoS ONE* 8.8 (2013), e70395.

Demarcation from the work of the co-authors

The author of this thesis, Michael Welter, developed scientific goals and questions to be answered in the Refs. [WBR08; WBR09; WR10; WR13; Wel+] together with the coauthors in collaborative effort. Subsequent model development, computer implementation, design of the experiments, calculations, and analysis of the results were performed by the first author alone, with the exceptions that Fredrich carried out the comparison with the Green's functions method [s. Wel+, Appendix S1, Fig. 3], and Rinneberg developed and analyzed the homogeneous compartment model [s. Wel+, "Homogeneous Three-Compartment Model of Blood Oxygenation"]. Rieger, Bartha and Rinneberg acted as supervisors giving inspiration through discussions and criticism. For the publication manuscripts, the Welter delivered the presentation of results, comprising figures and tables and other data. The co-authors supplied an introduction and discussion for the earlier papers [WBR08; WBR09]. Welter wrote drafts of other sections, or in case of the later papers [WR10; WR13; Wel+] he wrote a complete draft. After that, the coauthors revised the manuscript for better readability and additional remarks.

 Prof. Dr. Hebel Rinneberg, Berlin 5.10.15
Signature Coauthor

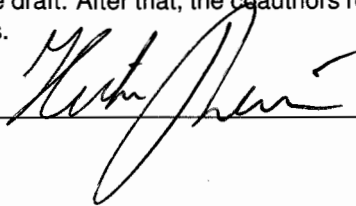
References

- [WBR08] M. Welter, K. Bartha, and H. Rieger. "Emergent vascular network inhomogeneities and resulting blood flow patterns in a growing tumor". In: *J. Theor. Biol.* 250.2 (Jan. 2008), pp. 257–280.
- [WBR09] M. Welter, K. Bartha, and H. Rieger. "Vascular remodelling of an arterio-venous blood vessel network during solid tumour growth". In: *J. Theor. Biol.* 259.3 (Aug. 2009), pp. 405–422.
- [Wel+] M. Welter et al. "Relation between tumor oxygenation, vascular remodeling, and blood flow: a computational model with applications to breast cancer."
- [WR10] M. Welter and H. Rieger. "Physical determinants of vascular network remodeling during tumor growth". In: *Eur Phys J E Soft Matter* 33.2 (Oct. 2010), pp. 149–163.
- [WR13] M. Welter and H. Rieger. "Interstitial fluid flow and drug delivery in vascularized tumors: a computational model". In: *PLoS ONE* 8.8 (2013), e70395.

Demarcation from the work of the co-authors

The author of this thesis, Michael Welter, developed scientific goals and questions to be answered in the Refs. [WBR08; WBR09; WR10; WR13; Wel+] together with the coauthors in collaborative effort. Subsequent model development, computer implementation, design of the experiments, calculations, and analysis of the results were performed by the first author alone, with the exceptions that Fredrich carried out the comparison with the Green's functions method [s. Wel+, Appendix S1, Fig. 3], and Rinneberg developed and analyzed the homogeneous compartment model [s. Wel+, "Homogeneous Three-Compartment Model of Blood Oxygenation"]. Rieger, Bartha and Rinneberg acted as supervisors giving inspiration through discussions and criticism. For the publication manuscripts, the Welter delivered the presentation of results, comprising figures and tables and other data. The co-authors supplied an introduction and discussion for the earlier papers [WBR08; WBR09]. Welter wrote drafts of other sections, or in case of the later papers [WR10; WR13; Wel+] he wrote a complete draft. After that, the coauthors revised the manuscript for better readability and additional remarks.

Signature Coauthor



References

- [WBR08] M. Welter, K. Bartha, and H. Rieger. "Emergent vascular network inhomogeneities and resulting blood flow patterns in a growing tumor". In: *J. Theor. Biol.* 250.2 (Jan. 2008), pp. 257–280.
- [WBR09] M. Welter, K. Bartha, and H. Rieger. "Vascular remodelling of an arterio-venous blood vessel network during solid tumour growth". In: *J. Theor. Biol.* 259.3 (Aug. 2009), pp. 405–422.
- [Wel+] M. Welter et al. "Relation between tumor oxygenation, vascular remodeling, and blood flow: a computational model with applications to breast cancer."
- [WR10] M. Welter and H. Rieger. "Physical determinants of vascular network remodeling during tumor growth". In: *Eur Phys J E Soft Matter* 33.2 (Oct. 2010), pp. 149–163.
- [WR13] M. Welter and H. Rieger. "Interstitial fluid flow and drug delivery in vascularized tumors: a computational model". In: *PLoS ONE* 8.8 (2013), e70395.